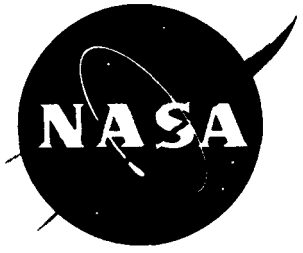

NASA Conference Publication 3272
Volume II

Joint Launch + One Year Science Review of USML–1 and USMP–1 with the Microgravity Measurement Group

Edited by
N. Ramachandran
Universities Space Research Association
Huntsville, Alabama

D.O. Frazier, S.L. Lehoczky, and C.R. Baugher
NASA, Marshall Space Flight Center
Marshall Space Flight Center, Alabama

Proceedings of a conference
held at Huntsville, Alabama
September 22–24, 1993

National Aeronautics and Space Administration
Marshall Space Flight Center • Marshall Space Flight Center, Alabama 35812

May 1994

Contents

Contents continued.

Contents continued.

Contents continued.

Contents concluded.

INTERFACE CONFIGURATION EXPERIMENT
PRELIMINARY RESULTS

Paul Concus*, Robert Finn+, and Mark Weislogel#

*Lawrence Berkeley Laboratory and Department of
Mathematics, University of California, Berkeley, CA.
+Department of Mathematics, Stanford University, Stanford, CA.
#NASA Lewis Research Center, Cleveland, OH.

ABSTRACT

The Interface Configuration Experiment (ICE) was carried out on USML-1 to investigate liquid-gas interfaces in certain rotationally-symmetric containers having prescribed, mathematically derived shapes. These containers have the property that they admit an entire continuum of distinct equilibrium rotationally-symmetric interfaces for a given liquid volume and contact angle. Furthermore, it can be shown that none of these interfaces can be stable. It was found, after the containers were filled in orbit, that an initial equilibrium interface from the symmetric continuum reoriented, when perturbed, to a stable interface that was not rotationally symmetric, in accordance with the mathematical theory.

INTRODUCTION

It is essential, when planning space-based operations, to be able to predict the configurations that fluids will assume in their containers under low-gravity conditions. For example, one would be in serious difficulty if one did not know in advance in what part of a fuel tank the liquid contents were to be found. Currently available mathematical theory can determine possible free-surface configurations for only a few simple containers, such as the right circular cylinder and the sphere. Even for these geometries, the present theory is incomplete for dealing with unaccustomed liquid configurations, such as a column or bridge extending across the interior of the container, that can be expected to occur under reduced gravity.

The classical theory, according to the Young-Laplace-Gauss formulation, characterizes stable fluid configurations as local minima of the surface-plus-gravitational mechanical energy. Based on this point of view we have been carrying out mathematical studies directed toward characterizing possible configurations of liquids under reduced gravity. In this connection we have calculated the shapes of rotationally symmetric "exotic" containers with the remarkable property that for given contact angle and

Joint "L+1" Science Review for USML-1 and USMP-1 with the Microgravity Measurement Group, September 22-24, 1993, Huntsville, Alabama, USA.

liquid volume, an infinity (in fact, an entire continuum) of distinct rotationally symmetric equilibrium configurations can appear, all of which have the same energy (Figure 1).[5,10] These symmetric equilibrium configurations turn out to be unstable, and it can be shown that particular deformations that are not rotationally symmetric yield configurations with lower energy.[4,10] By a careful construct, using a result of Ref. 11, it was possible to demonstrate a symmetric container that admits infinitely many symmetric equilibrium interfaces, but for which no interface that minimizes energy can be symmetric. This is in notable contrast with what happens in the familiar case of the right circular cylinder, for which the symmetric interface is stable, and no asymmetric ones can appear.[13]

There is presently no known way to determine mathematically the surfaces that minimize energy in the exotic containers. Numerical computations have suggested a number of particular non-rotationally-symmetric surfaces as local minima. As it is not clear to what extent the idealizations of the formal theory will be reflected in reality, it is of interest to determine experimentally what physically observable energy-minimizing configurations there might be. Our USML-1 experiment has been carried out for this purpose, both as an indication of the limitations of classical theory and as a guide to future theoretical study. A preliminary form of this paper is given in Ref. 8.

I. COMPUTED CONFIGURATIONS

According to the classical Young-Laplace-Gauss formulation, the mechanical energy ε of a partly filled container, arising from the associated surface and hydrostatic forces, is (Ref. 9, Chap. 1)

$$\varepsilon = \sigma(S - S^* \cos\gamma) + \text{gravitational energy} \qquad (1)$$

Here σ is the liquid-gas interfacial tension and $\cos\gamma$ is the liquid-solid relative adhesion coefficient, where γ is the contact angle between the liquid and the container; S denotes the area of the liquid-gas free surface and S^* the area of the portion of the container in contact with the liquid. The quantities σ and γ depend only on the materials and are independent of the container geometry and gravitational field. The classical formulation, upon which our mathematical study is based, does not encompass possible surface friction effects, such as hysteresis and contact line resistance, or thermodynamic Kelvin energy associated with evaporation and condensation. Configurations of liquid that yield a stationary value for ε subject to the constraint of fixed liquid volume are, according to the classical theory, equilibrium configurations. They will be stable, as well, if ε is locally minimized. In Ref. 5 exotic rotationally symmetric container shapes are calculated from (1) and the requirement that there be a continuum of rotationally symmetric liquid-gas free surfaces all having the same contact angle and enclosing the same volume of liquid with the container. Such container shapes, which were studied first in Ref. 12 for the

special case of zero gravity and contact angle $\pi/2$, can be obtained for any contact angle or gravity level.[5,10]

The container shown in Figure 1 is obtained by placing circular cylindrical extensions with disk ends on a calculated exotic container shape, in this case for zero gravity and contact angle 80°. The dashed curves depict members of the continuum of rotationally symmetric equilibrium interfaces. Although such containers can be constructed for any gravity and contact angle, only under microgravity conditions are they of sufficiently large scale to permit accurate physical experiment and observation. Of principal interest in this study is the case for which gravity is zero, or sufficiently small that the gravitational energy term can be neglected, so that (1) becomes

$$\varepsilon = \sigma(S - S^* \cos\gamma).$$

In order to obtain an indication of what stable interfaces there might be in an exotic container, such as the one in Figure 1, numerical calculations were carried out using a modified version of the Surface Evolver program[1] and the driving software reported in Ref. 2. The Surface Evolver seeks local minima of a discretized energy functional subject to prescribed constraints using a gradient descent method. Surfaces are approximated by a piecewise-linear triangulation, the form of which can be controlled to various degrees with commands available to the user. Under control of the user, the program adjusts the triangulated surface, step-by-step, in an attempt to decrease the energy. From the numerical and graphical output provided by the program, a user interprets whether a local minimum has been found.

Numerical results obtained with the Surface Evolver for the configuration depicted in Figure 1, but with container shape and liquid for contact angle 55°, are shown in Figure 2. (The value of 55° corresponds to the materials for which the USML-1 video images are shown below in the Video Images section). The computed surface depicted in Figure 2 is the lowest-energy one that was found using the Surface Evolver, starting from the initial horizontal planar member of the symmetric equilibrium interface continuum, to which a small volume-preserving perturbation had been added. Other local minima could be found by varying the form of the initial perturbation, but these had greater energy, although still less than that for the rotationally symmetric surface continuum.[2] The minimizing free surface is shown as a lighter surface against the darker, checked background of the container; both have been shaded by the (color) graphics display software. Triangulation mesh lines are in white. To expose the free surface to view, only half the container, lying to one side of a vertical plane through its axis of symmetry, is shown. This vertical plane is one about which the free surface possesses reflective symmetry. The exotic, bulge portion of the container and a small length of the circular cylindrical extensions are depicted. The view

for the upper figure is from a point on a horizontal plane through the maximal width of the bulge; the vertical symmetry plane of the free surface is in the plane of the paper. The liquid would lie below and to the left of the free surface. For the lower figure the viewpoint is slightly above the maximal-bulge plane and to the right of the one for the upper figure, to show the excursion of the surface across the bulge portion of the container.

II. EXPERIMENTAL APPARATUS

The vessels for the Interface Configuration Experiment, one of which is depicted in Figure 3, were fabricated at the NASA Lewis Research Center. Each weighs about 1.5 Kg, including the liquid contents, and measures approximately 9 x 9 x 18 cm. The interior was bored out of a solid rectangular block of acrylic plastic, to limit optical distortion. The coordinates for the bulged portion of the container were fed into a numerically controlled air bearing lathe, which performed the final machining operations. The surfaces were then lightly finished with cloth and a polishing compound. After polishing and annealing, the interior surface deviated less than 50 μm from the specified, calculated one.

The vessels were designed for use in the USML-1 Glovebox Experiment Module, which was provided by the European Space Agency/ESTEC. The Glovebox is a multi-user facility developed for experiments to be conducted on Spacelab missions beginning with USML-1. The purpose of the Glovebox is to provide a work area that is ergonomically sound and will allow a payload specialist to carry out operations using small quantities of toxic, irritant, or potentially infective materials, which must be prevented from contaminating the spacecraft atmosphere. Previously designed to handle biological experiments, the Glovebox has been adapted to handle fluids, combustion, and materials science experiments, to permit effective use of hands-on interaction by the payload specialists. ICE utilized the Glovebox primarily as a staging area and a level of containment in the event of fluid leaks. ICE was one of sixteen Glovebox experiments aboard the NASA Space Shuttle Columbia on USML-1 (STS-50).

III. EXPERIMENT DESCRIPTION

The general experimental procedure for ICE during the USML-1 flight was to partly fill the selected vessels with prescribed volumes of fluid and to record with two video cameras the fluid interface configurations that resulted.

Four vessels were fabricated for the tests. They are similar in construction to the vessel shown in Figure 3. The primary vessel components are the single-piece acrylic-plastic (transparent) body, an aluminum piston and control dial, stainless steel drive screw and two-port valve, and magnetized feet for securing the vessel to the Glovebox labjack. As indicated in Figure 3, the vessel is placed in the Glovebox in a horizontal position. One of the test fluids is an "immersion" fluid that has a refractive

index matched with that of the acrylic container, for reduction of optical distortions; it is a blend of hydrogenated terphenyl and an aliphatic hydrocarbon. Two of the vessels contained this fluid. The interiors of these vessels were coated with surface modifier FC-723 to produce a desired contact angle. Distilled water was used in the other two containers, which were not coated.

The fluids were lightly dyed in order to enhance visibility of the free surface. For the immersion fluid a ceres red dye was used, and for the water a blue food coloring was used, which was an aqueous solution of propylene glycol with propylparaben and sodium metabisulfite as preservatives. Both concentrations were so small that no measurable effects were detected on the values of surface tension or contact angle after the dye was introduced. Surface tension was measured by the Dunuoy ring method as 72.4 dyne/cm for the water and 32.4 dyne/cm for the immersion fluid, with a repeatable accuracy of ± 0.2 dyne/cm. The wedge method (Ref. 3, pp. 220 - 221), (Ref. 6, pp. 191 - 192), was used for measuring the contact angle of water with the acrylic plastic as 80° with a repeatable accuracy of ±2°. For the immersion fluid, a modified sessile drop method yielded a contact angle with the coated surface of approximately 55°. This method is more sensitive to hysteresis effects; the accuracy is estimated at ± 4°.

The interior surfaces of each vessel were cleaned with sequential rinses of a strong ethanol/distilled water solution and distilled water. The vessel was then allowed to dry in a pure nitrogen clean-room environment. Before being injected into the vessel reservoir, the fluid was filtered with P4 filter paper. The injection was carried out in the nitrogen environment. All seals on a vessel were lubricated with the particular fluid used for it, to eliminate possible contamination from other lubricants.

The two immersion-fluid-filled vessels were the same, the exotic container portion being constructed for the 55° contact angle measured for the materials; the second provided a repeat run for experiment control purposes. For the third vessel, which contained distilled water, the exotic container portion was constructed for the contact angle of 80°. A similar vessel was tested previously in the NASA Lewis Research Center Zero Gravity Facility five-second drop tower.[7] Although insufficient low-gravity time was available for a stable interface to be achieved, observations showed reorientation toward a particular asymmetric configuration. The 80° vessel tested on USML-1 permits comparison with these ground-based test results, and, more importantly, for obtaining information on the behavior resulting from disturbing the surfaces that form in space.

The fourth vessel also contained distilled water as test fluid, yet it differs from the others in that the container is not exotic; the bulge is a portion of a sphere, for which complete mathematical results are available. The infinite family of distinct rotationally symmetric equilibrium interfaces that are possible for the exotic containers cannot form. However, by rigid-body rotation of the liquid, an equilibrium surface in zero gravity can be tilted as desired with respect to the symmetry axis, without any change in

shape or energy. The results for this vessel can act as a control to compare with the behavior in the exotic containers.

The diagnostics for the experiment included two full-color 1:1 video cameras to record the fluid interface configurations, a Glovebox video camera with audio, and devices for the measurement of ambient Glovebox temperature and local acceleration levels.

IV. EXPERIMENT PROCEDURE

The crew procedures for carrying out ICE consisted of six steps: (1) unstow equipment, (2) set up Glovebox and install vessel, (3) fill vessel test volume with fluid, (4) observe equilibrium interfaces, (5) disturb interface configuration(s) to determine stability, (6) reverse fill procedure and stow. Up to 60 minutes was required for each vessel when it was tested independently. Less time was necessary when the vessels were tested sequentially.

To begin the experiment, a crew member unstowed the labjack, video cameras, multi-use arm and clamp, and the ICE vessel to be tested. The Glovebox power was switched on and the ICE vessel was placed (horizontally) on the labjack. One video camera was mounted to the front door of the Glovebox, and the other was directed down from the top, secured by the multi-use arm and clamp. The field of view for the cameras was centered on the bulge portion of the exotic container. Iterative adjustments of the cameras and vessel were necessary to center the field properly for both cameras. The Glovebox doors were then replaced with cuff attachments, and the cameras were turned on to record the interface configuration.

To carry out the fill procedure, the crew member opened the quarter-turn valve and turned the control dial on the vessel, displacing the entire fluid contents of the reservoir slowly into the exotic container. The volume of fluid corresponded to that for the symmetric family of equilibrium interfaces, as calculated for the planar member of the family (Figure 1). Time was then allowed for the fluid configuration to stabilize fully while being recorded by the cameras. Five minutes were allowed for the filling procedure. The crew member then disturbed the surface by tapping the container with a finger, lightly at first and then subsequently with moderately increasing force. New surfaces that formed in the container during the tapping procedure were given time to stabilize and to be captured on video. The tapping continued until the surface either broke up or consistently returned to a particular configuration, at which point the fill procedure was to be reversed to empty the exotic container test volume. The vessel and support equipment were then stowed.

V. VIDEO IMAGES

Because the Glovebox video recordings of ICE taken on board USML-1 started to be released only recently, there has not yet been opportunity for a complete analysis. However, frames from the videotapes shown in Figures 4 and 5 indicate qualitative behavior of the liquid for one of the 55° exotic containers. For the other exotic containers, the behavior was found to be similar.

Figure 4 shows views taken with the video camera that was directed downward from the top of the glovebox. The views correspond to looking down on the module and schematic of Figure 3 with the viewer behind the module, so that the container portion is on the left and piston and dial on the right. The first frame shows the equilibrium configuration after filling has been completed. This would correspond to the member of the continuum depicted in Figure 1 that is uppermost at the container axis. The subsequent sequence of four frames shows the reorientation following a perturbation resulting from payload specialist Lawrence DeLucas tapping the dial end of the module. The last frame depicts the configuration after the fluid again reached equilibrium. This last configuration was observed to be very stable to subsequent perturbations that were applied - even to those that were relatively large.

Figure 5 depicts the initial and final equilibrium shapes as viewed from the video camera mounted to the front door of the glovebox. Here the (dyed) liquid is better illuminated than in Figure 4, because the glovebox back-lighting is directly behind the liquid relative to the camera. Although the shadows and reflections make it difficult to discern the detailed shape of the final equilibrium interface in the black-and-white Figures 4 and 5, it is evident from the figures that the fluid reorients to a non-rotationally-symmetric shape, not unlike the computed lowest energy configuration shown in Figure 2.

VI. POSTFLIGHT DATA ANALYSIS

Taking into account video recording excerpts downlinked to Earth during the flight and comments made by the payload specialists, some qualitative remarks can be made. In all cases, the displacement of liquid from the reservoir to the container was reported as being accomplished successfully, and at the end of the filling procedure the observed free surface was generally in accordance with one that was predicted: a spherical cap corresponding to a particular member of the continuum of rotationally symmetric (unstable) equilibrium interfaces. The liquid then moved to an asymmetric configuration in the each of the three exotic containers after it was tapped by the payload specialist, in a manner similar to that shown in Figure 4. This is in accordance with mathematical predictions, and the shapes appeared to be in correspondence with the computed lowest energy configurations. The asymmetric configuration behaved very stably in response to subsequent induced disturbances. No configurations resembling those from other computed local-minimum energies at higher

energies were observed. The interface in the control vessel with spherical bulge did not exhibit the type of reorientation described above; this, too, is in accordance with theory.

Corroboration and quantitative evaluation of the results, as well as further assessment of effects of hysteresis and other factors, await complete analysis of the data.

VII. CONCLUDING REMARKS

The Interface Configuration Experiment (ICE) on the first NASA United States Microgravity Laboratory (USML-1), launched in June 1992, explored a striking behavior of liquid-vapor interfaces that has been predicted mathematically for certain "exotic" containers in a low-gravity environment. Results from video images show that an initial equilibrium interface from the rotationally symmetric continuum reoriented, when perturbed, to a stable interface that was not rotationally symmetric, as predicted by the idealized mathematical theory. The results indicate also the role of contact-line resistance forces (contact-angle hysteresis)in creating a barrier that must be overcome, in moving from the symmetric equilibrium configuration into asymmetric configurations of lower potential energy. More detailed and extensive experiments can be expected to yield further information on the significance of the findings and on sensitivity to effects not included in the present theory, such as those associated with contact-line resistance and with inaccuracies in measuring contact angles and in fabricating the vessels. The present and future experiments can contribute to determining the applicability of the existing theory and the ability of the theory to predict fluid interfacial configurations for arbitrary container geometries.

ACKNOWLEDGMENTS

We wish to thank V. Brady and M. Callahan for numerical determination of local energy minima and preparation of the graphical images shown in Figure 2; D. Gotti and the machine shops at the NASA Lewis Research Center for their role in designing and fabricating the flight units; and the USML-1 crew and NASA staff, whose impressive commitment and expertise made the experiment possible. This work was supported in part by the National Aeronautics and Space Administration under Grant NAG3-1143, by the National Science Foundation under Grant DMS89-02831, and by the Mathematical Sciences Subprogram of the Office of Energy Research, U. S. Department of Energy, under Contract Number DE-AC03-76SF00098.

REFERENCES

1. K.Brakke, *Surface Evolver* program, available by anonymous ftp from geom.umn.edu as file **evolver.tar.Z** in directory **pub**, The Geometry Center, 1300 So. 2nd St., Minneapolis, MN.

2. M. Callahan, P. Concus, and R. Finn, Energy minimizing capillary surfaces for exotic containers in *Computing Optimal Geometries* (with accompanying videotape), J. E. Taylor, ed., AMS Selected Lectures in Mathematics, Amer. Math. Soc., Providence, RI, 1991, pp. 13--15.

3. P. Concus and R. Finn, *On capillary free surfaces in a gravitational field*, Acta Math. 132 (1974), pp. 207--223.

4. P. Concus and R. Finn, *Instability of certain capillary surfaces,* Manuscr. Math. 63 (1989), pp. 209-213.

5. P. Concus and R. Finn, *Exotic containers for capillary surfaces,* J. Fluid Mech., 224 (1991), pp. 383-394; Corrigendum, J. Fluid Mech., 232 (1991), pp. 689--690.

6. P. Concus and R. Finn, *Capillary surfaces in microgravity, in Low-Gravity Fluid Dynamics and Transport Phenomena*, J. N. Koster and R. L. Sani, eds., Progress in Astronautics and Aeronautics, Vol.130, AIAA, Washington, DC, 1990, pp. 183--206.

7. P. Concus, R. Finn, and M. Weislogel, *Drop-tower experiments for capillary surfaces in an exotic container*, AIAA J., 30 (1992), pp. 134--137.

8. P. Concus, R. Finn, and M. Weislogel, *An interface configuration experiment on USML-1*, Paper AIAA 93-0253, 31st AIAA Aerospace Sciences Meeting, Reno, NV, Jan. 11-14, 1993.

9. R. Finn, *Equilibrium Capillary Surfaces*, Springer-Verlag, New York, 1986.

10. R. Finn, *Nonuniqueness and uniqueness of capillary surfaces*, Manuscr. Math. 61 (1988), pp. 347-372.

11. R Finn and T. I. Vogel, *On the volume infimum for liquid bridges*, Zeit. Anal. Anwend., 11 (1992), pp. 3-23.

12. R. Gulliver and S. Hildebrandt, *Boundary configurations spanning continua of minimal surfaces*, Manuscr. Math., 54 (1986), pp. 323--347.

13. T. I. Vogel, *Uniqueness for certain surfaces of prescribed mean curvature*, Pacific J. Math., 134 (1988), pp. 197--207.

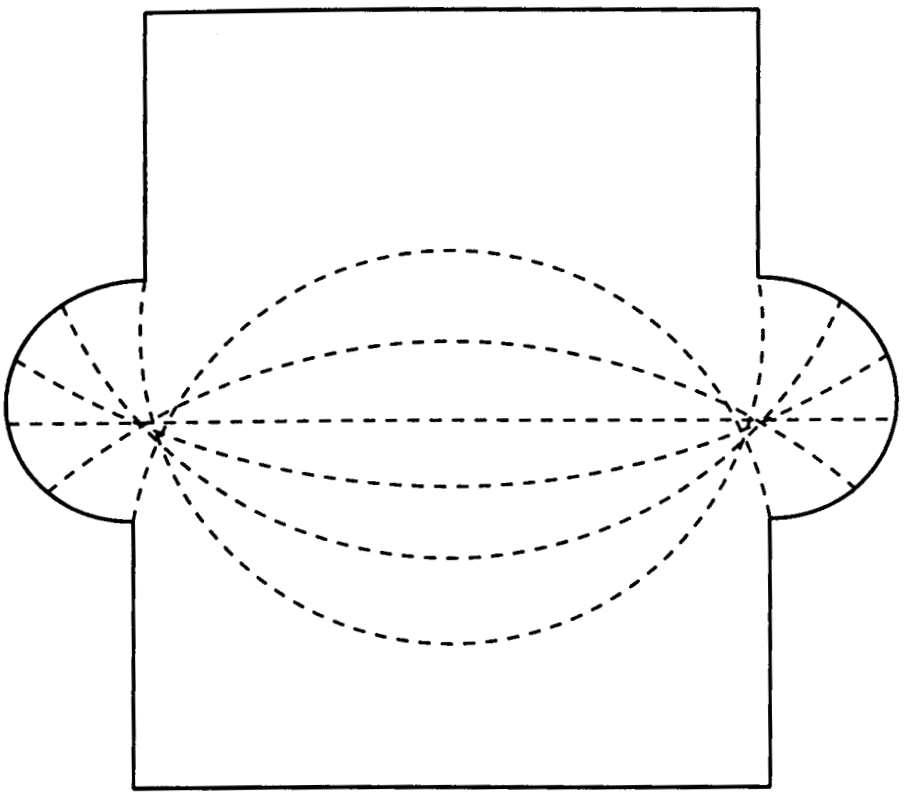

Figure 1 Axial section of an exotic container for contact angle 80° and zero gravity, depicting meridians (dashed curves) of members of the rotationally-symmetric equilibrium free surface continuum. All surfaces have the same contact angle and energy and enclose the same volume of liquid with the bottom of the container.

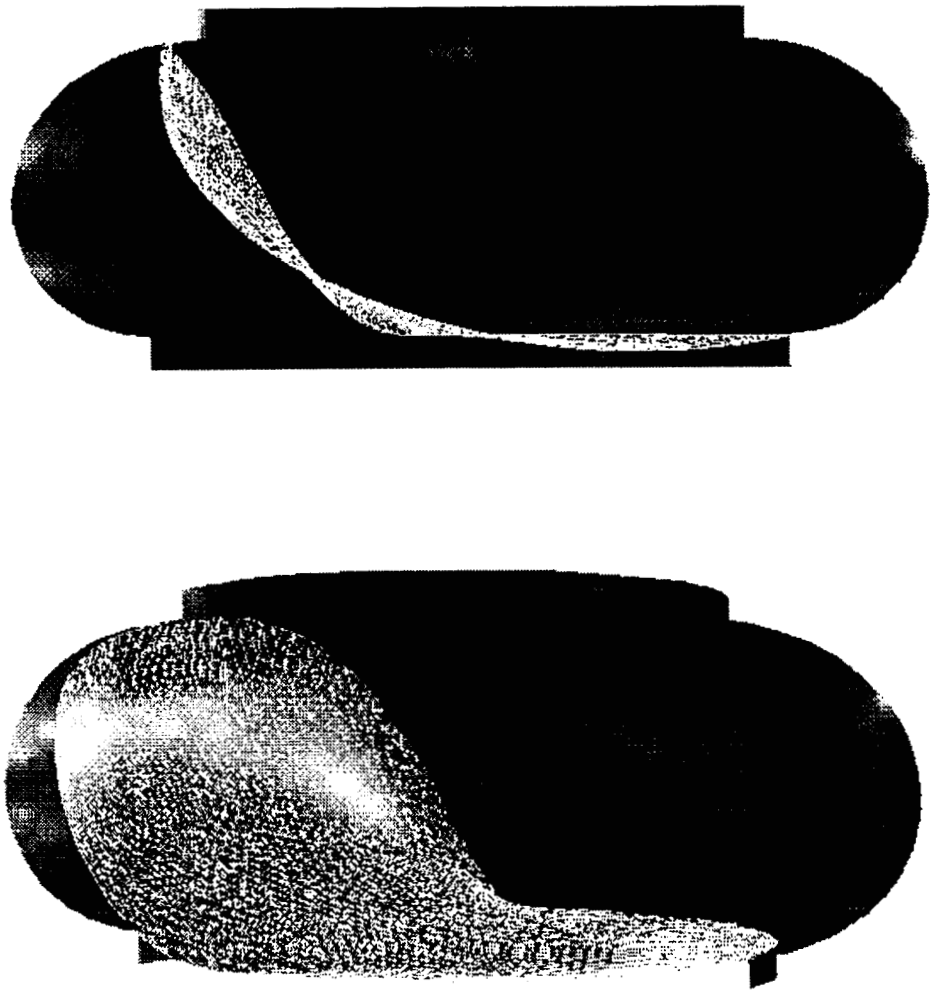

Figure 2 Two views of calculated energy-minimizing equilibrium interface in an exotic container. Zero gravity, $\gamma = 55°$.

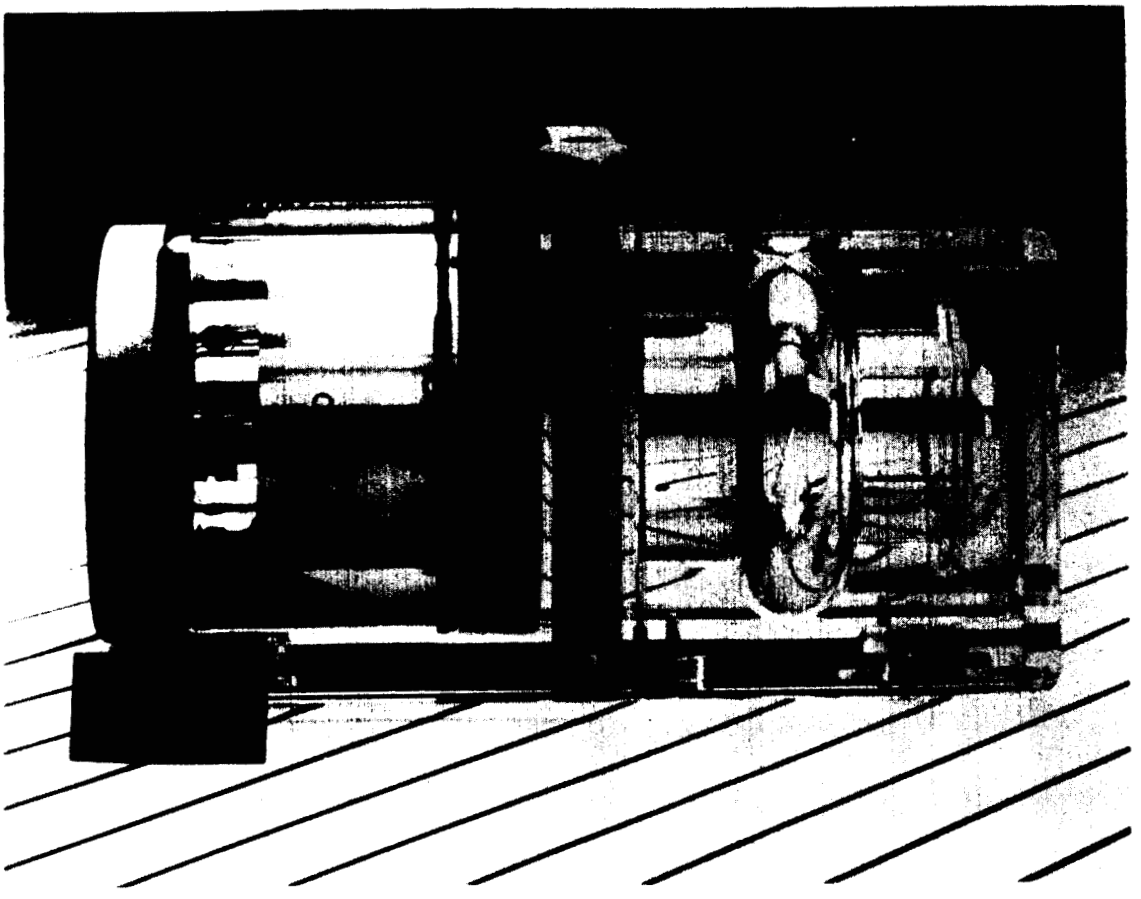

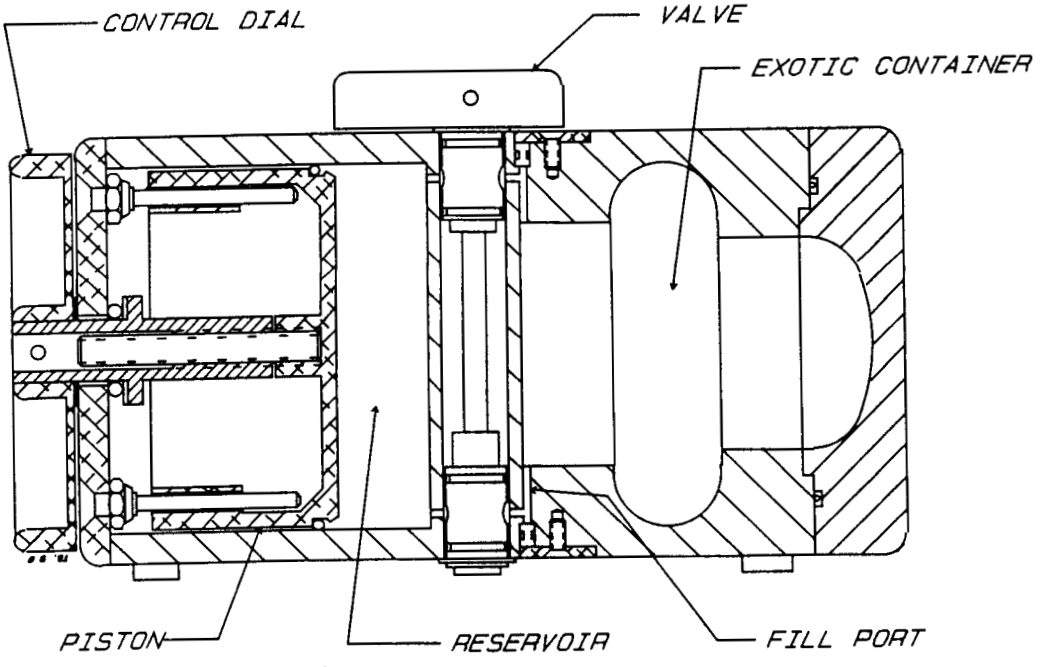

Figure 3 Flight module and schematic drawing of an interface configuration experiment vessel. Exotic container is for zero gravity and zero gravity, $\gamma = 55°$.

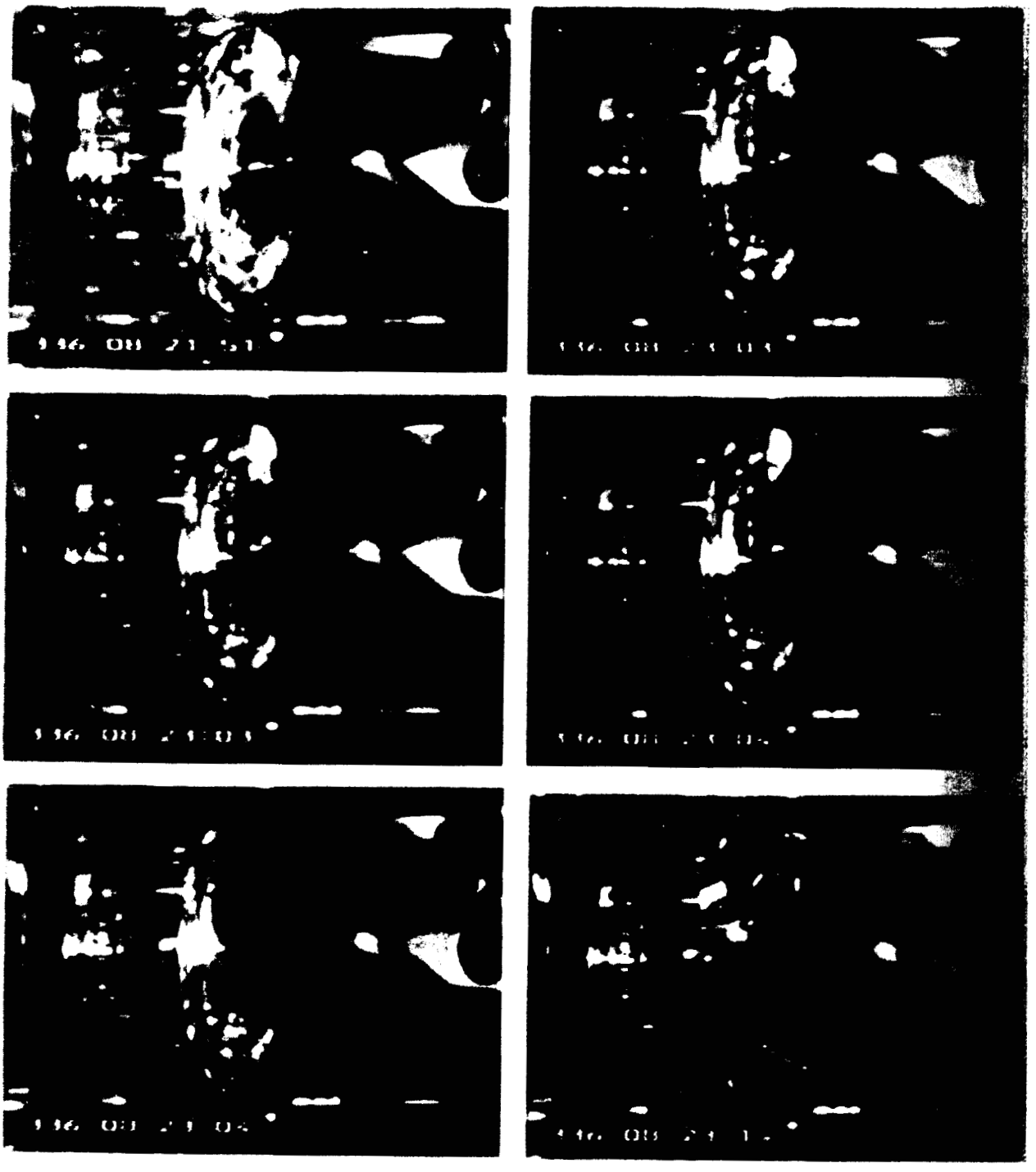

Figure 4 Sequence of video frames depicting transition from initial symmetric equilibrium interface (upper left) to stable asymmetric one (lower right). Top view.

Figure 5 Initial symmetric equilibrium interface (left) and stable asymmetric one (right). Front view.

Discussion

Question: *Were any other orientations tried in the experiment ?*

Answer: No. Everything was done in the Spacelab in the Glovebox with the vessel lying horizontally. That is the way it fit into the Glovebox and fit onto the lab jack. It had magnetic holes in the bottom, so there was no attempt to orient the container in any other way. Of course if there is no gravity at all, it wouldn't matter. There is some.

Question: *Were there any noticeable differences between the two runs you showed ?*

Answer: This is the second run. The first run, I believe, Larry tapped the vessel from the side, so it was an asymmetric perturbation which would encourage this configuration you saw on the slides here. The second one you saw was tapped on the end in an attempt to get a symmetric perturbation which would be less biased towards having the fluid move that way (as in the first run). But it always went to something like that.

Question: *Have you tried to correlate your results to SAMS data ?*

Answer: No. We would like to get the SAMS data and put it up along side to see if we could observe something. That is certainly on the list once we get all the tapes.

Question: *What is your next experiment on the lines shown here ?*

Answer: We have something that has been proposed and accepted for USML-2. But whether it is still on it we do not know, since the Glovebox is over-subscribed. It is actually a different sort of phenomenon. It is one of discontinuance dependence on configuration and contact angle whereby a small change in the container geometry or a small change in contact angle could cause large bulk motions of the fluid. We want to study that and possible applications; by which I mean determining contact angles in zero gravity in an accurate way.

CANDLE FLAMES IN MICROGRAVITY: USML-1 RESULTS -- 1 YEAR LATER

H. D. Ross*, D. L. Dietrich+, and J. S. T'ien#

*NASA Lewis Research Center
+Sverdrup Technology Inc., LeRC group
#Case Western Reserve University

ABSTRACT

Here we report on the sustained behavior of a candle flame in microgravity determined in the glovebox facility aboard the First United States Microgravity Laboratory. In a quiescent, microgravity environment, diffusive transport becomes the dominant mode of heat and mass transfer; whether the diffusive transport rate is fast enough to sustain low-gravity candle flames in air was unknown prior to this series of about 10 tests.

After an initial transient in which soot is observed, the microgravity candle flame in air becomes and remains hemispherical and blue (apparently soot-free) with a large flame standoff distance. Near flame extinction, spontaneous flame oscillations are regularly observed; these are explained as a flashback of flame through a premixed combustible gas followed by a retreat owed to flame quenching. The frequency of oscillations can be related to diffusive transport rates, and not to residual buoyant convective flow. The fact that the flame tip is the last point of the flame to survive suggests that it is the location of maximum fuel reactivity; this is unlike normal gravity, where the location of maximum fuel reactivity is the flame base.

The flame color, size, and shape behaved in a quasi-steady manner; the finite size of the glovebox, combined with the restricted passages of the candlebox, inhibited the observation of true steady-state burning. Nonetheless, through calculations, and inference from the series of shuttle tests, it is concluded that a candle can burn indefinitely in a large-enough ambient of air in microgravity.

After igniting one candle, a second candle in close proximity could not be lit. This may be due to wax coating the wick and/or local oxygen depletion around the second, unlit candle. Post-mission testing suggests that simultaneous ignition may overcome these behaviors and enable both candles to be ignited.

Joint "L+1" Science Review for USML-1 and USMP-1 with the Microgravity Measurement Group, September 22-24, 1993, Huntsville, Alabama, USA.

INTRODUCTION

The candle flame has fascinated scientists for over three hundred and fifty years. The first recorded experimental investigations into candle flames were by Dr. Robert Hooke in 1672 (Birch, 1757). He used the candle flame to investigate the nature of combustion, discovering, among other things, the function of oxygen, performing the first schlieren experiment (using candles as both the light and object sources), and observing what is now known as buoyant convection. Dr. Hooke recorded this last observation as "...besides the flame and smoke of a candle there is a continual stream rising up from it distinct from the air". In beginning a famous series of lectures and candle experiments in the 1830's and 1840's, Sir Michael Faraday stated "There is no better, there is no more open door by which you can enter into the study of natural philosophy (science) than by considering the phenomena of a candle...(Faraday, reprint 1988)." Since the time of Faraday's lectures, the burning of a candle has often been used to illustrate some of the complicated physico-chemical processes occurring in a flame [Walker (1978), Gaydon and Wolfhard (1979), Lyons (1985)]. Recently candles have been used to study flame flicker (Buckmaster and Peters, 1986), spontaneous, near-extinction flame oscillations (Chan and T'ien, 1978), electric field effects (Carleton and Weinberg, 1989) and enhanced gravitational effects on flames (Villermaux and Durox, 1993).

Despite the frequency with which a candle flame is used in combustion science, no computational model of its behavior is available. Qualitatively, of course, various aspects of candle burning have been understood for centuries (for a history of candle making and candles, see Sherman, 1993). The flame surface represents the location where fuel vapor and oxygen mix at high temperature and react exothermically. Radiative and conductive heat transfer from the flame melts the wax (typically a C20 to C35 hydrocarbon) at the candle base. The liquid wax rises by capillary action up the wick, bringing it into closer proximity to the flame. This close proximity causes the liquid wax to vaporize. The wax vapors then diffuse toward the flame surface, breaking down into smaller hydrocarbons enroute. Oxygen from the general atmosphere migrates toward the flame surface by diffusion and convection. The survival and location of the flame surface is determined by the requirement that all these processes balance continuously.

In normal gravity, buoyant convection develops due to the hot, less dense combustion products. This has several effects: (a) the hot products are carried away by buoyancy and fresh oxygen is carried toward the flame zone; (b) solid particles of soot form in the region between the flame and the wick and are convected upward, where they burn off, yielding the bright yellow tip of the flame; and (c) in overcoming the loss of heat due to buoyant convection, the flame anchors itself close to the wick. The combination of these effects causes the flame to be shaped like a tear drop. Near the flame tip, the convective velocities are estimated to be between 30 and 90 cm/sec.

Therefore, one of the essential elements needed to explain the shape, size, and color of candle flames is the presence of buoyant-induced convective flow which affects the heat and mass transfer processes. Questions are frequently asked regarding candle flame behavior if buoyancy forces are greatly reduced. In a quiescent, microgravity environment, diffusive transport becomes the dominant mode of heat and mass transfer; diffusive transport velocities are on the order of 1 cm/sec, and at this rate, most combustion systems become less flammable. Whether this transport rate is fast enough to sustain low-gravity candle flames in air was unknown prior to these tests. It should also be noted that the candle flame in low gravity is one which provides a potential for a steady, non-propagating, non-convective, diffusion flame, and as such it is a model system.

Chung and Law (Chung and Law, 1986) used low pressure in an attempt to minimize buoyancy driven flows in combusting systems. Low pressure, however, obviates the use of better-understood chemical kinetics, since an elevated oxygen concentration is required to prevent flame extinction. Furthermore, diffusive transport rates decrease and the mean free molecular path increases (which broadens the reaction zone thickness) as pressure is reduced. Finally, low pressure is not expected to diminish the convective flows to a negligible level for candle flames in air (see Appendix 1) despite a near-spherical flame shape.

Compared with those in normal gravity in the same atmospheric conditions, both the low-pressure and the low-gravity candle flames (described below) are different in that: (a) the shape is approximately spherical rather than elongated and (b) the main reaction zone, as indicated by the visible blue region, is much farther away from the wick. This distance, referred to as the flame standoff distance here, Rs, gives an indication of the magnitude of the heat flux from the flame to the liquid fuel in the wick. In normal gravity and 1 atm pressure, this distance is about 1 mm at the base of the flame; in low gravity or low pressure, it is about 5 mm. Thus the candle in low gravity or pressure produces a flame of much lower power (smaller wax mass burning rate per unit wick surface area) and, based on the diminished soot content, a lower flame temperature. for the reduced pressure, normal gravity case (see Appendix 1).

I. PREVIOUS AND RELATED MICROGRAVITY TESTS

In preparing for the shuttle flight, we utilized both the NASA Lewis Zero Gravity Facility (Lekan, 1989) which offers reported acceleration levels less than 10^{-6} ge with very little jitter for a period of 5.2 sec during the free-fall drop, and the NASA Lewis Learjet. In the former tests, we examined the effects of oxygen concentration, and diluent type on flame behavior (Ross *et al*, 1991). The range of oxygen concentrations that were tested spanned the lowest to highest concentrations expected in Spacelab (19-25% O2). At 19%, the soot content appeared minimal. As the oxygen concentration was raised from test

to test, the soot content, determined by the size and intensity of the yellow luminosity of the flame, increased. Regardless of the initial oxygen concentration, the luminosity of the soot diminished continuously throughout the time of the drop. In all cases, a blue outer rim remained, undiminished in intensity (based on visual observation). Because of the lack of convection and the presence of thermophoresis, the soot in low gravity is confined within the fuel-rich region defined by the blue zone. In normal gravity, soot convects across the blue reactive zone producing a much more luminous and larger, visible flame.

Also tested was the effect of ignition in 1ge versus microgravity. Ignited in 1ge, the flame's response to a change in gravitational level was immediate: within 0.04 sec after the drop start, the flame shape became nearly identical to its shape at the end of the drop. Thus, the sensitivity to g jitter is clearly apparent. Much more luminous soot was seen concentrated near the flame top, a residual effect of the 1g ignition and flame.

In the aircraft tests we conducted, as well as independent tests on NASA aircraft (Carleton and Weinberg, 1988), the residual acceleration level and jitter caused severe unsteadiness in the flames, which produced rapid soot flares and flame shape variations (Carleton, personal communication). The flames from our testing were elongated in the direction of the residual acceleration, very sooty, and often emitted smoke through an open tip. These differences from the drop-tower flames further showed how sensitive candle flames are to acceleration levels. Aircraft-based tests were also conducted with two candles (described below).

More recently (post-USML-1), tests were run in the 10 sec drop tower in Hokkaido, Japan; the results were consistent with the previously reported drop tower tests.

II. MOTIVATION FOR SHUTTLE FLIGHT TESTS

Extinction was not observed in any of the drop tower and aircraft experiments; in addition the soot content of the flames burning in air was still evolving at the end of the tests. A long duration, microgravity test then offered the possibility to determine the flame survivability, the sustained mass burning rate, and the flame behavior (e.g. flame oscillations) near extinction. Each of these phenomena was unknown. By having crew member involvement, thermocouple position could be changed to provide information about flame temperature at various locations around the flame surface, emulating the low pressure, normal gravity experiments. Also, the crew could manipulate the igniter or other variables to recover from unexpected events; this proved a vital feature of the candle flame experiments.

Flame interactions (two flames in near proximity) could also be observed. Because the apparent shape of the low-gravity candle flame is approximately spherical, its behavior may be analogous in some

ways to low-gravity droplet combustion. It is of interest here to see, in a purely quiescent environment, how two neighboring flames behave; following Williams (Williams, 1985), one might expect the flames to merge when the distance between the base of each hemispherical candle flame is less then 2 times the flame radius, Rf. From a heat transfer perspective, the influence of neighboring flames will help promote and sustain burning, since the heat losses from the flames are reduced by each other's presence. From a mass transfer perspective, however, both flames compete for the same oxidizer, also required for combustion. It is not known *a priori* whether the rate and amount of fuel consumption, and flame(s) lifetime will increase or decrease. For closely spaced candles, where one single envelope flame is established around both wicks, can a stable flame exist since the stabilization point (discussed below) of both flames is effectively quenched? If not, at what separation distance do the interactions become such that a steady flame will exist? Here again, the advantage of a simple space shuttle experiment is apparent: the separation distance and system behavior of two flames may be much more easily adjusted by a trained crew member than by some automated process.

The purposes of the experiments therefore were: to determine if wick-stabilized flames (candles) can be sustained in a purely diffusive, i.e. quiescent, environment or in the presence of very slow, sub-buoyant convective flows; to determine the effect of these processes on the sustained burning rate, flame shape and color; to determine if near-extinction flame oscillations occur in the absence of buoyantly-induced flow; and, finally, to study interactions between two, closely spaced diffusion flames.

III. HARDWARE DESCRIPTION

There were two modules needed to run the experiment: a *candle parts box*, containing cables, igniter wires, candle holders, etc. and a *candlebox* in which the candle was mounted. As shown in fig. 1, the faces of the plastic candlebox are 11.4 cm by 11.4 cm by 0.95 cm thick. There were about 100 0.32 cm diameter holes in each of the six faces. The holes permitted fresh oxidizer to reach the candle but prevented a glove or other material from being accidentally ignited. The box itself provided thermal mass to keep both the combustion products diffusing through the holes and the candlebox itself from being above touch temperature limits.

A candle was normally mounted in the center of the right face. For the two candle experiment, a second candle, whose position was adjustable, was mounted in the center of the left face. Also on the right face of the candlebox was a Viton-covered opening through which the igniter was pushed. Shown also is a translation stage which was capable of moving one or two thermocouples through the flame to obtain temperature; this was not utilized in the experiments.

Candles of 4.75 mm diameter, roughly 1.2 cm long were used; the type of candle was 80% paraffin wax with 20% stearic acid ($C_{18}H_{36}O_2$), a paraffin to impart toughness and reduce the dripping

characteristics. The melting temperature was about 68° C. The small size of the candles were to limit the available fuel to about 10 minutes of burning, and to guarantee that the experiment would not exceed Spacelab's maximum allowable concentrations of combustion products.

Ignition was via an electric-powered, hot-wire igniter. The igniter could only be activated if 2 switches, remotely located, were closed simultaneously and if an igniter wire was in place. A retractable shield was available to serve as a flame snuffer and to protect the bare wire in operations. The candlebox was permanently mounted on an aluminum stand 7.5 cm high to ensure its being centered in the glovebox. In the stand were thermocouple displays and electrical connectors. Magnets on the base of the stand held the candlebox to the bottom of the glovebox's working volume.

The flame(s) were observed in orthogonal views by video cameras and in one run by a 35 mm SLR camera (Nikon F4) containing ASA 1600 color film; the camera was operated using the intervalometer feature and aperture bracketing in order to be assured of proper timing between photos and film exposure, respectively. Electric power and video cameras were provided by the glovebox facility. The video data was either downlinked directly or stored on Spacelab video tapes, copies of which were provided after the mission. In addition, data was obtained from an accelerometer mounted to the underside of the floor of the glovebox working volume.

IV. OPERATIONAL SEQUENCE

During launch and reentry, the candlebox and candle parts box were stowed in a foam-padded drawer. In orbit, a payload crew member (either Dr. Bonnie Dunbar or Col. Carl Meade) placed the candlebox inside the glovebox; the candle parts box was attached to the outside of the glovebox. The crew member then removed from the candle parts box the candle(s) and igniter, and installs them inside the glovebox. After the electrical connections were made and verified, the crew set up the cameras focusing on a 2.5 cm x 2.5 cm area around the candle tip and on the thermocouple displays.

The crew member then activated the igniter and lighted the candle(s). Photography and temperature measurements continue until the flame burned to extinction. In some cases, the glovebox fan was then turned on to replenish the glovebox with Spacelab air. After about 1 minute, the next test proceeded.

V. DATA REDUCTION AND ANALYSIS

To ascertain the proper film development process, only 1 of the 4 rolls of color 35 mm film was developed and reviewed; following this review, the remaining rolls were developed. The video tapes were analyzed, frame by frame, on a digitized motion analyzer to determine the flame diameter and heights as functions of time from each test. Quantitative comparisons were made with normal gravity

behavior. In addition, the 3-axis readings from the Space Acceleration Measurement System (SAMS) sensor head C (125 samples / sec) were superimposed on the video tapes to synchronize the flame and accelerations, and facilitate correlation. At the time of this writing, the acceleration data was still being analyzed. The log of thruster firings is also being analyzed for potential effects on flame behavior and acceleration traces. Spacelab data suggests that the ambient oxygen concentration was 21.7% in Spacelab; it is assumed that this was the initial concentration in the glovebox prior to the first ignition attempt for each test.

VI. RESULTS

About ten single-candle flame tests were run with the following results. Immediately after ignition, the candle flame was spherical with a bright yellow core. After 8-10 seconds, the yellow, presumably from soot, disappeared, and the flame became blue and hemispherical; these behaviors are consistent with the earlier, short-duration studies (Carleton and Weinberg, 1989; Ross et al, 1991) Typically, the candle flame reached a nearly steady diameter of 1.5 cm (fig. 2). The mass of liquified wax grew, however, and unlike normal gravity, did not drip off because of the small Bond Number ($\rho g l/\sigma$, where ρ is the liquid density, g is the acceleration level, l is the characteristic length, i.e. effective diameter of the liquid, and σ is the surface tension). The shape of the liquid mass was not spheroidal (as might be expected in low gravity), because of the wick and the likely presence of thermocapillary convection. The extent of liquified material also suggests that the influence of thermal conduction from the flame, overwhelmed by buoyant convection in normal gravity, extended much farther into the solid wax in the microgravity tests.

Figure 3 shows the flame diameter and height as a function of time for a single candle experiment. Figure 3a shows that the flame diameter decreases with time for the first ten seconds, after which it maintains a steady value until just prior to extinction. The flame height, shown in fig. 3b on the other hand changed continuously with time until extinction. Figure 3a is just for a single flame, the temporal behavior of each experiment was different. Some flames reached *steady-state* with respect to both diameter and height, and for some both the flame diameter and height changed continuously. The flame diameter and height increased with time for some flames and decreased with time for others. The flames remained soot-free throughout the flame lifetime. Extinction occurred between 40 and 60 seconds for all flames except one[1]. One flame had a lifetime of 105 seconds; this flame started and

[1]For comparative purposes, a candle of identical composition as those used in the shuttle tests was burned in normal gravity in the following manner: a vertical, downward burn orientation (flame above candle), no candlebox, a rectangular sealed box filled with air (21% oxygen) with a physical volume of 12 liters (just under one-half the glovebox volume), the same candle diameter but about 6 cm length. The candle flame survived for 205-220 sec, 2 to 5 times the shuttle results; the longer-lived flame in normal gravity, despite the available oxygen being half that of the full glovebox, illustrates how buoyant convection maintains steep oxygen and combustion product concentration gradients and thereby enhances the local supply of oxygen to the flame zone.

stayed smaller than normal (approximately 0.6 cm) for a long time because it stabilized on only a portion of the wick. This smaller but longer-lived flame, supported by models and discussion described below suggest that oxygen depletion in the candlebox and the overall glovebox volume, combined with ongoing heat losses (e.g. flame radiation to the environment; conduction into the solid), led to extinction.

Surprisingly, each candle flame oscillated spontaneously about 5 seconds before extinction. The flame symmetrically traced back and forth along the candle axis in each cycle (fig. 4). The oscillation had a frequency of about 1 Hz with an amplitude that started small and continued to grow until extinction.

Another surprising result was the inability to sequentially ignite two, proximate candles oriented to face each other on a common axis. The crew attempted ignition with various wick separation distances (4-12 mm), ignition sequences, and igniter locations. After successfully lighting the first candle, the second candle could never be ignited; at no time was a stable flame(s) attained simultaneously on both. In one test, a single candle was lit and allowed to burn to extinction near an unlit second candle. Initially, the single candle flame was not affected by the presence of the second candle. With time, the flame grew closer until its tip was quenched by the wick of the unlit candle, immediately after which the surviving part of the flame rotated asymmetrically around the axis and then extinguished.

For a fraction of a second during one experiment, the residual acceleration level changed from $O(10^{-6}ge)$ to $O(10^{-3}ge)$ due probably to a crew movement (a review of the log book on shuttle thruster firing shows that thrusters were not the source of the increased acceleration). Before and several seconds after, the flame was hemispherical and dim. During and shortly after the disturbance, the flame remained hemispherical but became much more luminous, presumably due to enhanced soot production and burnout caused by a small buoyant flow. This appears to further demonstrate the sensitivity of even small flames to convection induced by seemingly benign accelerations; however given that this was the only occurrence of such behavior, it is difficult to state with certainty that this is the source. The acceleration environment was analyzed in terms of frequency content and mean-square spectral density (aka power spectral density). The 17 Hz dither for the shuttle antenna is readily apparent in the analysis. As expected, the flames do not appear to be responsive to the high-frequency components of acceleration.

Also in one test, flashes of flame appeared somewhat randomly in time and space. These were most likely a result of air bubbles trapped inside the solid wax. As the wax was heated and melted, these bubbles expanded and burst. The mixture of fuel vapor, satellite wax droplets, and air then ignited and quickly extinguished upon consumption of the fuel. The acceleration traces did not show any correlation with, i.e. response to, the appearances of the flashes.

VII. DISCUSSION

This investigation sought to provide some experimental evidence toward answering the commonly asked questions "will a candle burn indefinitely (or steadily[2]) in 'zero' gravity in a large volume of quiescent air." These types of questions are often asked because a greater accumulation of combustion products in the absence of buoyancy tends to make the candle less flammable. The classical theory for a spherically-shaped, diffusion flame, however, shows that steady combustion is possible in the absence of buoyancy if the chemical reaction kinetics are fast enough. The oxygen concentration profile, both at steady state, and in transition to steady state, for a spherical geometry are shown qualitatively on Figure 5. At the flame front itself (r = Rf), oxygen is completely consumed. The initially steep gradient in oxygen concentration (curve 1 in fig. 5) evolves as time continues, to a flatter gradient (curve 2), with oxygen depletion being apparent farther from the flame front. Eventually the oxygen concentration profile reaches steady state (bold curve) if the surroundings are effectively infinite. To experimentally test candle flammability in air in zero gravity, a long test duration is required because, in addition to the gas phase, the wick and the solid and liquid phases take substantial time to reach their steady states. Unfortunately, ambient oxygen depletion owed to the small glovebox volume and the candlebox complicates the test.

The flame lifetime in the glovebox was estimated, on the assumption that oxygen depletion leads to extinction, to understand the effects of the sealed volume. The estimate is based on solving (numerically) the transient, spherically-symmetric, species conservation equation for oxygen (Appendix 2). The boundary conditions are developed based on the assumption that the candle is a sink for oxygen, and there is no oxidizer flux at the glovebox wall. The analysis assumes a known constant wax mass burning rate, flame diameter (0.1 mg/sec and 1 cm respectively) and the product of the gas density and binary diffusion coefficient of oxygen into nitrogen is a constant (evaluated at 800 K). As shown on curve 4 on fig. 5, the non-infinite ambient suffers from ongoing oxygen depletion. Extinction occurs when the ambient can no longer supply the required oxidizer flux to the flame (curve 5).

The results show that for a candle burning in a spherical volume the approximate size of the glovebox, the flame lifetime will be on the order of three minutes. During this time, the ambient oxygen concentration is significantly depleted. The perforated candle box, however, serves as an impediment to oxygen diffusing to the flame. Modifying the analysis to account for the effect of the candle box shows that the flame lifetime decreases to on the order of 1 minute. During this time the oxygen concentration

---

[2] Steady state is achieved when the solid- (wax and wick), liquid-, and gas-phase behaviors become invariant with time. For candles burning in normal gravity, there are several initial transients, including the flame size, the wick lengths (the length coated in wax and the exposed length), and the volume of liquified wax. Eventually these reach a balance and the candle flame system is considered to be steady. Often stray air currents cause the flame to move about; also flame flicker is commonly observed in normal gravity. These variations from steady state are well-explained.

inside the candlebox decreases significantly while that outside the candlebox decreases only slightly. The analysis is admittedly not a comprehensive model of candle burning; specifically, the mass burning rate and flame radius may change as oxygen is depleted. This estimate supports the notion that flame extinction was caused by oxygen depletion. We also note, that the long-lived flame was small initially, thus consumed less oxygen, and this resulted in its significantly longer lifetime.

Despite the ability to obtain a true steady state being compromised by the sealed glovebox, we note that the gas phase was quasi-steady, since the flame was invariant over a characteristic gas-phase transport time (e.g. 1-3 x Rs^2/D, where Rs is the flame standoff distance, as previously defined, and D is the average molecular diffusion coefficient), and this time was much smaller than the characteristic time scale over which oxygen was depleted (e.g. Volume of glovebox / Volumetric rate of oxygen consumption, the latter quantity being estimated from equilibrium chemistry, a comparison of Rs in 1g and microgravity, and the known burning rates in normal gravity). Furthermore the flame survived the initial transient when heat loss into the solid is a maximum. Thus a single candle flame can survive indefinitely in zero gravity in air in a large-enough, quiescent, ambient air volume. This conclusion, admittedly, is reached through inference, rather than through experimental demonstration.

To discuss the actual mechanism of extinction, we define a local reactivity as the fuel vapor reaction rate per unit volume and note that it varies from point to point in the flame. Previous modeling results with similar flow configurations (Bergeson and T'ien, 1986) show that the maximum reactivity is located near the flame base for the normal gravity candle flame. The point of maximum reactivity serves as the flame stabilization region for the flame. In zero gravity, the visible flame is entirely blue and its shape is close to a hemisphere. The flame standoff distance is basically the same from any point in the flame. Based on the survival of the flame tip during oscillations, the response of the microgravity candle flame to the nearby, unlit candle, and previous temperature measurements of flames with similar shape and sizes (Chan and T'ien, 1978) one can deduce that in low-gravity the maximum reactivity is located at the top of the candle flame. Since the location of maximum reactivity is the strongest point in the flame, it is the last part to extinguish. In the shuttle experiment, oxygen is gradually depleted as the candle burns. With decreasing oxygen, the reactivity decreases everywhere. The base is the coolest part of the candle flame, hence the reactivity is the lowest and the flame base is the first point to extinguish.

Extinction of flames in normal gravity is usually due to blowoff (e.g. how one extinguishes a match) in which the residence time of fuel vapor in the reaction zone is too short compared to the chemical reaction time. The ratio of these times is known as a Damkohler number, and extinction corresponds to the condition when the Damkohler number falls below a critical value (Williams, 1979). In a quiescent, microgravity environment, the residence time becomes large, and this form of the

Damkohler number (based on adiabatic flame temperature) becomes large; therefore extinction must be due to a completely different mechanism (T'ien, 1986). Extinction in microgravity has sometimes been described as being caused by an accumulation of combustion products around the flame (e.g. Carleton and Weinberg, 1989), but this description, in isolation, is incomplete. Instead, we note that the chemical reaction time (and the rate of heat release), is indeed affected by the local oxygen concentration (linear dependence) which is coupled to the diffusive transport. However, the chemical reaction time and heat release are affected more strongly (exponential dependence) by the flame temperature. The peak candle flame temperature is less than the adiabatic flame temperature by ongoing conductive and radiative heat loss into the solid and to the surroundings. Flame extinction occurs when the lowered flame temperature, owed both to reduced oxygen transport rate and heat loss, decreases the rate of chemical heat release beyond that which can overcome the ongoing heat losses. At this point, chemical reaction effectively ceases.

The above discussion has concentrated on the importance of the gas phase, but the wick/liquid phase is also important in determining the characteristics of the candle flame. Since the fuel is evaporated from the surface of the wick, the mass burning rate of wax from the candle is a function of the length of exposed wick. In many instances (normal gravity) when a candle is first lit and the length of exposed wick is small and/or the mass of liquid wax is also small, the flames are small initially. As the burning proceeds, and the fuel heats up melting solid wax and exposing more wick the flame begins to grow until it reaches a steady-state size. While the wick dynamics cannot explain the significant differences between the normal gravity and reduced gravity flames, they can explain the differences between the different shuttle experiments. Specifically, even though the candles were nearly identical to start with, the length and severity of the ignition process created a different initial condition (length of exposed wick and/or mass of liquid wax) in each test. Also potentially contributing to the test-to-test variation was the variable oxygen concentration in the glovebox.

The flame oscillation before extinction is explained as a flame base retreat and flashback mechanism. As the ambient oxygen concentration decreases, the flame oscillations are initiated when the flame base begins to retreat. Because of their thermal inertia, the liquified wax and wick are still hot, so fuel vaporizes, and the fuel vapor and oxygen diffuse toward each other. Eventually a combustible mixture is formed and a rapid flashback of the flame occurs. This further depletes the ambient oxygen concentration, so that more of the base or weakest part of the flame (compared to the previous cycle) extinguishes, and the cycle repeats. The oscillations will continue, increasing in amplitude as the ambient oxygen is continuously depleted, until the ambient oxygen concentration becomes too low to sustain any part of the flame.

This type of oscillation has also been observed in candles in normal gravity at low pressure (0.14

atm). The frequencies of oscillation are different, however, 6-9 Hz in normal gravity, 0.14 atm versus 1 Hz in microgravity, 1 atm. Previously a buoyant convective flow, even at the low pressure condition, was suspected as being related to the oscillation cycle (Chan and T'ien, 1978). Analysis of the acceleration traces shows that oscillations occurred even in the "most quiet" environments on the shuttle, i.e. when there were no thruster firings and no obvious crew disturbances. At the measured background levels of 10^{-5} to 10^{-6} ge associated with these quiet periods, buoyant convection is estimated at much less than diffusive transport rates. Therefore buoyant convective flow does not appear to be required for the oscillation phenomena. Instead, we hypothesize that the different frequencies are due to the different diffusive transport rates (times) in the two environments and further assume that these transport rates are approximated by the time for fuel vapor transport from the wick to the flame surface. The time scale for diffusion is $1\text{-}3 \times Rs^2/D$; using measured values of Rs = 5.6 mm and 5 mm for μg and 1g, respectively, and an average molecular diffusion coefficient evaluated at 800 K for both, the estimated diffusion time is equal to 0.37 - 1.1 sec for the low-gravity flame and 0.04 - 0.12 sec for the normal gravity, 0.14 atm flame. The magnitude and the ratio of the two times (about 9) are in the range of the experimental data. The identification of time scales does not necessarily explain why oscillations have to occur; this requires a proper phase relationship between the involved processes. In addition, whether this observed oscillation is an instability (oscillation under constant environmental conditions) needs further investigation.

The inability to ignite two candles was somewhat surprising. The range of initial separation distances would produce near-optimal burning in normal gravity. Perhaps more significantly, aircraft-based testing, albeit limited, of the ignition procedure for two candles was successful. Since the candles were lighted *sequentially*, the first flame could have at least two undesirable effects on the unlit candle. First the heat from the first flame may have melted the wax of the unlit candle to the extent that the liquified wax coated the wick of the unlit candle; in this case, ignition is much more difficult to achieve, a result observed firsthand by the crew members. Second, and probably more likely, the wicks in microgravity were within 1 flame diameter, so the oxygen around the unlit candle may have been sufficiently depleted prior to ignition to be unable to support a flame. The aircraft tests did not reveal similar behavior because the residual acceleration level was higher (so residual convective flow provided oxygen locally and causing the large, first flame to promote ignition) and because the time between lighting the candles was greater in the space-based mission. Since the USML-1 mission, these were further investigated via experiments by D. Dietrich in the 10 sec drop tower in Hokkaido, Japan. To overcome both the deleterious possibilities, axially aligned candles were *simultaneously* ignited in the Hokkaido drop tests. At the same wick separation distance (about 1 cm) as in the shuttle tests, both candles were ignited and a merged, roughly elliptical flame was observed, whose temporal and spatial

characteristics were still evolving (neither extinction nor steady state was seen) at the end of the drop. This occurred whether or not the candles were ignited in 1g and then dropped, or if they were ignited in microgravity.

VIII. RECOMMENDATIONS FOR FURTHER RESEARCH

The existing shuttle-based hardware performed extremely well, revealed several new behaviors, was developed in a very short period of time and cost literally *orders of magnitude less* than most shuttle investigations. Further tests nonetheless could be beneficial.

Perhaps most importantly, the candle flame behavior should be examined in an experiment where the rate of ambient oxygen depletion is significantly less than in the earlier experiment. This could be readily accomplished since the new glovebox facility is larger and since the safety of the experiment has now been demonstrated. Design and operations will be changed to enable the effect on oxygen diffusion by the perforated box to be minimized. This might mean a wire cage with much larger free passages, the elimination of the cage completely, or use of a larger, but similarly styled box with a larger open volume. This design would not only enable the tests described below, but would verify the flame lifetime calculations and explanations described above. It would also allow for steady state in the gas, liquid and solid phases to be reached.

The previous two-candle, shuttle-based tests were compromised both by the ignition procedure and the close, initial spacing of the candles (which was necessitated by the size of the glovebox and candlebox). With a greater separation distance and a simultaneous ignition, two independent flames should be observable. The preliminary tests in the Hokkaido drop tower verified this behavior. Again, the behavior of these flames was still evolving at the end of the 10 sec test period. Further shuttle testing could involve a much further separation distance, now available because of a larger glovebox volume. At least three kinds of flame interaction tests could be performed: (1) simultaneous ignition of on-axis candles at various separation distances, with the flames allowed to burn to completion; (2) simultaneous ignition of on-axis candles at various separation distances, followed by the slow translation of one candle flame toward the other; and (3) off-axis flame interactions. The existing hardware, in a new, larger perforated container can be utilized for all of these investigations.

One question regarding experimental operations on the shuttle which has emerged since the mission is that the ignition process took longer on the shuttle than in drop facilities and or aircraft. The reasons for this are not yet clear. Variables have been discounted [e.g. that the wicks were too short in the shuttle tests (unlikely, since they were the same length as used on the ground), or the igniter power from the glovebox was lessened in space (also unlikely since this was well-characterized)]. It is only recently realized that the ignition time and method may be an important variable in many, quiescent

microgravity combustion experiments. The hot gas expansion associated with ignition may influence the observed flame behavior for far longer times than in normal gravity, where the ignition effect is swept away by buoyant convection. Hot gas expansion has been shown to influence flame spread behavior and even flame survivability (Ross, 1993). Since the mission, other igniter configurations than the one used on the shuttle tests have been examined, and it is believed that a simple change to a coiled wire should speed ignition and minimize the hot gas expansion effect.

The thermocouple measurements planned for USML-1 were never conducted, due to scheduling tradeoffs. These measurements would directly verify the location of maximum reactivity, and measure flame temperatures. Such measurements should be relatively accurate, since the flames are soot-free.

Finally, the effects of slow, controlled air flow over the candle flame can be examined. As noted above, these velocities would be between the diffusive transport velocities, estimated at about 1 cm/sec, and the buoyant convective velocities, estimated at 30-90 cm/sec, found on Earth. The effects of these flows on sooting behavior, flame lifetime, color, and temperature should be noted. Alternatively, various wick and candle diameters might be examined; Villermaux and Durox attributed gravitational effects on wick dynamics as having a significant influence on the flame position (relative to the wick) in their recently published, candle experiments conducted in a centrifuge.

CONCLUSIONS AND CONCLUDING REMARKS

The following conclusions were reached in this experiment.

The flame color, size, and shape behaved in a quasi-steady manner; the finite size of the glovebox, combined with the restricted passages of the candlebox, inhibited the observation of true steady-state burning. Nonetheless, through calculations, and inference from the series of shuttle tests, it is concluded that a candle can burn indefinitely in air in a large-enough, quiescent, microgravity environment.

After an initial transient in which soot is observed, the microgravity candle flame in air becomes and remains hemispherical and blue (apparently soot-free). During the time in which the candle burned, the mass of melted wax increased continuously, suggesting steady state had not yet been reached. The enlarged flame standoff distance, previously observed in drop tower tests, is maintained throughout the burning lifetime. Near extinction, spontaneous flame oscillations, explained as a flashback-quench phenomena, are regularly observed. The frequency of oscillations can be related to diffusive transport rates, and not to residual buoyant convective flow. The fact that the flame tip (the farthest from the solid wax) is the last point of the flame to survive suggests that it is the location of maximum reactivity; this is unlike normal gravity, where the location of maximum reactivity is the flame base.

Accelerations on the shuttle are generally below those which induce a significant buoyant flow for

these low-momentum, and therefore very sensitive, flames. As such the shuttle environment should be amenable to several other microgravity combustion experiments. An isolated departure on the order of 10^{-3} ge from the background levels of acceleration appeared to cause temporary sooting of the candle flame.

Two candles in close proximity could not be lit sequentially. This was unlike the experience in aircraft testing, and shows that, at least for these flames, aircraft testing with bolted-down hardware is a poor surrogate for the shuttle. The inability to light both candles in the shuttle experiment may be due to wax coating the wick and / or local oxygen depletion around the second, unlit candle. Post-mission testing suggests that simultaneous ignition may overcome these behaviors and enable both candles to be ignited.

The actions of Bonnie Dunbar and Carl Meade proved vital to the success of these candle flame experiments. The unexpected difficulty in igniting the candles could not have been overcome with software and automation, or at least without years of expensive development of such processes. Instead, the crew took appropriate on-the-spot action which enabled us to observe sustained burning. In addition, the color still photographs proved especially valuable, since they revealed the liquified mass clinging to the wick (invisible on the video cameras).

This seemingly simple experiment has yielded widespread interest from disparate groups -- primary and secondary school students; physics, chemistry, and engineering professors; combustion scientists; and the popular media (Encyclopedia Britannica, Cable News Network, the Associated Press, CBS, and local newspapers). The results continue to engender debates amongst the investigators as well as the forementioned groups, and this may be the most gratifying part of the experience.

ACKNOWLEDGMENTS

Appreciation is expressed to Kofi Kankam, a high-school summer student, and Richard DeLombard for helping to reduce the SAMS and USML-1 thruster data, respectively, and to Kurt Sacksteder and Peter Quinn for the idea and digitization, respectively, to superimpose the acceleration data on the candle flame video records. We also wish to acknowledge the consistent performance of the ESA-provided glovebox facility throughout the mission.

REFERENCES

1. Birch, Th. *The History of the Royal Society of London,* London (1757).

2. Borgeson, R. and T'ien, J. *Combust. Sci. Tech.*, **32**, 125-136 (1983).

3. Buckmaster, J. and Peters, N., *The Infinite Candle and its Stability - A Paradigm for Flickering*

Diffusion Flames; 21st. Symposium (Int'l) on Combustion; p. 1829-1836; (1986).

4. Carleton, F. and Weinberg, F. *Nature* **330**, 635-636 (1988).
5. Chan, W. and T'ien, J. *Combust. Sci. Tech.*, **18**, 139-143 (1978).
6. Chung, S.H. and Law, C. K. *Comb. and Flame*, **64**, 237 (1986).
7. Faraday, M., *The Chemical History of a Candle*; Chicago Review Press (1988).
8. Gaydon, A. and Wolfhard, H.,*Flames: Their Structure, Radiation, and Temperature*, Halstead (1979).
9. Lekan, J. AIAA Paper No. 89-0236, Aerospace Sciences Meeting, Reno, Nevada (1989).
10. Lyons, J. Chapter 2 in Fire, Scientific American Books, Inc. N. Y. (1985).
11. Ross, H., Sotos, R and T'ien, J. *Combust. Sci. Tech.*, **75**, 155-160 (1991).
12. Ross, H. *Neither Up Nor Down: A Perspective on Combustion in Microgravity*; invited presentation, Fall Tech. Mtg. of the Eastern States Section of The Combustion Institute (Oct 25-27, 1993).
13. Sherman, D. R., *Domestic Lighting: Candles, Lamps, and Torches in History*; The Compleat Anachronist, #68, Society for Creative Anachronism, Inc.(1993).
14. T'ien, J.S., Combustion and Flame, 65: 31-34 (1986).
15. Villermaux, E. and Durox, D. *Comb. and Flame*, (1993).
16. Walker, J. *Sci. Am.*, **238**, 4:154, (April, 1978).
17. Williams, F. A. Combustion Theory, 2nd Edition, Benjamin/Cummings, (1985).
18. Williams, F. A. *Fire Safety J.*, 3, 168 (1981).

Appendix 1

Estimating and Demonstrating Residual Convective Flow at Low Pressure in Normal Gravity

An order-of-magnitude analysis is made here to estimate the effect of reduced pressure on the buoyancy-induced velocity in air. The estimate can be based on a balance between gravitational force with either inertial or viscous terms in the momentum equation. Using inertia, we get

$$U_{iner} \sim \sqrt{gl\Delta\rho/\rho} \cong \sqrt{gl\Delta T/T}$$

where l is the height of the flame. It is clear that gas velocity is continuously accelerating and the highest velocity in the flame occurs at the flame tip. Using the viscous term, we get

$$U_{vis} \sim \delta^2 g \frac{\Delta\rho}{\mu} \cong \delta^2 \frac{g}{\mu} \rho \frac{\Delta T}{T}$$

where δ is the thickness of the viscous or thermal layer. The choice between eqn. (1) and eqn. (2) depends on the magnitude of the Grashof number:

$$Gr = \frac{\rho^2 l^3 g \Delta\rho}{\mu^2 \rho}$$

When Gr > 1, a boundary layer type of flow exists and it is more appropriate to use eqn. (1) since the boundary layer thickness adjusts its magnitude such that u_{buoy} becomes comparable to u_{iner}. When Gr < 1, eqn. (2) gives a better estimate of the magnitude of buoyancy-induced velocity in the flame and δ can be taken as the flame standoff distance, Rs. The pressure dependence in eqs. (1-3) comes from l, Rs, and ρ. The dependence of flame height, l, on pressure can not be determined simply from flame photographs because, at different pressure levels, the soot production varies and masks the actual height of the flame. If we select the blue boundary to define flame height (extrapolation required for sooty flames), the dependence of l on pressure is weak for candle flames. On the other hand, Rs exhibits a strong pressure dependence. At the bottom of the flame, Rs is about 1 mm at 1 atm; everywhere around the flame Rs is about 5 mm at 0.14 atm. The density ρ is proportional to pressure, but $\Delta\rho/\rho$ is about 1 (actually about 0.8) over the pressure range of interest. Thus from eqns (1-3) u_{iner} is only weakly dependent on pressure, u_{vis} can actually increase with decreasing pressure (if the increase of δ^2 is greater than the decrease of ρ), and Gr will decrease with pressure. Evaluating μ and ρ at 900K, we find at normal gravity for a range of selected l:

l (cm)	p (atm)	Gr	$Gr^{0.5}$	u_{iner} (cm/s)
1	1	464	21.5	36
1	0.14	8.6	2.2	36
0.5	1	58	7.6	25.5
0.5	0.14	1.1	1.04	25.5

From this table, we see that, even at low pressure, Gr > 1 for l = 0.5 - 1 cm (the observed low pressure flame height). Using eqn. (1), the buoyantly-induced velocity is estimated at 25 - 36 cm/sec. Thus it appears that the flow is not diminished sufficiently over the tested range of pressure and oxygen concentration, and as such it does not simulate the low convective flow in reduced gravity.

In support of these estimates, a few simple experiments were performed. A low-pressure, normal gravity candle flame was established inside a candlebox identical to that flown in the shuttle, but *without a top* placed inside a large (over 500 *l*) chamber. A top was then placed on the candlebox, and the flame quickly extinguished. Similarly, a low-pressure candle flame was established in a chamber in normal gravity, and then the chamber was released into freefall in the NASA Lewis 2.2 sec drop tower. Shortly after entry into microgravity, the flame extinguished. These demonstrate a significant, residual convective flow was present even in low pressure.

The molecular mean free path, Λ, is proportional to T/P. As pressure is lowered seven-fold (from 1 atm to 0.14 atm), the flame temperature diminishes only slightly (about 10%). Thus, the reduction in pressure has a stronger effect than the reduction in temperature, and Λ increases by about a factor of 6. This will reduce the number of molecular collisions in the reaction zone and broaden the reaction zone thickness.

Appendix 2

Oxygen Depletion Calculations

The problem being considered is that of a spherically symmetric candle flame with radius R1 and mass burning rate $\dot{m}$ burning in a spherical container of radius R2 that allows no oxygen to enter. The following assumptions are made in the development of the model.

1.) Spherical symmetry.

2.) No oxidizer leaks through the flame and the flame burns at stoichiometry at an infinitesimally thin flame front. The radius of the flame front is R1.

3.) The problem is one of oxygen diffusing in air. Neglect the products of combustion.

5.) Body forces on the two species are the same.

6.) No thermal diffusion or thermosolutal effects.

7.) Constant pressure.

8.) The product of the density and the binary diffusion coefficient is a constant.

The following parameters are assumed to be known and are specified.

1.) The mass burning rate of the candle wax, $\dot{m}$. This parameter is also assumed to be constant. Knowing the wax mass burning rate and by assumption (2) allows the mass flux of oxygen to the candle flame to be determined. This is the boundary condition at the flame.

2.) The initial ambient oxygen concentration. This is the initial condition for the unsteady computation.

The species conservation for oxygen conservation is given as follows (Williams, 1985).

$$\frac{\partial Y_o}{\partial t} + v_o \cdot (\nabla_x Y_o) = \frac{w_i}{\rho} - \frac{\left[\nabla_x \cdot (\rho Y_o \overline{V}_i)\right]}{\rho}$$

By assumption (1) we can write the differential operators as.

$$\nabla_x \rightarrow \frac{\partial}{\partial r}\ ,\ \nabla_x^2 \rightarrow \frac{1}{r^2}\frac{\partial}{\partial r}\left(r^2\frac{\partial}{\partial r}\right)$$

By assumptions (5), (6) and (7) Fick's law of diffusion is valid, and the product of the local oxygen mass fraction and diffusion velocity may be written as.

$$Y_o\overline{V}_o = -D(\nabla_x Y_o).$$

By assumption (8) the Stefan convective velocity may be written as

$$\dot{m} = 4\pi r^2 \rho v_o.$$

With this, the differential equation of oxygen conservation becomes

$$\frac{\partial Y_o}{\partial t} + v_o\frac{\partial Y_o}{\partial r} = \frac{D}{r^2}\frac{\partial}{\partial r}\left(r^2\frac{\partial Y_o}{\partial r}\right).$$

The initial and boundary conditions are:

at $t = 0$, r: $Y_O = Y_{O\infty}$

at $r = R1$, $t = t$: $\frac{\dot{m}}{\nu} = \left\{-4\pi r^2\rho\left(v_o + \overline{V}_o\right)Y_o\right\}_{r=R1}$

at $r = R2$, $t = t$: $\left\{\left(v_o + \overline{V}_o\right)Y_o\right\}_{r=R2} = 0$

The second boundary condition expresses the fact that the oxidizer mass flux to the flame must occur in stoichiometric proportion to the mass burning rate of the candle. The last boundary condition shows that no oxygen can enter from the outside to the inside of the container. ν is the stoichiometric fuel to oxygen (not air) mass ratio. The equation, initial and boundary conditions are then non-dimensionalized as follows.

$$\tilde{r} = \frac{r}{R2}\ ,\ \tau = \left(\frac{t}{R2^2/D}\right)$$

$$\frac{\partial Y_o}{\partial \tau} + \frac{\beta}{\tilde{r}^2}\frac{\partial Y_o}{\partial \tilde{r}} = \frac{1}{\tilde{r}^2}\frac{\partial}{\partial \tilde{r}}\left(\tilde{r}^2\frac{\partial Y_o}{\partial \tilde{r}}\right)$$

$$\beta = \gamma\delta\nu$$

$$\gamma = \frac{\dot{m}}{4\pi\rho(R1)D\nu}$$

$$\delta = \frac{R1}{R2}$$

at t=0, $\tilde{r} = \tilde{r}$: $Y_o = Y_{o\infty}$

at $t = \tau$, $\tilde{r} = \delta$: $\gamma\nu Y_o - \delta\frac{\partial Y_o}{\partial \tilde{r}} = -\gamma$

at t = t, $\tilde{r} = 1$: $\gamma\delta\nu Y_o - \frac{\partial Y_o}{\partial \tilde{r}} = 0$

The above system of equations was finite-differenced and solved for the oxygen mass fraction as a function of radial position and time. Only two parameters in the problem need to be specified, γ and δ. The following tabulation lists some of the values utilized.

$\dot{m}$ = 1.4 (10^{-7}) kg/s

D = 2.0 (10^{-4}) m^2/s (~1500 K)

R1 = 0.005 m

ν = 0.3

ρ = 0.25 kg/m^3 (~1500 K)

Resulting in: γ = 0.15

Using the outer dimension of the glovebox for R2, δ becomes

δ = 0.04

The ambient mass fraction must also be input, and its value is :

$Y_{o\infty}$ = 0.232

Results were compiled for different values of γ and a fixed δ. Below is a sample result for the oxygen mass fraction as a function of non-dimensional radius for δ=0.4 and γ=0.15. Extinction of the flame is defined as the time at which the oxygen mass fraction at the flame front is less than zero.

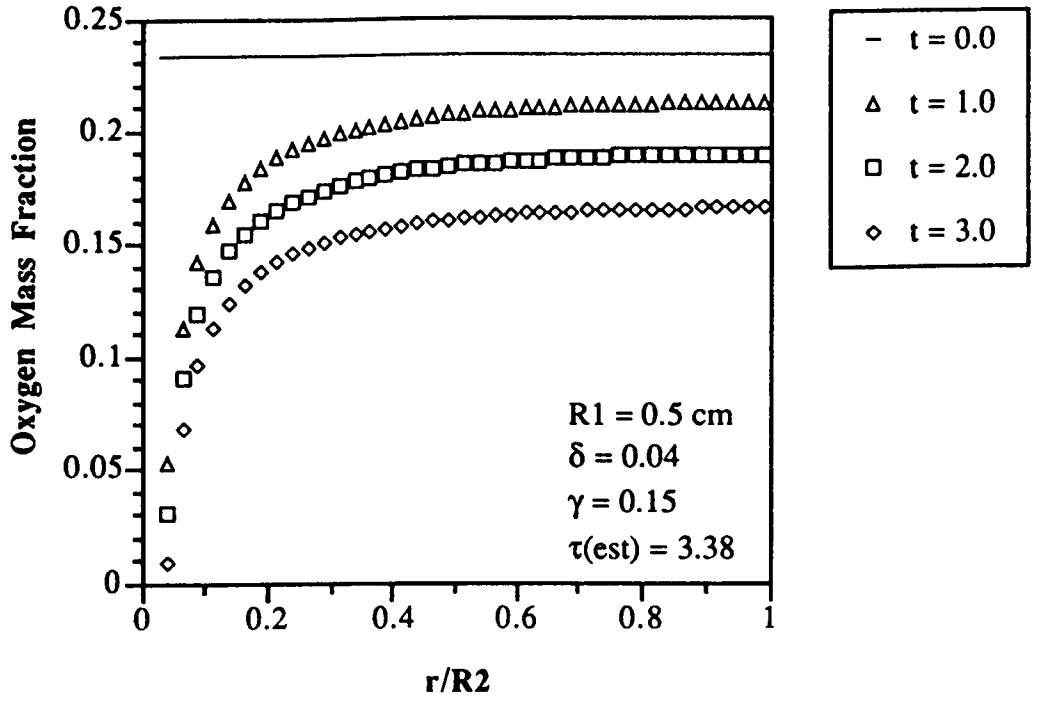

Converting to dimensional time using the given parameters shows that for the candle flame above the flame lifetime will be on the order of 4 minutes.

This result does not take into account the impediment to oxygen transport due to the candle box, so the analysis was modified to account the candle box. The surface area of the holes in the box comprised approximately 13% of the total surface area of the box. The model assumes that the candle flame is surrounded by a sphere with radius R2 with 13% free area for oxygen transport. This sphere is surrounded by another sphere with radius R3 in which the boundary condition is no oxygen transport. The spherically symmetric equations above are solved in the regions between R1-R2 and R2-R3 with the boundary conditions of known oxidizer flux at R1 and no oxidizer flux at R3. The interface between the two regions have equal and opposite fluxes; this is used to match the interfacial condition.

Below is a graph of the oxidizer mass fraction as a function of radius for the candle in the candle box surrounded by the glovebox (both times are non-dimensionalized by R2, but the value of R2 is different for the two figures).

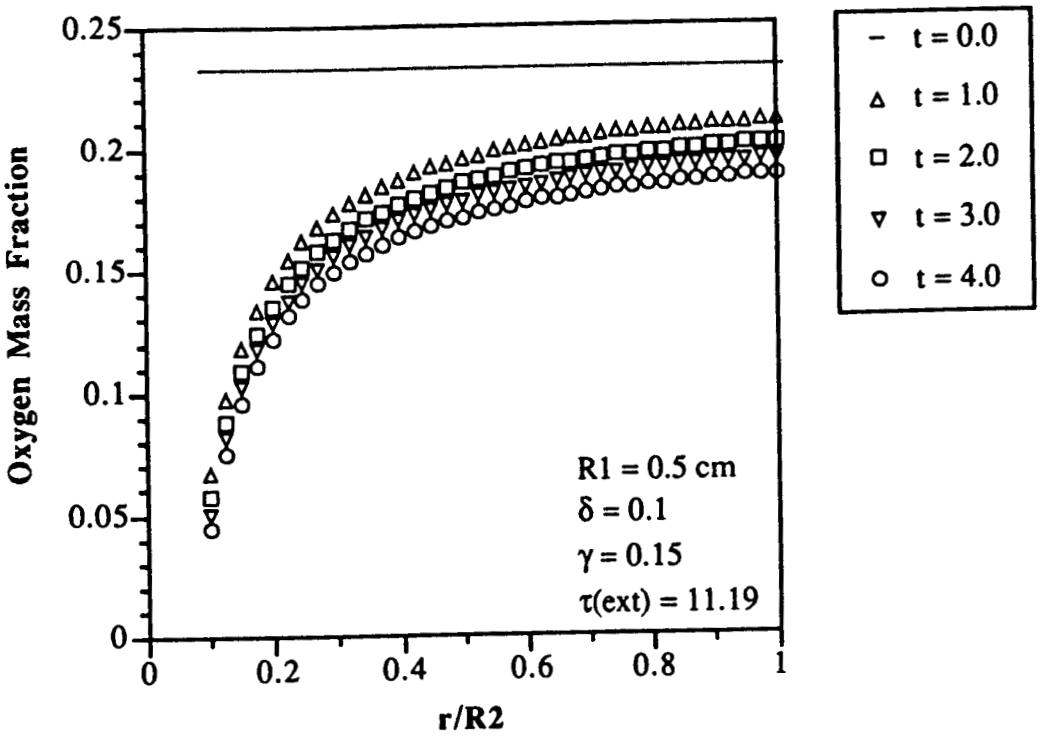

The actual time of extinction corresponds to about 2 minutes in this case.

The time at which the oxygen concentration at the flame front, or the flame lifetime, is very sensitive to the value of γ, the non-dimensional mass burning rate. Small values of γ lead to large flame lifetimes, and large values of γ to smaller flame lifetimes. In a more complete model of the candle flame, the mass burning rate and flame radius would be 'outputs' as opposed to 'inputs'. The value of γ is also temperature dependent since ρD is a function of temperature ($\rho D \sim T^{1/2}$). For the γ used above we assumed the density of air and the binary diffusion coefficient of oxygen into air at a mean temperature of 1500 K.

A few words about flame size are in order. The analysis above shows that the oxygen transport to the candle flame is, to a first approximation, determined by γ. γ is not necessarily fixed during the lifetime of the flame. In other words, as oxygen is depleted, the non-dimensional mass burning rate of the candle will change. Given the definition of γ though, it is impossible to know, without a more complete model, how the flame will respond as oxygen is depleted. The mass burning rate of the candle may decrease, the flame radius may increase, only one may change, or both may change. Further analysis of the results of Ross et al. (1990), however, suggests that the near quasi-steady flame size was nearly independent of the oxygen concentration from a 19% to a 25% oxygen ambient. Thus, we conclude that changes in the flame size as a result of oxygen depletion would not necessarily be expected.

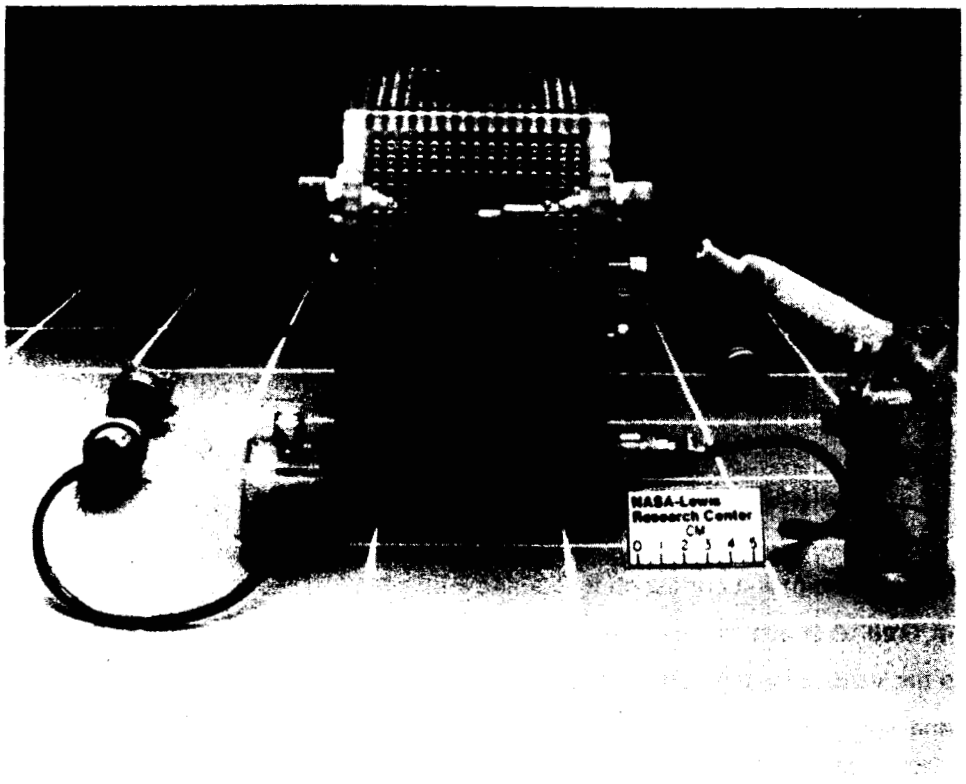

Figure 1 Hardware used in the Candle Flames in Microgravity experiment

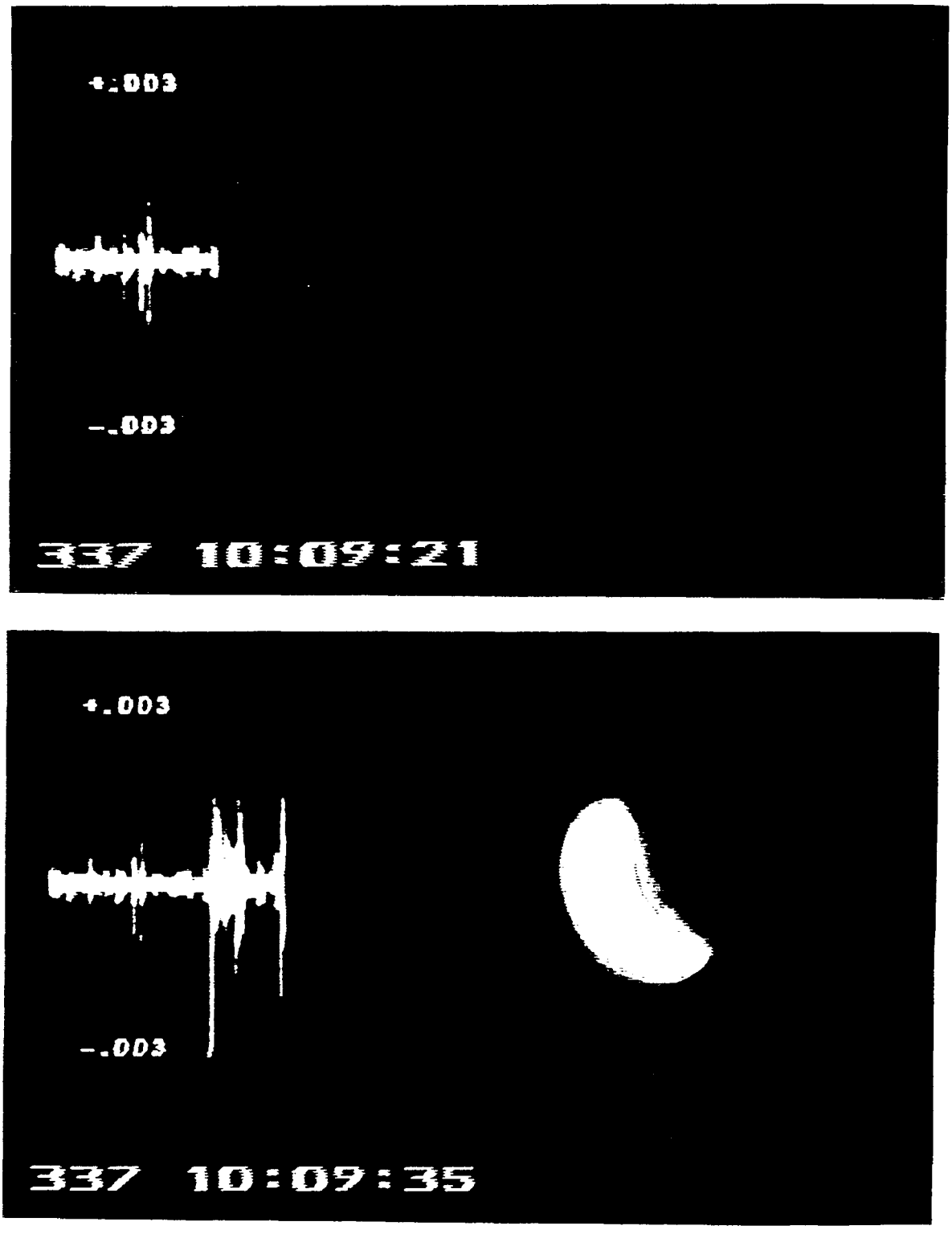

Figure 2 Candle flame in microgravity. On the right is the flame image. On the left is superimposed the SAMS acceleration data from the SAMS-x axis. The vertical scale is in m/sec^2, so divide by about 10 to obtain the value in terms of g_e. (a) Blue, hemispherical flame during quiet period; (b) 14 sec later, sooty flame apparently as a result of increased acceleration level.

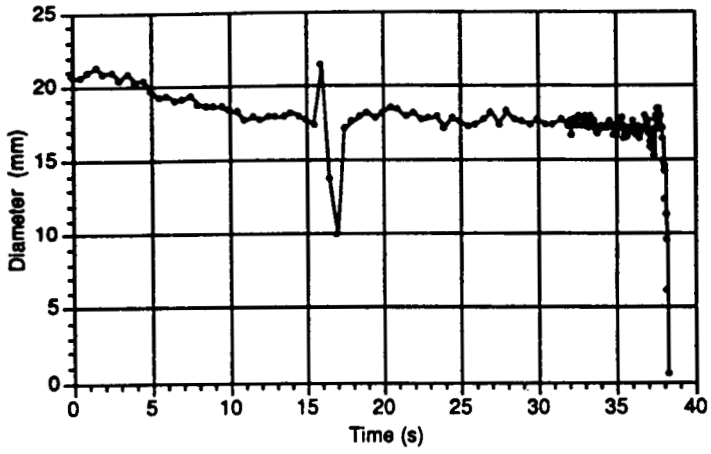

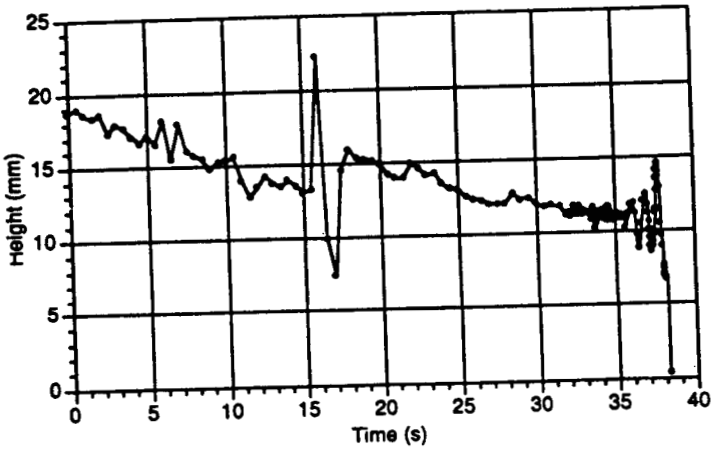

Figure 3 Evolution of flame shape (a) flame diameter; (b) flame height. Note the data showing a wide excursion at 17 sec is incorrect, a consequence of an error in the digitization of the motion analyzer.

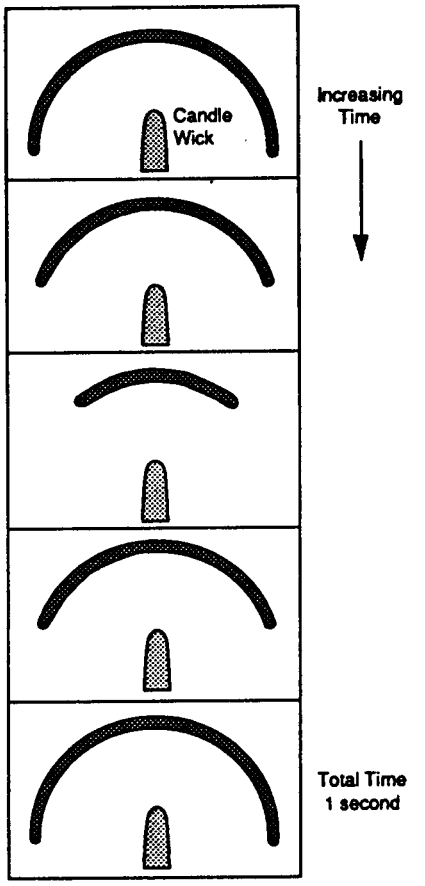

Figure 4 Near-extinction flame oscillations

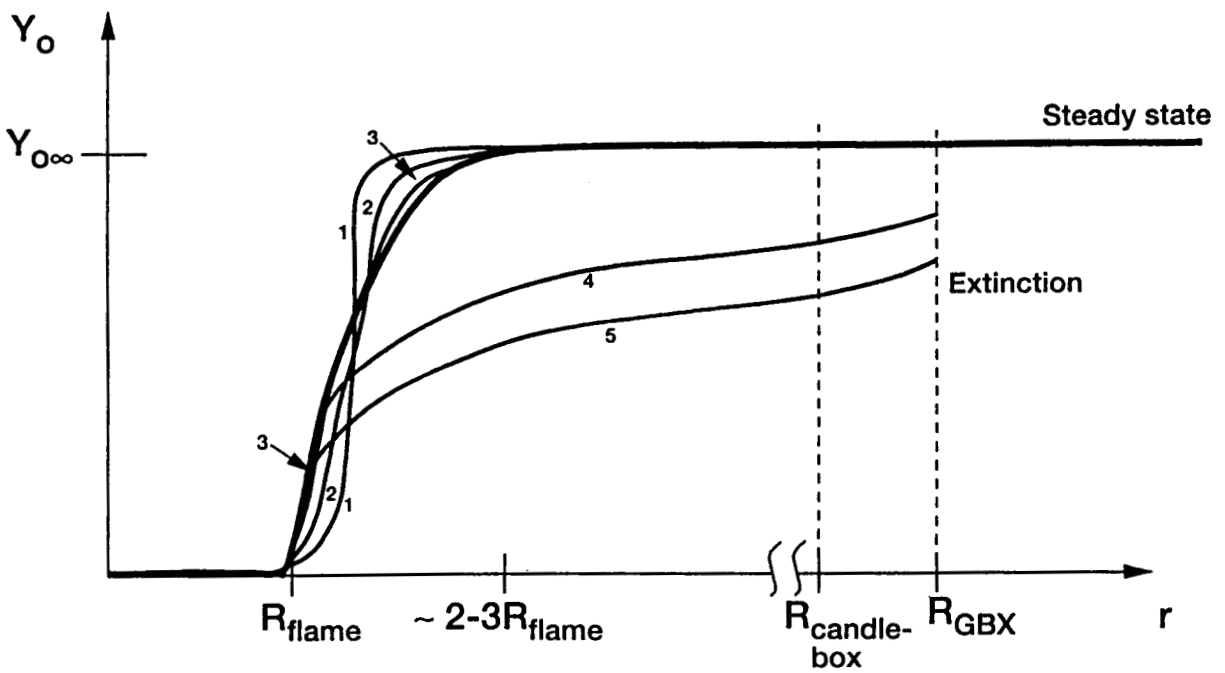

CD-93-64340

Figure 5 Oxygen concentration profile in the glovebox and at steady state in an infinite ambient with oxygen concentration $Y_{O\infty}$. Curve 1 shows the qualitative profile shortly after ignition, curve 2 at a slightly later time, curve 3 at a still later time, etc. Curves 4 and 5 show when the oxygen concentration in the far field has been somewhat depeleted.

PASSIVE ACCELEROMETER SYSTEM : MEASUREMENTS ON STS-50 (USML-1)

J. Iwan D. Alexander[1] and Melissa J. B. Rogers

Center for Microgravity and Materials Research
University of Alabama in Huntsville, Huntsville, Alabama.

ABSTRACT

The passive accelerometer system (PAS) is a simple moving ball accelerometer capable of measuring the small magnitude steady relative acceleration that occurs in a low Earth orbit spacecraft due to atmospheric drag and the Earth's gravity gradient. The accelerometer can be used when the spacecraft continuously rotates during the orbit such that some line of reference in the craft always points along the vector connecting the Earth's mass center with the spacecraft mass center. PAS was used successfully on the first United States Microgravity Laboratory (USML-1).

INTRODUCTION

The passive accelerometer system (PAS) was designed to measure the quasi-steady residual acceleration caused by a combination of atmospheric drag effects and the gravity gradient. This acceleration should be on the order of 10^{-6}g or less and is difficult to record accurately using conventional accelerometers. The acceleration is obtained indirectly by recording the motion of a small proof mass along an oriented tube filled with liquid. The trajectory and speed of the proof mass can then be used to find the residual acceleration indirectly using Stokes' Law [1-3]. Since the walls of the tube used in PAS affects the motion of the ball, the Ladenburg-Faxen-Francis [4] correction to Stokes' Law is applied.

I. APPARATUS AND OPERATION

The PAS consists of a 2 cm diameter glass tube with a wall thickness of 2mm. The tube is filled with water and contains a 0.2 cm diameter steel ball. At one end of the tube is a fill and pump port with a high vacuum stopcock valve. The tube is enclosed in a clear LEXAN tube. The LEXAN tube is sealed with two endcaps and is attached to modified camera tripod head to allow for

[1] This paper is dedicated to the memory of Dr. W.W. Fowlis who took part in many discussions about such an accelerometer with one of the authors.

a full range of orientations. The tripod head is mounted onto a steel plate which is backed with Velcro strips to allow for easy mounting to surfaces in the spacecraft. A pencil magnet is used to reposition the ball inside the tube.

A typical operation of PAS would be as follows:

The accelerometer tube is oriented such that the tube axis is approximately parallel to the estimated acceleration direction. The magnet is then used to position the proof mass at the end of the tube. The starting position of the proof mass is then recorded and a timer is started. At 1-2 minute intervals the payload specialist checks that the trajectory of the proof mass lies along the tube axis and records the time and position of the proof mass. If the angular deviation of the ball's trajectory from the tube axis is greater than 10 degrees, the tube is repositioned such that its axis lies along the trajectory of the proof mass. Each run is complete when the proof mass has traversed the length of the tube. Note that the attitude motion of the spacecraft must be one for which a quasi-steady gravity gradient acceleration is expected.

II. RESULTS

This section summarizes accelerometer readings made on STS-50 (USML-1) with PAS (Flight Deck) and OARE (Orbital Acceleration Research Experiment) on MET days 2&3, and a single data point from PAS taken near the Crystal Growth Furnace (CGF) on day 6. The PAS data represents an average over 8 measurements. Both the Flight Deck and OARE data are extrapolated to the CGF location. Both OARE and PAS data indicate that besides the gravity gradient and atmospheric drag effects, for the USML-1 mission there was an additional contribution to the quasi-steady residual acceleration vector. It contributed, approximately, an additional 0.5 mg acceleration along the negative x-direction (body coordinates see Fig. 1). This cannot be entirely accounted for by the Flash Evaporation System (FES)[2]. Note that the frame of reference of the residual accelerations presented here is taken to be the spacecraft frame and that the coordinate system refers to the "Orbiter body coordinates" (see Fig. 1). All acceleration vectors are represented in the form $\mathbf{a} = (a_x, a_y, a_z)$, where the components of **a** represent the projections of the total acceleration vector onto the x-,y- and z-body axes.

A. Flight deck accelerations

Readings were taken in Flight deck from days 1-5, and on remaining days measurements were made in the Spacelab. As can be seen from the table below, these readings produced consistent data

[2]R. Blanchard, OARE STS-50 Flight Data, final report, December, 1992.

and the PAS appeared to work best here. The flight deck readings form the best data set. Only the readings taken near the CGF in Spacelab produced a usable measurement. The remaining readings in Spacelab were either disturbed too frequently to yield useful data or the excursion of the ball was too small. Table I gives the ball velocities and associated acceleration for the flight deck.

At the flight deck location, the direction of the acceleration was chiefly along the positive x-body axis of the Orbiter. This is consistent at this location with the expected domination of the gravity gradient acceleration. Since we know the variation of the gravity gradient acceleration as a function of location [2,3] the flight deck results can be extrapolated to the CGF location.

B. Accelerations at the CGF location (extrapolated)

The acceleration, $\mathbf{a}^*$, calculated from extrapolated PAS Flight Deck data (MET days 2&3) is

$$\mathbf{a}^* = (-0.57, 0.14, -0.46)\ \mu g$$

This vector is illustrated in Fig. 2, and shows that the vector is tilted away from the CGF axis by about 15° in the y-z plane. The tilt direction is toward positive y. In the x-z plane the vector is tilted away from the CGF axis by about 50° toward negative x. The PAS measurement is compared to the two sets of OARE data given below. Each set has a mean vector and a maximum and minimum magnitude vector. The corresponding vectors are shown in Figs. 3-8.

The reading taken with PAS near the CGF yielded a magnitude of approximately 0.6 μg. The orientation of the tube was directed primarily along the negative x-axis, and tilted in toward the CM about 15 degrees (this is compatible with the (x,y) components of the acceleration measured in the Flight Deck and indicates that the gravity gradient component in the negative x-direction was augmented by an additional acceleration of about 0.5 μg magnitude, and that the drag was much smaller than 0.5 μg. The question is how much smaller? Here the PAS measurement made near CGF is inconclusive. The ball excursion distances were small, 1 cm, compared to 7cm in the Flight Deck. The reason for this was that the intermittent vernier firings disturbed the ball motion at 3-5 minute intervals. Only one reliable reading was obtained near the CGF and while the magnitude is a reliable measure, the orientation results are questionable when one considers the ball radius is such that excursions of 4-6 cm are necessary to distinguish the orientation of the residual acceleration vector. (A back-up accelerometer tube with a larger radius ball that would have moved further between vernier firings was available. Unfortunately, circumstances did not permit transmittal of a request for the tubes to be swapped).

REMARKS

- The PAS data and the OARE data both indicate that the net acceleration vector was not generally aligned with the CGF axis (see Figs. 3-8). If the drag had been 1 μg or greater then the

residual vector would have been closer to the CGF axis, although atmospheric density fluctuations will cause continuous orientation changes.

• Since the PAS location was displaced from the CGF along the x-axis the resultant vector would be expected to be oriented differently from the acceleration vector at the CGF due to gravity gradient effects.

• The resultant vector at CGF would only have lined up with the CGF axis if the drag had been 10^{-6} g. Had this been the case PAS would also have shown this orientation since drag would have dominated the gravity gradient. However, two things are apparent from CGF and OARE measurements:

• The gravity gradient acceleration along the x-axis is augmented by a 0.5 μg acceleration acting along negative x. This has the effect of tilting PAS away from the CGF axis.

• According to OARE and the PAS Flight Deck measurements, the actual drag was about 0.5 μg and OARE shows that at times it was lower. Under these conditions (even without the extra x-acceleration) the resultant acceleration vector would not have been aligned with the furnace axis but would be tilted at 25 degrees from the CGF toward positive y.

ACKNOWLEDGMENTS

The enthusiastic participation of the USML-1 crew and NASA's Glovebox support team is gratefully acknowledged.

Table 1. Flight deck data, days 1-5

U [cm s^{-1}]	Acceleration [cm s^{-2}]	Acceleration [g]
2.43×10^{-2}	4.34×10^{-3}	4.43×10^{-6}
2.52×10^{-2}	4.48×10^{-3}	4.57×10^{-6}
2.73×10^{-2}	4.87×10^{-3}	4.97×10^{-6}
2.49×10^{-2}	4.44×10^{-3}	4.53×10^{-6}
2.38×10^{-2}	4.23×10^{-3}	4.32×10^{-6}
2.57×10^{-2}	4.58×10^{-3}	4.67×10^{-6}
2.54×10^{-2}	4.53×10^{-3}	4.62×10^{-6}
2.56×10^{-2}	4.58×10^{-3}	4.67×10^{-6}

Maximum deviation in values 12% (occurred on same day)

Table 2. OARE data

set#1, FES off	Mean [μg]	Max [μg]	Min [μg]
a_X	-0.23	0.1	-0.5
a_Y	0.12	0.4	-0.1
a_Z	-0.75	-0.3	-1.0

set#2 , FES on	Mean [μg]	Max [μg]	Min [μg]
a_X	-0.6	-0.2	-0.8
a_Y	0.12	0.4	-0.1
a_Z	-0.4	-0.1	-0.65

REFERENCES

1. L. D. Landau and E. M. Lifshitz, Fluid Mechanics, Course of Theoretical Physics, Volume 6 (Pergamon, Oxford, 1979) p. 63.

2. J.I.D. Alexander, and C. A. Lundquist, AIAA Journal 26 (1988) 34.

3. J.I.D. Alexander, and C. A. Lundquist, J. Astr. Sci. 35 (1987) 193.

4. A. W. Francis, Physics 4 (1933) 403.

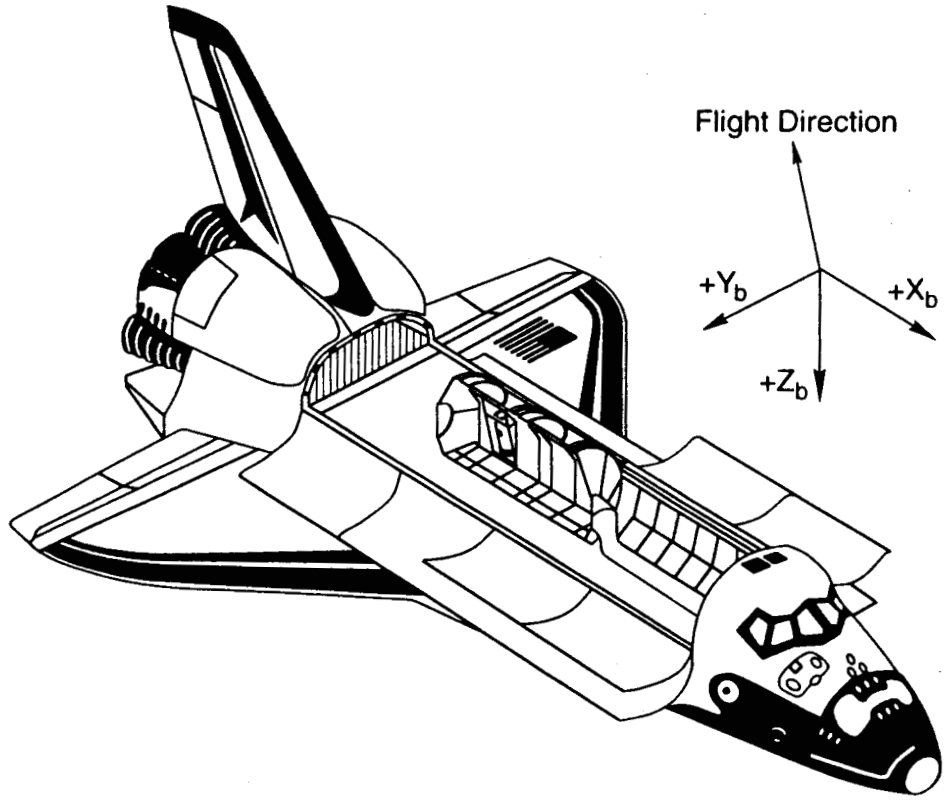

Figure 1

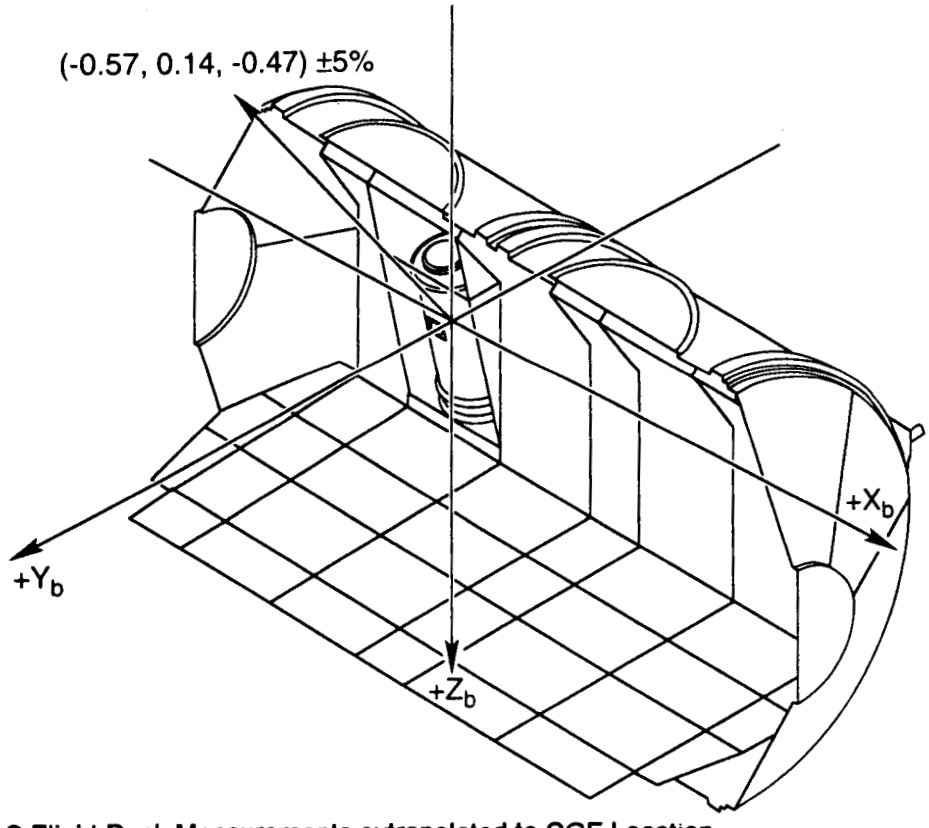

Figure 2 PAS Flight Deck Measurements extrapolated to CGF Location.

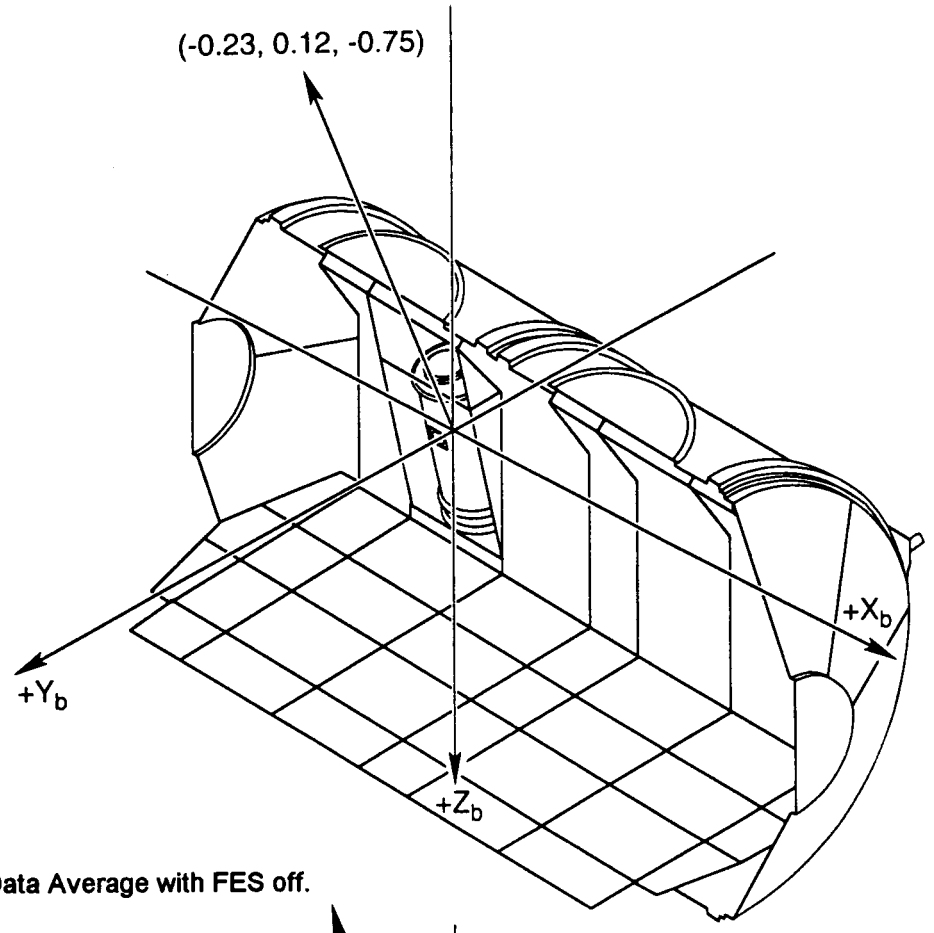

Figure 3 OARE Data Average with FES off.

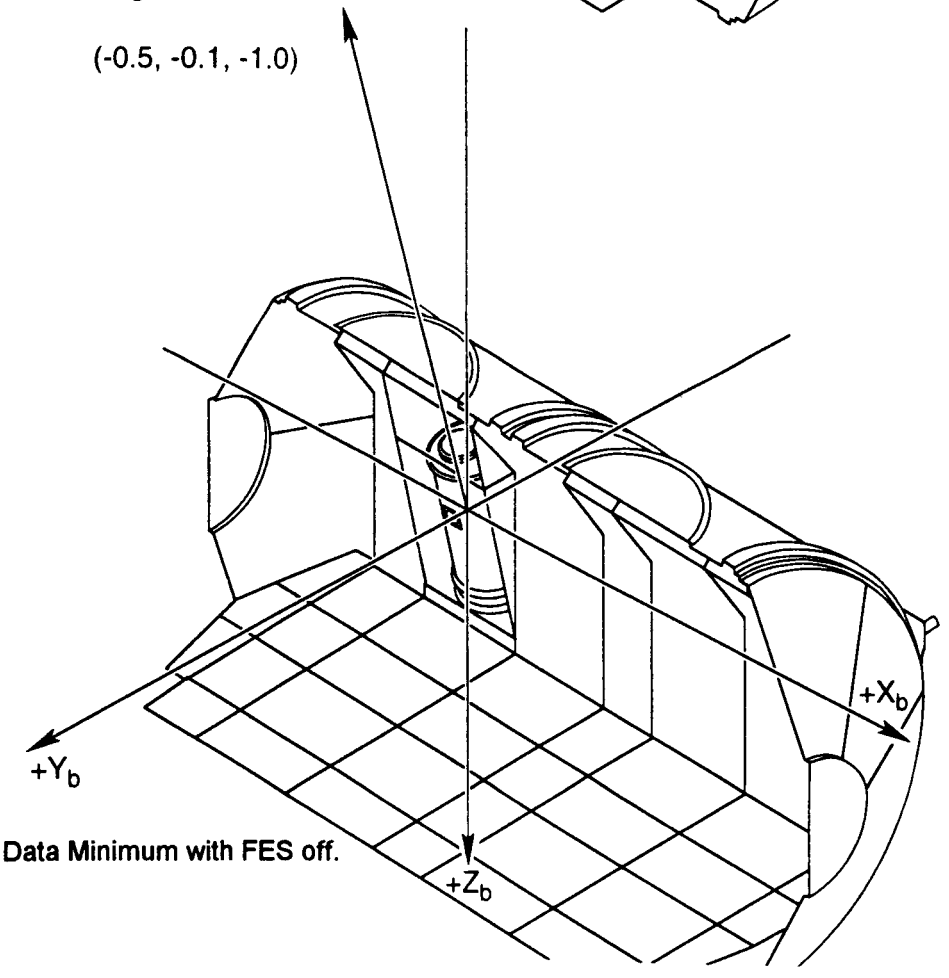

Figure 4 OARE Data Minimum with FES off.

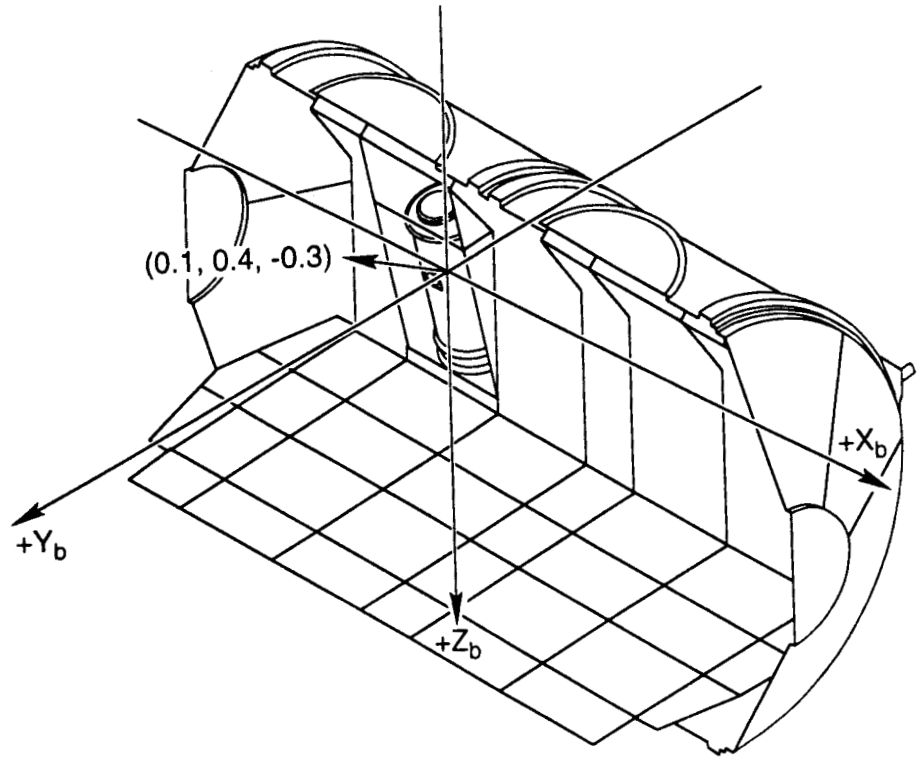

Figure 5 OARE Data Maximum with FES off.

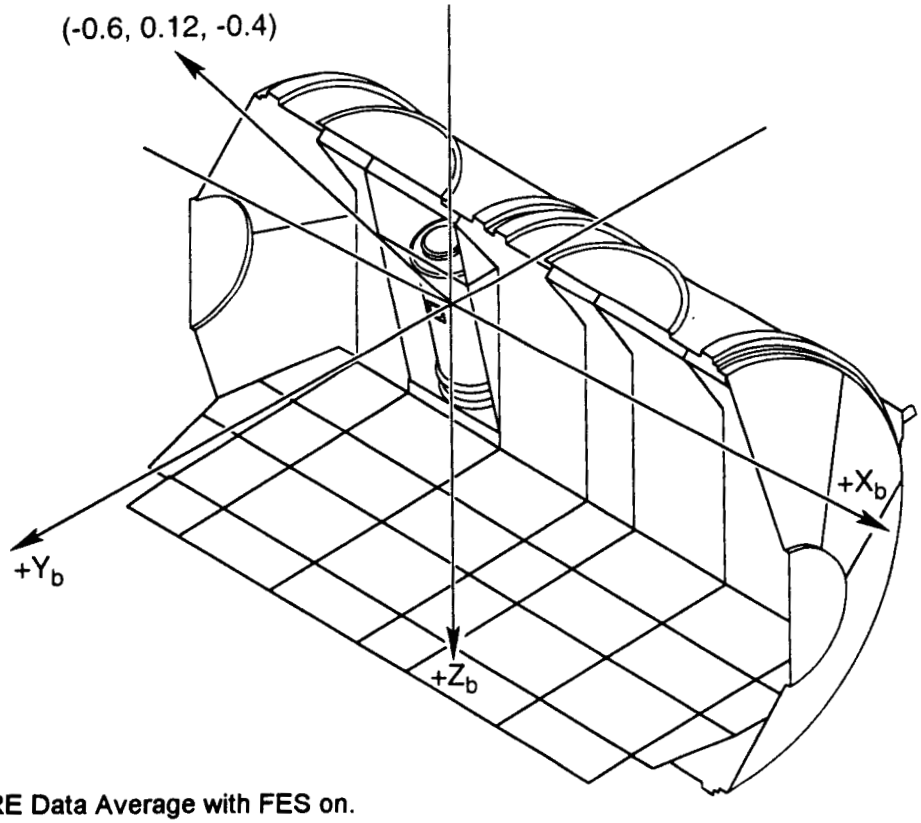

Figure 6 OARE Data Average with FES on.

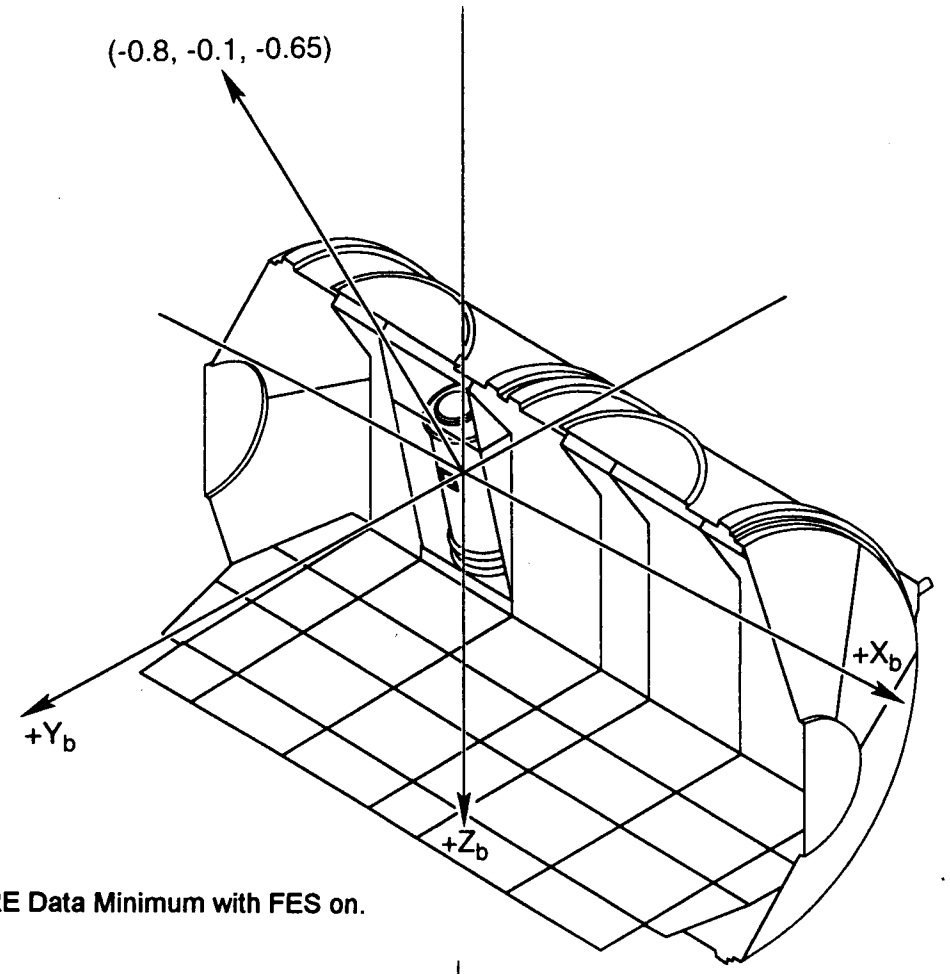

Figure 7 OARE Data Minimum with FES on.

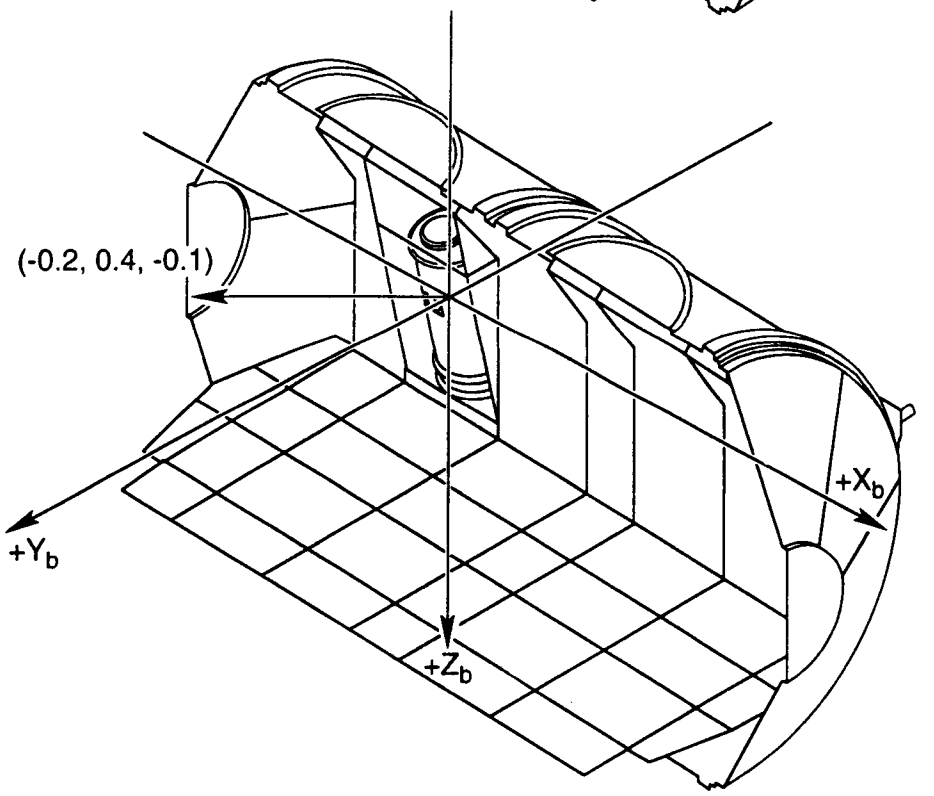

Figure 8 OARE Data Maximum with FES on.

Discussion

Question: *To what extent does the drag correction vary with the distance of the sphere from the wall ? It seems it would be another detail that you would have to subtract to get at the final numbers.*

Answer: Yes. We did some tests in our lab with different viscosity silicone oils. Mainly we used 500,000 centistokes and we wanted to get as close to the equivalent of 10^{-6} g's as we could, and I think that comes out to about 10^{-5} g's. If it is touching the wall, it is terrible. If it is slightly off axis then it is hard for me to quantify what that means because we were just basically dropping them in. If it kept greater than a radius away from the wall it affected the rate by approximately 5-10% or so; however, we got that much variation from dropping them down the middle anyway, so I couldn't really tell the difference. I had someone do about 20 or 30 of those drops.

Question: *I just have a couple of questions to ask. First of all, have you made any measurements at all or made any attempt to find out what effect magnetic fields will have from the Orbiter or even magnetic fields from Earth ?*

Answer: Well I have gathered that the crew got worried about that, and they moved some things around. Bonnie Dunbar may have a comment about that. When you put it too close to a strong magnet, it was sensitive. As far as it's response to weak fields, I mean it is hard for me to estimate. You would have to tell me what it was around. I understood the pilot had been concerned about one package that was in there that was able to move around that he thought might be affecting it, but you couldn't see anything.

Question: *Based on OARE data and your data, how far off was the CGF axis on an average ?*

Answer: That is a good question. For the answer to that, let me show some plots. This is an average with the flash evaporated system on and so you see some variation. It is different when it is off. This is only for a 3 day portion of the mission. So I think it can vary quite a lot, but you have got to look at the magnitude for when it is varied. There is an OARE measurement that we have, which is this one, which is pointing in almost the same direction for example as PAS was. You remember that you had about a half micro-g extra in that direction from some as yet unexplained origin plus it is almost a meter away from CGF. So you have gravity gradients of almost 0.4 micro-g's anyway, at that location, so you would expect it to be pointing away from flight direction unless you had it right on top of CGF. It is not as bad as it looked.

Question: *Do you have an idea how sensitive your system is ?*

Answer: I think I measured 10^{-6} g very well. I don't think I measured 10^{-7} g very well, because the environment that I was making the measurement in perturbed the heck out of the motion on that beebee on that time scale it took to measure 10^{-7} g with some confidence. So I would have to say, "yes, I can do it ", but I have to change the tube radius and the ball radius.

Question : *What was the amount of time you spent for each measurement ?*
Answer: In the flight deck? Approximately 4 minutes or so.

Question: *These are not momentary or instantaneous measurements then ?*
Answer: No. You must get a finite measurable excursion of the ball.

Question: *Over how long a period of time ?*
Answer: Well how ever long it takes.

Question: *Can you at least provide an estimate ?*
Answer: It varies. I am making a velocity measurement and it is an average velocity. So, for example, if I tell you to get an unambiguous angular measurement, I must have a 5 cm excursion of the ball. It is just how long it takes for it to move 5 cm. So if you watched it for 20 minutes, which is what the time is for the magnitude acceleration of that location, that is about how long it would have taken. Unfortunately that is not a good measurement because it is being perturbed all the time. I didn't want averages from the thrusters I just wanted to get the gravity gradient from the atmospheric drag.

Question: *I just want to make a comment quickly. Is it possible that you could redesign your instrument? Instead of being a long tube, to be a sphere or something of different dimensions and maybe containing 2 or 3 different ball sizes because the magnet that you were using was capable of moving the ball around even from about 6 inches away. So you could get to your ball, bring it to a starting point and then essentially watch where it tracks across and where it hits the sphere. That would give you all the angular information and the dimensions would give you the velocity roughly. Would this be a possible candidate?*
Answer: You can do that but then you have to start wondering, well, this is going to start getting a little bit complicated and I have to be careful, a lot more careful about how I track the motion of it. Then when you start adding up how much that costs and you think we can do much better than that and simply go and take a look at the standard accelerometer design and try to understand how to modify that design specifically for a 10^{-6}g measurement. Most of our accelerometers are much more jittery than that.

What we want to do here is to pick up that very quasi-steady motion and measure it not over a short time period but a long time period and try to find a way to eliminate the noise that is inherent in most accelerometer readings. You could take an idea that you could damp your accelerometer sufficiently, maybe using viscous means, take some ideas from a simple thing like that, and apply them to modern accelerometry and maybe that is the way to go. It is just going to be a question of what lengths you are going to have to go to. It can be improved drastically beyond this. That is a fact.

Question: *I saw two readings of the y component. One was 0.1 and the other was 0.4. I am not clear how you can get such a y variation. As I understand it, the y variation was in the gravity gradient field ?*
Answer: But if you remember because this thing was not flying exactly bay doors to the velocity vector you get a Y component. Now when the atmosphere density changes you will pick up that change on a component and that change is projected onto the Y axis.

Question: *That was only about 12°, right ?*
Answer: It doesn't matter. We have one magnitude along Z where the atmospheric drag is a micro-g.

Question: *There was some discussion on Lorentz force which would also have some sort of orbital frequency associated with it. I saw a pretty big number put up there for the static charge carried, a nontrivial fraction. Is that a totally trivial effect under the geomagnetic field or does that add up to something on the order of a fraction of the micro-g?*
Answer: I had always thought that based on the order of magnetic estimates that was around something times 10^{-8} g contribution but I am not an expert in that area myself. I would like to know more about that.

Question: *Do you see a difference in drag as you go in and out of the day/night terminator ?*
Answer: I didn't get my measurement in space where I would be able to say that. I only had 8 or 9 measurements in the flight deck alone, so there is not enough data to say so but I think yes you would see it.

SOLID SURFACE WETTING AND THE DEPLOYMENT OF DROPS IN MICROGRAVITY

E. H. Trinh and J. Depew

Jet Propulsion Laboratory
California Institute of Technology

ABSTRACT

The complete or partial deployment of liquid samples in low gravity is primarily influenced by the interfacial properties of the specific liquid and solid materials used because the overwhelming bias of the Earth gravitational acceleration is removed. This study addresses the engineering aspects of injecting and deploying drops of prescribed volume into an acoustic positioning chamber in microgravity. The specific problems of interest are the design, testing, and implementation of injector tips to be used in a simultaneously retracting dual-injector system used in the Drop Physics Module microgravity experiment facility. Prior to release, the liquid to be deployed must be retained within a restricted area at the very end of the injectors even under dynamic stimuli due to continuous injection flow as well as to the stepped motion of the injectors, and the final released drop must have a well determined volume as well as negligible residual linear or angular momentum from the deployment process. The outcome of Earth-based short-duration low gravity experiments had been the selection of two types of injector tips which were flown as back-up parts and were successfully utilized during the USML-1 Spacelab mission. The combination of a larger contact surface, liquid pinning with a sharp edge, and selective coating of strategic tip surfaces with a non-wetting compound has allowed a significant increase in the success rate of deployment of simple and compound drops of aqueous solutions of glycerol and silicone oil. The diameter of the samples studied in the Drop Physics Module ranged between 0.3 and 2.7 cm. The tests conducted on-orbit with a manually operated small device have allowed the calibration of the volume deployed for a few drop sizes. The design for improved tips to be used during the next USML flight is based on these results.

Joint "L+1" Science Review for USML-1 and USMP-1 with the Microgravity Measurement Group, September 22-24, 1993, Huntsville, Alabama, USA.

INTRODUCTION

The shape of the free surface of liquids in contact with solids remains a subject of great interest especially when the overriding influence of gravity is removed.[1,2] In addition to basic theoretical interest, the correct implementation of fluid management methods in low gravity relies on our understanding of the interfacial statics and dynamics between liquids and solid surfaces [3]. Even when one is interested in the observation of the behavior of completely free three dimensional liquid surfaces, the actual process of going from a contained liquid into a containerless environment is of primary importance. The study to be described below is a limited experimental investigation designed to develop, test, and implement a specific component for the controlled deployment of liquid samples in low gravity. It was designed as a low cost flight investigation in the framework of the USML-1 Glovebox facility and in support to the on-orbit operations of the Drop Physics Module, an experiment facility dedicated to the study of the dynamics and rheology of the surface of free drops in microgravity.

I. THE PROBLEM

The objectives of the investigation of the behavior of free drops in low gravity can only be rigorously satisfied when these drops are actually deployed in a well controlled manner with well defined volume and an uncontaminated surface. The weak acoustic positioning forces used in the Drop Physics Module (DPM)[4] will be effective at restraining the drop motion in a short amount of time only when the residual momentum imparted to the sample during the deployment process is negligible. The approach taken in this facility utilizes a pair of oppositely situated symmetrical injectors which simultaneously retract at high speed to leave a motionless drop in the center of the experiment chamber. This technique has been shown to be very effective when the liquid and solid deployment surface are characterized by a very large contact angle. The standard tips of the injectors are made of stainless steel and are 0.75 mm in diameter. The approach is thus to minimize contact between the drop and the injector tips by reducing their diameter to a minimum. The drop volume of interest ranged between 0.5 to 20 cm^3 . *Figure 1a* is a picture of the opposed injectors with the standard tips as they are positioned in the center of the DPM chamber without a drop, and Figure 1b shows them with a drop positioned in a desired configuration in microgravity.

Even for reasonably high contact angle (about 90° for distilled water and stainless steel) symmetrical wetting of both injector tips must be maintained in order to avoid spreading of the liquid over a single injector surface as shown in Figure 2. In this case contact was broken with the upper left injector and the liquid spread over the lower right injector surface. The subsequent remerging of the two drops produced a liquid bridge anchored at the edge of the V-shaped injector housing.

The majority of the liquids used for the drop physics experiments during the USML-1 Spacelab flight, however, displayed low contact angles with clean stainless steel surfaces. This made it quite difficult to maintain the configuration shown in figure 1b under the continuing mechanical impulses due to the liquid injection and the stepped motion of the retracting injectors. Liquids such as silicone oil and aqueous mixtures of organic surfactants will spread over the contacting solid surface upon very slight impulses. Figure 3 shows a case where a glycerol-water mixture has spread over the injector tip and past the V-shaped edge in the case of the lower right injector. The subsequent deployment was asymmetrical as evidenced by the non-simultaneous breaking of the liquid necks (Figure 3c). This asymmetry imparts linear momentum to the drop, and it results in translational oscillations of the sample in the acoustic pressure well.

The behavior of liquid bridges in low gravity has been investigated by others in the past both during parabolic flights as well as during Spacelab missions [5,6], and the characteristics of liquid-solid interfaces relating to the aspects of liquid management have also been addressed in both static[7] as well as dynamic cases[8]. In this instance we are concerned with the additional impact of the deployment dynamics on the behavior of the released drop.

II. OBJECTIVES

The objectives of this flight demonstration were simple and limited in scope: The first task was to experimentally study the dynamics of drop injection, containment, and deployment in order to design specific injector tips which would minimize all detrimental impact. The second task was to manufacture a set of tips for use in microgravity with a manually operated apparatus to be used in the Glovebox facility in order to calibrate the deployed volume. An important aspect of this investigation was the ability to also use these tips in the DPM facility, and consequently, a third objective was to utilize these tips in case difficulty was encountered during deployment in microgravity.

III. GROUND-BASED DEVELOPMENT

The process of injection, stabilization, and deployment of liquid samples can be carried out in a 15 to 20 seconds time period for liquid volumes less than 5 cm^3. This has made it possible to perform experimental tests during parabolic flights of the NASA KC-135 airplane prior to the USML-1 mission. The same manually operated mechanical drop deployment device built for the Shuttle Glovebox experiment was flown aboard the KC-135 to study the dynamics of drop injection and deployment with the standard small diameter injector tips as well as with a variety of custom-designed tips. Figure 4a is a photograph of the apparatus as operated in the KC-135, and Figure 4b shows the same device on the Spacelab Workbench as it was configured for the experimental runs during the USML-1 flight.

Only distilled water and silicone oil (100 cSt viscosity) were deployed during the parabolic flight tests as they were considered the best and worst cases as far as drop deployment was concerned. All the tips tested were coated with a commercial surface treatment (trade name Nyebar).

Distilled water did not spread over the coated small diameter (0.75 and 1.5 mm OD.) cylindrically shaped stainless steel and brass tips, and could be held between the opposing injectors and deployed without difficulty. The cohesive forces of water were able to overcome the adhesive forces between the liquid and the coated solid surfaces. This allowed the controlled deployment of water drops of up to 2 cm^3 in volume in an environment where the background residual acceleration was on the order of 0.05 G with transients on the order to 0.1 G (G is the magnitude of the Earth-based gravitational acceleration). *Figure 5* illustrates the effectiveness of the surface coating by showing the wetting of coated stainless steel tips by distilled water. Initially asymmetric wetting of the tips can be changed to symmetric wetting and positioning of the drop at the tip ends, allowing symmetric deployment of the sample.

Silicone oil, on the other hand, readily spread over the injector tip surface, and could not be deployed in a controlled manner by using small diameter cylindrical tips. Wider faced injector tips were thus designed in order to contain silicone oil and other spreading liquids. They allowed the demonstration of not only stable capture of oscillating liquid bridges, but also that of successful deployment of silicone oil drops as shown in Figure 6. Low gravity tests aboard the KC-135 have therefore established that the fast retraction of opposed injectors allowed the deployment of silicone oil drops of up to 2 cm^3 in volume with negligible residual momentum even with tips having a significant contact surface area (18 mm^2). This led to the selection of two tip designs for implementation in microgravity: type **a** tips have a flared out face of 9.5 mm in outer diameter and 1.75 mm in inner diameter and type **b** tips are cylindrical in shape with an outer diameter of 4.75 mm with a inner diameter of 1.55 mm. These two different designs are shown in Figures 7 where they have been mounted on the Drop Physics Modules injectors. Both these types of tips have 90 degrees sharply machined edges, and the flight units have been completely surface treated with a Nyebar solution through a dipping and bakeout procedure.

IV. EXPERIMENTS DURING THE USML-1 FLIGHT

Drop deployment experiments using the designed tips described above have been carried out both in the Drop Physics Module facility as well as on the Spacelab Workbench. Contrarily to initial plans, the tips were successfully used in the Drop Physics Module prior to tests in the Glovebox facility. Since feasibility had been demonstrated, the goals of the Glovebox demonstration were restricted to manual deployment and calibration of large drop volumes from 5 to 12 cm^3 .

A. Spacelab Workbench tests

Initially scheduled at the beginning of the mission for performance in the Glovebox facility, the drop deployment tests were postponed until the seventh day, and were carried out on the Spacelab workbench. The experimental set-up is shown in figure 4b, and the Orbiter video camcorder was used to record the experiments. The apparatus was gray-taped to the workbench surface, and existing Spacelab and workbench lighting were utilized.

Working well below the stability limit for liquid bridge (cylindrical zones with aspect ratio only up to 2.6 were generated), very symmetric manual injection and deployment of water, aqueous mixtures of glycerin, and surfactant solutions was carried out and video recorded or transmitted live to the ground. *Figure 8* shows the sequence of injection and deployment of a 5 cm^3 water drop.

Detailed observation of the dynamics of drop deployment reveals that for larger droplet volumes (greater than 5 cm^3) the majority of the liquid remains undisturbed and motionless as the injector withdraw symmetrically at high speed. The necks on both sides of the central drops elongate and break leaving no or several satellite droplets depending on the liquid viscosity. The small fraction of the liquid remaining on the injector faces (5 to 10%) appears to primarily depend on the size of the contacting surfaces and on the retraction velocity.

The results of the measurement of the deployed drop volumes are displayed in table I. These data have been gathered for distilled water and for the wide-faced tips. Three different desired volumes were investigated, and three different runs were carried out for each volume. The drops could not be captured in mid-air as planned, but they were retrieved from the walls of the Lucite chamber on which the liquid did not spread, thus allowing recovery of the entire sample. The volume measurements were obtained through a calibrated micrometer-driven syringe with an accuracy of 0.005 cm^3. The reproducibility obtained through this limited set of measurements indicate a volume reproducibility of +/-2 % at worst. Part of this variation might be attributable to the variation in retraction velocity inherent of the manually operated device. The stepper motor-controlled injection system of the Drop Physics Module provides more reproducibility in the retraction velocity as well as higher rates.

B. Drop Deployments in the Drop Physics Module

Both types of tips were successfully used during the experiment runs of the DPM facility for the deployment of simple as well as compound drops (a drop within a drop) of aqueous mixtures of glycerol, silicone oil, and hydrocarbon compounds. The sharp 90° edges of the tips contained the liquid within the required surfaces during the first injection and deployment, but the sudden stop at the end of the injector retraction invariably drove the liquid beyond the pinning edge, and allowed the spreading of the liquid

over the body of the tips. The liquid containment for silicone oil was so precarious that in one particular instance the bursting of a bubble caused the liquid to spread beyond the pinning edge.

Figure 9 displays a series of video frame printouts from a recorded deployment of a drop of water-glycerol mixture of 50 cSt viscosity using the cylindrically shaped tips (type **b**). Near perfect symmetry can be observed by noting the breaking points of the necks on each side of the drop as well as the symmetrical shapes of the residual shape oscillations. Figure 10 is a similar series of video frames depicting the deployment of a 100 cSt silicone oil drop using the wide-faced injector tips (type **a**). Good symmetry can be observed once again. The deployed sample remained motionless in both instances.

Type **b** tips were also successfully used to inject and to deploy compound drops of a water-glycerol solution into a silicone oil drop.

CONCLUDING REMARKS

Liquid wetting and spreading acquire greater importance in microgravity when one becomes concerned with containment and material contamination management. Notoriously difficult to handle liquids such as silicone oil and surfactant solutions must be restricted to limited areas by physical barriers such as a sharp pinning edge. Although this latter technique is not foolproof, it appears to be effective in normal acceleration conditions of the Space Shuttle. In the restricted area of drop deployment, the results of these low gravity tests show that a compromise involving a larger liquid-solid contacting area will still allow the reproducible deployment of drops with controlled volumes. Because orbital operation time is extremely valuable, drop deployment procedures which minimize liquid clean-up and sample translational oscillation damping times must be adopted.

Improvements based on these results will involve the elimination of sudden acceleration pulses in the direction tending to induce liquid spreading, sharper pinning edges (30 or 45° instead of 90°), slower liquid injection rates or larger injector bores, and finally real-time crew interaction with the injection/deployment mechanism.

ACKNOWLEDGMENTS

This work was carried out at the Jet Propulsion Laboratory, California Institute of Technology under contract to the National Aeronautics and Space Administration. The authors gratefully acknowledge the support and assistance of the MSFC USML-1 Glovebox engineering team.

REFERENCES

1. P. Concus and R. Finn, *On capillary free surfaces in the absence of gravity*, Acta Math. *132*, 177 (1974)

2. P. Concus and R. Finn, *Continuous and discontinuous disappearance of capillary surfaces" in Variational Methods for Free Surface Interfaces*, P. Concus and R. Finn (Eds.), Springer-Verlag, New York, Berlin, p. 197-204 (1987)

3. G. Smedley, *Containments for liquids at zero gravity*, Microgravity Sci. Technol. III *1*, 13 (1990)

4. A. Croonquist, *The Drop Physics Module on USML-1: DPM Hardware and Science,* Conference paper *AIAA 93-4309*, Am. Inst. of Aeronautics and Astronautics, Space Programs and Technologies Conference, Huntsville AL, Oct. 23, 1993

5. I. Martinez, Proceedings of the 6th European Symposium on Material Science in Microgravity conditions, ESA *SP-256*, 235 (1987)

6. J.F. Padday, Ibid., 251 (1987)

7. J.F. Padday, Ibid., 49 (1987)

8. D. Langbein, Ibid., 221 (1987)

TABLE I

Results of the measurement of the deployed drop volumes. The samples were retrieved with a micrometer-driven syringe, and the measured volumes are listed together with the desired injected volumes.

Injected Volume cm^3	Deployed Volume cm^3
5	4.45
5	4.35
5	4.52
7	6.28
7	6.20
7	6.30
12	11.65
12	11.45

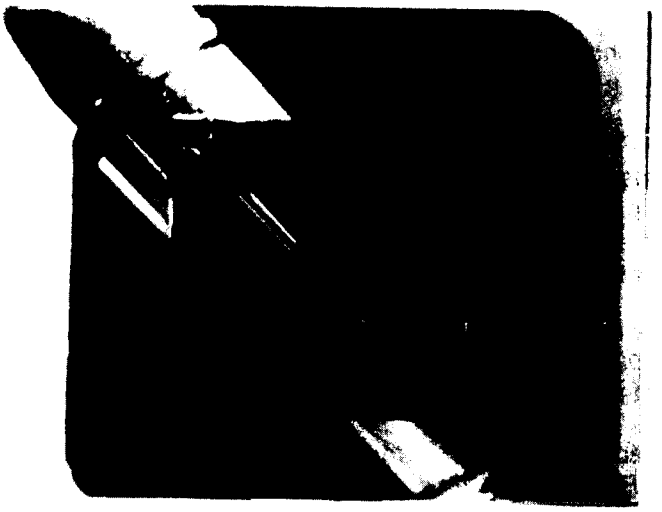

1a

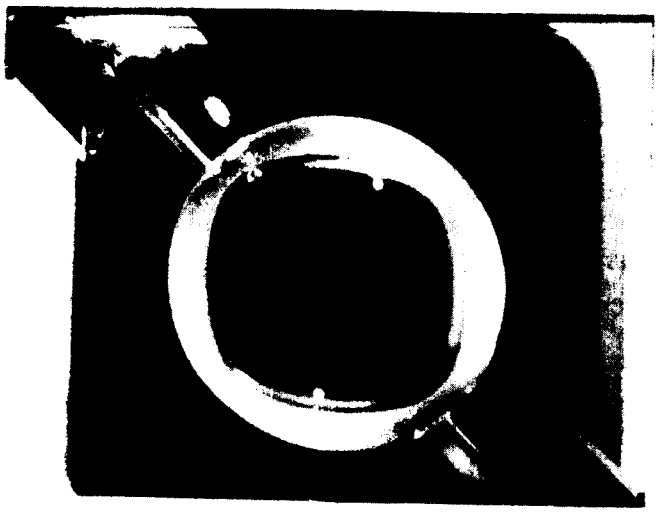

1b

Figure 1 1a. Small diameter standard DPM injector tips and housing as viewed along the Z axis of the experiment chamber

1b. Nominal configuration for a drop to be deployed. The small contact surface between the tips and the drop and the symmetrical retraction of the injectors insure that a very small fraction of the liquid remains on the injector tips and that minimal momentum is imparted to the released sample.

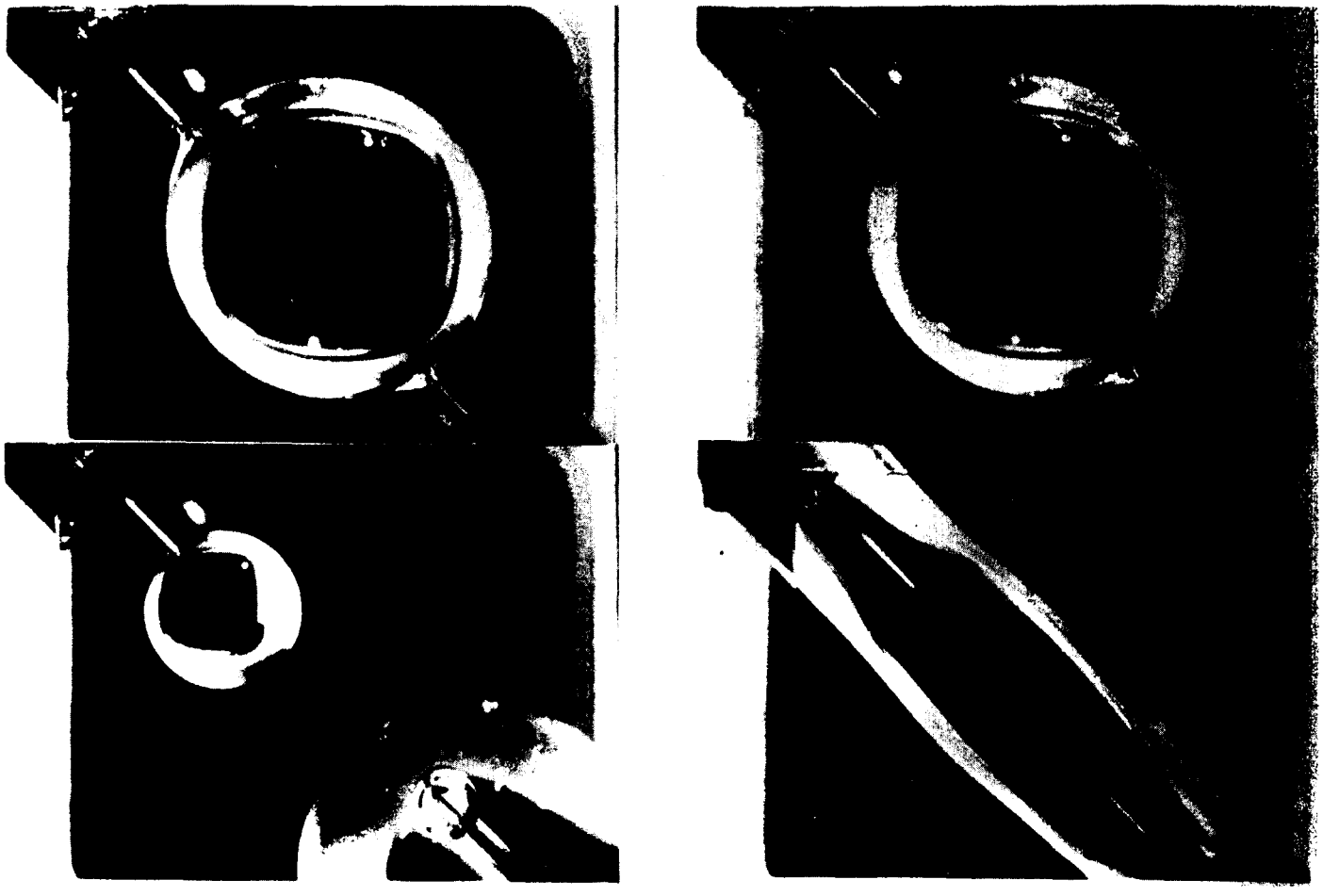

Figure 2 Still video frame sequence showing the loss of contact with one injector tip and the subsequent spreading of the liquid (distilled water) all the way to the injector housing collar (V-shaped solid surface). For a non-spreading liquid like water, this can be prevented by maintaining a larger contact surface with both tips.

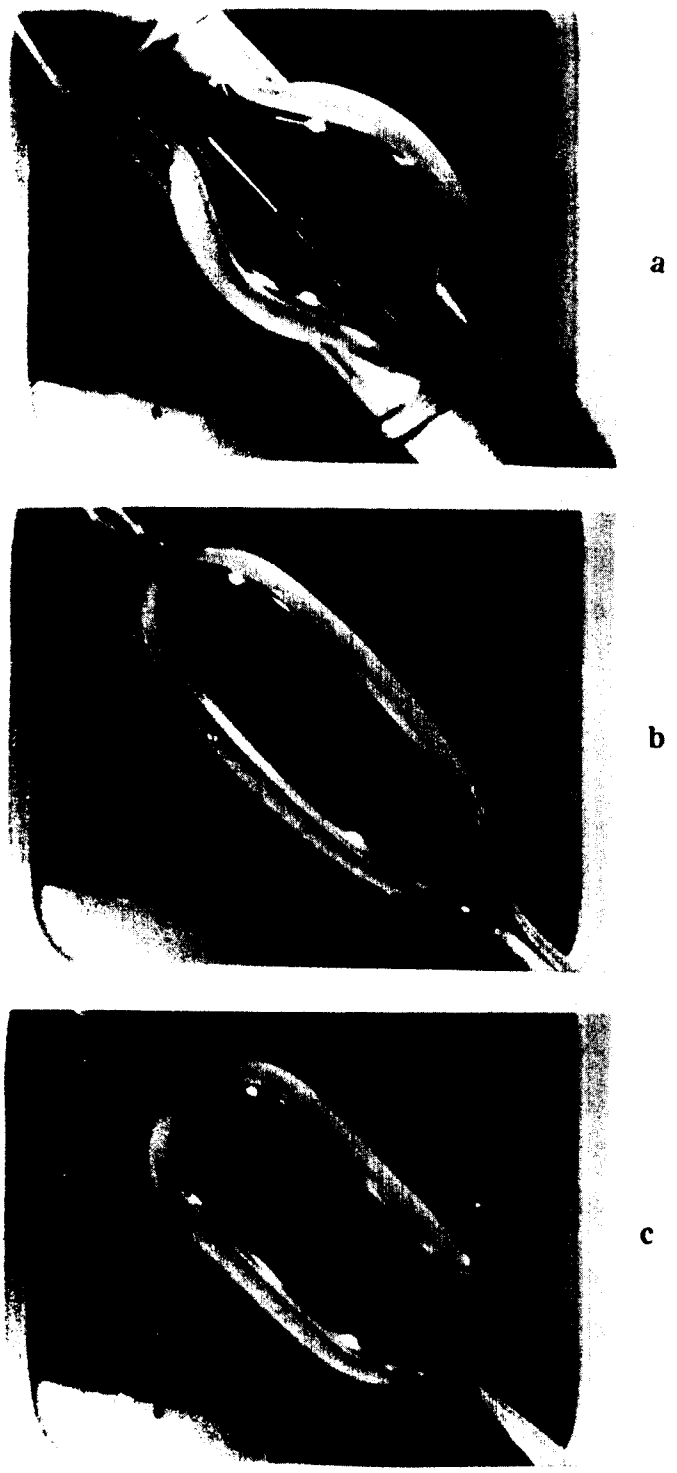

Figure 3 In these video frames a water-glycerol mixture has spread past the V-shaped housing to the O-ring on one side of the lower-right injector (a). Subsequent deployment creates an initial time lag in the breaking of the liquid neck connecting the drop to the more wetted injector (b and c). This unbalance does not necessarily result in the induction of linear momentum, but it influences the initial dynamics of the released sample.

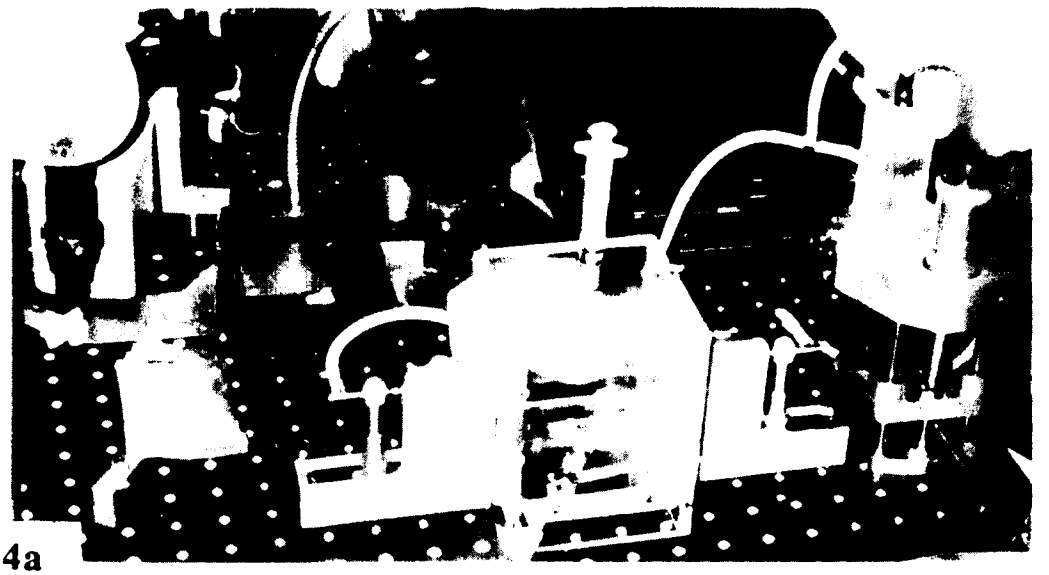

4a

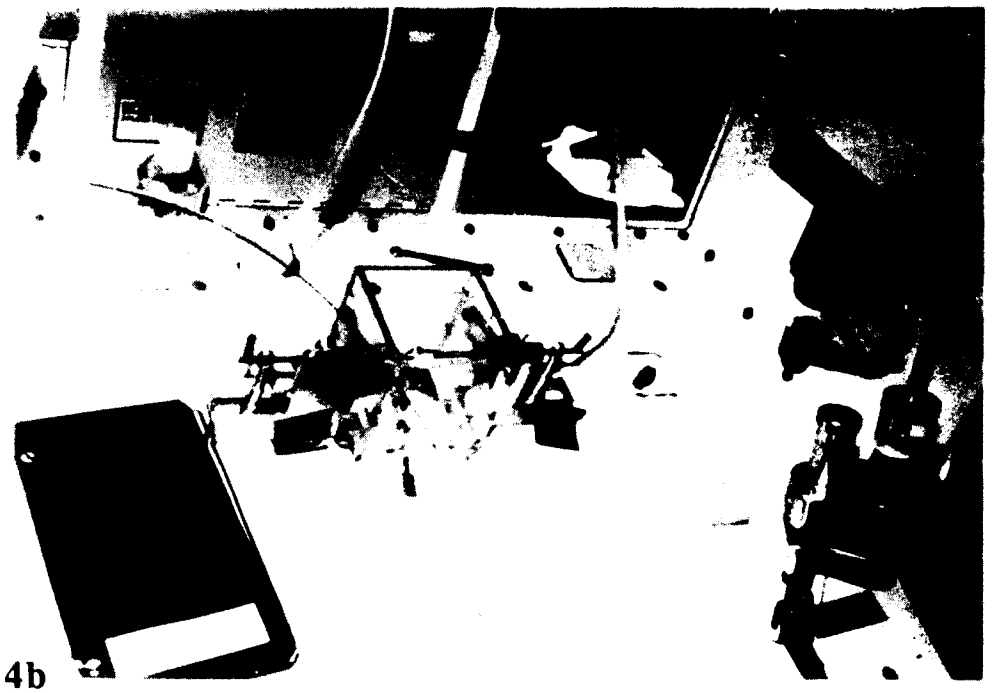

4b

Figure 4 4a. Manually operated Glovebox demonstration apparatus as installed on a breadboard during short duration low gravity tests aboard the NASA KC-135 aircraft.

4b. The same apparatus installed on the Spacelab Workbench during the USML-1 mission. The apparatus was taped to the work surface, and the operations were recorded and downlinked to the POCC using the Orbiter 8 mm video Camcorder.

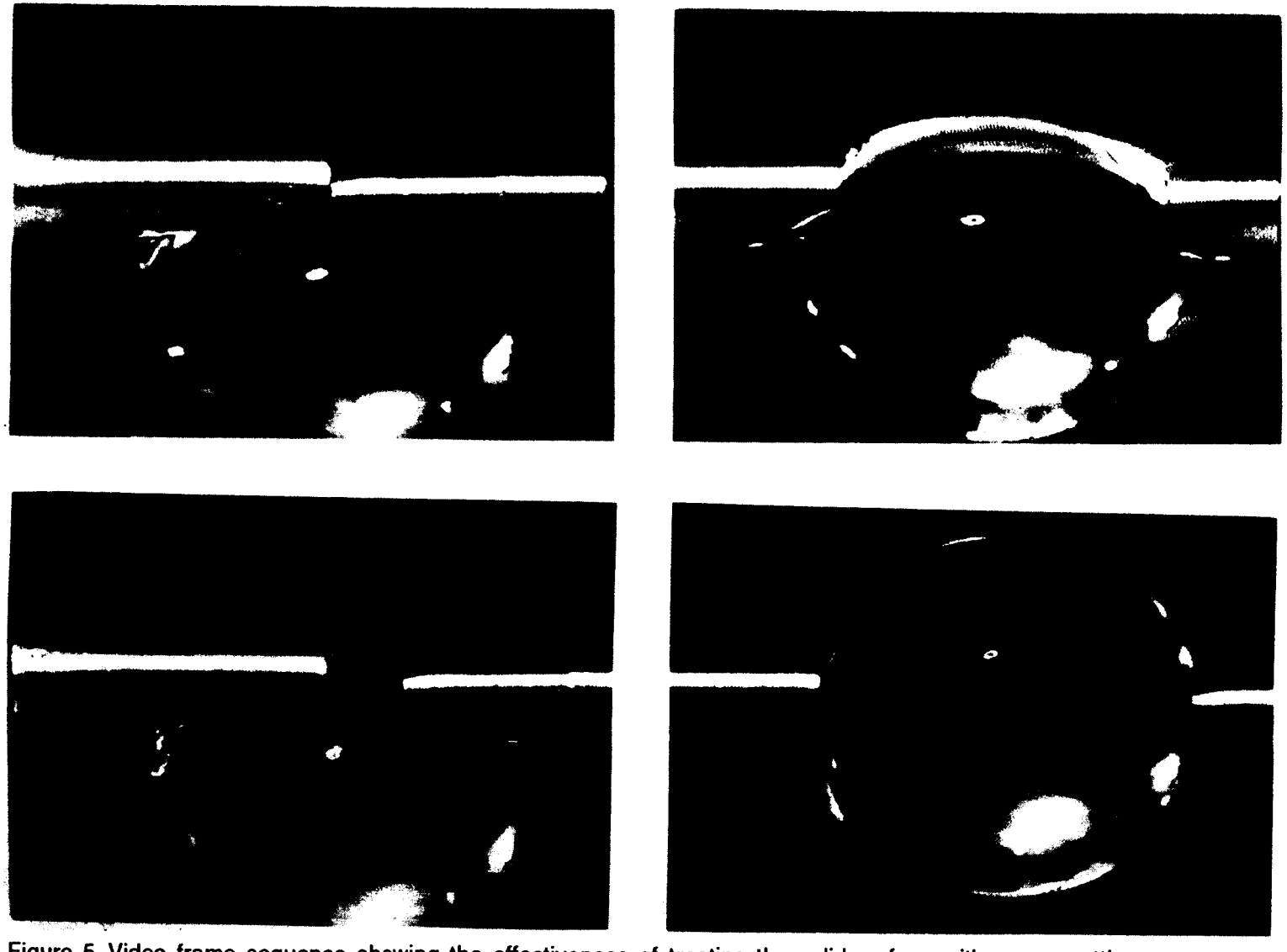

Figure 5 Video frame sequence showing the effectiveness of treating the solid surface with a non-wetting coating. From an initially asymmetrical attachment, the solid-liquid interfaces have been moved by the retracting injectors to allow a near-symmetrical positioning of the liquid between the injector tips.

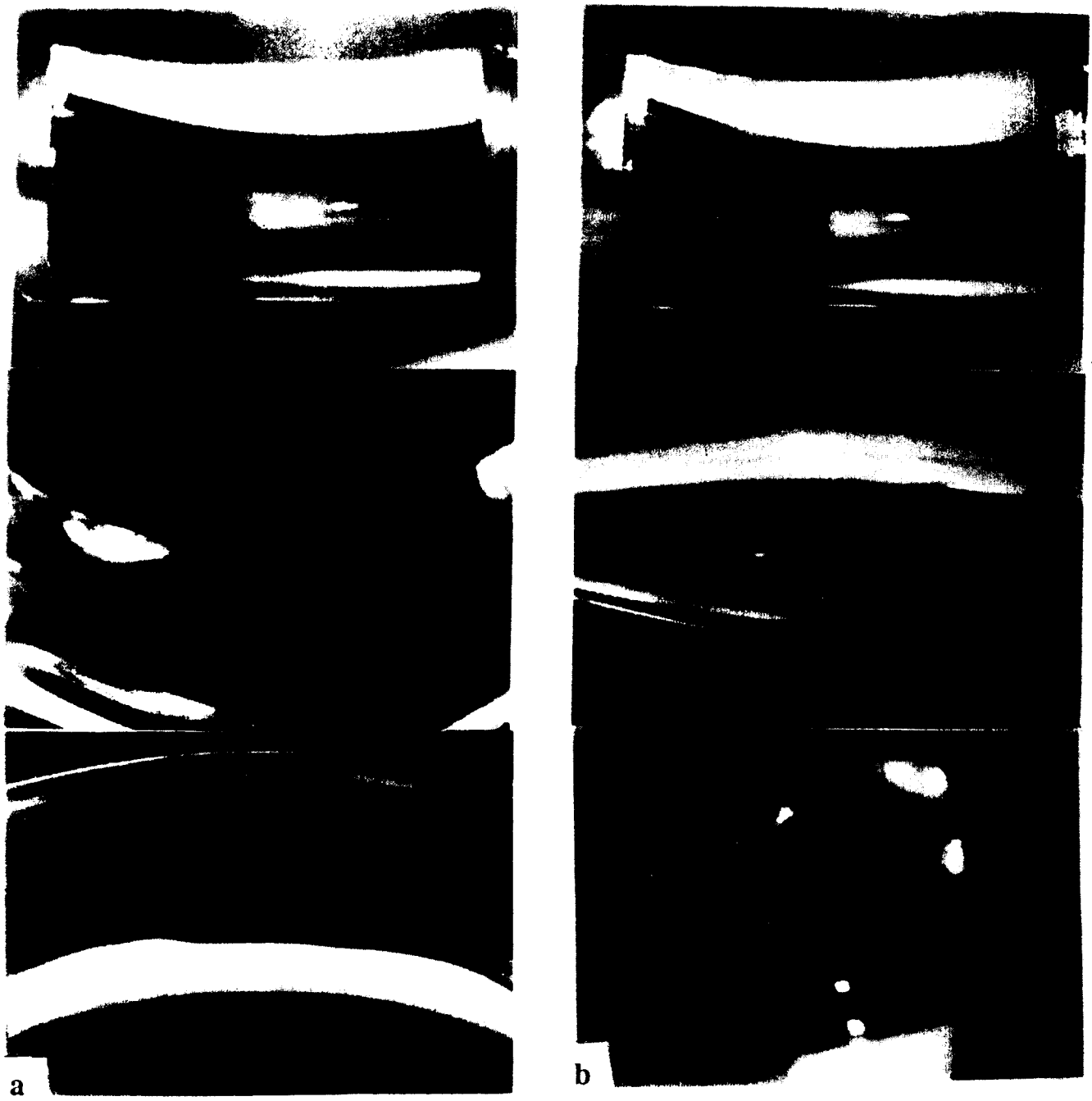

Figure 6 6a. Successful anchoring of silicone oil by a flared tip surface with 90^{o} sharp edge. The liquid bridge is stable even under the acceleration perturbations characteristics of the KC-135 flights.

6b. Deployment of silicone oil drops has been demonstrated in low gravity aboard the KC-135 . The deployed sample is released at the center of the initial liquid bridge with minimal residual linear momentum.

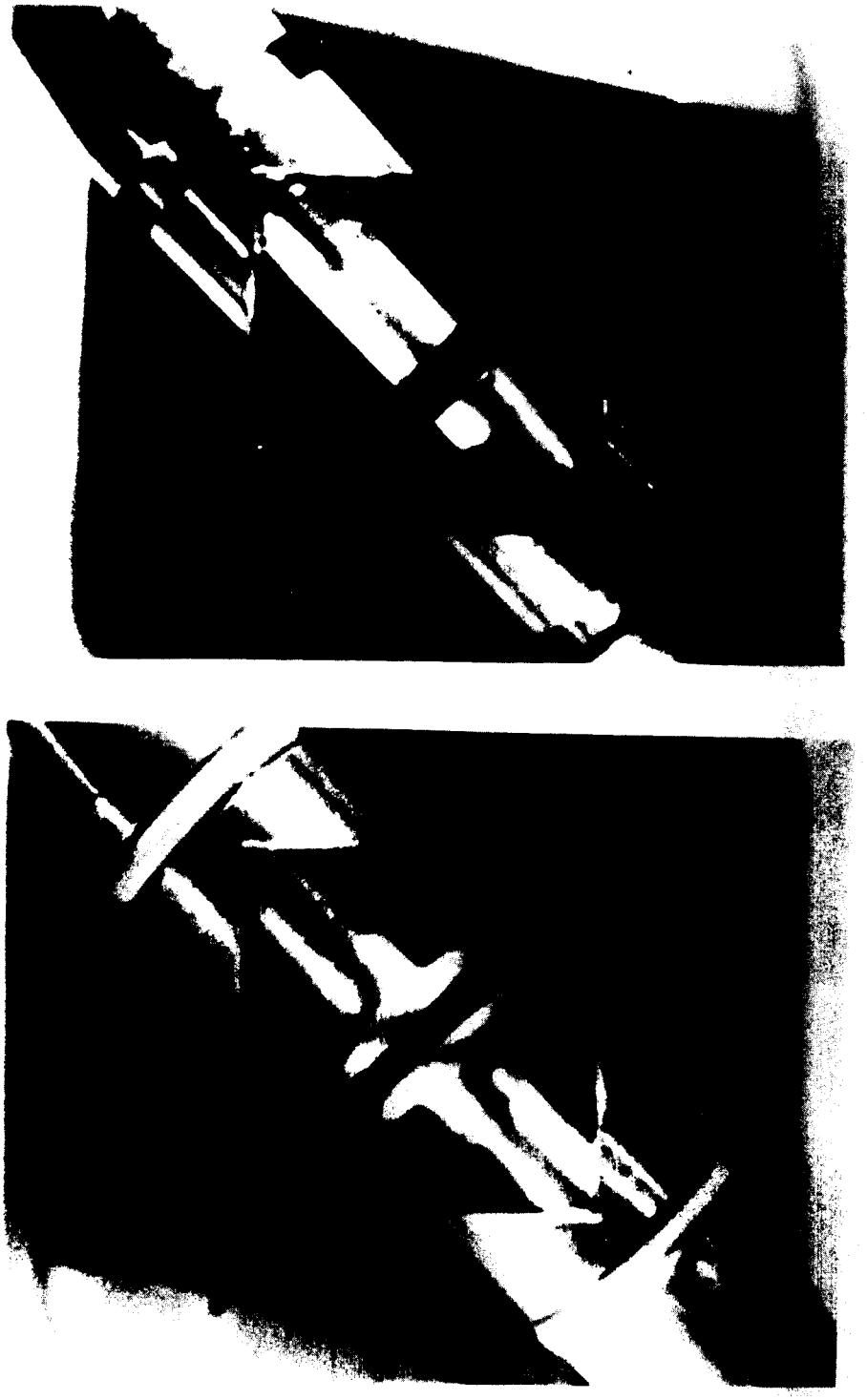

Figure 7 The two principal designs for the Glovebox demonstration tips as installed on the DPM injectors. Type **a** is a flared surface tip 9.5 mm in outer diameter and type **b** is cylindrically shaped with 4.75 mm in outer diameter. Both have been treated with a chemical non-wetting agent, and have a sharp 90 degrees pinning edge.

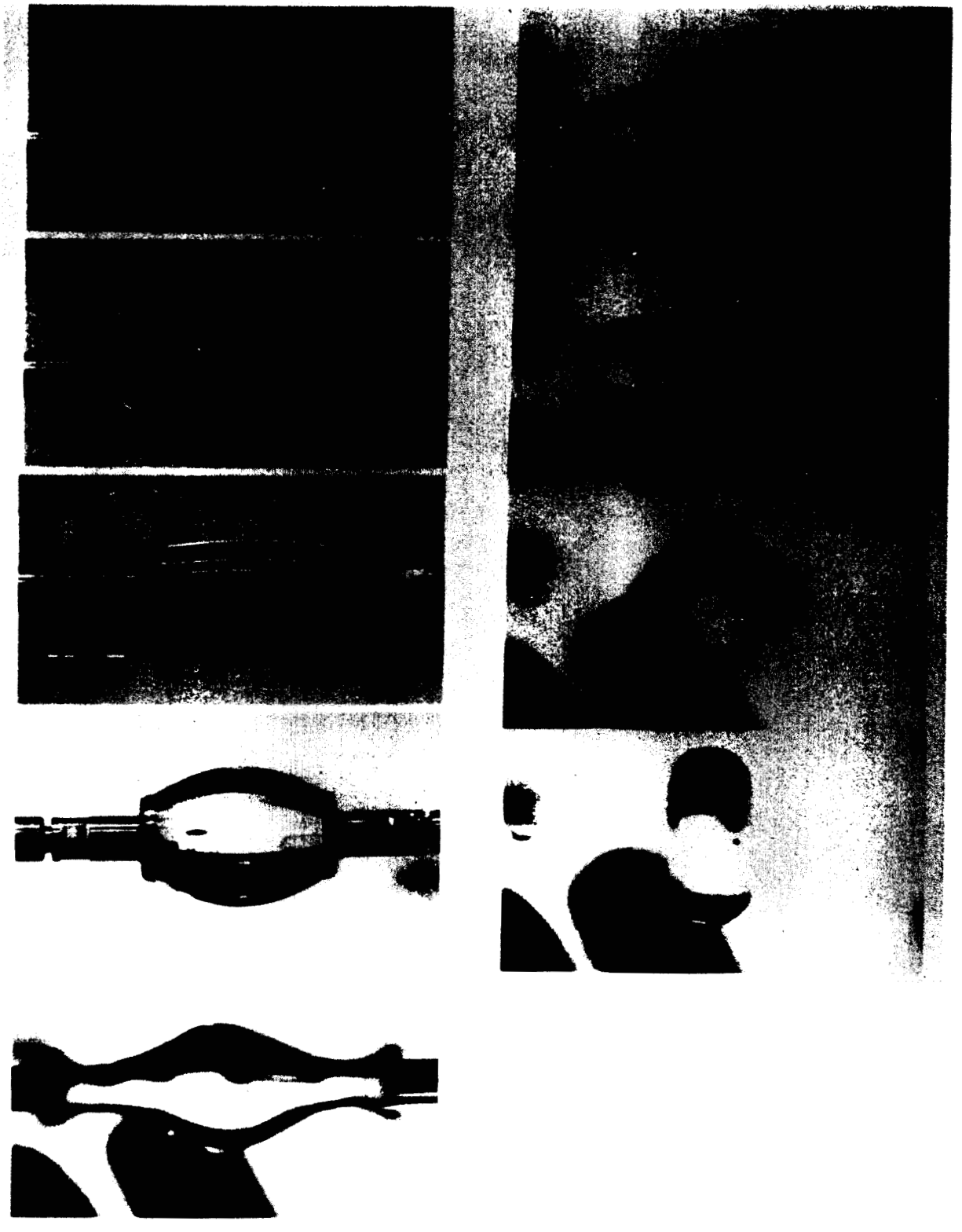

Figure 8 Video frame sequence showing the deployment of a 5 cm^3 water drop by the manually-operated apparatus on the Spacelab Workbench. Measurement of the deployed volume has been obtained by retrieving the sample after impact on the lucite walls. As shown by Table I, 5 to 10% of the injected volume remains on the tips, or is lost to the deployed drop through non-coalescing satellite droplets.

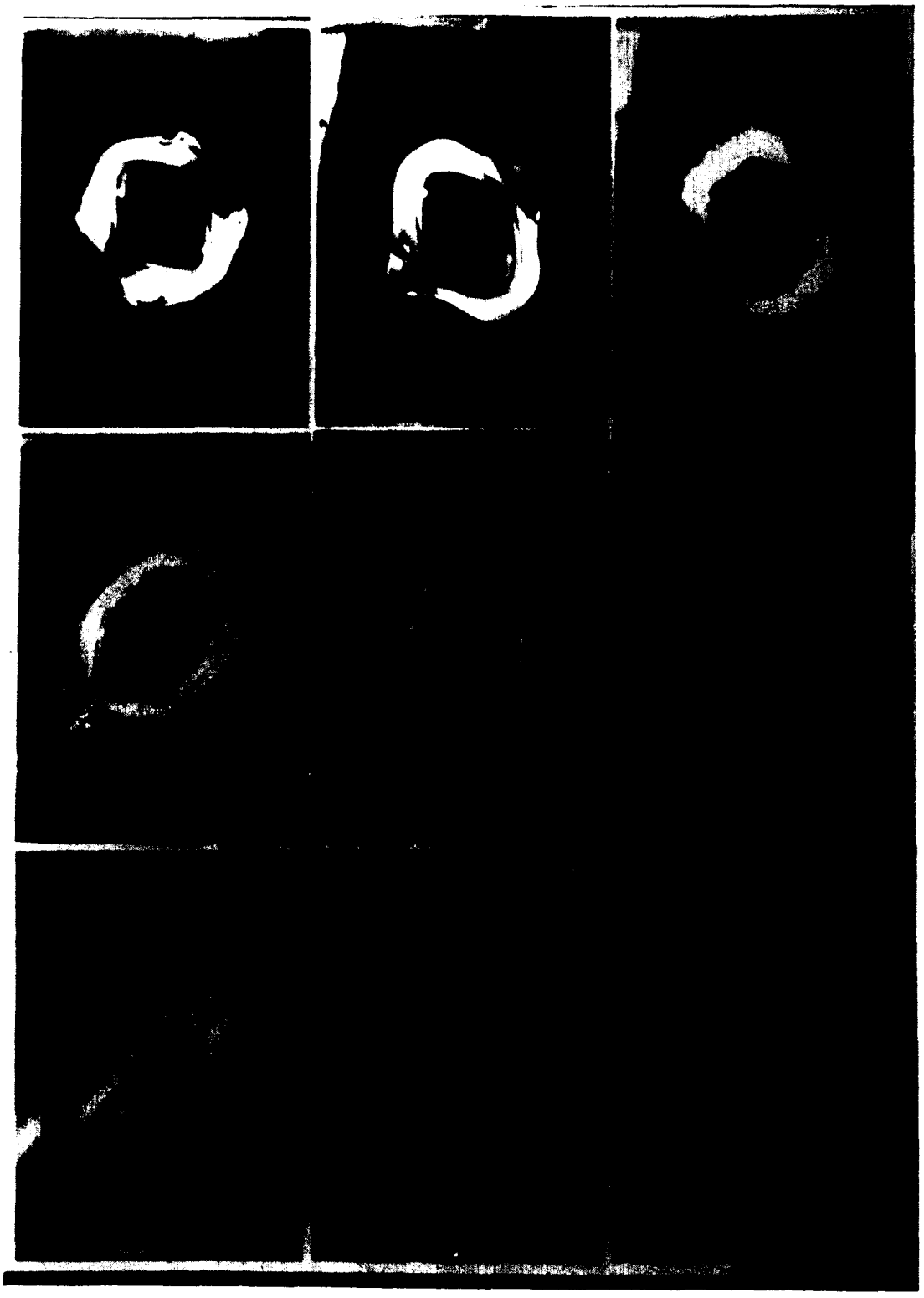

Figure 9 Video frame sequence of the top view of the deployment of a 50 cSt water-glycerol mixture using the type **b** injector tips in the DPM. Near-perfect symmetry can be observed by the shape of the drop and the simultaneous breakage of the two necks joining the liquid sample to the injector tips.

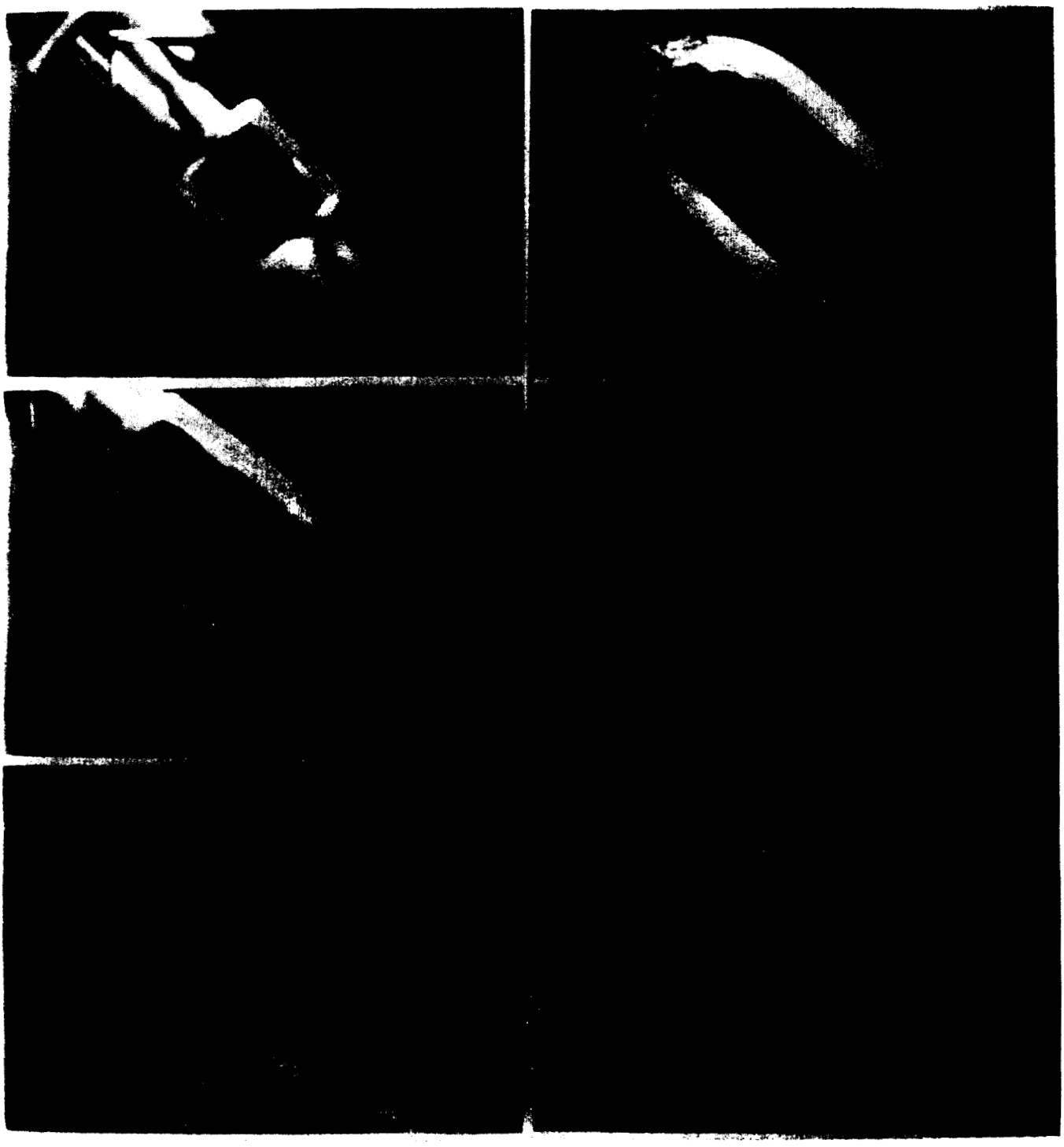

Figure 10 Video frame sequence showing the details of the deployment of a 100 cSt silicone oil drop using type a injector tips in the DPM.

Discussion

Question: *Your syringes are much larger than those used in PCG (Glovebox) experiment. You also have a lot of different types of fluids. What can you comment about the bubbles ?*

Answer: I don't want to talk about it. We had a lot of problems with bubble deployment. They were of different sources than yours. I think most of our bubble deployment problems came from the tubing that we are using. I am not really convinced of that. I think it is the way we connected the syringes to the deployment tips that was the weak point. There were places where we could generate bubbles, not by negative pressure, but by just flowing by entraining air. With bubbles, it is a major problem.

Question: *Did you suffer the mental retardation effect as Larry DeLucas ?*

Answer: I could not tell the difference. No. That is not true. Larry is very right. Things slow down tremendously. I had to take a lot more time to do things, things that seem to be really easy, and think about things a lot longer. That is the major part of things going real slow. Factors for this probably include the pressure that you have 200 people watching you, and great PIs talking to you. There is a great bit of pressure, and various sources contributing to that are many. I think that having a lot of fluids in your head does not help either. But I agree with Carl, I think after a few days I began to get in the groove, and I came up to 100%, or whatever level I am supposed to be at.

MARANGONI CONVECTION IN CLOSED CONTAINERS (MCCC)

Robert J. Naumann

Professor of Material Science
University of Alabama in Huntsville

ABSTRACT

The Marangoni Convection in Closed Containers experiment was designed to study the effects of a void space in a simulated Bridgman crystal growth configuration and to determine if surface tension driven convective flows that may result from thermal gradients along any free surfaces could affect the solidification process. This study was motivated by some of the results of the early directional solidification experiments on Skylab in which the ingot was smaller than the ampoule and appeared to have been in only partial contact with the wall. The Soviets observed similar effects which they attributed to the possibility that the fluid may have been in only partial contact with the wall due to the lack of hydrostatic pressure.

No evidence of partial wall contact was seen in either the case of wetting or nonwetting walls. A hemispherical bubble that was pinned to the wall formed in the case where the liquid did not wet the wall and a perfectly spherical bubble that did not touch the wall formed in the case where the liquid wet the wall. Marangoni convection was observed around the bubble which acted like a pump - driving a global flow throughout the chamber which was several orders of magnitude greater than the buoyancy-driven flows from the residual acceleration.

INTRODUCTION

The purpose of this experiment was to investigate the low gravity behavior of a simulated melt in a Bridgman or gradient freeze configuration in which a void is present to allow for thermal expansion. Some of the early directional solidification experiments on Skylab found the solidified ingot was smaller than the ampoule and appeared to have been in only partial contact with the wall[1]. The Soviets observed similar effects which they attributed to the possibility that in the absence of hydrostatic pressure the fluid may be suspended on microscopic asperities on the surface and thus may be in only partial contact with the wall[2]. If indeed there was only partial wetting at the wall, the heat transfer between the walls and the melt would be significantly altered and the no-slip boundary condition may no longer apply, opening the possibility for surface tension convection (Marangoni convection) to occur.

Joint "L+1" Science Review for USML-1 and USMP-1 with the Microgravity Measurement Group, September 22-24, 1993, Huntsville, Alabama, USA.

The primary objectives were (1.) to investigate the nature of the liquid-wall interface in the absence of hydrostatic pressure under both wetting and nonwetting conditions with particular emphasis on determining if there is complete or partial liquid-solid contact at the walls, and (2.) to assess the possible effects of Marangoni convection in closed containers with a void. A secondary objective was to examine the effects of transient accelerations due to crew motion and vernier thruster firings on a fluid with a thermally imposed density gradient in a partially filled container.

I. DESCRIPTION OF THE EXPERIMENT

The experiment apparatus consists of a control base and a pair of lexan sample tubes. The control base contains a simple light sheet illuminator to aid in observing marker particles in the fluid to map the flows. A 5 V Lumitex high intensity bulb is focused on one end of a fiber optic bundle. The opposite end of this bundle is spread into a fan to provide a line source. A 12 mm focal length cylindrical lens projects this line source through the sample tube. Two metal clips (broom holders from Ace Hardware) hold the sample tube in position over the light sheet illuminator.

The sample tubes were fabricated from 2.54 cm ID lexan tubing. A copper heater plug in the form of a piston is inserted into one end and a finned copper heat sink plug into the other leaving approximately 3 cm space for the working fluid. The fins unscrew for filling. Double O-ring seals are provided on both the heater and heat sink plug to prevent leakage.

Thermistors are imbedded in both the heater and the heat sink. Thermal control and monitoring of the heater is provided by a Radio-Shack temperature control module which controls the power to the heater through a Darlington transistor. A second Radio-Shack temperature control module monitors the temperature of the heat sink. A thermal fuse in the heater plug protects against overheating in the event of a failure of the thermal control module.

One sample tube was filled with 14 ml Krytox 143AZ leaving a 1 ml void. Krytox 143AZ is a fluorocarbon oil with viscosity of 5 cSt. This fluid readily wets the copper plugs as well as the lexan tube. Finding an acceptable non-wetting fluid was not so easy. Water was finally chosen by default even though it is well known that trace quantities of surface active contaminants, which are virtually impossible to avoid, will tend to suppress Marangoni flow. Lexan, which is initially not wet by water, will after several days absorb a layer of water and become wetted. This happens even with various protective coatings such as Nyebar or 3M FC730. For this reason it was decided to have the crew fill the tube in orbit.

II. EXPERIMENTAL RESULTS

Sample tube #1 was filled with water on orbit with no difficulty leaving a 1 ml void or bubble as requested. Marker particles were injected, and the sample tube was closed. The heat-up was nominal

with the heater temperature stabilizing at 45°C as programmed. The heat sink temperature rose from ambient (25°C) to approximately 30°C during the course of the experiment as predicted, verifying that the thermal gradient was established throughout the sample. Initially the bubble was located on the tube wall near the heat sink and showed no tendency to move. By mechanically jiggling the tube, the Mission Specialist was able to reposition the bubble near the hot end where the thermal gradient was steeper. The Mission Specialist reported no evidence of marker particle motion. This was not unexpected since, as mentioned previously, any trace of surface active contaminant will prevent Marangoni convection in water.

The primary purpose of this run was to examine the configuration of a fluid in an ampoule in which the ends were wetted (simulating the interaction between a melt and a forming solid) and the walls were highly nonwetting. It was speculated that under these circumstances there might be a tendency for the fluid to pull away from the walls because of the very large contact angle between the water and the Nyebar-coated lexan walls. However, the bubble appeared nearly hemispherical in shape and tended to remain pinned to the wall at one spot with significant contact line resistance. Video was to have been recorded for approximately 1 hour. These data will be examined to determine if vernier firings induce observable flows in a partially filled container with a thermally induced density gradient. (Unfortunately the tape with these data has not yet been located and may not have been recorded.)

Sample tube #2 containing Krytox 1 43AZ represents a system in which the fluid wetted both the walls and the ends. Again, at the beginning of the heating cycle, the bubble was located at the heat sink end near the wall. However, this time the bubble was perfectly spherical and did not actually touch the wall. After a few minutes of heating when the gradient reached the bubble, a rapid migration of the bubble toward the heated end was observed as would be expected from the Young-Bloch-Goldstein theory[3]. However, instead of remaining near the center of the tube (where presumably the fluid would be the warmest), the bubble migrated to the wall opposite the light source. Several times the Mission Specialist mechanically jiggled the bubble back to near the center of the sample tube, and each time the bubble migrated back to the same side. This direction was thought to be perpendicular to the residual gravity vector. Also when the Mission Specialist turned the apparatus 180°, the bubble migrated to the same wall. Apparently, the center of the tube near the heater is a position of unstable equilibrium or there is a thermal asymmetry in the copper heater plug.

Considerable motion of the marker particles in the fluid was observed. The flow was obviously being driven by the thermal gradient across the bubble, as would be expected. The flow was across the heater face to the bubble, around the bubble, and along the wall. In this sense, the bubble is acting as a pump - driving a circulating fluid flow in the sample tube with an estimated velocity ~0.5 cm/sec near the surface of the bubble.

Post flight testing revealed no measurable thermal asymmetry across the heater plug. Of course on Earth the fluid configuration is quite different than in low gravity. In the vertical thermally stable position (hot over cold) the bubble is flattened across the heater because of hydrostatic pressure and Marangoni convection is suppressed because of the stabilizing thermal gradient. In any other position, the heat transfer is significantly affected by buoyancy-driven convection.

Since the Krytox oil has a low thermal conductivity and the Marangoni convection was relatively large, heat transfer is dominated by the convective transport. Therefore, cold fluid is being brought to the heater plug by the flow and becomes heated as it flows along the heater face. If the bubble were exactly centered, the configuration would be unstable because any slight displacement would allow the fluid that traveled the greatest distance along the face to become hotter, thus reducing the interfacial energy of the bubble. Apparently, equilibrium is reached only when the bubble moves all the way to the wall where the fluid flowing in from the side has traveled the greatest distance along the heater face and has reached the highest temperature before encountering the bubble.

Even though most of the flow is concentrated in the hot end of the sample tube which would be away from the solidification interface in a solidification experiment, the effects of the flow could be important in disturbing the diffusion-controlled composition field many experimenters hope to achieve by operating in reduced gravity. This is illustrated in Fig. 1 which shows the computed streamlines resulting from a simulated bubble at one corner of the hot end. Note that the flow circulates throughout the fluid. Figures 2 and 3 show the computed horizontal and vertical velocity profiles taken in the mid-planes of the system. The flows near the cold end peak at ~2% of the surface velocity, which for this system would amount to about 10 microns/sec. This is several orders of magnitude higher than the estimated flow from the residual acceleration from drag and gravity gradient effects.

CONCLUSIONS

There was no evidence of partial wetting between the liquid and the walls in the MCCC experiment, either in the wetting or non-wetting configuration. In the non-wetting system, the void formed a hemispherical bubble that remained pinned to the walls with considerable contact line resistance.

The bubble in the Krytox oil migrated toward the heater as expected, but apparently the center of the heater is a position of unstable equilibrium as the bubble insisted on migrating to the wall. Marangoni convection around the bubble acted a pump circulating fluid throughout the volume. This effect was not observed in the tube containing water because the surface water contaminates with any trace quantity of surface active material and the contaminated surface blocks the interfacial flow. The possibility of flows driven by voids or bubbles in solutions or melts should be considered by experimenters wishing to use microgravity to suppress buoyancy driven flows. Such flows are global in nature and can be significantly

larger than buoyancy driven flows from residual accelerations, even in regions away from the bubble from the bubble.

REFERENCES

1. Proceedings of the 3rd Space Processing Symposium, Skylab Results, Report M-74-5, Marshall space Flight Center, June 1974

2. Scientific Foundations of Space Manufacturing (Ed. V. S. Avduyevsky), MIR Publishers, Moscow 1984

3. N. O. Young, J. S. Goldstein, and M. J. Bloch, J. Fluid Mech., 6,(1959) 124-126

ACKNOWLEDGMENT

The author wishes to thank the many people that helped in the various aspects of this experiment, especially Roger Chassay and Tony DeLoach in the MSFC project office for guiding me through the MSFC flight acceptance procedures, the USML crew for their patience in the training exercises and the preliminary experiments on the KC-135 and special thanks to Joe Prahl for his interest and helpful suggestions and to Carl Meade for the skill and dedication he exhibited in actually performing the experiment on USML-1.

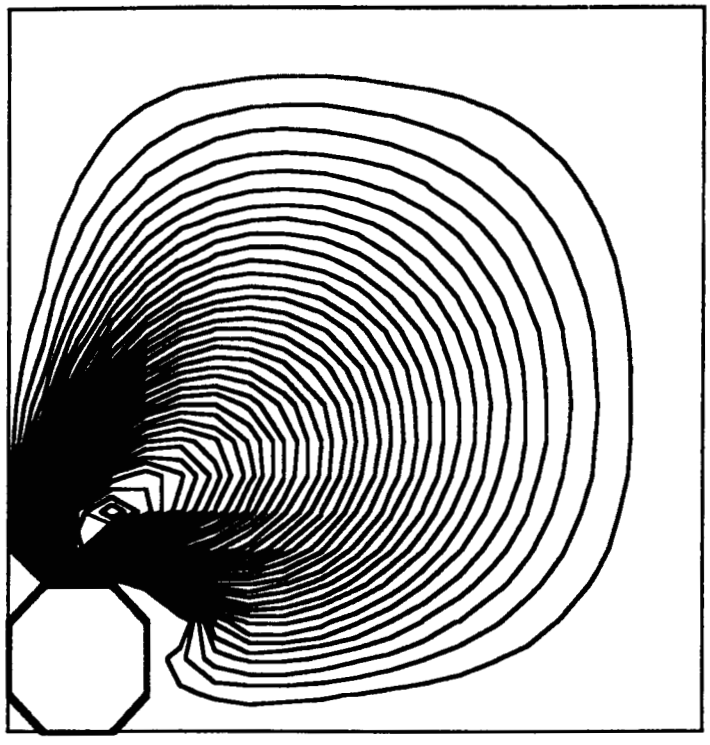

Figure 1 Computed stream function for flow driven by a bubble in the corner of a rectangular slot with differentially heated walls; hot (45°C) on the left and cold (25°C) on the right.

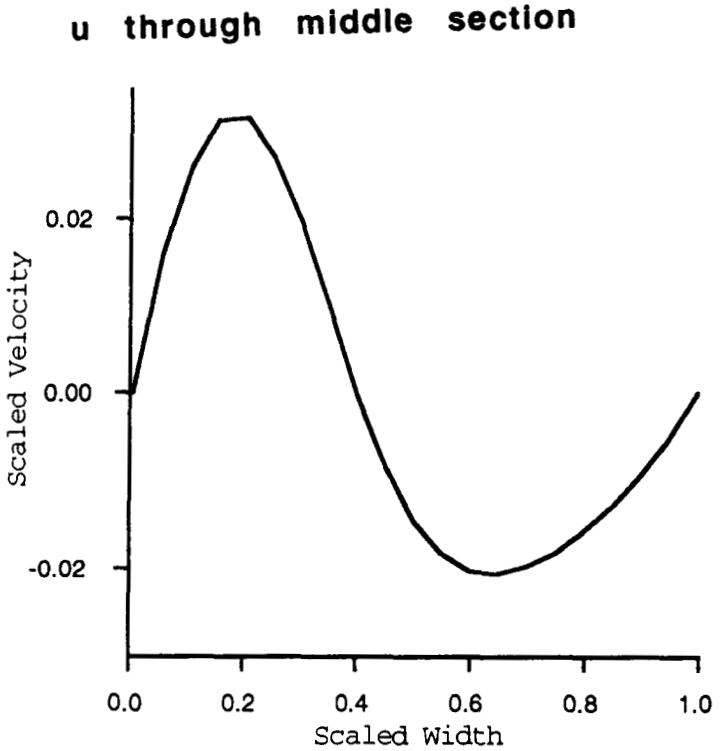

Figure 2 Horizontal velocity at mid-plane between the hot and cold walls scaled by the maximum velocity at the bubble interface.

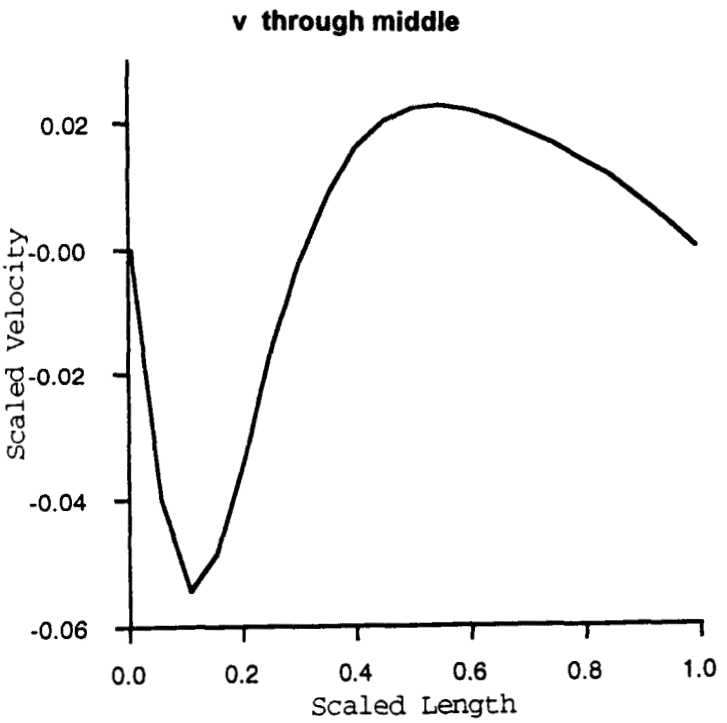

Figure 3 Vertical velocity at mid-plane between the top and bottom walls scaled by the maximum velocity at the bubble interface.

Discussion

Question: *I do not understand why the bubbles would go to the wall ?*

Answer: The walls are Lexan and they are very good insulators. I think the fact that you could get more flow along the surface along the heater probably causes it. Unfortunately the fluid in the cusp is shadowed by the light which is on the other side and so you really can't see what is going on in there. I am not totally convinced that explanation is right, but I can't think of a better one.

Question: *Does this have to do with Marangoni convection ?*

Answer: There was no separation from the wall. I could not detect any case where the fluid was not touching the wall with the wetting case and the only place it was not touching the wall with the nonwetting case was where the bubble was pinned to the wall. When you stop to think about it, that is really what you should expect to happen, because why would you expect the fluid to touch the surface at various points ? That creates a lot of surface energy whereas the fluid could get closer to the wall even if it does not like the wall and just form a little bit of air bubble surface. I think the Russian speculation on that certainly does not seem to work for water. It may work for other systems where the relevant surface energy between the liquid vapor is quite different from the liquid wall so you really do have to worry about all of those things. Maybe water just was not a good simulation of that, but we didn't see that affect at all.

MICROGRAVITY SMOLDERING COMBUSTION ON THE USML-1 SPACE SHUTTLE MISSION

Dennis P. Stocker*, Sandra L. Olson*, José L. Torero+ and A. Carlos Fernandez-Pello+

*NASA Lewis Research Center, Cleveland, Ohio
+Department of Mechanical Engineering, University of California, Berkeley, California.

ABSTRACT

Preliminary results from an experimental study of the smolder characteristics of a porous combustible material (flexible polyurethane foam) in normal and microgravity are presented. The experiments, limited in fuel sample size and power available for ignition, show that the smolder process was primarily controlled by heat losses from the reaction to the surrounding environment. In microgravity, the reduced heat losses due to the absence of natural convection result in only slightly higher temperatures in the quiescent microgravity test than in normal gravity, but a dramatically larger production of combustion products in all microgravity tests. Particularly significant is the proportionately larger amount of carbon monoxide and light organic compounds produced in microgravity, despite comparable temperatures and similar char patterns. This excessive production of fuel-rich combustion products may be a generic characteristic of smoldering polyurethane in microgravity, with an associated increase in the toxic hazard of smolder in spacecraft.

INTRODUCTION

Smoldering is a non-flaming surface combustion reaction that takes place in the interior of porous combustible materials. A smolder reaction will propagate through the porous material if enough heat, generated by the reaction and any external source, is transferred to the unburnt fuel to initiate a smolder surface reaction. However, for the smolder reaction to be sustained, oxygen must also be transported to the reaction zone. The balance between the transport of oxidizer and the transport of energy determines the rate and characteristics of the reaction (Ohlemiller[1], Drysdale[2], Torero[3], Torero, et al.[4]). When the smolder conditions are such that the resulting smolder reaction is vigorous, its rate of propagation is directly proportional to the rate of oxygen supply. When it is weak, however, the rate of heat loss determines whether the reaction will continue to propagate or eventually extinguish (Dosanjh, et al.[5], Torero[3]; Torero, et al.[4]).

Joint "L+1" Science Review for USML-1 and USMP-1 with the Microgravity Measurement Group, September 22-24, 1993, Huntsville, Alabama, USA.

Although smoldering is present in a variety of combustion processes, it is of particular interest in fire safety because of its role as a potential fire-initiation source. It can propagate slowly, undetected, for long periods of time, and suddenly undergo a transition to flaming. The products of smolder combustion themselves are toxic. Recently, with the planned establishment of a space station, there has been an increased interest in the study of smoldering in microgravity because of the potential danger of a smolder-initiated fire in remote facilities. The absence of gravity is expected to influence smoldering through its effect on the mass and heat transport within the smoldering material.

Although considerable work has been conducted to date on smoldering at normal gravity (reviews on the subject can be found in the works of Ohlemiller[1] and Drysdale[2]), very limited information is available on smolder in low gravity. This paper reports the first experimental study of smolder initiation in the extended period of microgravity that is available on the Space Shuttle. These tests are part of an ongoing broader program to study smolder in low gravity.

Cantwell and Fernandez-Pello[6,7], and Torero et al.[8], conducting experiments in a Drop Tower (NASA Lewis, 2.2 sec of ~10^{-5} g) and in KC-135 and Learjet aircraft following a parabolic trajectory (NASA, 20-25 sec ~10^{-2} g per parabola), made some preliminary observations of the effect of gravity changes on the smolder characteristics of polyurethane foam. However, due to the slow propagation of smolder, the short test periods provided only limited information about smoldering in microgravity.

These studies confirmed that in microgravity, as in normal gravity, smoldering is controlled by the balance between the oxygen supplied to the reaction zone and the heat transferred to and from the reaction zone to the virgin fuel ahead. The absence of gravity resulted in an enhancement of the fuel heating ahead of the reaction zone due to reduced natural convective cooling, but also resulted in a decrease in the smolder reaction temperature due to the reduction in oxygen supplied. From these works it was concluded that in microgravity, smoldering would be generally weaker than in normal gravity because of the reduction in the buoyancy-induced oxidizer flow. However, if smoldering occurred under conditions such that it is controlled by heat loss rather than oxidizer flow, then the reduction of convective heat loss in microgravity should result in increased temperatures and a resulting enhancement of the smolder process.

The present work attempts to provide further information about smoldering in a microgravity environment. To provide for extended periods of microgravity, a comprehensive smolder experiment was approved for testing on the Space Shuttle and is now under development. A preliminary set of tests were approved to specifically study the ignition and transition effects of low-gravity smolder. The Spacelab Glovebox on the United States Microgravity Laboratory mission, of the Space Shuttle Columbia, of June/July 1992 (USML-1, STS-50), was used for these preliminary tests. The use of the Glovebox limited the size of the fuel sample that could be tested and the power available for ignition, but

had the advantage of much reduced costs and development time. Although the small sample size and low ignition power limits the amount of information to be obtained from these preliminary experiments, the primary objective was to investigate the ignition characteristics for smolder propagation in microgravity. This information would be very useful in the design of the comprehensive smolder experiment to be carried out at a later time in the Space Shuttle.

A series of comparative tests were also conducted in normal gravity. The normal and microgravity smolder characteristics were determined from interpretation of the available temperature histories obtained at several locations within the sample, visual inspection of the smoldered foam sample, and analysis of the post-combustion gases.

I. EXPERIMENT

A. Flight Hardware

The flight hardware consisted of four experiment modules, two data displays, a control box, and four cables. Each module contained a cylindrical foam sample, with an embedded igniter, and a fan to produce a forced flow in the longitudinal direction. A photograph of the assembled hardware, with one module, is presented in Figure 1. The test variables during the experiment were the igniter geometry and the convective environment. Through the use of an axial igniter (as in Figure 1) and a plate igniter, both radial and axial smolder were investigated. For each igniter geometry, a test was conducted in a quiescent environment and with a low-velocity air flow for a total of four test conditions, as shown in Table I.

Each experiment module was a sealed polycarbonate box, nominally 0.15 m x 0.15 m x 0.20 m, filled with dry air at one atmosphere pressure. The fuel consisted of a 50 mm diameter, 80 mm long cylinder of open-cell, unretarded, white flexible polyurethane foam, with a 26.5 Kg/m^3 density and 0.975 void fraction, which weighed 4 grams. The fuel sample was positioned axisymmetrically in a polycarbonate tube, 76 mm in diameter, that had a fan at one end to provide a convective flow past the sample. The fan was oriented to pull the air past the foam, and screens were placed at both ends of the cylinder to improve flow uniformity. For the quiescent tests, large sections of the tube were removed to provide free exchange of air throughout the module. Hot-wire measurements of the fan-induced air flow indicated that the velocity around the foam sample was of the order of 100 mm/sec. Indirect observations indicate that the fan also induces a localized flow through the foam. No measurements were made, however, of this internal flow. The plate and axial igniters were resistively-heated elements, consisting of nickel-chromium wire sheathed in ceramic.

The axial igniter was 95 mm long and 3 mm in diameter, but only 42 mm of its center section was heated. The plate igniter was 7 mm thick, 51 mm in diameter and was sandwiched in the foam,

centered at 20 mm from the fan end of the fuel sample, such that the smolder wave propagated along the length of the sample in both directions away from the igniter. With the fan on, the air flow through the sample results in an opposed-flow smolder upstream of the igniter, and a forward-flow smolder in the downstream region. The axial igniter ignited the fuel sample along the centerline such that the smolder wave propagated radially outward toward the edges of the cylinder. The maximum igniter power was approximately 29 watts, due to Glovebox limits.

The foam sample was instrumented with six sheathed, cold-junction compensated, chromel-alumel thermocouples, 0.5 mm in sheath diameter, to measure the smolder reaction temperature and its propagation throughout the sample. A seventh thermocouple was used to measure the local gas-phase temperature outside the foam. The positions of the six thermocouples within the foam sample are indicated in Table II, for the modules with an axial igniter. The output of the thermocouples and the igniter current was recorded with a video camera through the use of two data displays (with four readings each). A second video camera viewed the side of the smoldering sample.

B. Experimental Procedure

Testing a single module at a time, the hardware was assembled by the crew member within the Glovebox. Prior to ignition, the fan was activated for those tests requiring air flow. The igniter was then energized and the current potentiometer was adjusted to the appropriate level. Power was applied for 10 to 24 minutes, depending on the test. The progress of the smolder reaction was observed for up to an hour through the temperature displays, the smoke production, and the discoloration or charring of the foam. After the test was completed, the hardware was disassembled and the module was stowed. The four planned smolder combustion tests were successfully conducted during the USML-1 mission, the first by Dr. Lawrence DeLucas, and the following three by Col. Carl Meade.

Following the mission, gas samples were drawn from the modules for analysis and the foam samples were removed for inspection. Normal-gravity tests were conducted in the flight hardware to allow comparison of the smolder characteristics in normal gravity and microgravity. These tests were identical to those conducted in space in regards to the igniter power, flow conditions, and time sequence. The comparison normal-gravity tests were conducted with the foam samples in a horizontal orientation, such that the gravity vector was perpendicular to the axis of the foam. Additional tests were performed with other foam orientations to observe the effect of gravity on the normal-gravity smolder.

The test nomenclature and specific test conditions are listed in Table I. The nomenclature used to describe the four tests is based on the order that the tests were conducted in during the USML-1 mission. During the first microgravity test (1.0), there was a malfunction which affected the display for thermocouples 5 to 7. During the mission, it was not clear whether the malfunction also affected the

igniter current reading which was on the same display. The uncertainty about the igniter current and a concern about exceeding the Glovebox power limits prompted the authors to have Dr. DeLucas reduce the igniter power to a level determined from normal-gravity igniter characterization testing. However, the resulting heating rate was less than desired, so the igniter power was then increased to an intermediate level, bringing the heating rate to an acceptable level. The malfunction did not reoccur during the mission; it was later determined to be the result of a failed reference junction, for thermocouples 5 to 7, located on that single module. Tests 2.x to 4.x were all conducted with the maximum ignition power available from the Glovebox.

During test 2.0, the fan was shut off at approx. 8 minutes, per the nominal test procedure, because the measured igniter temperature fell below the desired level. The igniter temperatures also fell below the desired level in test 4.0, but at the authors instruction, Col. Meade kept the fan on, in order to simplify the interpretation of the results. As previously described, these procedures were duplicated in the comparison normal-gravity testing.

II. RESULTS

The test results are based on the temperature histories provided by the thermocouples, a visual inspection of the burnt foam samples, and the composition of the post-combustion gases. Since the temperature data for the plate igniter tests (3.0 and 4.0) is not yet available, the results and conclusions will primarily deal with the axial-igniter tests (1.x and 2.x). The results from the plate-igniter tests are only briefly reported.

A. Temperature Histories

The temperature histories provided by thermocouples 1 to 4 in the microgravity and normal-gravity experiments for test 1 (axial igniter/fan off) and test 2 (axial igniter/fan on) are presented in Figures 2 and 3, respectively. The temperature histories for the other thermocouples will not be presented here. They were positioned near the surface of the foam to detect flaming, which did not occur in any of the tests. Note that the thermocouple temperatures have not been corrected for heat loss. Given the relative mass of the thermocouples as compared to that of the foam, it is possible that the measured temperatures were significantly affected by conductive losses. Normal-gravity tests also suggest that the temperatures may have been depressed due to the thermocouple's compression of the foam, which may have locally inhibited smolder.

The result of the irregular ignition profile in test 1.x, as previously described, can be seen in Figure 2 for both microgravity and normal-gravity runs. It is evident from the temperature histories that the smolder self-extinguished at both gravity conditions. All four thermocouples reached peak

temperatures at about the same time. If the smolder was self-propagating, the temperature histories would indicate the radial propagation of the smolder wave, with peaks of about 400°C displaced in time. All four temperatures dropped after the peak temperature was reached, even though the igniter was still energized. The temperatures dropped rapidly after the igniter was turned off at 9.5 minutes, which demonstrates the large conductive losses for these small samples. The igniter current was held steady at 3.9 amps from 4.0 to 9.5 minutes, so the initial drop in temperature must be due to a decrease in the heat of the reaction, as will be discussed later.

From a comparison of the microgravity and normal-gravity temperature profiles, it appears that gravity had a limited effect on the temperature histories. The peak temperatures were greater in microgravity than normal gravity for all four thermocouples, with the difference increasing with distance from the igniter. Whereas the peak temperature difference was about 16°C at the igniter, it was 50°C at thermocouple 4, which is 5 mm from the foam surface. The temperature difference is presumably due to buoyant cooling in normal gravity, which would be most strongly felt near the surface of the foam.

The temperature histories for test 2.x, shown in Figure 3, can be more easily interpreted, as the igniter was held at a constant power. In general, the temperature profiles are similar to those for test 1, except for the irregular heating profile in test 1. Extinction is again indicated by the temperature profiles; the temperatures drop slightly while the igniter is energized, and rapidly when the igniter is turned off. However, test 2.x has the unusual feature that the fan was initially on, and then turned off at approximately 8 minutes. Deactivating the fan caused the igniter temperature to gradually increase about 23°C in microgravity, until the igniter was turned off. Meanwhile, at thermocouples 2 to 4, the temperature rose 35 to 43°C in microgravity. In normal-gravity, the deactivation of the fan caused a minor temperature increase of 6 to 11°C. After the fan was shut off, the temperatures were found to increase the most at the thermocouples nearest the foam surface, in both microgravity and normal gravity. This observation is not surprising, since the convective heat loss is the strongest near the foam surface. The temperature increase associated with the fan deactivation was presumably smaller in normal gravity due to the continued presence of the buoyant cooling.

The contribution from the igniter was measured in normal gravity by insulating the igniter with fiberglass insulation and recording the temperature history in the absence of smolder. This data is plotted in Figure 4 along with the igniter temperatures from runs 2.0 and 2.1. The resulting difference in temperatures is approximately the contribution from the exothermic smolder reaction. In both tests, it can be deduced that the reaction started at approximately 1.5 minutes and increased until 4 minutes, at which time the reaction decayed to extinction. Extinction appears to have occurred at some point between 4 and 7 minutes. The differences in the two tests is not believed to be significant. In test 2.x, it is also notable that the peak temperatures (prior to the fan deactivation) for the two gravity conditions are

within 15°C of each other, for all four thermocouples. This suggests that the low forced flow may have been comparable to any buoyant effects during the smolder. The temperature histories of Figures 2 and 3 can be used to roughly calculate smolder propagation velocities using the method previously developed for ground-based experiments (Torero, et al.[4]). The smolder velocity is calculated from the known distance between two consecutive thermocouples and the time lapse for a given temperature to be attained by the thermocouple. That time is determined by the intersection of the tangent to the temperature curve at the inflection point and a horizontal line at the pre-established temperature (350°C). This technique is not truly applicable for this experiment since the measured temperatures did not reach 350°C, except at the igniter. However, approximate information about the smolder propagation velocity can be obtained by extrapolating the tangent of the temperature curve (at the inflection point) until it reaches the 350°C. From the temperature histories of run 2.0, using this technique, it is found that the resulting smolder velocity decays from approximately 0.08 mm/s between thermocouples 1 and 2, to 0.04 between thermocouples 2 and 3, and to 0.02 mm/s between thermocouples 3 and 4. Thus, the smolder was not steady but decayed to extinction. Similar trends are obtained from the temperature histories of test 1. For an average smolder velocity of 0.04 mm/s, and a smolder wave propagating for approximately 18 mm (from thermocouple 1 to 4), the smolder time was estimated to be 7.5 minutes, which is roughly consistent with the temperature profiles of Figure 3. The smolder propagation velocities obtained for the normal-gravity tests experiments are similar. The calculated smolder velocities are of the same order of magnitude as those measured in larger experiments of opposed-flow smolder at low flow velocities (0.5 mm/sec) and natural convection smolder (Torero[4]). They correspond to the "weak" smolder cases tested. The maximum smolder velocities measured in those experiments were obtained for flow velocities of 3 mm/sec and were of the order of 0.15 mm/sec.

B. Char Patterns

During the testing, the smoldering foam was observed to expand and smoke, much of which later condensed as a yellow residue on the module interior. Upon removal after testing, the samples were cut open to reveal the extent of the smolder propagation. Photographs of the smoldered samples from tests 1.x and 2.x are shown with microgravity samples in Figures 5 and normal gravity samples in Figure 6, respectively. Each sample was cut in half on its axis; the interior view of a single half is shown. The normal-gravity tests were conducted with the sample in a horizontal orientation; with the gravity vector oriented down.

The plane of the cut for each sample was selected to include the igniter thermocouple. In most of the samples, the position of the igniter thermocouple can be seen as a narrow dark line. The dark line results from charring from the hot thermocouple, suggesting that thermocouple measurements could

have been significantly affected due to conductive heat loss along the thermocouple. The narrow width of the charred line implies that the conduction along the thermocouple had a localized effect and probably did not effect the smolder propagation in general. This is not surprising, given the foam's low thermal diffusivity compared to that of the thermocouple sheath.

In the char pattern for test 1.0, it can be seen that smolder propagated symmetrically outward from the igniter, in an oval shape. The dark charred region extends to within about 1 cm of the sample edge, except at the ends of the sample. A pyrolysis zone, typical of foam exposed to low temperatures, is visible as a light brown discoloration. This zone is roughly 5 mm thick, indicating that the smolder reactions reached within about 5 mm of the surface. Accounting for the limited propagation at the ends, it is estimated that the char and pyrolysis regions include about 50% of the sample volume. Based on previous studies (Ohlemiller[1]; Torero[3]), the extent of the propagation was somewhat surprising for the low temperatures measured. However, it is in approximate agreement with the propagation velocities estimated from the temperature histories.

The char pattern from normal-gravity test 1.1 was found to be similar to the pattern from test 1.0. The visible extent of propagation was similar in both tests, but there were two notable differences.

First, large voids, on the order of 1 cm long, were created in the normal-gravity char region, whereas there were none apparent in the microgravity char. The voids were found in other, but not all, of the normal-gravity tests and none of the microgravity tests. It is speculated that the voids result from gravitational forces on the weakened polymeric structure, but it is not clear what controls their occurrence. A close comparison of the char structure of the microgravity and normal-gravity tests also shows significant differences. The normal-gravity voids had a crust of melted material which appeared to clog the foam pores. Microscopic observation of the normal-gravity char showed that discolored filaments in some cases had melted into spheres. Furthermore, strong signs of fuel pyrolysis could also be observed at the edges of the char region. These observations are typical of a low temperature smolder process (Dosanjh[5], Torero[3]). In contrast, the char in the microgravity samples was more typical of high temperature smolder with a fibrous, relatively dense structure, despite the similar temperature profiles.

Second, the effect of gravity is also evident even in the presence of forced convection in that the normal-gravity smolder did not propagate as far in the downward direction. In normal-gravity, natural convection induces an upward air flow, inhibiting the downward (opposed) propagation of the smolder, as seen in Figure 6.

With the fan-induced concurrent flow in test 2.x, the smolder also propagated substantially farther toward the fan, particularly in microgravity. The dark char, with forced flow in microgravity (test 2.0), reached within about 5 mm of the fan end of the sample, whereas the char was roughly 1 cm from

the end without flow (tests 1.0 and 1.1). The char, with forced flow in normal-gravity (test 2.1), was also about 1 cm from the end. The pyrolysis zone, with forced flow at either gravity level, reached to (or nearly to) the end of the foam, unlike the quiescent tests. A close inspection of the samples from test 2.x has also revealed significant concentrations of tar at the fan end of the sample, again particularly in microgravity.

In the upstream end of the foam, the forced flow had a minimal effect in microgravity. The shape of the dark char region appears to be slightly more streamlined (≈1 mm) with flow (test 2.0), than without (test 1.0). The char region with flow is slightly wider within 0 to 2 cm of the upstream end. Convective effects noted at both ends of the fan thus suggest that the smolder and pyrolysis were enhanced by convective mass transport in this region.

Except for the fan end, normal-gravity tests with the foam oriented vertically so that the forced flow opposed the buoyant flow show smolder patterns that are similar to the microgravity ones. This suggests that the two convective effects counteract one another in this region. At the fan end, however, the char patterns indicate that in this region, the fan-induced flow enhances smolder, especially in microgravity. Whether the fan-induced flow is stronger or weaker than that induced by natural convection is difficult to determine, since we do not have direct measurements of the flow velocity inside the foam, we can only use this type of indirect observation to infer the flow pattern in the sample interior.

The tests with the plate igniter show similar results to those for the axial igniter. The char region forms a hemisphere with the center plane at the igniter, except downstream from the igniter in the microgravity experiment when the fan is on, where the smolder is enhanced, as in the test 2.0. The dark char region extends about as far from the igniter as with the axial igniter. However, it appears that the light-colored pyrolysis zone extends somewhat further along the axis, away from the fan, presumably due to the distance from the foam surface and the subsequent insulation from heat losses.

C. Gas Analyses

The results of the analyses of the post-combustion gases are presented in Table III, for the microgravity and normal-gravity tests. Only the major components have been included in this report. The results are based on analyses, performed at the Toxicology Laboratory at NASA Johnson, with both Gas Chromatography (GC) and Gas Chromatography/Mass Spectrometry (GC/MS).

Oxygen depletion and the production of carbon dioxide, carbon monoxide, and hydrocarbon species are good indicators of the combustion reaction characteristics. However, in interpreting the data, it should be kept in mind that smoldering is a low-temperature surface reaction that is generally oxygen limited. It is seen that the microgravity smolder tests produced significant amounts of carbon monoxide and carbon dioxide, as well as a number of light organic compounds. These species are characteristic of

pyrolysis and oxygen-limited combustion. It is believed that the chlorinated compounds are contaminants resulting from the methylene chloride that was used to solvent bond the joints in the polycarbonate modules.

Comparison of the species concentrations reveals that the amounts of the gaseous products roughly corresponds to the time that the igniter was on, for a specific gravity level. This observation suggests that fuel pyrolysis may have contributed significantly to the production of gaseous components.

Microgravity test 2.0 (axial igniter, fan on) produced the largest concentrations of combustion products. This test did have the greatest smolder propagation, particularly toward the fan. However, the difference between the products of tests 1.0 and 2.0 is far too great to only result from this difference in the smolder propagation. This implies that the smolder consumed a larger amount of fuel per unit volume in microgravity than normal gravity.

The normal-gravity tests produced these species in substantially smaller amounts than the microgravity tests. This is somewhat surprising, since the extent of smolder propagation as apparent in the char patterns was not strongly effected by gravity for any of the tests. Yet in all cases, the amount of carbon monoxide was much greater (89 to 3900 ppm) than that produced in normal gravity (<3 to 6 ppm). This suggests that the reaction may have been oxygen limited. In most cases, the microgravity tests produced twice as much carbon dioxide as the normal-gravity tests. It must be kept in mind that the measured temperatures were too low for the gas-phase oxidation of carbon monoxide (Glassman[9]).

Methane is evident in the microgravity cases at 17 to 570 ppm, whereas no methane above 5 ppm is detected in the normal gravity samples. Also, propene is present in the microgravity samples at 12 to 107 ppm, and it is not detected (limit = 0.2 ppm) in the normal gravity ones. Other products (e.g., 2-propanol) are detected in the microgravity samples and are undetected, or weakly detected, in the normal-gravity samples.

III. DISCUSSION

A. Heat Losses

That heat losses are an important factor in the smolder propagation for the present experimental conditions in microgravity as well as normal gravity is somewhat unexpected and specific to the smolder (not flaming) combustion process. Since air has such a low thermal conductivity and mass diffusivity, one would expect that with the absence of natural convection in microgravity, the heat losses to the environment would be small and that the deterrent to the progress of the reaction would be a small supply of oxidizer to the reaction zone.

However, these concepts are somewhat modified by the fact that the smolder process is very slow, and consequently, the characteristic time for smolder propagation can be significantly smaller than

that for diffusion of heat and mass. With a thermal diffusivity for air of $5x10^{-5}$ m^2/s and a characteristic length of 25 mm (based on the foam radius), the characteristic times for heat and mass diffusion are of the order of 12.5 seconds (Lewis number assumed unity), which is relatively small compared with the characteristic time of smolder propagation, which with a smolder velocity of 0.05 mm/s and a characteristic sample length of 25 mm is of the order of 500 seconds. The diffusive time scale agrees well with the experimental time scales for cooling after the igniter is deactivated. Thus, from the point of view of transport of mass and heat, the smolder reaction is basically stationary and there is ample time for the heat and mass to diffuse to and from the reaction zone.

If the sample size is small, as it is in this case, the percentage of the heat generated by the smolder reaction that is transferred by conduction to the surroundings becomes increasingly significant as the smolder propagates away from the igniter and the contribution of the external heat source (igniter) is diminished. When the percentage of heat generated by smolder becomes insufficient to overcome the heat losses due to conduction, the smolder reaction weakens and extinguishes. Under these conditions, the smolder process is very sensitive to heat losses, and consequently controlled by heat transfer processes (Torero, et al.[4]). The oxidizer and combustion products have enough time to be transported in and out of the reaction zone at their corresponding diffusion rates which, although small, should be sufficient to support at least a weak smolder reaction. If the sample size were increased, however, and the ratio of heat losses to heat generation decreases, the smolder process would becomes increasingly controlled by the supply of oxidizer, and it may reach the point that diffusion of oxidizer may not be sufficient to sustain the reaction.

B. Mass Transfer

Because of the similarity in the temperature fields and the extent of the char patterns, it is surprising that such dramatic differences in the combustion products are noted. The key to understanding this may be in the flow fields in microgravity as compared to normal gravity. In the absence of buoyant convection, the flow is strictly due to the fan, when it is activated. Due to the relative pressure drops in the annulus around the foam and through the foam, most of the air flow is believed to travel around the perimeter of the foam except near the ends of the foam when the two pressure drops become comparable. Significant flow through the foam end in microgravity is observed via the tarring in microgravity Run 2, which supports this flow analysis.

If the flow in microgravity is primarily annular except as noted above, then the primary source of mass transport within the central region of the foam is diffusion. This would provide longer residence times in the reaction zone for the heavy fuel fractions, and may result in a higher degree of fuel cracking. In normal gravity, the local buoyant flows generated within the foam results in shorter residence times in

the reaction zone, and thus in fewer cracked fuel components and a greater degree of recondensation of heavy fuels on the pyrolyzing fuel.

CONCLUSIONS

The present experiments, although limited in fuel sample size and igniter power, provided valuable information about the smolder characteristics of a porous polymeric fuel in microgravity. The following conclusions can be drawn from these preliminary tests.

(1) Temperatures in microgravity were in general similar to those measured in normal gravity, with only a slight increase in microgravity temperatures noted in the quiescent test, where convective losses are effectively eliminated. The effect of the fan as a source of convective cooling is clearly noted in microgravity, and provides cooling of similar magnitude as normal gravity natural convection.

(2) Char patterns were also similar between normal and microgravity samples, with the effect of gravitational orientation having a minor effect on the char patterns. The major differences note were 1) the char was more uniform and fibrous in microgravity as compared with the irregular voids found in the char from normal gravity; and 2) significant deposits of tar were discovered at the fan end of the sample from run 2.0. This indicates the presence of the flow through the foam end, which presumably enhanced the deposition of the tars in this region.

(3) Under the present conditions of fuel size and external heating, the smolder process was in a "weak" regime because the heat losses from the reaction zone were significant in comparison to the heat generated by the reaction. Under these conditions, smolder was primarily limited by heat losses from the reaction to the surrounding environment. This is in contrast to the short-duration aircraft tests which indicated that the oxygen supply was the controlling mechanism for larger samples. It remains to be demonstrated which mechanism is truly controlling when both extended microgravity periods and large sample sizes are available.

(4) Despite similar temperatures and visible extent of smolder, significant production of light combustion gases was found to have occurred in microgravity, possibly due to the longer residence times in microgravity due to the absence of natural convection. Of particular note, the microgravity levels of carbon monoxide were orders of magnitude higher than that observed in the normal-gravity tests. This may be a specific result of smoldering in a microgravity environment, which would imply that microgravity smolder products may be more toxic than smolder products produced on Earth.

ACKNOWLEDGMENTS

The authors would like to acknowledge the contributions of the many NASA personnel that made this space experiment possible. In particular, we would like to thank the Toxicology Branch of NASA Johnson, who conducted the gas analyses, specifically John F. Boyd, Millie P. Martin, Lily Y. Wang, Tom Linero, and John James. We would like to thank the USML-1 crew for their design suggestions and for their hard work during experiment training and simulations. Special thanks go to Col. Carl J. Meade and Dr. Lawrence J. DeLucas for their interest and dedication while conducting the experiments during the USML-1 mission.

REFERENCES

1. Ohlemiller, T.J., Prog. Energy Combust. Sci., **11**, 277,1986.

2. Drysdale, D., An Introduction to Fire Dynamics, p. 265, John Wiley,1987.

3. Torero, J.L., *Buoyancy Effects on Smoldering Combustion of Polyurethane Foam*, Ph.D. Thesis, University of California, Berkeley, 1992.

4. Torero, J.L., Kitano, M. and Fernandez-Pello, A.C., Combust. Sci. Tech., **91**, 1-3, 95,1993.

5. Dosanjh, S.S., Peterson, J., Fernandez-Pello, A.C., and Pagni, P.J., Acta Astronautica, **13**, No. 11/22, 689,1987.

6. Cantwell, E., and Fernandez-Pello, A.C., 28th Aerospace Science Meeting, paper # AIAA-90-0648,1990.

7. Cantwell, E. and Fernandez-Pello, A.C, *Smoldering Combustion Under Low Gravity Conditions,* 1990 Fall Meeting, WSS/CI, San Diego, CA., 1990.

8. Torero, J.L., Fernandez-Pello, A.C., and Urban D., *Experimental Observations of the Effect of Gravity on Smoldering Combustion,* submitted to the AIAA Journal. Also paper # AIAA-93-0829, 31st Aerospace Science Meeting, Reno, NV, 1993.

9. Glassman, I., Combustion, Academic Press, 63, 1987.

TABLE I: TEST CONDITIONS

Run	Gravity	Igniter Shape	Ignition Current (amps)	Ignition Time (min)	Air flow	Notes
1.0 1.1	µG 1G	Axial	4.2 to 2.5 to 3.9	9.5 9.5	No	Irregular ignition profile, due to data display malfunction
2.0 2.1	µG 1G	Axial	4.2	15.5 15.5	Yes	Fan turned off at approximately 8 minutes
3.0 3.1	µG 1G	Plate	4.2	_22 15.0	No	Igniter turned off for brief time at approximately 18 minutes
4.0 4.1	µG 1G	Plate	4.2	24.3 15.0	Yes	Fan kept on, contrary to nominal procedure (at the authors' direction)

TABLE II: THERMOCOUPLE POSITIONS AXIAL IGNITER (1.x AND 2.x)

TC	Position (mm)	
	Radial (from axis)	Axial (from fan end)
1	2 (at igniter)	50
2	10	45
3	15	40
4	20	35
5	5	2
6	10	7

TABLE III: ANALYSIS OF THE POST-COMBUSTION GAS SAMPLES

Compound	Microgravity				Normal-Gravity			
	1.0	2.0	3.0	4.0	1.1	2.1	3.1	4.1
Oxygen	21%	19%	21%	20%	20%	20%	20%	20%
Nitrogen	78%	79%	78%	78%	79%	79%	79%	79%
Hydrogen	ND	40	ND	ND	ND	ND	ND	ND
Methane	17	570	96	180	ND	ND	ND	ND
Carbon Monoxide	89	3900	150	610	4.0	Trace	Trace	5.5
Carbon Dioxide	2300	7400	7600	10700	2100	3000	3300	3800
Propene	15.2	107	12.1	43.8	—	—	—	—
Acetaldehyde	6.33	117	36.4	85.1	120	66	66	150
Propanone	25.8	47.7	4.89	40.9	41	18	13	26
Propanal	ND	7.91	ND	ND	13	4.4	ND	9.1
2-Propanol	6.08	19.0	0.18	13.2	3.7	1.0	0.83	3.7
Dichloromethane	63.5	70.7	70.3	49.7	46	26	44	46

ND: Not detected; limit is 3 ppm for carbon monoxide, and 5 ppm for hydrogen and methane.
Trace: Amount detected is sufficient for compound identification only.
— : Not reported in analysis.

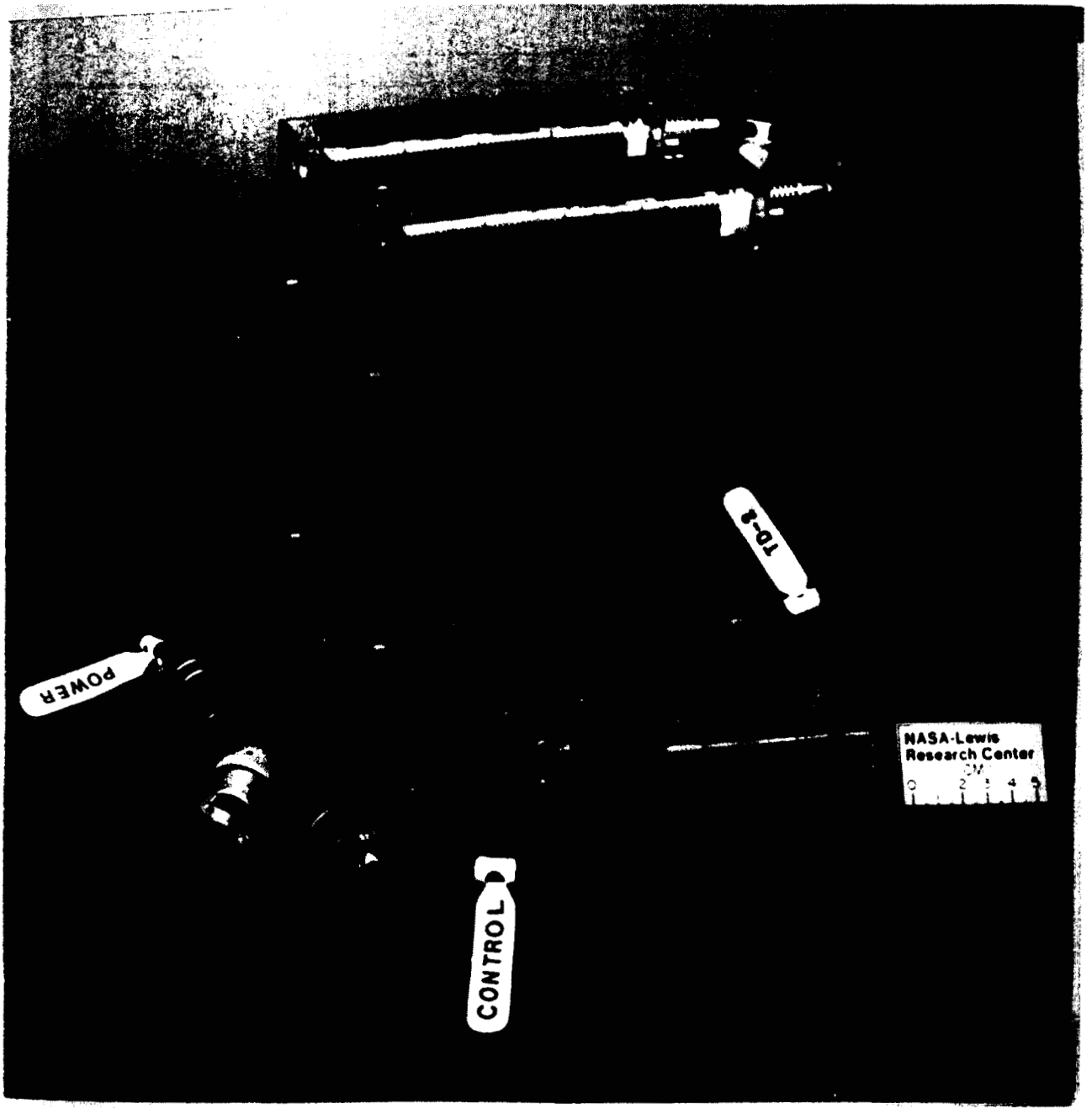

Figure 1 Flight Hardware assembled for a test with an axial igniter.

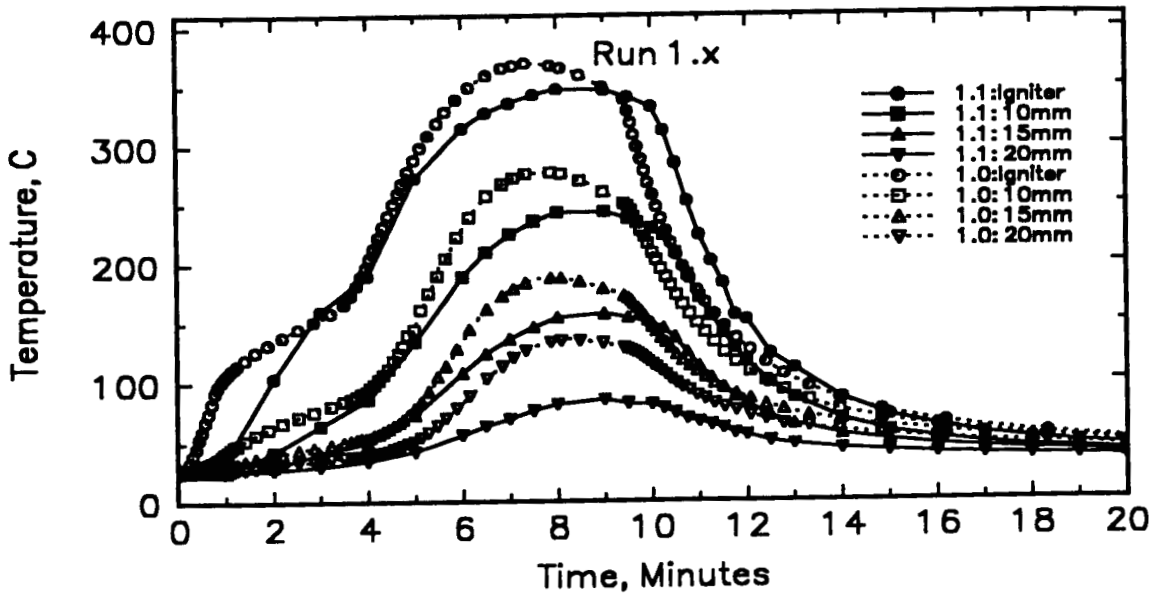

Figure 2 Temperature data from Runs 1.0 and 1.1; (Fan off); Thermocouples 1 to 4.

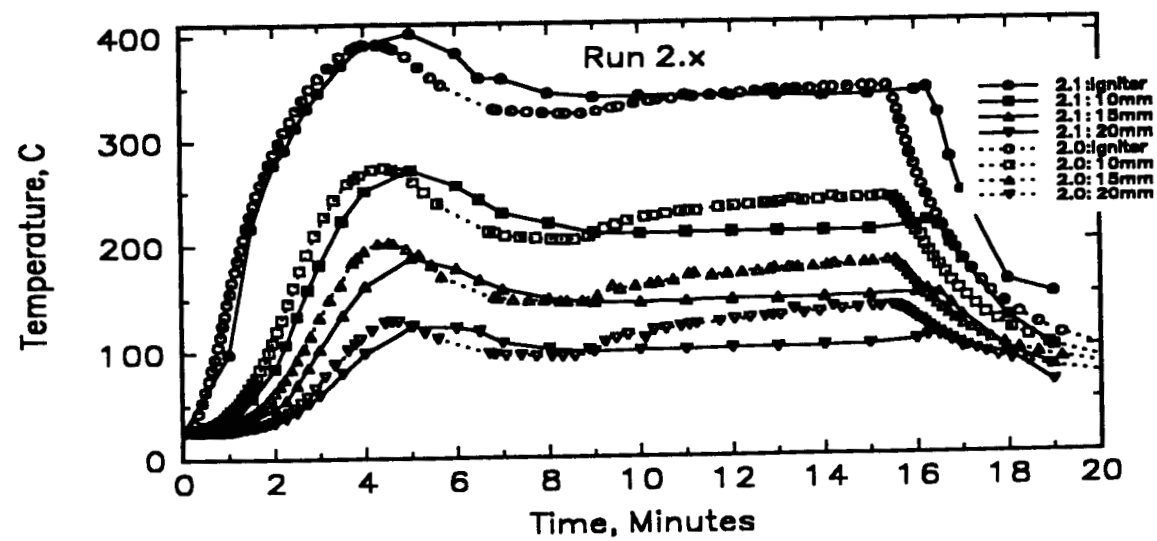

Figure 3 Temperature data from Runs 2.0 and 2.1 (Fan on); Thermocouples 1 to 4.

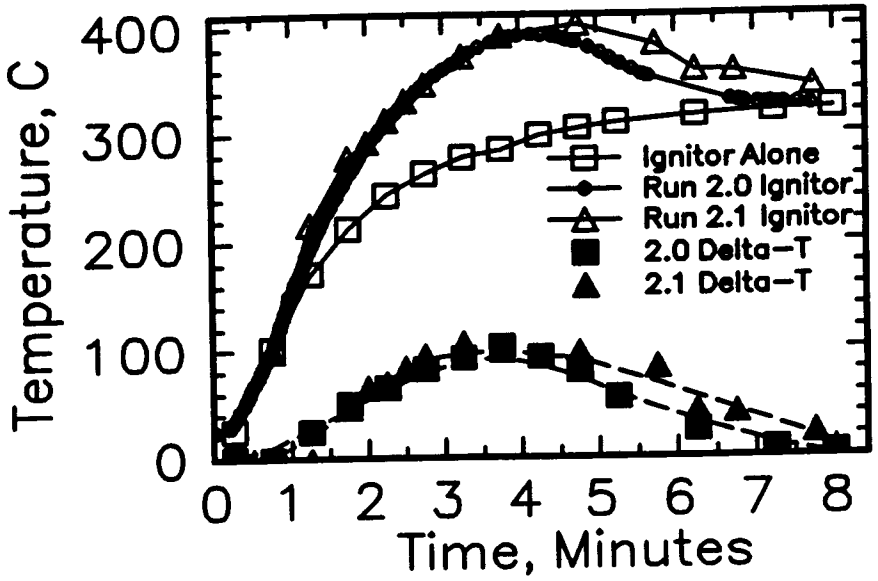

Figure 4 Igniter Temperature Comparison.

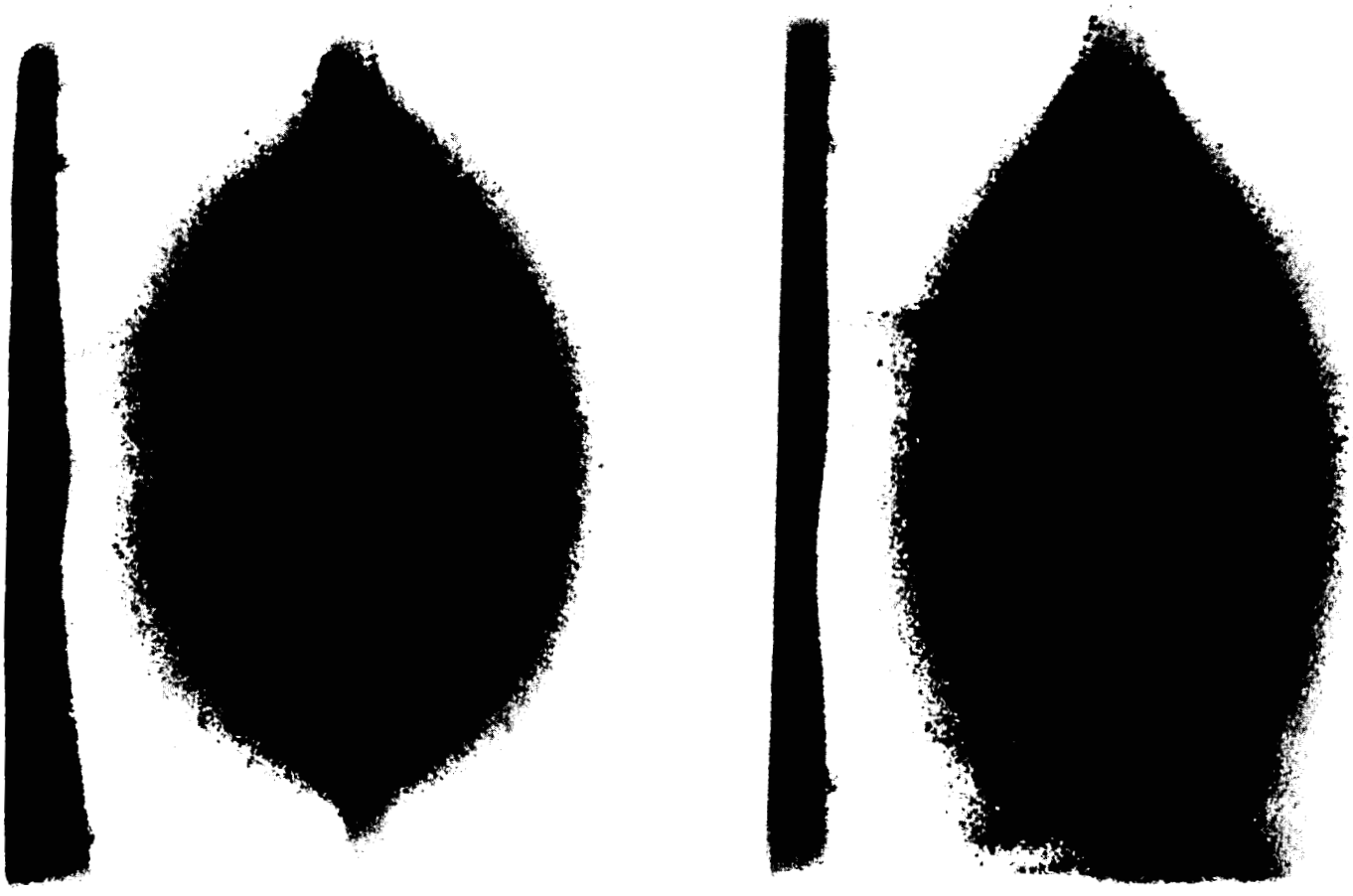

Figure 5 Foam Samples, from Runs 1.0 (Left) and 2.0 (Right), Fan end at base of figure. Samples are 8 cm long.

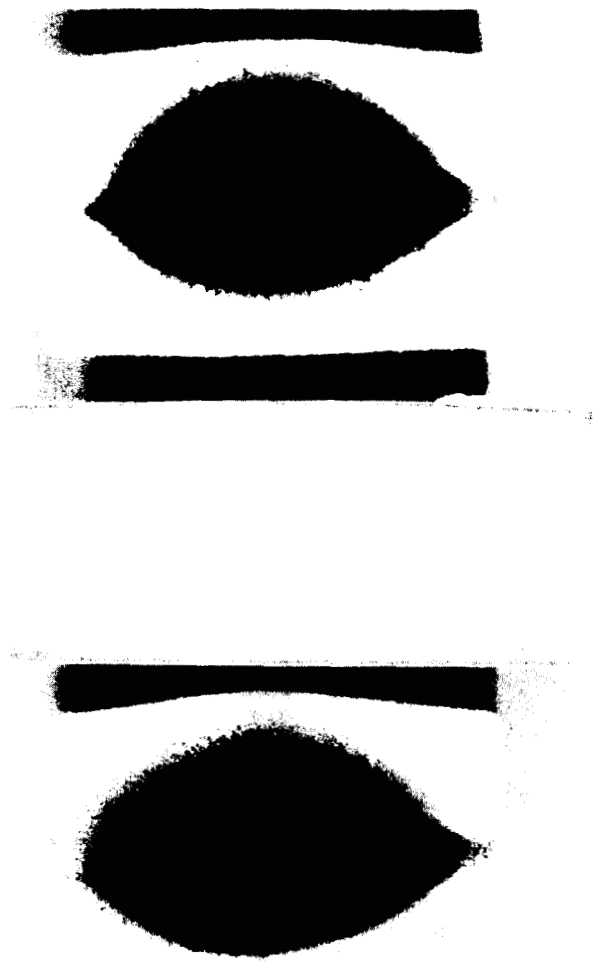

Figure 6 Foam Samples, from Runs 1.1 (Top) and 2.1 (Bottom), Fan end at left, Gravity Vector down. Samples are 8 cm long.

Discussion

(Speaker: Carlos Fernandez-Pello, University of California, Berkeley, California)

Question: *When you see a lot of CO produced in a reaction that under other conditions does not produce a lot of CO, my naive view is that somehow I have limited the amount of oxygen getting to this combustion process, and that is why I don't go to completion in that reaction. Is that consistent with your interpretation of these results?*

Answer: Yes. Basically I think what happens is the supply of oxidizer is by diffusion and what we have in microgravity is we have a higher temperature, with higher pyrolysis of the fuel, and an attempt to react more than in normal gravity. We are comparing normal and microgravity. In normal gravity the convective flow cools the reaction and prevents this from occurring, but in microgravity there is not enough oxidizer to oxidize the CO to CO_2. One thing that is a bit deceiving, also, is that this is a surface reaction, so when we think of the oxidation process in the gas phase, that occurs at above 1000°C. Here, in the experiment, the temperatures are of the order of 400°C, so the concepts that apply to the oxidation process in flames do not apply here. But basically you are right.

WIRE INSULATION FLAMMABILITY EXPERIMENT: USML-1

1 YEAR POST MISSION SUMMARY

Paul S. Greenberg*, Kurt R. Sacksteder* and Takashi Kashiwagi+

*NASA Lewis Research Center, Cleveland, OH
+National Institute of Standards and Technology, Gaithersburg, MD.

ABSTRACT

Herein we report the results from the Wire Insulation Flammability (WIF) Experiment performed in the Glovebox Facility on the USML-1 mission. This experiment explored various aspects of electrically induced fire scenarios in a reduced gravity environment. Under quiescent microgravity conditions, heat and mass transfer are dominated by diffusive and radiative transport; while in normal-gravity buoyancy-induced convection often dominates. Of considerable scientific and practical interest is the intermediate situation of combustion occurring in the presence of imposed gas flows, with lower characteristic velocities than those induced by buoyancy in normal gravity. Two distinct cases naturally arise: flow direction opposed to, or concurrent with, the flame spread direction. Two tests of each kind were conducted in the WIF experiment, providing the first controlled demonstration of flame spreading in forced convection ever conducted in space.

Four test modules were flown. The wire insulation, 1.5 mm in diameter, was polyethylene, extruded onto nichrome wire. Temperatures of the wire cores and insulation heated in quiescent and flowing environments were measured. Video and still-camera images of the samples, burning in air flowing at approximately 10 cm/sec, were recorded to obtain flame characteristics including spread rate, structure and temperature. Flame spread rates in concurrent flow were approximately twice those in opposed flow.

Several unexpected and unique microgravity combustion phenomena were observed. In concurrent and opposed flow regimes, the spreading flames stabilized around a bead of molten insulation material, within which bubble nucleation was observed. An ignition attempt without flow created a quiescent cloud of vaporized fuel which ignited dramatically yet failed to sustain normal flame spread. Finally, all tests produced substantial soot agglomerates, particularly the concurrent flow tests; and the collected soot has a morphology very distinct from soot formed in normal gravity flames.

Joint "L+1" Science Review for USML-1 and USMP-1 with the Microgravity Measurement Group, September 22-24, 1993, Huntsville, Alabama, USA.

INTRODUCTION

Combustion is a ubiquitous phenomenon that affects nearly everyone in some way either as an energy source for cooking, heating, transportation, electrical power generation, and a variety of industrial processes, or as a destructive agent in fires. Some people believe civilization began when mankind conceived the concept of controlling fire, yet after thousands of years uncontrolled fires still cause tremendous injury and property damage. Because of its importance to modern civilization, combustion has been the object of scientific study for over a century. Still, many questions remain to be answered.

Convection plays a role in most combustion phenomenon, providing the necessary oxidizer and affecting the chemical reaction rates and the distribution of the heat released in the flame. In normal gravity, buoyant convection introduces additional complexity: the heat released in the flame induces the density gradient upon which gravity acts to induce flow. Some normal gravity flames are completely dominated by buoyant convection, even though convection would cease without that flame.

Flame spreading tests have been conducted using thin fuels in microgravity situations, where buoyant convection is suppressed. In spacecraft experiments, (e.g. the Solid Surface Combustion Experiment[1]) flames were ignited in quiescent atmospheres with an elevated oxygen content. These tests demonstrated diffusional mechanisms can be sufficient alone to sustain flame spreading. In ground-based facilities (i.e. drop towers and parabolic aircraft) convection at very low speeds has sustained flames at much lower concentrations of atmospheric oxygen[2,3,4] than quiescent microgravity tests similarly configured. The ground-based tests, however, were limited to very thin fuels (e.g. tissue paper); practical fuels, which are thicker, require more test time than is available. One objective of the Wire Insulation Flammability Experiment was to obtain the first extended observations of low-speed convection in flames spreading over fuels resembling engineering materials.

The WIF experiment also provided an opportunity to conduct a simple heat transfer experiment. On Earth, buoyant convection plays a role in the disposition of heat generated by resistance (joule) heating in electrical wires. Ratings for the current carrying capacity of wires rely partially upon buoyant convective cooling to dissipate the energy of joule heating. Similarly, the cooling of electrical components is commonly accomplished using finned heat-sink structures that also rely upon buoyant cooling. In microgravity buoyant convection is suppressed, and electrical systems in spacecraft are cooled by other means (e.gs. cold plates, forced convection, heat exchangers, and heat conducted through the wires). Joule heating rates in quiescent and very-low-speed flows were measured with the WIF experiment for comparison with tests in normal-gravity buoyant environments.

I. EXPERIMENTAL OBJECTIVES

The Wire Insulation Flammability Experiment (WIF) was designed to obtain test data on two related phenomena:

(1) Observe and measure the joule heating of electrical wire in a quiescent, then low-speed forced-flow environments, for comparison with normal-gravity behavior and with established tests for rating spacecraft electrical systems.

(2) Observe and measure the ignition and spreading of a flame over the insulation of overheated electrical wire in very-low-speed flows in microgravity. Distinguish between flames spreading in concurrent and opposed flow, and compare with flame spreading in normal gravity.

To obtain these desired observations, four experiments were conceived, two each in concurrent and opposed flows.

II. EXPERIMENT HARDWARE

Four nearly-identical WIF test modules, designated WIF-A,B,C, and D (see figure 1) were built for the STS-50 mission. The modules were designed to function inside the Glovebox Experiment Facility (GBX) which provided electrical power, flowing air, and photographic capability.

Each module consisted of a combustion chamber (see figure 2) open at both ends, configured as a miniature wind tunnel. At one end a flexible duct was provided for connection to the GBX air circulation system, the air supply for the experiment. A small bending flag anemometer, made from the jewel-bearing movement of an electrical meter, was positioned in the tunnel to indicate the airflow velocity. A metal screen covered the exit port to cool the gases exiting the WIF module and to contain any particulates released during combustion.

A single insulated wire sample, 1.5 mm diameter, 110 mm long, was mounted axially in the duct, parallel to the airflow direction. The sample consisted of polyethylene insulation extruded onto a 0.75 mm nichrome wire core. The sample was connected to circuitry design to provide current for joule heating the nichrome core. At one end of the sample, a kanthol igniter wire was wound around the insulation. In two modules, the ignitor was located near the flow exit so that the flame spread direction would be opposed to the airflow direction; in the others, the ignitor was located near the entrance for concurrent-flow flame spreading.

The electrical power deposited in the test wire cores via joule heating was controlled by calibrated ballast resistors. The power deposition in the WIF modules A-D were 1.27, 1.49, 1.59, and 1.75 watts, respectively. The resistances were selected to achieve different steady temperatures in the wire samples near the melting point of the insulation, based on tests in a vacuum in normal gravity.

Four Type K, 0.07 mm wire diameter thermocouples were placed inside the sample to measure wire temperatures and insulation temperatures near, but below, the surface. Two additional thermocouples were located in the gas phase, 2.5 mm and 1.5 mm from the insulation surface, to

measure the flame temperatures. A window in the tunnel was framed by six thermocouple-temperature displays (see figure 2). This window configuration was designed to allow simultaneous imaging of the flame and the thermocouple displays using the glovebox video. A second window in the tunnel presented an orthogonal perspective used for 35 mm still photographs.

Two 10 cc vacuum bottles, located behind the combustion chamber, were connected through a solenoid valve to small-diameter metal sampling tubes, that terminated near the wire sample. The vacuum bottles were designed for collecting gaseous samples of the off-gassing and combustion products for post-flight chemical analysis. Two transmission electron microscope grids, approximately 3 mm in diameter, were attached to each exit screen for post-flight analysis of any captured particles.

The crew controlled the WIF modules using a small control box outside the GBX. The controlled functions included: wire heating, ignition, and gas sampling (2 samples per module). The control functions were actuated with momentary switches to prevent inadvertant overheating, etc.

III. EXPERIMENT OPERATIONS

Following installation of a test module and the photography devices, and establishing electrical connections, the nominal test procedures were a sequence of crew actions for wire heating then ignition. The first phase of the experiment consisted of recording temperatures of the sample during preheating - first in a quiescent (no-flow) environment. The crew member was to actuate the electrical current flow, stopping when the predetermined insulation temperature was reached. The first of two gas samples were to be taken at this time. Next, the airflow was to be activated and adjusted using observations of the anemometer. The wire heating was then to be repeated in the convective cooling regime.

When the wire insulation reached a predetermined temperature, the crew member was to terminate the wire heating and then activate the ignitor. Upon observing ignition, the crew member was to deactivate the ignitor and trigger the motor-driven still camera. During the spreading of the flame, the second vacuum bottle was to be momentarily opened for collecting a sample of the combustion products. Video images of the temperature displays and the spreading flame were to be recorded throughout the heating and burning processes.

IV. TEST RESULTS AND DISCUSSION

A. SAMPLE PREHEATING

Electrical power levels required to heat the WIF wire samples were determined in ground based tests conducted in air at normal gravity, in a vacuum at normal gravity, and in air in reduced gravity aircraft (Learjet) tests. Heating rates that would conserve USML-1 crew time yet maintain nearly uniform insulation temperature were sought. Figure 3 shows plots of temperature versus time for three power

levels (1.22, 1.5, and 1.82 watts), comparing results of the three test environments. The reduced-gravity/air and the normal-gravity/vacuum chamber results were similar for the available aircraft test time. In the vacuum tests, at low heating rates the insulation reached a steady temperature below 100°C where the polyethylene began to melt, while at higher heating rates the temperature rose quickly to excessive temperatures. Temperatures in normal-gravity/air were always lower than the other environments. The vacuum test data were used to specify heater power levels for the WIF flight samples.

Figure 4 shows comparisons of insulation temperatures sensed by thermocouples embedded near the insulation surface as they increased during heating in a quiescent atmosphere then under flow (approximately 10 cm/sec) for three heater power levels (WIF-A,B, and D). In WIF-C, heating in a flow was not performed. Peak temperatures were reached in successively shorter times at higher heater power levels. The heating rates were affected to different extents by the low-speed convection. In the WIF-A and D tests, airflow slowed the heating rate compared to the quiescent case. In WIF-B, the quiescent heating profile is not smooth, suggesting that the heater power was not applied continuously, and the quiescent/convective comparison is difficult. More detailed analysis will be required to complete the comparison of the two environments on wire insulation heating rates.

B. IGNITION AND FLAME SPREADING

Successful ignition of the insulation material was achieved in all four tests. Two of the WIF burning experiments, WIF-A and WIF-C were conducted with flames spreading in concurrent flows, the others, WIF-B and WIF-D, were conducted in opposed flows. Learjet flame spreading tests provided estimates of flame luminosity used to preset the brightness of the thermocouple displays. Generally the WIF flames were much brighter than the flames observed in the Learjet tests, complicating the temperature display observations. The disparity in brightness is attributed to the (sub-atmospheric) cabin pressure in the aircraft in which the experiments were conducted. Additionally, the WIF tests produced surprising amounts of soot, and a molten fuel effect not observable in normal gravity.

C. CONCURRENT FLOW FLAME SPREADING

WIF-A. The first burning test, WIF-A, configured for concurrent-flow conditions, did not ignite on the first attempt. On the second attempt, the igniter was activated for a longer time and the sample ignited. The flame was significantly brighter than the Learjet flame and saturated the video imaging device. The video record shows that as the flame spread, the image brightness pulsated. The pulsations may have been caused by flow velocity fluctuations, however no fluctuations were indicated by the anemometer. The exposure meter in the 35 mm still camera responded quickly enough to these variations to provide

good, clearly resolved exposures. Figure 5 is a black and white reproduction of a single still color frame from the WIF-A flame. A thin blue flame stabilized where the air flow first met the flame, followed immediately downstream a very bright yellow region. The color of the flame gradually changed from the bright yellow to red nearer the downstream flame tip. These visibly luminous regions are associated with thermal radiation from hot soot particles produced in the flame.

The tip of the flame in this concurrent flow case was open, rather than coming to a pointed tip. Soot escaped visibly from the flame, often in large thread-like structures. The overexposed video image precluded quantitative measurements of their length, but fluctuations in the flux of escaping soot particles, apparently in concert with the brightness variations, were observed.

The stabilization region of the flame propagated as the insulation near the flame disappeared from the wire. Normally described as a burnout front, the consumption of fuel in this case combined fuel vaporization and the flow of molten insulation material. The molten material accumulated, forming a continuously growing, quasi-spherical bead two to three times the initial diameter of the insulation (see figure 6). This shape was assumed presumably to achieve a minimum surface energy configuration in the presence of surface tension. The molten bead in the concurrent flow test grew and was not always symmetric with respect to the wire. Near the downstream end of the sample, the gas-phase thermocouple, 1.5 mm from the insulation surface, was occluded by the molten fuel.

Unlike the opposed flow cases described below, the surface of the fuel near the flame in WIF-A, as seen in the still photographs, was discolored and opaque. A gray/brown color persisted throughout the burning time, and was apparently caused by the deposition of soot from the flame onto the surface. In a few of the still photographs, the opaque fuel surface appears to have been fractured or chipped, with an irregularly shaped gap in an otherwise uniformly brown surface. We speculate that a part of the surface soot layer may have been ejected by a bursting vapor bubble.

WIF-C. In the third test, WIF-C, the air-flow was not activated prior to ignition (nor during the heating phase.) A torroidal cloud of vapor or condensed pyrolysis products formed around the igniter and was rendered visible by the scattering of light emitted by the hot ignitor (see figure 7a). Upon reaching a diameter of approximately 30 mm, the cloud ignited suddenly (see figure 7b). The hot gas expansion wave associated with the ignition not only reached but overwhelmed the anemometer flag located 75 mm away.

After the ignition of the cloud the video recording shows an overexposed stationary flame stabilized about the igniter, which also appears to have remained energized (see figure 7c). Over the next several seconds the incipient flame and the hot igniter melted the insulation material in their vicinity, and soot deposition blackened the fuel surface beginning approximately 10 mm from the igniter. The

molten fuel flowed away from igniter, eventually baring the wire between the ignitor and the receding fuel.

Approximately 17 seconds after ignition the GBX air flow was activated. A flame around the igniter became immediately discernible but did not spread beyond the blackened surface downstream. For several seconds the stationary flame bathed the blackened fuel surface which appeared to accumulate soot emitted from the flame and to partially melt and recede an additional 5-6 mm. The flame continued burning until the insulation material near the igniter coil was consumed, approximately 38 seconds after ignition. We speculate that the downstream fuel failed to ignite under the combined effect of oxygen depletion and retarded fuel vaporization, suppressed by the layer of soot on the fuel surface.

D. OPPOSED FLOW FLAME SPREADING

WIF-B. Following ignition, the brightness of the flame in the WIF-B test saturated the video camera, and no structure of the spreading flame is discernible in the video recording. To compensate, Mission Specialist (MS) Carl Meade temporarily extracted the video camera from the GBX while the burn was in progress and reduced the lens aperture to improve the exposure of the spreading flame. The comparative brightness of the thermocouple displays, configured for compatibility with the Learjet flames, was thereby brought below the detection threshold of the video camera for the remainder of the test.

A single frame of this flame is shown in Figure 8. Molten insulation material flowed into an ellipsoidal bead just inside the leading edge of the flame. Approximately 1 mm ahead of the visible flame, a melting front in the virgin fuel is visible in the still photographs, seen as a change from translucence to transparence. A dark surface layer, about 1-2 mm in length, appears near the flame stabilization point. Similar observations have been made of polyethylene material radiatively heated in air in normal gravity, but not when heated in a nitrogen atmosphere. This discoloration may indicate that some degree of oxidative degradation of polyethylene occurred at the fuel surface.

Throughout the opposed flow tests, the flame stabilization region and the accumulation of molten fuel under the flame remained symmetric with respect to the wire axis. The size of the molten bead reached a steady size and shape, as shown in Figure 8, within 15-18 seconds.

The still photographs also showed vapor bubbles in the molten fuel. Evidence of the bursting of these bubbles was more clear in the video recording where small jets of flame briefly deform the flame near or in the flame stabilization region. In some instances these disruptions were accompanied by observations of small satellite flames, presumably burning particles of fuel created as the bubble burst. These disruptive events were the principal perturbations of the spreading flames.

The still photographs resolve the flame shape during a short time window and emphasize any captured perturbations of the flame. The video record emphasizes the average shape, though the source of the flame perturbations (e.g. bursting bubbles) are made more clear. In the video record the side, or visible outer boundary, of the spreading flame seems parallel to the wire (and flow) axis and the tip of the flame is completely open (i.e. the end of the luminous region is perpendicular to the flow direction), while the still photographs show some curvature of the flame tip back toward the fuel surface. The still photos show the fuel ball entirely inside the visible flame while the leading edge of the flame in the video appeared to be stabilized at a point nearly 90° around from the leading edge of the molten fuel ball. These distinctions are all attributed to greater sensitivity of the film to the dim blue portions of the flames.

According to the video record, as the flame reached the end of the fuel sample the side of the flame, previously parallel to the flow direction, diverged downstream (see Figure 9). At the same time the visible flame stabilization region moved forward to the front of the spherical molten fuel ball. In this non-spreading flame, more frequent disruptions were observed, caused by the ejection of material (polyethylene fragments and/or burst vapor bubbles) from the molten fuel ball. We speculate that the higher rate of vapor/fragment production was caused by the accumulation of the energy used earlier for flame spreading. This process continued until the spherical mass of fuel was completely consumed.

WIF-D. The fourth test was also configured for opposed flow conditions and resembled WIF-B in appearance. MS Meade replaced the monochrome video camera used in the previous tests with a color camera and, as before, reduced the lens aperture to eliminate the saturation in the video image. In this case the thermocouple displays remained visible because, although the color array is less sensitive overall than its monochrome counterpart, its color balance was in favor of the displays.

Acting on a suggestion of Professor J.S. T'ien, the WIF investigators decided to obtain a direct comparison between flames in opposed flow and quiescent conditions. When the WIF-D flame had spread nearly to the end of the sample, the air-flow was switched off. Figure 10 shows the ensuing sequence reproduced from the video recording. The visible flame quenched rapidly, receding downstream from the former stabilization region. The remaining polyethylene material cooled and solidified around the wire core in a nearly spherical bead 4-5 mm in diameter, shown near the right-hand end of Figure 11.

E. FLAME SPREAD RATES AND LENGTHS

The 35 mm photographic sequences provided the better resolution of the flame structure, particularly where precise visualization of the leading blue edge of the flame (essentially invisible in the

video record) was needed. Thus while lacking the time resolution of the video record, the still photographs were used to obtain the flame spread rates of tests WIF-A,B, and D. Flame position data from these measurements are shown in Figure 12. We estimate that the error in each position measurement is less than 0.01 cm, which in the propagation of error analysis[5] indicates an uncertainty in the spread rate measurement of less than 0.001 cm/sec. The spread rate results are summarized in Table 1.

F. MICROGRAVITY OPPOSED FLOW.

The measured spread rates for the two opposed-flow cases differ by only 6%, having values of 0.070 and 0.066 cm/sec for WIF-B and WIF-D respectively. Sample heating just prior to ignition (see also Figure 4 B and D) left the insulation temperature higher in the WIF-B test than in the WIF-D test. Higher bulk fuel temperatures reduce fuel preheating requirements and may explain the faster flame spread rate[6].

G. MICROGRAVITY CONCURRENT FLOW.

In concurrent flow, WIF-A, the visible downstream tip of the flame spread at 0.16 cm/sec; while the base of the flame (where the flame is stabilized and the fuel burnout occurs) spread at 0.12 cm/sec. The length of the flame therefore grew slowly throughout the test at about 0.04 cm/sec. Thus even in the extended test time provided by the glovebox this fuel did not reach an equilibrium flame length in a concurrent flow. While steady flame lengths and propagation rates in concurrent flow have been predicted[7] it is not clear what length of WIF-type fuel would be required to observe steady propagation.

H. NORMAL GRAVITY.

Flame spreading tests of the WIF fuel were performed in normal-gravity, ignited either at the sample top or at the bottom, to observe buoyant opposed or concurrent flows (respectively) interacting with the flame. Tests were also conducted in a horizontal configuration. Still photographs and video images were recorded during these tests for direct comparison with the WIF results. The molten fuel frequently dripped in all the normal gravity tests, and the dripped fuel was collected and weighed. A summary of the flame spread rates, averaged over multiple tests, is shown in Table 2.

I. COMPARISON OF CONCURRENT FLOW RESULTS.

The spreading of the flame tip in the upward case was too rapid to measure in the images obtained, i.e. the flame length exceeded the length of the fuel sample within about three seconds. Additionally, small cross currents in the laboratory air perturbed the flame symmetry with respect to the

fuel. The data imply an upward flame spread rate of at least several centimeters per second for samples of this size, compared to the WIF-A result of 0.16 cm/sec. The flame spreading and fuel heating processes were in many ways not comparable to the microgravity concurrent forced-flow case of WIF-A.

The speeds of the fuel burnout front in the normal-gravity upward test and the WIF-A concurrent flow test were similar (0.13 and 0.12 cm/sec, respectively). The molten fuel in the case of the WIF-A experiment accumulated as described above, and the burnout front propagated at a rate controlled by the rates of fuel melting and fuel vaporization. In the normal-gravity upward burning case, however, the burnout front propagation is strongly influenced by dripping, losing approximately 1/3 of the total fuel mass over the entire test. The similar WIF and normal gravity burnout rates therefore appear to be coincidental.

J. COMPARISON OF OPPOSED FLOW RESULTS.

The downward spreading experiments provide a closer comparison between normal-gravity and microgravity spreading. The microgravity spread rate in a low-speed opposed flow, 0.07 cm/sec, is much slower than the normal-gravity spread rate of 0.24 cm/sec. The bright, sooty image of the WIF flames preclude the simple explanation, oxygen deprivation, for the spread rate difference. It is reasonable to infer that the influences of radiative losses, identified in thin fuel flame spreading tests,[1] play a similar role here.

The behavior of the molten fuel seems to contribute to flame spread rates. In normal-gravity tests significant fuel mass dripped from the sample, 1/2 to 3/4 of the original fuel amount. In the several tests conducted, higher downward spread rates correlated with lower amount of fuel lost to dripping. We speculate that in the downward burning case the dripping may have provided an additional forward heat transfer mechanism in which the molten fuel flows downward along and preheats the virgin fuel, some fraction cooling enough to re-solidify. Where more fuel re-solidifies (and does not ultimately drip), more heat is provided to the virgin fuel, enhancing spreading.

In microgravity, that spreading mechanism is absent - all the fuel vaporizes. However, a thermocapillary flow of molten fuel from the vicinity of the flame toward the virgin fuel is conceivable, though not certain. While an appropriate surface tension difference exists between behind the flame and ahead of the flame, without a detailed surface temperature profile it is not clear if the fuel could flow, by capillarity, past the flame leading edge. Surface tension may affect flame spreading in a secondary way by altering the surface area and streamwise length of the mass of vaporizing fuel.

The quenching demonstrated at the end of WIF-D demonstrated the enhancement by convection of flammability for this fuel in microgravity. In ground-based testing of thin fuels, similar enhancements of microgravity flammability have been observed, and flame-spread rates in air are higher in 5-10

cm/sec opposed flows than in either normal gravity or quiescent microgravity conditions.[2,3,4] An analogous reduced-gravity enhancement by convection of flame spread rates is suggested by the WIF-D result.

K. FLAME TEMPERATURES

Temperature histories of the various thermocouples during the burning phase of the WIF tests were obtained from the video record of the temperature displays. Figure 13 shows the temperature histories obtained for the WIF-A and WIF-D experiments. In the WIF-A experiment (concurrent flow flame spreading) the first peak in the gas-phase temperature represents the passage of the flame tip, followed about 20 seconds later by the higher peak of the flame stabilization region. The later gas-phase temperature profile shows, in contrast, the effect of the thermocouple being occluded by the molten ball of fuel. The temperature reported for the melted fuel, about 520°C, is higher than expected and may be influenced by heat conducted along the thermocouple leads from the flame. The highest temperature measured in the concurrent flow flame was 1060°C.

In the WIF-D experiment (opposed flow flame spreading) the first peak in the gas-phase temperature represents the leading edge of the flame where the flame is stabilized in the flow, and is the highest temperature recorded in the test, about 1000°C. The gas-phase temperature dips lower after the initial peak then displays a second and lower peak representing the trailing edge of the flame. The temperature of the insulation shows a rapid rise to the pyrolysis temperature as the flame approaches, remains flat as the fuel vaporizes, then at burnout increases briefly to a high gas-phase temperature.

The temperature data from these experiments provide an opportunity to compare the global characteristics of flames spreading in concurrent and opposed flows in microgravity. Additional analysis of these temperatures has been proposed that will formulate estimates of heat transfer mechanisms in the flame, both in the flame spread direction and between the flame, the insulation and the wire.

L. SOOT AND PARTICULATE PRODUCTION

In all four tests, the bright yellow-orange color of the flames indicate that significant quantities of soot were produced. In the video recordings, soot can be seen escaping from the flame, most prolifically in the opposed-flow tests. In the normal-gravity tests of this material, this visible passing of soot from the flame was not so easily observed, perhaps because gas velocities (buoyant) are much higher than in the WIF tests (forced) at the downstream end of the flames. In normal-gravity tests, though, some soot does escape and can be collected from the plume above the flames.

In the opposed-flow WIF tests, strand-like soot structures, with lengths of approximately 10 cm, were observed downstream of the flame. The overexposure of the video record in WIF-A did not provide

similar quantitative imaging of the soot escaping from the concurrent-flow flame. Soot escaping from each of the flames accumulated on the exit screens of the test modules. The long soot strands observed leaving the opposed-flow flames were visible in the post-flight inspection of those exit screens. These exit screens, shown in figure 14, are noticeably more soot laden than the concurrent case.

Transmission electron microscopic analysis of the primary particles of the soot revealed mean diameters of 31 nanometers in the opposed-flow tests; primaries formed under concurrent flow conditions exhibited a mean diameter of 27 nanometers. These mean diameters differ by less than one standard deviation, and the apparent difference might prove to be statistically insignificant. Primaries formed under conditions of normal gravity exhibit, in comparison, a mean diameter of 13 nanometers. These results are consistent with contemporary microgravity soot measurements made in gaseous diffusion flames in drop towers.

Of additional interest is the discovery of polyethylene particles on the exit screen of module WIF-C. We speculate that these particles, 100 to 200 nanometers in diameter, are from the visible fuel-vapor cloud observed during the quiescent ignition attempt, and were carried downstream and condensed either in transit or by contact with the cold exit screen.

Many small bubbles were visible within the molten region, particularly in the opposed flow cases. Since the boiling temperatures of some polyethylene degradation products (range from C_1 to C_{100} or higher)[8] are much less than the degradation temperature of polyethylene, when the degradation products are formed inside the sample they are immediately superheated and form bubbles. These bubbles grow by accumulation of degradation products through diffusion in the molten polyethylene. When they become sufficiently large and close to the surface, the pressure in the bubbles is sufficient to cause a sudden rupture, ejecting fragments of the molten polyethylene into the gas phase. The ejection of small burning polymer fragments were often observed during the flame spread process.

CONCLUSIONS

The WIF experiment has provided a significant introductory database for electrical wire insulation overheating and burning in a low-speed convecting environment, a database impossible to create in normal gravity.

The analysis of the insulation temperature data, isolated from the wire and gas-phase temperatures, provided a simple observation of convective cooling effects in two of the four tests. We expect, however, that further analysis of the temperature data will yield quantitative convective heat transfer estimates in the low-speed flow regime that is unique to these tests.

The acquired data on flame size, structure, spread rates and temperatures, the behavior of the molten fuel, the soot production phenomena, etc. are instructive, particularly insofar as some aspects of

the observed behavior have not been previously observed. The behavior we have described of the molten fuel, the prodigious production and size of the soot agglomerates, the formation and bursting of fuel vapor bubbles in a spreading flame, and the transient quenching in an abruptly-created quiescent environment are all phenomena seen first in these tests. Among the more quantitative results are the observation that between the concurrent and opposed flow tests, the opposed flow tests propagate slower and produce more soot. As expected from a glovebox experiment program these data are not conclusive; yet they have already provided a stimulation for additional analysis of the existing data. We hope, for example, to extract additional heat transfer estimates from the temperatures observed during flame spreading. We hope that these data will also inspire the development of some modeling effort to clarify some of the unexpected observations.

REFERENCES

1. Bhattacharjee, S., Altenkirch, R.A., and Sacksteder, K.R., "Implications of Spread Rate and Temperature Measurements in Flame Spread Over a Thin Fuel in a Quiescent, Microgravity, Space-Based Environment," *Combust. Sci. Tech.*, 91, pp.225-242, (1993).

2. Olson, S.L., Ferkul, P.V., and T'ien J.S., "Near-Limit Flame Spread Over a Thin Solid Fuel in Microgravity," *Twenty-Second Symposium (International) on Combustion*, the Combustion Institute, pp. 1213-1222, (1988).

3. Olson, S.L., "Mechanisms of Microgravity Flame Spread Over a Thin Solid Fuel: Oxygen and Opposed Flow Effects," *Combust. Sci. and Tech.*, 76, pp. 233-249, (1991).

4. Sacksteder, K.R., and T'ien, J.S., "Buoyant Downward Diffusion Flame Spread and Extinction in Partial-Gravity Accelerations," submitted to the *Twenty-Fifth Symposium (International) on Combustion*, (1993).

5. Press, W.H., Flannery, B.P., Teukolsky, S.A., and Vetterling, W.T., *Numerical Recipes, the Art of Scientific Computing,* Cambridge University Press, pp. 505-506 (1986).

6. Borgeson, R.A., and T'ien, J.S., "Modeling the Fuel Temperature Effect on Flame Spread Limits in Opposed Flow," *Combust. Sci. and Tech.*, 32, pp. 125-136, (1983).

7. Grayson, G.D., Sacksteder, K.R., Ferkul, P.V., and T'ien, J.S., "Flame Spreading Over a Thin Solid in Low Speed Concurrent Flow: Drop Tower Experimental Results and Comparison with Theory," *Microgravity Sci. Technol.*, to appear.

8. Madorski, S.L., *Thermal Degradation of Organic Polymers*, John Wiley and Sons, Chapter 4, 1964.

Table 1. Initial Fuel Temperature, Flame Spread Rates and Flame Lengths in 10 cm/sec Forced Air Flow

Flame Spreading Direction	Insulation Temperature at Ignition	Leading Edge Propagation Speed	Fuel Burnout-Front Speed	Flame Length
Concurrent (WIF-A)	75-85°C	0.16 cm/sec	0.12 cm/sec	1.8-2.6+ cm
Opposed (WIF-B)	80°C	0.070 cm/sec	-	1.8 cm
Opposed (WIF-D)	70°C	0.066 cm/sec	-	1.9 cm

Table 2. Normal Gravity Flame Spreading Results

Flame Spreading Direction	Flame Leading Edge Propagation Speed	Fuel Burnout-Front Speed
Upward	-	0.13 cm/sec
Downward	0.24 cm/sec	0.18 cm/sec
Horizontal	0.14 cm/sec	0.13 cm/sec

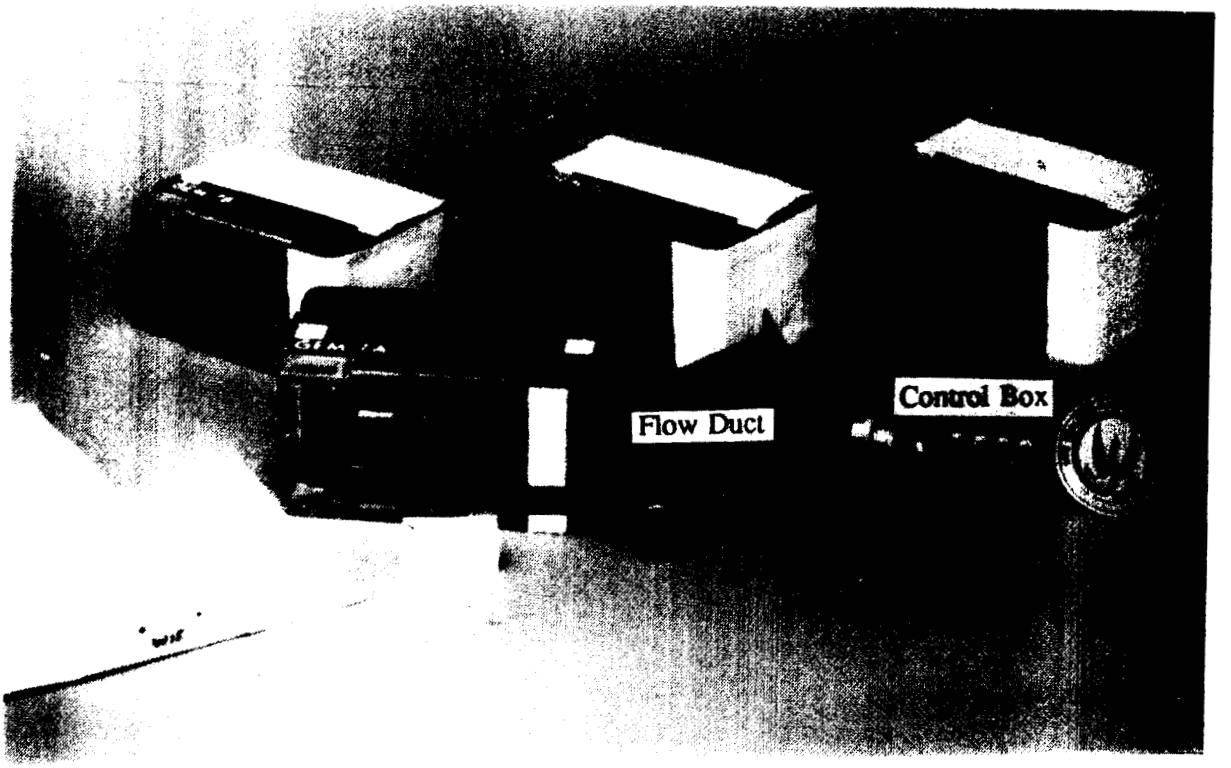

Figure 1 The WIF Flight Hardware.

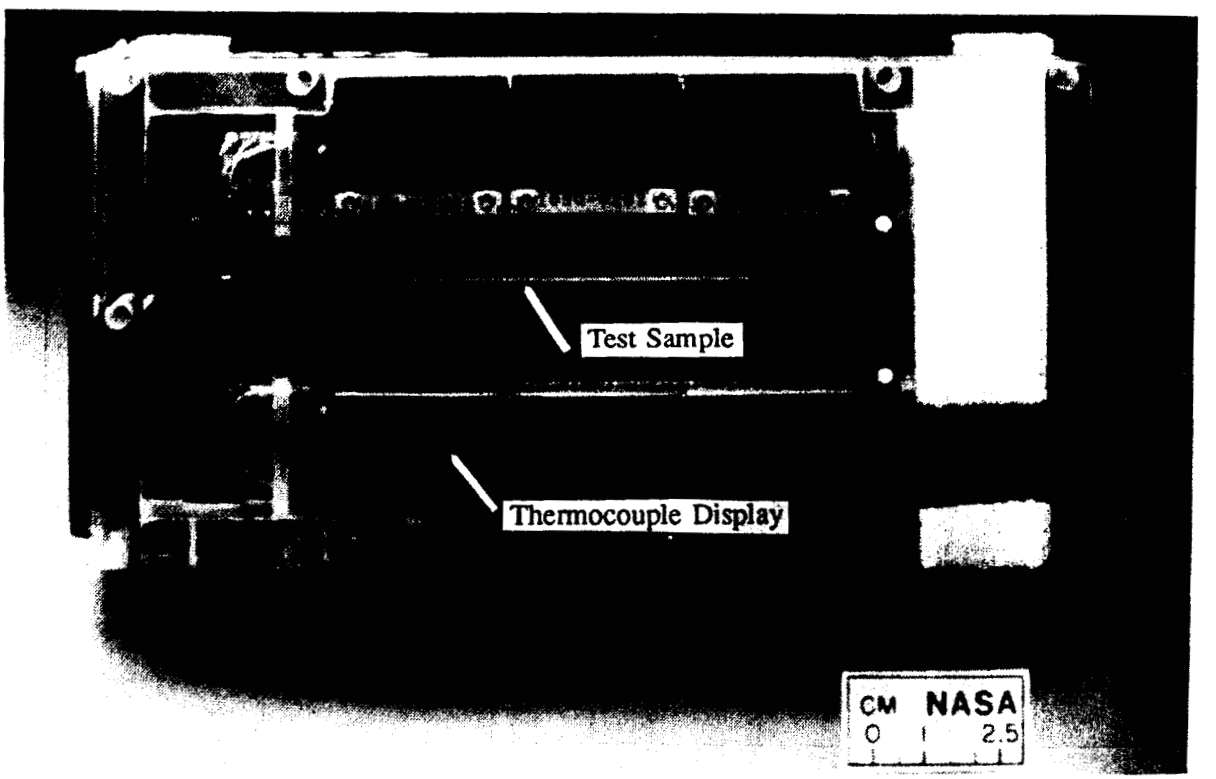

Figure 2 WIF Module: Temperature Displays and Test Sample.

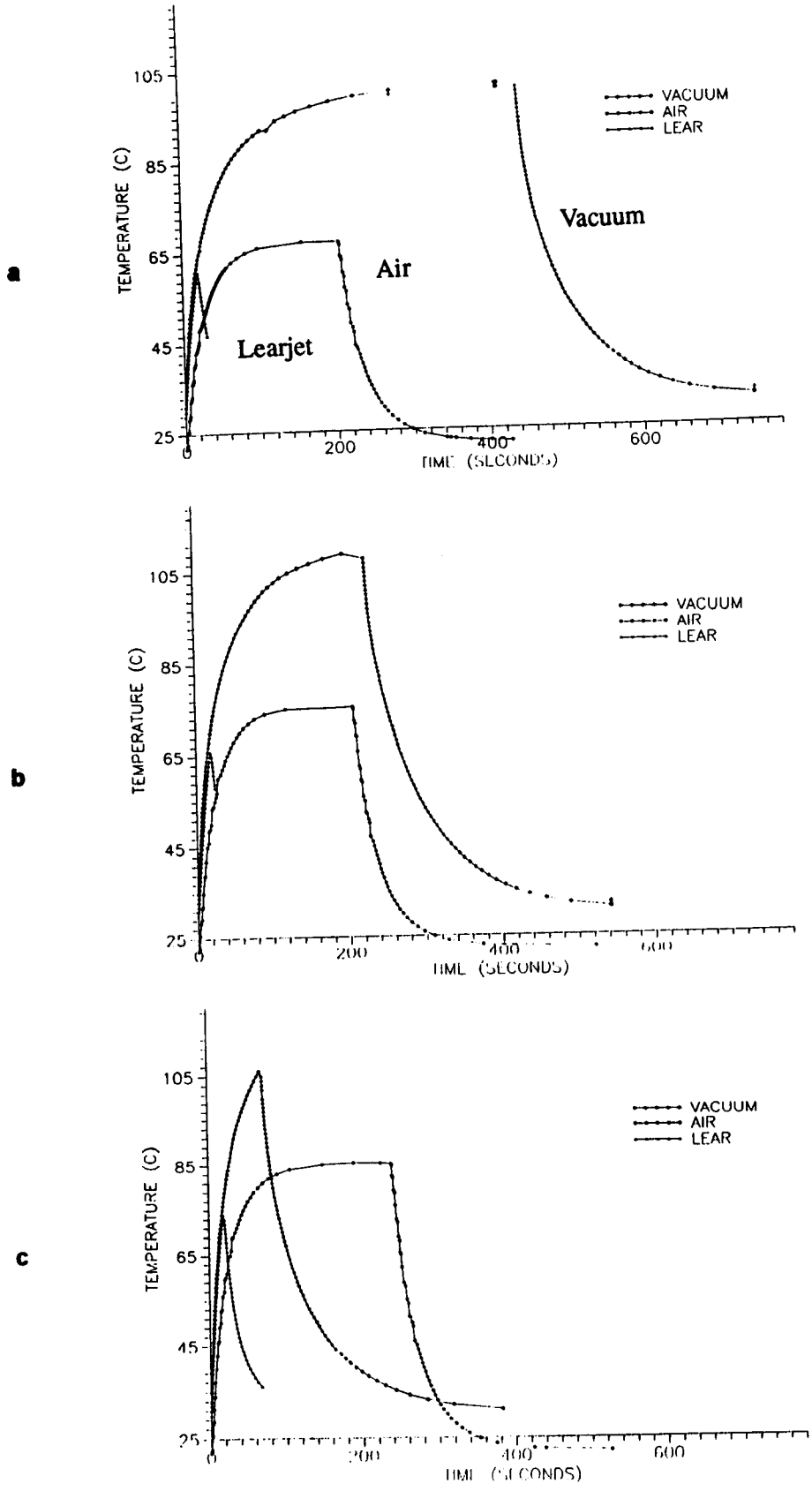

Figure 3 Ground-based wire heating rates, a) 1.22 Watts input power, b) 1.5 Watts input power, c) 1.82 Watts input power.

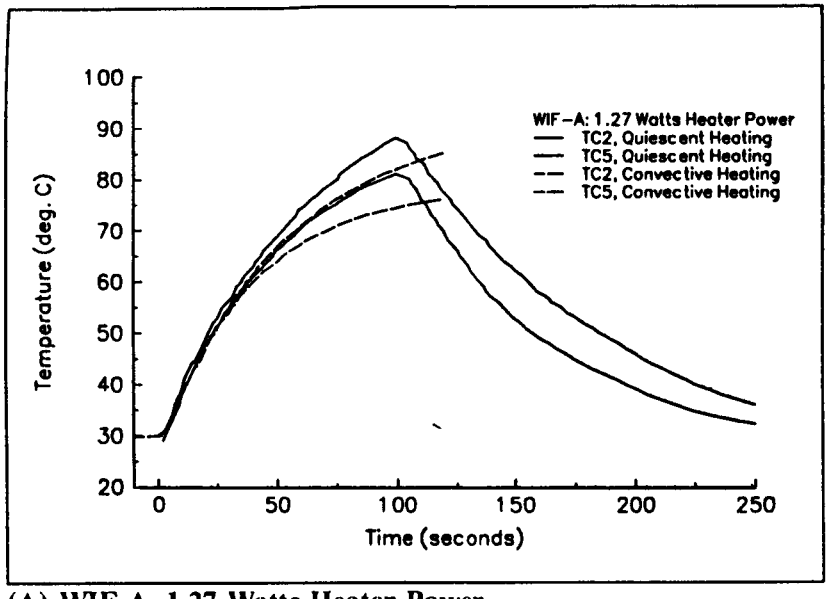

(A) WIF-A, 1.27 Watts Heater Power

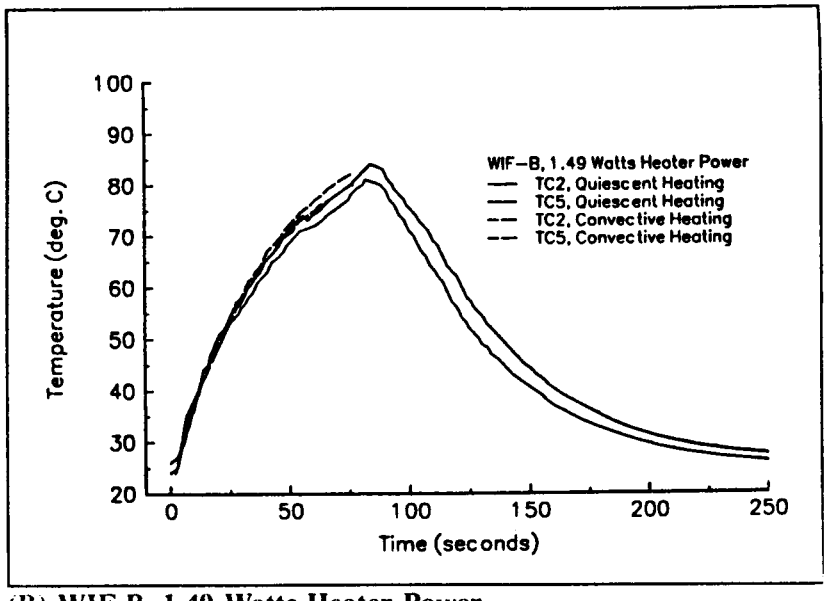

(B) WIF-B, 1.49 Watts Heater Power

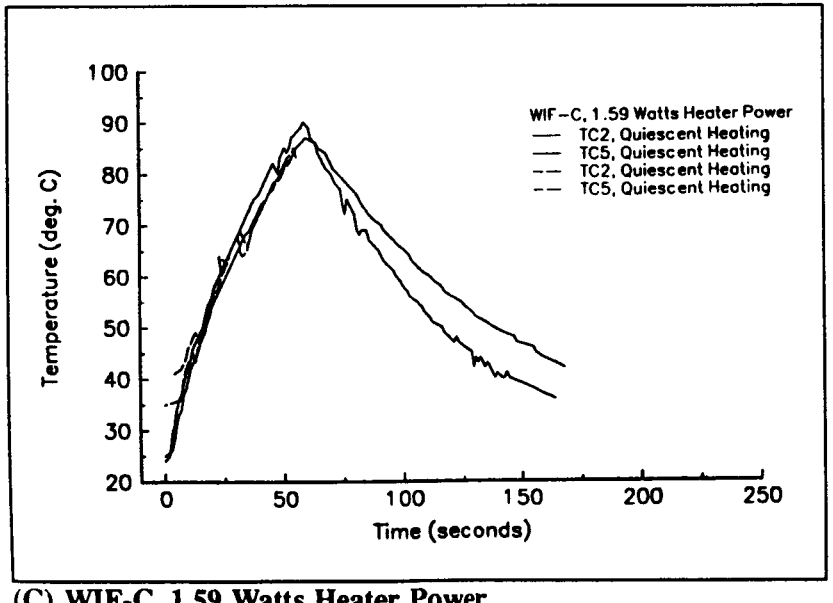

(C) WIF-C, 1.59 Watts Heater Power

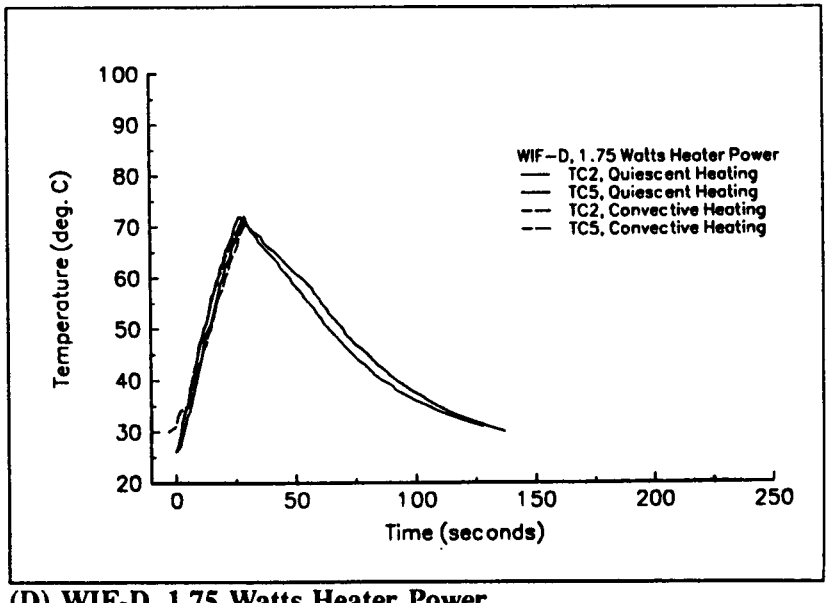

(D) WIF-D, 1.75 Watts Heater Power

Figure 4 Comparison of Quiescent and Convective Heating Rates.

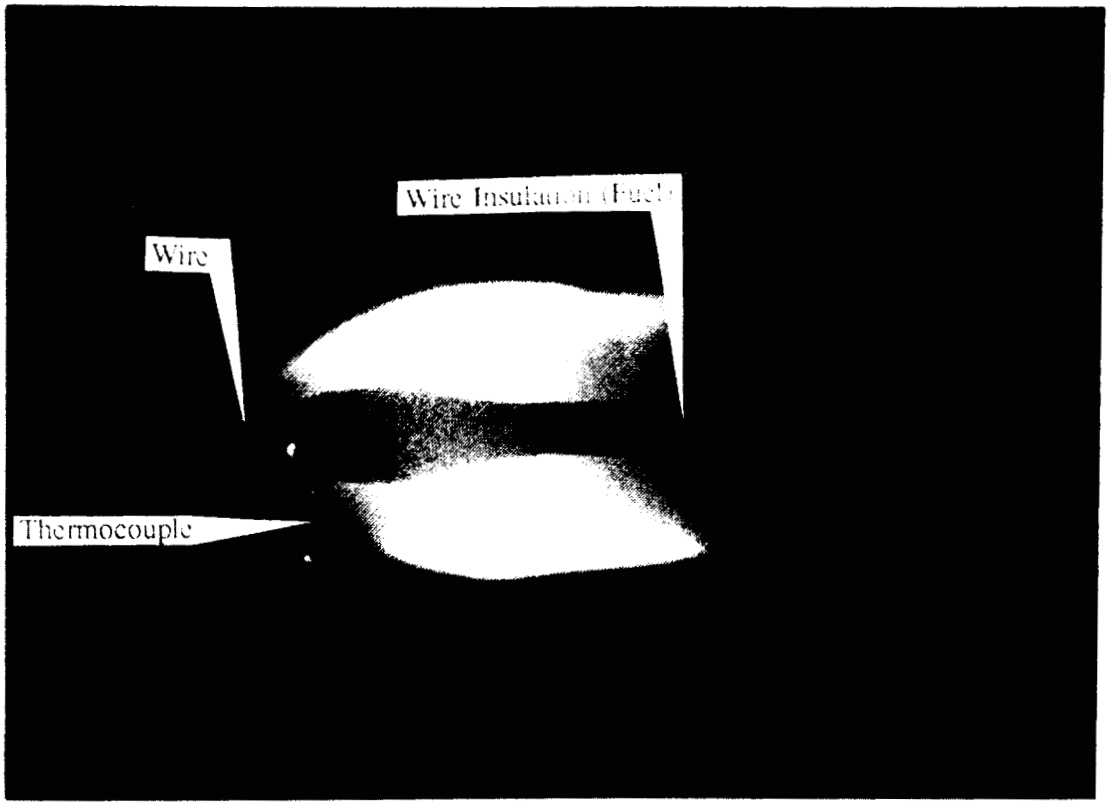

Figure 5 WIF-A, Concurrent Flow Flame; Accumulating Molten-Fuel Bead.

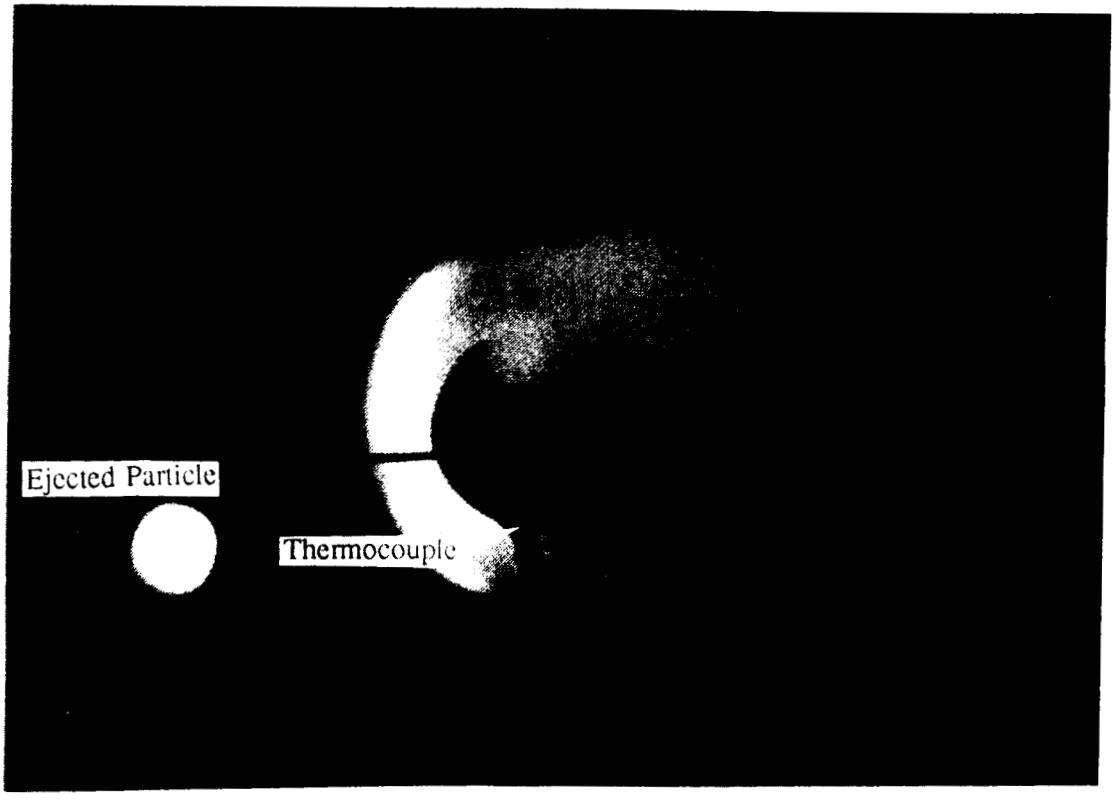

Figure 6 WIF-A, Concurrent Flow Flame; Molten-Fuel Occluding Thermocouple.

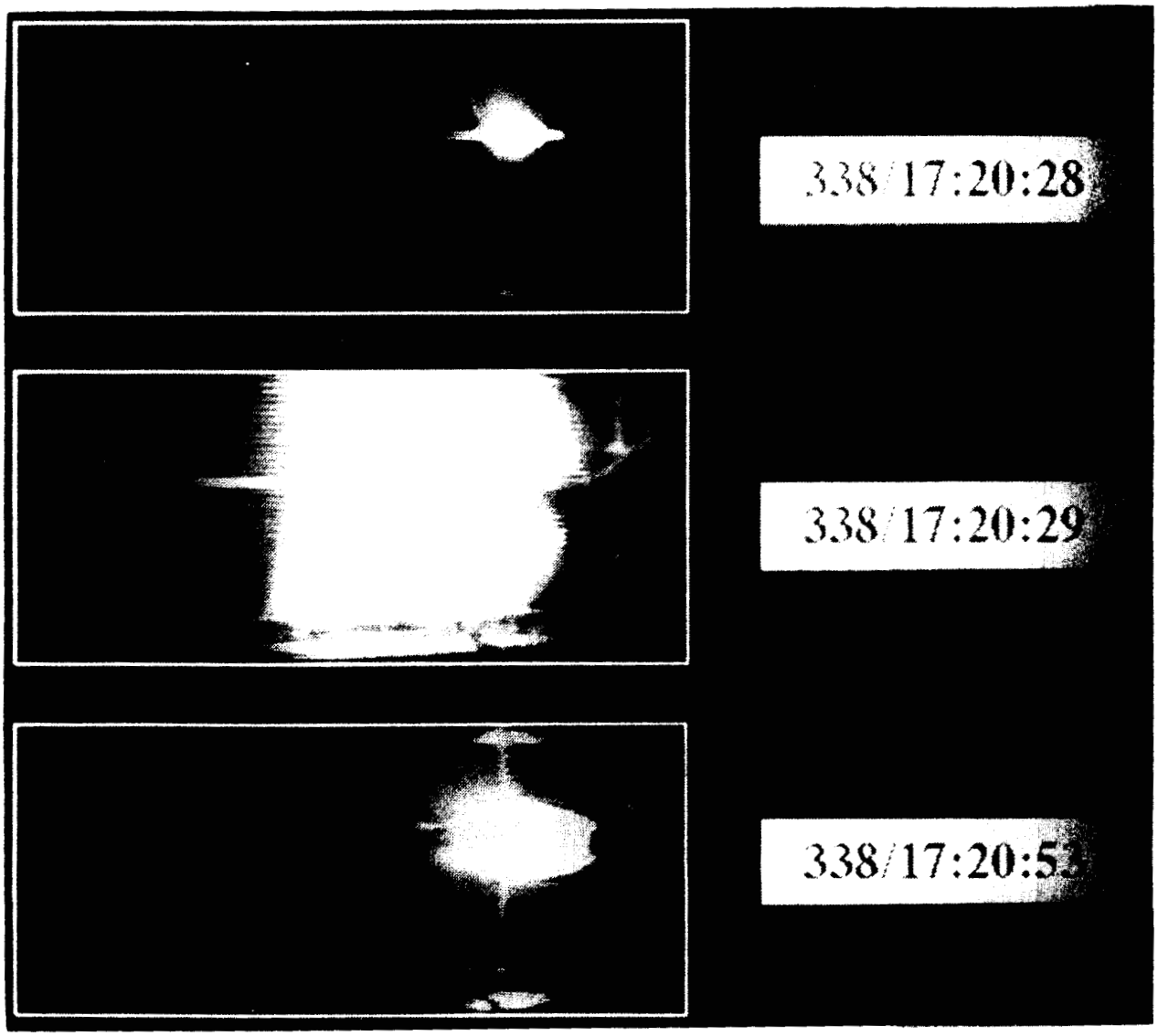

Figure 7 WIF-C, Ignition of Fuel Vapor in Quiescent Air.

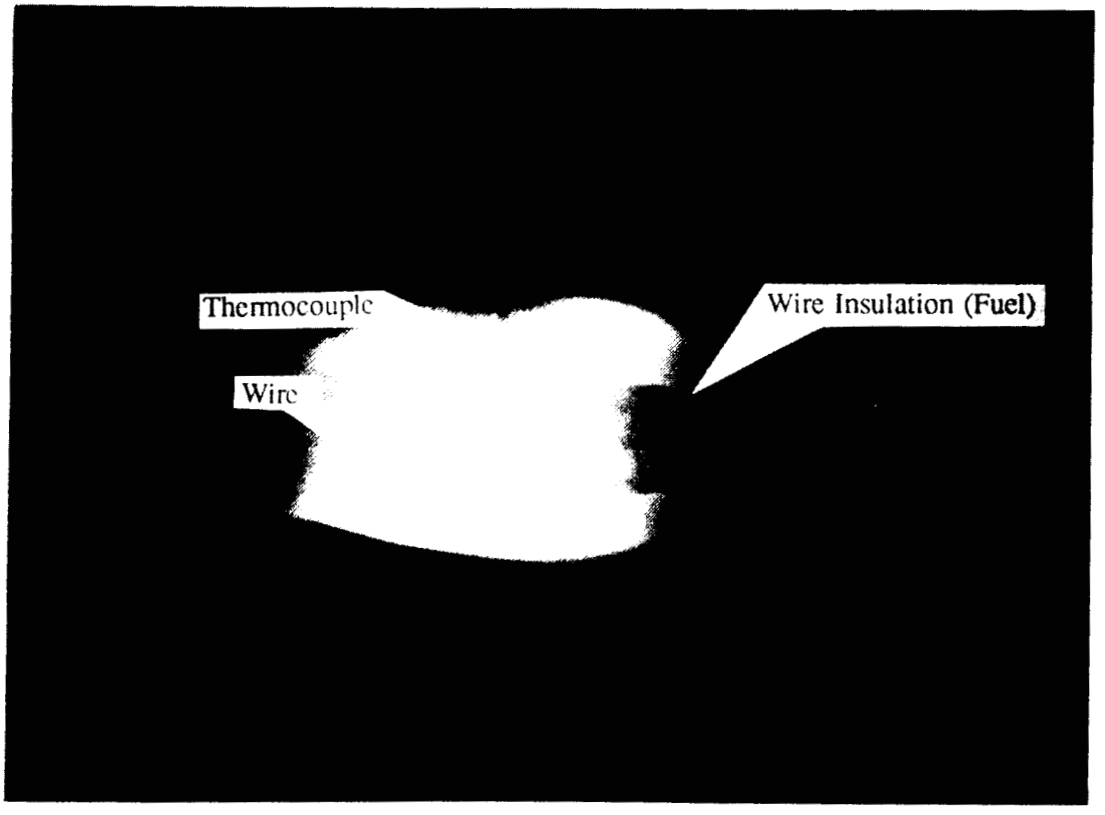

Figure 8 WIF-B, Opposed Flow Flame; Accumulating Molten-Fuel Bead (from Film)

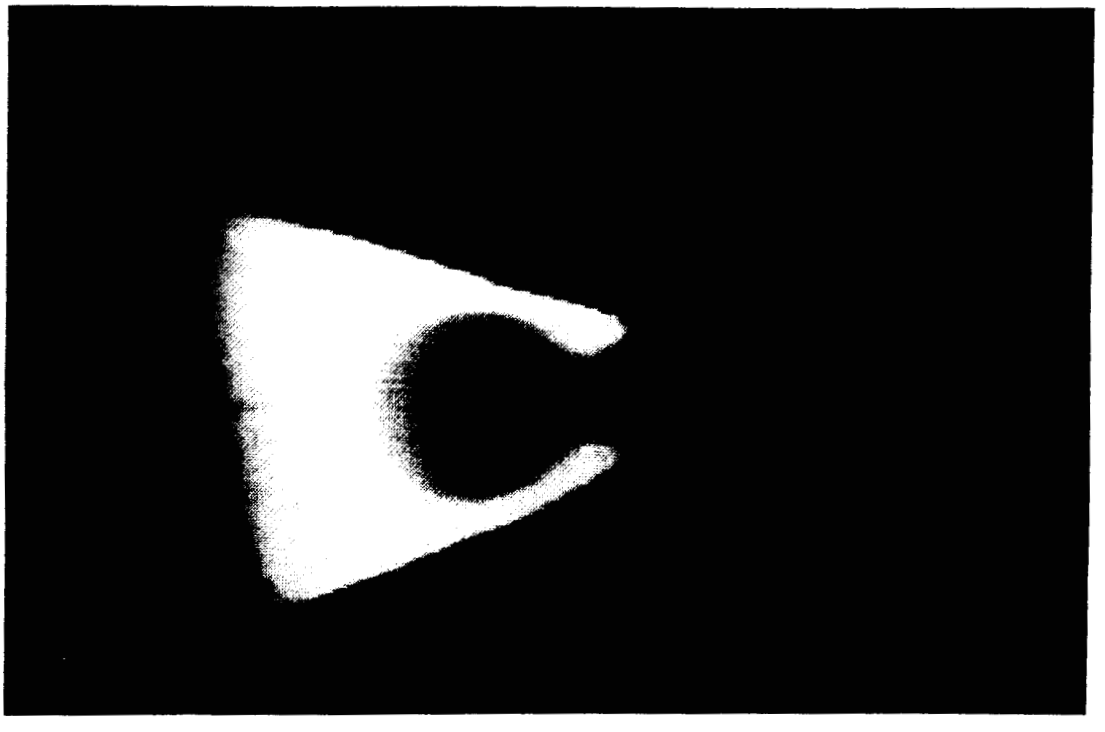

Figure 9 Opposed Flow Flame; Flame Structure at the Fuel End (from Video).

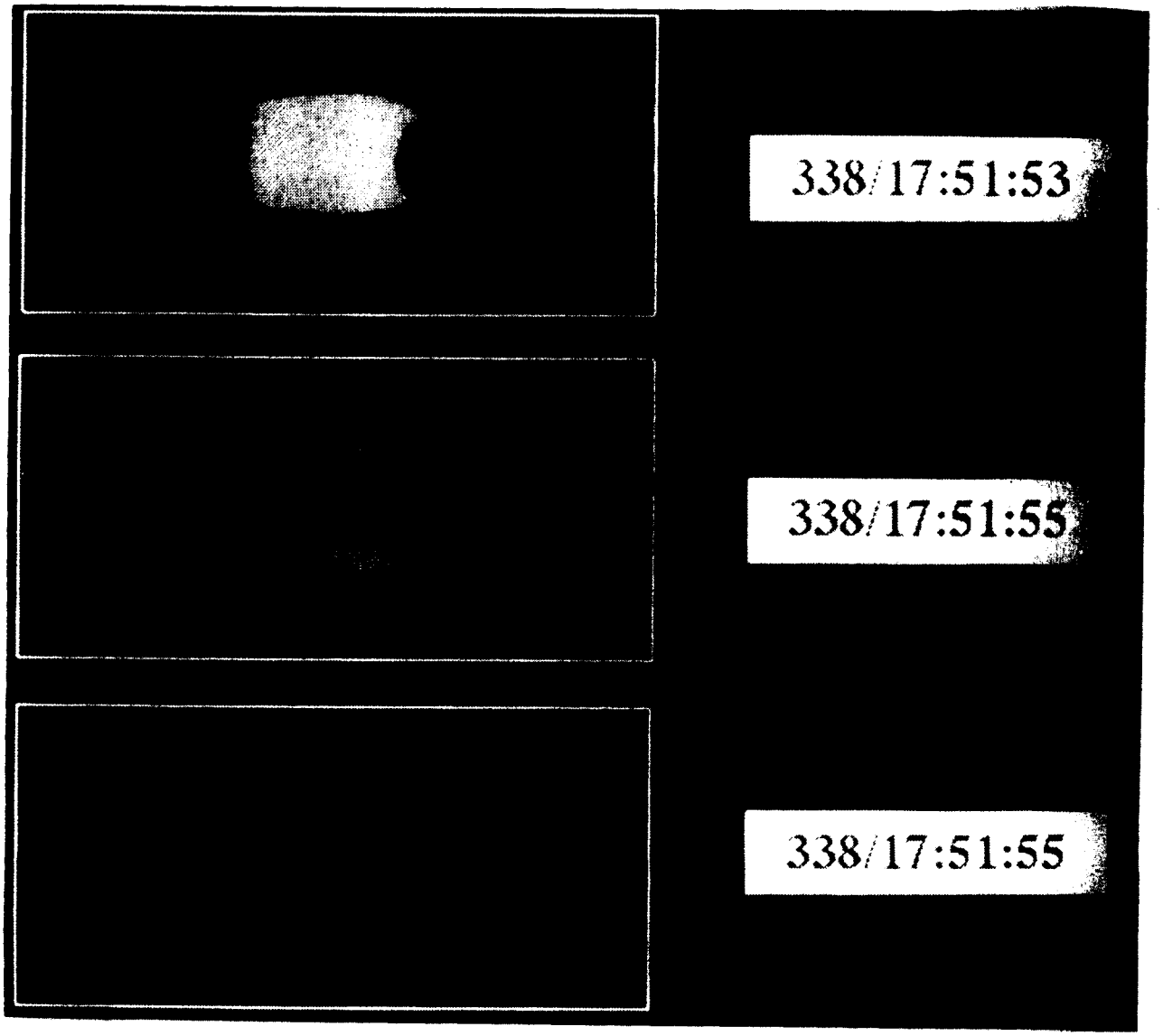

Figure 10 WIF-D, Opposed Flow Flame; Quenching as Flow Stops (from Video).

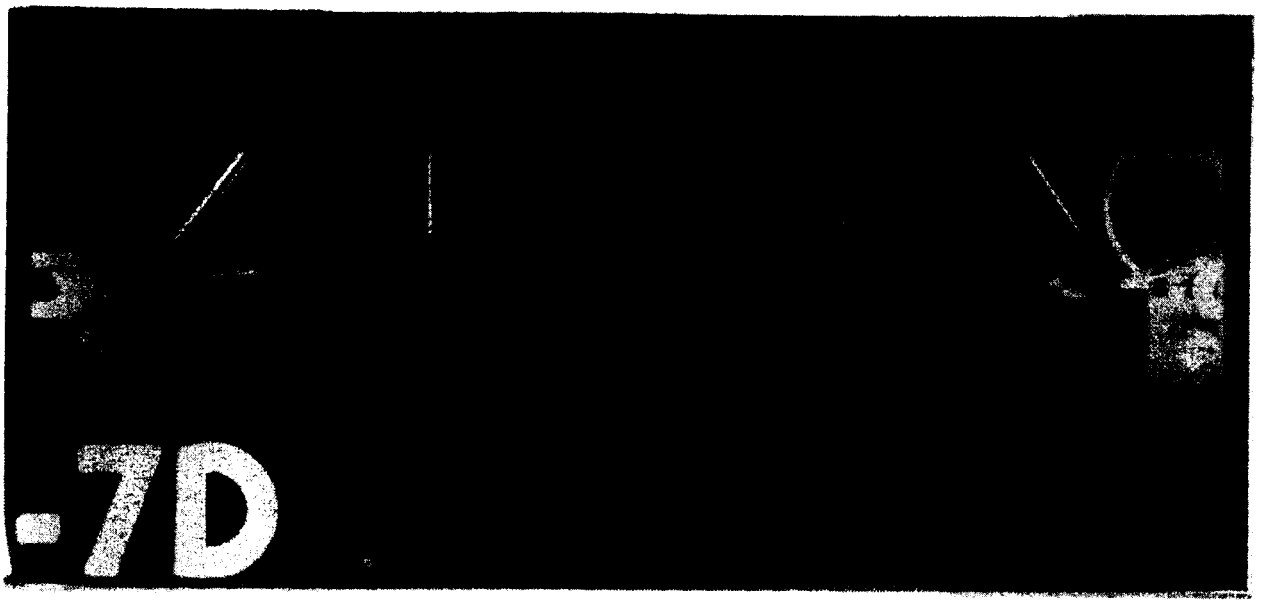

Figure 11 WIF-D, Opposed Flow Flame; Quenched Shape of Molten Fuel (from Film).

a.

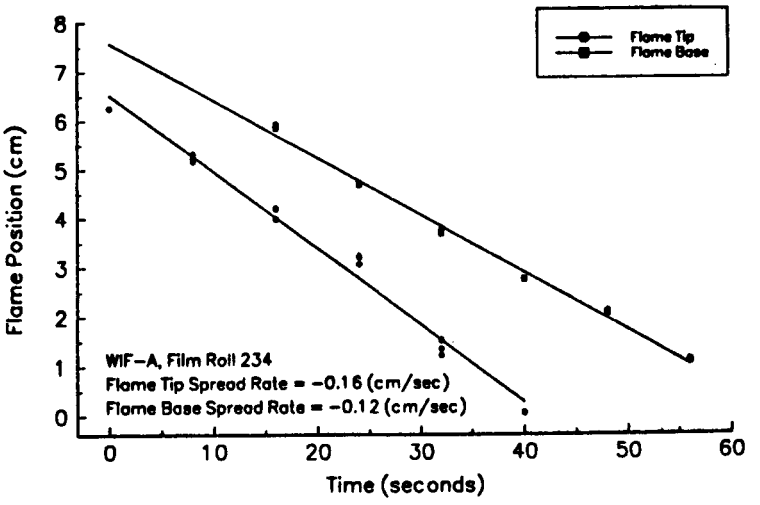

b.

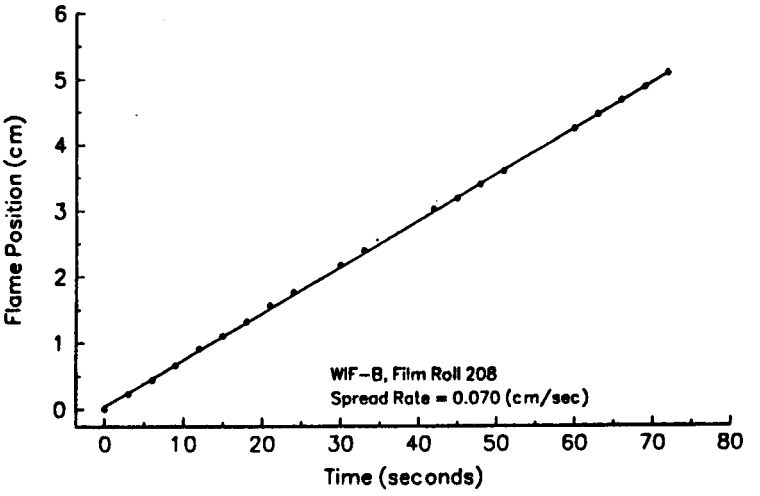

c.

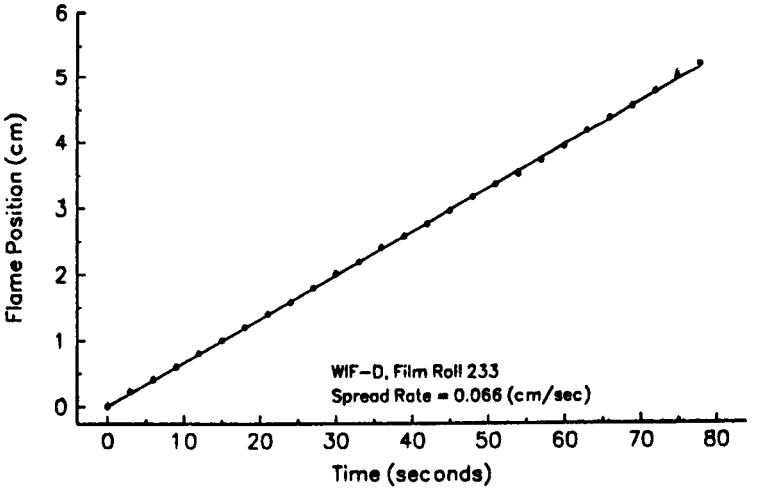

Figure 12 Flame Spread Rate (from film data) a) WIF-A, Concurrent flow flame, b) WIF-B, Opposed flow flame, c) WIF-D, Opposed flow flame.

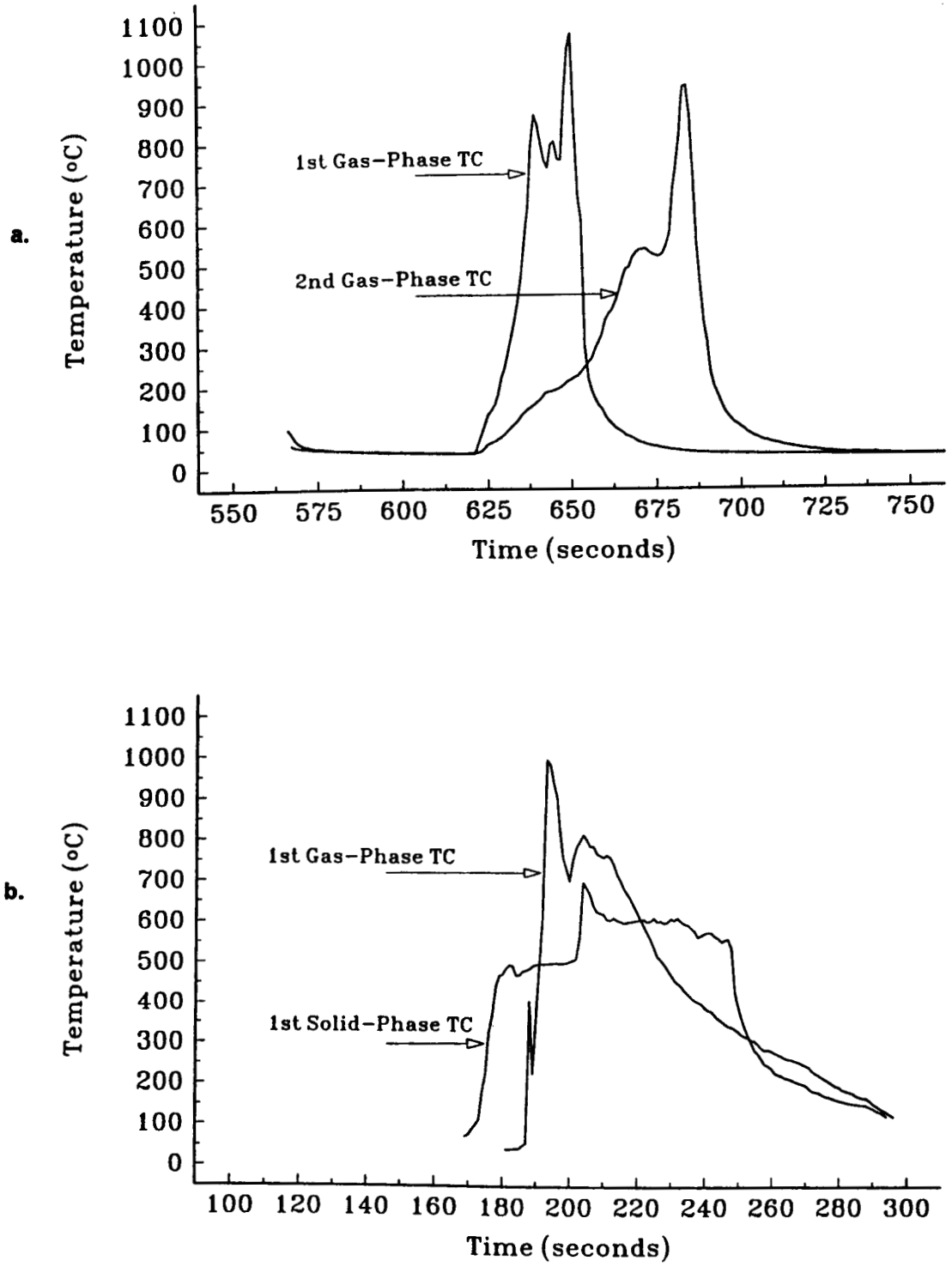

Figure 13 Temperatures during flame spreading, a) WIF-A, Concurrent flow flame, b) WIF-D, Opposed flow flame.

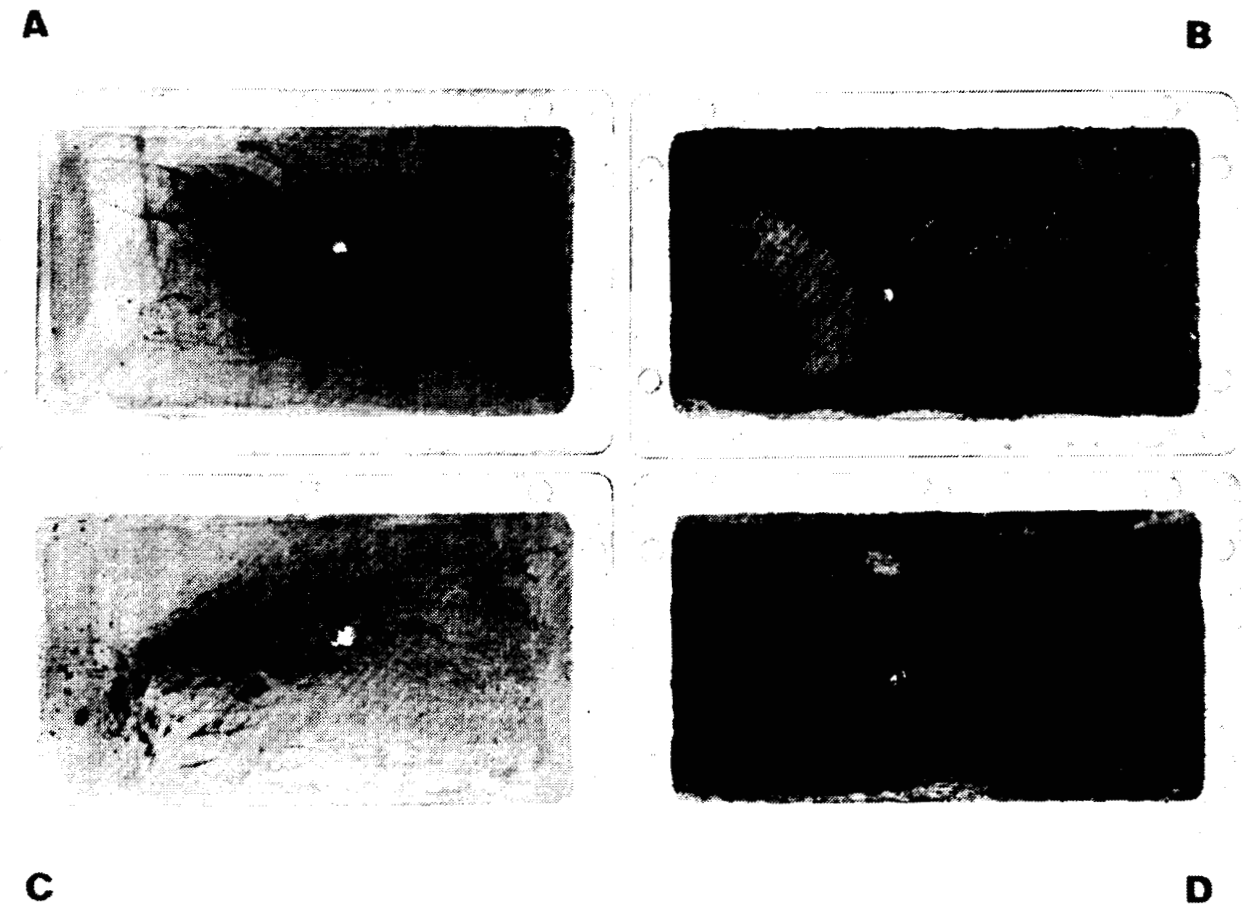

Figure 14 Accumulated Soot on WIF Module Exit Screens.

FIBER PULLING IN MICROGRAVITY (FPM)

Robert J. Naumann
Professor of Material Science
University of Alabama in Huntsville

ABSTRACT

The Fiber Pulling in Microgravity experiment sought to separate the role of gravity drainage from capillarity effects in the break-up of slender cylindrical liquid columns. Both effects tend to limit the parameter range of viscosity and surface tension over which fibers can be successfully drawn.

Slender liquid strands of various materials were pulled manually by the Mission Specialist to well beyond the Rayleigh stability limit and the breakup was observed. The time required for break-up was estimated and compared with theory. The break-up times for silicone oil correlated with viscosity as would be expected. Interestingly, strands of corn syrup and honey broke up almost immediately, making it impossible to draw fibers from these materials in the absence of gravity.

INTRODUCTION

Long liquid strands are inherently unstable and capillarity effects will cause the column to pinch-off and break up if the length is more than the circumference. Also gravity causes the liquid to slump and eventually pinch-off. Generally, the more viscous the liquid, the longer it takes for the stand to break, other things being equal. Drawing fibers from viscous liquids is a widely used process in many industries. The trick is to cause the liquid to solidify before breakup-up can occur. Many interesting exotic heavy metals and fluoride glass systems have a low viscosity in the melt which make it difficult to draw them into fibers. If it can be shown that gravity drainage is a limiting factor in fiber drawing, a good case could be made for using microgravity to draw fibers from lower viscosity melts that are encountered in some of the more

I. DESCRIPTION OF THE EXPERIMENT

The fiber pulling apparatus consisted of lexan base and six 3 ml syringes which contained fluids of varying viscosities. The range of viscosities were chosen to represent low to moderate values for glass melts. The fluids involved and their properties are listed in Table 1. In addition to the Dow 200 fluids that are well-characterized, honey and white corn syrup were also included. This was done for two reasons; one, because the experiment had been written up as a potential student participation experiment and it

was desired to use at least some materials that were familiar and easily accessible to students, and two, it might be interesting to vary the type of material to explore a different region of parameter space.

Table 1. Fluids used in fiber pulling experiment

Fluid	Surface tension	Viscosity
Dow 200 Silicone oil	21.5 dynes/cm	100,000 cSt
Dow 200 Silicone oil	21.5 dynes/cm	73,000 cSt
Dow 200 Silicone oil	21.5 dynes/cm	45,000 cSt
Beechwood honey	TBD dynes/cm	15,000 cSt
Dow 200 Silicone oil	21.5 dynes/cm	11,000 cSt
White Corn syrup (Kayro)	TBD dynes/cm	7,200 cSt

It should also be pointed out that the mechanism for forming liquid strings in normal gravity is quite different than in low-gravity in that gravity drainage is helping pull the liquid into a strand. In low-gravity, attempts to pull liquid strings by simply dipping a object into the fluid and removing it were unsuccessful as we discovered during the KC-135 training flights prior to this mission. Without the help of gravity drainage, the viscous forces are simply not strong enough to overcome the inertia of the liquid and the strand immediately breaks. In order to deploy a liquid strand, it is necessary to extrude the liquid as the syringe is moved to avoid accelerating the liquid in the strand.

II. EXPERIMENTAL RESULTS

A syringe containing the fluid of choice was selected and inserted through a guide hole in the experiment base. A small amount of fluid was squeezed onto a pedestal supported by the base to anchor the liquid strand. The syringe was then slowly withdrawn while extruding fluid in an attempt to form a thin liquid strand approximately 5 cm long. The syringe was then clamped in place and the break-up of the column was recorded on video. Of primary interest was the time required for the capillary instability to cause the column to thin and separate as a function of column diameter, viscosity and surface tension. Attempts to pull long slender liquid strands were made using all 6 sample materials although some difficulty was encountered in manually trying to keep a constant diameter as the liquid column is drawn. Also the liquid column tended to snake around as it was being deployed. Strands of liquid approximately 4 mm in diameter were successfully pulled from all of the silicone oils, including the 11,000 cSt. material

which does not tend form liquid strings in normal gravity. The time to break-up due to capillarity effects ranged from 10 seconds for the 11,000 cSt. silicone oil to approximately 70 seconds for the 100,000 cSt. silicone oil. Strangely, both the honey and the corn syrup, which easily form liquid strings in normal gravity, would not form strands in reduced gravity. Instead, they broke almost immediately in any attempt to draw them into fibers. Accurate values for their surface tension have not yet been determined, but since they a aqueous solutions, their surface tensions are possibly two or more times greater than the silicone oils. Given their relatively low viscosities, the break-up time was probably too short to be observed.

In 1892 Lord Rayleigh[1] obtained a solution for the break-up of slender liquid columns, both for the inertial dominated case and for the viscous dominated case. The time constant for the latter is given by

$$\tau = 6\mu a/\sigma$$

Inserting μ = 1000 gm/cm sec (100,000 cSt.), a = 0.2 cm, and σ = 21.5 dynes/cm, τ = 56 sec. Similarly, for the 1100 cSt. silicone oil, t = 6 sec. These compare favorably to the observed break-up times of 70 sec. and 10 sec. respectively. (It should be noted that e-folding times for thinning are being compared against actual break-up times.)

CONCLUSIONS

The observed time required for a long slender column of silicone oil to break up is in reasonable agreement with the prediction from the theory developed in 1892 by Lord Rayleigh. This is probably the first attempt to actually test of this theory since there is really no way to perform such a test on Earth without gravity interfering. It was difficult to get an accurate measure of the initial diameter of the liquid column since there was some variation in diameter due to the manual deployment technique used. Also, there is some uncertainty in when the time should start since it takes several seconds to deploy the strand, during which some thinning has already begun. Greater accuracy could probably be obtained with a mechanical deployment system which could meter the fluid more accurately than by hand.

It is interesting to note that in the case of honey and corn syrup, the breakup time was too short to allow strands to be deployed in microgravity; yet these substances readily for liquid strands in the presence for gravity. Apparently gravity drainage helps stabilize these strands against break-up due to capillarity effects by continuing to supply new fluid to areas that have begun to thin.

REFERENCE

1. Lord Rayleigh, Phil. Mag. S. 5., 34 (1892) 145-155

ACKNOWLEDGMENT

The author wishes to thank the many people that helped in the various aspects of this experiment, especially Roger Chassay and Tony DeLoach in the MSFC project office for guiding me through the MSFC flight acceptance procedures, the USML crew for their patience in the training exercises and the preliminary experiments on the KC-135 and special thanks to Joe Prahl for his interest and helpful suggestions and to Carl Meade for the skill and dedication he exhibited in actually performing the experiment on USML-1.

Discussion

Question: *In squeezing the material out of the syringe you actually get compression flow. Have you ever tried to do this in extensional flow ? If you do it in extensional flow you get polymers there and you will actually extend those polymers and then your viscosity will be at least 3 times that in compressional flow, and that could stabilize you ?*

Answer: Well certainly. All of these fluids that we are dealing with are non Newtonian and of course the theory was developed for Newtonian fluids so right away you have got a problem there. The problem in trying to do it by extensional flows though, is the fact that without gravity drainage to help pull that out, you just can't pull a strand. There is just not enough strength, if you will, or whatever it takes in a column to overcome the inertia and that is why you couldn't just dip a stick in there and pull it out from the stick. It just doesn't want to pull. So what we were trying to do was to deploy the strand without having to accelerate the mass of the strand. So that is why we thought, well if we simply lay it out as we go along, then we will have no inertial forces to overcome or to accelerate and hopefully we will have gotten the force-free deployment scheme. And of course you can only do that to a certain degree of accuracy by trying to squeeze it out in your hand. The other problem of course was the silicone oil was sticky and was always getting in between the guide that Carl was working with, and also, the syringes that we were trying to work with had a slight taper to them. So they tend to want to hang up and there is a lot of stiction and it could use a little bit more human engineering. But as it turned out real well for a first cut experiment, I think we were able to do a pretty decent experiment. Carl did a beautiful job with the technique of trying to work that.

Question: *In keeping with the bubbles of the morning when you pushed on that syringe was there any evidence of bubbles being generated ?*

Answer: That is interesting. We didn't really see any bubbles. Again, the fluid is very viscous and I don't know why we didn't really see any. What we tried to do in a couple of cases when Carl didn't get a string to be pulled very well, he would go back in and try to aspirate the little blob by pulling back on the syringe. When he did that you always got bubbles in it. But then if you tried to deploy it with bubbles in it you had all sorts of problems because bubbles would come out and cause the thing to break up. But we did not seem to have problems just extruding from the fluid that was in the syringe the first time. If there were any bubbles in there, I surely did not see any evidence of it. I don't know why there should have been, come to think of it.

Question: *When you start considering the low viscosity and low surface tension for certain classes of optical materials, did you get any insight from what you have done here for how you might consider doing something like that in microgravity ?*

Answer: Well, yes. The range of viscosity we chose was roughly around 10 kilo centistoke, if you like that unit, but that is the way they are advertised up to 100,000 centistoke and that is roughly the range. The 100,000 value is sort of the low end of the optical fibers that you would pull from silicon or silica. The 10 k was down more of what you would expect of the fluoride systems as I understand it. I guess the conclusion that I would have reached here, was that these were pretty fat fibers and they had to be fat to last long enough to be measured. I am under the opinion of what I have seen so far, that the gravity drainage is a very stabilizing effect in pulling fibers and probably you would run into very serious trouble if you tried to do very thin fibers in microgravity. I am not sure there is an advantage to doing that from what I have seen so far. I will have to look at that much more carefully before I make a blatant statement but I guess what I am saying is, you can pull strands a lot easier on Earth than you can in microgravity because of the gravity drainage effect. Rather than being something that hurts you it seems to help you.

NUCLEATION OF CRYSTALS FROM SOLUTION IN MICROGRAVITY

(USML-1 GLOVEBOX (GBX) INVESTIGATION)

Roger L. Kroes, Donald A. Reiss, and Sandor L. Lehoczky

Space Science Laboratory
Marshall Space Flight Center, Huntsville, AL.

ABSTRACT

A new method for initiating nucleation from solutions in microgravity which avoids nucleation on container walls and other surfaces is described. This method consists of injecting a small quantity of highly concentrated, heated solution into the interior of a lightly supersaturated, cooler host growth solution. It was tested successfully on USML-1, producing a large number of LAP crystals whose longest dimension averaged 1 mm.

BACKGROUND

There are two approaches to growing crystals from solution in microgravity; (1) seeded crystal growth, and (2) nucleated growth. In seeded crystal growth one starts with a high quality seed crystal, immerses it in a slightly supersaturated growth solution , and the seed crystal grows by the process of new growth layering on the seed. The growth rate is controlled by the degree of supersaturation of the growth solution; a low degree of supersaturation producing a low growth rate which is conducive to high crystal quality. A difficulty arises when evaluating the quality of the new growth area and relating it's quality to the microgravity processing environment. Defects and imperfections in the seed are often propagated into the new growth region. Ambiguities arise, therefore, when trying to interpret the characteristics of the new growth area because the effects of the seed may mask the effects of the growth environment.

In nucleated crystal growth, one produces a highly supersaturated solution in which over time spontaneous nucleation takes place and crystallites appear. The degree of supersaturation can be adjusted to provide optimum growth rates for the crystallites, which then grow to large size. Since these crystals were not grown from seeds their structural quality is not influenced by the quality of an underlying seed, and a relationship can be made between their quality and the microgravity processing conditions from which they were produced.

Another advantage of growing crystals from nucleated solutions is that it can offer a greater degree of flexibility compared to seeded growth. There are ways to control the number and size

distributions of crystals produced. Careful control of the nucleation process can produce anywhere from a very few to a great many crystallites. The growth of these crystallites into large single crystals can be controlled by adjusting the degree of supersaturation of the growth solution.

The favorable condition for nucleation is a high degree of supersaturation. The onset time for nucleation, along with the rate of nucleation, is governed by a curve which displays a very sharp increase in the nucleation rate over a narrow range of supersaturation. The favorable condition for the growth of crystallites into high quality large crystals is a low growth rate achieved by a low degree of supersaturation. Figure 1 shows the dependence of the nucleation rate, the growth rate and the mean crystal size on supersaturation.

A serious problem arises when nucleating in microgravity. The usual procedure used in a one-g environment is to cool the walls of a container of solution to drive the solution into supersaturation. Because of the absence of convection in microgravity, cooling the walls of the container only cools the adjacent solution leaving the interior solution to cool very slowly by conductive heat transport. Crystallites tend to nucleate first on the walls of the container, and do not form in the interior until a much later time when conductive heat transport has finally cooled the interior. As a result, control over the nucleation and growth rates will not be sufficient to produce the desired numbers of crystals of large size and high quality.

A new method for initiating nucleation from solutions in microgravity which avoids wall nucleation problems and adds considerable flexibility to the whole process has been developed by the authors.[2] This method consists of injecting a small quantity of highly concentrated, heated solution into the interior of a lightly supersaturated, cooler host growth solution. The injected solution, which is heated to above its saturation temperature, quickly cools in the presence of the cooler, lightly saturated host solution and forms a highly localized, highly supersaturated zone in which nucleation is soon initiated. Once crystallites form, they grow in the favorable concentration and temperature environment provided by the host solution. Considerable flexibility is offered by the combinations of injection solution and host solution temperatures and concentrations which can be chosen. It should be noted that because the rate of thermal diffusion is an order of magnitude greater than mass diffusion, the small globule of injected solution cools quickly and only slowly diffuses into the host solution, providing the needed time for the nucleation process to occur.

I. EXPERIMENT

The objective of this investigation, which was flown in the GBX facility onboard USML-1 launched on STS-50 from the Kennedy Space Center on June 25, 1992, was to demonstrate and evaluate the above described new technique for initiating and controlling the nucleation of crystals from

solution in a microgravity environment. Figure 3 shows the experiment apparatus. It consists of a fluid transfer unit (FTU), solution reservoirs, experiment cells, and a temperature probe and display. Aqueous solutions of L-Arginine Phosphate Monohydrate (LAP) , $C_6H_{14}N_4O_2$- H_3PO_4-H_2O, were used for both the nucleating and growth solutions. Three sequential runs were planned using nucleating solutions of LAP with concentrations of 42g, 38g, and 34g of LAP in 100g of H_2O. These were to be injected into growth cells filled with a host solution with a concentration of 18g LAP in 100g of H_2O. Figure 2 shows the solubility curve for LAP. At one end of each solution reservoir was an interior electric heater, a thermistor, a magnetic coupled stirrer, and a transfer port. At the other end was a piston used to drive the transfer of solution from the reservoir. On top of each reservoir was a electrical terminal for connection to the FTU controller. On top of each growth cell were ports for (1) filling with host solution, (2) injection of the nucleating solution, (3) a vent for exhausting air as the cell is filled, (4) a check valve with overfill chamber, and (5) a feed through for the temperature probe. The reservoirs containing the host solutions held a volume of 93 ml of which 70 ml were the maximum transferable. The reservoirs containing the nucleating solutions had an internal volume of 49 ml, however only about 0.99 ml of solution were injected for any given nucleation run. The growth cells had an internal volume of 67 ml. The FTU contained a Tattletale microprocessor programmed to control the heating, stirring, and transfer of solutions form the reservoirs. It also had a temperature display indicating the solution temperature in the reservoir being processed.

Mission constraints necessitated the stowage of the experiment solutions at ambient temperature (about 25·C) in their reservoirs for many weeks prior to launch. Because all of the concentrations used in the experiment are above saturation at room temperature, it was anticipated that crystallites would precipitate out of solution in the reservoirs during this stowage period, therefore the experiment was designed with the capability of heating and stirring the solution to dissolve the precipitated material.

II. PROCEDURE

The FTU was placed in the glovebox and connected to the glovebox power through two cables, one of which supplied 12 VDC for the electronics and the stirring motor and the other supplied 24 VDC for the heater and the stepper motor which pumped the solutions. A host solution reservoir was inserted into the FTU and the heater/thermistor cable was connected. The host solution was heated to 55·C and held at that temperature with stirring until all precipitated solute had dissolved. The solution was pumped through a flexible transfer tube and quick-disconnect fittings into the nucleation cell, which was then allowed to cool to glovebox ambient temperature (about 27·C). While the cell was cooling, the reservoir containing the nucleating solution was heated to 60·C and held at that temperature with stirring until the precipitated material was dissolved. When the cell reached ambient temperature, a Lexan injection tube

was connected to the injection reservoir, and hot solution was manually driven into the tube assembly by turning a knob on the FTU in order to purge all air from the assembly. The injection tube was then quickly inserted into the nucleation cell and a knob on the FTU was slowly turned to inject about 1 ml of the nucleating solution into the host solution. The solution transfer tube was then disconnected using the quick disconnect fitting, and the cell was bagged and attached to the laboratory module wall for periodic photography as nucleation occurred and the crystallites grew. The growth phase lasted for about 5 days.

III. Results

Nucleation did not occur in the first run because a number of large air bubbles were introduced into the host solution during experiment cell filling. These bubbles dispersed the nucleating solution in the host solution as it was injected, preventing the formation of the highly supersaturated region required for nucleation to occur. In the second run, the cell was filled more slowly by using the manual fill knob on the FTU instead of the filling motor. No bubbles were introduced in this case. The 34g LAP/100g H_2O nucleating solution was selected for this run, and it was successfully injected into the center of the cell, producing a nucleating region about 12 mm in diameter. Profuse nucleation occurred approximately 15 seconds after injection, producing a large number of crystallites. The crystallites eventually drifted to the wall of the cell opposite the end of the injection tube under the influence of residual gravity. Figure 3, taken during the flight, shows the cell with crystals. A few of them are still suspended near the center of the cell in the microgravity environment of the Spacelab module. The largest of the crystals grew to dimensions of about 3 x 5 x 0.5 mm. Most of the crystals were about 1 mm in their longest dimension. These were difficult to measure because they had clumped together after the flight and could not be separated without breakage. A total of 4.34g of crystals were recovered from the cell after it was returned to the laboratory. The third planned run could not be performed because of time constraints.

CONCLUSION

This experiment successfully demonstrated the value of our new method of initiating nucleation in a solution in microgravity in providing significantly better control over nucleation and growth processes than conventional techniques. A predetermined volume of nucleating solution was deployed in the desired location in a growth solution-filled cell. Nucleation was restricted to this well defined region near the center of the cell, and crystallites were grown. The nucleation onset time was much shorter than expected based on the results of ground control experiments using the same concentrations. In these experiments a series of solutions of various concentrations were prepared and loaded into test tubes which were then sealed and allowed to cool to room temperature. These tubes were inspected periodically, and the time of the appearance of visible nucleation was noted. The reason for the

difference between ground-based and flight onset times has not yet been determined, but turbulence in the nucleating solution during injection, and the high cooling rate may have been important factors. Further experiments will emphasize the optimization of the solution concentrations to improve control of the nucleation rate. With finer control over nucleation, this method will permit more precise control over growth parameters which control crystal characteristics.

REFERENCES

1. J. Nyvlt, O. Sohnel, M. Matuchova and M. Kroul, *The Kinetics of Industrial Crystallization,* Elsevier, NY, p35

2. U. S. Patent No. 5,173,087, Crystal Growth in a Microgravity Environment, December 22, 1992

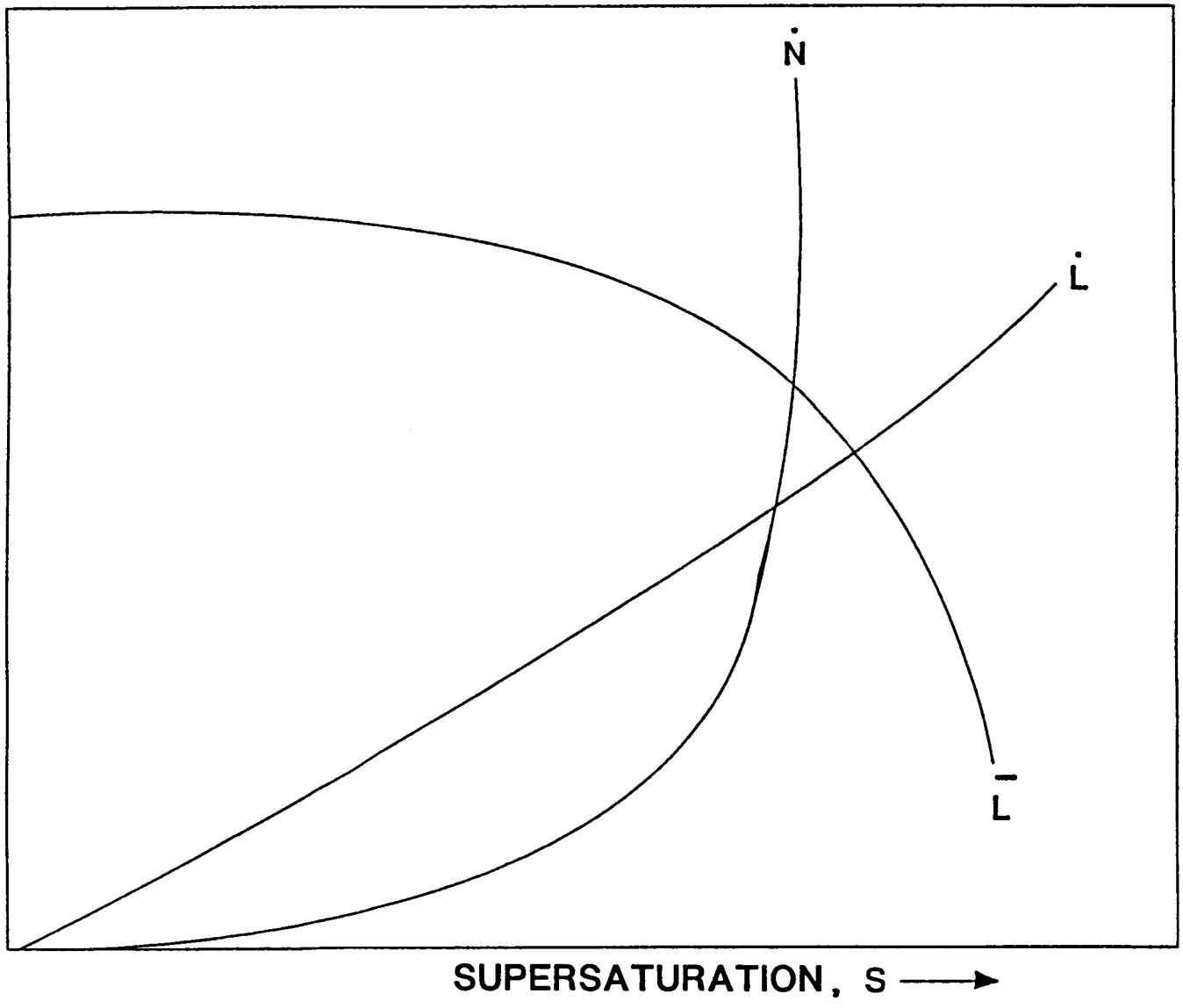

Figure 1 Dependence of the nucleation rate ($\dot{N}$), the crystal growth rate ($\dot{L}$), and the mean crystal size ($\bar{L}$) on the supersaturation (S).[1]

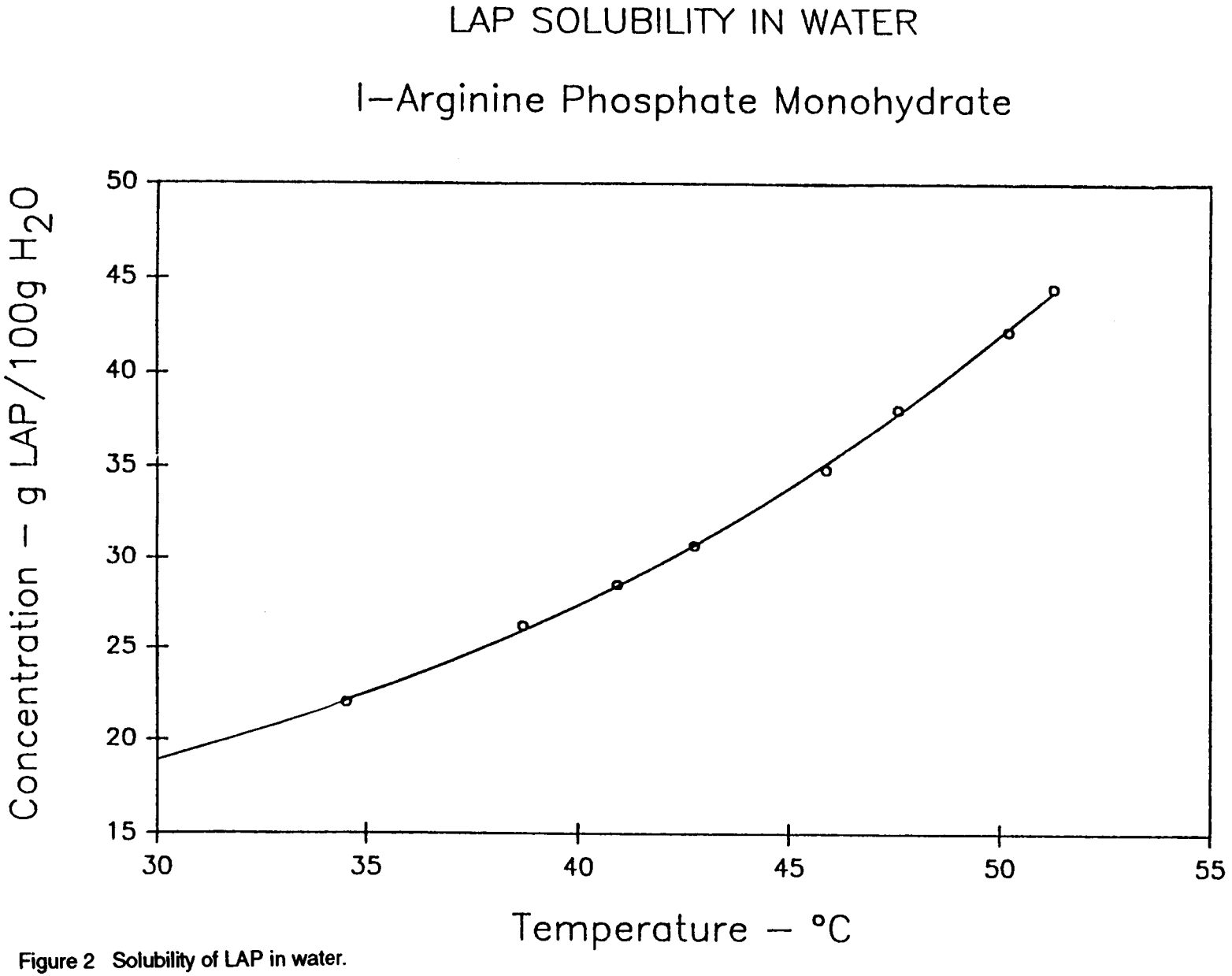

Figure 2 Solubility of LAP in water.

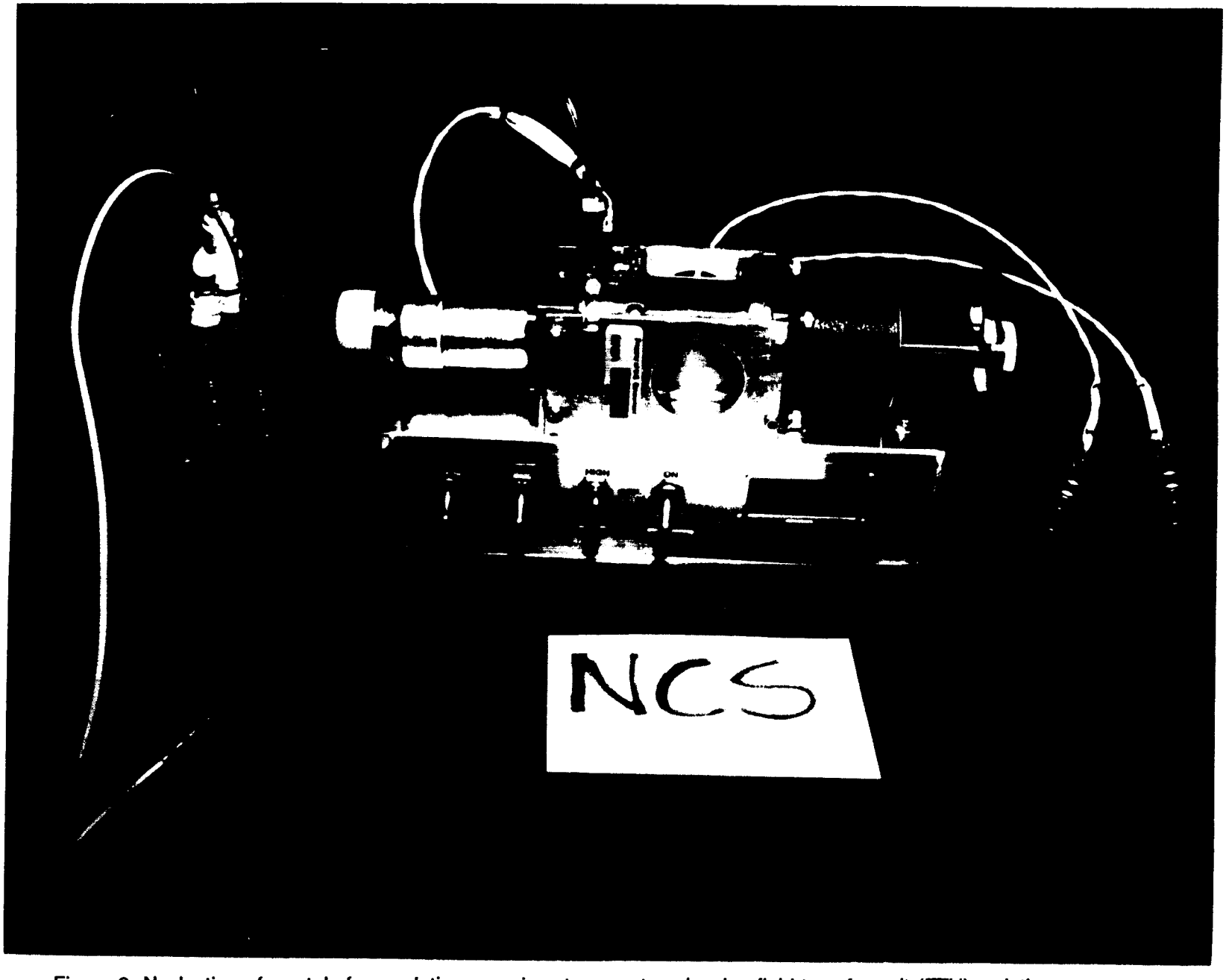

Figure 3 Nucleation of crystals from solution experiment apparatus showing fluid transfer unit (FTU), solution reservoir (mounted in FTU), experiment cell, and temperature display.

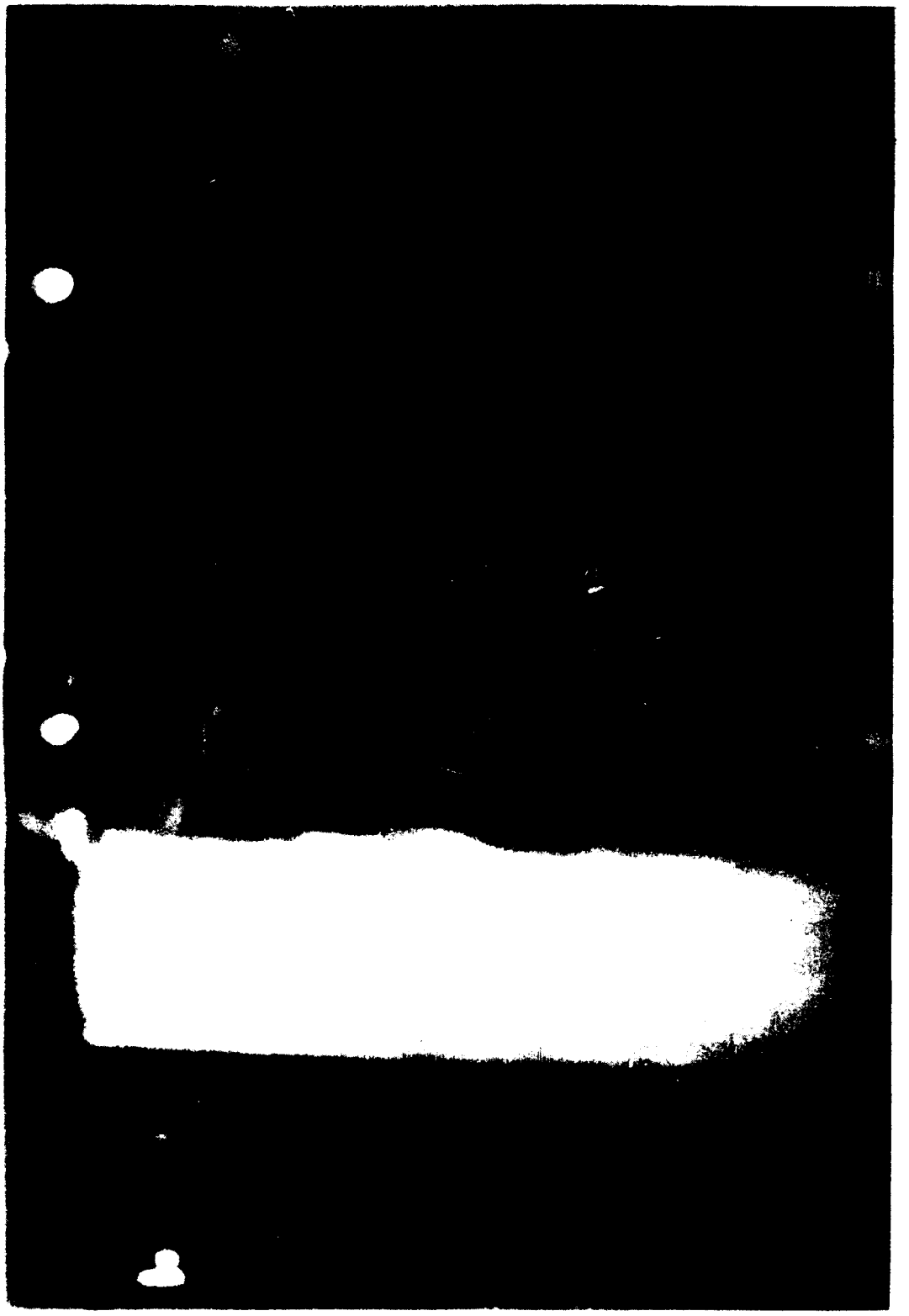

Figure 4 Experiment cell containing growing crystals, taken during flight of USML-1.

Discussion
(Speaker: Donald Reiss, NASA MSFC)

Question: *Did you do anything to agitate the solution to make sure there was not basically a local heavier concentration because as you were trying to dissolve the crystals, the nutrient had to diffuse into the solute ?*

Answer: Are you talking about the reservoir before we injected it ?

Question: *Yes*

Answer: Yes. Again, because we had problems with the stirrer, we did have Carl manually agitate the apparatus repeatedly. I think it was every 10 minutes, or so, until he could see that certainly there was no solid material in there; but, we tried to get as good mixing as we could under the circumstances.

Question: *Could you comment on what the possibility was of getting pre-embryonic or embryonic sizes while it was coming down the tube ?*

Answer: That is certainly a possibility if you get some substantial cooling in there. We had no way of measuring it. The way we tried to avoid it was just to heat the solution well enough above equilibrium. That and, then of course, the tubing itself is an insulated material, so we were hoping that if we worked quickly enough that we wouldn't have time to cool into supersaturation before that injection took place. The equilibrium temperature was 45 and we heated to 60. We are just assuming that we are reasonably under-saturated before we did the injection. I didn't see in the video any salt particles coming out of the tube. It looked clean.

Question: *Did you purge the tube ?*

Answer: Yes, we did purge the tube.

Question: *But critical nuclei sizes are below what you could see ?*

Answer: Yes, you wouldn't be able to see it.

OSCILLATORY DYNAMICS OF SINGLE BUBBLES AND AGGLOMERATION IN A SOUND FIELD IN MICROGRAVITY

Philip L. Marston*, Eugene H. Trinh+, Jon Depew+, and Thomas J. Asaki*

*Department of Physics, Washington State University, Pullman, WA
+MS 183-401, Jet Propulsion Laboratory, 4800 Oak Grove Drive, Pasadena, CA.

ABSTRACT

A dual-frequency acoustic levitator containing water was developed for studying bubble and drop dynamics in low gravity. It was flown on USML-1 where it was used in the Glovebox facility. High frequency (21 or 63 kHz) ultrasonic waves were modulated by low frequencies to excite shape oscillations on bubbles and oil drops ultrasonically trapped in the water. Bubble diameters were typically close to 1 cm or larger. When such large bubbles are acoustically trapped on the Earth, the acoustic radiation pressure needed to overcome buoyancy tends to shift the natural frequency for quadrupole (n = 2) oscillations above the prediction of Lamb's equation. In low gravity, a much weaker trapping force was used and measurements of n = 2 and 3 mode frequencies were closer to the ideal case. Other video observations in low gravity include: (i) the transient reappearance of a bulge where a small bubble has coalesced with a large one, (ii) observations of the dynamics of bubbles coated by oil indicating that shape oscillations can shift a coated bubble away from the oil-water interface of the coating giving a centering of the core, and (iii) the agglomeration of bubbles induced by the sound field.

INTRODUCTION

A. Background and Motivation

Acoustic standing waves have long been used as a method for trapping very small bubbles in liquids in a normal gravitational field (1g). Early descriptions of this trapping are summarized in Refs. 1 and 2 and most applications of the technique to the study of bubble dynamics concern the trapping by acoustic radiation pressure of very small bubbles (typically <100 μm in radius) at the pressure antinode of the standing wave.[3] For reasons described in Ref. 1 and reviewed in Sec. I, bubbles larger than a critical size determined by the acoustic frequency are pushed away from pressure antinodes and are attracted to the pressure nodes of a standing wave. This attraction to pressure nodes (due to the radiation pressure or average force on a bubble) is important to the experiments to be summarized since we are primarily concerned with bubbles larger than the aforementioned critical size associated with the

monopole resonance of a bubble. For the ultrasonic frequencies used in the flight apparatus (see Sec. II) the resonant radius R_0 was approximately 150 μm or 50 μm, depending on which acoustic mode of the levitator was driven.

Shape Oscillations: One of the objectives of the flight experiments was to study the dynamics of shape oscillations of bubbles in which the principal restoring force results from surface tension. In the absence of buoyancy and acoustic radiation stresses, the bubble has a spherical shape. Lamb predicted that in the absence of viscous dissipation, the natural frequency for the nth order shape oscillation mode is given by[4]

$$f_n = \frac{1}{2\pi}\left\{\frac{\sigma n(n+1)(n-1)(n+2)}{R^3\left[n\rho_o + (n+1)\rho_i\right]}\right\}^{1/2}, n \geq 2 \qquad (1)$$

where R is the bubble radius, σ denotes the surface tension, ρ_0 is the density of the outer medium (water), and ρ_i is the density of the inner gas (air). For example, if R = 5 mm, then the frequency of the quadrupole shape oscillation mode of a bubble in water is predicted to f_2 = 13.2 Hz. In this example, and even for much smaller bubbles, the frequencies predicted by Eq. (1) are generally so low that direct coupling of an acoustic wave of frequency f_n is impractical as well as weak because the acoustic wavelength is very much larger than bubble size. An alternate acoustic method of exciting shape oscillation on bubbles based on the low-frequency modulation of ultrasonic radiation stresses was proposed by Marston[5,6] as part of an investigation of radiation-pressure excitation of oscillations of drops.[7] One complication to the investigation of such modes on the Earth is that the acoustic radiation stresses needed to counteract the buoyancy can be sufficient to significantly distort the equilibrium shape of a bubble. Preflight experiments[8] (reviewed in Sec. I) demonstrated that this is greater for large bubbles where oscillations are slow and (as reviewed below) effects of viscous dissipation are weakest. One complication of static distortion is that different azimuthal modes for a given n are no longer degenerate but are usually closely spaced.

The viscosity of the liquid surrounding the bubble as well as that of the gas dissipates the energy of shape oscillations. The presence of surfactants on the bubble can cause additional dissipation as well as a shift of the surface tension σ. One effect of dissipation is to broaden the resonance peaks of different values of the mode index n such that the resonances are less distinct for small bubbles.[5] Dissipation also causes the decay in the amplitude of freely oscillating bubbles.[5,9] For the investigation of modal properties based on either steady-state resonance features or on free decay, it can be advantageous to consider bubbles larger than approximately 1 mm diameter. For bubbles that have

clean interfaces and are not much smaller than 1 mm, the mechanical quality factor or Q of a bubble shape oscillation mode is predicted to vary approximately as[5,8] $R^{1/2}$ where R is the bubble radius.

Bubble Agglomeration and Coalescence: Consider now the dynamics of bubbles in an unmodulated ultrasonic field such that shape oscillations are not being driven. The primary effect of the acoustic field is to cause an attraction to special locations in the standing wave as noted earlier. This manifestation of the radiation force is sometimes referred to as the primary Bjerknes force.[10,11] As a result of this force, bubbles in different regions of an acoustic standing wavefield should, depending on their size, tend to agglomerate at pressure nodes or antinodes.[1] Depending on their size, the agglomeration of bubbles may be enhanced by a mutual force of attraction that results from a type of acoustic radiation pressure of a wave by one bubble on a neighboring bubble. This is known as the secondary Bjerknes force and for small bubbles varies approximately as x^{-2} where x is the distance between the centers of the bubbles.[10,11] Detailed experimental investigation of this secondary force have been carried out primarily with very low frequency pressure variations.[10] The agglomeration of bubbles in low gravity in response to both the primary and secondary Bjerknes forces may be of practical value in microgravity since it may facilitate the collection and removal of bubbles from liquids. This may prove useful for experiments in fluid dynamics where bubbles can be a complication or in processes involving freezing or crystallization from solutions where bubbles are undesirable.

As a consequence of agglomeration, the liquid film separating adjacent bubbles may break giving rise to coalescence. The dynamics of this process is of general interest in physical oceanography and in ocean acoustics because of the importance of bubbles to air-sea exchange processes and to ambient noise. For the case in which one of the bubbles is much smaller than the adjacent bubble, some of the dynamics can be anticipated by considering the oscillations on a bubble with an initial bulge off to one side. The evolution of the resulting capillary wave traveling around the surface of the bubble is complicated by the dispersive character of capillary waves. Longuet-Higgins[12] has given an approximate analytical solution to the surface evolution when the initial deviation from a spherical shape is a Gaussian function of the polar angle. The analysis, which neglects viscosity, predicts repeated appearances of bulges at both the original site of coalescence and the opposite pole. Since the analysis neglects viscous dissipation, experiments are merited to confirm the presence of such transient bulges for real liquids.

An additional aspect of coalescence concerns the possible effects of surfactants. It is not easy to anticipate if surfactants should always inhibit coalescence through the stabilization of the film between adjacent bubbles or whether there can be cases where coalescence is enhanced.

Core Centering of a Bubble: There has been ongoing interest in a core-centering mechanism reported by Lee *et al.*[13] and in subsequent experiments. Theoretical investigations indicate that the

centering of the core occurs in response to shape oscillations of the surrounding liquid shell as a result of Bernoulli's law.[14] The emphasis has been on situations where air is the outermost fluid. There appears to have been no observation reported for the case of the core being a gas bubble with the outer-most fluid being a liquid separated from the bubble by an immiscible liquid. Microgravity provides an excellent opportunity to investigate such a system since the density of the coating (silicone oil in the experiment performed) need not be matched with that of the outer liquid (water).

B. Summary of Flight Objectives

From the above considerations and from experiments in 1g carried out during the development of the flight hardware, objectives for the flight experiments were formulated that may be summarized as follows: (a) investigate the shape oscillation modes of bubbles for comparison with experiments carried out in 1g; (b) look for the agglomeration of bubbles in an ultrasonic standing wave without the complication of gravitational buoyancy; (c) investigate the coalescence with a large bubble; (d) investigate the effects of surfactant injection; and (e) look for core-centering in response to shape oscillations on the oil shell around a bubble core.

I. PREFLIGHT EXPERIMENTS AND APPARATUS DESIGN

A. Ultrasonic Trapping of Large Bubbles in Rectangular Chambers

An approximation that has long been used for insight concerning the trapping of bubbles in a standing wave is to approximate the radiation pressure or primary Bjerknes force as[2,10]

$$F(x,y,z) \approx -\left\langle V(t)\nabla p_a(x,y,z,t)\right\rangle \qquad (2)$$

where x, y, and z are spatial coordinates, V(t) denotes the oscillating volume of the bubble, < > is a time average, and p_a is the pressure of the incident acoustic standing wave evaluated at the position of the bubble center but neglecting the presence of the bubble. An alternate approach, evaluation of projections of the acoustic radiation stress on the bubble's surface,[6] is known to reduce to a similar final result for small bubbles in an appropriate limit.[15] The bubble has a monopole resonance that affects the phase relationship between V and p and the sign of F. For the purposes of the present discussion it is sufficient to use the simplest approximation for the resonant bubble radius[1,2,11]

$$R_o = (3p_\infty \gamma / \rho_o)^{1/2} / 2\pi f_a \approx 3.2\text{mm} / f_a(\text{KHz}) \qquad (3)$$

where f_a is the acoustic frequency, $p_\infty \approx 1$ atm is the static pressure, ρ_0 is the density of water and γ is the effective polytropic exponent of the gas in the bubble. (For a bubble contained in a closed levitation chamber, R_0 may be shifted from this value; however, that is not central to the general design considerations that follow.) The response phase for bubble radii $R < R_0$ is such that when p_a is large

V(t) is small so F is directed toward pressure antinodes as for conventional acoustic levitation of small bubbles.[3] For the large bubbles studied in low gravity $R > R_0$ and the sign of F is reversed, being directed toward pressure nodes. Experiments carried out in 1g confirm the attraction of large bubbles to velocity antinodes but the levitation position is offset from the antinode due to buoyancy.[8] The experiments showed that it is possible to trap bubbles in 1g having diameters as large as 12 mm with a 22 kHz standing wave in a rectangular chamber. The general magnitude of the required acoustic pressure amplitude was comparable to 1 atm. It is noteworthy that for large bubbles significant deviations from Eq. (2) may be anticipated and the radiation force may be calculated from the distribution of acoustic radiation stresses on the surface of the bubble including dipole scattering in the analysis.

Rectangular levitation chambers had been previously developed for the purpose of studying the shape oscillations of oil drops in water.[16,17] The flight chamber, Fig. 1, differs from ones used for ground-based studies of bubble dynamics[8,18] primarily in the capping of the chamber with a Plexiglas plate for containment of the water. As described in Ref. 8, the ultrasonic wave is excited by a piezoelectric ceramic transducer coupled by a metal plate to the chamber.

B. Shape-Oscillations Observed in 1g

In 1g, bubbles with R from 0.8 mm to 6 mm were trapped slightly above the principal centrally located velocity antinode (or pressure node) of a rectangular levitation cell in a 22 kHz standing wave.[8] The larger bubbles clearly had an oblate equilibrium shape that may be qualitatively understood as follows. Since the bubble lies close to a velocity antinode, the relative velocity from the acoustic wave is large near the equator of the bubble and the average pressure there is reduced relative to the average pressure at the poles of the bubble. The flattening of the bubble predicted by this qualitative consideration is in agreement with the sign predicted by an analysis in Ref. 6. Notice that the response is analogous to the levitation of drops in air that also become oblate close to velocity antinodes.[6,19]

Shape oscillations are induced by modulating the amplitude of the drive voltage at the desired oscillation frequency f_m so that the voltage applied to the transducer is[8]

$$v(t) = v_T\left[1 + M\cos(2\pi f_m t)\right]\cos(2\pi f_a t) \qquad (4)$$

where $0 \le M \le 1$ and M determines the modulation level. The procedure for determining the frequency of the quadrupole or $n = 2$ mode of a bubble involves tuning f_m to maximize the response of the mode.[8] Figure 2 compares predictions based on Lamb's equation, Ea. (1), with measurements obtained by this procedure. The measurements taken in 1g are discussed in Ref. 8 and the important result is that there is a significant deviation from Eq. (1) for large bubbles. One correction used in Fig. 2 was to plot the radius as that of a spherical bubble having the same volume as the oblate levitated

bubble, however, that correction is inadequate to explain the deviation. The deviation appears to be a consequence of the large acoustic radiation stresses needed in 1g to counteract buoyancy.

C. Apparatus Design for the Experiment on USML-1

The acoustic frequencies f_a that produced standing waves of significant amplitude in the rectangular chamber were investigated and it was found that in addition to f_a near 21 kHz, appreciable standing waves could be achieved for f_a close to 63 kHz. (The precise values for f_a depended on the height of the water and the temperature.) Measurements indicated that the nodes and antinodes of the higher frequency standing wave were more closely spaced than the 22 kHz pattern shown in Ref. 8. To provide an alternative radiation pressure distribution a dual-frequency electronics driver (and modulator) was designed that is diagrammed in Fig. 3. Tests made in simulated low gravity on KC-135 flights with a prototype levitation chamber suggested that the ability to drive the transducer at about 63 kHz may be useful for stable trapping of bubbles in low gravity. Consequently, the extra complication to allow for carrier frequencies at $f_a = f_0 \approx 21$ kHz and $f_a = 3f_0$ was appropriate as was subsequently verified on USML-1. A digital display could be switched to measure either the modulation frequency f_m or to give a measure of the current delivered to the output power amplifier. The switch was located at the base of the levitator. Tuning f_a to maximize the current increases the amplitude of the ultrasonic wave. The DC voltage supply for the circuit was supplied by the Glovebox.

The inner dimensions of the Plexiglas box forming the top of the levitation chamber were 3.5 in. x 3.5 in. x 2.75 in. giving a volume of 552 cm^3. The actual volume available for water was slightly larger due to a narrow gap, sealed by an O-ring, between the box and the aluminum base and because water wetted a gap between the cylindrical transducer and the base. The walls and top of the chamber were transparent so that the dynamics of bubbles could be recorded with a Glovebox TV camera. After the sealed chamber was tested to meet safety requirements, distilled water was inserted at the Kennedy Space Center through an opening that was resealed. An air bubble was left in the chamber to allow for an anticipated expansion of water resulting from any temperature variations during the nearly 4 months prior to launch.

II. SPACELAB (USML-1) RESULTS AND DISCUSSION

The experiment was scheduled for 3 hr. 15 min. of operation on MET day 11 with only intermittent real-time down link of TV video. The experiment was operated by E. Trinh.

A. Shape Oscillation Modes of Bubbles in Low Gravity

There was sufficient air in the chamber that it was not necessary to inject air through the septum except for experiments described in Sec. II.D. (Postflight measurement of the volume of air in the

chamber gave 2.4 cm^3.) The air could be partitioned into bubbles by manual agitation of the chamber. For stable trapping of bubbles away from the sides of the chamber the frequency fa = $3f_o \approx 63$ kHz was selected. The modulation frequency fm was adjusted to maximize the response apparent to the operator. The size of the bubbles was measured by using the septum as a reference dimension in the video records. Real-time estimates were consistent with such measurements. Generally the equilibrium shapes of the large bubbles were far closer to spherical than when they are trapped in 1-g; the equilibrium deviation from sphericity (due to the acoustic field) being a few percent or less in low gravity.

Resonance frequencies were measured for two bubbles. Bubble 1 had a diameter D = 14.9 mm and the resonances for the n = 2 and 3 modes were respectively at 6.8 and 12.7 Hz. These agree with theoretical estimates from Eq. (1) of 7.2 and 13.2 Hz. Bubble 2 had D = 8.8 mm and measured n = 2 and 3 frequencies of 15.9 and 29.8 Hz which also agree with Eq. (1) though this bubble was trapped near the plate driven by the transducer and the plate may have perturbed that flow. The resonances for these bubbles are plotted as + symbols in Fig. 2 where the frequencies are far closer to the ideal theory and any results available in 1 g for such large bubbles. The oscillation amplitudes achievable were generally smaller than for similar experiments[8] in 1 g. This may have been a consequence of perturbation of the ultrasonic resonances of the chamber by the quality of enclosed air.

B. Bubble Agglomeration and Coalescence

Bubbles having diameters ranging from 1 to 15 mm were dispersed by agitation of the chamber. The bubbles migrated in response to the steady 63 kHz ultrasonic wave. In the recorded words of the operator, "Turning on the (acoustic) field . . . gathers them up in about the same place." Figure 4 reproduces a video record showing acoustically gathered bubbles. Video records of the migration suggest that while primary Bjerknes forces and viscous drag are most important in determining the trajectories, secondary Bjerknes attraction may also contribute in certain situations.

A remarkable feature of video records like Fig. 4 is that the bubbles, once gathered, did not tend to naturally coalesce. Nevertheless, a few coalescence events were recorded on video but it is noteworthy that these were seen within 60 seconds after a dilute surfactant was injected through a hypodermic needle at the surface of a large bubble. The solution was sodium dodecylsulphate (SDS) at 0. 75 of CMC (critical micelle concentration) prior to injection. The amount of surfactant injected was such that postflight measurements of the water indicated that the surface tension σ was reduced to 63 ± 1 dyn/cm.

The clearest sequence recorded shows a 2 mm radius bubble popping into a 15 mm diameter bubble with a negligible sound field present. Coalescence launches a wave that disperses and travels around the bubble. Waves converge back at the point of coalescence to produce transient bulges. The

first and strongest convergence occurs about 5 video frames (i.e. 5/30 ≈ 0.17 sec) after coalescence. The angular width of the initial bulge corresponds to the width of the small coalescing bubble and this width is close to the width of an initial Gaussian bulge considered in a calculation by Longuet-Higgins.[12] The predicted time for convergence is $1.9(R^3/\sigma)^{1/2}$ = 0.16 sec where σ = 63 dyn/cm and R = 7.5 mm is the initial radius of the large bubble. The observed interval of 0.17 sec is close to the predicted value. Evidently, the initial condition assumed by Longuet-Higgins, in which the n = 4 and 5 modes were most strongly excited, well approximate the conditions for this coalescence event.

C. Shift in Bubble Modes Produced by the Surfactant

The resonance frequencies of the n = 2 and 3 modes were measured for a bubble with D = 15 mm giving respectively 6.2 and 11.9 Hz. These are close to the calculated values with σ = 63 dyn/cm from Eq. (1) of 6.7 and 12.3 Hz. The difference may partially be from a lowering of the frequency due to the additional inertia of the oscillating boundary layer near the bubble that is neglected in Eq. (1). (See e.g. Refs. 5 and 9.) Comparison with the measurements in Sec. II.A shows that the principal reduction in frequency is a consequence of the reduction in the surface tension caused by the injected SDS solution.

D. Oscillations of Compound Bubbles in Silicone Oil Drops in Water and Evidence of Core Centering

Preflight experiments in 1 g demonstrated that it was possible to coat the wall of an acoustically levitated bubble with a thin liquid layer immiscible in water. To prevent the pooling of the layer at the bottom of the bubble, it was necessary to closely match the density of the layer to that of water by mixing silicone oil and CCl_4. This difficulty in generating such levitated coated bubbles in 1 g and interest in core centering reviewed in the introduction (A) motivated observations of the dynamics of compound bubbles on USML-1 in which the coating was pure silicone oil (Dow Corning 200) having a viscosity of 2 cS and a density of 0.87 g/cm^3. Since the measurements were taken after the injection of the SDS surfactant, the interfacial tension with water was lower than the ideal value for clean water of about 25 dyn/cm. Silicone oil is more compressible than water and the ultrasonic mode of the levitation cell near 21 kHz was used to trap compound bubbles and drops of silicone oil in low gravity.

The most important of the observations were made with a compound bubble in which the outer diameter of the oil coating was 5 to 6 mm and the average thickness of the coating was ≈ 1 mm. For the generation of centering of the core in other liquid shell systems, the relevant mode is thought to be the "sloshing mode" in which the outer and inner surfaces move out of phase such that the shell is thickest either at its poles or its equator depending on the phase of the oscillation cycle.[14] Unfortunately the resonance frequency of the sloshing mode for this system appeared to be lower (but close to) the lowest

available modulation frequency f_m of 4.5 Hz. (The apparent low frequency of this mode is supported by calculations.) Nevertheless, when f_m was reduced to 4.5 Hz, weak oscillations of the compound bubble could be seen and the enclosed bubble drifted away from the outer wall of the silicone oil shell. A video record after the drift is shown in Fig. 5(a). This is to be contrasted with the situation in the absence of modulation where the bubble tended to drift to an outer wall of the shell producing an eccentric compound bubble. Note that while only one profile view was recorded on video, the operator could view the bubble's response from more than a single profile. His recorded observations were, "(It) doesn't take much to get bubble centering in this system. Little oscillation amplitude is required." These appear to be the first observations of shape-oscillation induced core centering in a fluid system of this type where the inner fluid is gas and the outer-most fluid is liquid.

The aforementioned behavior of easy centering may be contrasted with a case where the enclose bubble had a diameter of only 1 mm while the outer diameter of the oil drop was about 7 mm. In that case, the quadrupole mode of the drop was strongly excited giving aspect ratios as large as 2-to-1 during the oscillations. The small enclosed bubble remained at one pole of the drop showing no evidence of a core centering force, Fig. 5(b) and (c). Consequently, core centering of bubbles appears to be inhibited for bubbles that are much smaller than the surrounding drop.

E. Cavitation Plumes from an Oil Drop in Low Gravity

During the course of observations of a 2 cm diameter 2 cS silicone oil drop, an unanticipated sequence occurred. Transient acoustic cavitation at or near the surface of the drop affected the stability of the drop. The cavitation ejected a plum from the drop extending about 1 cm into the liquid. Related plumes have been photographed for drops of oil acoustically levitated in water on the Earth and the plume is thought to contain mm-sized oil drops.[20] In low gravity, without buoyancy the ejected mist remained in the vicinity of the drop, surrounding it after a few seconds. Subsequently the combined drop and cloud of mist became unstable in the sound field and moved out of the field of view of the camera. It is unclear whether the absence of buoyancy may have exacerbated the consequences of ultrasonic cavitation in the drop.

III. SUPPLEMENTAL OBSERVATIONS

The development and testing of the flight apparatus and supporting ground based experiments gave the first observations of large acoustically levitated bubbles. Two types of supplemental observations of the dynamics of large levitated bubbles are noteworthy. (i) Figure 6 shows oscillations of an 8 mm diameter bubble in 1 g driven by amplitude modulation of a 22 kHz ultrasonic wave. The oblate and prolate shapes have been captured by strobe lighting. On the upper surface of the bubble in each of

the pictures a capillary roughening is visible. The roughening typically has a length scale of a few 100 μm. It appears to be excited by a large amplitude ultrasonic field since the contrast in the surface usually is modulated along with the ultrasonic amplitude. The roughening is probably a manifestation of parametrically excited capillary waves. Thresholds of such waves have been previously studied for other applications.[21] (ii) It was often possible to drive quadrupole oscillations of sufficient amplitude to break up a bubble into two bubbles. The analogous break-up of drops driven at quadrupole resonance by modulated radiation pressure has been previously reported.[7,16,17] Neither of the processes in (i) or (ii) was observable on USML-1, probably because of insufficient sound amplitude.

Comparison of the USML-1 measurements of resonance frequencies for bubbles plotted in Fig. 2 with the theory for spherical bubbles and with the preflight measurements in 1 g illustrates an advantage of low gravity. For experiments on the Earth, to reduce the biases due to levitation field, the bubbles need to be as small as 1 to 2 mm diameter. A quantitative light scattering method was developed for measuring both the frequency and dissipation of the shape modes of such bubbles. (The method, partially summarized in Ref. 18, extends an optical extinction method previously used for drops.[19]) Recent measurements show that the damping of the quadrupole mode can be as low as the value calculated for an ideal clean interface between air and water.[5,9] Furthermore, the mode properties were found to be a sensitive non-contact probe of the bubble's surface.

CONCLUSIONS

The measurements of quadrupole resonance frequencies performed in microgravity and summarized in Section II.A confirm that the strong acoustic levitation field used on the Earth can bias the resonance frequencies. As summarized in Section III, a method has been found (partially based on insight from that result) that simplifies the interpretation of measurements in 1 g. Such measurements have application to the probing of interfacial properties. Other observations in microgravity, summarized in Sections II.B - II.E illustrate various aspects of bubble dynamics without the complication of gravitationally induced buoyancy. Of these observations the following are especially noteworthy: the agglomeration of bubbles in a ultrasonic field, the observations of capillary waves induced by coalescence, and the evidence for core centering in the compound bubble system in response to shape oscillations. Ground based experiments have expanded our ability to trap bubbles as large as 12 mm diameter and, as described in Ref. 8, have advanced the development of stable levitators. During the course of this work the mechanism for exciting shape oscillations on bubbles proposed in Refs. 5 and 6 has been confirmed. Discoveries from supporting ground based investigations of the dynamics of levitated bubbles are summarized in Sections I.B and III.

ACKNOWLEDGMENTS

The development of the microgravity experiment was supported by NASA through the Glovebox program. Supplemental experiments carried out at Washington State University were supported by the U.S. Office of Naval Research. The authors acknowledge the assistance of the Glovebox and Drop Physics Module teams during the USML-1 mission and Jet Propulsion Laboratory (JPL) staff during the hardware development and testing. C. Boswell of JPL solved several problems on the design and construction of the compact electronics shown in Fig. 3.

REFERENCES

1. F. G. Blake, "Bjerknes forces in stationary sound fields," J. Acoust. Soc. Am. **21**, 551 (1949).

2. A. I. Eller, "Force on a bubble in a standing acoustic wave," J. Acoust. Soc. Am. **43**, 170-171 (1968).

3. R. G. Holt and L. A. Crum, "Acoustically forced oscillations of air bubbles in water: Experimental results," J. Acoust. Soc. Am. **91**, 1924-1932 (1992).

4. H. Lamb, *Hydrodynamics* (Dover, New York, 1945).

5. P. L. Marston, "Shape oscillation and static deformation of drops and bubbles driven by modulated radiation stresses—theory," J. Acoust. Soc. Am. **67**, 15-26 (1980).

6. P. L. Marston, S. E. LoPorto-Arione, and G. L. Pullen, "Quadrupole projection of the radiation pressure on a compressible sphere," J. Acoust. Soc. Am. **69**, 1499-1501 (1981).

7. P. L. Marston and R. E. Apfel, "Acoustically forced shape oscillation of hydrocarbon drops levitated in water," J. Colloid Interface Sci. **68**, 280-286 (1979); "Quadrupole resonance of drops driven by modulated acoustic radiation pressure—experimental properties," J. Acoust. Soc. Am. **67**, 27-37 (1980).

8. T. J. Asaki, P. L. Marston, and E. H. Trinh, "Shape oscillations of bubbles in water driven by modulated ultrasonic radiation pressure: Observations and detection with scattered laser light," J. Acoust. Soc. Am. **93**, 706-713 (1993).

9. C. A. Miller and L. E. Scriven, "The oscillations of a fluid droplet immersed in another fluid," J. Fluid Mech. **32**, 417-435 (1968).

10. L. A. Crum, "Bjerknes forces on bubbles in a stationary sound field," J. Acoust. Soc. Am. **57**, 1363-1370 (1975).

11. A. Prosperetti, "Bubble dynamics: A review and some recent results," Appl. Sci. Res. **38**, 145-164 (1982).

12. M. S. Longuet-Higgins, "Monopole emission of sound by asymmetric bubble oscillations. Part 2. An initial-value problem," J. Fluid Mech. **201**, 543-565 (1989).

13. M. C. Lee, I. Feng, D. D. Elleman, T. G. Wang, and A. T. Young, " Coating of glass microballoons using an acoustic technique," J. Vac. Sci. Technol. **20**, 1123-1124 (1982).

14. N. A. Pelekasis, J. A. Tsamopoulos, and G. D. Manolis, "Nonlinear oscillations of liquid shells in zero gravity," J. Fluid Mech. **230**, 541-582 (1991).

15. C. P. Lee and T. G. Wang, "Acoustic radiation force on a bubble," J. Acoust. Soc. Am. **93**, 1637-1640 (1993).

16. E. Trinh and T. G. Wang, "Large-amplitude free and driven drop-shape oscillations: experimental observations," J. Fluid Mech. **122**, 315-338 (1982).

17. P. L. Marston and S. G. Goosby, "Ultrasonically stimulated low-frequency oscillation and breakup of immiscible liquid drops: Photographs," Phys. Fluids **28**, 1233-1242 (1985).

18. T. J. Asaki, P. L. Marston, and E. H. Trinh, "Shape oscillations of bubbles in water driven by modulated ultrasonic radiation pressure," in *Advances in Nonlinear Acoustics*, edited by H. Hobaek (World Scientific, Singapore, 1993), pp. 424-429.

19. E. H. Trinh, P. L. Marston, and J. L. Robey, "Acoustic measurement of the surface tension of levitated drops," J. Colloid Interface Sci. **124**, 95-103 (1988).

20. E. A. Gardner and R. E. Apfel, "Using acoustics to study and stimulate the coalescence of oil drops surrounded by water," J. Colloid Interface Sci. **159**, 226-237 (1993).

21. R. P. Brand and W. C. Nyborg, "Parametrically excited surface waves," J. Acoust. Soc. Am. **37**, 509-515 (1965).

Figure 1 Photograph of the chamber of water flown on USML-1. The aluminum base of the chamber houses a piezoelectric ceramic transducer that generates an ultrasonic standing wave in the water. A 1/2 inch diameter septum on one Plexiglas wall was penetrated by needles during the experiment to facilitate the injection of fluids. The bulb on the upper left served as a ballast during the experiment but was sealed off during launch.

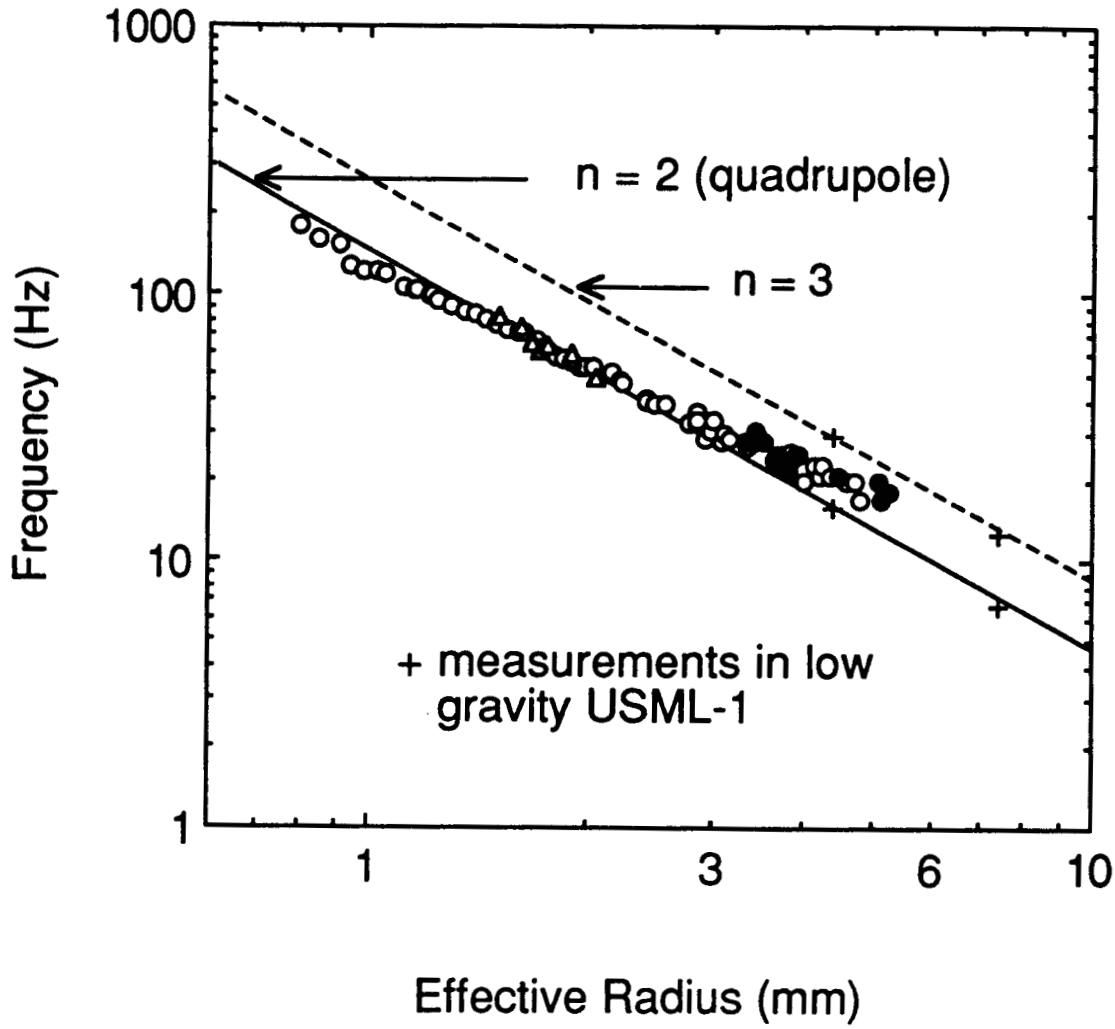

Figure 2 Preflight measurements of resonance frequencies for a wide range of bubble sizes in water are compared with measurements taken on USML-1 shown as + symbols. Also shown is the theoretical result from Eq. (1) which neglects a viscous correction that is small for large bubbles. The circles are based on maximization of the visible quadrupole response and the triangles are based on a light scattering method (see Ref. 8). In 1 g the levitation field distorts the bubbles and the circles where the equilibrium aspect ratio exceeded 1.3 are filled in. To reduce the effect of this bias, our data from Ref. 8 has been replotted here using an effective radius corresponding to that of a spherical bubble having the same volume. The USML-1 measurements (see Section II.A) were unbiased since they were taken on nearly spherical bubbles. They included observations of the n = 3 mode.

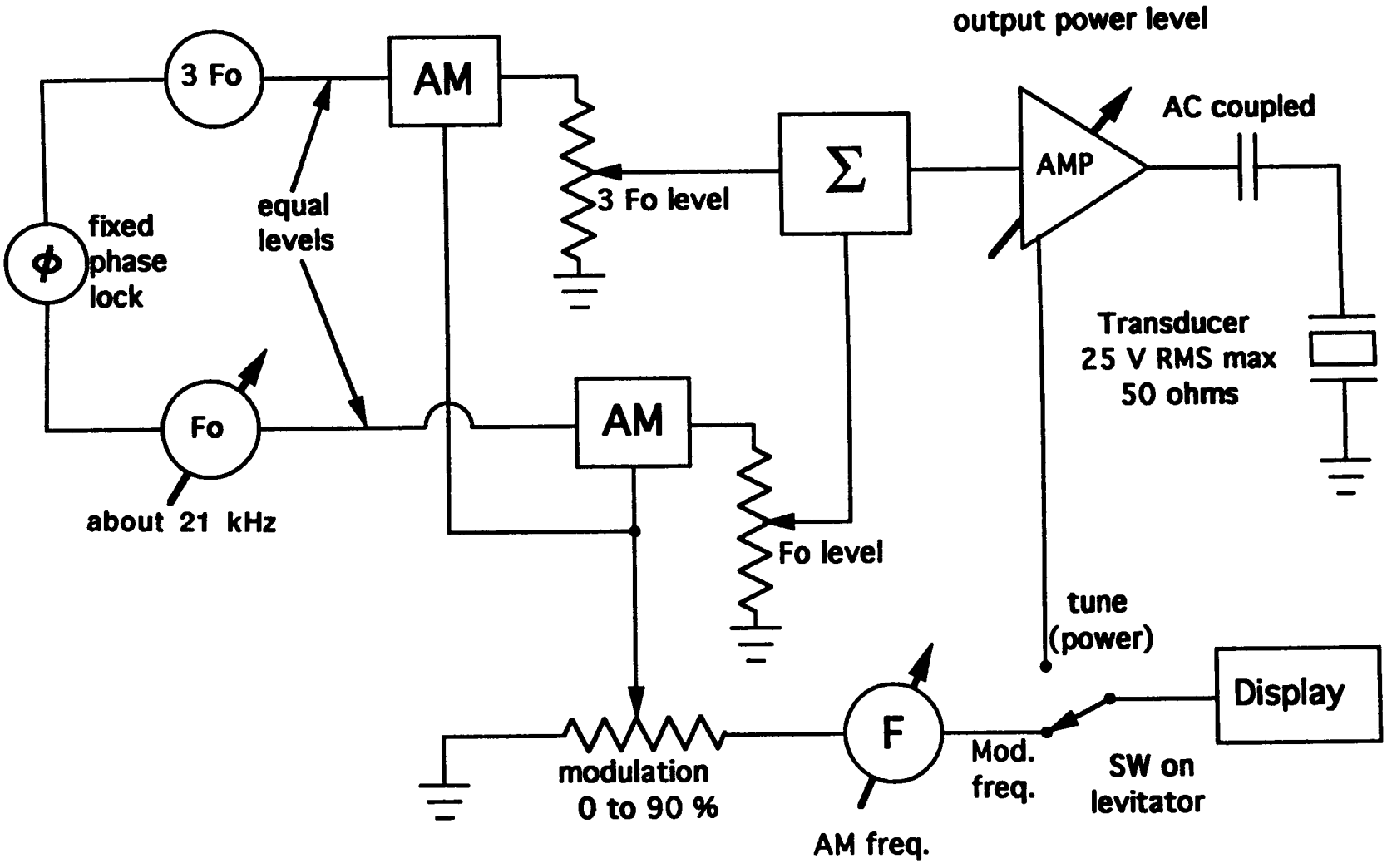

Figure 3 Circuit used to generate the modulated transducer voltages for the USML-1 experiment. The dual-frequency design enhanced the flexibility of the experiment.

Figure 4 Video record of bubbles agglomerated together in low gravity in response to a 63 kHz ultrasonic standing wave. In the absence of gravitational buoyancy, a weak ultrasonic standing wave was sufficient to induce agglomeration.

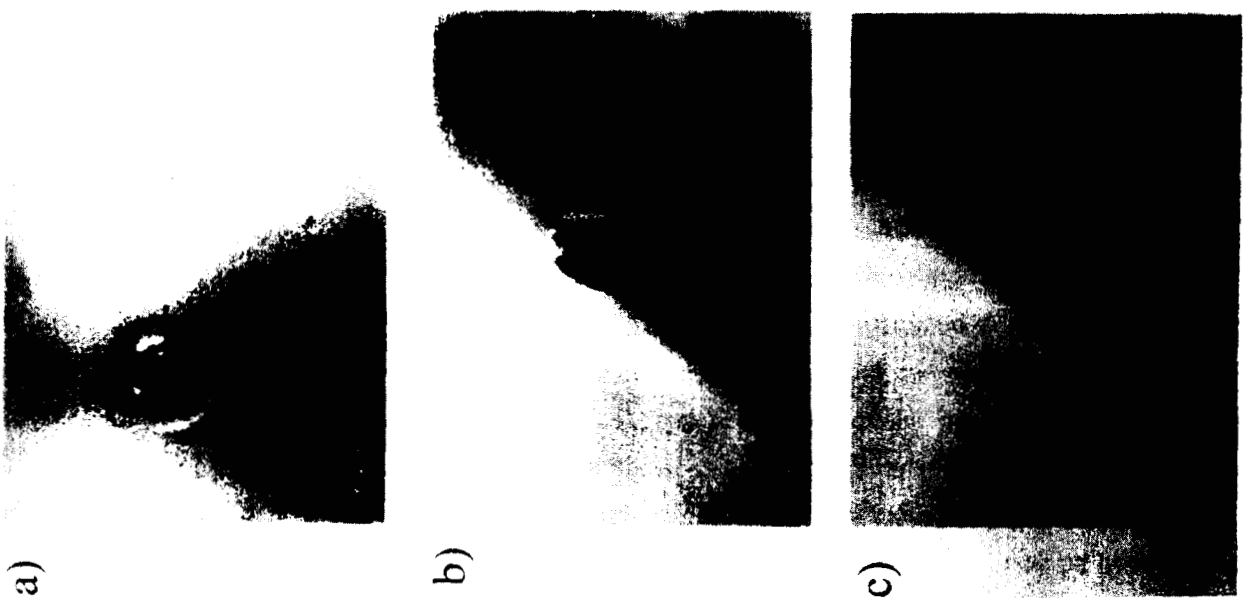

Figure 5 Low-gravity observations of a compound drop-bubble system. (a) shows a bubble contained in an oil drop in water subjected to low amplitude shape oscillations. In response to the oscillations the bubble core moves away from the wall of the drop. The density of the oil differs from the density of the surrounding water. (b) and (c) show a case where the bubble was much smaller than the drop. Prolate and oblate phases of the oscillating drop are shown. The bubble, visible at the upper end, shows no evidence of a centering force, unlike the case in (a).

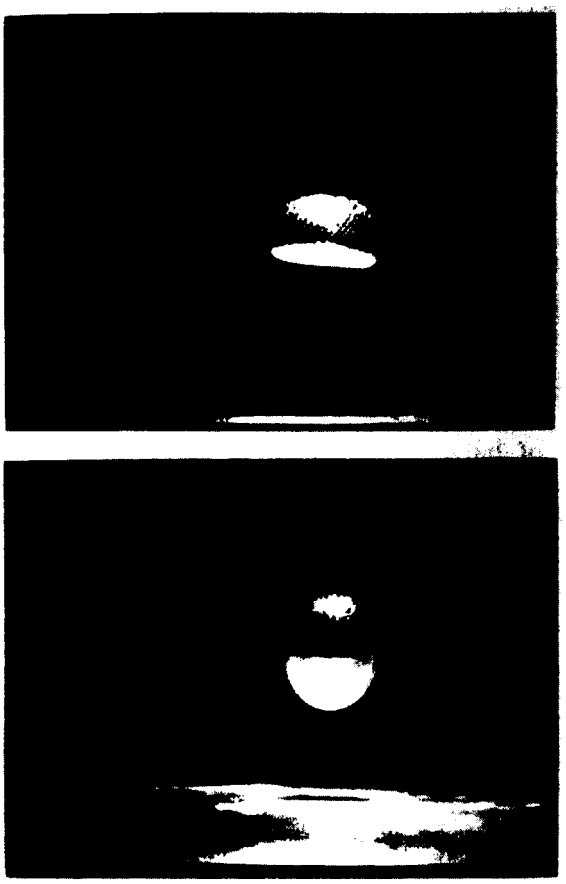

Figure 6 Oblate and prolate phases of an 8 mm diameter bubble oscillating in the n = 2 mode in 1 g. Capillary roughening is visible on the upper surface that is coupled to the strong ultrasonic field.

DOUBLE FLOAT ZONE (DFZ)

Robert J. Naumann
Professor of Material Science
University of Alabama in Huntsville

ABSTRACT

The Double Float Zone experiment explored the feasibility of a quasi-containerless process in which a solidifying material is suspended by two liquid bridges of its own melt. One of the issues that must be considered is how far the liquid bridges could be extended before instabilities set in. The concept was tested using a mechanical model in which lexan rods represented the solid and the melt was simulated by water.

The double float zone proved to be quite stable for modest lengths of the liquid bridges; however, an unexpected asymmetry in the position of the float piece was observed. It was possible to extend one bridge to nearly the Rayleigh limit (length equal circumference), but not both. There seems to be an instability imposed by the differential capillary pressure in the two liquid regions.

INTRODUCTION

One attribute of reduced gravity that has received relatively attention is the possibility of deploying liquid configurations that would be quite impossible in normal gravity. For example, it should be possible to suspend a solid object by two liquid bridges in a double float zone configuration. Such a configuration could be useful for allowing a portion of a melt to solidify while being suspended only by its own melt. Unlike a levitated containerless process, which is more or less restricted to spherical or nearly spherical shapes, this quasi-containerless process is inherently simpler and can produce a final product in wider variety of shapes such as rods or possibly even sheets. All of the advantages of the fully containerless process, e.g. the elimination of container-induced contamination and heterogeneous nucleation site, are retained. The departure from near-spherical geometry provides greater surface area to volume which can be useful in removing heat rapidly from larger objects, thus it may be possible to trap metastable or amorphous phases in larger samples than would be possible with a spherical geometry.

It is well-known that a liquid bridge becomes unstable when its length exceeds its circumference[1]. However, the stability of a double float zone in which the liquid bridges are coupled through the motion of a suspended solid has not been considered. It would be well to understand these

stability limits before attempting experiments with high temperature melts. Therefore the primary objective of this experiment was to investigate the stability limits of this unique solid-liquid configuration.

Since liquids with free surfaces are very susceptible to spacecraft vibrations, a simple passive isolation platform was also developed and tested as a secondary objective.

I. DESCRIPTION OF THE EXPERIMENT

The (DFZ) apparatus consists of a lexan base with two clamps to hold two 1 cm dia. lexan support rods along a common axis. The clamps allow the distance between the rods to be easily adjusted. Each rod is drilled along its axis to accept a stainless steel alignment wire. A Teflon liner is placed in the hole to prevent the working fluid (water) from wicking back into the hole as the alignment wire is withdrawn. A 1 cm dia. x 4 cm lexan rod served as a typical float piece. Other float pieces consisted of rods of different lengths and geometries. The end faces of the rods were coated with EHEC CST103, a sucrose-like coating to improve the wettability of the lexan. Teflon shrink tube was placed over the cylindrical surfaces to act as an anti-spread barrier.

The Mission Specialist positions the float piece between the support rods by engaging the alignment wire into dimples on each face of the float piece. The rods are adjusted to leave a gap of approximately 1 cm between the float piece and the support rod on each side. These gaps are filled with water using a syringe. The alignment wires are then slowly withdrawn leaving the float piece suspended by the two liquid bridges. The bridges are extended by pulling the alignment wires farther apart and adding more water until the configuration becomes unstable and breaks up. The procedure is recorded on video.

The passive vibration isolator consists of an isolation plate in the form of a thin steel sheet that is suspended in a frame by flat rubber bands, each with a half twist[2]. The restoring force is provided by the flexing rather than stretching of the rubber bands, thus providing the very high compliance needed to reduce the natural frequency to the order of 1 Hz. The experiment is attached to the isolation plate by magnetic strips, and the frame is also mounted to the Glovebox floor by magnetic strips. A manual caging mechanism consisting of 4 half-discs with deep grooves around their peripheries was used to lock the isolation platform is place when desired.

II. EXPERIMENTAL RESULTS

Single zones of extended length were initially deployed and observed with the isolator caged and uncaged. The spacecraft environment was sufficiently quiet so that vibrations of the liquid column were not seen either with the platform caged or uncaged. The Mission Specialist displaced the experiment several times from its equilibrium position and it slowly returned with a period of approximately 1 sec.

The motions were quickly damped with only a slight overshoot. The equilibrium position was not quite in the center of the frame however, indicating the need for either being able to adjust the rubber bands mechanically in orbit or to be able to accurately apply loads on the order of 1 !19 on Earth for final adjustment.

Double float zones of various lengths were established using the flat ended rods. These configurations were remarkably stable even when they were intentionally perturbed by the Mission Specialist. A curious phenomena was observed, however. The center float seemed to be more attracted toward one support rod that the other. Adding more fluid to the short zone seemed to exacerbate the effect. In fact, at one point the short zone was bulging while the long zone was pinched in - totally defying the expected behavior! It was demonstrated this was not a residual gravity effect since the residual g-vector was perpendicular to the direction of offset and turning the apparatus around produced the same effect.

This effect can be understood by recalling that the capillary pressure in the liquid bridges is proportional to the sum of both the radial and the transverse curvature. For a given volume of the liquid zone and fixed radius R0 at the end points, the capillary pressure exhibits a minimum at some length. The position of this minimum depends on the amount of liquid in the bridge as shown in Figure 1. For convenience lengths are scaled by R0 and a dimensionless volume is defined in terms of the dimensionless length when the shape is cylindrical. Thus a liquid bridge whose volume is such that its shape is cylindrical when its length is equal to its radius R0 (L1 in Fig. 1) has a minimum pressure when the length is slightly longer than L/R0. On the other hand, a liquid bridge with volume such that it is cylindrical when its length is 5 R0 (L5 in Fig. 1) has this minimum at less than 5 L/R0.

The consequence of this may be seen in Fig. 2 in which the pressures for the left hand bridge with dimensionless volume =1 (L1) and the right hand bridge with dimensionless volume =1 (R1) are plotted against each other for a combined spacing of 3. Note the cusp in the intersection of the two plots that indicates that the mid-point position of the floating piece is unstable. The pressure in both bridges must be equal and minimum. Therefore, the float will either go to the left or right of the center to the point where the pressure curve is minimum. Say it moves to the left so that the left hand bridge is shorter than the right hand bridge. Now if liquid is added to the short left hand bridge to increase its volume to L2 without increasing the spacing between the two end pieces, the left hand bridge would increase in length to 2 as one would intuitively expect.

Now consider the case where the end pieces are set so the combined length is 9 (Fig. 3). If both left hand and right hand sides are each filled to a dimensionless volume of 4, stable equilibrium is reached when one leg is near 3 and the other near 6. This is getting very close to the Raleigh limit of 2π. Let's say the left hand side length is 3 and the right hand leg is 6. Now if liquid is added to the left to

increase its volume to 5, The spacing will not change appreciably because the pressure is not increased significantly in the left hand leg. This would explain the observed counterintuitive phenomena that adding fluid to the short leg did not increase its length.

One can see how an instability might arise at less than a combined length of 4π. If both bridges filled so their volume was 5 and the end pieces were set so the combined zone lengths were 11, pressure equilibrium would result in zone lengths of 4 and 7. This would cause one of the zones to exceed the Rayleigh limit and rupture. This type of rupture was seen during the experiment.

A sheet and a double sheet float zone was also established. From the limited video down-link available during this period, it did appear that a stable sheet of some length could be established although there was considerable bulging in the center, as would be expected. The flat float piece was captured and held by the two flat liquid bridges, but it tended to cock or rotate approximately 20° in the plane of the sheet. This appeared to be caused by unequal wetting along the faces of the support rods and the flat float piece.

CONCLUSIONS

A simple passive vibration isolation platform using a rubber band suspension was successfully demonstrated.

The stability limits of the double float zone configuration were investigated. An unexpected phenomena was found in that the float piece would not remain centered and filling the short zone would not cause it to lengthen. This was explained in terms of the variation of capillary pressure as a function of zone length due to the combined zone curvature.

It was found that this pressure behavior could reduce the limit of stability below the combined Rayleigh limit of 4π.

REFERENCE

1. Lord Rayleigh, Phil. Mag. S. 5., 34 (1892)145-155.

2. R. J. Naumann, A Passive Vibration Isolation Device for Small Space Experiments, Patent Applied for, MSFC Case Number 262084-1-CU, November 1991.

ACKNOWLEDGMENT

The author wishes to thank the many people that helped in the various aspects of this experiment, especially Roger Chassay and Tony DeLoach in the MSFC project office for guiding me through the MSFC flight acceptance procedures, the USML crew for their patience in the training

exercises and the preliminary experiments on the KC-135 and special thanks to Joe Prahl for his interest and helpful suggestions and to Carl Meade for the skill and dedication he exhibited in actually performing the experiment on USML-1.

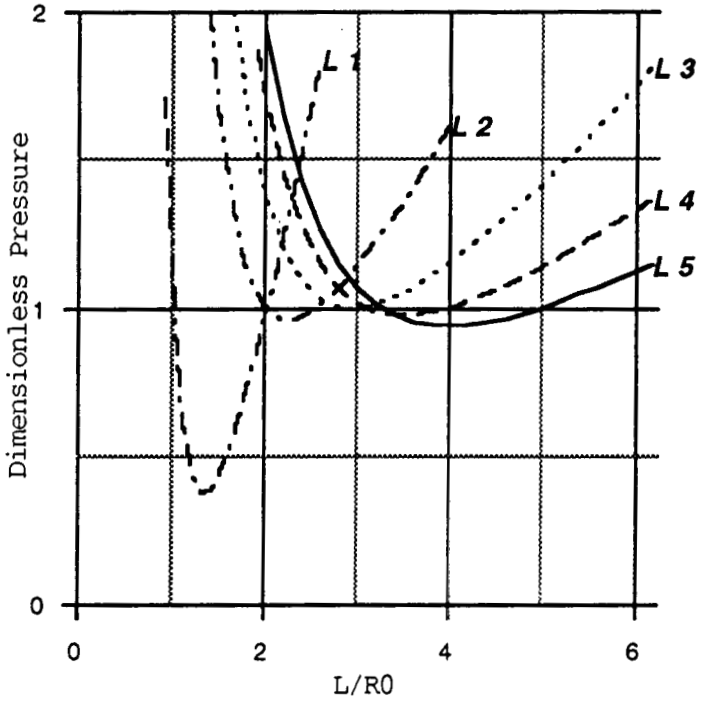

Figure 1 Pressure behavior as a function of dimensionless length for various dimensionless volumes.

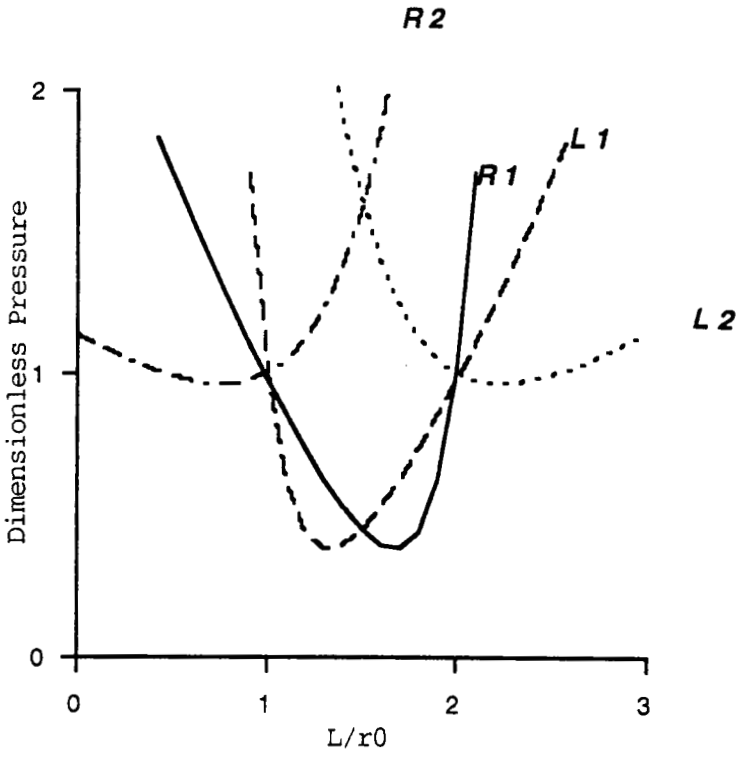

Figure 2 Pressure curves for the left hand (L1 and L2) and the right hand (R1 and R2) legs for a combined zone length of 3R0.

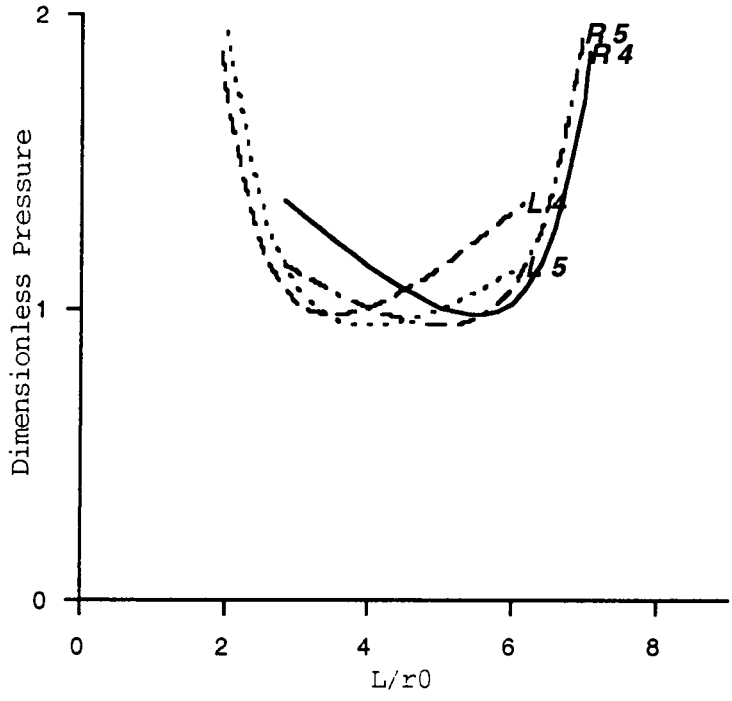

Figure 3 Pressure curves for the left hand (L1 and L2) and the right hand (R1 and R2) legs for a combined zone length of 9R0.

Discussion

Question: *Because you had that center portion in there, there is nothing that says that all 3 rods have to stay a constant diameter. Would you care to speculate what would happen if you had different diameters?*

Answer: Oh you mean if you had a solidifying material in there where the diameter was going to be fixed by contact angle? Yes. I forgot to mention the fact the contact angle here was a little bit artificial because to make sure we did not spread on these rods I had to use Lexan. Lexan, again, does not wet very well so we had to actually coat the inside portion of it, where the water was, with a little brew that Milton Harris cooked up called EHEC, I don't know what that stands for, but it is a sucrose-like material that makes the Lexan wettable to water. But then, to keep it from spreading, we took a little piece of Teflon shrink wrap and put it over the top to pin it so we knew that it was going to stay the same diameter. Now, of course, if you had a melt, that would be a totally different picture. You would have to be very careful about how you did that.

Question: *What if the tube were a capillary communication device? What if solid 2 was hollow instead of being solid ?*

Answer: Where the water can flow back and forth to it? That means the fluid can exchange from one to the other right? So you don't have a fixed volume. Then, you could allow liquid to flow over the top of it, I suppose, so it could communicate. My first guess would be you would then be subject to the Rayleigh instability of the single leg depending on how long it took for the liquid to communicate back. Then you would just have an extended bridge, wouldn't you, where the capillary waves would go all the way across. That is an interesting question. We were trying to simulate something that would be a melt in the middle of it. The reason for putting the Teflon over that, we figured that if it was below the melting point, at that time, the liquid couldn't really flow over it. We actually did do this with different kind of configuration tools. We had some with rounded noses to look at different wetting effects and contact angle effects. They did pretty much the same thing though.

Question: *Would the problem be like a double balloon situation, where the small balloon would fill the big balloon ?*

Answer: Yes. I think that is probably right. It would probably exacerbate the situation wouldn't it ? Because if you wanted to pump from the small to the large then that would shove the thing over.

Question: *To put that in the context of a dynamic process where you have tubes moving from one end to the other, how would expect the things to change if they were dynamic ?* Would that stabilize it or destabilize it ?

Answer: You mean if you are actually melting something and trying to move the zone ? Well. Actually in a way it was sort of dynamic because we had Carl moving the rod and then adding more to it. So we were doing it stepwise instead of continuous. We were trying to simulate something like that and I think that if you were filling at the same rate that you were pulling as you would be in the developing case, I don't know what will happen. I think you would still see the same instability, though, because of this pressure, the way this pressure function works. I guess in response to Roger's comment, I didn't actually model what was in here, I was just trying to get some plausible explanation of it. Unfortunately the tapes I got are in the wrong format for me to do the digital analysis on it. I am still trying to get that corrected and so once we do that I will actually be able to measure the distances and maybe the volume, or, at least the deformation of the liquid bridge and come up with something a little more definitive. I was just trying to get a plausible model here that would try to explain something like that, and I think we are on the right track; but, I don't think that is a definitive explanation yet.

OSCILLATORY THERMOCAPILLARY FLOW EXPERIMENT

(OTFE)

Y. Kamotani*, S. Ostrach* and A. Pline^

*Department of Mechanical and Aerospace Engineering
Case Western Reserve University, Cleveland, Ohio
^NASA Lewis Research Center, Cleveland, Ohio.

ABSTRACT

An experiment was performed on oscillatory thermocapillary flow in the Glovebox aboard the USML-1 Spacelab which was launched in July, 1992. Cylindrical containers of 1 and 3 cm in diameter were used. Silicone oils of 2 and 5 cSt viscosity were the test fluids. The fluid was heated by a cylindrical heater placed along the centerline of the container. The diameter of the heater was 10% of the container diameter. The fluid motion was studied by flow visualization. Although oscillations were observed briefly, bubbles generated in the fluid during the experiment disturbed the flow substantially so that the critical temperature differences could not be determined.

INTRODUCTION

One unique aspect of a low-gravity environment is that surface tension becomes a dominant force and can generate significant flows and associated heat and mass transfer. Although there is both experimental and numerical evidence of steady and transient thermocapillary flows, the detailed nature and extent of oscillatory flows under a variety of conditions remains to be determined as does some of the basic physics, which is not completely understood. In a one-g environment the flow coexists with buoyancy driven flow and is usually overshadowed by it except for flows in very small dimensions.

More than a decade ago German scientists showed the existence of a surface tension induced oscillatory flow state. Because the mechanism for this oscillation phenomenon involves complex physics and cannot be studied easily either analytically or numerically, experimental study of this problem has become the subject of significant scientific importance. Extensive research has been conducted both terrestrially and in space to determine the onset conditions for this oscillatory state.

Much of the past work on oscillatory thermocapillary flow has been done in the so-called

half-zone simulation of floating zone melting in which a liquid column is suspended vertically between two differentially heated metal rods. High Prandtl (Pr > 5) fluids have been used to simplify the experiments. Schwabe and Scharmann (1979), Chun and Wuest (1979), Chun (1980a,1980b), Schwabe et al. (1982), Preisser et al. (1983), Schwabe et al. (1990), Velten et al. (1991) all experimentally studied oscillatory thermocapillary flow. They all assumed that for given Pr and zone dimensions there is a critical Marangoni number (Ma_{cr}) beyond which oscillations occur. Ma_{cr} was found to be about 10^4 for high Pr fluids in the ground-based tests. However, in the thermocapillary flow experiment on the D-1 mission by Napolitano et al. (1986) with a large (diameter = 6 cm) half-zone no oscillations were found, although Ma was as large as $4x10^5$. Monti and Fortezza (1991) conducted half-zone experiments with silicone oils (1.8 cm diam) aboard sounding rockets. The values of Ma_{cr} were found to be at least one order of magnitude higher than 1-g values. Clearly the use of Ma_{cr} to characterize the onset of oscillations is not appropriate. Also, Kamotani et al. (1984) investigated the onset of oscillations under various conditions. They found that Ma alone cannot specify the onset of oscillations and suggested the flexibility of the free surface to be another important factor controlling the onset. It was suggested that a coupling among the velocity and temperature fields and the free surface deformation were responsible for the oscillations. Based on that idea a surface deformation parameter S was proposed. The parameter S correlates well the onset conditions measured under various conditions with high Prandtl fluids (Ostrach et al. 1985).

Theoretically the transition to oscillatory thermocapillary flow in the half-zone configuration has been treated as a form of hydrodynamic instability with an undeformable free surface (Xu and Davis 1984, Shen et al. 1990, Neitzel et al. 1991, 1993). In all those analyses the models do not accurately simulate the actual situations and, moreover, because of the assumption of undeformable free surface the instability criteria are based on Ma, which does not agree with the experimental results discussed above.

Much less information is available on oscillatory thermocapillary flow in other configurations. Lee and Kamotani (1991) studied the oscillation phenomenon in a rectangular container. Kamotani et al. (1992) studied the oscillation phenomenon in a circular container with a cylindrical heater placed along the centerline. That experiment showed that the S parameter can correlate the onset conditions and that the flow structure during oscillations is quite different from that in the half-zone configuration. An organized three-dimensional free surface motion was observed.

Despite all the past work the importance of the deformable free surface is not yet fully understood and our physical model for the oscillations and the S parameter need more experimental confirmation especially in microgravity tests. The Surface Tension Driven Convection Experiment

(STDCE) was designed to study thermocapillary flow in microgravity but its main objective was to investigate steady and transient (non-oscillatory) flow.
Therefore, the Oscillatory Thermocapillary Flow Experiment (OTFE) was conceived to study oscillatory flow in the Glovebox aboard USML-1.

The OTFE was designed to measure the conditions for the onset of oscillations in circular containers. The ranges of Ma and S were chosen to obtain the oscillatory state. 1 and 3 cm diameter cylindrical containers were used with 2 and 5 cSt silicone oils as test fluids. A cylindrical heater was placed at the center of each container with its diameter equal to 10% of the container diameter. The flow was studied by flow visualization. At present we have not received a complete set of video tapes containing the flow visualization and temperature data, so the present paper is based on a preliminary analysis of the data.

I. EXPERIMENTAL APPARATUS AND PROCEDURE

The experimental configuration of the OTFE was the CT configuration of the STDCE but the test fluids and the chamber sizes were different. 1 and 3 cm diameter chambers were used in the OTFE with 2 and 5 cSt viscosity silicone oils as the test fluids. The OTFE consisted of four separate modules, each accommodating one chamber diameter and one fluid viscosity. Each module was configured around a base plate. The module is sketched in Fig.1a and its cross-section showing the test chamber is drawn in Fig.1b.

The top of each plate consisted of a reservoir and piston type pump connected to the test chamber via small diameter copper tubing. The reservoirs are constructed of Lexan to provide optical access. Small tracer particles were mixed with the fluid in the reservoir for flow visualization. A small ball bearing was also placed in the reservoir to provide a method to mix the particles homogeneously in the fluid prior to operation. There were two valves which isolated the reservoir which were opened prior to filling. Each test chamber was cylindrical and constructed of copper with a coaxial resistive heating element. The diameter of the heater was 10% of the chamber diameter as in the STDCE. The bottom wall was made of ceramic. The resistive element was sealed into the ceramic using a fillet of high temperature epoxy. A knife sharp 90 degree edge was machined into the test chamber wall to retain or 'pin' the fluid. Because there was no active cooling of the side walls, the mass of the copper chamber was sized appropriately for the amount of heat produced by the heater. The lid to the test chamber was also Lexan with an anti-reflective coating to reduce reflections. The internal walls of the test chamber were blackened to reduce unwanted reflections. The entire fluid system on the base plate was a closed system. The air displaced from the chamber during filling filled the gap created behind the piston. The test chamber

was instrumented with two type-T thermocouples, one placed just under the pinning edge and one protruding into the fluid. The latter thermocouple was positioned at the half-radius location in the radial direction and one-third of depth away from the free surface in the axial direction. The heater also had a type-T thermocouple placed at the same height as the thermocouple in the wall.

The heater and thermocouple leads were routed through the base plate to a printed circuit board on the other side. This circuit board contained signal conditioning electronics and LED displays for three thermocouples and a heater power control circuit. The LEDs had a 10 Hz display rate. The power to the heater was varied via a transistor circuit. As the gate voltage of the transistor was increased, current flowed through the heater, thus increasing the power to the heater. The ranges of heater power available were 0-10 W for 1 cm chambers and 0-13 W for 3 cm chambers. The thermocouple displays and the transistor circuit utilized the Glovebox ± 12 VDC line while the heater was powered using the Glovebox +5 VDC line.

The OTFE utilized two video signals for data recording on Spacelab VCRs. A black and white camera with 1:1 lens was attached to the PCG microscope to view, through the top of the Glovebox, the flow field in the chamber and a color camera with 1:1 lens was attached to the door to view the LED displays. These two video signals comprised the OTFE data. Therefore, both signals were recorded simultaneously and time stamped to insure that they can be temporally correlated. From these video records, the time of the transition from steady to oscillatory flow, as observed on the flow data, can be correlated with the temperature data yielding the critical temperature difference ΔT_{cr}. Also, the bulk flow temperature can be plotted as a function of time, yielding the oscillation amplitude and frequency. The overall experimental arrangement is sketched in Fig. 2.

An outline of the experimental procedure was as follows.

1. Unstow module and mix particles.
2. Configure module in Glovebox and power up (Fig. 2).
3. Configure video cameras.
4. Fill chamber.
5. Increase power in a stepwise manner while watching for oscillations.
6. After oscillations are observed, decrease power below point; increase power in smaller steps until oscillations are reached again: continue procedure transition is precisely defined.
7. Power down and wait for module to cool.
8. Empty chamber.
9. Reconfigure Glovebox with another module or stow Glovebox hardware.

II. PARAMETRIC RANGES

The important dimensionless parameters for the present experiment are : Ma (Marangoni number) = $\sigma_T \Delta TR/\mu\alpha$, Pr (Prandtl number) = ν/α, Ar (aspect ratio) = H/R, Hr (relative heater size) = D_H/D, where σ_T is the temperature coefficient of surface tension, ΔT the temperature difference between the heater and the chamber side wall, H the fluid depth, D the chamber diameter, R the radius, D_H the heater diameter, ν the fluid kinematic viscosity, μ the dynamic viscosity, and α the thermal diffusivity. For the onset of oscillations the surface deformation parameter S, which is defined as $S = \sigma_T \Delta T/\sigma$ (1/Pr), is also important. Also, in our concept of the oscillation mechanism the onset is delayed if the inertia forces associated with the flow become important or if the Reynolds number R_σ (= Ma/Pr) becomes large.

Both Ar and Hr were fixed at Ar = 2.0 and Hr = 0.1 in the OTFE. For each fluid the ranges of parameters covered in the tests were as follows. For 2 cSt fluid : Pr = 28 (at 25 °C), $Ma < 8 \times 10^5$, $S < 0.015$. For 5 cSt fluid : Pr = 63 (at 25 °C), $Ma < 6 \times 10^5$, $S < 0.01$. In our ground-based experiments (Kamotani et al., 1992) the flow was found to become oscillatory around $Ma = 6.5 \times 10^4$ (for 4 mm dia. container) and S=0.007, so the values of both Ma and S in the OTFE exceed those values. In comparison, the parametric ranges of the STDCE were : $Ma \leq 3.1 \times 10^5$, $S \leq 0.0025$, and $78 \leq Pr \leq 97$. Therefore, the value of Ma exceeded Ma_{cr} but the parameter S was below the critical value in the STDCE.

III. RESULTS AND DISCUSSIONS

Total four tests were conducted as originally planned but the module for 5 cSt-3 cm was not used, instead the module for 2 cSt-1 cm was used twice for the reason explained below. All the tests were marred by bubbles generated in the fluid beyond a certain heater temperature and the flow was very much disturbed before the critical temperature was reached. Because of that the present experiment did not give us the critical temperature differences for the oscillations. Since the bubble problem was so serious, it is discussed first.

After filling the chamber with the fluid before each test the fluid looked bubble-free, except in the first test for 2 cSt-1 cm, and it remained so until the heater temperature reached a certain value. Until then the flow was steady and very axisymmetric. When the heater temperature, measured by the thermocouple touching the top of the heater, became around 60 -70 °C, a bubble was seen to form near the bottom of the heater and it became larger as time went on. Referring to Fig.1b the heater element was heated along its entire length including the part inside the ceramic bottom. Therefore, unlike the part exposed to the fluid where convection removed heat from the heater, the part in the bottom wall experienced much less heat transfer and consequently that part

became much hotter. That situation itself did not give us a problem in our ground-based testing. However, for the space modules epoxy was used to seal the gap between the heater and the bottom wall (see Fig.1b). The epoxy was needed to stop fluid leakage through the gap during the pressure test for space qualification. It turned out that the epoxy generated vapor when it became very hot and in the absence of buoyancy the vapor bubble stayed near the epoxy and grew. The bubbles not only disturbed the flow field as they got bigger but they also created thermocapillary flow around them because of non-uniform temperature distributions over their interfaces with the fluid. For those reasons the flow field was very much altered. Attempts were made to remove the bubbles but they reappeared when the heater got hot and the test was halted. In our ground-based tests conducted after the space experiment the same bubble generation was observed over the epoxy surface around the same heater temperature as in the space tests, although the bubbles rose to the surface in one-g.

The flow visualization and temperature data were recorded on video tapes but so far we have not received all the tapes for the OTFE especially the flow visualization tapes. We also recorded the downlinked video, mainly the flow visualization data, at the POCC but the video did not cover all the tests. For that reason our analysis of those data is not yet complete.

Fig.3 shows the variation of the heater, side wall and fluid temperatures in the first test with the 2 cSt-1 cm module. The time is measured from the start of heating. Because the video camera was not properly positioned, the heater temperature could not be read in the first three minutes. The time of the vapor generation from the epoxy is indicated in the figure but in this test there were two small bubbles in the fluid even before that time. It seemed that they drifted into the test chamber through the fluid filling line shortly after the start of the test. Their size was about the heater diameter. Despite the presence of those two small bubbles the flow was very steady and nearly toroidal motion was observed over a large part of the test section until the epoxy vapor generation became noticeable, at which time the temperature difference ΔT was about 32 °C. After that the bubble attached to the bottom of the heater grew larger and around time = 18 min. the bubble size became almost equal to the container radius and the flow became very three-dimensional. The test was stopped shortly thereafter.

The critical temperature difference measured in the ground-based test using the same module was 40 °C ($S_{cr}=0.007$), so the bubble generation in the space test began before that ΔT. As discussed above, the flow remained steady and the flow structure was nearly toroidal up to about $\Delta T=32$ °C, based on which one can say that the flow was not oscillatory even at Ma $=1.3\times10^5$. That value of Ma was twice as large as the 'critical' Ma measured in the ground based tests.

Fig. 4 shows the variation of temperatures in the second test with the 2 cSt-3 cm module. In this test the heater power was increased faster than in the first test because we thought, at that time, that by doing so we could get into the oscillatory state before the bubble generation. However, the flow became very disturbed and three-dimensional by the bubble generation starting around $\Delta T = 35$ °C. Just when the bubble activity became noticeable, the heater temperature decreased noticeably as seen in Fig. 4 but the reason for that is not yet known. Unlike in the first test no bubbles were present before that time and the flow was very axisymmetric and toroidal. Therefore, one can conclude that no oscillations were observed up to Ma = 5.1×10^5 ($\Delta T = 35$ °C), which was 7.8 times larger than Ma_{cr} determined in our ground-based tests and $S_{cr} = 0.007$ (ΔT_{cr} = 40 °C) was not reached because of the bubble disturbances.

Much of the flow visualization and temperature tapes are not yet available for the third test with the 5 cSt-1 cm module. The bubble problem was worse in this test because the heater temperature was generally higher than in the tests with 2 cSt oil. The typical back-and-forth motion of particles associated with the oscillatory state was seen briefly but at present we do not know at what time and at what ΔT it appeared.

For the fourth test it was decided to repeat the 2 cSt-1 cm test rather than the originally scheduled 5 cSt-3 cm test because the bubble problem was expected to be worse in the latter case. Also we decided to heat up very slowly in this test to see whether it had any effect on the bubble generation. Fig. 5 shows the temperature variations during the test. The fluid was bubble-free and the flow was very axisymmetric until about $\Delta T = 30$ °C, at which point the bubble generation began to be noticeable. As in the second test, the heater temperature reading was unstable for some time after the bubble activity began. The size of bubbles grew with increasing temperature. When ΔT was about 38 °C the flow appeared to go through a sudden transition although the bubble activities did not show any sudden change at that point. After the transition the flow path changed and became three-dimensional. Although the transition occurred near $S_{cr} = 0.007$ ($\Delta T_{cr} = 40$ °C), whether the transition was related to oscillatory thermocapillary flow could not be determined .

CONCLUSIONS

Some conclusions from the present experiment are as follows.

1. Although steady thermocapillary flow was observed, the vapor bubbles generated by the epoxy fillet disturbed the flow before it became oscillatory so that the critical temperature differences were not determined. However, indications of oscillations were seen in some tests.

2. The flow remained steady even at Ma which was 7.8 times larger than the 'critical' Marangoni number determined in our ground-based tests, which shows that the Marangoni number is not the

appropriate parameter to describe the onset of oscillations.

ACKNOWLEDGMENTS

The authors wish to express their appreciation to Drs. Eugene Trinh and Bonnie Dunbar who conducted the OTFE aboard USML-1. To set up the experimental system properly was not an easy task but they performed the work very well. We also acknowledge the financial support of NASA for this experiment.

REFERENCES

Chun,C.-H., 1980a, "Experiments on Steady and Oscillatory Temperature Distribution in a Floating Zone due to the Marangoni Convection," Acta Astronautica, Vol.7, pp. 479-488.

Chun,C.-H., 1980b, "Marangoni Convection in a Floating Zone under Reduced Gravity," J. Crystal Growth, Vol.48, pp. 600-610.

Chun,C.-H. and Wuest,W., 1979, "Experiments on the Transition from Steady to the Oscillatory Marangoni Convection of a Floating Zone under Reduced Gravity Effect," Acta Astronautica, Vol. 6, pp. 1073-1082.

Kamotani,Y., Ostrach,S., and Vargas,M., 1984, "Oscillatory Thermocapillary Convection in a Simulated Floating Zone Configuration," J. Crystal Growth, Vol.66, pp. 83-90.

Kamotani,Y, Lee,J.H., Ostrach,S., and Pline,A., 1992, "An Experimental Study of Oscillatory Thermocapillary Convection in Cylindrical Containers," Phys. Fluids A, Vol.4, 955-962.

Lee,K.J. and Kamotani,Y., 1991, "Combined Thermocapillary and Natural Convection in Rectangular Enclosures," In Proceedings of the 3rd ASME/JSME Thermal Engineering Conference, Reno, Nevada,
pp. 115-120.

Monti,R. and Fortezza,F., 1991, "The Scientific Results of the Experiment on Oscillatory Marangoni Flow Performed in Telescience on Texus 23," Microgravity Quarterly, Vol.1, pp. 163-171.

Napolitano,L.G., Monti,R., and Russo,G., 1986, "Marangoni Convection in One- and Two-Liquids Floating Zones," Naturwissenschaften, Vol.73, pp. 352-355.

Neitzel,G.P., Law,C.C., Jankowski, D.F., and Mittlemann,H.D., 1991, "Energy Stability of Thermocapillary Convection in a Model of the Floating-Zone Crystal-Growth Process. II: Nonaxisymmetric Disturbances." Phys. Fluids A, Vol.3, pp. 2841-2846.

Neitzel,G.P., Chang,K.T., Jankowski, D.F., and Mittlemann, H.D., 1993, "Linear Stability Theory of Thermocapillary Convection in a Model of the Floating-Zone Crystal Growth Process," Phys. Fluids A, Vol.5, pp. 108-114.

Ostrach,S., Kamotani,Y., and Lai,C.L., 1985, "Oscillatory Thermocapillary Flows," PCH Physico-Chemical Hydrodynamics, Vol.6, pp. 585-599.

Preisser,F., Schwabe,D., and Scharmann,A., 1983, "Steady and Oscillatory Thermocapillary Convection in Liquid Columns with Free Cylindrical Surface," J. Fluid Mech. Vol.126, pp. 545-567.

Schwabe,D. and Scharmann,A., 1979, "Some Evidence for the Existence and Magnitude of a Critical Marangoni Number for the Onset of Oscillatory Flow in Crystal Growth Melts," J. Crystal Growth, Vol.46, pp. 125-131.

Schwabe,D., Velten,R., and Scharmann,A., 1990, "The Instability of Surface Tension Driven Flow in Models for Floating Zones under Normal and Reduced Gravity," J. Crystal Growth, Vol.99. pp. 1258-
1264.

Shen,Y., Neitzel,G.P., Jankowski,D.F., and Mittlemann,H.D., 1990, "Energy Stability of Thermocapillary Convection in a Model of the Float-Zone Crystal-Growth Process," J. Fluid Mech., Vol.217, pp. 639-660.

Velten,R., Schwabe,D., and Scharmann,A., 1991, "The Periodic Instability of Thermocapillary Convection in Cylindrical Liquid Bridges," Phy. Fluids A, Vol.3, pp. 267-279.

Xu,J-J. and Davis,S.H., 1984, "Convective Thermocapillary Instabilities in Liquid Bridges," Phys. Fluids, Vol.27, pp. 1102-1107.

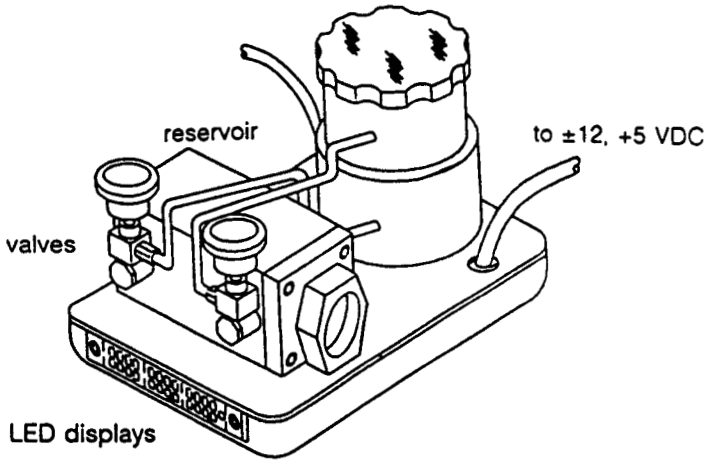

(a) Sketch of test module

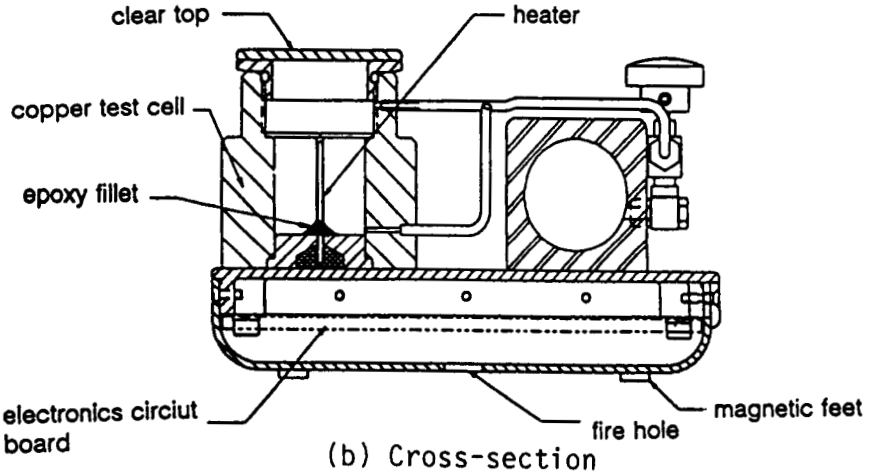

(b) Cross-section

Figure 1 Sketch of test module for OTFE.

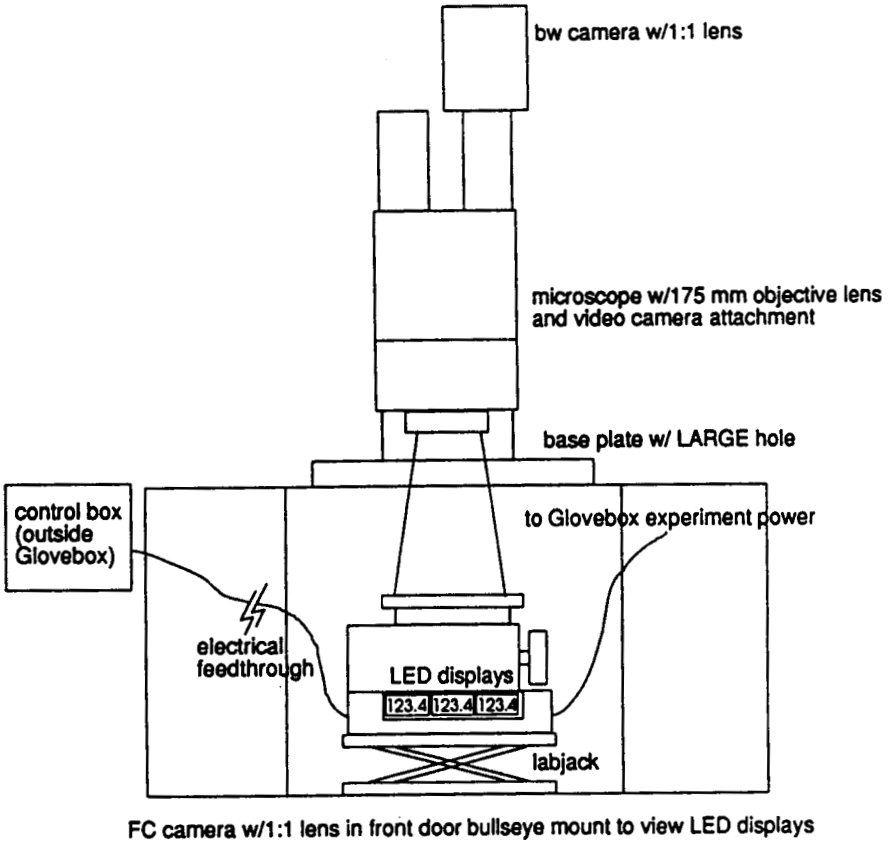

Figure 2 Experimental arrangement of OTFE.

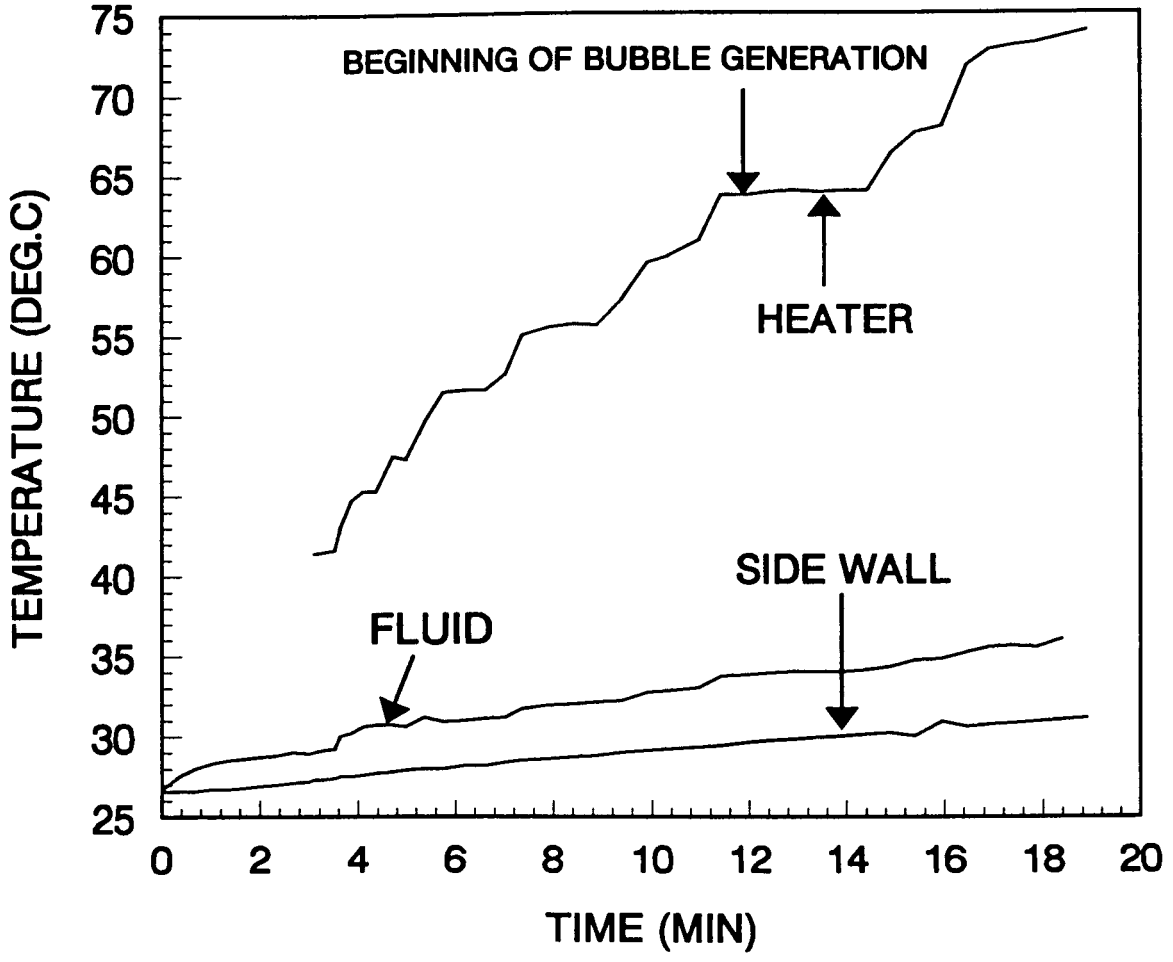

Figure 3 Temperature variations in Test 1 with 2 cSt-1 cm module.

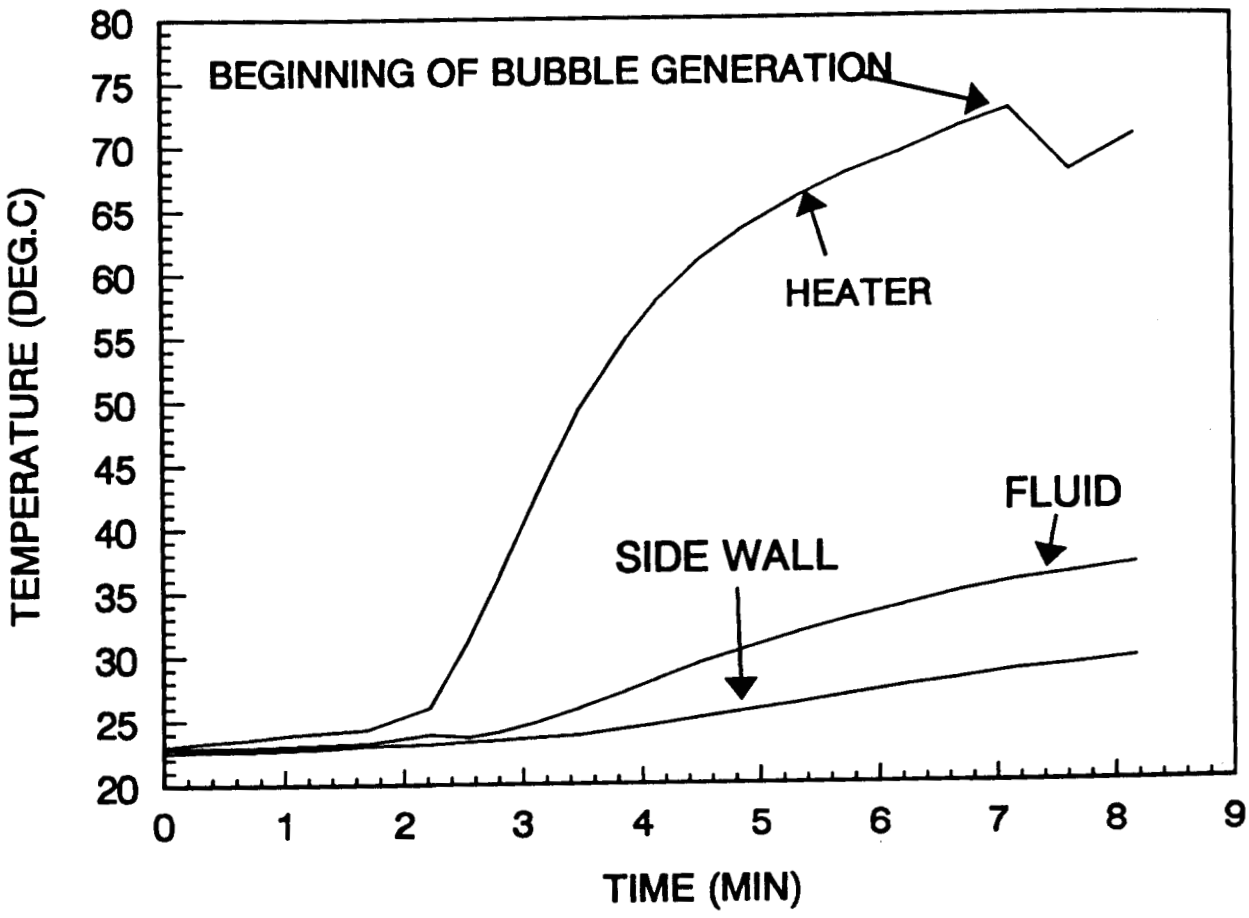

Figure 4 Temperature variations in Test 2 with 2 cSt-3 cm module.

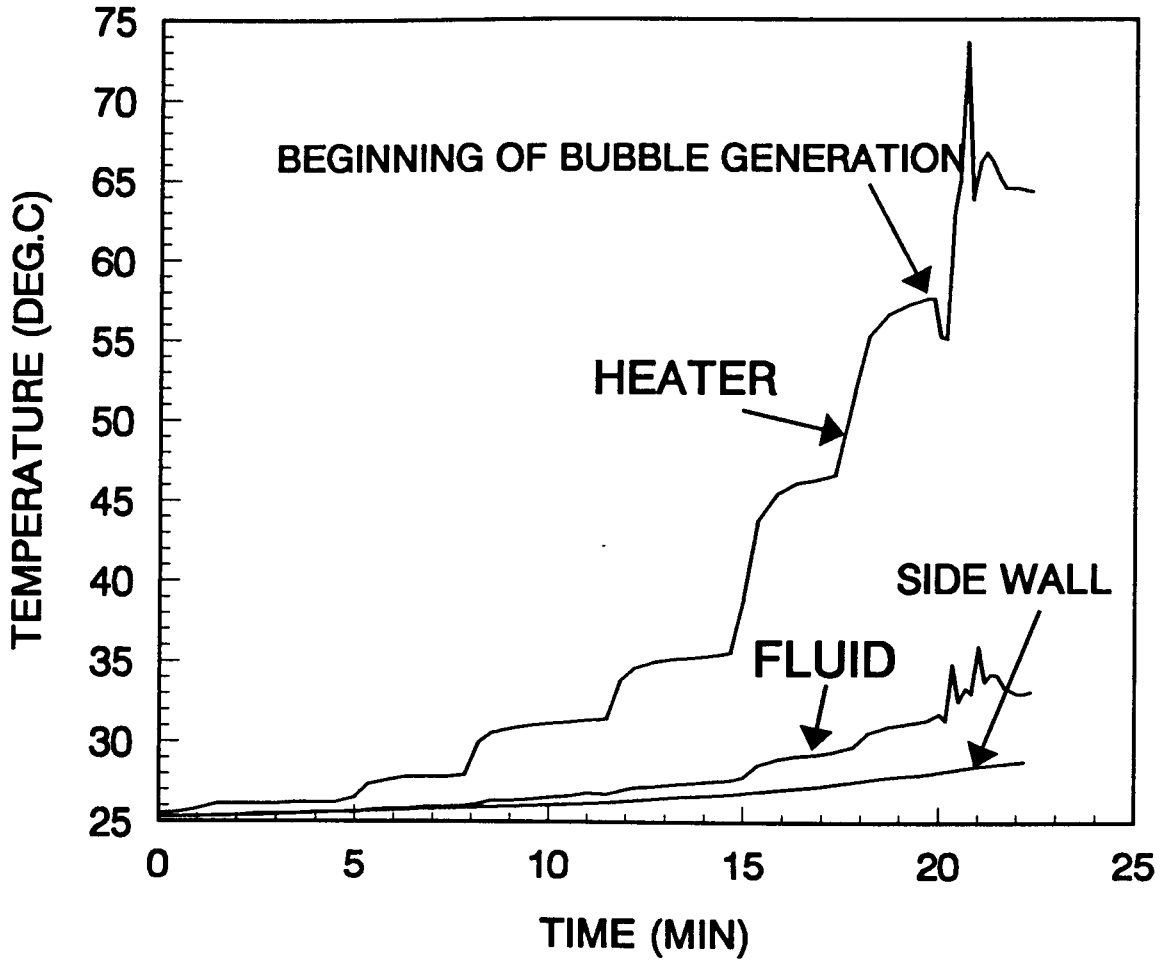

Figure 5 Temperature variations in Test 4 with 2 cSt-1 cm module.

Discussion
(Speaker: Y. Kamotani, CWRU)

Question: *On USML-2, what steps are being taken to circumvent the bubble problem ?*

Answer: Okay, to avoid the bubble problem; Now in 1g, the bottom wall is made of Teflon and the heater just goes through the gasket and there is no epoxy. That is supposed to be sufficient. According to our KC-135 flight results, no bubbles were created. So that is what we used in 1g, but for this experiment, we changed the design and paid the price. Also in STDCE-2, we follow the same parametric ranges and aspect ratio but in OTFE-2 we want to study the aspect ratio effect. We want to make it deeper.

PARTICLE DISPERSION EXPERIMENT (PDE): PRELIMINARY RESULTS FROM THE USML-1 GLOVEBOX

John R. Marshall

SETI Institute
NASA Ames Research Center, MS 239-12, Moffett Field, CA.

ABSTRACT

The Particle Dispersion Experiment was designed to test technologies for future Space Shuttle and Space Station experiments that will be concerned with the dispersion of aerosols and related particulate clouds. PDE successfully tested a gas-pulse method of dispersing granular materials inside eight modular experiment chambers. The technique further demonstrated the ability of an air pulse to redisperse particles once they are already free-floating in a chamber. PDE was also designed to enable a limited parametric study of the aggregation of the dispersed particles caused by electrical interparticle forces. Such forces are prevalent on natural materials when dust is injected into planetary atmospheres by volcanic eruptions, meteorite impact, and dust storms. Electrostatic aggregation is inevitable in natural dust clouds, and is a major factor controlling the longevity of the dust palls. The PDE experiments showed that aggregation experiments can be conducted in small experiment chambers, that aggregating natural materials form amorphous and filamental structures, and that aggregation can lead to the formation of "giant" (>cm) particle clusters with commensurately large electrical fields around them. The observed growth of the electrical fields has important implications for our understanding of the aggregation process, and of course, important ramifications for the behavior of natural dust clouds.

INTRODUCTION

Science Background

Large quantities of dust can be injected into planetary atmospheres by several processes. It has been speculated that the impact of a large meteorite or comet with a planet such as Earth could create a dust pall of global proportions; this idea has received wide-spread popular attention as a possible cause of the demise of the dinosaurs at the end of the Cretaceous period. Since the Cretaceous bolide was not a rare event in Earth's history, there must have been many other occasions when dust contamination of the atmosphere by impact caused disruptive effects on the

Joint "L+1" Science Review for USML-1 and USMP-1 with the Microgravity Measurement Group, September 22-24, 1993, Huntsville, Alabama, USA.

evolution of Earth's global ecosystem. Certainly, local and regional ecosystems will have been devastated by meteorite impact.

Volcanic eruptions and dust storms are also mechanisms for creating dust palls; ash clouds created by individual volcanoes are well known from both recent and historical eruptions, although significant effects of these events are geographically limited. In the geological past, however, there may have been periods of intense volcanism when eruptions were both more violent and more frequent, and volcanism may have resulted is short-term modification of global climate. Likewise, dust storms on Earth have both local and regional effects, with relatively minor global effects. Again, in the geological past, there may have been much more extensive activity. For example, at the end of the last Ice Age when receding ice fronts left behind vast unvegetated tracts of the Earth covered in glacially-crushed rock, there was potential for large-scale raising of dust. The Pleistocene loess deposits (long-distance fall-out material from dust storms) bear witness to extensive dust storm activity associated with the last Ice Age.

In order to assess the climatic and ecological effects of dust-raising events, an understanding is required of the factors that control the period of dust suspension. This is poorly understood because there is no firm understanding of the rate and mode of aggregation of the suspended particles. Aggregation of material into larger clusters will obviously accelerate the dust settling process, and aggregation is inevitable because the particles will be electrically charged. This charging results from the electrification inherent in the comminution processes that generate the dust. Meteorite impacts, volcanic eruptions, and dust storms cause charging by material breakage, by triboelectrification, and by creating an association of suspended particles with electrically-charged atmospheric conditions (weather fronts).

The Particle Dispersion Experiment is in response to this need for a better understanding of the aggregation process; the need to conduct the experiment in microgravity derives from: 1) the fact that normal laboratory experiments are limited to brief periods of observation because settling rapidly removes aggregates from the experiment chamber, 2) there is a need to remove gravity-related forces such as convection and aerodynamic settling drag so that the interparticle electrical forces responsible for aggregation can be isolated and studied, 3) a microgravity environment prevents collapse of weak and delicate aggregate structures under their own weight.

Technology testing

It is planned to ultimately conduct more extensive aggregation experiments aboard Space Station Freedom as part of an experiment package for the Gas-Grain Simulation Facility (GGSF). The GGSF is planned as a multi-user Station facility for conducting a wide range of aerosol-type

experiments that deal with cloud physics, atmospheric dust, atmospheric aerosols, solar nebula accretion, satellite particle rings, etc. The experiments will serve the disciplines of exobiology, planetary geology, astronomy, climatology, physics, and chemistry. However, much precursor work (both on the ground and in reduced gravity) is needed to define the technologies and techniques appropriate for the facility. In order to conduct experiments involving dispersed liquid or solid particles, some initial dispersion condition has to be created that is controllable, repeatable, and definable. It is not intuitively obvious how this can be done and, therefore, the Particle Dispersion Experiment would be a preliminary attempt to test some rudimentary concepts.

The Experiment

As noted above, the PDE served both technological and scientific inquiry. The approach was to limit the scope of the technology testing to one injection/dispersion method that seemed the simplest and that probably had the greatest chance of success. No simple method could be envisaged that would enable an experiment to be initialized from a quiescent air volume. The dispersion technique therefore adopted the approach of creating dynamic rather than static isotropy of particle distribution as a starting point for an aggregation experiment. Because little was known about the likely outcome of the tests, sand-size material was used instead of dust, even though the latter is ultimately the material of interest. The use of sand simplified the imaging of individual particles, as well as simplifying the manipulation of the material. It was not intended to be a perfect surrogate for dust, but simply a material from which some useful first lessons could be learned. It was, however, directly appropriate as a representative of the coarser fractions lofted into atmospheres by volcanic eruptions and meteorite impacts.

The objective of the experiment was to test a method of dispersing particles in microgravity and to then conduct an aggregation experiment should the dispersion prove successful. Particles would be dispersed in an experiment chamber and their subsequent behavior would be captured on the Glovebox video tapes. Eight experiment modules were used to enable a range of particle sizes (105-125, 354-420, and 707-840 micron diameter quartz sand) to be tested, and to provide a means of testing repeatability. The video tapes of the experiments would be used to ascertain: 1) the rate of aggregation and the aggregation phases and thresholds, 2) the shapes of aggregates and aggregate growth modes, 3) the configuration and strength of electrical fields around aggregates judged from the direction of motion and velocity of particles, 4) the ability of aggregation to cleanse the experiment volume of monomer and small-cluster units.

I. FLIGHT HARDWARE DESCRIPTION

A. Engineering

The experimental hardware is depicted in Figure 1 and consists of one pump unit and eight interchangeable modules that plug into the pump. The pump unit provides the pressure for a momentary pulse of air that injects a small charge of particles into a module. The experiment begins at the moment that the particles are released into the experiment chamber of the module.

The pump unit of 1.0 kg and 0.002 m^3 consists of a small hand-operated (rotating crank) piston that compresses air into a 100 cm^3 pressure container to about 15 psig (indicated by a tiny dowel gauge at the left side of the apparatus). The air is drawn in and filtered through a one-way valve at the front of the apparatus. The handle at the left side is for gripping the apparatus during operation of the pump. All valve interiors can be accessed by a malfunction tool if valve adjustments become necessary.

Each of the eight modules contains its own cubic experiment volume of 125 cm^3 which is viewed through two large (5 x 5 cm) windows at either side of the module. The insides of the windows are coated with indium tin oxide and nichrome to prevent electrical charge build-up. The lower part of each module plugs into the pump and contains a $\approx$ 2-3 cm^3 cavity in which the sand particles reside; the particles are trapped by a wire screen at the lower end of the cavity and by an air-tight spring-loaded shutter at the top end which separates the particles from the experiment chamber. The shutter is released by operating a standard photographic shutter cable which attaches to the outside of the module. This type of release mechanism prevents the operator from disturbing the experiment during shutter firing because there is no "hard" coupling of the apparatus with the operator. A safety catch prevents the shutter from operating if the module is not mounted in the pump unit. Air released into the modules from the pump is immediately vented through eight side ports covered with wire mesh; the mesh is fine enough to retain the particles.

B. Operations

To conduct an experiment, a module is plugged into the pump unit and locked into place. The socket on the module makes a pressure seal when mated with the pump. The pump is operated until the pressure indicator shows full pressurization; two safety valves prevent pressures in excess of the desired maximum. The cable release is attached to the outside of the module and operated after the module is positioned correctly with respect to lighting and camera angles. Operating the cable releases the shutter which holds back both the particles and the pressurized air. A momentary pulse of air subsequently "spits" the particles at high velocity into the module's experiment chamber. Motion of the particles continues for a few seconds before damping due to air

drag. When the experiment is complete (after observation of particle behavior for ≈15-20 minutes), the module is unplugged and replaced with the next module.

Three of the eight modules were designated as "trial" modules; these already had particles floating freely in them so that camera focusing and lighting arrangements could be made prior to use of the "sand-firing" modules. They also provided the operator with a preliminary understanding of the likely behavior of the particles in the other modules. In the trial modules, air could be fired at the particles in the chamber to cause dispersion of material. A screen separated the shutter from the experimental chamber so that particles could not drift back into the mechanism of the module. Thus, the air (without a particle charge) could be fired into the chamber as often as desired. To enable the module and pump to be pressurized, the shutter was closed each time by a latching pin which was provided as part of the tethered "tool kit" for the apparatus.

C. Design rationale

The design of the PDE reflected a deliberate attempt to reduce safety problems, eliminate interfaces, and minimize use of Glovebox resources so that the experiment had a high degree of autonomy and self-reliance. This was the motivation behind the use of a hand-cranked air pump which avoided the need for on-board stowage of high-pressure gas containers; the pump also provided nominally unlimited amounts of compressed air. Large windows enabled use of Glovebox lighting so that batteries or power interfaces could be eliminated, and the use of interchangeable modules reduced the potential hazards of material changeouts as would have been necessary if only one chamber had been available. The use of many modules also eliminated the possibility of a single-point failure, while the incorporation of access ports and a tool kit on the pump acted as contingencies for potential malfunctions.

II. RESULTS OF TECHNOLOGY TESTING

A. Dispersion

The USML-1 experiment demonstrated that an air pulse will provide an extremely efficient method of dispersing particles in a relatively small experimental chamber. So far as the naked eye was concerned, the dispersion occurred instantaneously. On a frame-by-frame analysis of the video tapes, it could be ascertained that the injected particles had already ricocheted around the module several times after only 1/30 second (standard framing rate on the video tapes). The injection energy of the pellet of particles was more than sufficient to cause randomization of the particle distribution and a "dynamic isotropy" in the experiment volume. A frame-by-frame analysis of the first few seconds of the experiments showed that the random distribution of particles was

maintained as motion was gradually damped by air resistance. This random distribution has been judged qualitatively to date, but it is planned to conduct a quantitative characterization using an appropriate statistical method that evaluates the concentration of particles in a two-dimensional plane. If there had been no adhesion of particles to the wall, the concentration of particles would have been 0.016 gm/cm^3 (2 gm injected into 125 cm^3 chamber).

It was also discovered that the particles could be redispersed inside the modules by firing a pulse of air at free-floating materials; the dispersion appeared to be just as effective as that produced by the initial particle injection into the modules (Fig. 2). It should be noted, however, that the operator assisted this process by careful "rocking" of the modules until the bulk of the wall-adhering material was induced to float into the middle of the chamber where it was struck by the air pulse. This provided a perfectly acceptable method of restarting an experiment after the initial insertion, and for reduced gravity experiments where motion of the apparatus is possible, this should point to a very simple method for dispersion.

B. Operator Manipulation of Particles

Prior to the experiment there were insufficient data to assess the effect of manipulating the particles by motion of the apparatus. Therefore, the crew operator conducted several trials in which the apparatus was shaken from side to side in order to remove particles from the module walls. This manipulation proved that there was little force attracting the particles to the walls -- the particles were very easy to dislodge and it was equally easy to manipulate the particle clumps into exactly desired locations where their motion could be halted by careful oscillation of the module's position. This was used very effectively for placing the particles over the air nozzle so that the air pulse could be used to redisperse materials as just noted. Although the particles could be easily manipulated, no amount of module agitation could redisperse the particles, nor fragment aggregates to below a certain cluster size of several millimeters.

C. Visibility and Imaging

There was initial concern that visibility might be reduced through the experiment chambers as a result of material adhering to the windows. However, the windows stayed relatively clear of particles and the focus of the camera at the center plane of the modules (3 cm from the windows) rendered the few adhering particles virtually invisible. Particle concentrations in the modules were insufficiently high to cause any detrimental reduction in visibility and light transmission. The imaging of the particles as silhouettes against the backlighting worked extremely well, particularly with the relatively shallow depth of focus. It is noted that the use of trial modules with particles

already floating in the chambers proved to be absolutely essential for setting-up the lighting and camera focus prior to operation of the sand-firing modules.

The shallow focal depth of the camera (≈1cm) prevented too much overlapping information in the third (z) dimension which would have confused measurement of aggregate shapes. Sweeping the focus of the camera through the full depth of the modules at the end of each experiment added information from the third dimension.

During the long run-out times of the experiments (periods up to 20 minutes), several abrupt shifts in the floating particles were observed. Presumably, it was the apparatus (i.e. the space craft) that moved, giving the appearance of a relative shift in the frame of reference. This motion was later attributed to vernier rocket firings for orbital adjustments. Although this slightly disturbed the experiment, it was found to be a useful method of determining which particles were free floating and which were adhering to the windows, since the latter did not obviously appear to move.

D. Adhesion to the walls

It was observed by the experiment operator, and confirmed by calculation of final dispersion densities from the video tapes, that greater than 50% of the material came to rest on the walls within the first few seconds of the experiment. For the smallest particle size (≈115 microns), this was partly due to residual air currents that carried material to the walls. For the two larger sizes of material (which continued to ricochet around the chamber for longer periods), the final distribution of particles depended upon the reasonably high probability that a particle would be within adhesion range of a wall at a time when its energy had declined to something less than that required for resisting the wall/particle adhesion force. It is suspected, but not yet statistically proven, that to increase the initial energy of the particles would do little, if anything, to change the final particle distribution -- higher particle energy will simply delay the same end result. Despite significant losses to the walls, this did not jeopardize the experiments; sufficient material remained in the free space to enable aggregation experiments.

III. RESULTS OF AGGREGATION EXPERIMENTS

A. Dispersion and aggregation phases

Damping phase: The initial jet of material into the experiment chamber remained definable as a jet for only one still frame of the video, and must therefore have had a maximum lifetime of 1/30 second. Thereafter, the particles ricocheted around the chamber in elastic collisions, and were additionally driven by the turbulent motion of the dispersing air pulse. After two frames the dispersion was complete -- every part of the experiment volume was filled with a dense cloud of

rapidly-moving particles. This chaotic and violent motion continued for several seconds during which time an increasing number of grains became resolvable as their motion slowed. The cloud had such a high state of kinetic energy that all motion *appeared* to be driven by the impulse energy from their injection. As discussed later, this motion is probably retarded to some appreciable extent by interparticle forces which add a measure of internal friction to the motion of a gas/grain mixture. During this damping phase, particle motion was chaotic and omnidirectional.

Equilibration phase: This was the most important aggregation phase of the experiments. Particle motion had damped sufficiently to allow aggregates to form without disruption; the attraction forces between particles now superseded the disruptive forces from aerodynamic and collisional processes. Aggregates formed while there was still particle motion and, indeed, this motion appeared essential for bringing particles in close enough proximity to one another to enable aggregation. Thus, there was a narrow time window when particle motion was sufficiently low to prevent aggregate disruption, but sufficiently high to cause particle interactions. Particle motion was driven very obviously by interparticle electrical forces attaining equilibrium. Motion was still omnidirectional in the cloud as a whole although it was locally focused around aggregation centers. The equilibration phase lasted only a few seconds.

Quiescent phase: After equilibration, particle motion appeared to have ceased by judging with the naked eye. However, there was very slow aggregate growth (orders of magnitude slower than in the equilibration phase) during the quiescent phase and particles were brought together by both weakly-interacting electrical forces (that also slowly changed configuration), and by relative motion of clusters owing to differential settling rates. The slow settling (as well as intermittent rocket firings) caused predominantly unidirectional particle motion over the experiment run-out times of 15-20 minutes.

B. Shapes of aggregates

All particle sizes displayed a tendency to form both irregular clusters and organized filamental structures, although the filaments were most pronounced for the 354-420 micron material. A dozen or so particles would typically constitute one of these filaments (Fig. 3). The formation of filaments suggests some preferential stacking or orientation of the particles such as might occur if each grain exhibited electrical polarity, although there were no direct measurements of electrical fields to substantiate this claim. The giant aggregates described below were generally amorphous in shape although some had fractal-like "tentacles" or curling filaments evolving from their central bulk. On one side of one of the giant aggregates, growth appeared to be occurring by the stacking of particles on the ends of filaments extending from the main aggregate body.

C. *Giant aggregates and electrical fields*

Figure 4 shows an aggregate 5-6 cm in length -- occupying the full size of the experiment chamber. These aggregates were the result of accumulations near the chamber walls, but subsequent operator manipulation of the apparatus propelled the clusters into the center of the chamber. Nonetheless, the aggregates illustrate the tendency for particles to remain as one unit despite dislodgement. Attempts by the operator to fragment the aggregates were only partially successful despite fairly vigorous agitation of the apparatus. Unfortunately, motion of the particles in the vicinity of these aggregates is not apparent from the still-frame images. On the video film the motion is quite dramatic -- particles from the furthest reaches of the experiment chamber are being pulled towards the aggregates at velocities up to 1 cm/sec. The "infall" of particles showed no apparent preferred direction.

It was clear from these images that the electrical fields surrounding the aggregates were able to influence particles for distances at least equal to the aggregate diameters. Although these giant aggregates were not grown in the center of the chambers, it might be reasonable to assume that such aggregates could grow from a cloud if the initial cloud density were sufficiently high. Figure 5 illustrates two possible scenarios for aggregate evolution from an initial monodisperse particle cloud. In one case, it is (traditionally) assumed that the electrical fields around individual particles remain constant in strength during their incorporation into an aggregate, and that the net strength of a field around an aggregate is no greater than the sum of its parts (individual grains). The resulting aggregates continue to grow until the effect of their electrical fields on surrounding material ceases to be significant. At this point, there is a large size distribution for the aggregates, and many monomers remain. Aggregation also ceases at this point. In the other case (that observed in PDE), the electrical field strength (and thus, its sphere of influence, or effective diameter) grows as the aggregate mass increases. This situation could enable the appearance of very large clusters that completely scavenge their surrounds and always remain in (effective) electrical contact with one another. The theoretical (but unlikely) outcome is one single aggregate.

A model of the electrical fields around all of the aggregates observed (small clusters, long filaments, and amorphous giants) is still under development. The model will examine to what extent, if any, that the chamber itself contributes to the aggregate configurations. Independent observations from other aggregation experiments at both 1 g and at reduced g suggest that the USML-1 results are not an artifact of the experimental apparatus.

IV. IMPLICATIONS, CONCLUSIONS, & RECOMMENDATIONS

A. Technology testing

- The results of the technology testing demonstrate that particles can easily be dispersed in a microgravity environment using an air pulse technique, and that the air pulse can be used to re-disperse material if apparatus motion is possible.
- The dispersion technique was able to create a random distribution of materials required for the initiation of an aggregate experiment. The particles (at least, of the types tested) had also been sufficiently de-agglomerated so that monomers and very small clusters (two's and three's) constituted the initial cloud.
- Wall losses consume the majority of particles, even with apparently weak wall attraction. This factor must be taken into account in any future microgravity experiments. Losses can be compensated for by use of sufficiently high initial cloud densities.
- Future work might profit from tests in microgravity of wall vibrators or some means of intermittently rapping the walls in order to dislodge particles and gently impel them into the center of the experiment volume. Controlled vibration/rapping may enable accurate positioning with respect to a particle disperser such as an air jet.
- This type of experiment where there are brief periods of high interaction of the experiment with the crew, is absolutely essential as a precursor to more sophisticated experiments on Space Station where crew time will be at a premium and much autonomous function will be required of an experiment.

B. Aggregation

- There are aerodynamic implications of the observed aggregate shapes. The tendency for particles to form delicate filaments rather than amorphous or spheroidal clusters means that the aerodynamic drag on an aggregate will be greater. This could result in more rapid fragmentation, but it could also increase the ability of particle clusters to stay in suspension, at least compared to spheroidal structures.
- The observed aggregation phases imply for the natural world that most of the aggregation in a cloud will occur very rapidly after the injection of the dust into an atmosphere unless the cloud already begins as a very dilute suspension. Aggregation thereafter may take days or weeks, and motion of the air will be an important factor in bringing particles in close proximity to one another.
- There are significant scientific implications of the growth of giant electrical fields. If this phenomenon is indeed real and can be extrapolated to the natural environment, it implies that inside very dense dust clouds (such as the eruption plume of a volcano) there may be a tendency to

generate enormous aggregates, aerodynamic disruption notwithstanding, thus greatly accelerating precipitation from the cloud. It might also be surmised that the growth of electrical fields might significantly influence the internal motion of the cloud and the rate at which cloud dispersion can occur. It is probable that aggregation undergoes many cycles; aggregates form, then become disrupted by turbulence or during free fall, and the particles continue to recombine and separate for many cycles. This will cause exchanges of electrical charges and offer some interesting possibilities for the evolution of the electrical status of the cloud and its particulate components.

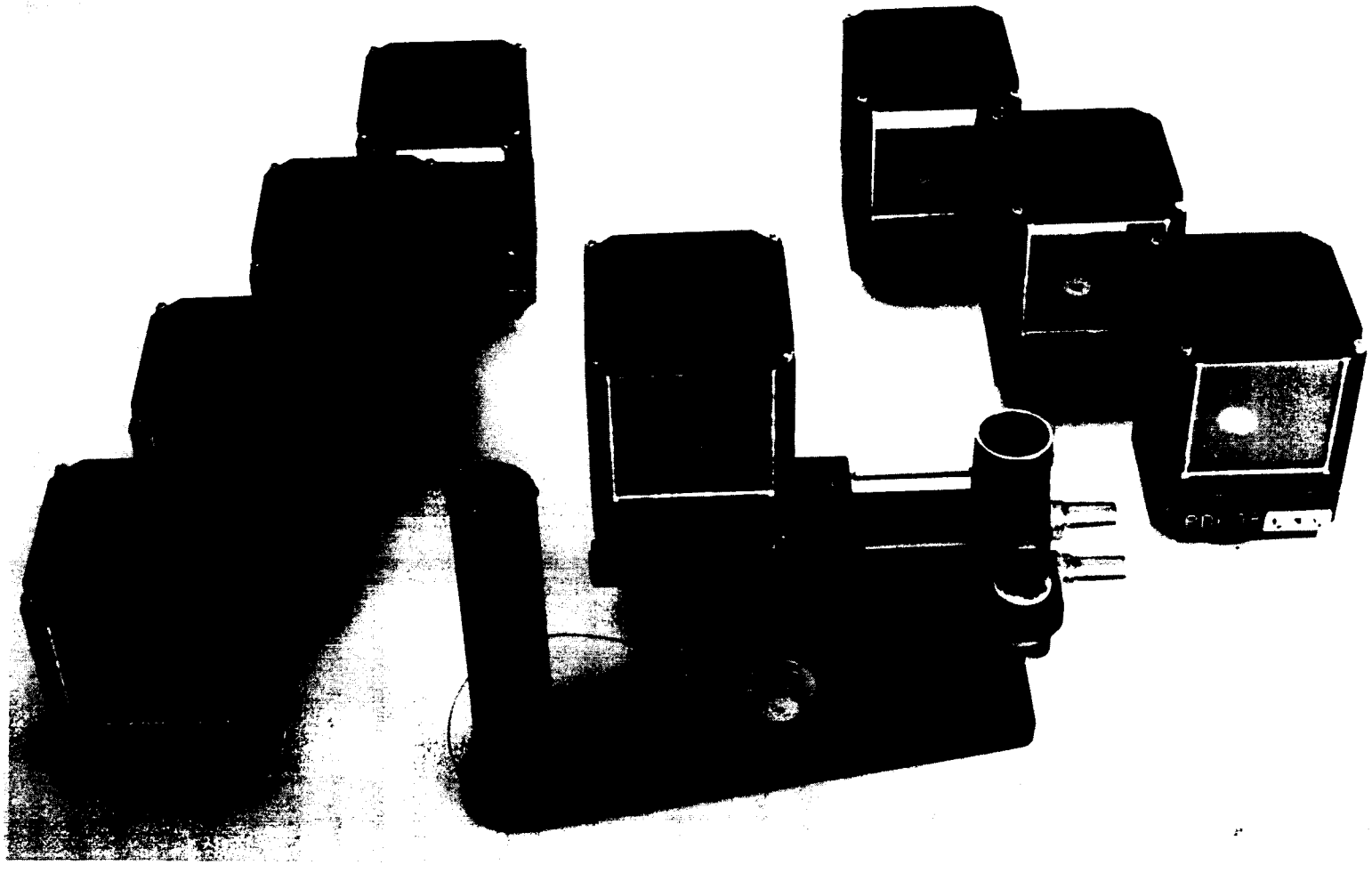

Figure 1 Particle dispersion experiment flight hardware for USML-1 Glovebox showing pump unit and eight modules.

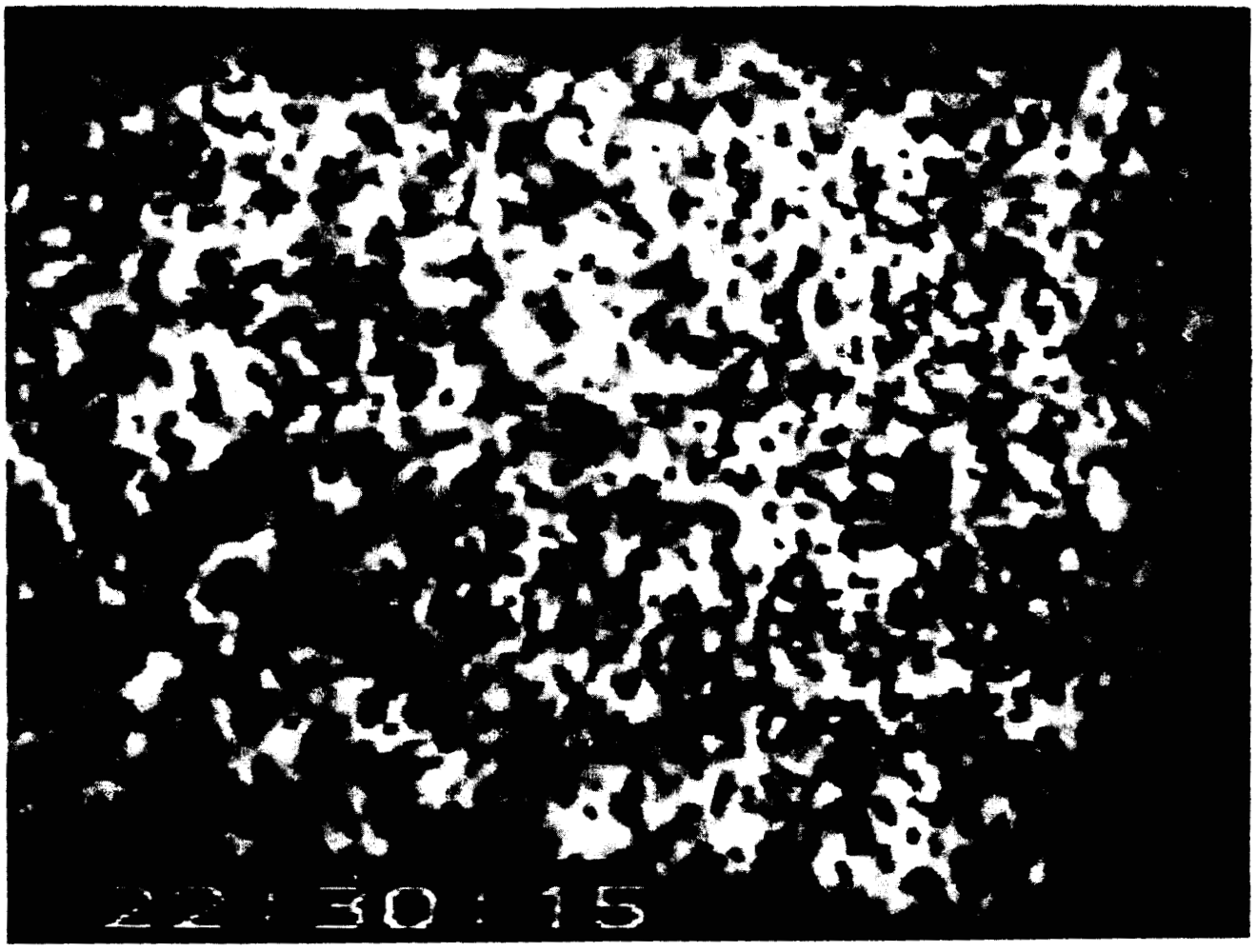

Figure 2 Dispersion of 354-420 micron particles caused by an air pulse. The image is 3 seconds after the pulse struck the aggregate in Figure 4. Field of view is 5 cm across.

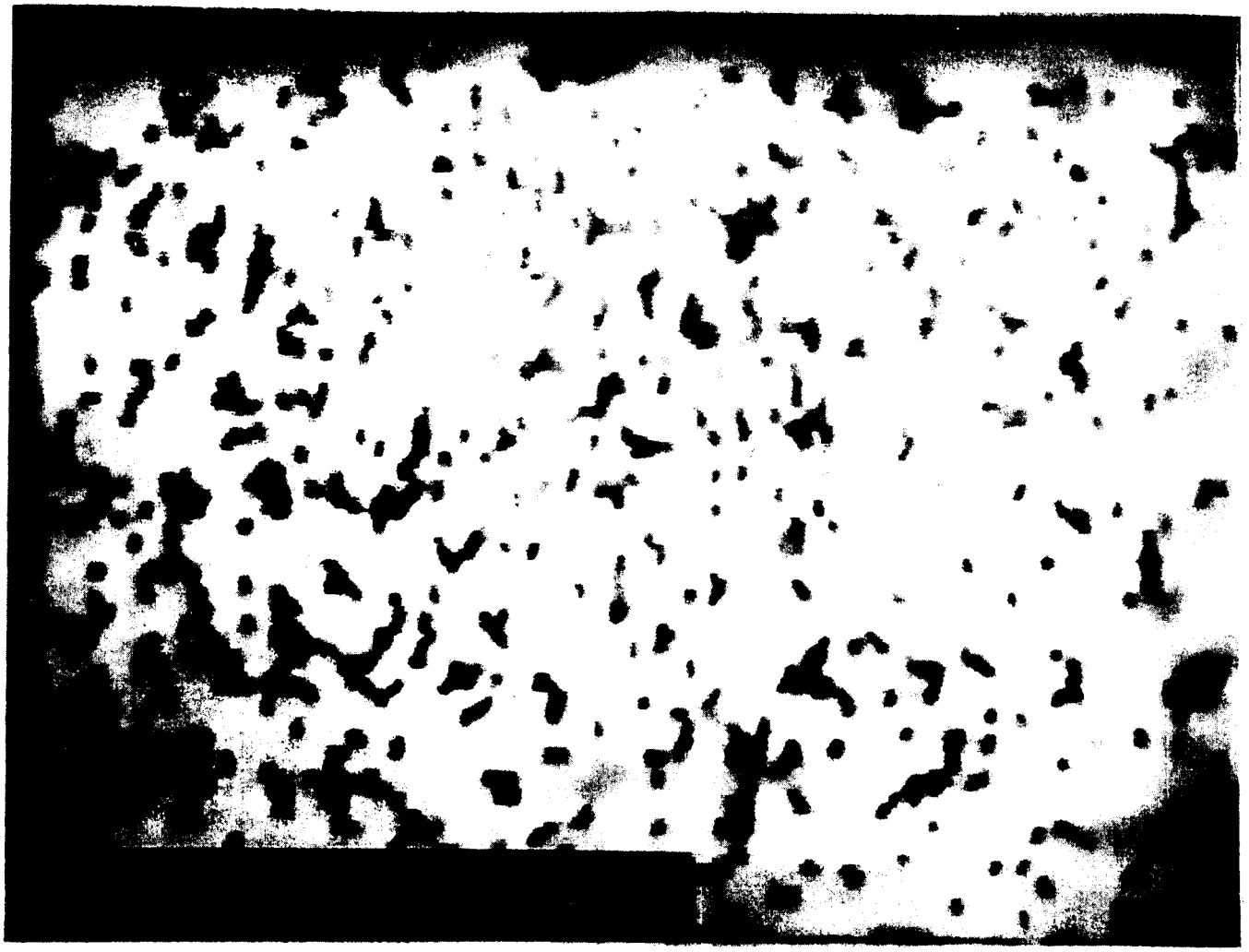

Figure 3 Filamental aggregates formed from 707-840 micron particles. Field of view is 5 cm across.

Figure 4 "Giant" aggregate formed from 354-420 micron particles. Field of view is 5 cm across.

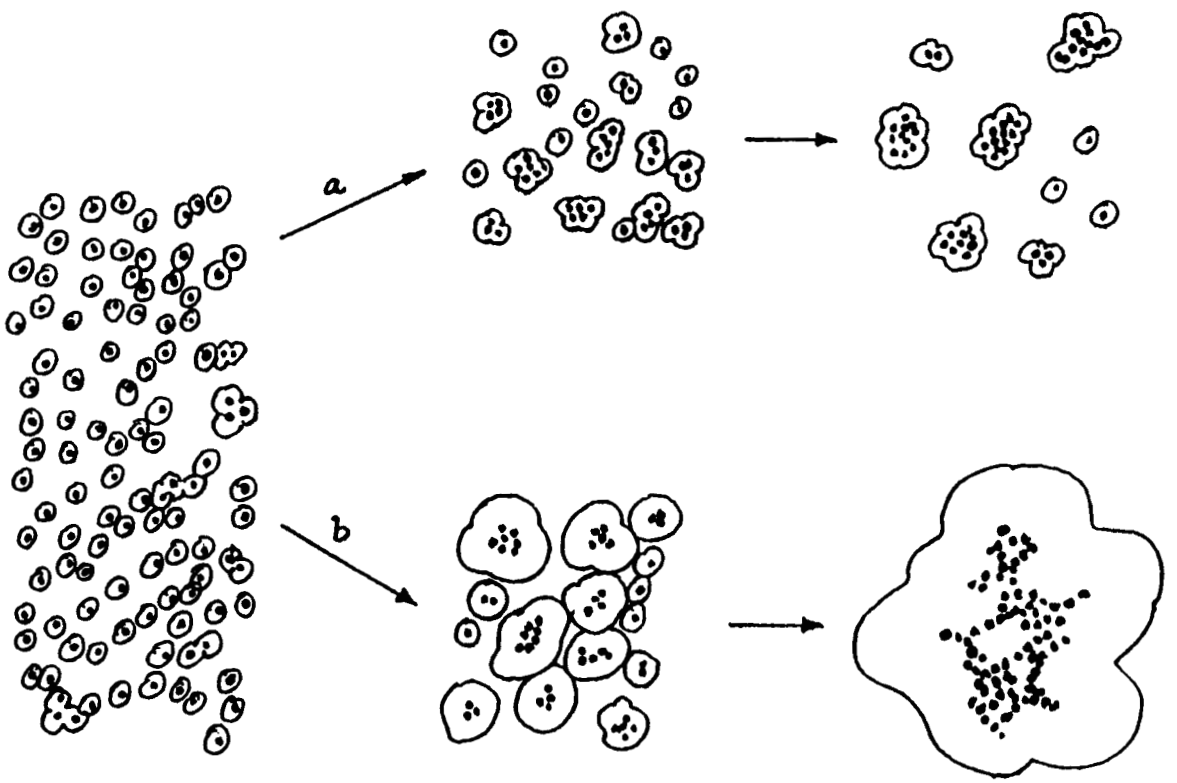

Figure 5 Growth of aggregates from a particle cloud. Path 'a' assumes electrical fields around particles to be constant strength. Path 'b' assumes increasing field strength as observed in PDE. Electrical "spheres" around particles are not intended to denote field boundaries, but practical limits of influence.

ESA ACTIVITIES ON MICROGRAVITY AND MICRODYNAMICS

H. R. Stark and **C. Stavrinidis**

ESA/ESTEC, Noordwijk, The Netherlands

ABSTRACT

The utilization of the low gravity environment of Earth orbiting spacecraft provides new opportunities for experiment performance and applications in the field of fluid physics, material, life and biological sciences. However, the environment is not quiescent onboard of Earth orbiting spacecraft as well as scientific satellites with very high pointing stability requirements. It is affected by various acceleration sources and constituents that arise under typical orbital and operational conditions. Microvibrations affect microgravity experiments during their performance in space and they affect the line-of-sight stability of instruments. Such effects need to be taken into account during the spacecraft development, mission planning and operation, and post mission analysis.

The paper provides an overview on the ESA microgravity and microdynamics activities in the field and applications of ongoing projects and programs. A review is given on microgravity payload sensitivities, disturbance sources, micropointing stability requirements of satellites and scientific experiments. Microdynamics control approaches, plans and philosophies are presented which are employed in various project and programs. Supporting technology tasks are presented which are performed in the framework of ESA R&D activities which shall provide the scientific projects and programs with adequate solutions.

INTRODUCTION

The realization of research and manufacturing activities in space under low gravity environment, mentioned in literature as microgravity environment, is a dominant prospective and utilization challenge of space flight missions. Future space laboratory modules for example the Columbus Attached Laboratory, Europe's contribution to the International Space Station Freedom, and space platforms as Eureca, the European carrier for microgravity payloads, provide new opportunities for the performance of fluid physics, material science, life and biological science experiments in space which cannot otherwise be performed on Earth because of the constraining effects of the Earth's gravitational field. However, the environment associated with Earth orbiting vehicles or scientific spacecraft is not quiescent but rather is a dynamic environment which results from many sources. Attitude control actuation, on-board

machinery, payload operation, re-configurations, servicing activities, docking/berthing and other impacts will introduce perturbation forces and torques which generate accelerated motions of the spacecraft and its payload. The on-board disturbances span from a broad range of frequencies, well beyond the AOCS control bandwidth, up to frequencies as high as 1000 Hz. It has been recognized that microvibrations affect microgravity experiments in space as well as the line-of-sight stability (jitter) of scientific instruments. Such effects need to be taken into account during the satellite development, mission planning and operation, and postflight analysis of space flight experiments. An overview is presented on Agency microgravity and microdynamics activities with respect to the nature and magnitude of disturbances, and the effect of such disturbances on scientific payloads.

In order to maintain a controlled low disturbance environment, it is necessary to implement low disturbance concepts in the program organization. Such concepts are presented that are related to the technology activities which support the microgravity environment control, and are briefly reviewed for various flight opportunities.

The technology activities include:

- the development of prediction and verification analysis tools,
- the development of on-ground verification test methods,
- the development of high sensitive acceleration sensors and on-orbit acceleration measurement systems,
- the development of compatible hardware and isolation technology,
- the performance of in-orbit experiment, their comparison with on-ground reference measurements and prediction analysis,
- the development of payload and experiment isolation technology.

I. MICROGRAVITY AND MICRODYNAMICS SENSITIVITIES

A. Microgravity Payload Sensitivities

It was the aim of different studies and workshops performed on behalf of ESA and NASA to develop a microgravity payload acceleration threshold level criterion and to derive from that an allowable acceleration spectrum for the spacecraft design [1-5]. The acceleration threshold of individual processes was investigated with regard to the sensitivity of steady state accelerations and the variation of these sensitivities for sinusoidal disturbances, and step function excitations, as well as the variation of this sensitivity with size of crystal and container, etc.

The basic physical mechanisms affected by micro-accelerations are found to be similar in the three major areas of microgravity research, namely fluid sciences, material sciences, and life sciences:

- effects of convection,

- effects of particle accelerations, including buoyancy and sedimentation,
- effects of pressure.

An overview on the performed ESA activities on the determination of allowable g-levels for microgravity payloads are given in Table 2-1.

Various analyses of the effects of micro-accelerations on fluid systems have been published which concentrate on:

- temperature and concentration gradients [1],
- particle movements [6].

According to the study on "Allowable G-levels for Microgravity Payloads" [1] performed by Battelle and Techno System in 1983-84, it is not the displacement of the liquid but the resulting change of temperature or concentration which critically affects many micro-acceleration experiments depending on fluid processes. In addition, an important limit on allowable residual accelerations is given by the accuracy or values of other experiment parameters. In general, it must be ensured that competing effects caused by residual accelerations are small compared to the effects aimed at the particular experiment. Microgravity payload sensitivity analyses were related to quasi-static low level accelerations and to the effect of monochromatic (discrete frequency) excitations. They did not account for example for multiple frequency excitation. Sensitivity studies are still continued and need to be updated by experiences in orbit. Scientists recommended to perform micro-g payload threshold stimuli experiments on orbit during future missions to gain the necessary experience. Individual physical processes which couple low level acceleration into materials processing systems have been investigated theoretically. Most of these investigations have considered only static accelerations, although some have treated monochromatic, time- varying accelerations. Theoretical investigations of coupled effects were not found, such as simultaneous surface tension and buoyancy-driven convection.

A summary of the effects of single-frequency g-jitter on several materials processes may be seen by Fig. 1, which is taken from [5]. The tolerance curves are calculated on the basis of single-frequency disturbances, which were directed in a particular direction. The results on directional solidification for an idealized Bridgman crystal growth indicate that there is some cause of concern, even at steady background levels of residual acceleration; especially in the light of the extreme sensitivity of melt growth processes to very slight misalignments of the body-force vector.

At present, a simple acceleration versus frequency plot, as shown in Fig. 2, can certainly not provide more than qualitative guidelines for the designer. In view of the broad uncertainties that still prevail in the question of acceptable levels of residual accelerations, that way of presentation may at present be most helpful, until other arguments gain acceptance.

B. Microdynamics Sensitivities

A brief reminder of term definitions with respect to pointing stability and pointing error sources is given, followed by the presentation of current and future ESA project requirements.

Definition Of Terms: The stability is usually associated to a period of time. Therefore it is defined as long term stability, medium term stability and short term stability. The accurate term definition is project dependent but the concepts can be summarized by the following:

Short term stability defines the allowed error during the exposure time of one frame or during the correlation time of two or several frames (in case of a fine pointing sensor). The period of time is considered in the range of a few seconds to several hours.

Medium term stability defines the accuracy required between two in-flight realignment or calibrations. The order of magnitude of duration of this period is a few months (up to six).

Long term stability is the stability required between the last ground alignment check and the end of life (EOL) of the satellite and is typically of several years.

In reference [7] a standard framework has been established for the analysis of satellite attitude control and attitude determination accuracy. Four time-varying functions are generally applied in specifying and controlling system performance:

- Absolute Pointing Error (APE)
- Relative Pointing Error (RPE)
- Absolute Pointing Drift (APD)
- Absolute Measurement Accuracy (AMA)

The RPE is a measure of the pointing stability of the payload. Its spectral content is determined by the time interval of definition, which often arises naturally from the physical properties of the payload. For instance, for imaging instruments which accumulate photons over discrete integration periods, image quality is dependent on the stability of the payload attitude during the integration periods.

Pointing Error Sources: Pointing error sources can be classified according to their time dependence.

Long Term Effects consist of bias errors and drift errors.

A bias error is a residual fixed offset error which is stable throughout the spacecraft mission. Drift errors are variations due to aging effects which appear slow in time but have no periodic character.

Medium/Long Term Effects result from error sources which are very often of harmonic nature. their period of oscillation is normally of the order of the orbital or half orbital period (period may be also shorter or longer). The error has a mean of zero so that it does not contribute to the bias errors. The amplitude and phase may also vary (drift) with time. Thermoelastic deformations are an example of harmonic errors which are often related to the orbital period (eclipse and hot case).

Short Term Effects are often considered as random errors because they vary in an unpredictable manner, and in short duration as compared to the orbital period. They are assumed to have a Gaussian distribution with standard deviation s_i. Mechanical disturbances may be generated by reaction wheels unbalances or bearing defects, onboard tape recorders, scanning mechanisms, shutters, thermal shocks, thermal loads created by time-lining of units, etc.

Long Term Effects	Error
1g/0g deflection	bias error
thermal difference between thermal prevision and S/C temperature in post	bias error
moisture release	drift error
material aging (dimensional unstability and thermo-optical properties)	drift error
electronic component aging	drift error

Budgeting Of Error Sources

The compilation of errors is done as following:

- bias and drift: $b_t = (\alpha \times \Sigma B_i^2)^{1/2}$
- harmonic errors:

  errors having the same period are summed as following: $hp_j = \Sigma H_i$,

  unless it can be demonstrated that they do not occur in phase: $h_t = (\beta \times \Sigma hp_j^2)^{1/2}$
- random errors: $r_t = (\gamma \times \Sigma \sigma_i^2)^{1/2}$

The overall total error is then $E = (b_t^2 + h_t^2 + r_t^2)^{1/2}$.

When possible, calibration is used to reduce the effect of bias, drift and harmonic errors. The value of the canceled error has then to be replaced by the calibration error and the inter calibration interval residual error which must both be identified with their appropriate error classification.

The pointing error reduction actually achieved depends on the calibration strategy. If calibration is not performed frequently enough and with sufficiently accurate references, aliasing (errors which are introduced when harmonic errors at the time of calibration cannot be differentiated from the bias and drift errors) and calibration errors will adversely affect the overall pointing. Therefore, a good assessment of the medium term/long term stability problems is necessary to be able to set up an appropriate calibration strategy utilizing finite element methods for the analysis. The main concern for the pointing stability is the short term pointing accuracy which employs an adequate understanding of the medium to high frequency

content of the structural behavior and its interaction with the scientific instrument and/or spacecraft control.

The problems to be addressed by the system engineer, particularly in relation with microdynamics requirement, are:

- to allocate margins for microvibration errors in a manner which (in statistical terms) ensures compliance with payload requirements without forcing over-design,
- to predict the level of microvibrations at subsystem and system level based on detailed knowledge of microvibration sources, analysis and test results.

In practice it is likely that each of these above steps will be iterated several times, accounting for changes in payload or non-compliance in certain areas of the design.

The establishment and implementation of meaningful pointing stability requirements necessitates the identification of experiment requirements combined with a common understanding by structural and attitude/dynamic control engineers. In general it is considered that sophisticated evaluation capabilities are available. However, difficulties arise in quantifying accurately low disturbances that cannot be measured easily on-ground e.g. structural/mechanical thermal shocks.

C. Project Pointing Stability Requirements

Hubble Space Telescope (HST)

The pointing stability requirement for the Hubble Space Telescope while in fine locking is 0.007 arc-sec (rms) over 24 hours.

Solar And Heliospheric Observatory (SOHO)

The pointing stability requirements for SOHO are summarized in the table below. The short term stability requirement for the experiments is given with respect to the experiment aiming axis.

SOHO Pointing Stability	Requirement
short term stability - period duration 1 mn to 2 hours	1" to 3" 30" to 90" (roll)
medium term stability - period duration 6 months	10" to 30" 3 to 5 (roll)
long term stability	3' 60'(roll)

Furthermore, a list of SOHO experiments and corresponding pointing stability requirements is given in Table 2.

X-Ray Multi Mirror (XMM) Mission And INTEGRAL

The requirements for both missions are defined in terms of

- Absolute Measurement Accuracy (AMA)
- Absolute Pointing Drift (APD) - 1 hour
- Relative Pointing Error (RPE) - over 2 mn
- Relative Pointing Error (RPE) - over 10 sec

The following tables summarize the XMM requirements which are much more stringent than the INTEGRAL requirements.

Absolute Measurement Accuracy	
Systematic Pointing Error	
• non calibrated biases	
- STR* random bias	
- random bias (θ_X = 40")	3.3"
• commissioning calibration error	1.3"
- FSS**/STR random bias (θ_X = 30")	
• very long term drift	1.3"
- FSS aging (θ_X = 45")	
- FSS/STR structure aging (θ_X = 45")	1.5"
Medium Term Pointing Drift	1.5"
• structure FSS/STR thermo-elastic (θ_X = 45")	0.75"
Specification = 5.0"	Allocation = 5.0"

* STR = Star Tracker

**FSS = Fine Sun Sensor

Absolute Pointing Drift (1 hour)	
• structure FSS/STR thermo-elastic	0.75"
• FSS internal thermoelastic (θ_X < 1")	neglig.
Specification = 5.0"	Allocation = 0.75"

Relative Pointing Error (2 mn)	
• measurement errors	4.0"
• actuation errors	2.5"
• high frequency jitter	1.0"
Specification = 5.0"	Allocation = 4.8""

Relative Pointing Stability (10 sec)	
• measurement errors }	
• actuation errors }	0.15"
• high frequency jitter	0.2"
Specification = 0.25"	Allocation = 0.25"

Polar Platform (PPF) - ENVISAT

This Earth Observation Satellite is a multi-instrument polar platform on a sun synchronous orbit. The requirements have therefore to be specified for each instrument depending on their calibration strategy and on their specific needs. The following figures were derived for the POEM project and are subject to change with the ENVISAT redirection of the project.

Pointing Accuracy	
• bias	0.07 deg
• harmonics	0.04 deg
• random	0.001 deg

Pointing Stability		
Instrument	**Time Interval**	**Stability**
SCIAMACHY I/F	1.6 sec	0.002 deg
MIPAS I/F	4.0 sec	0.005 deg
MIPAS I/F	75.0 sec	0.015 deg
GOMOS I/F	0.05 sec	0.008 deg

The pointing rate error is

- less than 0.004 deg/s for each axis for all instruments except MIPAS,

- less than 0.002 deg/s for each axis for MIPAS in the frequency range [0,∞].

The pointing errors over the frequency without bias errors can be enveloped by the curves given in Fig. 3. Linear disturbances without biases at instrument interface can be assessed by multiplying the values given by the curve by the lever arm between instrument interface and satellite center of gravity.

D. The Disturbance Sources

In Table 3 a brief summary is provided for microdynamics disturbance sources which stems from onboard subsystems and equipment, payloads, automation and robotics and others.
Their characteristics over a broad frequency bandwidth are shown in Fig. 4 to Fig. 6.

II. PROGRAMMATIC APPROACH

Different approaches can be followed to achieve the scientific objectives for a low disturbed environment onboard a spacecraft:

- development of low disturbance techniques and technology,
- implementation of isolation techniques (isolation of disturbance or receiver),
- optimization of transmission paths (i.e. active damping components, damping layers),
- operations optimization - time and frequency multiplexing.

In all fields ESA has initiated R&D activities to provide the scientific projects and programs with adequate solutions as presented in the subsequent chapters.

The methodology discussed in the following section has emerged from work carried out under various projects and programs such as Spacelab D-1 and D-2, the design and development of the European Retrievable Carrier (EURECA), and the design and planned utilization of the future Space Station and Columbus elements [8].

A. System Specification Implementation

As an example, the Microgravity environment control strategy is outlined which is implemented in the Columbus program. Microgravity environment control starts with the definition of a spacecraft system level design requirement, which is developed from the microgravity payload sensitivities as described in section 2. As a reference, the specifications for the Columbus Attached Pressurized Module (APM), also known as Columbus Attached Laboratory (CAL), as part of the Space Station Freedom (SSF) is given in the following.

Columbus Attached Laboratory (CAL): The CAL microgravity environment requirements are specified in Columbus System Requirement Document (SRD), Doc. No. COL-RQ-ESA-000 (Issue 1). These requirements apply only to the structure interface between the CAL and payload racks. They are

not applicable to the microgravity environment at payload to rack interfaces, payload to floor interfaces or payload interfaces on the external viewing platform.

The induced perturbations of the microgravity environment as caused by all sources of the CAL systems and subsystems shall not exceed:

- time domain acceleration limits of 10^{-4} m/s^2,
- frequency domain acceleration limits (Fig. 7).

The time domain acceleration limit is defined by the composite acceleration amplitude with frequencies up to 0.1 Hz. The frequency domain limit is defined as a 1/3-octave band rms-acceleration level spectrum between 0.1 Hz and 1000 Hz.

The requirements apply only to the design of the CAL and do not take into account microgravity disturbances caused by the Space Station, the crew, the payload and the Lab Support Equipment such as robotics, central process visualization system, freezer/coolers, general purpose workbench. These requirements apply during "quiescent" conditions, i.e. during nominal system and payload operation periods when no maintenance or servicing of the APM is performed.

B. Microgravity Environment Control Concept

Background Information: For a controlled microgravity environment onboard a spacecraft, the spacecraft system has to be designed according to a spacecraft system level requirement. The spacecraft has to be controlled, optimized where necessary, and finally verified, such that the desired goal is met at all stages of the spacecraft design processes, from the equipment, via subsystems to the integrated system qualification and in-orbit measurement (Fig. 8).

As a reference document and sole source, a Microgravity Environment Control Plan is to be issued which contain as a summary all microgravity environment requirements, subrequirements, verification requirements, test requirements, analysis and simulation requirements.

Microgravity Environment Control Plan: As a reference, the Columbus APM Microgravity Environment Control Plan PL 121 3800 005 is described in the following. The plan organizes all activities, from system level down to equipment level, to ensure that the system level microgravity environment is achieved. It provides guidelines for the implementation and verification of the microgravity environment requirements as derived from the Columbus System Requirement Document (CSRD). Furthermore, the plan defines the design and verification tasks, subrequirements and responsibilities at flight configuration level, subsystem level and equipment level.

The corresponding microgravity control approach is such that the system flight configuration level microgravity requirements are broken down into subsystem and equipment requirements. These

lower level requirements are based on budget allocations resulting from analyses which identify the disturbance sources.

The requirements are defined so as to allow design optimization and verification at various level such as equipment level, subsystem level and flight configuration. The verification approach is based on review of design, similarity, analysis and test.

Microgravity Environment Analysis Approach and Concept: For the microgravity analysis and reliable microgravity quality assessment of orbital systems, a global, comprehensive mathematical microgravity model is under development which yields as output the microgravity acceleration levels and field values, including the detailed spatial, temporal and spectral distributions, and which is capable of dealing with both quasi-stationary and time-variable sources and disturbances (Fig. 9).

A unified mathematical model extending over the entire frequency range of interest for the users cannot be formulated for the acceleration field and, therefore, systematic representations of the various microgravity constituents are used over suitably chosen frequency subranges. Representative model elements are defined and formulated and their superposition will provide a characterization and realistic representation of the overall effect [8,9].

As shown in Fig. 9, the overall global micro-gravity model is constituted of model elements such as the

- mission model of the orbital system,
- gravity gradient model,
- atmospheric drag model,
- attitude dynamics and control model (controlled S/C dynamics simulation model),
- low frequency structural dynamics model (Finite Element Model),
- high frequency structural dynamics model (mathematical equivalent of empirical model).

Detailed information and discussion of the mathematical contents of the above-mentioned model elements are given in [8,9].

With respect to the microgravity environment control, the microgravity dynamic disturbances of subsystems and equipment need to be controlled in the frequency domain over a frequency range of 0.1 Hz to 1000 Hz. This is done on basis of input-to-output transfer functions, as shown in Fig. 10, covering both the structural borne and the airborne transmission path. This transfer function approach allows subsystem and equipment supplier to verify their budget level requirements in terms of maximum allowable subsystem/equipment interface force or allowable resulting response which are specified at the receiver locations (= payload interface). The transfer function application by subsystem and equipment supplier avoids the need for distribution and handling complex simulation programs or finite element structural dynamics models for the satellite system. The determination of the forcing functions of the

disturbance sources form a vital part of the microgravity environment control approach at equipment and subsystem level. These are determined by analysis and/or test.

III. TECHNIQUES AND TECHNOLOGIES

A. General

The preferred approach in the overall microgravity and microdynamics environment control is the incorporation of vibration reduction principles into the basic design. If the design optimization of subsystem equipment is not adequate, secondary methods need to be implemented. These secondary methods essentially involve the attenuation, isolation and damping of induced vibrations in three areas:

- at the vibration source,
- on the vibration transmission path,
- at the sensitive receiver (= the payload).

Technology tasks supporting the microgravity and microdynamics environment control for various flight opportunities are briefly reviewed.

The technology support will be presented in the following areas:

- evaluation and prediction tools to characterize and predict microgravity and microdynamics disturbances, and to facilitate ground verification tests, in-flight experiment execution, evaluation of test data;
- on-orbit acceleration measurement systems;
- active control of microgravity vibrations, e.g. microgravity isolation mount (MGIM) facility, application of piezo-actuators, vibration suppression by active shape control of flexible appendages;
- microgravity compatible technologies e.g. technology development of low noise actuators and microgravity compatible driver for robot drives and joints;
- in-orbit microgravity and microdynamics experiment measurements in preparation for COLUMBUS and scientific spacecraft (Eureca, Spacelab, Olympus, Sounding rockets experiments).

B. Modeling and Prediction Analysis

AMEDA (Algorithm of Microgravity Environment Dynamic Analysis): The microgravity environment dynamic disturbances computational model is used for the prediction of broad band vibration response spectra at sensitive microgravity payload locations in the frequency range 0.1 Hz to 1000 Hz. It will form the second part of the overall microgravity environment prediction model, which is structured in Fig. 9, covering the requirement verification in the frequency domain. The acceleration responses in this frequency range are governed by the dynamics of the flexible spacecraft structure and

the dynamics of the disturbance source forcing functions. Microgravity dynamic disturbances in this frequency range shall be analyzed by three submodel elements:

1. controlled flexible spacecraft dynamics with feedback responses from multi-body simulations between 0.1 Hz and about 10 Hz by utilization of the ESA/MIDAS software;

2. low frequency structural dynamics using finite element models with responses between 0.1 Hz and about 100 Hz, by utilization of the MSC/NASTRAN software;

3. high frequency structural dynamics with responses between 3 Hz and 1000 Hz on the basis of test data, by utilization of Digital Signal Analyzer GENRAD 2517 with SDRC IDEAS-TDAS/RTA software.

AMEDA has been developed in the frame of the TRP study "Microgravity Dynamics Disturbances" [9]. It is intended to further extend the capabilities of the program to be able to predict the influences of acoustic disturbance sources.

Fluid Representation In Microgravity Spacecraft Models: Models and software modules have been developed to present and analyze the behavior of fluids in tanks under microgravity in non-spinning conditions. These models are used in connection with structural spacecraft models to predict the overall dynamic behavior of the spacecraft including effects related to small motion of the fluid considering surface tension and an arbitrary microgravity field.

In this frame the identification and modeling of free surface of the fluids in tanks when subjected to the above conditions has been developed and completed.

A further development is the representation of arbitrary shaped membrane tanks. The membranes control the fluid position in tanks in flight and under microgravity conditions.

GENSTEP: In regions of high modal density, vibration is often modeled statistically using a method known as statistical energy analysis (SEA). Work has been carried out for a number of years using an in-house code called GENSTEP, developed by British Aerospace and the Institute of Sound and Vibration Research (ISVR) at Southampton University.

The latest application of the program is the modeling of the vibration environment on ARTEMIS in a contract for Alenia. The study is aimed principally at quantifying the SILEX interface environment and is a follow-on to the recently completed study on vibration transmission through the Olympus bus. The models built by ISVR and tested using in-orbit data are capable of being used to predict the effect of equipment on highly sensitive payloads. In particular, work has been done to show the effect on the vibration environment of equipment location on a panel. A contract is being placed with ISVR for the continued development of the GENSTEP program and for a revision of the ESA Structural Acoustics Design Manual. These include improvements in dealing with concentrated (as opposed to distributed)

dynamic loading and the production of a PC version of the program. The ability to link SEA with other prediction methods is also being investigated.

C. On-orbit Acceleration Measurement Systems

The thorough measurement of the actual microgravity environment at the sites of sensitive microgravity payloads is of utmost interest for the microgravity payload specialists and experimenters. The most current European in-orbit measurement system is the Microgravity Measurement Assembly (MMA), which has been developed for ESA [10]. It is designed to monitor on-ground and in-orbit disturbance accelerations aboard Spacelab. The MMA is a central measurement facility for continuous and time correlated monitoring of broadband acceleration responses in the Spacelab module. It is designed to monitor the microgravity environment close to microgravity sensitive experiments through their processing period and to present residual acceleration time histories and frequency spectra to demonstrate the quality of the microgravity environment at any time for payload investigators. The MMA is using a new generation of micro-mechanical acceleration detectors which can be installed very close to scientific experiments due to their small dimensions and mass. The key element of the accelerometer sensor is a miniature and highly sensitive capacitive accelerometer based on silicon micromachining technology [11].

The extension of the MMA with the provision of additional DC-sensors is currently under study. The DC sensors shall monitor and cover the quasi-static accelerations which are experienced by an Earth orbiting microgravity spacecraft. During the Spacelab D2 mission the MMA was operational for over 200 hours and run without any technical or operational problems. The additional request by experimenters to utilize the MMA during this mission, and the results gained during the mission fully justified the necessity of a centralized microgravity measurement system combined with real-time data transmission and real-time data processing for on-line support to microgravity experimenters.

D. Microgravity And Microdynamics Compatible Hardware Technology

Identification And Characterization Of Disturbances Sources: As part of the Very High Pointing Accuracy AOCS TRP study, microvibration tests were carried out on ball and magnetic bearing wheels from European manufacturers (Aerospatiale, BAe and Teldix) to provide data for space missions with stringent pointing stability requirements, and to predict the microvibrations induced into the platform by these type of attitude control actuators (Table 2).

A new activity being submitted is aimed at developing standard test methods for equipment so that characterization of sources can be better defined. The work is aimed at providing vibration data in a standard form about sources at assembly level. The structural interaction of the source and typical

spacecraft panels will be investigated so that improved understanding of the mounting-point impedance of the device can be obtained. This is necessary if the coupling of the source vibration into the structure is to be modeled adequately. Free-free and seismic mountings will be designed and recommendations will be made to ensure that equipment is mounted to minimize the effects of on-ground testing.

Microgravity Compatible Drive: The need of automation and robotics is expected to grow substantially in on-going and future space programs where laboratory internal operations and servicing are involved. This especially concerns microgravity experiments and possibly space production in the future.

The microgravity requirements for the new generation of experiments to be flown on COLUMBUS are very severe and conventional mechanical components such as drive motors and gear systems as would be found for example in manipulator joints are incompatible with these requirements. Studies are initiated and on-going to build up the technology enabling drive/traction system for automation and robotics which are compatible with the extremely low vibration levels. Under ESA's Technical Research Program, a study has been initiated to obtain insight of the possibilities and limitations offered by tension terrestrial drive technologies.

The study objectives are the development, manufacturing and subsequent verification and validation by test of a breadboard of a microgravity compatible drive.

Development Of A Magnetic Gearbox: Major attention is being spent on robot linear and rotary joints, to limit backlash, motion irregularities etc. An innovative development is ongoing to develop a magnetic gearbox with integrated drive motor to provide high quality and very high torque density robot joints (20 Nm/kg compared to 2 Nm/kg conventionally).

Development Of Active Damping Components: Future space missions will employ large and flexible lightweight structures with high performance requirements such as high pointing accuracy and stability and high shape precision. These requirements demand new technologies to attenuate efficiently in-orbit dynamic disturbances induced to the flexible structure by e.g. the spacecraft attitude maneuvers. As a result the concept of actively controlled or adaptive structures becomes increasingly important for these missions. New materials where active components are fully integrated into the structure form a significant part of the active damping concepts.

A study activity has been initiated as part of ESA's Technical Research Program to develop active damping components that are usable as standard devices, and leads to the direction of developing active space structures. In the first instance the definition and the design of active damping components is the main objective of this study. The complexity of active damping design is mainly due to the fact that the active components in such structures in general perform a dual function as:

- passive structural elements, i.e. as load carrying members,

- active elements, i.e. as sensors or actuators.

Microgravity Payloads Disturbances: The general objective of this TRP activity is to support the community of microgravity payload developers in planning, design, development, operation and verification of microgravity aspects of their hardware. For the accomplishment of the objectives the following activities are planned:

- characterization of microgravity payload disturbance sources and recommendation of disturbance reduction methods with the aim to establish a comprehensive microgravity payload design compliant with the stringent microgravity requirements;
- evaluation and definition of an on-ground microgravity disturbance source test facility to provide the payload developer with a tool to verify the compliance of the design with the requirements on component and instrument level;
- establishment of computational payload models;
- definition of post-hoc countermeasures for disturbances, the most relevant and promising of which are to be defined and to be tested at laboratory level.

E. Isolation Technology

A survey of potential microgravity payloads revealed that some payloads, such as crystal growth and fluid physics experiments, are particularly demanding in their requirement for an ultra-low gravity environment. To cope with these stringent microgravity requirements, a Microgravity Isolation Mount (MGIM) is being developed as a facility which will be accommodated within the standard rack system of the COLUMBUS laboratories. It will serve to isolate sensitive experimental payloads from the vibrations ambient on the spacecraft structure.

The MGIM is an active suspension system where the experimental payloads are mounted on a central platform. Around the platform small modules are located containing actuators and sensors to control the platform's motion in all six degrees of freedom. Long-term the control system ensures that the platform and payload remain central within its enclosure but are also isolated from short-term disturbances of the spacecraft structure [12].

F. In-orbit Experiments

Slosh Test Orbital Facility (STOF) program: The Slosh Test Orbital Facility (STOF) program has the main objective to perform in-orbit experimental verification of predicted motions of a spacecraft with partially filled liquid tank in response to a sequence of commanded torques or forces. Originator is the National Aerospace Laboratory NLR in Amsterdam. The STOF program consists in the development of several small spacecraft, denoted Sloshsat, carrying the experiment and the related instrumentation.

In the frame of the Technology Demonstration Program Phase 2, the Agency intends to perform the first development and flight of Sloshsat in cooperation with NASA Lewis Research Center. Sloshsat will be ejected from a Hitchhiker cross bay structure in early 1996, and the investigations will mainly concern sloshing (small and large amplitude) in a non-spinning configuration and liquid motions in a spinning configuration. The flight data will support the development of mathematical models for spacecraft/liquid dynamics and the design of liquid management techniques in microgravity. In particular, prediction of in-flight responses by the software developed under 4.2.2 is foreseen as well as test analysis correlation.

On-Orbit Structural Dynamics Transfer Function Experiment: In the frame of the Spacelab D2 mission, the Transfer Function Experiment, called the "Hammer Experiment", has been performed to investigate the transmissibility characteristics inside the Spacelab module under near weightlessness.

Hereby, the Microgravity Measurement Assembly (MMA) has been extended by a calibrated impulse hammer that enables the measurement of structural dynamics transfer function on-ground and in-orbit. The experiment objectives and fundamental subjects which will be addressed during subsequent evaluation are:

- the comparison of the transfer function characteristics measured on-ground and in-orbit,
- the update and adaptation of mathematical models and methods,
- the determination and validation of the universal linear transfer function as defined for Spacelab, and
- the derivation and establishment of local transfer functions for categories and groups of disturbance sources and receivers.

This activity has been initiated by the Agency and is performed in close cooperation with the Institute for Space Simulation at DLR, Cologne, Germany.

PAX Experiment On Olympus: Olympus is carrying the first continuous transmission vibration monitor and extensive studies have been made on the various applications for the data relayed to ground [13]. It has been possible to isolate many different noise sources on Olympus, even though only one measurement location is available. In addition, long-term monitoring of these signals has been used to confirm correct functioning of on-board systems and to improve spacecraft operation. To do this effectively requires automatic analysis of the data stream, owing to the high data rate of transmission. A successful event recognition system has been constructed and numerous other detection techniques have been investigated [14]. Work will commence shortly on developing a general purpose monitoring system based on the methods developed for analyzing the vibration data.

CONCLUDING REMARKS

Microgravity payload and microdynamics activities have been presented as they are encountered in the development and operation of payloads with low disturbance and high pointing requirements. The system approach covers science requirements, payload and equipment state-of-the-art developments, and satellite configuration and operation constraints. Meaningful advancement in this area can only be achieved by adequate participation and interdisciplinary interaction of all parties.

ACKNOWLEDGMENT

This paper was established, to a significant extent, as a result of internal ESA/ESTEC workshops on "Microgravity and Microdynamics" and technical meetings with the project and program teams concerned. Particular thanks are due to E. Slachmuylders, for the initiation of the internal workshops, fruitful discussions and contribution. The authors wish to acknowledge following colleagues for their contributions towards the establishment of the paper: P. G. Buchwald, P. Clancy, P. Collins, A. McGrath, M. Nati, W. De Peuter, J. L. Parquet, C. Philippe, A. Robinson, R. Roumeas.

REFERENCES

1. *C. Tiby, D. Langbein,* "Allowable G-Levels for Microgravity Payloads", ESA Contract No. 5504/83/F/FS(SC), Final Report, September 1984

2. *Teledyne Brown Engineering, Advanced Programs Department,* "Low Acceleration Characterization of Space Station Environment", SP 85-MSFC-2928, Final Report, Rev. B, October 1985

3. *R.J. Naumann,* "Gravity Level Estimates and Effects", NASA Marshall Space Flight Center, August 1985

4. *J.I.D. Alexander,* "Low Gravity Experiment Sensitivity to Residual Acceleration: A Review", Microgravity Sci. Technol. III (1990) 2, pp. 52-68

5. *E.S. Nelson,* "An Examination of Anticipated g-Jitter on Space Station and its Effects on Materials Processes", NASA Tech. Memo. 103775, April 1991

6. *E.G. Lierke,* "Tolerable G-Level for Spherical Samples in a Fluid Matrix", In BDPU Phase B Final Report, ESA Contract 6590/86/NL/JS, November 1986

7. Handbook of Satellite Pointing Errors and their Statistical Treatment, ESA-CR(P) 1364

8. *W.E. Knabe*, "Methodology for Microgravity Quality Assessment, Implementation and Verification of Orbital Systems: A Challenge for Microgravity Engineering Science", IAF-89-451, Malaga, Spain, October 1989

9. *D. Eilers, B. Kotzias, S. Portigliotti, H. Stark,* "Microgravity Environment Dynamic Disturbances", IAF-90-345, October 1990

10. *D. Eilers, I. Gerhard, B. Hofer, F. Rudolf, W. Brungs*, "Microgravity Measurement Assembly (MMA) for Spacelab Module Missions", IAF-88, October 1988

11. "Solid State Accelerometer Development", Final Presentation, ESTEC, June 14, 1989

12. *R.G. Owens, D.I. Jones, A.R. Iwens*, "Integration of a Microgravity Isolation Mount (MGIM) within a COLUMBUS single rack", Acta Astronautica, 22, 1990, 119-128

13. *D. Tunbridge*, "The 'PAX' Experiment on Olympus", ESA Bulletin number 64

14. *S. Dyne, P. Collins, D. Tunbridge*, "Satellite Mechanical Health Monitoring", IEE Colloquium "Advanced Vibration Measurement Techniques and Instrumentation for the Early Prediction of Failure", Final Report

Table 1 ESA G-Level Study Activities

Year	Title and Contractor	Areas Covered	Results
1982-84	Microgravity Level required by the Payload during the operational phase of EURECA (Battelle)	Crystal Growth modeled (Navier Stokes) in a spherical Cavity (Oscillatory Convection)	EURECA Specification
1983-84	Allowable G-Levels for Microgravity Payloads (Battelle and Techno System)	Fluid and Material Experiments by Modeling (Navier Stokes Equation)	Tolerability for a) FS Expt. with temp. gradient b) Crystal Growth by THM c) Soret effect Constancy at Low Frequency, dependence at high frequency
1986-87	Study on Allowable G Levels for Spacelab, Columbus and Eureca (Techno-System, Battelle, CENG)	Liquid columns, particle in spherical container, Marangoni Flows, Critical Point, Crystal Growth, Metallurgy	General conclusions of earlier studies confirmed, effects of pulses examined.
1988-89	Study of allowable G-Levels for Spacelab, Columbus and Eureca (Techno-System, Battelle, CENG, University of Trondheim)	Included life sciences, but chiefly concentrated on diffusion, solid particles in liquid, solidification in dilute alloys	10^{-3} g for life sciences, concept of dose = acceleration x time emphasized

Table 2 SOHO Experiments Pointing Stability Requirements

SOHO experiment	Short-term Pointing Stability Requirement	Mid-term Pointing Stability Requirement	Long-term Pointing Stability Requirement	Flight Corrective System for Pointing
CDS	0.45"	23.3"	3'	Yes
EIT	0.45"	13.8"	2.1'	No
GOLF	0.45"	51.8"	3'	No
MDI	2.67"	4.32"	3'	Yes
SUMER	0.45"	23.3"	3' (per axis)	Yes
UVCS	(0.7")* per axis	(5.57")** per axis	3.43' (per axis)	Yes
LASCO	2.67"	4.32" per month	3'	Yes

* duration 15' expected for UVCS (2 hours)

** duration 16 months for UVCS (2 years)

Table 3 Microdynamics Disturbance Source

Spacecraft/Onboard Disturbances	Caused By
Guidance, Navigation and Control (GNC)	• GNC S/S hardware induced disturbances • control strategy/momentum management induced disturbances
ECLS/TCS	• pulsating flow rate and pressure • turbulence and wake phenomena
Structure and Mechanisms	• stick-slip effect, door closing, latch-up • ORU, rack and drawer exchange • docking/berthing mechanisms
Electrical Power (EPS)	• solar array (thermal deformations) • solar array drive/rotation • mechanical power relays
Data Handling	• HDRR (high data rate recorder) • Antenna Pointing Mechanisms (APM)
Payload and Instruments Complements	• stepper motors, steering mirrors, scanners • active mechanical coolers • filter wheels
Automation and Robotics (A&R)	• mechanical and electrical noise from motors, gears, guidance, digital control etc.
Crew Induced Disturbances	

Table 4 Microvibration Test Results On Ball And Magnetic Bearing Wheels

Project	Measurement	Moment [Nm]	Bearing (Company)
SOHO	45 Nms (3860 rpm)	0.2 Nm	Ball bearing (BAe)
DR-3	3 Nms (3320 rpm)	0.1 Nm	Ball bearing (Teldix)
RSR-14	20 Nms(2720 rpm)	0.2 Nm	Ball bearing (Teldix)
MW-X	60 Nms(6000 rpm)	0.1 Nm	Magnetic bearing (Teldix)
SPOT4	40 Nms(2550 rpm)	0.45 Nm	Magnetic bearing (Aerospatiale)

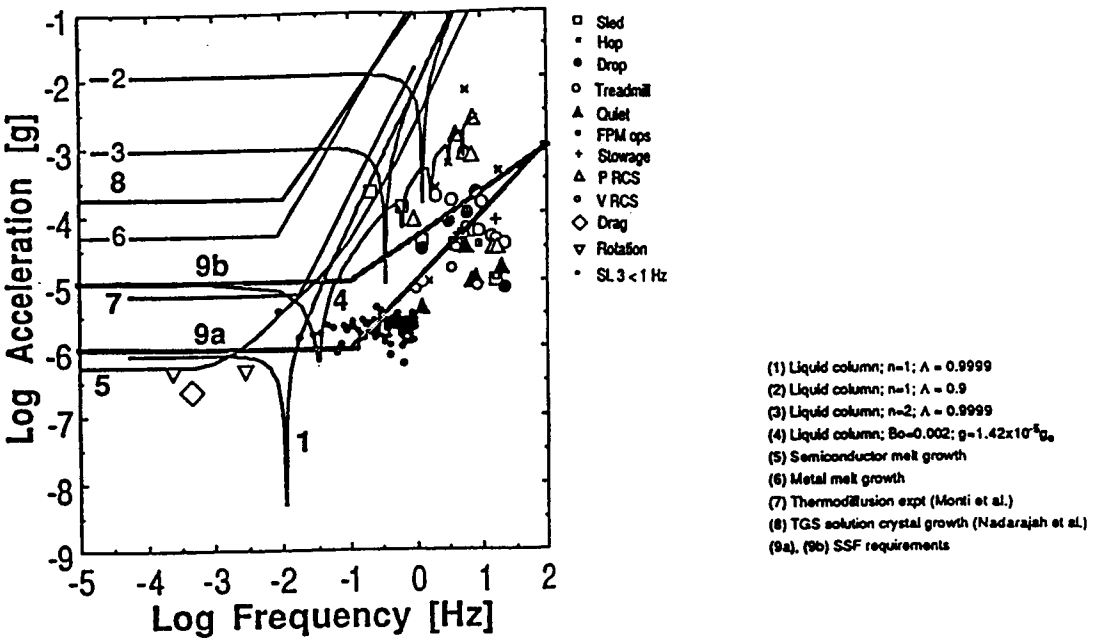

Figure 1 Tolerable G-Levels Calculated For Single-Frequency Harmonic Disturbances And In-Orbit Measured Acceleration Peaks From Shuttle Spacelab Missions

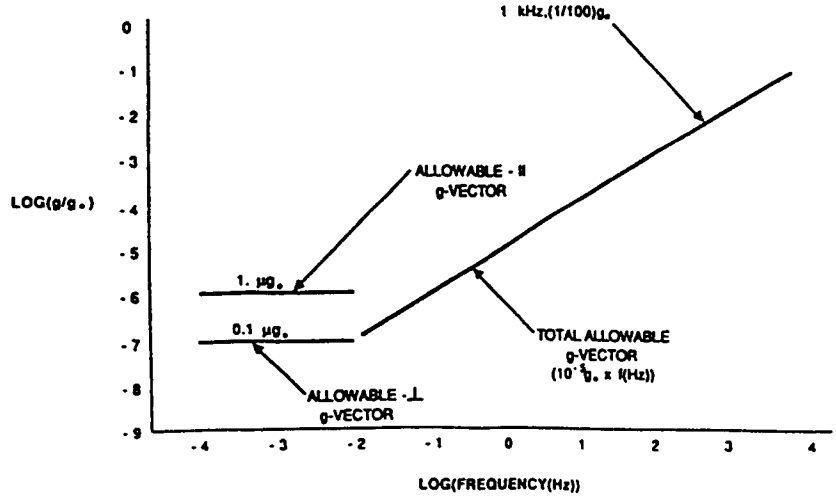

Figure 2 G-Level Tolerance For Monochromatic Oscillating Disturbances

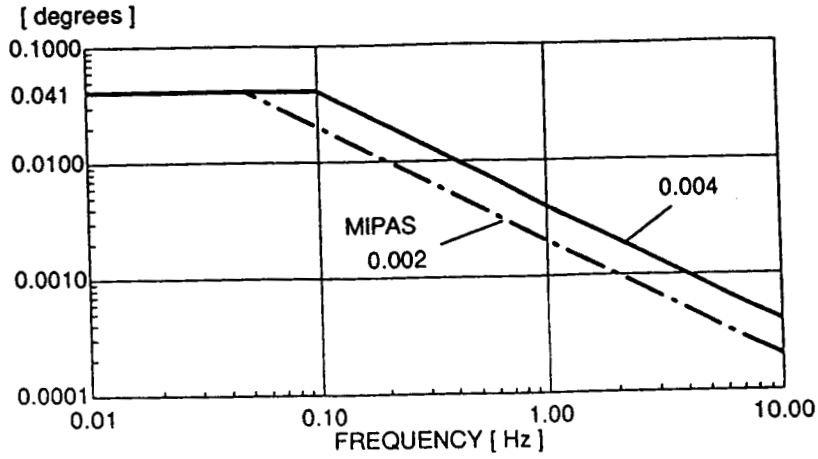

Figure 3 PPF-ENVISAT Pointing Error Specification

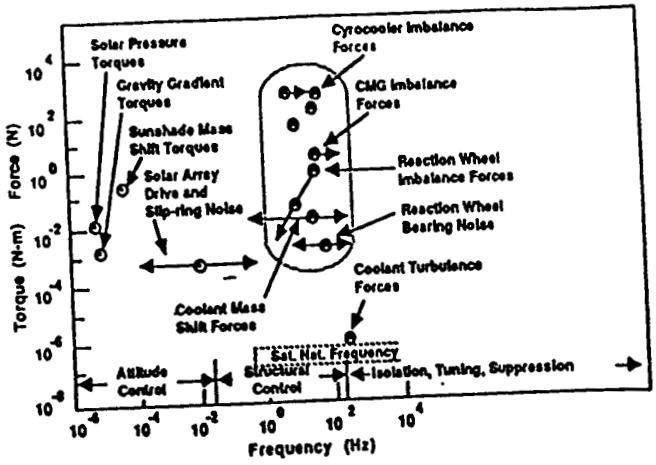

Figure 4 Typical Spacecraft Disturbances

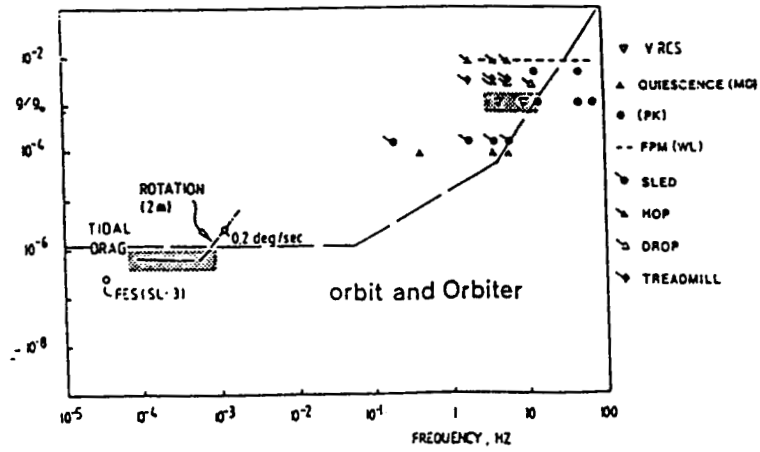

Figure 5 Spacelab D1 On-orbit Acceleration Response Spectrum - Summary

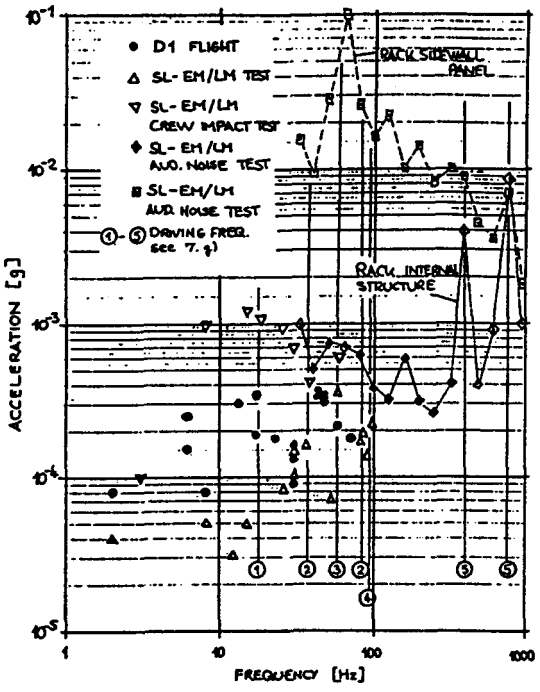

Figure 6 Comparison Of On-Ground And In-Orbit Measured Acceleration Responses (Spacelab)

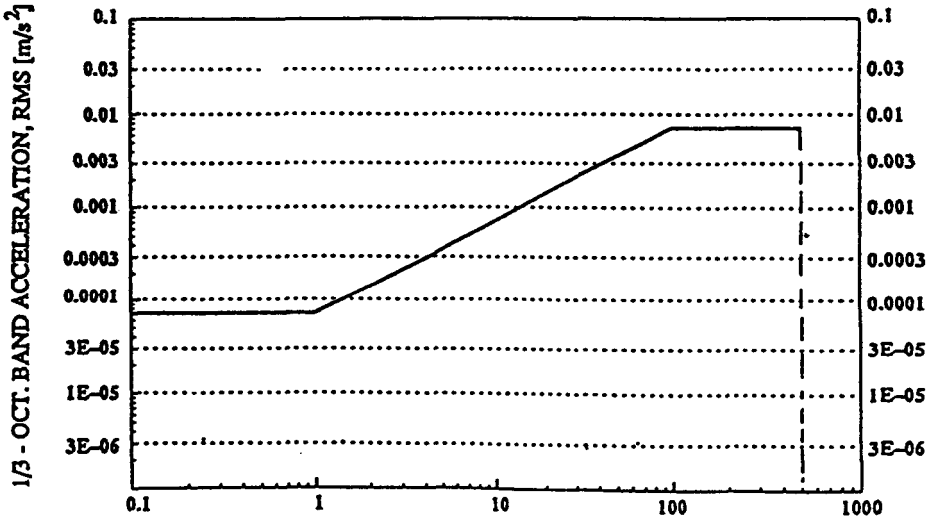

Figure 7 CAL (APM) Microgravity Environment Specification Specified From 0.1 Hz To 500 Hz Acceleration Spectrum At Module-To-Payload Rack Interfaces

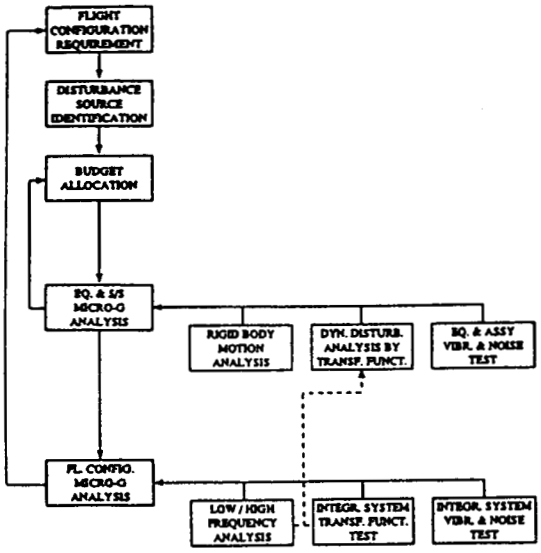

Figure 8 CAL Microgravity Environment Control Concept

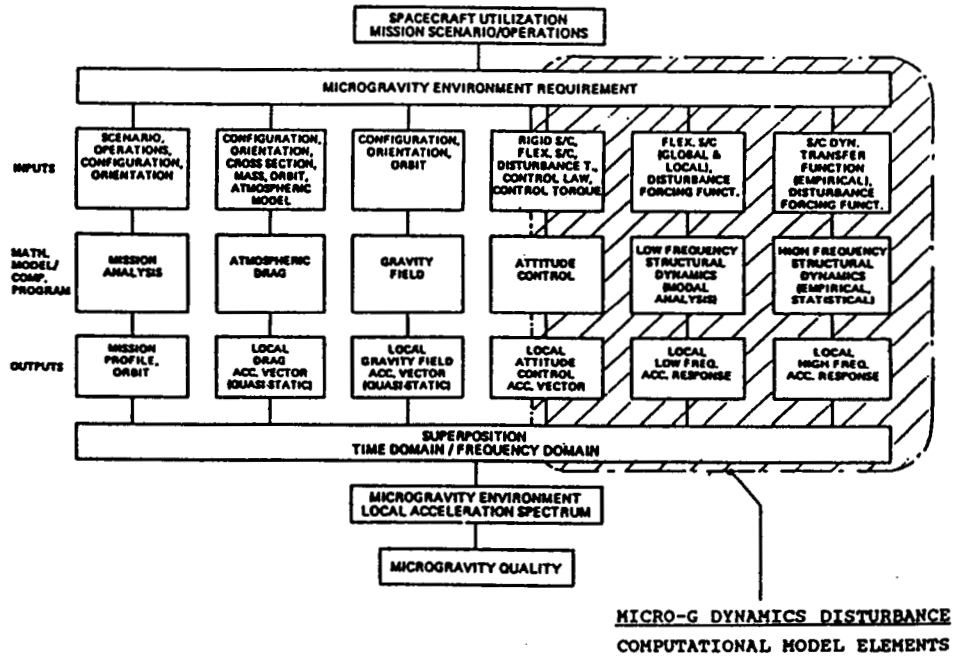

Figure 9 Flight Configuration Microgravity Environment Analysis (Microgravity Computational Model)

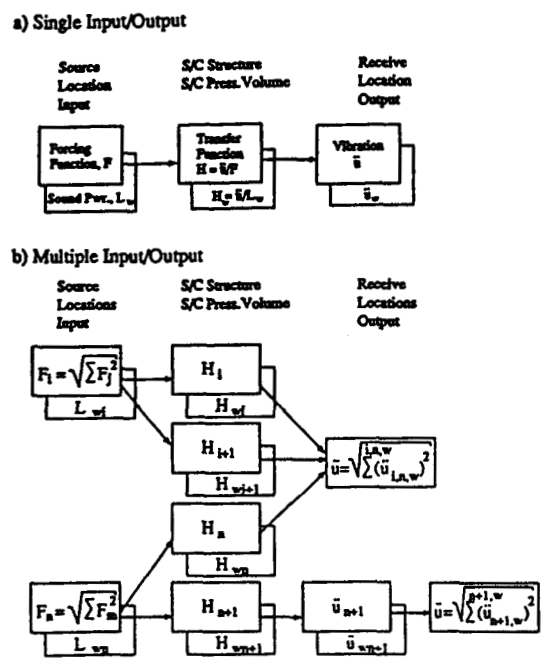

Figure 10 Microgravity Environment Dynamic Disturbance Control (Structure-borne And Airborne Transmission Paths

Discussion

Question: *How do you calibrate the hammer itself ?*

Answer: Now for each hammer you get calibration curves. Each hammer has a serial number and calibration and hence this is known.

Question: *Now, this is on the ground, correct ?*

Answer: Yes, this is done on the ground. We use the same hammer on the orbit, of course, to have the same reference.

Question: *So you do not have anything special for space applications ?*

Answer: No, we don't have to. This should be stable for the life of the hammer.

Question: *About your data, are you recording it or are you pre-windowing it ?*

Answer: The hammer was actually hooked up to the MMA. So it was complimentary to the MMA and by this we got the data also real time to the ground. We used the MMA as such and the hammer was plugged in and so we got the data down to our ground station. We also got real time feedback about impact and gave also indication to the astronaut whether it was right or not, whether he should repeat it or not.

Question: *What was your sampling rate ?*

Answer: We had a sampling rate of 300 samples per second.

Question: *What was the range of force you could exert on the structure ?*

Answer: We limited the force of the hammer to 200 Newton. But the hammer is able to go out to 1250 Newton

Question: *Did you have a range like increments of 10 Newtons or 20 Newtons ?*

Answer: We did a different investigation. Our first loop was to have a constant force and check the repeatability of one location to the other and also see whether this is valid, whether we have really a linear structure behavior or whether we have non-linearity in the structure. During the third cycle we used different levels of force which give us also an indication whether there is linear nature or nonlinear nature in the structure.

Question: *It is surprising how repeatable it is. Once you have done a few and you get this comfort zone you are doing the same thing over and over again. It is amazing. Seems like it is very well controlled ?*
Answer: We were surprised too. It was so stable because the object was to hit one location 5 times after the last with a pause in-between (about 15 seconds).

Comment: Another experiment was to find the difference between the behavior of the structure on ground and in orbit if any. The dynamic behavior and principle does not include any dependence on g but the boundary conditions of the system do. My question is what is the difference and if there is one there is a need for an investigation. That is one point. Stark also did extensive count measurements after the mission sequence tests when Spacelab was fully integrated. The dynamic system was equivalent to that in orbit and he is going to compare that data, the flight data, to the ground data. He will also do lots of modeling to predict the differences if any between ground and orbit.

Question: *Obviously you can't really do a true impulse especially in a situation where you can't really see a certain level of force so you don't dent the spacecraft. One way to verify that you have truly excited the frequencies of interest is to do a sinusoidal disturbance on the ground to compare the results or to put a cushion over the hammer and to give you a signal richer in lower frequency components. Did you look at that part ?*
Answer: Yes, we looked at that in the very beginning when we defined the experiment. There are better ways to do this, but since we had the MMA it was easy for us just to hook it up to a hammer, with all its known limitations. But I think we got a fairly good shape and attenuation of the frequencies with the hammer which we verified.

MICROGRAVITY DATA ANALYSIS AND THE MIR ENVIRONMENT

Jean-Pierre Granier* and **Pascale Faucher+**

*CNES (France)
+Europe Informatique (France)

ABSTRACT

This paper presents a new method to process the Megabytes of micro-acceleration data provided by the microgravity environment measurement. The Europe Informatique Company has developed under a CNES contract an Automatic Post-Processing Tool for the analysis of the MIR micro-acceleration environment data. The measurements have been performed during the ANTARES (August 92) and the Post-ANTARES flight (Autumn 92). The main objective of the microgravity Classification Tool is to provide a help for the analyst engineer. The classification principle is a comparison of the different computed distances between a signal to test and some representative signals contained in a data base. The classification tool selects the nearest class which contains the characteristic parameters of an event and associates this event to the initial signal.

Three data bases are associated with each module of the MIR station, one per axis. Each classification base contains the events organized into classes. A test has been performed on the KVANT 2 classification base. The first analysis has shown excellent classification results with a ratio of good classification between 81 % and 90 % depending of the axis.

INTRODUCTION

One of the most important problems with the micro-acceleration measurement is the post-processing of megabytes of data. A solution may be an Automatic Post-Processing. The CNES has developed a new tool for the post processing of the MIR microacceleration environment data. The Microgravity Environment Classification Tool is designed to detect the different events occurred during the measurement, to recognize these events, to classify them and to provide a report to the analyst engineer. This new tool is interfaced with the signal processing software DYNAWORKS developed by the INTESPACE Company.

I. OBJECTIVES

The objective of the "Microaccéléromètre" experiment is to perform a microvibration analysis of the MIR station. A lot of measurements have been performed in the different modules of the MIR station. This system has been used before the French flight ANTARES, during the flight and after this flight. That represents about 1 Gigabytes of information to process. The data are separated into files ranging from several seconds to several minutes. Each file is analyzed in the time and frequency domains to evaluate the main frequencies and the different levels encountered during the measurements.

Such a work may be realized by the microgravity Classification. The objectives of this software are to organize the environment knowledge into a data base, to use this data base to recognize the signals to evaluate, to classify them in accordance with the identified events and finally to present the results to the engineer in order to have a quick look on the contain of the signal.

The organization in a data base provides a very easy way to complete the knowledge of the environment by adding new events.

II. CLASSIFICATION PRINCIPLE

The classification is a signal analysis tool, using the similarity between data to perform a selection and to recognize unknown signals.

There are two types of classifications :

- The Unsupervised Classification :

It is used to determine the links between the elements of a set. This type of classification has been used to verify the links between the time signals which made up the different classification bases. The signals chosen for building a class have about the same kind of frequency signature. This classification allows to choose the relevant parameters of the model.

- The Supervised Classification :

This Classification is used to determine the class of a new element by comparison of the element characteristic parameters to class characteristic parameters.

There are different steps in the classification process :

- The signal modeling
- The extraction of the characteristic parameters
- The choice of a mathematical distance to compare the elements
- The use of a selection criterion to detect new events

III. SIGNAL MODELING

There are a lot of possibilities for signal representation. We have chosen two complementary methods to represent the signals :

- The Histogram Model
- The Auto Regressive Model

A. Histogram Model

It is a classical representation of the magnitude of a signal. It is useful for a statistic analysis. The interval between the maximum and the minimum reached by the signal is divided into equal intervals. Then we compute the number of sample in each interval. That provides a representation of the signal.

B. Auto Regressive Model

The Auto Regressive representation is often used in the signal processing domain. The signal representation is given by :

$$s_n = -\sum_{k=1}^{p} a_k s_{n-k} + e_n$$

with s_n are the samples

e_n is a white noise

p is the number of samples

and a_k are the model parameters

We have selected the MORF algorithm to compute the model parameters for the excellent results it provides with a few number of samples.

IV. CHARACTERISTIC PARAMETERS CHOICE

The N signals used in a classification base are represented by p parameters that provides a N x p space for a base. We have applied the FISHER criterion to reduce the number of significant parameters by computing the relevance of each parameter. The parameter reduction decreases the memory space used and the calculation time.

The relevance of each parameter takes into account the variations in its class and regard to the other classes. A relevant parameter has a low variance in its class and high variance in the other classes. The relevances are normalized to unity. An example of the representation of the relevance for 13 order model is shown in Fig. 1. In this case, the relevant parameters are : 1, 3, 5 and 8.

V. DISTANCE MEASUREMENT

One objective of the classification is to compare the signal to the different classes. It is equivalent to compare the relevant parameter vector to the vector which represents each class. This vector is defined as the average of the class vectors.

The choice of the mathematical distance is fundamental to obtain good results.

A mathematical distance is given by :

$$d^2(V,V_a) = (V - V_a)^T Q^{-1} (V - V_a)$$

with V is the vector

V_a is the average vector of a class

and Q is a weighting matrix

The Euclidean distance provides the identity weighting matrix. Its disadvantage is that all the parameters have the same weight, besides it doesn't take into account the relative importance of the parameters. We have selected the Mahalanobis distance because it provides a full weighting matrix. This matrix is built with the covariance between the parameters of the different vectors making up a class. This mathematical distance provides excellent results with the microvibration data.

VI. UNSUPERVISED CLASSIFICATION

The aim of the unsupervised classification is to search links or similarities between the different elements of a set. Using a mathematical distance, we compare the parameter vectors each other to select the two nearest. Then we group these elements and start another comparison step and so on, until the end. We obtain a hierarchical classification.

An example of two hierarchical classifications computed on the 72 elements of a test data base is shown in Fig. 2. It uses a 16 order model, the difference between the two representation is the selected parameters. The elements are organized by groups representing the events measured in the station. On the right diagram, the unsupervised hierarchical classification has detected 6 classes, that confirms the estimation made a priori.

VII. SELECTION CRITERION

The classification process uses selection functions to estimate the more probable class for the element to classify. These functions compare the Mahalanobis distances between the new element and the barycenter of each class. The nearest barycenter provides the belonging class. This method is useful and minimizes the number of calculations to compute because we just need to compute K distances if K

is the number of classes in the classification data base. The selection principle we use is very simple and provides excellent results. We compute the distances to the different classes barycenter. Then we select the two lowest and apply the reject criterion. The element belongs to the class which corresponds to the lowest distance, if the difference between the two selected distances is greater than 25 %. Otherwise, the element is declared to belong to the Unknown class.

VIII. DATA BASE ORGANIZATION

In order to increase the classification performances, the classification data base is organized into three data bases, one per axis. Each data base corresponds to a MIR station module. For a module, the classification data base contains the different events organized by classes.

A class is equivalent to a number, for example here are the classes used for the KVANT 2 module :

Class N° 1	=>	Fan disturbances
Class N° 2	=>	Compressor disturbances
Class N° 3	=>	CMG system at nominal speed
Class N° 4	=>	CMG ON but not running
Class N° 5	=>	Fan and Compressor high level disturbances
Class N° 6	=>	Fan and Compressor low level disturbances
Class N° 7	=>	Fan and Compressor high level disturbances plus high frequencies phenomenon
Class N° -1	=>	Unknown

IX. RESULTS ANALYSIS

A. Test Results

The Microgravity Environment Classification Tool has been tested on a KVANT 2 test base. This test base contains 1839 elements of one second length with only 12 % of contiguous elements. These results are summarized in the following array.

KVANT 2 AXES	RIGHT CLASSIFICATION	ERRORS	
		WRONG CLASS	UNKNOWN
X	87.75 %	5.80 %	6.45 %
Y	80.85 %	10.15 %	9.00 %
Z	89.45 %	6.10 %	4.45 %

B. Results on Unknown Files

Some recorded files haven't any information about the axes orientation in the KVANT 2 module, but the crew has noted that the CMG was running at nominal speed. In this case, the classification tool has found one and only one solution for the axes distribution. In an other files the crew has noted that during the measurement recording, the CMG was running at nominal speed. The classification has detected the right event during the first minute and then has found the unknown type. After a spectrogram analysis, it was possible to see the CMG speed decreasing.

CONCLUSIONS

The Microgravity Environment Classification Tool is adapted to the post-processing of a great deal of data on which we have enough information to realize a classification data base. The first tests obtained with this tool are promising in regard with the good results already reached. The data base organization allows very easy modifications without changing the classification performances.

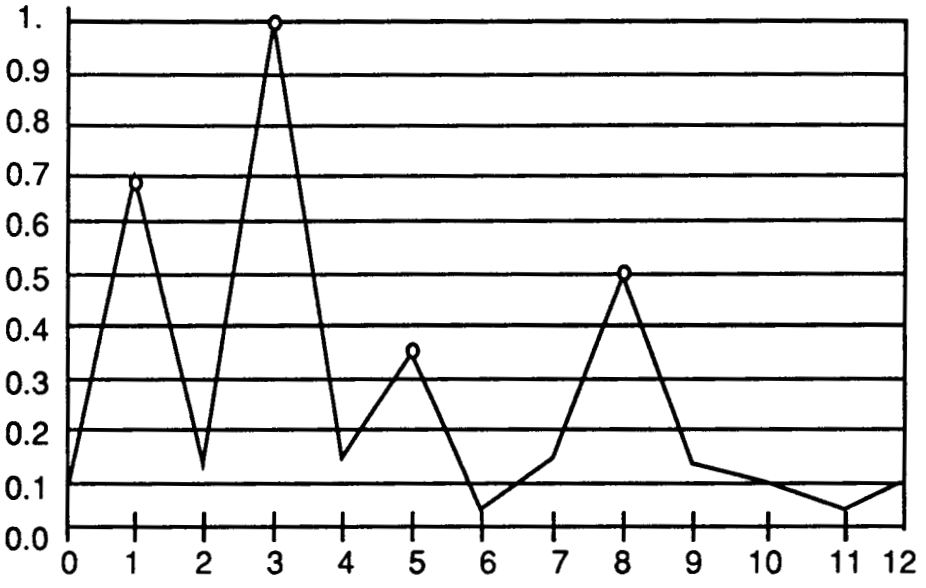

Figure 1 Representation of the relevance for 13 order model; Relevant parameters are : 1, 3, 5 and 8.

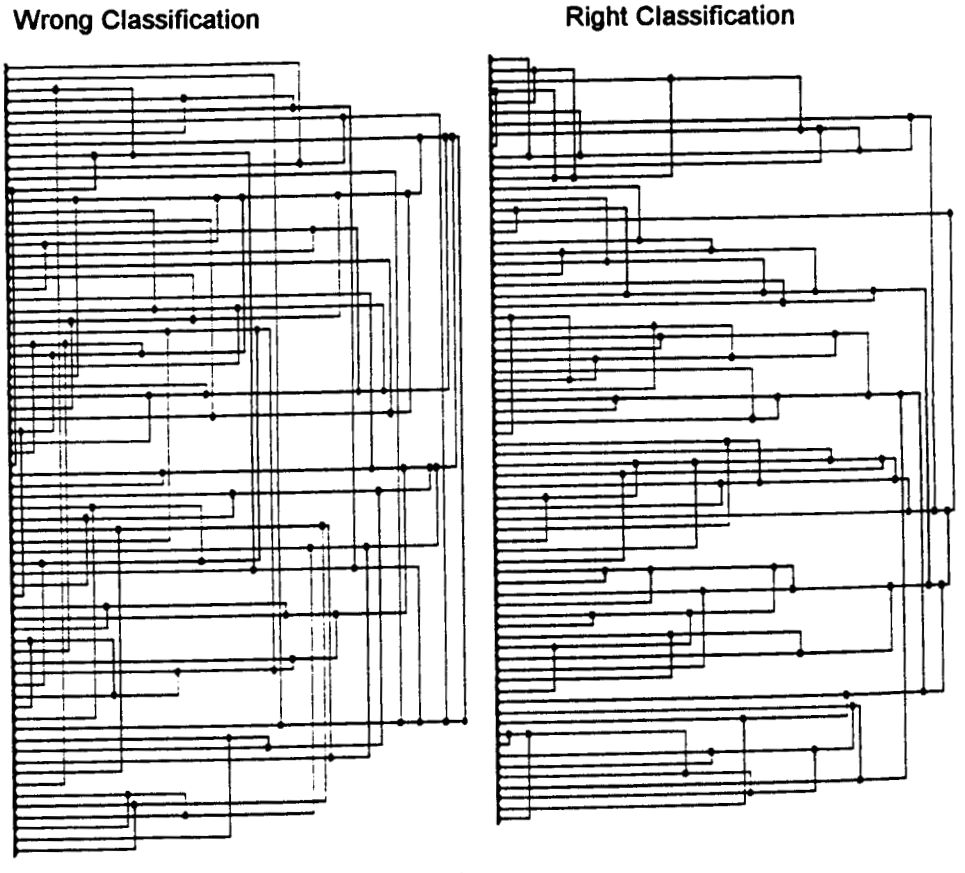

Figure 2 Unsupervised Hierarchical Classification.

Discussion

Question: *Could you tell us what you characterized on the MIR as far as the acceleration level is concerned ?*

Answer: What we did first was measure the disturbance sources. We report high levels here because we were near the sources. I should point out that the levels measured on the Kristall module and sometimes in the Ground-2 module were very quiet. For this analysis, however, I looked at high level disturbance effects.

Question: *Since you took the measurements close to the disturbance, when you moved the accelerometer pack to another location, there would still be signatures from that other source. Could you determine to what level there was damping through the station or did you find that the magnitudes stayed pretty much the same ?*

Answer: That is what we measured last time and we are still in the process of analyzing it. We used two accelerometer systems. One always stayed at the same point and the other one was moveable from one disturbance source to another in order to recognize maybe another source and also to measure the transmission between the two points. We also used a hammer to put yet another disturbance near the moving accelerometer, but we do not have all the results analyzed yet.

Question: *What is the lowest frequency you measured on the MIR ?*

Answer: I think the low frequencies were of the order of 0.5 to 1.6 Hz.

Comment: We did take MIR data from our last MGMG meeting and compared it to the shuttle data. For the most part, it was not much different in a way except for one important factor, that is, the MIR data went up quite a bit at the lower frequencies: in the 01. to 1 Hz area. MIR was substantially above the Shuttle in that area and in other areas it was not too bad. of course, that area is important for material science experiments.

Question: *What was the highest disturbance source that you identified ?*

Answer: I think it was the compressor system. The first measurements we made were on the control panel of, I think, the main module with a sensor with a maximum range of 0.1g and 32 of the 3 accelerometers were saturated. We identified the system. It was the first time the crew ever used it. We called ground control and told them that our data indicated saturated levels. You should know that on the MIR, every module has its own compressor and fan system and the crew can individually control them.

Microgravity Measurement Group

Jean-Pierre Granier, CNES
and
Charles R. Baugher, MSFC

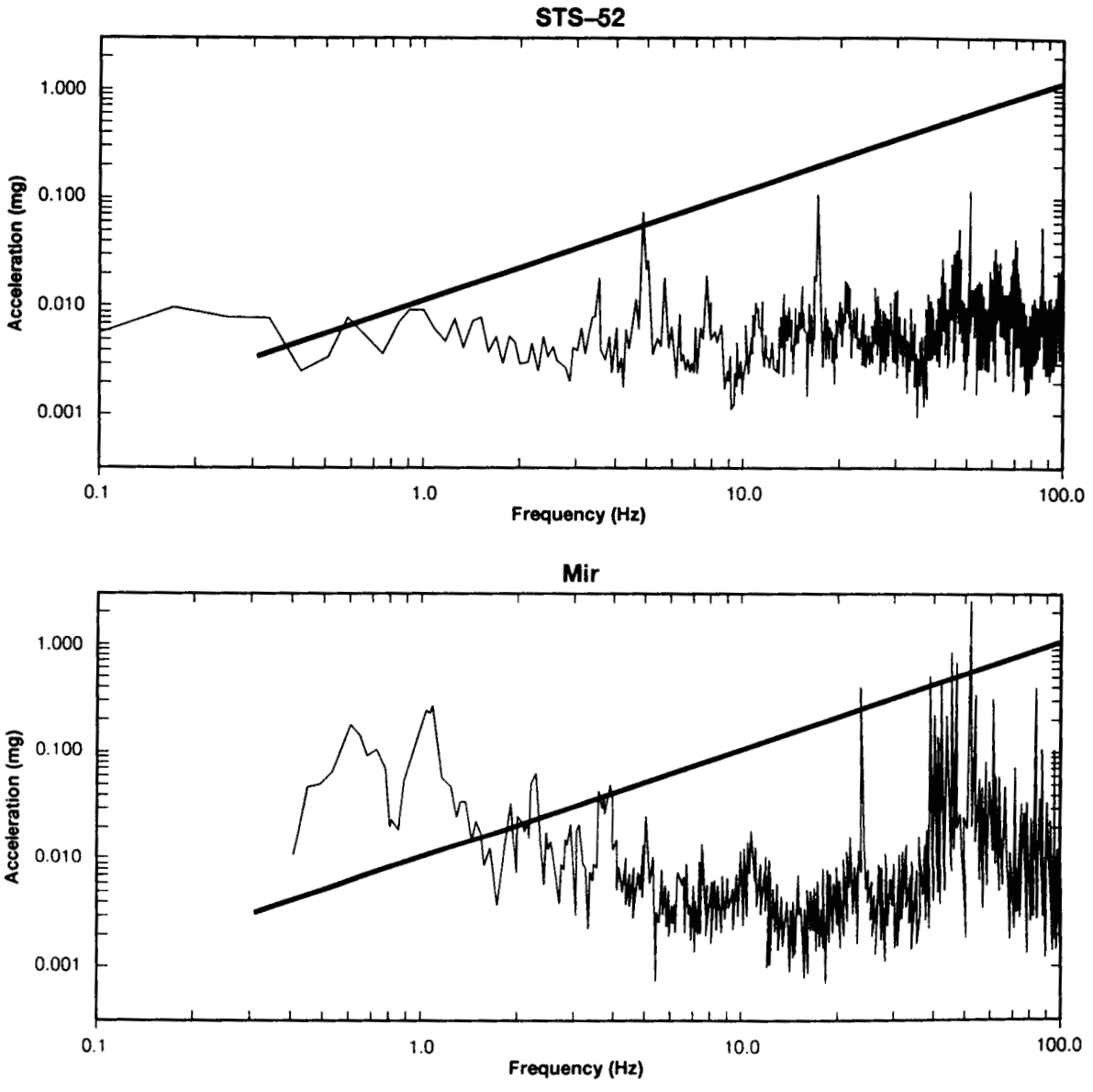

Comparison of the STS and Mir Vibration Environment. These two curves show the Russian Mir and STS vibration environment under similar analysis approaches. As can be seen from the plots, the larger Mir is characterized by structural modes at much lower frequencies than those evident in the smaller STS. The U.S. Space Station can be expected to similarly show considerable enhancement at frequencies around, and below, 1 Hertz.

ORBITAL ACCELERATION RESEARCH EXPERIMENT INSTRUMENT PERFORMANCE ON STS-50

Patrick J. McNally
Canopus Systems, Inc.
Ann Arbor, MI.

ABSTRACT

The Orbital Acceleration Research Experiment (OARE) instrument performance for the STS 50 mission is described, with particular attention given to bias calibrations and bias stability. The STS 50 mission results show extremely stable sensor output, resolving the in-flight anomalies from the STS 40 mission. In order to determine absolute acceleration levels on the shuttle to frequencies well below 1 Hz, instrument drifts with respect to several variables need to be modeled and removed from the data. Since OARE is the first accelerometer system to include a complete calibration subsystem, the OARE results will define how the miniature electrostatic accelerometer (MESA) operates over 14 day missions.

The OARE sensor collects three axes of data, each with three commandable dynamic ranges. Most of the STS 50 mission had the sensor in the "C" range, representing a resolution of 3.05 nano-g and dynamic range of 100 micro-g in the X axis and a resolution of 4.6 nano-g and dynamic range of 150 micro-g in the Y and Z axes. The bias results as a function of time after the launch event are described. The X axis bias level (sensor cylindrical axis) is shown to decay with a time constant of ~42 hours from an initial value of ~40 micro-g. The X axis continues to take valid data during this decay period. This decay is not seen on the Y and Z axes and is probably due to dielectric charging of the ceramic insulator material which surrounds the cylindrical axis electrodes.

The bias results as a function of sensor range and axis are illustrated with several charts. This data shows a variation of bias with range due to the pick-off null offset of the sensor and the reference voltage range scaling. The bias results as a function of temperature are also illustrated with several charts. Bias-temperature coefficients for the MESA are -0.036 micro-g/°C for the X axis, +0.027 micro-g/°C for the Y axis, and -0.019 micro-g/°C for the Z axis.

The OARE output is very stable even though the shuttle is very noisy (by nano-g standards) and accelerations change direction and magnitude often. Through modeling of errors related to sensor range, accurate estimates of bias and scale factor parameters for the most sensitive range can be made by

comparing data from the less sensitive ranges. This technique can be used to achieve greater performance from the OARE instrument even in the presence of large disturbances from the shuttle.

I. OARE SYSTEM DESCRIPTION

A photograph of the OARE instrument with the top cover removed is shown in figure 1. The OARE instrument consists of an electrostatic suspended proof mass and associated electronics, a precision indexing and rate table with associated electronics, an 8086 based computer with 4 Mbytes EEPROM storage, input/output electronics, and power conditioning electronics. The overall system is designed to collect, time tag, and store three axis acceleration signals in the DC to 1 Hz bandwidth over a 14 day mission, including periodic in-flight calibration of the sensor bias and scale factors. Associated temperatures, voltages, and other housekeeping measurements are also made.

The OARE instrument is built around the Miniature Electrostatic Accelerometer, or MESA. An exploded view of the MESA is shown in figure 2. This view shows a hollow, cylindrical proof mass, two X axis forcer ring electrodes, a cylindrical carrier with the Y and Z axis electrodes, and a protective case. The sensor proof mass is constrained to remain centered between the forcer rings and cylindrical carrier electrodes. The control loop uses capacitive feedback to modify an applied electrode voltage. Each loop also has a reference voltage to vary the dynamic range of the output. The reference voltage and the feedback voltage, called the forcing voltage are combined on the electrode to null the proof mass under an applied acceleration. The proof mass is centered in the gap as closely as possible in a direction normal to the gravity vector with a factory adjustment. Three dynamic ranges are provided with an associated system resolution summarized in table 1. The MESA sensor is packaged together with the constrainment loop electronics and output conditioning filters in a unit called the OARE Sensor Subassembly (OSS).

The OSS is rigidly mounted to a two axis precision indexing table. The table and sensor together make up the Sensor/Table Assembly (STA) (figure 3). The table features brushless DC torque motors controlled by an 8088 microprocessor. Position feedback is obtained from 16 bit optical encoders on each axis. The table is capable of precision positioning and tracking input position ramps.

For bias calibrations, the table is alternately rotated by the inner and outer gimbal motors by 180 degrees, providing a reversal of the input signal for first the X sensor axis and then the Y/Z sensor axes. Position accuracy is specified at 30 arc-seconds or better, but actual test results show settling within 7 arc-seconds. Each table flip is performed in less than 5 seconds to make sure that the input signal does not change from one bias calibration sample to the next. The bias measurement is equal to the difference of the two measurements divided by two.

For scale factor calibrations, one gimbal motor is "slewed" at a constant rotation rate while the other remains at a fixed position. Inner gimbal slews provide a centripetal acceleration input to the X sensor axis, outer gimbal slews provide a similar acceleration input to the Y/Z sensor axes simultaneously. The table is required to slew between two positions with a rate stability better than 0.1%, and an acceleration-deceleration time within 150 msec.

On-board signal processing is used to condition and convert the analog voltage output signal into a digital word for storage. The analog voltage is first put through a 6 pole 1 Hz Bessel anti-aliasing filter. The Bessel filter was chosen for fastest settling to a steady state level with zero overshoot. The 6 poles and 1 Hz cutoff were chosen to provide 96 db of signal attenuation at the Nyquist frequency of 5 Hz.

The output of the Bessel filter is taken to a sample and hold and a 16 bit analog to digital converter. Each of the sensor axes signals is sampled at a uniform rate of 10 samples per second. Engineering data is also sampled at a lower rate. All data is time tagged with a resolution of 1 millisecond.

After sampling and conversion, the data is both buffered for transmission to the payload tape recorder and passed to the adaptive trimmed mean filter. The adaptive trimmed mean filter is a batch filter run nominally every 25 seconds on the previous 50 seconds worth of data. The filter sorts the data set, calculates the mean and the 'Q' statistic, a measure of the data spread, then trims a set percentage of the data based on the value of the 'Q' statistic. Finally, the mean of the trimmed data set is calculated and stored, along with the average deviation value and the 'Q' statistic value. The filter has been shown to be highly effective at removing outliers without affecting the majority of the samples.

A. In-Flight Calibrations

The bias and scale factor calibration is a sequence of sensor and table commands issued by the OARE computer. A bias calibration is performed first, starting with the C range. Three measurements are made, corresponding with the normal X, then the Opposite X/Normal Y & Z, and finally the opposite Y & Z measurement. The sensor is commanded to B range and the sequence is repeated, and then again for A range.

A scale factor calibration for a given axis and range consists of two sets of three measurements. First, the table is moved to the midpoint of the slew and a measurement of the signal level at the midpoint is made. Then the sensor is returned to the start position and the table is slewed at constant rate from the start to end position while a scale factor measurement is made. Finally, the table is returned to the midpoint position for a final measurement of the signal level. The entire sequence of three data sets is repeated for each range/axis combination (where Y and Z are taken together) so that

two measurements are made with a centripetal acceleration - a low angular rate measurement and a high angular rate measurement.

With each calibration data set is recorded the sensor temperature, the average deviation of the sample, and the 'Q' statistic value. The temperature is provided for extrapolation of calibration results between calibration activities. The average deviation and 'Q' statistic provide a measure of the noise in the background environment when the sample was taken.

In-flight calibration assumes the input signal does not shift significantly during the calibration and the sensor output settles quickly to a new input level after a table movement and change in amplifier range. The OARE software design allows for some modifications to the calibration sequence, frequency, data set length, and table positions through the use of mission re-loadable control parameters called "adaptation parameters".

II. OARE PERFORMANCE ON STS - 50

The performance during STS 50 is discussed during this section. For measuring the low frequency disturbances with high sensitivity (below 1 micro-g), the system output must be stable and definable between calibrations. The OARE design philosophy is to perform calibrations as often as required to take out system drifts and obtain a new absolute reference level. The process of performing a calibration is disruptive to the collection of low frequency data, however, and the operations goal is to minimize the number of required calibrations. Since both system drift and the signal to measure are within the low frequency bandpass, modeling is required to separate the two effects.

The original calibration design assumptions were reviewed against the STS 50 experience. The design assumes that during a calibration, the input signal does not shift level significantly. If a large disruption occurs during the calibration, the system is designed to sense the event and defer the calibration until after the disruption (for instance, after an attitude correction maneuver). The design assumes that the sensor output settles quickly to a steady input from the calibration table, especially for the higher range calibrations which require faster table movements, and therefore have less gimbal travel in which to collect data. The design further assumes that the sensor output does not shift significantly between calibrations spaced several hours apart. This allows modeling of the known effects on the calibration parameters (such as temperature).

The original design assumption that the external signal level is constant throughout the calibration activity is not valid for many calibrations, as seen in figure 4. Note that output is given in data counts. When bias level is plotted with the signal level at each calibration, large variations in signal are seen. This is also evident when the noise measurement for each calibration is plotted with the bias level.

Therefore, care must be taken in selecting bias calibrations which occur during quiet times on the Orbiter.

The original design assumption that the sensor output settles quickly to a steady input from the calibration table is entirely valid for the X and Z sensor channels, but the Y sensor channel exhibits additional settling delays. Figure 5 shows the output settling in counts at the beginning of a scale factor slew in all three axes. The Y axis output takes about 1.5 seconds longer to settle to a steady state value than the X and Z axes. This effect must be removed in post processing of the data.

A. Bias Modeling

Overall instrument bias can be modeled as a function of several variables. First of all, because the instrument sensitivity depends on the stabilization of the electrostatic fields, charge deposition on the proof mass and the ceramic forcer rings can cause induced forces on the proof mass, resulting in an apparent acceleration signal. Second, because the sensor force balance loops are nulled in a "1 g" environment, the pick-off null can be offset from the reference voltage force balance, also resulting in an apparent acceleration signal. The MESA sensor is also subject to temperature effects from changes in internal dimensions. These various effects can be amplified by range changes and are also of different criticality in the cylindrical (x axis) and the radial (y or z axes).

B. Sensor Range Effects

Slight errors in the pick-off null offset from the final factory adjustment can cause an induced bias from the reference voltage. If the input signal is zero, a pick-off null offset will cause the sensor to be attracted to one electrode. This induced bias can be amplified with output range changes. This effect is measured quite accurately by the in-flight bias calibrations, even though the ground adjustments and calibrations tried to eliminate this effect completely. Plots of the bias in counts over time in each range, for each axis are shown in figures 6, 7, and 8.

The flight bias calibration data was reviewed to determine the dependency of the induced bias on reference voltage. Linear regression was used on the average range dependent bias levels to determine the best fit. The data for all three axes are shown in table 2, where the results have been converted to micro-g's. From this data, it is seen that a significant component of the in-flight bias is due to the null offset. Again, this component can only be removed from the flight data because bias calibrations were performed in a micro-gravity environment.

C. Temperature Effects on Bias

Changes in the sensor gap from temperature changes can also cause an induced bias. The sensor temperature is measured throughout the mission, including during all calibrations. Temperature trends can then be correlated with shifts in bias. Typical bias in counts versus temperature dependency is shown in figure 9 for the X axis in B range and figure 10 for the Y axis in B range. In-flight bias temperature coefficients were estimated using a least squares fit to bias versus temperature scatter plots for the entire mission. The sensor X axis showed the greatest temperature sensitivity of -0.036 μg/°C. The Y and Z axes had bias temperature coefficients of +0.027 μg/°C and -0.019 μg/°C respectively.

The bias temperature sensitivity is also amplified by range changes. This effect is due to the change in gap error with temperature, and the subsequent effect of gap error and reference voltage on the induced bias. Given bias temperature coefficient measurements in all three ranges, a simple model of bias temperature coefficient versus reference voltage can be developed for each axis. The model inputs and results are summarized in table 3 where results have been converted to micro-g units.

D. Bias Effects as a Function of Time

During the first several days of the STS 50 mission, the X axis bias settled from an initial value of near 4 μg to a final value of 1 μg in the C range. This settling was coincident with three events: 1) initial power on (several hours before launch), 2) launch vibration, and 3) thermal stabilization of the shuttle and the instrument. The primary effects of thermal stabilization can be removed through bias temperature coefficients calculated for the rest of the mission. Also, from inspecting the output settling after power cycles during the mission, the effects of power cycling are shown to be minimal.

Figure 4 shows the settling of the X axis output bias after launch. This bias settling is due to dielectric charging of the ceramic forcer ring assemblies. The dielectric charging appears to be due to the shock and vibration associated with launch. This charging is induced through launch vibrations.

Even small amounts of charge on the forcer rings can result in a dramatic bias shift. This effect has been observed on other flights of the MESA without a calibration system. Note that this bias shift can be removed accurately from the data because periodic bias calibrations had been performed throughout the first few days of the mission. The bias change is proportional to the surface potential on the ceramic portion of the forcer. An exponential time decay can be fit to this curve, with a time constant of approximately 43 hours.

SUMMARY AND CONCLUSIONS

Shuttle noise has a potentially large, but as yet unquantified effect on calibration accuracy, especially if calibrations are taken only a few times during the entire mission. For STS 50, plots of the

noise levels and signal level changes during calibrations were used to select "good" calibrations for further analysis. The next flight of OARE is STS 58, where calibrations will be planned for the sleep period. More analytical work is required in this area to understand the calibration accuracy.

After an initial settling period, the OARE output is very stable. The shock and vibration induced settling of the X axis during STS 50 was not seen in any ground test. Bias calibrations throughout this settling period allow this effect to be removed.

The magnitudes of the bias temperature coefficients could not be accurately measured in ground tests, where the limitations of the ground environment provide errors on the order of several hundred nano-g. In flight results have shown that the bias-temperature coefficients are extremely low, up to three orders of magnitude less, when compared with inertial grade pendulous accelerometers.

Multi-ranging sensor designs such as the OSS allow in-flight measurements in higher ranges to be applied to certain effects in the lower ranges. For instance, the absolute magnitude of bias and bias temperature coefficient can be more accurately measured in the sensor A range, then applied to the C range where measurements may be noisy. This modeling technique needs to be exploited more fully for future missions of the OARE instrument.

The OARE instrument design demonstrates that accurate in-flight bias and scale factor calibrations can be reliably performed with available hardware. Accurate, periodic in-flight calibration should be considered a requirement for all future accelerometers designed to measure low frequency disturbances.

Table 1: OARE Dynamic Range and Resolution

Range	Full Scale X Axis (10^{-6} g)	Y, Z Axis (10^{-6} g)
A	10000	25000
B	1000	1900
C	100	150
Range	**Resolution X Axis (10^{-9} g)**	**Y, Z Axis (10^{-9} g)**
A	305	763
B	30.5	58
C	3.05	4.6

Table 2: Bias versus Reference Voltage Squared

	Cyl. Axis		
Ref. Volt.^{2}	.12V^2 (C)	1.2V^2 (B)	16 V^2 (A)
X axis Bias	-0.87 μg	-1.30 μg	-7.19μg
	Radial Axes		
Ref. Volt.^{2}	1.44 V^2 (C)	3.24V^2 (B)	36 V^2 (A)
Y Axis Bias	1.31 μg	1.29 μg	0.91 μg
Z Axis Bias	-7.20 μg	-13.62 μg	-127.4 μg

Table 3: Bias Temperature Coefficient vs. Reference Voltage Squared

	Cyl. Axis		
Ref. Volt.^{2}	0.12 V^2 (C)	1.2 V^2 (B)	16 V^2 (A)
X axis Bias TC (μg/°C)	-0.036	-0.0386	-0.101
	Radial Axes		
Ref. Volt.^{2}	1.44 V^2 (C)	3.24 V^2 (B)	36 V^2 (A)
Y Axis Bias TC (μg/°C)	+0.027	+0.054	+0.539
Z Axis Bias TC (μg/°C)	-0.019	-0.0239	-0.264

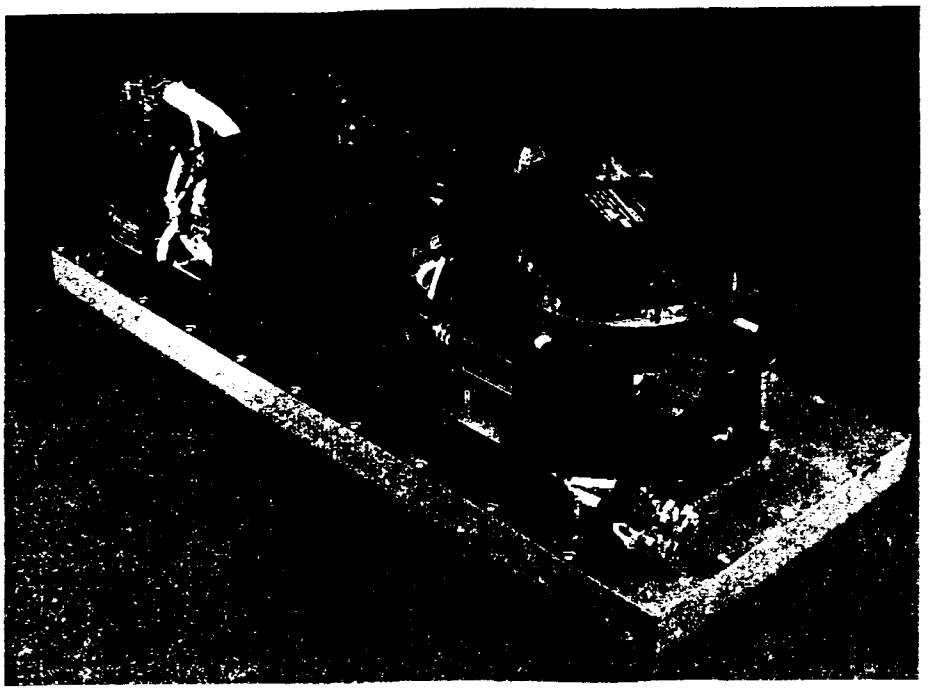

Figure 1 OARE Instrument with Cover Removed

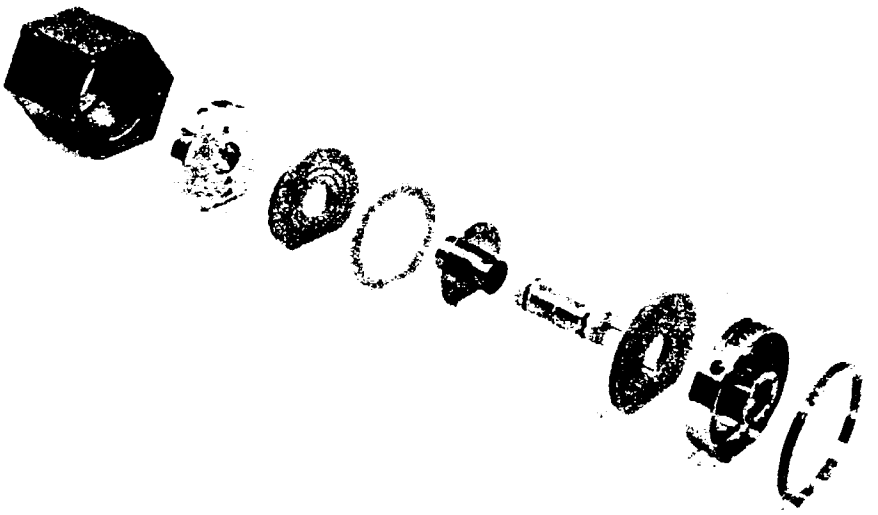

Figure 2 Miniature Electrostatic Sensor Components

Figure 3 Sensor/Table Assembly

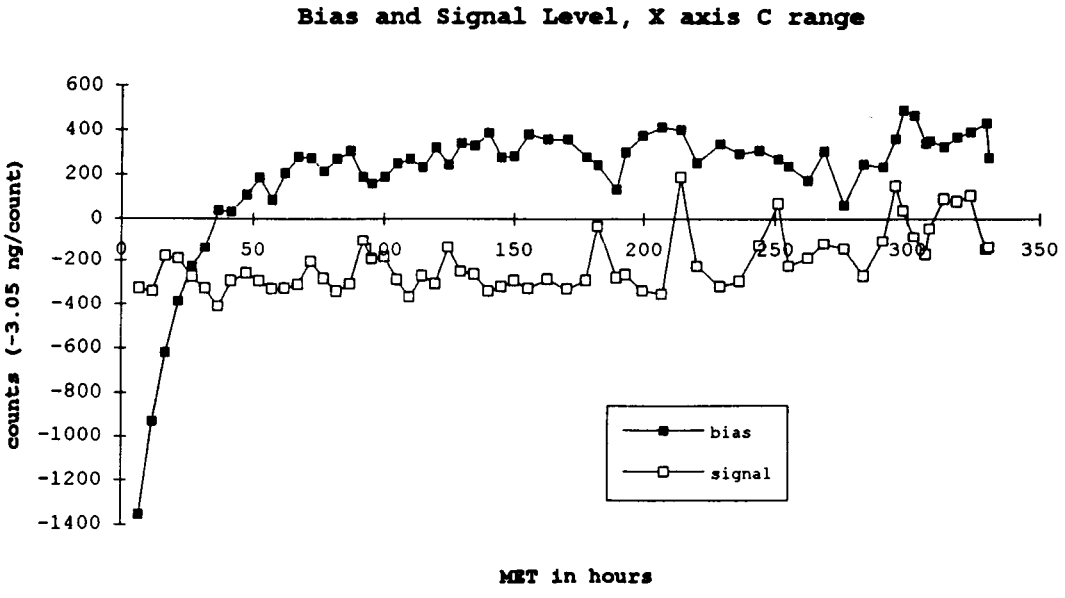

Figure 4 Large Signal Variations Affects Bias Calibration Accuracy

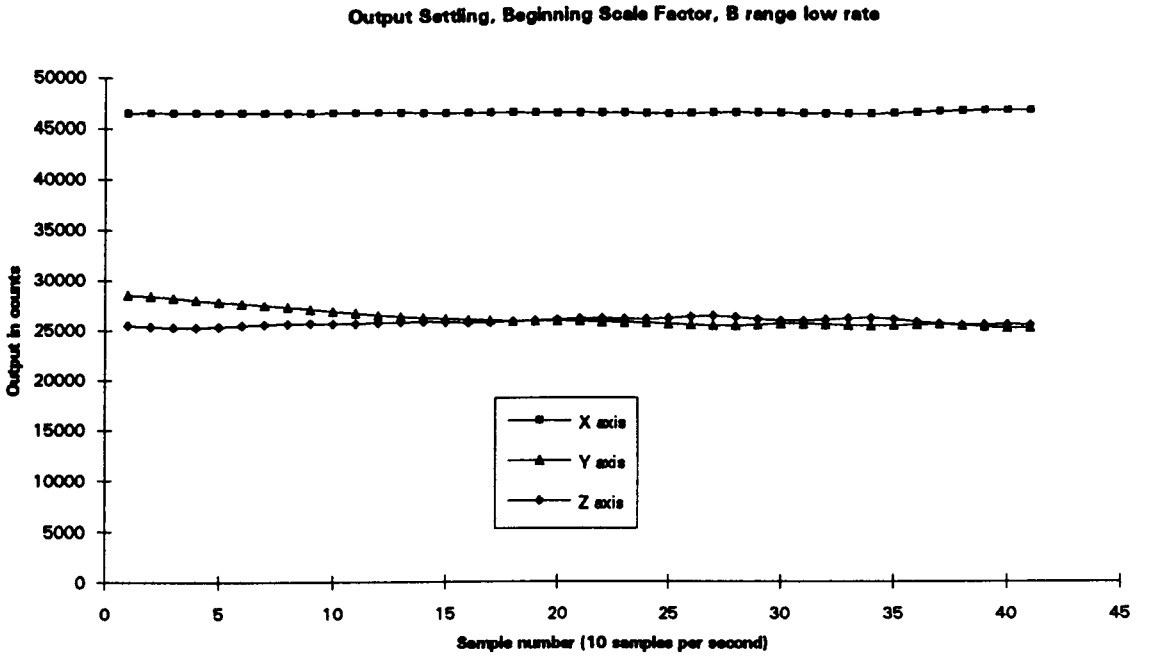

Figure 5 Y Axis Output Settling is not as Rapid as X and Z Axes

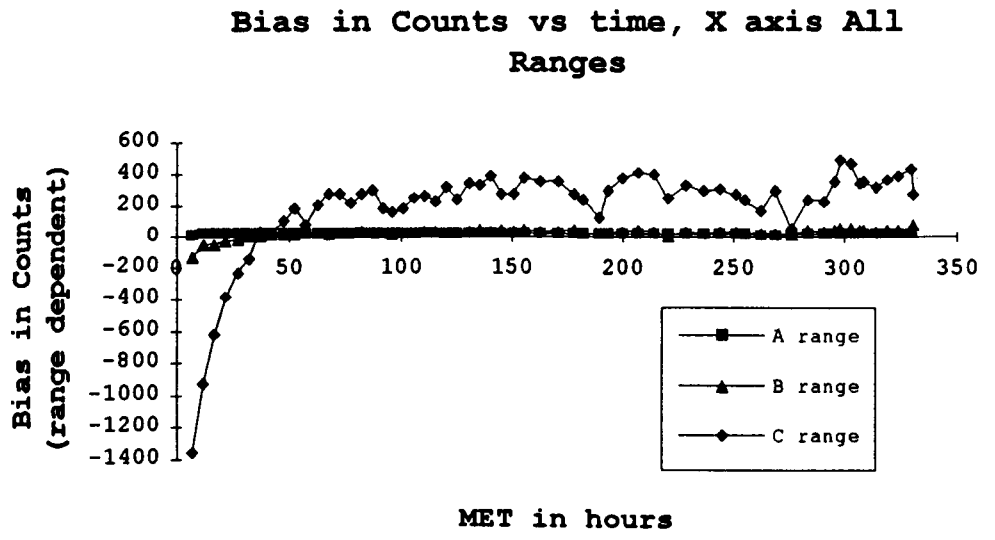

Figure 6 X axis Bias versus Range Shows Dependency on Reference Voltage

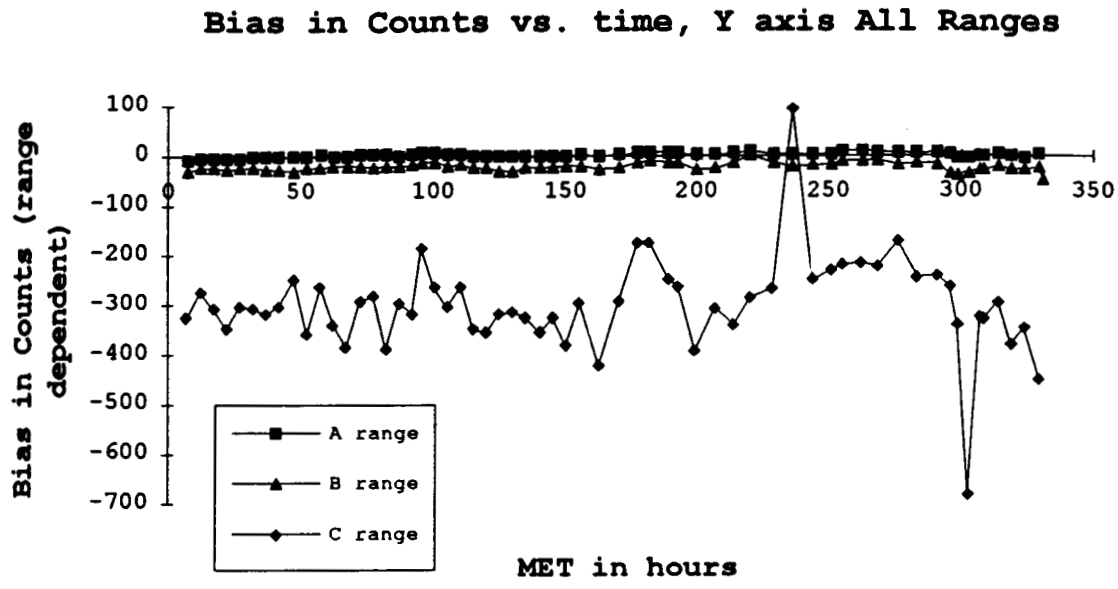

Figure 7 Y Axis Bias versus Range Shows Dependency on Reference Voltage

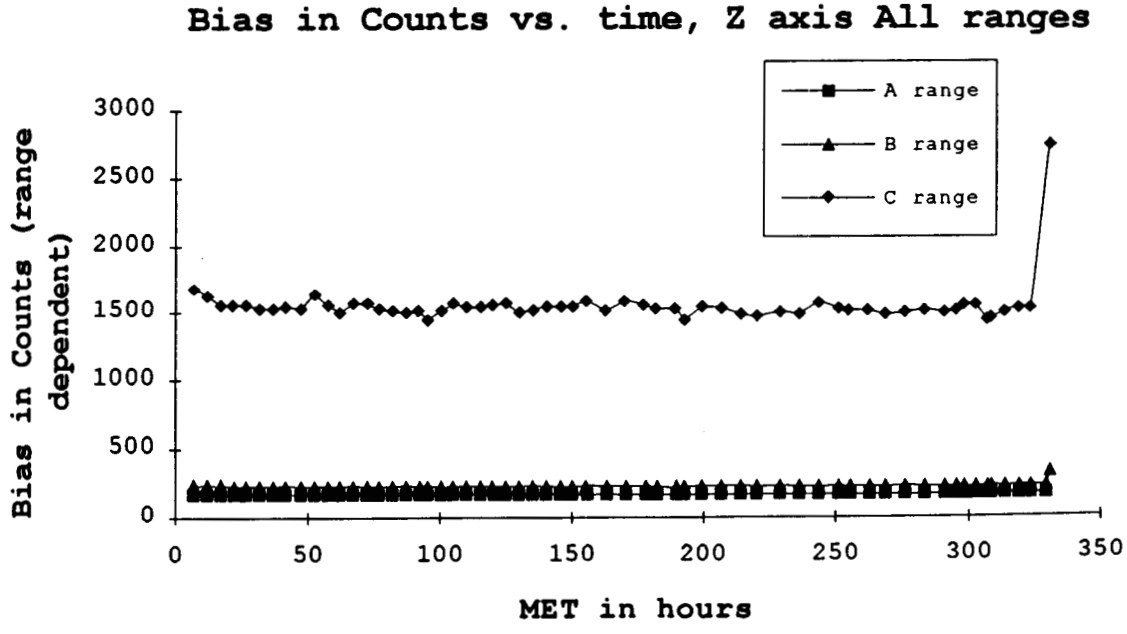

Figure 8 Z Axis Bias versus Range Shows Dependency on Reference Voltage

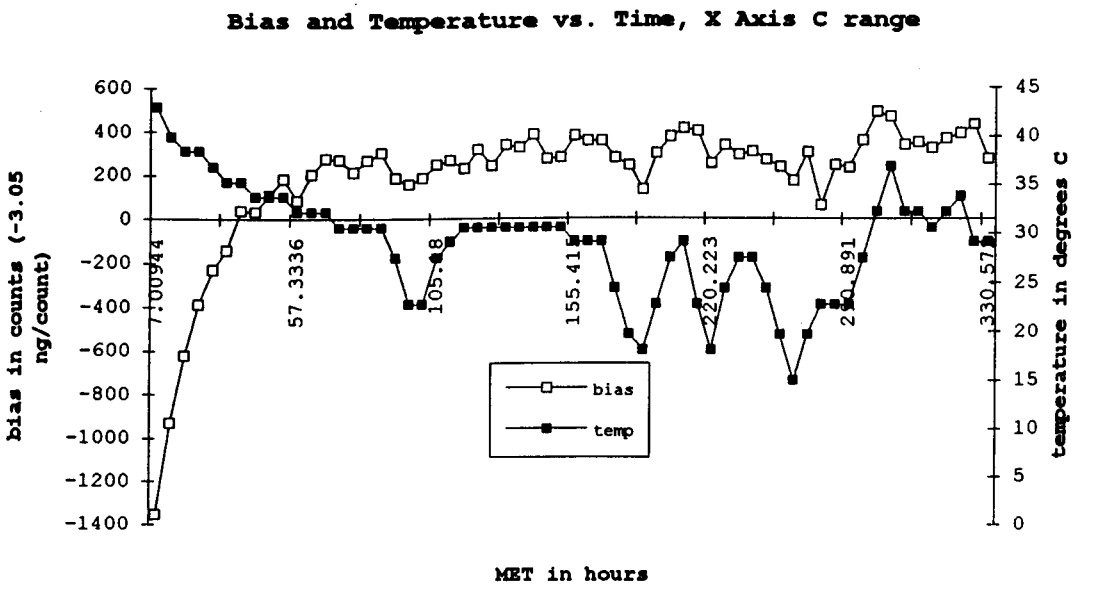

Figure 9 X Axis C Range Bias and Temperature Data used to derive Bias-Temperature Coefficients

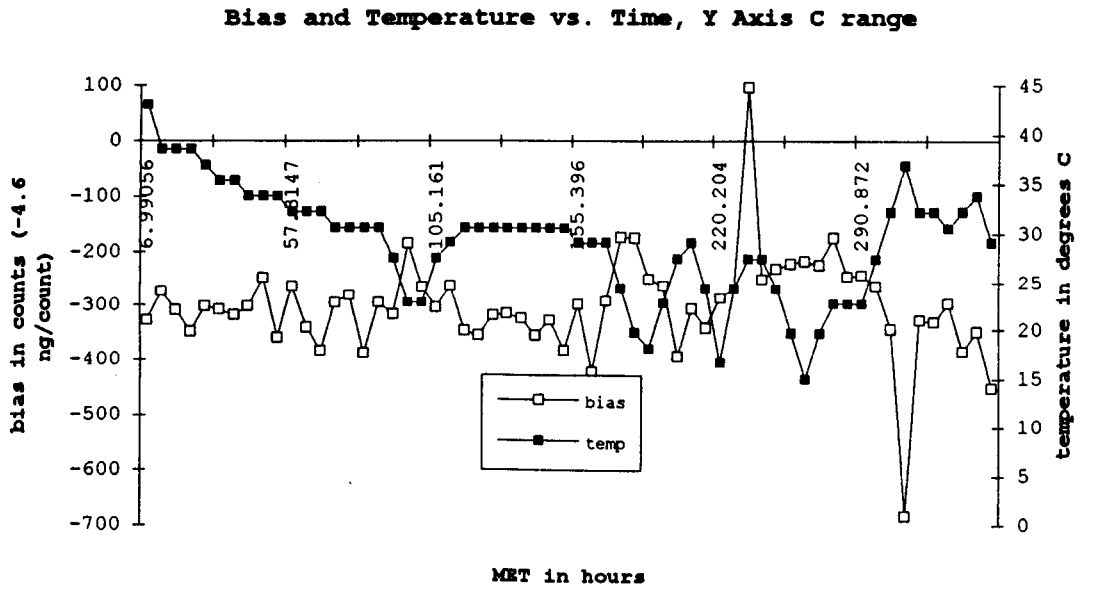

Figure 10: Y Axis C Range Bias and Temperature Data used to derive Bias-Temperature Coefficients

POSITIVE ENERGY GROWTH EFFECTS ON USML-1

Brian P. Matisak* and **Melissa J. B. Rogers**[+]

Teledyne Brown Engineering, Huntsville, Alabama
[+]Center for Microgravity and Materials Research
University of Alabama-Huntsville, Huntsville, Alabama.

ABSTRACT

The successful execution of the STS-50 mission established a number of milestones for Space Shuttle flights. The STS-50 flight, which carried the USML-1 payload, set a record for the longest Shuttle flight to date as well as the longest time in maintaining one fixed LVLH attitude. Maintaining this LVLH attitude resulted in positive energy growth contributions which impacted EOM landing opportunities. The attitude deadband also provided a significant effect to the altitude gain over the 14-day flight. The saturation of VRCS jet firings may have had an impact to the steady-state acceleration environment. No formal evidence linking VRCS jet firings with post-flight accelerometer data exists at the time of this writing.

INTRODUCTION

The successful execution of the First United States Microgravity Laboratory (USML-1) payload aboard the Shuttle set a number of milestones for manned space flight. The 14-day flight is currently the longest Shuttle flight to date. Furthermore, the flight also set a record for the longest duration in one fixed local-vertical, local-horizontal (LVLH) attitude. This attitude, known as the Crystal Growth Furnace (CGF) attitude, was required for each of the four CGF principal investigators (PIs) during USML-1 Spacelab Operations. Due to the required CGF attitude during the flight, coupled with the direction of specific Vernier Reaction Control System (VRCS) thruster jets, it was estimated pre-mission that the Orbiter would actually gain, not drop, in altitude during Spacelab Operations. Johnson Space Center (JSC) engineers[1] determined pre-mission that this gain in altitude may impact end of mission (EOM) landing opportunities. It is a generic rule for each Shuttle flight to maximize EOM landing opportunities. As a result, a strategy was developed to bring back those lost landing opportunities by conducting a series of retrograde Primary Reaction Control System (PRCS) trim burns near the end of Spacelab Operations. The purpose of this paper is to review details of the positive energy growth for the USML-1 flight and describe how the two

centers developed a method of conducting the trim burns without impacts to the USML-1 payload. The transient acceleration environment within the USML-1 module due to periodic VRCS jet firings will also be discussed in this paper.

I. USML-1 CGF ATTITUDE DESCRIPTION

One of the major experiments aboard the USML-1 flight was the CGF experiment. The intention of each of the four CGF PIs was to take advantage of the low frequency level steady-state microgravity environment aboard the Shuttle in an effort to grow crystals of high uniformity that otherwise could not be matched on the ground. Ideally, each of the CGF PIs wished to grow their crystals along an axial growth axis without any steady-state acceleration components acting perpendicular to this axial growth axis (see Figure 1). This perpendicular acceleration component, if large enough, could conceivably cause convective flows within the crystal sample. A significant amount of convective flow can be detrimental to the uniformity of each crystal.

One can conceivably minimize perpendicular steady-state acceleration components acting at the sample location by placing the crystal sample along the Orbiter center of gravity (cg). Due to the fact that the USML-1 Orbiter cg was located approximately in the middle of the Spacelab module between Racks 9 and 10^2, and was constantly moving due to the change in the mass properties of the Orbiter during the flight, it was impossible to provide the CGF PIs with the ideal configuration for optimum crystal growth. Due to the location of the CGF in Rack 9 of the Spacelab module, gravity-gradient accelerations were present and impossible to completely mask during realtime operations. Based on this information, the CGF PIs requested what is commonly known today as the CGF attitude. This attitude is defined as tail-to-Earth (-X/LV), payload bay into the velocity vector (-Z/VV), with an additional -12° roll angle to align the velocity vector along the CGF long axis (see Figure 2). While this attitude did not eliminate steady-state acceleration components perpendicular to the CGF long axis, it was determined that this component would not vary significantly due to the fact that the expected gravity-gradient component (a function of distance away from the cg) would not significantly vary. The perpendicular components at the CGF sample location were predicted pre-mission to be $\leq$ 0.10 mg along the Orbiter X-body axis and $\leq$ 0.20 mg along the Orbiter Y-body axis. Both components were deemed acceptable by the CGF PIs prior to flight. This attitude was subsequently flown during the majority of USML-1 operations.

II. VRCS CONFIGURATION

During nominal payload operations, the VRCS thruster jets are used to maintain nominal attitude control. The VRCS is comprised of six thruster jets (as seen in Figure 3), with each jet or

series of jets providing a specific purpose in maintaining attitude control.[3] This system is non-redundant; that is, if one VRCS jet should fail, the system will shut down and a backup digital autopilot (DAP) configuration, known as the alternate digital autopilot (ALT DAP), must be employed as a means of maintaining attitude control. The ALT DAP configuration requires the use of six PRCS jets to maintain attitude control.[4] Figure 4 provides the direction cosine matrix for the location, direction, and thrust values for each of the six VRCS jets. The six VRCS jets are labeled as jets F5R, F5L, L5D, R5D, R5R, and L5L.[5]

III. ORBITAL MECHANIC EFFECTS DUE TO POSITIVE ENERGY GROWTH

Beginning with the Vis-Viva equation[6]

$$v^2 = \mu (2 / r - 1 / a)$$

one can derive the relationship between the change in Orbiter velocity (Δv) with the change in semi-major axis (Δa) by first taking the derivative of the Vis-Viva equation, leaving

$$2v \Delta v = \mu a^{-2} \Delta a$$

by applying some key relationships to the previous equation one arrives at

$$\Delta a = (2a^{3/2} / \mu^{1/2}) (2a / r - 1)^{1/2} \Delta v$$

substituting the relationship

$$\tau / \pi = 2a^{3/2} / \mu^{1/2}$$

leaves

$$\Delta a = (\tau / \pi) (2a / r - 1)^{1/2} \Delta v$$

For circular orbits, a ~ r; applying this assumption, one arrives at the equation relating the change in velocity (Δv) to the change in semi-major axis (Δa) as

$$\Delta a = (\tau / \pi) \Delta v$$

where τ is the orbital period of the Orbiter. The formula states that for every change in the velocity (Δv) acting along the flight path (velocity vector, $\overline{v}$), a corresponding change in the semi-major axis (Δa) of the Orbiter results. In order for this effect to have a significant impact to mission planning, two criteria must be met:

1. the Orbiter attitude must be configured such that VRCS jets F5R, F5L, R5D, and L5D must be aligned along or very close to and act in the direction of the velocity vector, $\overline{v}$.
2. this attitude must be maintained for a long period of time for significant positive energy growth (altitude gain) effects to become evident.

Both conditions were met with the CGF attitude. JSC and MSFC engineers conducted pre-mission calculations and determined that based on an expected venting force (due to VRCS jet firings) of 0.16 lbf, the net altitude gain due to VRCS contributions alone would be approximately 200 feet/rev.[7]

The USML-1 flight marked the first time that positive energy growth significantly impacted mission operations. JSC flight controllers have shown their ability to be able to accurately determine pre-mission altitude decay due to drag effects. These pre-mission calculations are critical because they determine the position of the Orbiter near EOM. Knowing the location of the Orbiter near EOM is essential for assessing landing opportunities. Two conditions must be met in order to land the Orbiter for extended duration flights:

1. landing opportunities must occur in daylight.
2. Orbiter must be within a 770 nautical mile cross range radius of the landing site[8].

With the addition of the positive energy growth contributions, JSC flight controllers determined that some of the EOM landing opportunities were lost. JSC engineers also determined that these lost landing opportunities could be recovered by conducting two PRCS retrograde trim burns. These burns would be conducted by maneuvering the Orbiter to a tail-into-the-velocity vector attitude (-X/VV) and fire PRCS jets R3A and L3A (see Figures 3 and 4) in a direction opposite to the velocity vector in order to slow down the Orbiter. A loss in Orbiter velocity causes the Orbiter to drop in altitude. It was the intention of JSC flight controllers to provide a large enough Δv to counteract the positive energy growth effects.

Due to the fact that these two PRCS burns (one at the Orbiter apogee, followed 45 minutes later by another PRCS burn at Orbiter perigee) cause accelerations within the Orbiter of 10^{-2} g, it was imperative for the MSFC mission design team to provide the JSC mission design team a 1.5 hour (one rev) window in order for JSC flight controllers to maneuver the Orbiter from the CGF attitude to the PRCS burn attitude, conduct the burns, and maneuver back to the CGF attitude. Due

to the number of g-sensitive experiments compacted within the USML-1 timeline, it was difficult for the MSFC mission design team to find a window. The MSFC team was fortunately able to locate a window near the end of Spacelab Operations from 11/06 MET to 11/08 MET for JSC to conduct the burns, should the burns be deemed necessary.

IV. REALTIME EXECUTION OF THE PRCS TRIM BURNS

The positive energy growth contributions that were predicted pre-mission occurred as expected. It was determined realtime that due to on-orbit orbital parameters only one PRCS burn would be required. However, due to some unexpected events that occurred realtime, an opportunity to conduct the burn was moved to earlier in the flight. The +X-axis PRCS burn was completed at approximately 4/00:27 MET and successfully dropped the Orbiter altitude approximately 5 kilometers (2.7 nautical miles). Figure 5 details the USML-1 semi-major axis history. From the figure one can see that as the attitude deadband was tightened from 0.5°/axis to 0.1°/axis (due to the forward VRCS jet temperature problems, discussed in detail in the next section of this report), more VRCS jet firings resulted, causing a positive altitude gain only during periods while the CGF attitude was held.

As it turned out, this PRCS burn to bring in lost landing opportunities could not be taken advantage of at the nominal EOM landing day due to bad weather at the designated landing site. As a result, the USML-1 crew was required to stay in orbit for an extra day. However, the PRCS trim burn did provide additional landing opportunities at EOM+1 and EOM+2 if such opportunities were deemed necessary.

V. VRCS JET FIRING TRANSIENT ACCELERATIONS

From Figures 3 and 4 one can see the direction of each VRCS jet firing. During USML-1 realtime operations it was determined that by not including a two degree pitch angle in the CGF attitude (to allow the Orbiter X-principal axis to be aligned with the local radius vector), the Orbiter exhibited a tendency to constantly want to pitch up. As a result of this tendency, the aft VRCS down jets (L5D, R5D) were required to fire more than expected. Due to the fact that the forward VRCS jets (F5L, F5R) were not firing enough to satisfy VRCS jet temperature requirements, coupled with the desire on behalf of the CGF PI teams to maintain the CGF attitude, JSC and MSFC flight controllers decided to tighten the VRCS attitude deadband to 0.1°/axis to force these forward VRCS jets to fire. This decision was made and incorporated into the timeline at approximately 120 hours MET. As a result, the steady-state acceleration environment ($\leq 10^{-6}$ g) was saturated by a series of transient accelerations ($\leq 10^{-4}$ g) caused by numerous VRCS jet firings that resulted due

to the tight deadband. Based on realtime VRCS jet data, VRCS jet firings (while incorporating the 0.1°/axis attitude deadband) occurred approximately once per minute. What impacts to the steady-state acceleration environment resulted from this saturation of transient acceleration pulses? OARE accelerometer data[9] and PAS accelerometer data[10] suggest an additional 0.5 mg acceleration along the Orbiter X-body axis (which corresponds approximately to a constant 0.12 lbf along the X-body axis) was evident during flight that was not expected pre-mission. JSC flight controllers could not pinpoint any significant fluid leaks during flight that may have caused this additional acceleration contribution. It has been suggested that the continuous pulsing of the VRCS jets could have been a source of this continuous acceleration contribution. However, basic physics formulas dictate that once a force (VRCS jet firings) ceases to exist, the corresponding acceleration (resulting from the VRCS jet firings) also ceases to exist. As of this writing, it is not clear to these authors where this additional force originated. Due to the small force corresponding to this acceleration it may be difficult to ever find this unknown source.

CONCLUSIONS

The source of the additional acceleration (as seen from OARE and PAS accelerometer data) along the Orbiter X-body axis for the USML-1 flight is unfortunately not known at the time of this writing. On a positive note regarding the flight, MSFC and JSC mission design engineers were presented with an unprecedented opportunity in Shuttle flight history to observe the effects of significant positive energy growth to mission planning. Early detection of the positive energy growth and careful timelining of this phenomenon enabled MSFC flight controllers to conduct experiment operations without major impacts to the microgravity timeline while JSC flight controllers were able to maximize EOM landing opportunities. Critical and timely interaction between JSC and MSFC mission design teams regarding this and other issues affecting the USML-1 payload resulted in the successful execution of the USML-1 flight.

REFERENCES

1. personal communication with JSC/DM22 regarding STS-50 landing opportunities assessment, JSC, Houston, Texas, October 1991.

2. *Data Change Notification to the Shuttle Operational Data Book, Volume II*, NSTS-08934, Amendment 254, August 1992.

3. *Shuttle Operational Data Book, Volume One*, JSC-08934 (Vol.1), Revision E, January 1988.

4. "ALT DAP and Loss of VRCS On STS-42", Jeff Davis/DF62, JSC, Houston, Texas, July 1991.

5. *Shuttle Operational Data Book, Volume One*, JSC-08934 (Vol. 1), Revision E, January 1988.

6. Roy, A.E., *Orbital Motion,* Adam Hilger, Bristol and Philadelphia, 1988.

7. personal communication with JSC/DM42, as documented in Teledyne Brown Engineering Memo OPS(MDB)92-122, April 1992.

8. *STS-50 Flight Requirements Document, Level A Groundrules and Constraints, Appendix A*, NSTS-17462A-50, Appendix A, October 1991.

9. "Preliminary OARE Absolute Acceleration Measurements on STS-50", R. C. Blanchard, J.Y. Nicholson, J.R. Ritter, LaRc, Hampton, Virginia, NASA TM-107724, February 1993.

10. "A Note on the Extrapolation of PAS and OARE Acceleration Measurements to the CGF Location on STS-50", J. I. D. Alexander, M. J. B. Rogers, Center for Microgravity and Materials Research, University of Alabama-Huntsville, Huntsville, Alabama, September 1993.

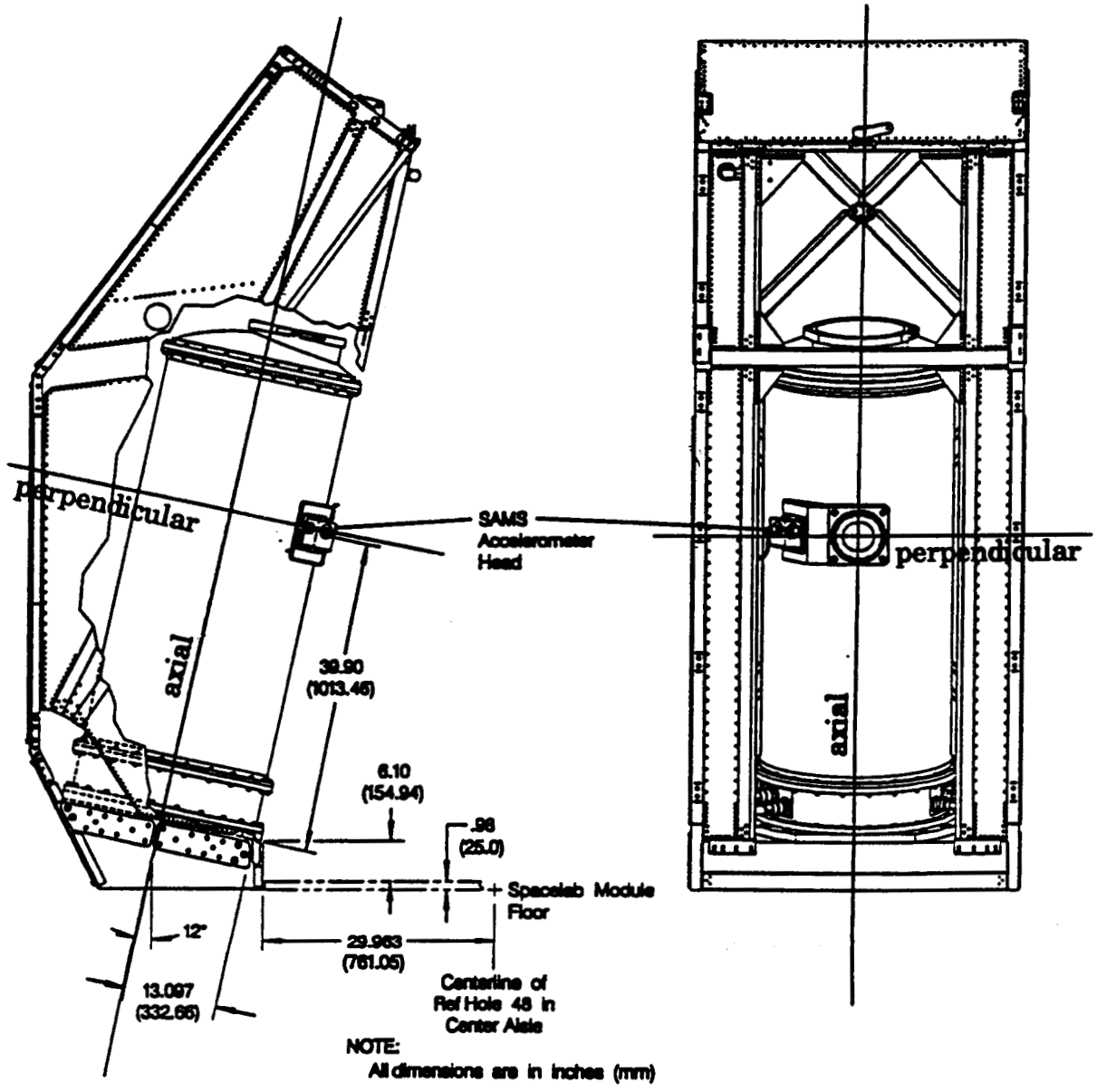

Figure 1 USML-1 Crystal Growth Furnace.

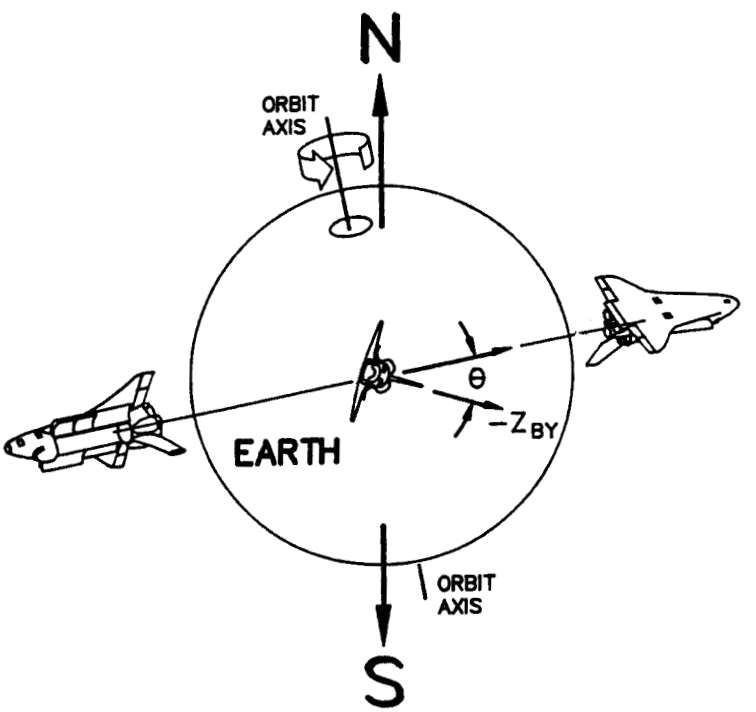

NOTE:
θ IS THE ROLL ANGLE ALIGNING THE CGF SAMPLE WITH THE VELOCITY VECTOR.

Figure 2 USML-1 Crystal Growth Furnace Attitude.

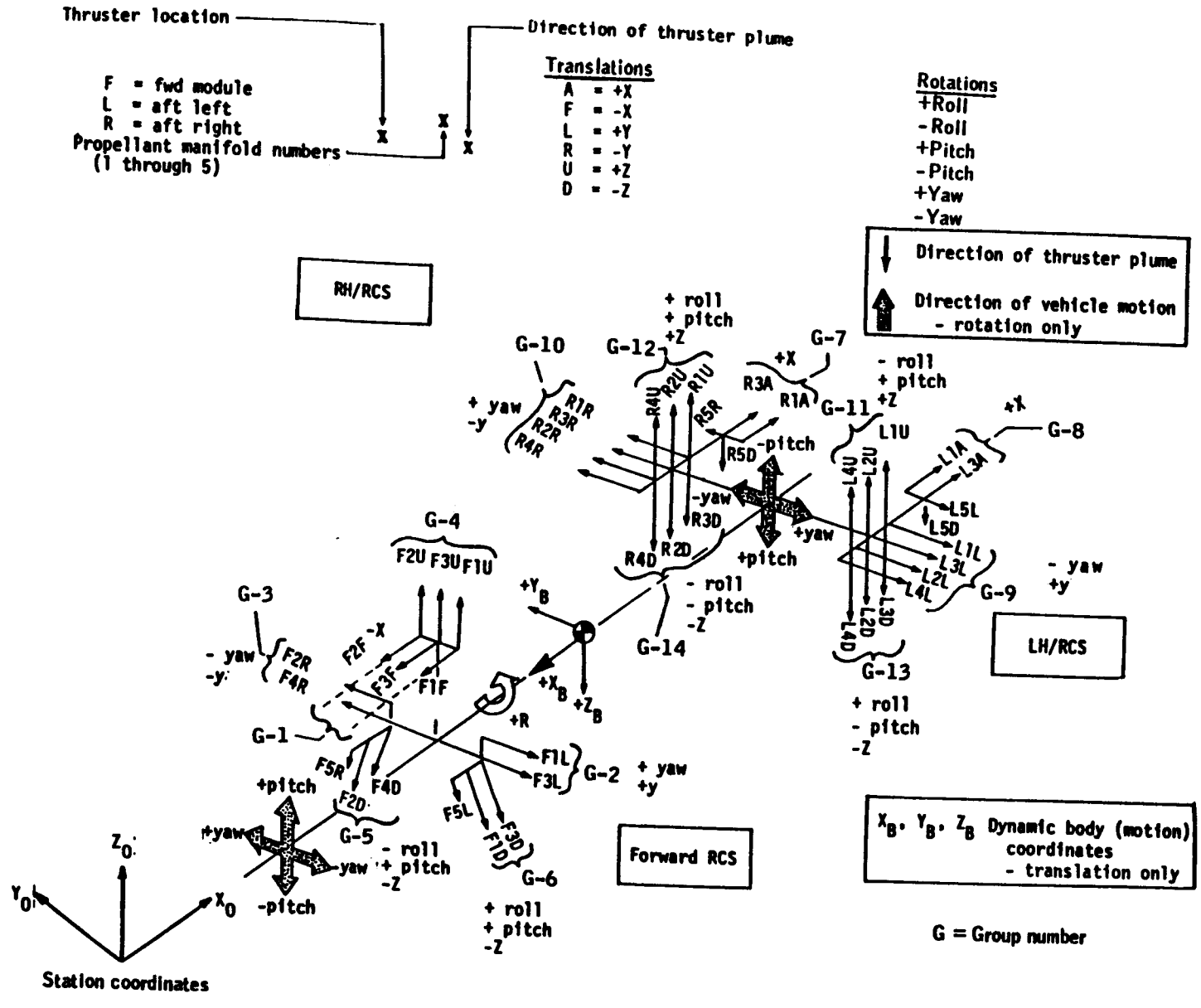

Figure 3 Orbiter Reaction Control System (RCS) Jet Configurations.

Thruster number	Thrust[a] direction	Scarf angle ϕ, deg	Thrust angle θ, deg	Axial component thrust[f], lb	Radial component thrust[f], lb	Resultant thrust[f] (F_t), lb	Thrust vector[b] location, in	Thruster mount attach points, in		
								X_0	Y_0	Z_0
F2F	-X	64.8	7.93	879.4	122.6	887.9	20.56	327.277	14.654	392.955
F3F	-X	65.0	7.94	879.5	122.7	888.0	20.66	327.383	0.0	394.450
F1F	-X	64.8	7.93	879.4	122.6	887.9	20.56	327.277	-14.654	392.955
F1L	+Y	22.8	2.10	873.6	32.0	874.2	13.87	362.671	-55.631	373.728
F3L	+Y	15.4	1.38	870.3	21.0	870.6	13.07	364.708	-58.579	359.250
F2R	-Y	22.8	2.10	873.6	32.0	874.2	13.87	362.671	55.631	373.728
F4R	-Y	15.4	1.38	870.3	21.0	870.6	13.07	364.708	58.579	359.250
F2U	+Z	24.1	2.25	874.4	34.3	875.1	13.88	350.925	14.394	399.588
F3U	+Z	22.7	2.09	873.5	31.9	874.1	13.71	350.917	0.0	400.818
F1U	+Z	24.1	2.25	874.4	34.3	875.1	13.88	350.925	-14.394	399.588
F2D[c]	-Z	59.5	7.18	881.7	111.0	888.6	19.29	333.840	49.814	372.350
F1D[c]	-Z	59.5	7.18	881.7	111.0	888.6	19.29	333.840	-49.814	372.350
F4D[c]	-Z	57.8	6.96	879.3	107.4	885.9	18.93	348.440	54.839	373.566
F3D[c]	-Z	57.8	6.96	879.3	107.4	885.9	18.93	348.440	-54.839	373.566
FSR[e] (Vernier)	-Z	59.5	7.18	23.3	3.1	24.5	9.75	324.350	53.830	357.900
FSL[c] (Vernier)	-Z	59.5	7.18	23.3	3.1	24.5	9.75	324.350	-53.830	357.900
R3A[d]	+X	0.0	0.0	870.0	0.0	870.0	0.0	1555.293	137.00	473.058
R1A[d]	+X	0.0	0.0	870.0	0.0	870.0	0.0	1555.293	124.00	473.058
L3A[d]	+X	0.0	0.0	870.0	0.0	870.0	0.0	1555.293	-137.00	473.058
L1A[d]	+X	0.0	0.0	870.0	0.0	870.0	0.0	1555.293	-124.00	473.058
L4L	+Y	16.3	1.47	870.5	22.4	870.8	13.10	1516.00	-136.77	459.00
L2L	+Y	16.3	1.47	870.5	22.4	870.8	13.10	1529.00	-136.77	459.00
L3L	+Y	16.3	1.47	870.5	22.4	870.8	13.10	1542.00	-136.77	459.00
L1L	+Y	16.3	1.47	870.5	22.4	870.8	13.10	1555.00	-136.77	459.00
R4R	-Y	16.3	1.47	870.5	22.4	870.8	13.10	1516.00	136.77	459.00
R2R	-Y	16.3	1.47	870.5	22.4	870.8	13.10	1529.00	136.77	459.00
R3R	-Y	16.3	1.47	870.5	22.4	870.8	13.10	1542.00	136.77	459.00
R1R	-Y	16.3	1.47	870.5	22.4	870.8	13.10	1555.00	136.77	459.00
L4U	+Z	0.0	0.0	870.0	0.0	870.0	0.0	1516.00	-132.00	480.50
L2U	+Z	0.0	0.0	870.0	0.0	870.0	0.0	1529.00	-132.00	480.50
L1U	+Z	0.0	0.0	870.0	0.0	870.0	0.0	1542.00	-132.00	480.50
R4U	+Z	0.0	0.0	870.0	0.0	870.0	0.0	1516.00	132.00	480.50
R2U	+Z	0.0	0.0	870.0	0.0	870.0	0.0	1529.00	132.00	480.50
R1U	+Z	0.0	0.0	870.0	0.0	870.0	0.0	1542.00	132.00	480.50
L4D[e]	-Z	0.0	0.0	870.0	0.0	870.0	0.0	1516.00	-111.945	437.403
L2D[e]	-Z	0.0	0.0	870.0	0.0	870.0	0.0	1529.00	-111.00	440.00
L3D[e]	-Z	0.0	0.0	870.0	0.0	870.0	0.0	1542.00	-110.055	442.597
R4D[e]	-Z	0.0	0.0	870.0	0.0	870.0	0.0	1516.00	111.945	437.403
R2D[e]	-Z	0.0	0.0	870.0	0.0	870.0	0.0	1529.00	111.00	440.00
R3D[e]	-Z	0.0	0.0	870.0	0.0	870.0	0.0	1542.00	110.055	442.597
L5D (Vernier)	-Z	0.0	0.0	24.09	0.0	24.09	0.0	1565.00	-118.00	455.44
R5D (Vernier)	-Z	0.0	0.0	24.09	0.0	24.09	0.0	1565.00	118.00	455.44
R5R (Vernier)	-Y	16.3	1.47	24.0	0.6	24.0	6.19	1565.00	143.68	459.00
L5L (Vernier)	+Y	16.3	1.47	24.0	0.6	24.0	6.19	1565.00	-143.68	459.00

[a]Translational direction.
[b]Distance from mount attach point, along thruster centerline.
[c]Canted 37° outboard in the Y-Z plane.
[d]Canted up 10° in the X-Y plane.
[e]Canted aft 12° in the X-Y plane and 20° outboard in the Y-Z plane.
[f]For impingement effects above 475,000 feet, refer to Aerodynamic Design Data Book, Vol. I (SD72-SH-0060-1L-7 Appendix C).
[g]For impingement effects, refer to EX32/8202-24.

Figure 4 Thrust Values and Locations of Orbiter RCS Jets.

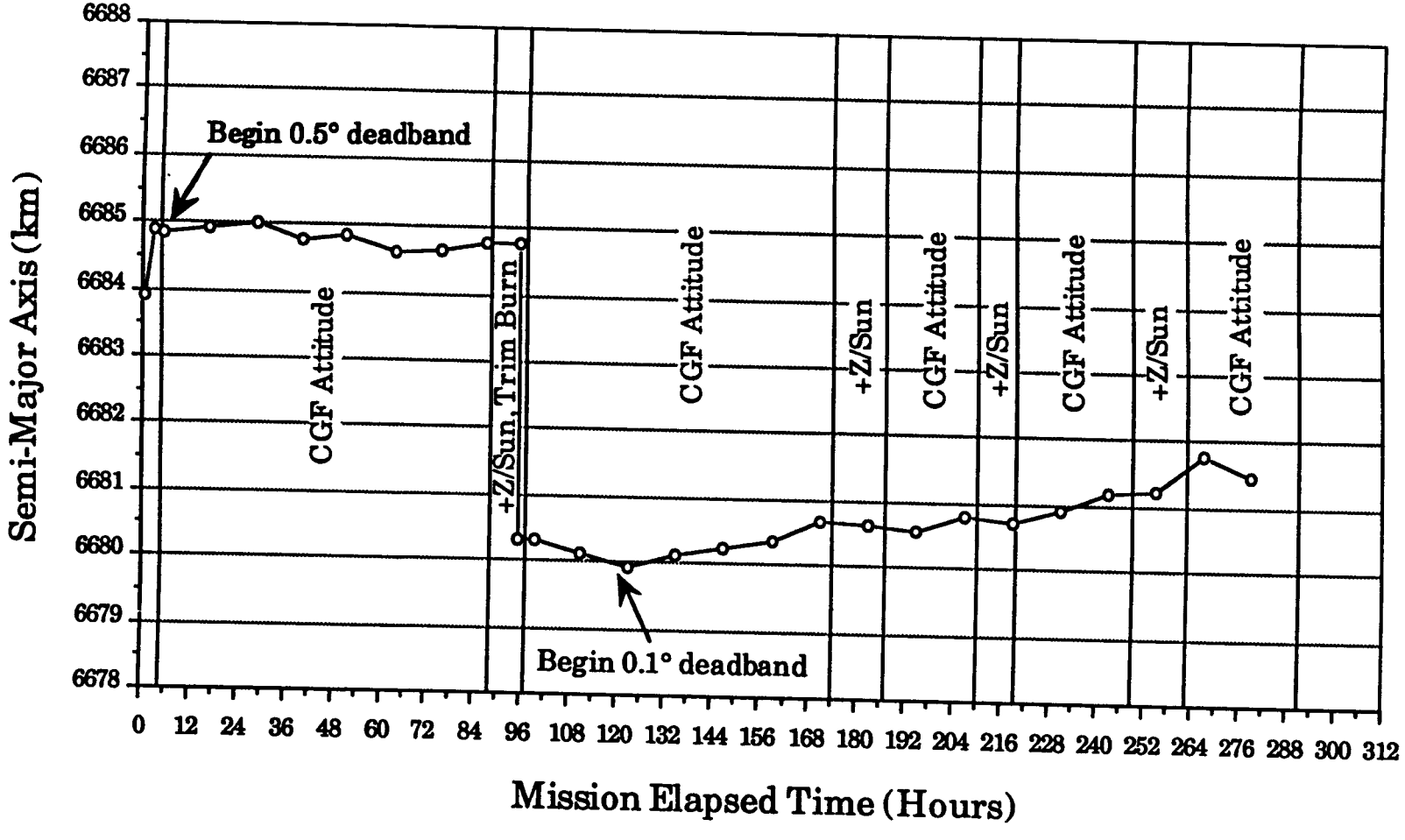

Figure 5 USML-1 Semi-Major Axis History.

SUMMARY STATUS OF THE SPACE ACCELERATION MEASUREMENT SYSTEM (SAMS) - SEPTEMBER 1993

Richard DeLombard
NASA Lewis Research Center, Cleveland, Ohio.

ABSTRACT

The Space Acceleration Measurement System (SAMS) was developed to measure the microgravity acceleration environment to which NASA science payloads are exposed during microgravity science missions on the shuttle. Six flight units have been fabricated to date. The inaugural flight of a SAMS unit was on STS-40 in June 1991 as part of the First Spacelab Life Sciences mission. Since that time, SAMS has flown on six additional missions and gathered eighteen gigabytes of data representing sixty-eight days of microgravity environment. The SAMS units have been flown in the shuttle middeck and cargo bay, in the Spacelab module, and in the Spacehab module.

This paper summarizes the missions and experiments which SAMS has supported. The quantity of data and the utilization of the SAMS data is described.

Future activities are briefly described for the SAMS project and the Microgravity Measurement and Analysis Project (MMAP) to support science experiments and scientists with microgravity environment measurement and analysis.

Joint "L+1" Science Review for USML-1 and USMP-1 with the Microgravity Measurement Group, September 22-24, 1993, Huntsville, Alabama, USA.

Acronyms

ACAP	Acceleration Characterization and Analysis Project
BIMDA	Bio-Serve /ITA Materials Dispersion Apparatus
CD-ROM	Compact Disk Read Only Memory
CGF	Crystal Growth Furnace
EURECA	European Retrievable Carrier
FMPT	First Materials Processing Test
IML	International Microgravity Laboratory
KSC	NASA Kennedy Space Center
LeRC	NASA Lewis Research Center
LPE	Lambda Point Experiment
MEPHISTO	Matérial pour l'Etude des Phénoménes Intéressant la Solidification sur Terre et en Orbite
MMAP	Microgravity Measurement and Analysis Project
MPESS	Mission Peculiar Experiment Support Structure
MSAD	Microgravity Science and Applications Division
MSFC	NASA Marshall Space Flight Center
NASDA	National Space Development Agency of Japan
OARE	Orbital Acceleration Research Experiment
PCG	Protein Crystal Growth
PI	Principal Investigator
POCC	Payload Operations Control Center
SAMS	Space Acceleration Measurement System
SH	Spacehab
SL-J	Spacelab J
SLS	Spacelab Life Sciences
SMIDEX	Shuttle Middeck Experiment
SMSP	Shuttle-Mir Science Program
SSCE	Solid Surface Combustion Experiment
STDCE	Surface Tension Driven Convection Experiment
USML	United States Microgravity Laboratory
USMP	United State Microgravity Payload

1.0 BACKGROUND

1.1 Need for General Purpose Accelerometer

The mission of NASA's microgravity science program is to utilize the unique characteristics of the space environment, primarily the near absence of accelerations, to expand man's knowledge of physics, chemistry, materials and fluid sciences, and biotechnology; to understand the role of gravity in materials processing; and, where possible, to demonstrate the feasibility of space production of improved materials that have high technological, and possible commercial, utility.

Environmental factors (e.g., temperature, pressure, acceleration level) are typically measured during microgravity science missions to characterize the conditions to which the experiments are exposed. In the past, many science experiments, which were particularly sensitive to acceleration levels, had incorporated an accelerometer within the experiment package. The need for a general purpose acceleration measurement system arose from those numerous special purpose accelerometers. A general purpose system was desired which could be utilized as a standard to measure the microgravity environment for many diverse experiments in different locations on the Orbiter. Such a system should also be capable of multiple flights and configurations for the support of different experiments on successive missions.

The SAMS project was conceived in 1986 to develop such a general purpose instrument to measure low-levels of acceleration at experiment locations on the space shuttle Orbiter. The SAMS project was assigned to the NASA Lewis Research Center (LeRC) by the NASA Headquarters Office of Space Science and Applications, Microgravity Science and Applications Division (MSAD). The primary experiments to be supported are those funded by the MSAD, although other experiments are occasionally supported through arrangements with MSAD.

1.2 Development of SAMS Flight Units

Four general purpose "middeck-style" SAMS units were fabricated in-house at LeRC by 1990. This style of unit is capable of operation in the shuttle middeck, Spacelab module single and double racks, Spacelab module center aisle, and in the Spacehab module. The first unit was delivered to the NASA Kennedy Space Center (KSC) on March 26, 1990 for integration into the first Spacelab Life Sciences (SLS-1) mission (STS-40).

Two specialized "cargo bay-style" SAMS units were fabricated in-house at LeRC by late 1991. This style of unit is capable of operation in the shuttle cargo bay on a Mission Peculiar Experiment Support Structure (MPESS). These two units were delivered to KSC in April 1992 for integration into the first United State Microgravity Payload (USMP-1) mission (STS-52). These units were made expressly for the USMP-series of missions. These two styles of SAMS units are described in reference 1.

Each of the SAMS units may be connected to three remote triaxial sensor heads by umbilical cables. The response of each of these sensor heads may be individually set to one of six low-pass frequencies. This provides the capability to tailor the sensor head response to the needs of the science experiment being supported.

2.0 SAMS FLIGHT OPERATIONS AND RESULTS

The SAMS units have flown on seven shuttle science missions to date with a wide range of carriers and sensor head frequency responses. The accumulated data continues to provide insight into the microgravity environment experienced on-board the shuttle. The data continues to be used in the analysis of science data from a variety of experiments on the past missions. Efforts are also on-going in planning modifications to future missions for such areas as crew exercise methods and vehicle structural investigations. These are using past SAMS data as well as acquiring new data from the future flights.

2.1 Missions and Experiments

Table 3 lists the various missions which have included a SAMS unit along with the pertinent characteristics of the mission and the SAMS unit. These missions have ranged from missions with intensive science operations (e.g., USML-1) to missions involving satellite launches with a few science experiments on-board (e.g., STS-43). Typically, for primary microgravity science missions, the shuttle flies in a favorable attitude with a minimum number of attitude changes which may disturb the experiments. This results in a fairly "quiet" mission with relatively little disturbance to the microgravity environment. For other missions, the "quiet" microgravity environment may be maintained for a short period of time, but other segments of the missions may be subject to high levels of acceleration as other activities are conducted.

The main purpose of the SLS-1 mission was to study the mechanisms, magnitudes, and time courses of certain physiological changes that occur during space flight and to investigate the consequences of the body's adoption to microgravity and readjustment to 1-g [ref. 2]. The Solid Surface Combustion Experiment (SSCE) flew on this mission, one in a series of eight SSCE flights. The SAMS unit A measured the acceleration environment for the SSCE principal investigator (PI) and also to acquire data to enable a study of the transmission of accelerations through the Spacelab module structure. SLS-1 was launched on June 5, 1991 and operated for nine days with SAMS recording for 168 hours, resulting in 0.37 gigabytes of data.

The Protein Crystal Growth (PCG) and the Bio-Serve /ITA Materials Dispersion Apparatus (BIMDA) flew on the STS-43 mission along with a re-flight of SSCE and the SAMS unit E. The acceleration environment was measured on a locker door between PCG and BIMDA to support the PI's

associated with those experiments. The acceleration environment was measured directly on the SSCE apparatus to support the PI associated with SSCE. A sensor head was also located on the crew exercise treadmill to measure the effects of this device on the microgravity environment. STS-43 was launched on August 2, 1991, and operated on-orbit for nine days with SAMS recording data for 186.5 hours, resulting in 2.70 gigabytes of data.

The first International Microgravity Laboratory (IML-1), the first United States Microgravity Laboratory (USML-1), and the Spacelab J (SL-J) missions were dedicated microgravity science missions. Each had a multitude of experiments which were operated during the course of the mission.

The IML-1 mission is the first in a series of shuttle flights dedicated to fundamental materials and life sciences research. As part of this series of missions, scientists from around the world have developed experiments that crew members completed inside the Spacelab module [ref. 3]. For IML-1, the primary experiments supported were those operated in the Fluid Experiment System (FES) and the Vapor Crystal Growth System (VCGS) apparatus. Sensor heads were also located near the Microgravity Vestibular Investigations rotating chair. The sensor heads were arranged to allow the vibrations generated by the chair to be compared with the vibration levels experienced in the rack. This data will contribute to the study of acceleration transfer through the vehicle structure. IML-1 was launched on January 22, 1992, and operated on-orbit for eight days with SAMS recording data for 162.5 hours, resulting in 4.63 gigabytes of data.

The USML-series of missions is one part of a science and technology program that will open NASA's next great era of discovery. This new era is certain to revolutionize the way we think about space and our world as dramatically as did the Apollo lunar missions. USML-1 flew in orbit for fourteen days, providing greater opportunities for research in materials science, fluid dynamics, biotechnology, and combustion science. In addition, the missions will also provide much of the experience in performing research in space and in the design of instruments needed for space station operations and the programs to follow in the 21st century [ref. 4].

For USML-1, the primary experiments supported by SAMS were the Surface Tension Driven Convection Experiment (STDCE), the Crystal Growth Furnace (CGF) and a multitude of experiments operated within the glovebox. USML-1 was launched on June 25, 1992 with SAMS recording data for 294 hours, resulting in 1.36 gigabytes of data.

Spacelab J was a joint venture between NASA and the National Space Development Agency of Japan (NASDA). Using the Spacelab module, forty-three experiments - thirty-four sponsored by NASDA and nine sponsored by NASA - were performed in the areas of microgravity materials and life sciences [ref. 5]. The SAMS sensor heads were mounted within the First Materials Processing Test (FMPT) equipment supplied by NASDA. There were multiple experiments operated within the FMPT equipment,

both materials science and life science experiments. SL-J was launched on August 18, 1992, and operated on-orbit for twelve days with SAMS recording data for 169 hours, resulting in 2.44 gigabytes of data.

USMP-1 and the first Spacehab module (SH-1) missions were shared missions which included microgravity science experiments as well as other primary payloads.

Six days of STS-52 were flown in a "quiet" mode and attitude for the USMP-1 microgravity science to be conducted. The remainder of the mission was occupied with other activities, such as a satellite launch and experiments involving remote manipulator arm operations. The microgravity science experiments on USMP-1 were the Lambda Point Experiment (LPE) and the Matérial pour l'Etude des Phénoménes Intéressant la Solidification sur Terre et en Orbite (MEPHISTO). The MEPHISTO apparatus was supplied by the French Centre National d'Etudes Spatiales. During this mission, the SAMS units sent some data via shuttle downlink to the Payload Operations Control Center (POCC) at the NASA Marshall Space Flight Center (MSFC). The remainder of the data was recorded on optical disks. The downlinked data allowed near-real-time decisions to be made by the PI's based on the microgravity environment. USMP-1 was launched on October 22, 1992 and operated on-orbit for ten days with SAMS acquiring data for 228 hours, resulting in 2.97 gigabytes of data.

A major objective of the STS-57 mission was devoted to the capture and return to Earth of the European Retrievable Carrier (EURECA) which had been launched one year earlier. The maiden flight of the Spacehab module (SH-1) was the other primary payload on STS-57. There were a variety of commercial and NASA experiments carried inside the Spacehab module. One SAMS sensor head was mounted near the Environmental Control Life Support System Flight Experiment on the starboard side of the forward bulkhead. Another sensor head was mounted to the module structure in a similar fashion on the port side of that bulkhead. The third sensor head was mounted to the door of a stowage locker toward the center of that bulkhead. STS-57 was launched on June 21, 1992, and operated on-orbit for ten days with SAMS recording data for 162 hours, resulting in 3.38 gigabytes of data.

More detailed information on these missions and experiments may be obtained by consulting various reports and descriptive literature produced for each mission.

2.2 Carriers

The SAMS "middeck-style" units were originally designed to be mounted in the middeck of the shuttle by occupying one of the stowage locker locations. Many missions have included microgravity payloads in the middeck.

The Spacelab module was designed as a space laboratory to be installed in the cargo bay of the shuttle and accessed via a tunnel from the middeck. Typically, the module is mounted toward the rear of

the cargo bay and envelops the vehicle center of mass while on-orbit. By design, the "middeck-style" SAMS unit can also be mounted in the Shuttle Middeck Experiment (SMIDEX) racks developed for the Spacelab module. Also, as part of the SAMS design, different components may be used to mount the SAMS unit to the center aisle floor of the Spacelab module.

The Spacehab module was expressly designed to accommodate experiments and lockers from the shuttle middeck. The "middeck-style" SAMS units mount directly in the module. The Spacehab module is mounted toward the forward end of the shuttle cargo bay and is also accessed via a tunnel from the middeck.

The MPESS carriers are truss structures designed to carry equipment in the shuttle cargo bay. The carriers attach to the Orbiter cargo bay sills and keel and may be mounted in nearly any location along the cargo bay. The MPESS carriers utilized by the USMP-series of missions incorporate subsystem equipment to supply power, thermal control and data services to the experiments.

2.3 Data Quantity

There are several different ways in which to describe the quantity of data acquired by SAMS on the various missions. One way is for the characterization of the shuttle microgravity environment. This environment has now been measured by a common instrument to an extent not accomplished before. The SAMS data allows comparison of environments for different missions as done in reference 6. This will also allow predictions to be made about the environment of future missions and will contribute toward the understanding of environments to be expected on space stations. To this end, SAMS has gathered data for an accumulated total of 68 days of on-orbit shuttle operations. This includes approximately 55 days of microgravity conditions.

Another way of describing the data quantity is the total time that the data represents. Since the three sensor heads are measuring different local environments, the total quantity of data acquired is significant for characterizing the local environment of various locations within the Spacelab module (for example). To this end, SAMS data represents 214 days of data from triaxial sensor heads.

Another way of describing the data quantity is the sheer quantity of data points measured during SAMS operations. This is indicative of the amount of data storage required to store the data or through which to search to find characteristics, trends, or other significant facets of the environment. To this end, SAMS data represents over four million samples of acceleration data. After data processing, this represents 17.9 gigabytes of acceleration data stored on computer disks.

For ease of access, the processed mission data has been put on compact disk read only memory (CD-ROM). This convenient form of data dissemination has been utilized for its de-facto standard across

many computer platforms and the data capacity of each disk. There have been twenty-three CD-ROM's prepared at the present time for five of the first seven missions.

2.4 Utilization of Data

For the first six SAMS missions, the Acceleration Characterization and Analysis Project (ACAP) at MSFC has analyzed the mission data. Summary reports have been prepared by ACAP to assist users in understanding the vast amount of data. ACAP has also prepared special analyses on occasion for characterizing certain aspects of shuttle and experiment operations. Correlation of acceleration data with the results from the science experiments will lead to a better understanding of the science. This also leads to a better understanding of the microgravity environment requirements of the experiment. Some of the reports and papers prepared with SAMS data are listed in the bibliography. Examples of these analyses are given below.

SAMS data was utilized in near-real-time during the USMP-1 mission by the LPE and MEPHISTO experiment teams to ascertain the microgravity environment and the effect of it on their experiment operation and data.

The SAMS data from the USML-1 mission has been extensively reviewed by ACAP for the PI's associated with the CGF.

Correlation of the thruster firing data with the SAMS acceleration data and observed events on glovebox combustion flames has been accomplished.

SAMS data has been used to examine the signature vibration patterns of the Ku-band communications antenna, crew activity, satellite launches, remote manipulator system operations, experiment generated vibrations, and the Life Sciences Laboratory Equipment refrigerator/freezer.

Some of the SAMS data has been utilized to better understand the isolation of crew exercise equipment so that this necessary activity will have a minimal effect on the microgravity environment.

2.5 Carrier Characterization

An objective of the SAMS data acquisition program is to enable characterization of the various microgravity science experiment carriers and locations within the carriers. On the multiple missions with SAMS units on-board, the coverage of carriers by frequency response measurements are shown in table 2. Covering the ranges of frequency response for the various carriers will facilitate the prediction of environment for future experiments.

2.6 Supported Science

The various types of science that have been supported by the SAMS measurements are combustion, fluids, materials, fundamental, and life science disciplines. Some of the experiments have indicated a strong need for direct measurement of the acceleration environment within the experiment. In these cases, the SAMS sensor head has been mounted within or on the experiment apparatus. This enhances the correlation of the acceleration data with the science data. The various science experiments supported by SAMS are listed in table 3. Other science experiments on these missions utilize the SAMS data even though they do not have a sensor head directly mounted to the experiment.

3.0 FUTURE ACTIVITIES

3.1 Future Missions

The SAMS units will continue to support the future microgravity shuttle science missions, such as the USML, IML and USMP series of missions. The SAMS project is also participating in the Shuttle-Mir Science Program (SMSP) and will install a SAMS unit on the Mir space station in early 1994. Another type of SAMS unit is currently under development to support the science experiments to be flown on the international space station.

The future missions for SAMS are listed in table 4 with the current scheduled launch date and the primary science experiments being supported.

A standard SAMS unit is being modified, along with shipping containers, procedures, launch containers, etc., to facilitate the launch of SAMS on a Progress vehicle to the space station Mir. The SAMS sensor heads will be used to measure the acceleration environment in various locations throughout Mir and will support some of the experiments planned for the SMSP. It is expected that SAMS will remain operational on Mir for approximately fifteen months with the possibility that operations may continue for several years.

A new SAMS unit is under development that will take advantage of the services and opportunities presented by the international space station. This new SAMS unit will not require dedicated cables from the sensor heads to the SAMS unit and will have enhanced data processing capabilities. Master control of the SAMS unit and the sensor heads will be accomplished by the SAMS project. Control of sensor head and data processing characteristics will be accomplished by the PI's at their operations center in near-real-time. Display of SAMS data by downlink will be made at the PI's operations center.

3.2 Data Dissemination

In the very near future, the processed SAMS data will be available from a file server connected to the Internet. This will simplify both data access by the PI's and data dissemination by SAMS. Eventually, the summary reports prepared for each mission will be available in a multi-media format on the file server.

For SAMS on the international space station, some of the data will be available to PI's in near-real-time via downlink. The remainder of the data will be recorded for later downlink or return of storage media via shuttle re-supply missions. Processed data will then be available on CD-ROM and/or file server format.

3.3 OARE Operations

Under a different NASA project, the Orbital Acceleration Research Experiment (OARE) was designed and flown to measure the aerodynamic drag on the Orbiter vehicle during orbital flight. The sensors used in this accelerometer are more sensitive than the sensors used in SAMS and OARE was designed specifically to measure the very low frequency accelerations in the quasi-steady regime. This accelerometer has operated on STS-40 and STS-50. In early 1993, MSAD acquired the flight equipment and ground equipment infrastructure of the OARE project. The OARE will now be flown on the shuttle Columbia in concert with the SAMS units to support the science experiments. This data will continue to be useful for aerodynamic analyses for the Orbiter vehicle.

3.4 Microgravity Measurement And Analysis Project

A consolidation of the SAMS project and the ACAP project was initiated in mid-1993 resulting in the Microgravity Measurement and Analysis Project (MMAP) at LeRC. The MMAP will expand the roles of the previous projects to better serve the PI's needs for microgravity data, analysis and interpretation.

CONCLUDING REMARKS

Over a two year period, the SAMS instrument has acquired a vast amount of data which supports the efforts of a variety of activities. The SAMS data is being applied to the analysis of the microgravity science data for which the device was originally intended. The SAMS units will continue to be flown in support of future missions, carriers and experiments.

The SAMS data forms a vast amount of information from which analyses and studies may be performed, such as, prediction of future mission environments, recommended carriers, recommended shuttle attitudes, effects of vibration isolation systems, etc.

In the near future, comparisons may be made between the microgravity environment of the shuttle and the Mir space station. In the not-so-distant future, a similar comparison may be made between the international space station, Mir and the shuttle.

REFERENCES

1. R. DeLombard, B. D. Finley, and C. R. Baugher, "Development of and Flight Results From the Space Acceleration Measurement System (SAMS)," NASA TM 105652 (AIAA 92-0354), January 1992.

2. Spacelab Life Sciences 1, brochure number NP-120, NASA Lyndon B. Johnson Space Center.

3. First International Microgravity Laboratory, brochure, NASA Marshall Space Flight Center.

4. The First United States Microgravity Laboratory, brochure, NASA Marshall Space Flight Center.

5. Spacelab J, brochure, NASA Marshall Space Flight Center.

6. C. R. Baugher, G. L. Martin, R. DeLombard, "Low-Frequency Vibration Environment for Five Shuttle Missions," NASA TM 106059, also AIAA 93-0832, March 1993.

Bibliography

1. NASA TM 105301, November 1991, R. DeLombard and B. D. Finley (Sverdrup Technology, Inc.) "Space Acceleration Measurement System Description and Operations on the First Spacelab Life Sciences Mission".

2. NASA CP-10094, Richard DeLombard, "Science Objectives of the Early Space Acceleration Measurement System Missions", Prepared for the International Workshop on Vibration Isolation Technology for Microgravity Science Applications, NASA LeRC, April 23-25, 1991.

3. NASA TM 105261, William M. Foster II, "Thermal Verification Testing of Commercial Printed-Circuit Boards for Spaceflight", Prepared for the 1992 Annual Reliability and Maintainability Symposium sponsored by the Institute of Electrical and Electronics Engineers, Las Vegas, Nevada, January 21-23, 1992.

4. NASA TM 105300, January 1992, John E. Thomas, Rex B. Peters (Sundstrand Data Control, Inc.), Brian D. Finley (Sverdrup Technology, Inc.), "Space Acceleration Measurement System Triaxial Sensor Head Error Budget".

5. NASA TM 105652, AIAA 92-0354, January 6-9, 1992, R. DeLombard, B. D. Finley (Sverdrup Technology, Inc.) and C. R. Baugher (NASA MSFC), "Development of and Flight Results from the Space Acceleration Measurement System (SAMS)", Prepared for the 30th Aerospace Sciences Meeting and Exhibit sponsored by the American Institute of Aeronautics and Astronautics, Reno, Nevada, January 6-9, 1992.

6. NASA TM 105960, May 1993, Richard DeLombard, "Proposed Ground-Based Control of Accelerometer on Space Station Freedom", Prepared for the 39th International Instrumentation Symposium sponsored by the Instrument Society of America, Albuquerque, New Mexico, May 2-6, 1993.

7. AIAA 93-0832, January 1993, C. R. Baugher, G. L. Martin, R. DeLombard, "Review of Shuttle Vibration Environment", Prepared for the 31st Aerospace Sciences Meeting and Exhibit sponsored by the American Institute of Aeronautics and Astronautics, Reno, Nevada, January 11-14, 1993. Also NASA TM 106059, March 1993.

8. M. J. B. Rogers, C. R. Baugher, R. DeLombard, et. al. "Low Gravity Environment On-Board Columbia During STS-40", Prepared for the 31st Aerospace Sciences Meeting and Exhibit sponsored by the American Institute of Aeronautics and Astronautics, Reno, Nevada, January 11-14, 1993.

10. IAF-90-350, October 6-12, 1990, G. L. Martin, C. R. Baugher, R. DeLombard, "Vibration Environment: Acceleration Mapping Strategy and Microgravity Requirements for Spacelab and Space Station".

11. Project Report, 1992, C. R. Baugher and F. H. Henderson (Teledyne Brown Engineering); "Early Summary Report of Mission Acceleration Measurements from STS-40".

12. Project Report, February 28, 1992, C. R. Baugher and F. H. Henderson (Teledyne Brown Engineering); "Early Summary Report of Mission Acceleration Measurements from STS-43".

13. Project Report, June 1992 (draft),C. R. Baugher and F. H. Henderson (Teledyne Brown Engineering); "Early Summary Report of Mission Acceleration Measurements from STS-42".

14. Project Report, March 31, 1993, C. R. Baugher and F. H. Henderson (Teledyne Brown Engineering); "Summary Report of Mission Acceleration Measurements from STS-47".

15. Project Report, June 18, 1993, C. R. Baugher and F. H. Henderson (Teledyne Brown Engineering); "STS-50 Summary Report of Mission Acceleration Measurements".

16. Project Report, August 2, 1993 (draft), C. R. Baugher and F. H. Henderson (Teledyne Brown Engineering); "STS-52 Mission Acceleration Measurements Summary and Sensor Report".

17. Project Report, February 28, 1992, C. R. Baugher and F. H. Henderson (Teledyne Brown Engineering); "Sensor Report for STS-40 & STS-43".

18. Project Report, May 28, 1993, C. R. Baugher and F. H. Henderson (Teledyne Brown Engineering); "STS-42 Sensor Report".

19. Project Report, May 21, 1993 (draft), C. R. Baugher and F. H. Henderson (Teledyne Brown Engineering); "STS-47 Sensor Report".

20. Project Report, May 11, 1993 (draft), C. R. Baugher and F. H. Henderson (Teledyne Brown Engineering); "STS-50 Sensor Report".

Table 1: Missions Supported by SAMS

Mission	Microgravity Payload Category	Microgravity Carrier	SAMS Unit	Frequency Responses
SLS-1	Primary	Spacelab module	A	5, 5, 5
STS-43	Secondary	Shuttle middeck	E	50, 50, 2.5
IML-1	Primary	Spacelab module	D	100, 100, 2.5
USML-1	Primary	Spacelab module	C	25, 5, 2.5
SL-J	Primary	Spacelab module	E	50, 50, 2.5
USMP-1	Primary	MPESS	F G	25, 10 100, 100
SH-1	Secondary	Spacehab module	A	100, 50, 5

Table 2: Frequency Coverage of Carriers by SAMS Measurements

	Sensor Head Frequency Response (Hertz)					
Carrier	2.5	5	10	25	50	100
Middeck	STS-43				STS-43	
Spacelab Module	IML-1, USML-1, SL-J	USML-1, SLS-1		USML-1	SL-J	IML-1
MPESS			USMP-1	USMP-1		USMP-1
Spacehab Module		SH-1			SH-1	SH-1

Table 3: Science Experiments Supported by SAMS

Science Category	Mission	Experiment
Combustion	SLS-1	Solid Surface Combustion Experiment
Fluids	IML-1	Fluid Experiment System
	USML-1	Glovebox experiments
	USML-1	Surface Tension Driven Convection Experiment
Materials	STS-43	Protein Crystal Growth
	STS-43	Bio-Serve /ITA Materials Dispersion Apparatus
	USML-1	Crystal Growth Furnace
	USML-1	Glovebox experiments
	SL-J	First Materials Processing Test - Material Science
	USMP-1	MEPHISTO
Fundamental	IML-1	Critical Point Facility
	USMP-1	Lambda Point Experiment
Life	SLS-1	Crew activity
	USML-1	Isolated crew exercise ergometer
	SL-J	First Materials Processing Test - Life Science
	SL-J	Frog Embryology Experiment
	SH-1	Environmental Control Life Support System Flight Experiment

Table 4: Future Microgravity Science Missions for SAMS

Mission	Launch Date	Experiments
SH-2	1/20/94	General carrier measurements
USMP-2	2/24/94	Advanced Automated Directional Solidification Furnace
		MEPHISTO
		Critical Fluid Light Scattering Experiment
		Isothermal Dendritic Growth Experiment
IML-2	6/23/94	Bubble Drop Particle Unit
		Critical Point Facility
		Electromagnetic Containerless Processing Facility
Shuttle - Mir Science Program	3/94	Carrier characterization
Middeck missions	2 per year	Various middeck microgravity experiments
USMP-3	10/95	Advanced Automated Directional Solidification Furnace
		MEPHISTO
		Gravity Probe - B
USML-2	9/95	Surface Tension Driven Convection Experiment
		Crystal Growth Furnace
		Glovebox experiments
		Mechanics of Granular Materials
International space station	6/97	Various station facility-class experiments, such as Space Station Furnace Facility, Combustion Module, Fluids Module

Discussion

Question: *How are the accelerometer heads configured ? Are they close to the cg ?*

Answer: It really varies by mission. On IML-1 they were fairly close. We had a sensor head toward the top of the rack and the base of the rack and out in the center aisle right in front of that rack. In SL-J the two Japanese experiments were on either side of the aisle, so we kind of had them opposite. On USML-I, I think they were fairly close to the CG but again across the center aisle around the Glovebox and surface tension and across the aisle on the CGF. You can look at the charts and see where those are, but I think, typically, they have been back toward the back of the module. Somewhat near the CG. We had three sensor heads in the Middeck. We were kind of spread out because PCG and BIMDA (Bio-Serve /ITA Materials Dispersion Apparatus), were at one side of the Middeck area and Solid Surface Combustion Experiment was at the other end and the treadmill was over in the floor in the middle. So it was kind of a distributed set of data there.

NASA ULTRA-SENSITIVE MINIATURE ACCELEROMETER

Frank T. Hartley* **and Paul M. Zavracky**+

*Supervisor Advanced Test and Measurement
California Institute of Technology, Jet Propulsion Laboratory
+Professor Microsensor Laboratory, Northeastern University

ABSTRACT

Using micro-machined silicon technology, an ultra-sensitive miniature accelerometer can be constructed which meets the requirements for microgravity experiments in the space environment. Such an accelerometer will have a full scale sensitivity of 10^{-2} g a resolution of 10^{-8} g, low cross-axis sensitivity, and low temperature sensitivity. Mass of the device is approximately five grams and its footprint is 2 cm x 2 cm. Innovative features of the accelerometer, which are patented, are: electrostatic caging to withstand handling shock up to 150 g, in-situ calibration, in situ performance characterization, and both static and dynamic compensation. The transducer operates on a force balance principle wherein the displacement of the proof mass is monitored by measuring tunneling electron current flow between a conductive tip and a fixed platen. The four major parts of the accelerometer are tip die, incorporating the tunneling tip and four field plates for controlling pitch and roll of the proof mass; two proof mass dies, attached to the surrounding frame by sets of four "crab-leg" springs; and a force plate die. The four parts are fuse-bonded into a complete assembly. External electrical connections are made at bond pads on the front surface of the force plate die. Materials and processes used in the construction of the transducer are compatible with volume production.

INTRODUCTION

Microgravity accelerometers used in the harsh environment of space must measure extremely small static and near-static events. Typical applications are experiments on the space shuttle, free flyers, space station, sounding rockets, etc.

The Micro Gravity Acceleration (MGA) sensor is a spring/mass type using a unique "crab-leg" spring support configuration and electrostatic platen force for control of mass movement. Design features of the MGA sensor include electron tunneling tip position detection, electrostatic force feedback, pitch and roll control, electrostatic compensation, and low off-axis sensitivity. A tunneling electron tip provides precision proof mass positioning and measurement for closed-loop

Joint "L+1" Science Review for USML-1 and USMP-1 with the Microgravity Measurement Group, September 22-24, 1993, Huntsville, Alabama, USA.

6. NASA TM 105960, May 1993, Richard DeLombard, "Proposed Ground-Based Control of Accelerometer on Space Station Freedom", Prepared for the 39th International Instrumentation Symposium sponsored by the Instrument Society of America, Albuquerque, New Mexico, May 2-6, 1993.

7. AIAA 93-0832, January 1993, C. R. Baugher, G. L. Martin, R. DeLombard, "Review of Shuttle Vibration Environment", Prepared for the 31st Aerospace Sciences Meeting and Exhibit sponsored by the American Institute of Aeronautics and Astronautics, Reno, Nevada, January 11-14, 1993. Also NASA TM 106059, March 1993.

8. M. J. B. Rogers, C. R. Baugher, R. DeLombard, et. al. "Low Gravity Environment On-Board Columbia During STS-40", Prepared for the 31st Aerospace Sciences Meeting and Exhibit sponsored by the American Institute of Aeronautics and Astronautics, Reno, Nevada, January 11-14, 1993.

10. IAF-90-350, October 6-12, 1990, G. L. Martin, C. R. Baugher, R. DeLombard, "Vibration Environment: Acceleration Mapping Strategy and Microgravity Requirements for Spacelab and Space Station".

11. Project Report, 1992, C. R. Baugher and F. H. Henderson (Teledyne Brown Engineering); "Early Summary Report of Mission Acceleration Measurements from STS-40".

12. Project Report, February 28, 1992, C. R. Baugher and F. H. Henderson (Teledyne Brown Engineering); "Early Summary Report of Mission Acceleration Measurements from STS-43".

13. Project Report, June 1992 (draft),C. R. Baugher and F. H. Henderson (Teledyne Brown Engineering); "Early Summary Report of Mission Acceleration Measurements from STS-42".

14. Project Report, March 31, 1993, C. R. Baugher and F. H. Henderson (Teledyne Brown Engineering); "Summary Report of Mission Acceleration Measurements from STS-47".

15. Project Report, June 18, 1993, C. R. Baugher and F. H. Henderson (Teledyne Brown Engineering); "STS-50 Summary Report of Mission Acceleration Measurements".

16. Project Report, August 2, 1993 (draft), C. R. Baugher and F. H. Henderson (Teledyne Brown Engineering); "STS-52 Mission Acceleration Measurements Summary and Sensor Report".

17. Project Report, February 28, 1992, C. R. Baugher and F. H. Henderson (Teledyne Brown Engineering); "Sensor Report for STS-40 & STS-43".

18. Project Report, May 28, 1993, C. R. Baugher and F. H. Henderson (Teledyne Brown Engineering); "STS-42 Sensor Report".

19. Project Report, May 21, 1993 (draft), C. R. Baugher and F. H. Henderson (Teledyne Brown Engineering); "STS-47 Sensor Report".

20. Project Report, May 11, 1993 (draft), C. R. Baugher and F. H. Henderson (Teledyne Brown Engineering); "STS-50 Sensor Report".

Table 1: Missions Supported by SAMS

Mission	Microgravity Payload Category	Microgravity Carrier	SAMS Unit	Frequency Responses
SLS-1	Primary	Spacelab module	A	5, 5, 5
STS-43	Secondary	Shuttle middeck	E	50, 50, 2.5
IML-1	Primary	Spacelab module	D	100, 100, 2.5
USML-1	Primary	Spacelab module	C	25, 5, 2.5
SL-J	Primary	Spacelab module	E	50, 50, 2.5
USMP-1	Primary	MPESS	F G	25, 10 100, 100
SH-1	Secondary	Spacehab module	A	100, 50, 5

Table 2: Frequency Coverage of Carriers by SAMS Measurements

	Sensor Head Frequency Response (Hertz)					
Carrier	2.5	5	10	25	50	100
Middeck	STS-43				STS-43	
Spacelab Module	IML-1, USML-1, SL-J	USML-1, SLS-1		USML-1	SL-J	IML-1
MPESS			USMP-1	USMP-1		USMP-1
Spacehab Module		SH-1			SH-1	SH-1

Table 3: Science Experiments Supported by SAMS

Science Category	Mission	Experiment
Combustion	SLS-1	Solid Surface Combustion Experiment
Fluids	IML-1	Fluid Experiment System
	USML-1	Glovebox experiments
	USML-1	Surface Tension Driven Convection Experiment
Materials	STS-43	Protein Crystal Growth
	STS-43	Bio-Serve /ITA Materials Dispersion Apparatus
	USML-1	Crystal Growth Furnace
	USML-1	Glovebox experiments
	SL-J	First Materials Processing Test - Material Science
	USMP-1	MEPHISTO
Fundamental	IML-1	Critical Point Facility
	USMP-1	Lambda Point Experiment
Life	SLS-1	Crew activity
	USML-1	Isolated crew exercise ergometer
	SL-J	First Materials Processing Test - Life Science
	SL-J	Frog Embryology Experiment
	SH-1	Environmental Control Life Support System Flight Experiment

Table 4: Future Microgravity Science Missions for SAMS

Mission	Launch Date	Experiments
SH-2	1/20/94	General carrier measurements
USMP-2	2/24/94	Advanced Automated Directional Solidification Furnace
		MEPHISTO
		Critical Fluid Light Scattering Experiment
		Isothermal Dendritic Growth Experiment
IML-2	6/23/94	Bubble Drop Particle Unit
		Critical Point Facility
		Electromagnetic Containerless Processing Facility
Shuttle - Mir Science Program	3/94	Carrier characterization
Middeck missions	2 per year	Various middeck microgravity experiments
USMP-3	10/95	Advanced Automated Directional Solidification Furnace
		MEPHISTO
		Gravity Probe - B
USML-2	9/95	Surface Tension Driven Convection Experiment
		Crystal Growth Furnace
		Glovebox experiments
		Mechanics of Granular Materials
International space station	6/97	Various station facility-class experiments, such as Space Station Furnace Facility, Combustion Module, Fluids Module

Discussion

Question: *How are the accelerometer heads configured ? Are they close to the cg ?*

Answer: It really varies by mission. On IML-1 they were fairly close. We had a sensor head toward the top of the rack and the base of the rack and out in the center aisle right in front of that rack. In SL-J the two Japanese experiments were on either side of the aisle, so we kind of had them opposite. On USML-I, I think they were fairly close to the CG but again across the center aisle around the Glovebox and surface tension and across the aisle on the CGF. You can look at the charts and see where those are, but I think, typically, they have been back toward the back of the module. Somewhat near the CG. We had three sensor heads in the Middeck. We were kind of spread out because PCG and BIMDA (Bio-Serve /ITA Materials Dispersion Apparatus), were at one side of the Middeck area and Solid Surface Combustion Experiment was at the other end and the treadmill was over in the floor in the middle. So it was kind of a distributed set of data there.

NASA ULTRA-SENSITIVE MINIATURE ACCELEROMETER

Frank T. Hartley* **and Paul M. Zavracky** +

*Supervisor Advanced Test and Measurement
California Institute of Technology, Jet Propulsion Laboratory
+Professor Microsensor Laboratory, Northeastern University

ABSTRACT

Using micro-machined silicon technology, an ultra-sensitive miniature accelerometer can be constructed which meets the requirements for microgravity experiments in the space environment. Such an accelerometer will have a full scale sensitivity of 10^{-2} g a resolution of 10^{-8} g, low cross-axis sensitivity, and low temperature sensitivity. Mass of the device is approximately five grams and its footprint is 2 cm x 2 cm. Innovative features of the accelerometer, which are patented, are: electrostatic caging to withstand handling shock up to 150 g, in-situ calibration, in situ performance characterization, and both static and dynamic compensation. The transducer operates on a force balance principle wherein the displacement of the proof mass is monitored by measuring tunneling electron current flow between a conductive tip and a fixed platen. The four major parts of the accelerometer are tip die, incorporating the tunneling tip and four field plates for controlling pitch and roll of the proof mass; two proof mass dies, attached to the surrounding frame by sets of four "crab-leg" springs; and a force plate die. The four parts are fuse-bonded into a complete assembly. External electrical connections are made at bond pads on the front surface of the force plate die. Materials and processes used in the construction of the transducer are compatible with volume production.

INTRODUCTION

Microgravity accelerometers used in the harsh environment of space must measure extremely small static and near-static events. Typical applications are experiments on the space shuttle, free flyers, space station, sounding rockets, etc.

The Micro Gravity Acceleration (MGA) sensor is a spring/mass type using a unique "crab-leg" spring support configuration and electrostatic platen force for control of mass movement. Design features of the MGA sensor include electron tunneling tip position detection, electrostatic force feedback, pitch and roll control, electrostatic compensation, and low off-axis sensitivity. A tunneling electron tip provides precision proof mass positioning and measurement for closed-loop

Joint "L+1" Science Review for USML-1 and USMP-1 with the Microgravity Measurement Group, September 22-24, 1993, Huntsville, Alabama, USA.

control of the sensor. The resulting accelerometer will have a small, 2 cm x 2 cm x 0.6 cm package envelope, a proof mass of 0.2 gm., and a light, 5 gm. (2 oz) total weight. The targeted operating amplitude range is 10^{-8} to 10^{-2} g with 10^{-9} g resolution and a natural resonance of 12.5 Hertz. The sensitivity, small size and light weight package characteristics are desirable attributes to monitor and control microgravity experiments. The electrostatic force platen design can provide an offset for a constant acceleration field (i.e. Earth gravity). Microgravity acceleration changes can be sensed and measured in the presence of a constant field up to 1 g. The electrostatic parking design provides non-operational high acceleration (150 g) load tolerance.

The new simplified lightweight microgravity accelerometer uses micro-machined silicon technology. The spring-supported transducer employs a force balance principle based on electrostaticaly attracted platens. This technique is expected to provide an ultra high sensitivity when the tunneling tip measurement of proximity error is used to hold the mass motionless via a current feedback process. The variation in voltage necessary to maintain mass positioning as a result of this feedback loop will be related to the square root of variation in magnitude of the applied acceleration.

The unique mass-support mechanism uses a dual, four-point crab leg suspension arrangement. This support method minimizes the undesirable cross-axis sensitivity typically present with small transducers. The supported mass is brought into close proximity to the tunneling tip and held stationary using a feedback technique. An added benefit of this technique is that in situ calibration is possible. A known dynamic electrostatic excitation may be applied to the force plate which simulates the result of, and is indistinguishable from, an actual acceleration. Verification of transducer performance and sensitivity values can be undertaken in this manner.

The characteristics cited for improvement over current microgravity accelerometer technology include: a decreased size and mass, higher sensitivity, simplified calibration procedures, health monitoring, and a decreased cost per unit. A novel feature of the desired transducer is that it can be dynamically calibrated in place. In-place calibrations are expected to be highly important when sensitivity changes of the unit might take place over long periods of time, such as during operation on space station or long duration planetary missions.

I. SPECIFICATIONS

The specific technical objectives for the microgravity accelerometer development are:

1. Dimensions: < 2 x 2 x 0.6 cm
2. Total mass: < 5 grams
3. Proof mass: 0.2 grams

4. Amplitude precision range: 10^{-8} to 10^{-2} g
5. Resolution: 10^{-9} g
6. Bandwidth: Static to 10 Hz
7. Cross Axis Sensitivity: < 0.1% of reading
8. Temperature sensitivity: < 0.01%/°C
9. Operating temperature limits: -20 to +80°C
10. Non-operating temperature limits: -40 to +90°C
11. Non-operating shock limit without affecting calibration: >150 g
12. In-situ static and dynamic calibration during operation
13. In-situ health monitoring and characterization
14. Self test/calibration: internal electrostatic force
15. System interface: Micro computer regulated precision ADC and DAC units

II. INNOVATIONS

The MGA sensor is an autonomous transducer which provides functional verification as well as perpetual calibration, offset and coefficient compensation. Several innovative features are unique and are patented.

A. Calibration

The electrostatic attractive force exerted by an electric field between the force plate and the proof mass cannot be differentiated from either the seismic acceleration or mechanical restoration forces. The desired force arises from an applied voltage on the force plate which is previously correlated to a predetermined force on the movable member. By observing the response of the feedback controller to the applied voltage on the force plate, the entire device may be calibrated. In fact, a large range of applied voltages corresponding to a range of applied forces may be used in succession to internally calibrate the micromachined transducer. The advantage is that the device is readily calibrated or re-calibrated remotely and with great precision without any external calibration equipment of the type typically required.

B. Characterization

In order to characterize various parameters (such as frequency response) of a micro-machined transducer, the desired force applied by the control apparatus is a test stimulus signal. This range of parameters may include, for example, frequency response, phase response, linearity, hysteresis and the like.

C. Static and Dynamic Compensation

It may be desired to compensate for a large ambient force so that only small differentials are measured by the micro-machined transducer. The desired force is one which is equal and opposite to the force exerted on the movable member by the ambient force. This type of compensation requires the desired force to be fairly constant over time, and is therefore a type of static compensation.

Three micro-machined accelerometers may be integrated in an inertial sensor, each accelerometer being aligned, to within a manufacturing error, along a respective one of three orthogonal axes. The resulting cross-coupling between measurements otherwise deemed to be orthogonal is measured precisely after assembly of the inertial measurement device. During calibration and operation, the vector forces are measured using two known orthogonal forces to determine the proper correction for the third individual sensor. The same process is repeated to determine the correction for each of the sensors in a triaxial configuration. These correction factors are then applied to the appropriate accelerometer's force plate and the cross axis error in the measured data is compensated for.

A fixed bias may be deployed in determining the static characterization of a transducer, such as providing "free" levitation of a sensor element in a fixed gravitational field.

A small single cell battery of about a volt, can create a large attractive force between two micro-structured platens. With a good insulator, the leakage current is negligible, permitting maintenance of a retention force for the cell life of about a decade. In micro-structured accelerometer, application of this electrostatic retention facilitates a simple mechanism for caging the proof mass that will withstand accelerations in excess of 150 g for launch, etc.

III. MECHANICAL DESCRIPTION

The transducer design is based on a four die configuration as shown in Figure 1. The top die in the figure is referred to as the tip die which is shown in more detail in Figure 2. The tip die has at its center an electron tunneling tip. The tip will be approximately 3.75 μm high. Two identical dies are bonded together to form the proof mass. These dies are comprised of a border region and the proof mass as shown in the center of Figure 3. The proof mass is 1 cm (10,000 μm) across. The lowest die is referred to as the force plate. Figure 4 presents the top and bottom views of this die.

IV. CONSTRUCTION

A. Tip Die

The tip die, the most complicated structure in the assembly, has its basic fabrication process illustrated in Figure 5. Key specifications of the tip die are listed in Table 1. It not only incorporates the tunneling tip, but contains 4 field plates to control the pitch and roll of the proof mass as well as its position. The tip die must also accommodate the bonding method use to assemble the four separate dies that comprise the accelerometer. Two separate metal layers are required. The first layer is isolated from the second by a 0.5 μm oxide layer. The first metal layer is used as the tip metal. A three metal composite is used consisting of chrome/gold/chrome. Chrome layers are used to enhance adhesion to the substrate (nitride coated silicon) and to the isolation oxide layer. The top chrome layer of this composite metal layer is removed to expose the gold layer as the tip metal.

The second metal layer, the same metal used as the bonding layer, is aluminum/germanium, the preferred choice because it is easily deposited, inexpensive and has a low bonding temperature.

The center region of the die is recessed with respect to the bond perimeter and bond pads. This is required to obtain a spacing between the field plates and the proof mass. When this die is bonded to the proof mass, the perimeter will form a hermetic seal with the bond pads, mechanically bonded and electrically connected to their counterparts on the proof-mass die. This electrical connection scheme is a key feature of the design. By interconnecting the die in the bonding processes, all electrical connections to the completed accelerometer can be made from its front surface.

The electrically insulating oxide layer is removed from the tip and its surrounding area, exposing the tip metal. The electrical contact to the tip is accomplished with the first metal layer which is connected by a single thin lead to the bond pad. The second metal layer which forms the field plates, bond perimeter and bond pads is deposited above the first metal layer. The cross in the center of the bond perimeter, which is electrically grounded, is used to shield the tip metal lead from the influence of the electric fields that will exist in the vicinity of the field plates. Because of the recessed nature of the center of the die, the center cross of the bond perimeter will not take part in the bonding process. The cross is open at the very center to expose the tip below.

To connect the force plates electrically to the bond pads, holes are cut in the oxide layer above the first metal in the vicinity of the force plates. This allows the force plates to contact the first metal layer. The first metal layer is patterned in such a way as to connect each force plate electrically to its associated bond pad. The bond pads also contain a connection between first and second metal.

B. Proof Mass Die

Key specifications of the proof mass die are given in Table 2 and the basic steps in the fabrication process are shown in Figure 6. The proof mass is assembled from two identical die. The top dimension is 1 cm or 10,000 μm. The proof mass is held to the surrounding frame by a set of springs affectionately referred to as 'crab legs.' The target thickness of the crab legs is 25 μm. Each individual crab leg is divided into three spring sections, two short ones and one long one. The length of the short sections is 5000 μm, but the length of the long spring is 9800 μm, due the requirement to clear the corner ties. The corner ties play no role in the normal motion of the proof mass and do not alter the stiffness of the device in its sensitive axis. These ties are added to increase the stiffness to pitch, roll and yaw.

The proof mass die is maintained at essentially ground potential and the surface of the proof mass is completely covered by metal. At the perimeter of the die, electrical contact between bond pads is routed to facilitate the scheme of front surface contact only, as described above.

The eutectic bonding metal is applied before the anisotropic etch procedure to prevent metal deposition on the backs of the springs.

C. Force Plate Die

Key specifications of the force plate die appear in Table 3 and the basic steps in the fabrication process are shown in Figure 7.

The force plate die, similar to the tip die, uses a two metal process to provide a bond perimeter which is not electrically connected to the force plate. A contact pad to this perimeter metal is provided in order to set the potential. The force plate is fabricated in first metal, which may simply be a single chrome layer similar to that used on the tip wafer. The force plate must be covered with a thin 1000 A oxide layer . The purpose of this oxide layer is to prevent an electrical contact between the proof mass and the force plate when the proof mass is being clamped electrostaticaly. Choices for the bond perimeter and contact layer (second metal) are identical to those described for the tip wafer.

The 'top view' section of Figure 4 shows the locations of the bond pads and specifies their various functions

CONCLUSIONS

Silicon micromachining is rapidly becoming the dominant method for producing state-of-the-art sensors in the world today. Even laboratory tunneling tip accelerometers have been developed but, until now no one has resolved how the delicate mechanisms of sensitive accelerometers can be protected and a robust sensor engineered.

The recursive design process that resolved the mechanisms and machining processes to realize them has been arduous but rewarding. The MGA sensor described in this paper will provide experimenters with the capability for highly sensitive acceleration measurements using a device of extremely small size and mass. This sensor has patented innovative features which include in situ calibration, in-situ characterization and self test, state and dynamic compensation, and caging. The sensor also has low cross-axis sensitivity and negligible temperature sensitivity (10^{-5} $\mu g/°C$). Materials and processes used in the construction of the transducer are compatible with volume production.

ACKNOWLEDGMENTS

This paper represents the results of one phase of research carried out at the Jet Propulsion Laboratory, California Institute of Technology and at the Microsensor Laboratory, Northeastern University under contract with the National Aeronautics and Space Administration.

Table 1: Key Specifications of the Tip Die

Design Characteristic	Specification	Tolerance
Tip to Ground Capacitance	100 pf	+/-20 pf
Control Plate to Substrate Capacitance	100 pf	+/-20 pf
Control Plate to Proof Mass Capacitance	100 pf	+/-1 μf
Control Plate to Tip Ground Capacitance	0.2 pf	max.
Voltage to overcome 1g	5	+/-1
Tip to Proof Mass Proximity	0	+/-0.2 μm
Tip Height	3.5 μm	+/-0.5 μm
Bond Metal Thickness	1 μm	+/-0.1 μm
Insulating Layer Thickness	0.5 μm	+/-0.05 μm

Table 2: Key Specifications of the Proof Mass Die

Design Characteristic	Specification	Tolerance
Mass	0.18 gm	+/-0.005 gm
Volume of Proof Mass	7.55×10^{-2} cm^3	
Spring Thickness	25 μm	+/-5 μm
Spring Width	100 μm	+/-5μm
Spring Length	5000/9800 μm	+/-5 μm

Table 3: Key Specifications of the Force Plate Die

Design Characteristic	Specification	Tolerance
Force Plate to Substrate Capacitance	5 x 10^{-2} μf	+/-2 x 10^{-2} μf
Voltage to overcome 1g	10	+/-2
Bond Metal Thickness	1 μm	+/-0.1 μm
Insulating Layer Thickness	1000 A	+/-250 A
Depth of Depression	5 μm	+/-0.05 μm
Max. Holding Voltage	10	
Holding Force @ 1.4v	96 g to 265 g	

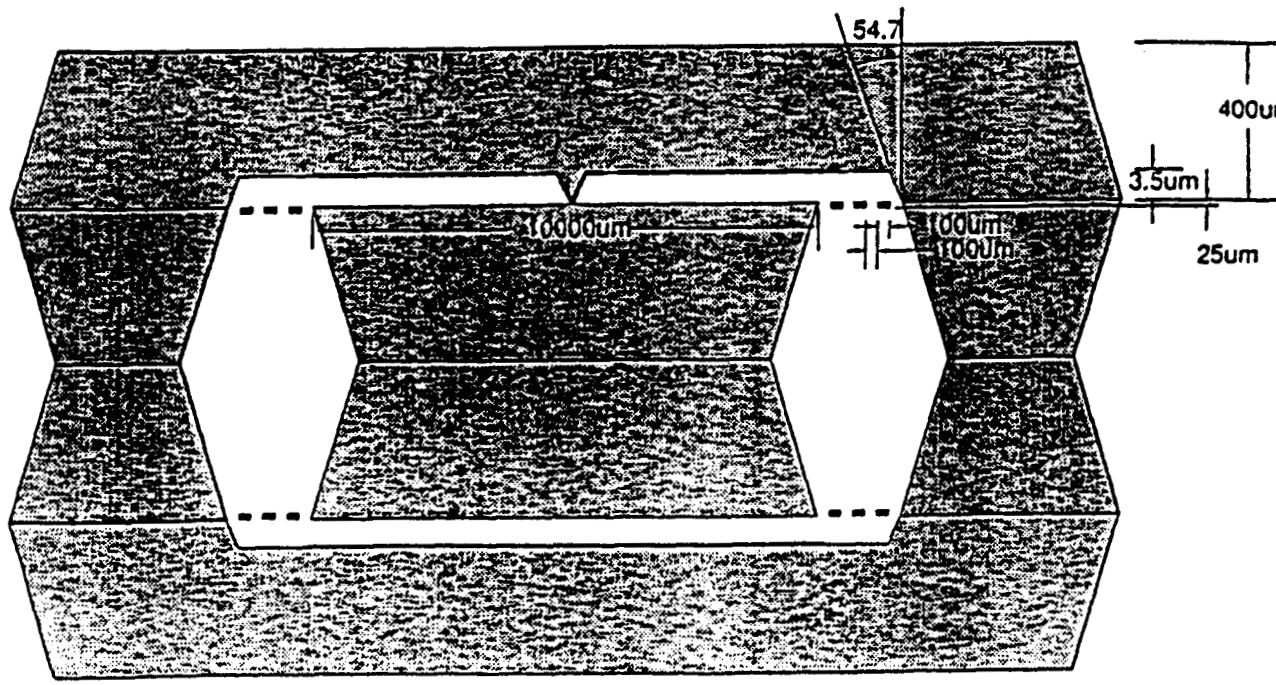

Figure 1 Accelerometer Assembly.

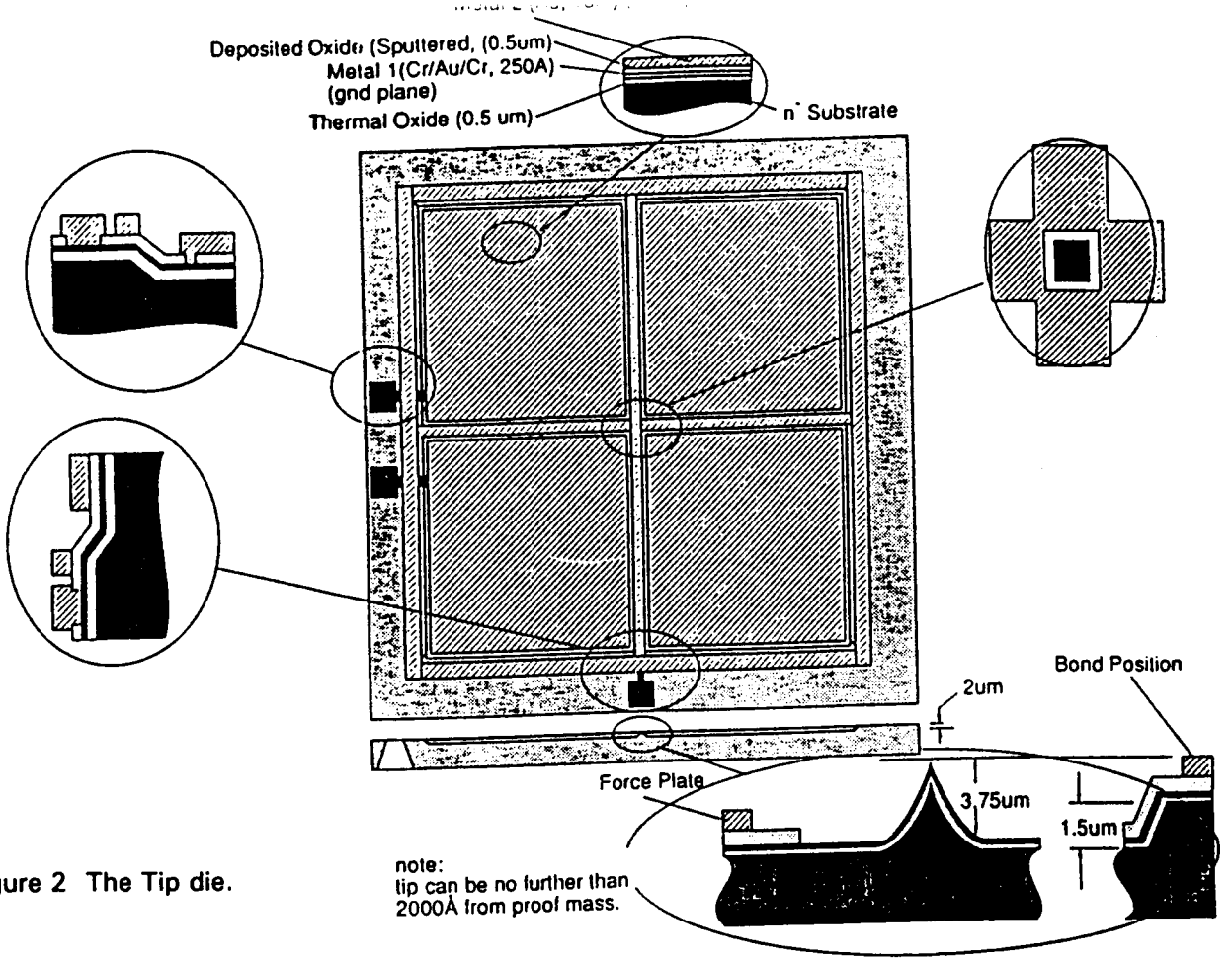

Figure 2 The Tip die.

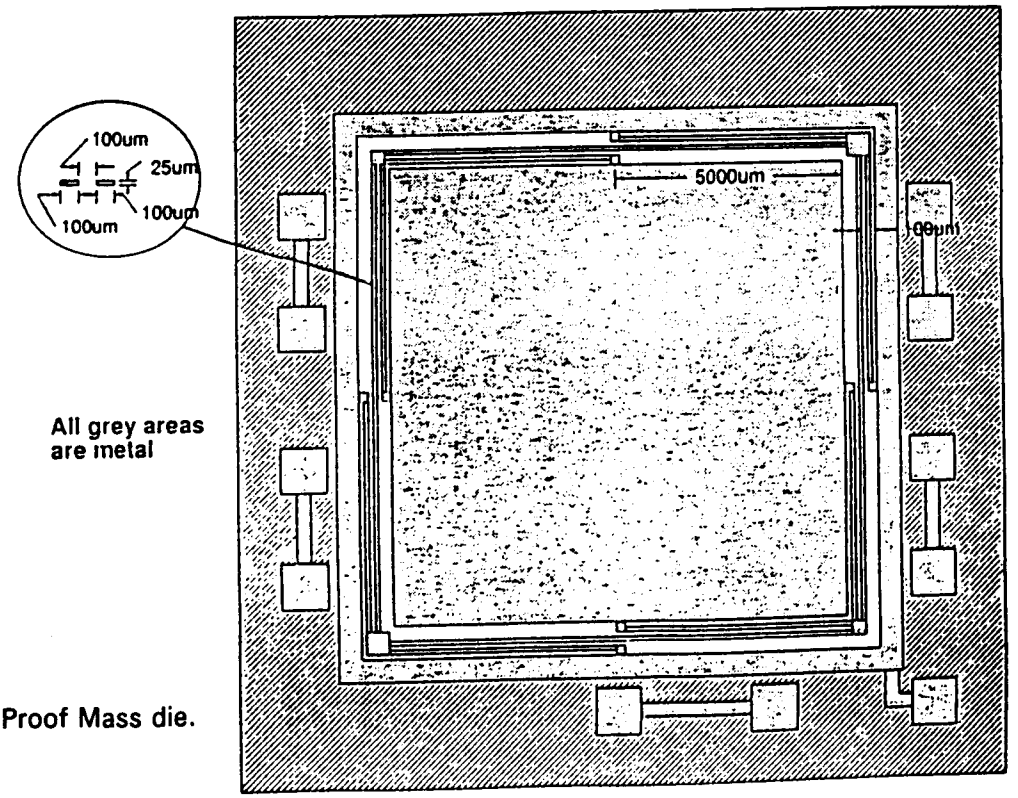

Figure 3 The Proof Mass die.

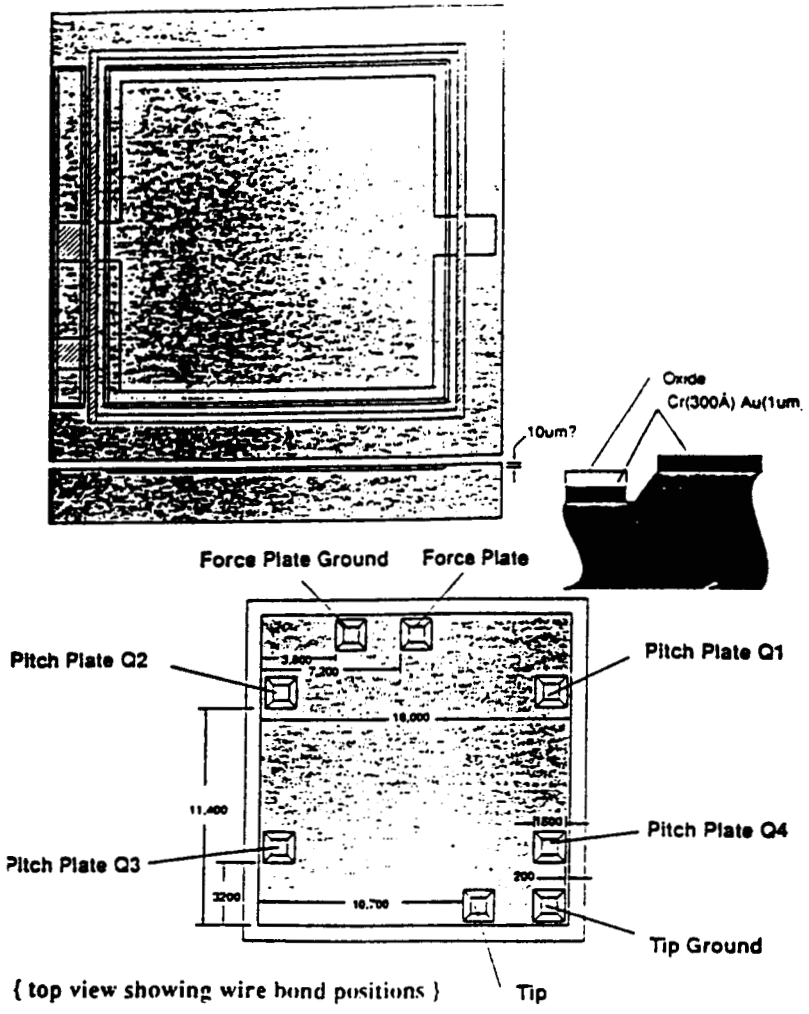

Figure 4 Force plate die.

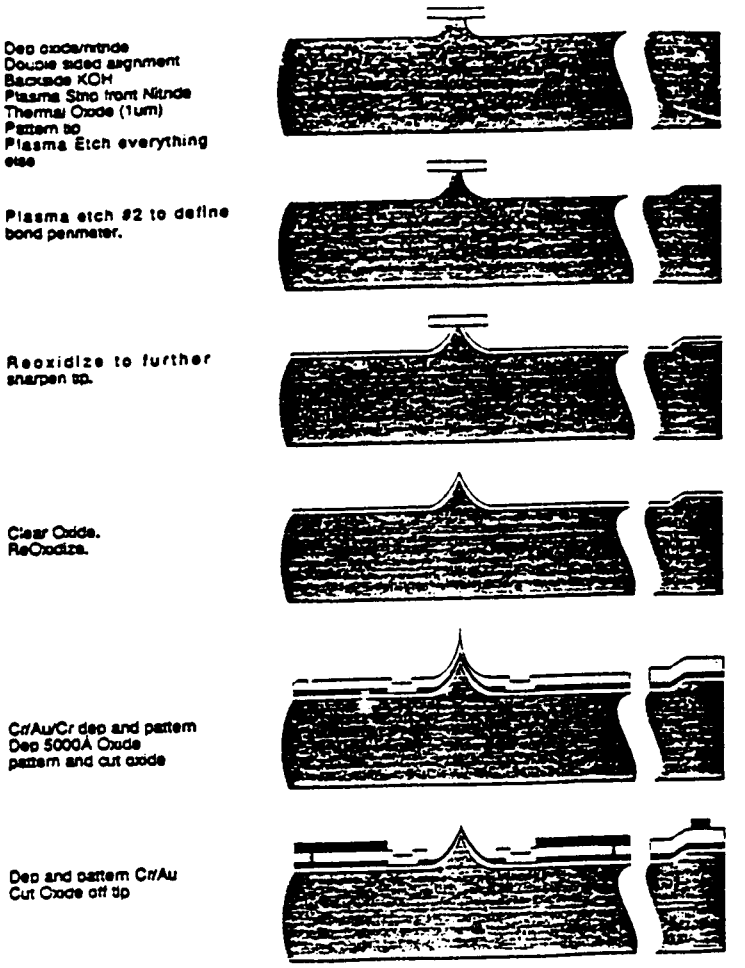

Figure 5 Tip Die fabrication process.

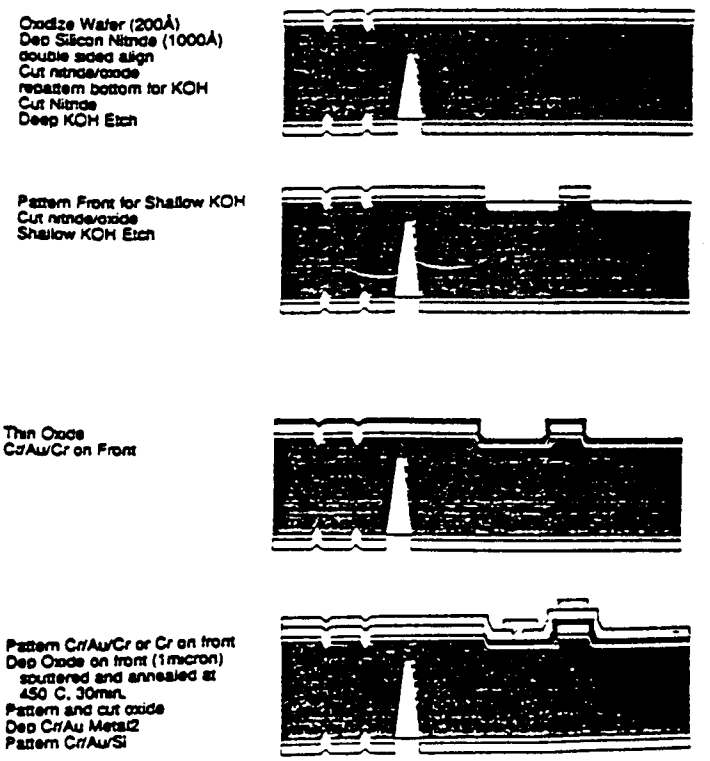

Figure 6 Proof mass die fabrication process.

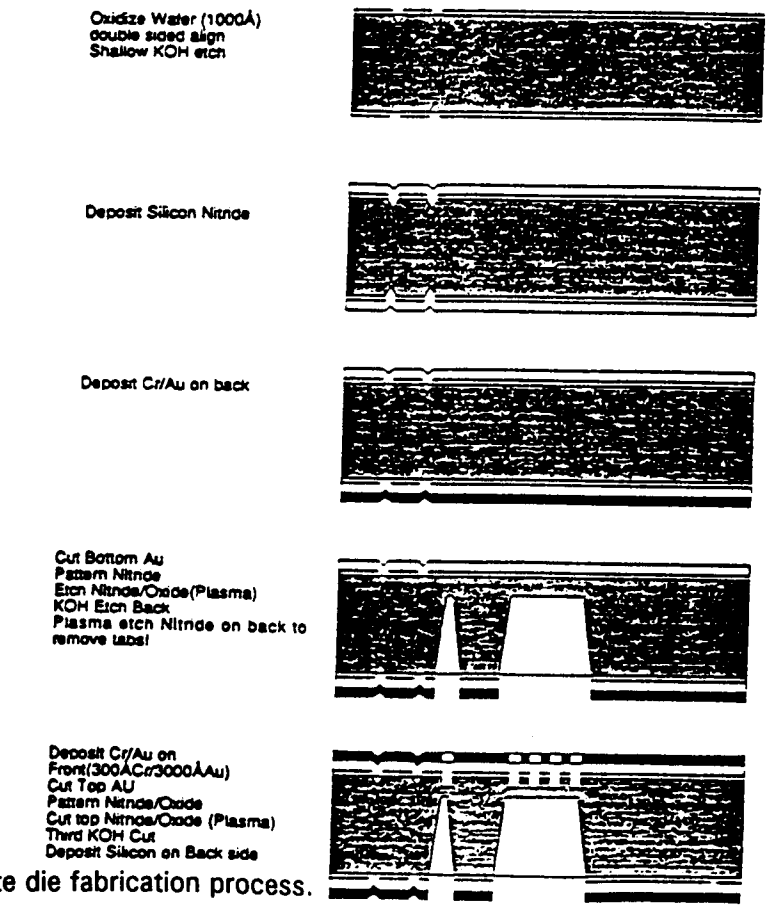

Figure 7 Force plate die fabrication process.

Discussion

Question: *I wondered if you looked at the stability of this tip ?*

Answer: We haven't put the thing together yet in its entirety. I don't think there is much issue about the stability of silicon as a material and the precision with which you can machine and those other issues. So if you are talking about dimensional stability of the device itself, that is not going to be an issue. In terms of the tip, an issue will be breaking it or contaminating it, but, again, even in terms of the contamination we are looking at in these systems, we can have it in a vacuum and there is not going to be any oxidation. I am not anticipating any problems with that.

Question: *Any direct mechanical connection between the case and the proof mass, and how those change with temperature and time will affect bias. How do you stabilize those grab springs ?*

Answer: Well, in silicon I don't think we are going to have to worry about stabilizing it.

Question: *Those dimensions will shift as the thing heats up or cools off. Will that be of any effect ?*

Answer: As I have indicated, I do not think there is going to be a problem. It is not going to be a stability problem. The dimensional changes are still quite small, and I don't think they are going to have an effect on this. The other one that we were looking at was what the growth of the pier would be due to thermal expansion, and because we are only working with micrometers, that is not a significant issue. But again, we have in situ calibration in this, and we will be tracking those temperature variations and can accommodate them.

FURTHER ENHANCEMENTS IN NANO-G ACCELEROMETRY: THE CUBE MESA

Patrick J. McNally*, Robert W. Dietrich+ and William G. Lange+

*Canopus Systems, Inc.
+Canopus Products, Inc.

ABSTRACT

This paper discusses an evolution of the cylindrical proofmass Miniature Electrostatic Accelerometer used on the Orbital Acceleration Research Experiment into a cube shaped proofmass, known as the Cube MESA. The current approach of the OARE instrument using the cylindrical proofmass is briefly summarized. The Cube MESA design is explained and compared with the cylindrical MESA. A low cost approach to obtaining flight experience with a Cube MESA while utilizing a major portion of the OARE flight hardware is proposed.

INTRODUCTION

The primary objective of the OARE was to develop a system capability for accurate measurement of aerodynamic acceleration along the Shuttle Orbiter's principal axes in the free-molecular flow (on-orbit) regime and in the rarefied flow transition (re-entry) regime. To attain the scientific measurement objective, the system had to provide for nano-g resolution measurements in a narrow-band frequency range compatible with near orbital period intervals, wide dynamic range to cover milli-g to nano-g signal levels, on-orbit calibration of bias and scale factor and the ability to perform the signal measurements and calibration in the presence of interfering acceleration signals such as Orbiter structural vibration, crew-induced noise, thruster signals and other perturbation forces such as gravity gradient, mass-dumping, solar pressure, and magnetic field.

During several feasibility studies and in the preliminary design phase, it was determined that the required long-term, low frequency, high resolution and wide range acceleration measurement characteristics could only be provided by an electrostatic suspension accelerometer with its dual servo loop high gain electronic constrainment system leading to the flight proven cylindrical MESA choice for the OARE system.

The OARE instrument has been shown to provide valuable data for microgravity research, in addition to the original objective of providing aerodynamic acceleration data. The composite

requirements of space station experiment sensitivity to g-jitter has been summarized in a frequency vs. disturbance amplitude plot (ref. 1), shown in figure 1. The low frequency (from 0.1 Hz to 10^{-6} Hz) and high sensitivity (from 1μg to 1 nano-g) corner of this figure is critical for comparison with space materials processing results. The OARE system is currently providing measurements for this portion of the requirement curve using a cylindrical proof mass.

The OARE cylindrical MESA uses a flanged cylinder proofmass originally developed as a single axis linear accelerometer. Figure 2 compares the cylindrical MESA electrode configuration with the Cube MESA electrode configuration. Figure 3 illustrates the type of data obtained by OARE over a 45 hour period along the Shuttle velocity vector (ref. 2). Over this period, drag variations of $\pm$ 0.6 ug from the day/night atmospheric effect are clearly visible. Also, a variation of 0.5 ug with a period of approximately 26 hours is apparent. Preliminary data analysis shows that the cylindrical MESA appears capable of isolating signal magnitudes of 100 nano-g with frequencies as low as 10^{-5} Hz

I. CUBE MESA DESCRIPTION

The Cube MESA mechanical assembly is shown in figure 4. The cube proofmass, made of beryllium, has a nominal 0.5 inch edge dimension. Facing each of the six sides of this proofmass is a dual electrode forcer assembly. An individual electrode and the corresponding electrode at the opposite face of the cube are used in each of the six constrainment loops. The electrodes are oriented to provide 6 DOF constrainment of the cube proofmass. The nominal 0.002 inch gap between the electrodes and the proofmass is maintained by a combination of the cylindrical-shaped cage into which all six forcer assemblies are mounted and the temperature compensating spacer. The cage assembly is mounted inside the hermetically sealed hexagonal-shaped housing, with the 12 electrode terminals exiting radially at both ends. The housing is hermetically sealed and filled with a mixture of 90% dry nitrogen and 10% helium at a nominal pressure of 1 atmosphere. This gas provides the viscous damping required for stable constrainment loop operation as well as protecting the proofmass during any high-g environment, even when unpowered. The housing has three mounting pads which are used to secure it to a mounting bracket in the Cube MESA.

A prototype Cube MESA mechanical and electrical assembly was developed under an IR&D program originally at Bell Aerospace and now at Canopus Products. The hardware developed under this program is shown in figure 5.

The 6 constrainment loops in the Cube MESA are identical in design. They are based on the design of the cross-axes constrainment loops used in the cylindrical proofmass MESA, but require less electronic gain because of the flat surfaces of the cube proofmass. The output of each of the 6 constrainment loops contains a combination of linear and angular acceleration data. The desired 6

outputs (3 linear acceleration outputs and 3 angular acceleration outputs) are obtained by combining the outputs of each pair of constrainment loops. Each of the 3 linear acceleration outputs is obtained by summing the outputs of the constrainment loops utilizing the electrodes facing opposite surfaces of the cube proofmass. Similarly, each of the 3 angular acceleration outputs is obtained by differencing the outputs of its pair of constrainment loops. A block diagram of the force rebalance constrainment loops for each Cube MESA axis is presented in figure 6.

II. CUBE MESA COMPARED WITH CYLINDRICAL MESA

The Cube MESA provides 3 linear acceleration outputs and 3 angular acceleration outputs from the 6 constrainment loops used to constrain the cube proofmass in all 6 degrees of freedom (DOF). The 6 DOF constrainment maintains the cube proofmass in the same position relative to the constrainment loop electrodes; this causes the Cube MESA to be almost insensitive to slight deviations of the proofmass from the ideal cubical shape. By comparison, the cylindrical proofmass used in present MESA accelerometers can be constrained in only 5 DOF. The lack of rotational constraint around the cylindrical axis allows the proofmass to rotate relative to the cross-axes electrodes; this causes the performance of the two cross-axes to vary slightly in the presence of even very small (micro-inch) deviations of the proofmass from the ideal cylindrical shape.

The mechanical design of the Cube MESA incorporates several design improvements over that used in the cylindrical proofmass MESA. Because of the symmetry of the cube proofmass, only one forcer assembly design is required instead of two; this reduces costs and provides interchangeability of all 6 forcer assemblies. Because only flat surfaces (no curved surfaces) are used, the machining and assembly operations are simplified. The use of temperature compensating spacers in the Cube MESA reduces the scale factor temperature sensitivity.

An additional benefit of the Cube MESA is that "1G" constrainment can be applied in all three axes (vs. only two axes for the cylindrical proofmass MESA). This allows ground-based determination of the alignment of all axes by the use of a "nulling" technique rather than the less accurate "peaking" technique required for some measurements on the cylindrical proofmass MESA.

III. JUSTIFICATION FOR CUBE MESA

There are three primary justifications for changing from a cylindrical MESA design to a cube MESA design for future microgravity experiments:

1) lower life-cycle costs from manufacturing and test through operation

2) improved flight performance by reducing the effects of disturbances on the sensor accuracy

3) additional angular acceleration data

This section describes the supporting data and analyses for justification #2 and #3.

Performance gains are anticipated with the cube MESA from two primary differences: 1) the cube MESA design eliminates the curved electrodes from the cylindrical design, greatly reducing cross coupling and errors due to proof mass and electrode machining tolerances, and 2) the cube MESA controls 6 degrees of freedom vs. 5 for the cylinder, eliminating errors from proof mass rotation.

Currently, the curved electrode design causes several error effects, basically due to asymmetry of the three sensing axes. (see figure 7). First, a "negative spring" force is developed when a proof mass displacement along one cross axis causes a resulting loop imbalance in the other cross axis. Second, due to machining tolerances and handling impact, the cylinder is actually a "squashed can", with a different "squash" axis at each end. This effect causes a coupling between cross axes as well as a net torque about the uncontrolled cylindrical axis when undergoing an acceleration. Third, due to electrode deposition accuracy, an effect known as the "barber pole effect" results from non-symmetric placement of the cross axes electrodes around the cylinder. Since the cube MESA has point symmetry, all of these effects are greatly reduced, with an expected performance gain of a factor of 3 in sensitivity.

By controlling only 5 degrees of freedom, the cylinder is free to rotate around it's axis, introducing a coupling between the cylindrical axes and the cross axes. A ground-based proof mass roll test of the cylinder was conducted with results shown in figure 8. This figure shows that a component of gravity is coupled into the x axis with varying amount, depending upon the rotation angle of the cylinder. The Cube MESA design eliminates this effect, with an additional expected improvement in overall sensitivity by a factor of 2.

The bias temperature coefficient for the X axis from STS 50 was measured as -36 nano-g/°C. This effect is due to dimensional changes to the proof mass gap, and to expansion of the forcer rings coupled to the sensor case. The Cube MESA is expected to provide an order of magnitude or better improvement to the scale factor/temperature coefficient through the use of temperature compensating spacer rings and elimination of the X axis forcer ring design used in the cylindrical MESA. Bias/temperature coefficients will also improve due to the overall symmetry of the cube. A similar redesign of the cylindrical MESA to add compensating spacer rings is extremely difficult.

There are currently no sensors on the Shuttle which accurately measure angular accelerations. Estimates of acceleration are made by twice differentiating IMU orientation data, a very noisy process. The Cube MESA instrument will provide direct, sensitive angular acceleration data, with bias compensation. This data can be used directly to estimate external moments on the shuttle, or integrated to provide estimates of shuttle rates and attitude in conjunction with IMU data.

IV. CUBE MESA FLIGHT EXPERIMENT APPROACH

The Cube MESA sensor assembly can be designed to exactly match the existing OARE Sensor/Table Assembly (STA) mechanical interfaces and volume envelope. Additionally, electrical functions can be accommodated using the existing STA wiring. To add the angular outputs, the constrainment disable function wires (no longer needed with the Cube MESA) and redundant wiring would be utilized. Additionally, minor changes between the connecting cable to the OARE Interface Subsystem (OIS) and two circuit boards internal to the OIS, the Analog-Digital Converter Card (ADC) and the Sensor Low Pass Filter Card (SLPF) would be needed. All changes could be made as new assemblies. The existing OARE system would not change, and could be restored by replacing the new Cube MESA assemblies with the existing OARE assemblies. Additionally, the assemblies that are being changed are not sensitive to handling, therefore, the changeout and replacement could be handled with minimal risk to the existing OARE hardware.

CONCLUSIONS

The OARE instrument is currently providing low frequency high sensitivity linear acceleration measurements of the on-orbit micro-gravity environment with a cylindrical shaped MESA accelerometer. In-flight calibration and specialized data processing are used in the OARE design to achieve performance already demonstrated for signals below 1 ug and 0.00001 Hz (10^{-5} Hz). The cube MESA design directly addresses areas of the cylindrical MESA design where performance improvements can be made. The performance gains of a cube MESA design cannot be quantified without a direct comparison of flight results. A methodology for obtaining flight performance data for a cube MESA design is proposed, utilizing the OARE instrument as a test platform with the cube MESA temporarily replacing the cylindrical MESA.

REFERENCES

1. "Preliminary OARE Absolute Acceleration Measurements on STS-50," NASA Technical Memorandum 107724, R. Blanchard, J. Nicholson, J. Ritter,

2. "An Examination of Anticipated g-Jitter on Space Station and its Effects on Materials Processes," NASA TM 103775, Emily S. Nelson, NASA LeRC, May 1991.

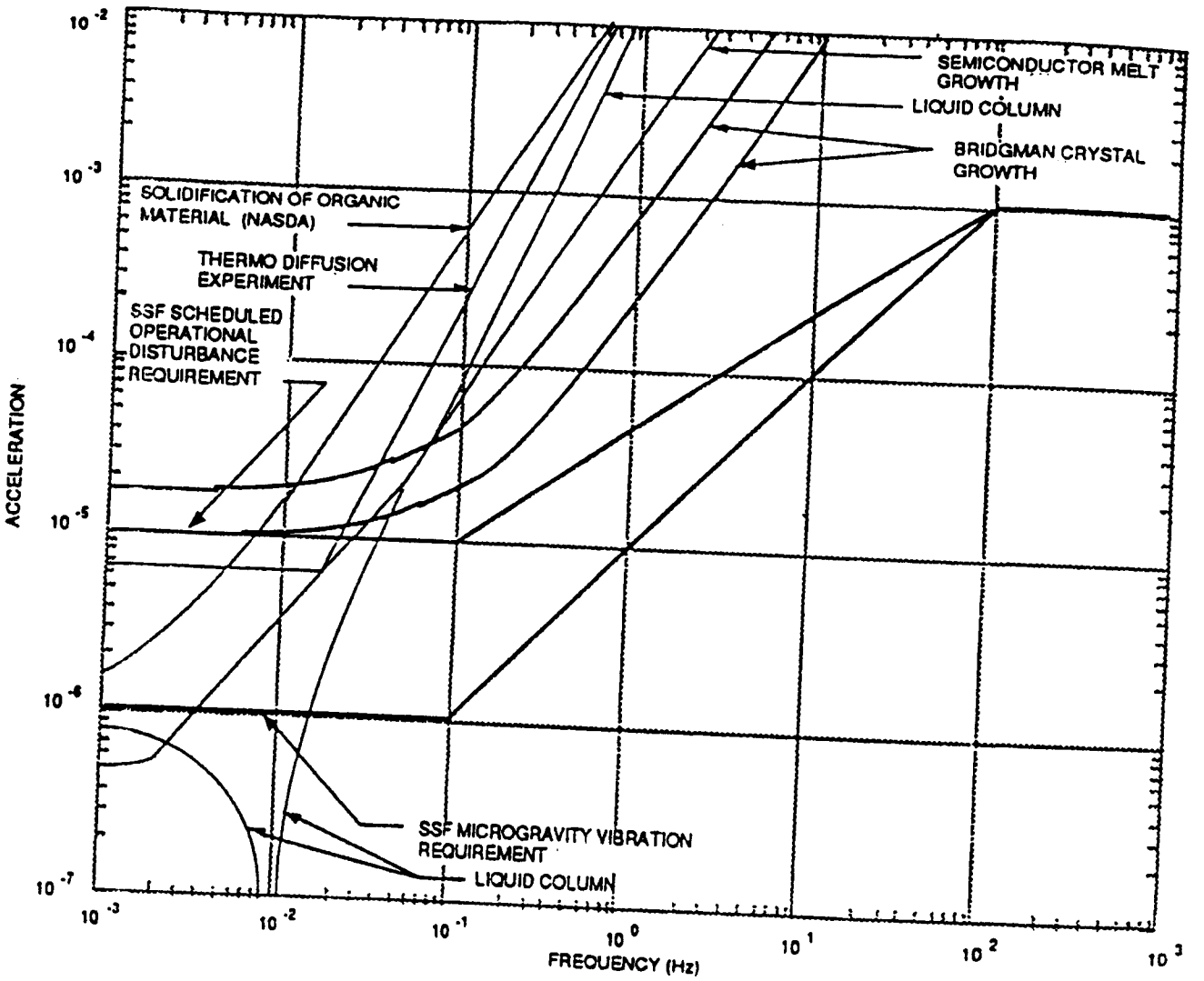

Figure 1 Measuring the Low Frequency/High Sensitivity Acceleration Requirement is Critical for Space Materials Processing Success.

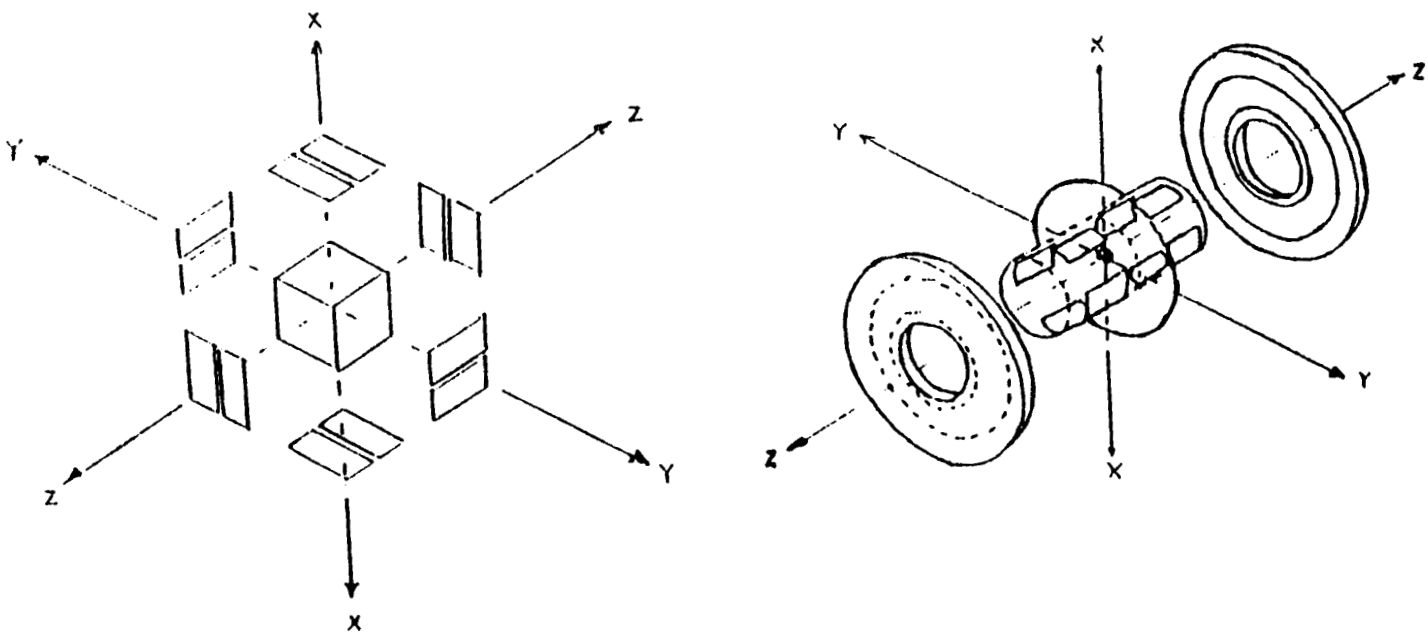

Figure 2 Comparison of Electrode Configuration and Proof Mass for the Cube and Cylindrical MESAs.

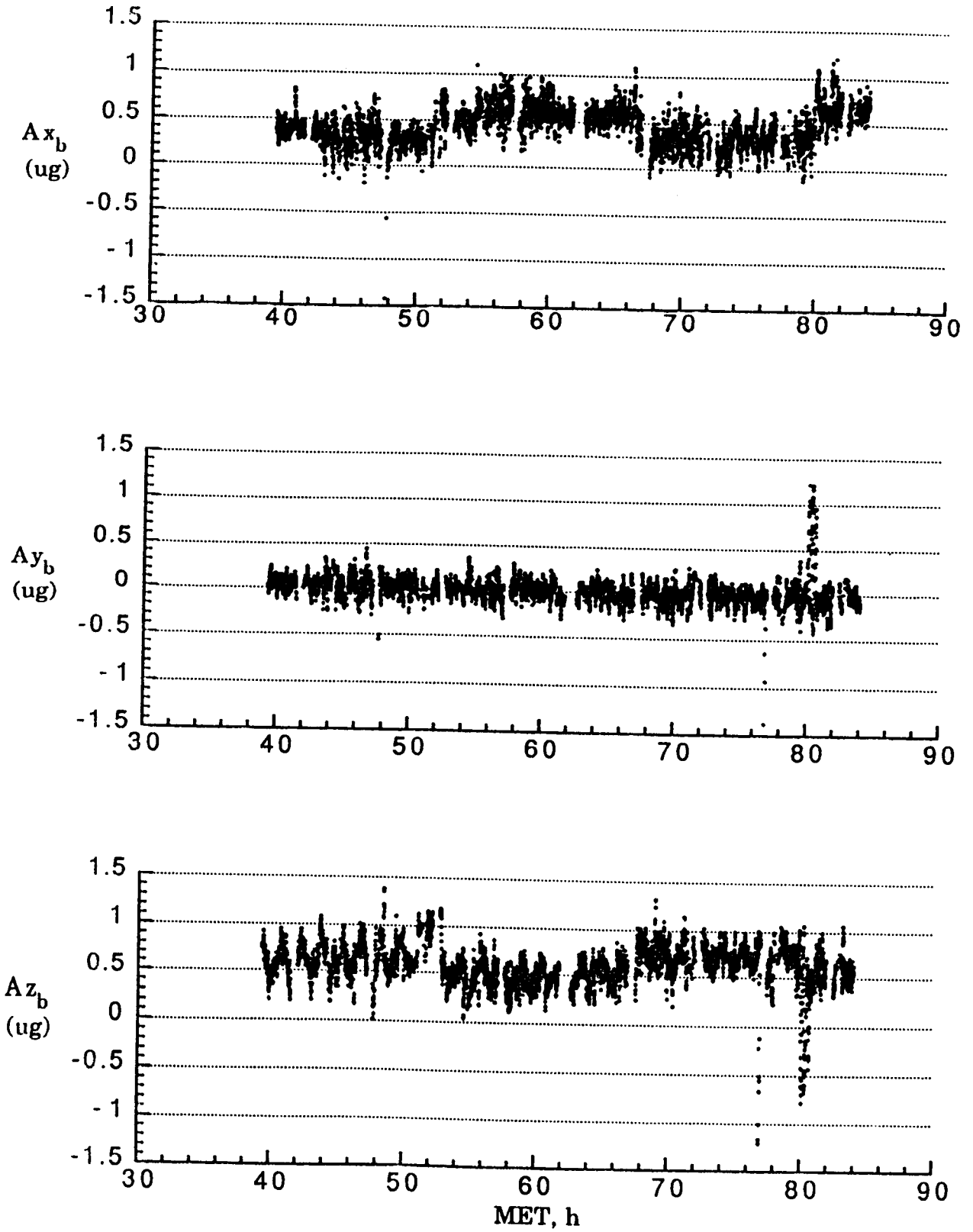

Figure 3 OARE Measurements from STS 50 Demonstrate Cylindrical MESA Sensitivity at Very Low Frequencies.

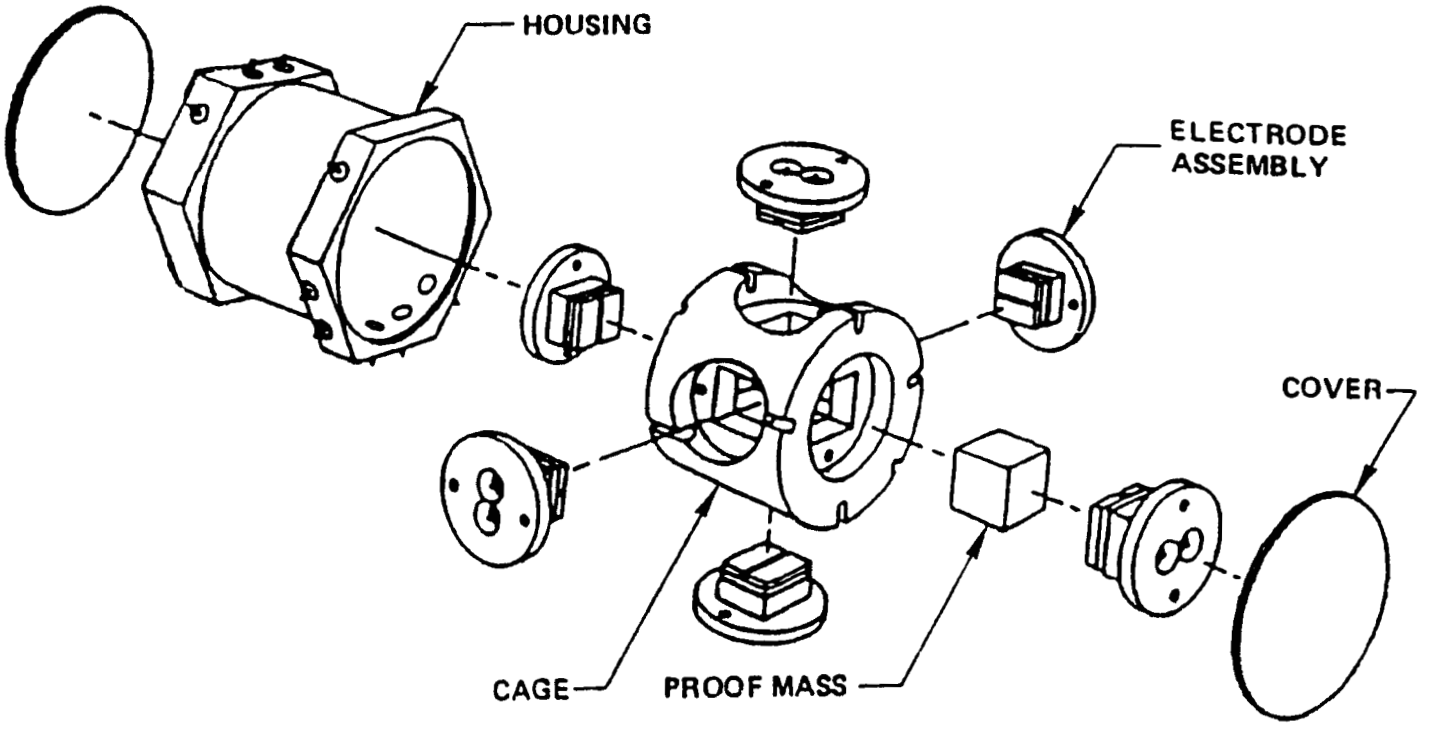

Figure 4 Cube MESA Mechanical Assembly Illustrates Fully Symmetric Design with Fewer Precision Parts Required and Interchangeable Axes.

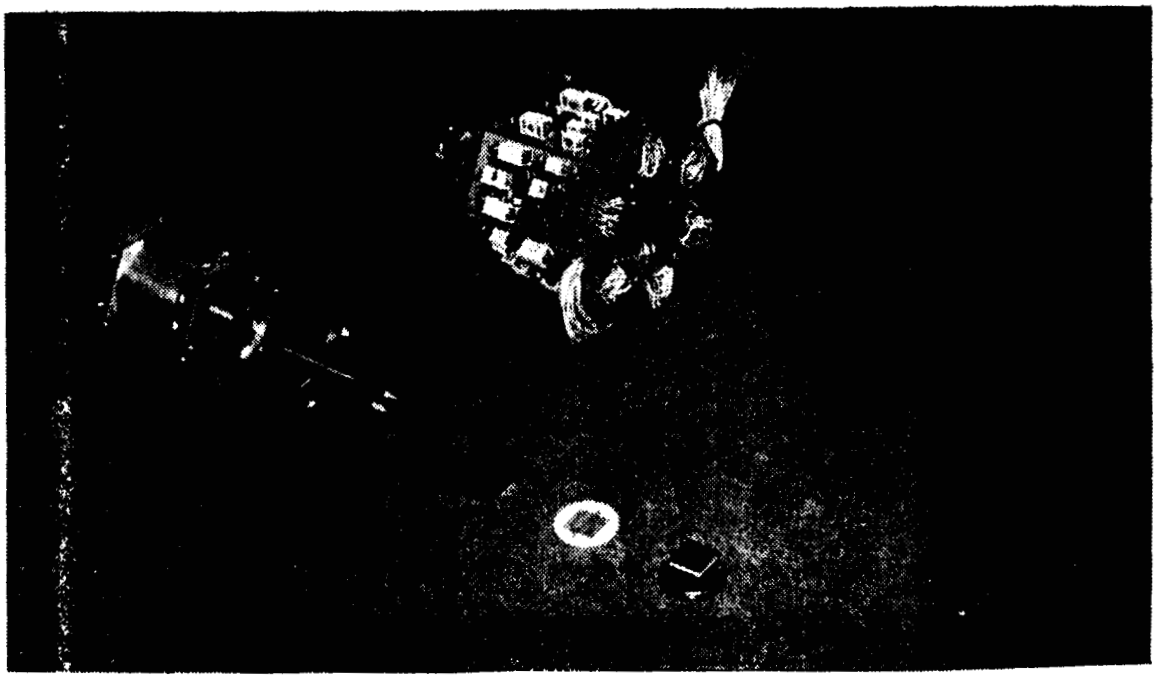

Figure 5 Cube MESA Prototype Hardware includes Mechanical and Electrical Components for Complete 6 Degree of Freedom Constrainment.

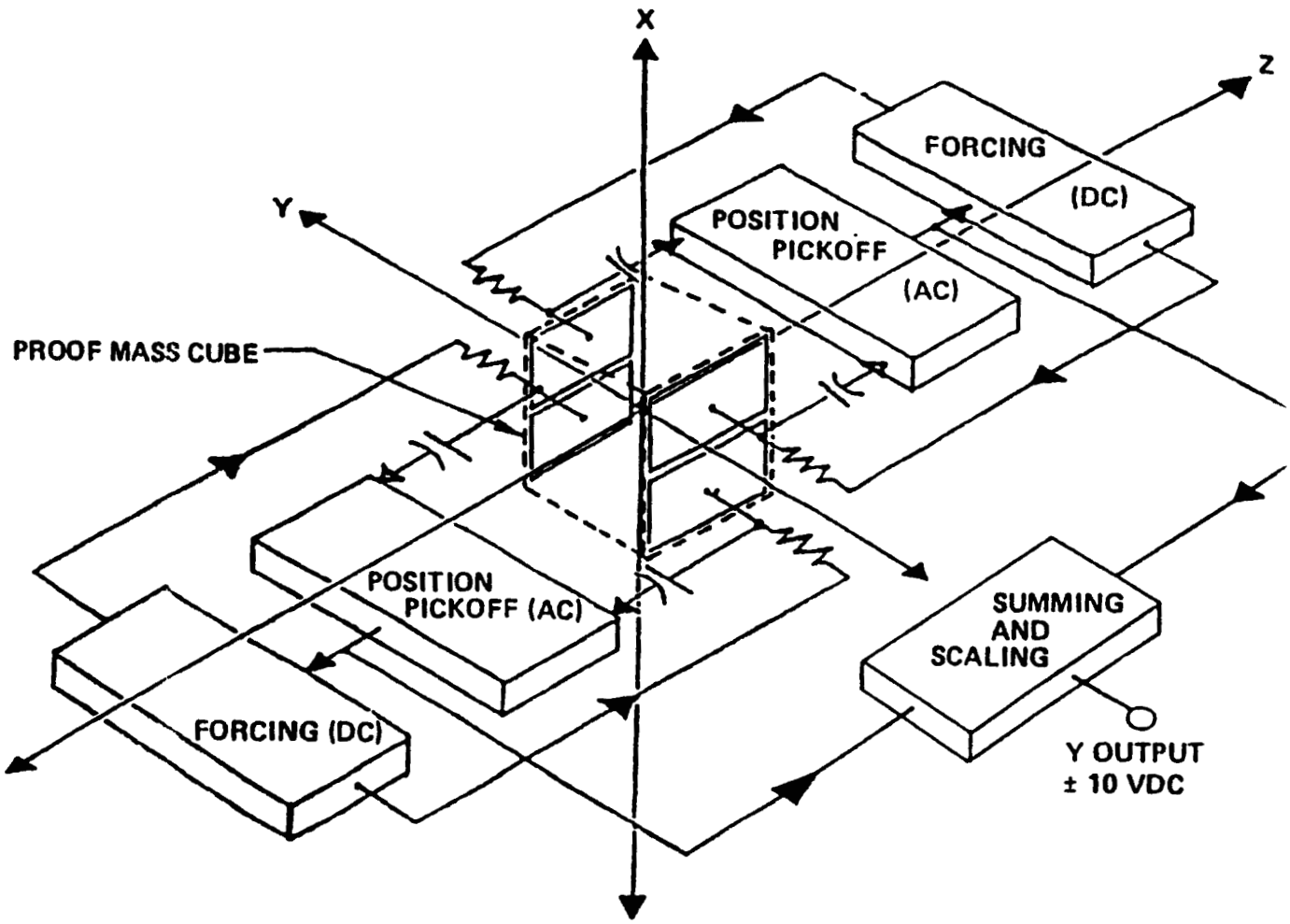

Figure 6 Cube MESA Force Rebalance Constrainment Loops, Based on the Flight-Proven Cylindrical Design.

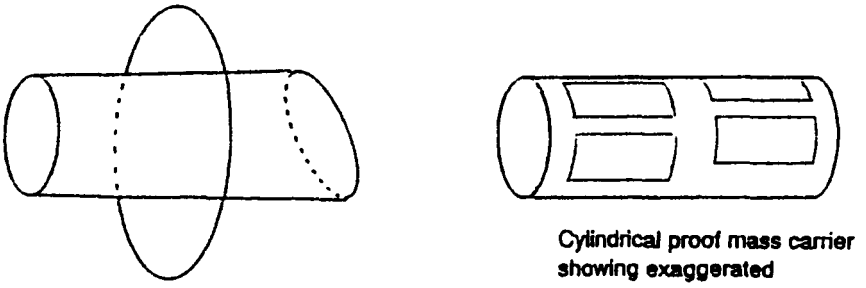

Cylindrical proof mass showing exaggerated taper and "squashed" ends

Cylindrical proof mass carrier showing exaggerated "barber pole effect"

Figure 7 Some Machining Errors for the Cylindrical MESA that are Eliminated with the Cube MESA.

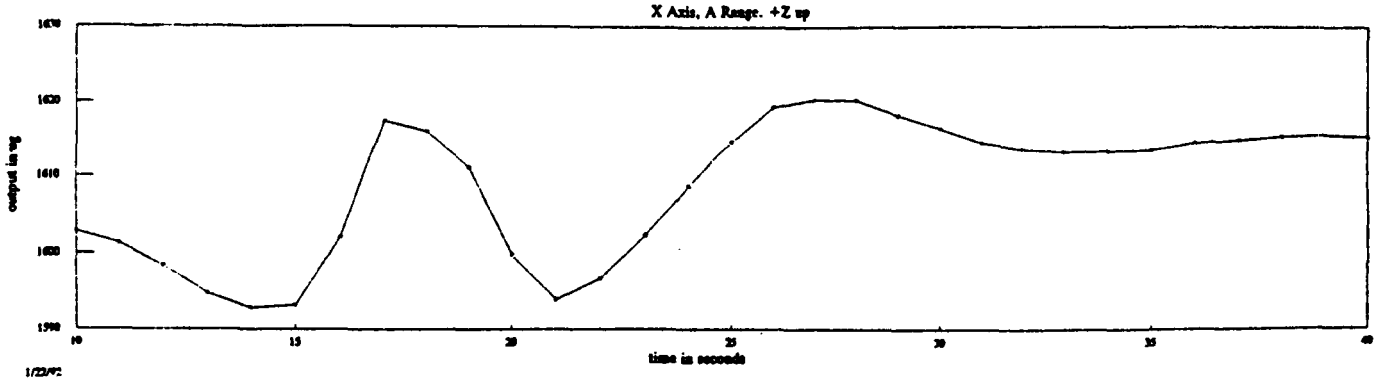

Figure 8 Roll Test of Cylindrical MESA Demonstrates Induced Error from Uncontrolled Degree of Freedom, Eliminated with the Cube MESA.

MICROGRAVITY MEASUREMENT ASSEMBLY (MMA) - A CENTRALIZED ON-BOARD MEASUREMENT FACILITY

Ingo Gerhard

DASA/ERNO Raumfahrttechnik GmbH
Hünefeldstr. 1-5
28199 Bremen, Germany

ABSTRACT

The Microgravity Measurement Assembly (MMA) is a centralized measurement facility for ground and on-orbit disturbance accelerations, currently designed for Spacelab applications, and has demonstrated it's full functionality the first time during the German Spacelab Mission D-2 in April / May 1993.

The system is using a new generation of micromechanical acceleration detectors. Small dimensions of the triaxial sensor packages allow for installation very close to scientific experiments. The mass is significantly reduced compared to previously used systems. The system capability to connect up to seven sensors to the central MMA computer lead for the D-2 mission to the following system configuration: Four of these mini-sensor packages have been installed near to the most g-sensitive experiments inside Spacelab racks. In addition two mobile sensor packages were available to be handled by the astronauts inside the cabin. These sensors could be installed near to various vibration sources like pumps, centrifuges etc. or any other location.

An impact hammer inducing defined forces was used together with MMA in order to support determination of structural transfer functions on-ground as well as on-orbit.

All data were collected and formatted by the MMA computer and send via High Rate Multiplexer to the ground. On ground the MMA Ground Station processed the data on-line to support either the other experiments or the transfer function determination.

Thus, for the first time, synchronized and comparable precision acceleration data were available in real time on ground for on-line judgment of the microgravity environment desired for experiment success, offering the possibility e.g. of experiment repetition in case of excessive g-disturbances. Furthermore MMA allows for immediate feedback to the crew concerning the microgravity effects of their own body movements with the aim to improve crew training towards lower crew induced disturbances.

The MMA on-board system and ground station is planned to be utilized for further Spacelab Missions and in modified configuration also for MIR.

Joint "L+1" Science Review for USML-1 and USMP-1 with the Microgravity Measurement Group, September 22-24, 1993, Huntsville, Alabama, USA.

INTRODUCTION

Results derived up to now from spaceborne microgravity research indicated, that for successful performance of a number of experiments a better micro-g environment was necessary than available on previous Spacelab Mission.

A first step in improving microgravity quality aboard Spacelab and future orbital research carriers as Columbus, is a thorough measurement of the actual micro-g environment given in a manned Spacelab Mission at the locations of microgravity experiments, as well as the empiric investigation of disturbance transfer functions of the spacecraft structure under weightlessness [4]. The results of such measurements provide on one hand precise information about experiment environmental conditions and on the other hand they can be used to derive design support information for either future Spacelab Missions or e.g. the Columbus program, with the overall goal of reducing disturbance accelerations caused by man and machine.

Acceleration measurement at various experiment locations is not new for Spacelab Missions. The German Spacelab Mission D1 was equipped with different types of accelerometers, with measurement capabilities limited by the individual data storage and transmission constraints. Thus, direct correlation of measured data was rather limited. A further disadvantage of previous measurement systems was, that the individual sensors provided data only for the time the individual payload was active and sensitive. Disturbances generated, e.g. , during activation of one payload element, by crew handling or acceleration / deceleration of vacuum pumps, etc. was measured by other payloads, but could not be correlated with local response measurements.

Post flight data evaluation of D1 acceleration data resulted in the conclusion, that additional standardization and centralization of detectors would improve micro-g investigations [1].

Furthermore a necessity for quick look analyses of acceleration data already during mission was recognized. The problem here was to find a way of computerized data reduction and production of easy to interpret summary plots in order to handle the large amount of data obtained from a set of acceleration measurement devices.

Thus, the demand arose for a centralized micro-g measurement facility for Spacelab Module Missions with a number of identical detectors, with identical data processing and transmission and a ground station for data reduction and providing quick look information during mission.

The flight hardware of this facility should be usable as well in orbit as on ground before mission. Comparison of ground and orbit measurements should enable predictions of expected on-orbit disturbances for future missions.

I. DESIGN REQUIREMENTS FOR MMA

MMA is designed to be a reusable facility for Spacelab module missions to be operated autonomously, independent of payload operation and throughout the whole mission duration. MMA is planned to be flown on at least 3 Spacelab Missions within the next 10 years.

Accelerations in three orthogonal axes are measured at four experiment locations with identical detectors inside racks. The Microgravity Sensor Packages (MSP) should be as small as possible in order to allow for installation close to scientific experiments and should have low masses to minimize the needed resources. Acceleration measurements should be possible as well in orbit as on ground before mission with identical hardware and precision, as far as the measurable quantities on ground, the induced vibrations, are concerned. Furthermore two additional mobile sensor packages, operated by the crew and to be flown as stowage item, should be usable at arbitrary positions inside the Spacelab module in order to measure e.g. accelerations at disturbance sources like water pump, centrifuges etc. MMA should provide an interface for an impact hammer set, operated by the astronauts, enabling measurements for later structural dynamics transfer function calculation under weightlessness for the determination of disturbance source to receiver transmissibility.

Fig. 1 shows the MMA measurement range and schematically, the main sources of disturbance acceleration to be encountered during Spacelab Missions. These are the shuttle Orbital Maneuvering System (OMS), the Primary and Vernier Reaction Control System (PRCS, VRCS), aerodynamic drag and gravity gradient, furthermore effects of crew, payload and machinery. The indicated typical payload requirement curve reflects the fact, that in general the sensitivity of microgravity payload to disturbing accelerations increases toward lower frequencies.

The scenario shown in Fig. 1 lead to a MMA measurement range from micro-g to 100 mg in acceleration amplitudes and from 0.1 to 100 Hz (without suppression of DC) in the frequency domain, with a resolution of 3.06 micro-g and an accuracy of better than 10 % per decade.

MMA consist of flight hardware to be integrated into Spacelab and of a ground station, enabling data storage and quick look analyses of acceleration data during checkout and mission. Among others as quick look data a A4 size paper print-out per sensor package over each 15 minutes with peak acceleration value information was foreseen. A further requirement to MMA was a modular hardware and software design offering flexibility for future extensions and modifications.

II. MMA SYSTEM CONCEPT AND ACCOMMODATION FOR D-2

MMA is a real-time data acquisition and processing system consisting of a flight- and a ground unit. Both units are connected by a real-time data transmission link.

The MMA on-board system provides a distributed network of sensors at selected locations inside

the Spacelab module and integrates the output of experiment dedicated and mobile sensor packages into a coherent data stream inside the Microgravity Measurement Electronics (MME) computer. This unit delivers the data, marked with a highly homogeny timing information, to the Spacelab Command and Data Management System (CDMS). Via orbiter telemetry and various satellite links, data are transmitted to the German Space Operation Center (GSOC) in Oberpfaffenhofen. The GSOC receives the data in the same way as they are transmitted by the MMA on board system and delivers them to the MMA ground station.

The ground station stores all data and processes them for on-line data evaluation and experimenters support and provides the capability for post-mission data analyses. The Block Diagram for the MMA D-2 configuration, is shown in Fig. 2. Four Microgravity Sensor Packages (MSP) with 3-axial micro-mechanical detectors are integrated into those Spacelab experiment racks, containing the most g-sensitive experiments. For D-2 the MSP were located in MEDEA, Biolabor, HOLOP and Werkstofflabor together with their dedicated Microgravity Sensor Electronics (MSE) which convert the analog sensor outputs into digital data streams.

Two additional mobile packages were available to be attached to different predefined locations within the Spacelab cabin on experiment request. All these units were connected to the central MMA computer inside Rack # 12, the mobile ones via the MMA front panel. The 7th MMA sensor channel was used for the impact hammer in order to support the transfer function measurement experiment. This assembly, the impact hammer and its dedicated electronics box, was also connected via the front panel to the MMA computer.

Microgravity Measurement Assembly Key Features

- 3-axis acceleration measurement in six identical sensor packages
- Low gravity measurement range: $3 \times 10^{-6}g$ to $100 \times 10^{-3}g$
- Frequency measurement range: < 0.1 to 100 Hz
- Miniaturized sensor packages, solid-state accelerometers
- Time-synchronized format
- Complete mission coverage
- Data display and analysis on ground in real-time
- Structural transfer function analysis available from impact hammer

III. MICROGRAVITY SENSOR PACKAGE

Key components of the MMA are the Microgravity Sensor Packages (MSP). The core element of the accelerometer sensor is a micromechanical chip which detects the on-board microgravity

disturbances in the first instance. It contains a movable plate which is suspended by flexure bars. This plate acts as an inertial mass and as a capacity plate. An acceleration perpendicular to the surface deflects the plate. This deflection is transformed to an electrical signal by measuring the associated capacity variations between the movable plate and fixed electrodes placed on either side [2]. The structure of the micromechanical chip is illustrated in Fig. 3.

This device represents a significant advantage over conventional sensors, offers improved sensitivity and greatly reduces weight. Three such accelerometers are mounted orthogonally on a precision machined metal block, and are assembled together with three integrated circuits to form a hybrid sensor head, as shown in Fig. 4. This hybrid is combined with additional electronics to form the Microgravity Sensor Package (MSP), as shown in Fig. 5.

The output of one MSP consist of three analog signals for the accelerations and one temperature sensor signal. As input, each MSP receives power lines and a self check signal to stimulate the MSP internal self check generation, which gives information on the mechanical and electrical health state of this unit.

Microgravity Sensor Package: Main Components and Performance Characteristics

- Micromechanical Accelerometer Chip

  Working range: ± 0.1 g

  Size: 5,5 mm x 8,3 mm x 1,4 mm

  Inertial mass: 14×10^{-3}g

  Suspension: 1 bar
  length 1 mm
  width 2 mm
  height 10 µm

- Hybrid sensor head containing triaxial accelerometer unit and 3 pre-amplifiers
- Electrostatic self-test stimulation source
- 3 synchronous accelerometer signal demodulators
- Temperature sensor
- Low gravity measurement range (absolute): 3×10^{-6}g to 100×10^{-3}g
- Operating temperature range: 5° C to 70° C
- Sensitivity (at 20° C): 100 V/g ± 2 %
- Frequency measurement range: < 0.1 to 100 Hz
- Frequency response from 0 to 10 Hz: within ± 0.2 dB, 0 to 100 Hz: within ± 2 dB
- Power consumption: 1,1 W
- Dimensions: H: 33, W: 87, L: 63 mm

- Mass: approx. 165 g

IV. MICROGRAVITY SENSOR ELECTRONICS

To minimize the size of the MSP, the electronics for conversion of the analog sensor output to digital values is located in a second box, the Microgravity Sensor Electronics (MSE). This unit is the interface between MSP and the central system computer (MME).

MSE processes the analog sensor signals by filtering with a sixth order Butterworth low pass filter, multiplexing and digitizing them with a 16 bit A/D converter, and then processes the digital data by a micro controller and transmit them using a RS 422 interface, to the MME.

The combination of MSP and MSE is called a Microgravity Sensor Assembly, as shown in Fig. 6. This combination is used for both rack-installed (fixed) assemblies as well as the mobile assemblies. The difference is, as shown here, that the mobile assemblies are equipped with fastening straps and double-sided Velcro^{TM} tape as well as a special attachment kit for the MSP to enable universal installation within the Spacelab module cabin.

Microgravity Sensor Electronics Key Features:

- Three differential input stages
- Three Butterworth lowpass filters of 6th order
- Temperature amplifier with current to voltage converter
- Four channel analog multiplexer
- 16 bit analog / digital converter
- High precision voltage reference
- Micro-controller with internal data memory and external ROM
- RS422 interface driver
- MSP self test driver
- DC/DC converter for MSE and MSP power supply
- Resolution: 3.06 µg
- Serial interface: 38.4 K Baud
- Power consumption: 5.1 W (with MSP connected)
- Dimensions: H: 85, W: 88, L. 128 mm
- Mass: 925 g

V. MICROGRAVITY MEASUREMENT ELECTRONICS (MME)

The MME is the central data acquisition, processing and transmission computer of MMA. This MODUS-computer is a standard computer developed by DASA and used for many other space

applications like EURECA, the IML experiment Critical Point Facility and the D-2 experiments Anthrorack and Biolabor. The computer is based on a real time operating system using a 8086 CPU instruction set. It is a modular system including digital and analog standard boards for signal receiving and special CDMS boards to communicate with the Spacelab CMDS.

MME provides for up to seven interfaces to MSA's, interface to the Spacelab HRM and RAU as well as to the time synchronization input UCSU of the Spacelab system and to the 28 V DC Power bus.

In the D-2 configuration, MME acquires the four rack mounted MSA data streams as well as the three data streams of the mobile equipment, the two mobile MSA's and the impact hammer, which are connected via the MMA front panel (see Fig. 8).

The general tasks of the real-time software are the packaging of the data, formatting of a 164,8 kbps data stream which is send via High Rate Multiplexer (HRM) to the ground. A subset of the HRM data as well as some more health data of the MMA are send via Remote Acquisition Unit (RAU) to the Spacelab system. All data are marked with a highly precise time information for later comparison with experiment data on-ground.

The MME is not only the data kernel of the system. Also the power for all components is converted inside the MME box and distributed to MSE's and MSP'S. This concept makes the MMA measurements independent of the actual operation status of the rack which contains the sensors. So it is possible, not only to detect the experiment disturbances, but also the µg-environment of the Spacelab itself, even so the sensor hosting racks itself are passive.

Microgravity Measurement Electronic Key Features:

- Standard Computer for Space Applications
- High performance, space proven low-power microprocessor 80C86 with timers, interrupt handling and on-board supervision capability using the real-time operation system ERTOS
- Standard interface connections to Spacelab Exp. RAU, HRM and 28 V DC power
- Accepts up to 7 Microgravity Sensor Assemblies
- Includes stabilized power supply for MSE/MSP operation
- Control Front Panel status (mobile MSA power) via digital input
- Synchronized system time signals via digital output to the MSE's
- HRM interface: 164,8 kbps
- ECIO / RAU interface: 512 bps
- Power consumption:
- 23,2 W (computer only)

-- 60.0 W (with 5 MSA's on)
- Dimension: H: 195, W: 226, L: 436 mm
- Mass: 8.52 kg

VI. IMPACT HAMMER ASSEMBLY

The Impact Hammer Assembly consist of a modified industrial impact hammer and an adapted MSE, the so called Hammer-MSE (H-MSE) see Fig. 8. It was used during D-2 mission for inducing and determination of transfer function measurement inputs. The hammer was used to stimulate Spacelab rack structures with predefined forces. These forces are detected by a hammer internal force sensor and transmitted via the H-MSE to the on-board computer and were here integrated into the data frame containing the MSP data. These time correlated data from hammer and MSP's allow for calculation of structure transfer functions.

The system was used during KSC checkout phase to support the ground transfer function determination as well as later on during mission to support the identical measurement sequence during flight. The ground station was used for data processing, display and to give a feedback on-line to the crew during both measurement sessions. Figure 9 shows the impact hammer.

Impact Hammer Assembly Key Features:

- Force Range: -1250 N to +1250 N
- Resolution: 16 bit, 1 LSB = 38.14 mN
- Error: < 2 %
- Noise: < 60 mN
- Band width: 0.1 to 100 Hz

VII. MMA GROUND STATION

The MMA Ground Station was developed to provide on-ground the capability to process the MMA data on-line during checkout and mission. The GST should support the KSC checkout phase including the ground-transfer-function measurements and the whole mission in support of other experiments as well as the in flight transfer-function measurements.

These requirements led to a system which had to be able to receive data via High Rate Demultiplexer (HRDM) and also via the GSOC LAN. It had to store all data and in parallel it had to support data replay requests from the users side. To support the above mentioned tasks the GST needs further a comfortable data display system with hardcopy capabilities.

The GST was split in two main components, see also Fig. 10. The first part is the '386 based

Front-End PC which provides the interfaces to HRDM and GSOC, reformats the MMA data and sent them to optical disks or on request in parallel to the second system part, the Display Unit (DU). The Front-End PC provide for a storage capacity of twice 7 h MMA data on each optical disk so that all D-2 mission provided MMA data could be stored on approx. 15 disks. The Front-End PC display show the major GST health data as well as collected MMA on-board housekeeping data.

The link to the DU was established using a transputer interface with fiber optical connection.

The Display Unit itself is a Unix system with CADA-X based display software.

It provides for processing and display of acceleration data in various formats, e.g. display of peak values in real time and replay on screen and paper, real time evaluation of the transfer function experiment and a lot of further functions to support other experimenters during mission.

A. Development

Initial development of the Microgravity Measurement Assembly was carried out by Deutsche Aerospace/Erno as prime contractor to the German Aerospace Research Institute (DLR), and completed under contract to the European Space Agency (ESA), which is now responsible for this facility. Deutsche Aerospace also developed the Microgravity Sensor Electronics, the Measurement Electronics (MODUS computer), and the Impact Hammer unit, as well as all software. The Microgravity Sensor Package was developed by CIR of Switzerland, as subcontractor to Erno. The solid state accelerometer was developed by CSEM of Switzerland, under contract to ESA.

The ground station development was split in two parts: The Front-End PC was developed by Deutsche Aerospace/Erno, the Display Unit by SAS and Trasys (Belgium). Both units were developed under ESA contracts.

VIII. MMA APPLICATION FOR OTHER SPACELAB MISSIONS

The MMA was operational during D-2 mission for over 200 h and operated without any technical or operational problems. The MMA data was processed by the MMA ground station and distributed in GSOC (German Space Operation Control Center) to the experimenters in real-time. No essential modifications have to be planned for further Spacelab flights.

Due to the modular system design and the standard interface between the central computer and the sensor assemblies, also an adaptation of new sensors, e.g. a DC sensor or an other micromechanical sensor type of smaller size, both under ESA development, could be very easily realized. The fact that MMA has only mechanical and minimum thermal interfaces to racks containing MMA sensors should allow for simple adaptation of the system to other mission configurations.

The ground station was a prototype for other standard systems. The handling during tests and mission show that here some improvements for both machines could be helpful for further applications to

support, more as it has done already during D-2, the experimenter requests as fast as possible.

IX. MMA APPLICATION FOR MIR

MMA is a flight qualified (D-2) equipment. Accommodation of the system for an MIR mission should be possible. In the meantime initial discussions on MIR flight opportunities and system configuration has been performed. Figure 12 shows a possible configuration suitable for a MIR mission.

The above shown MMA for MIR is based on the assumption that four sensor assemblies are sufficient for a MIR application. All MMA sensor assemblies are mobile and could be connected to the MMA computer located in a 19" housing via a front panel similar to the Spacelab D-2 version.

For the data storage two optical disk drives are foreseen. Each disk side is capable in this configuration to record approximately 12 hours of MMA data.

The required and available resources on MIR are the 28 V DC power interface and a line to the MIR clock to provide MMA with precise time information. Optional a high rate data interface should be provided for the MMA acceleration data. Such an interface would allow for an on-line data evaluation on-ground using the MMA ground station. Due to the limited availability of this link for MMA (or other experiments) it will only be possible to control well predefined events on-board MIR.

Using this optional mode, experiment events which need µg-control and feedback from ground could be monitored via the direct link to ground. All other µg-relevant experiment phases could be recorded on optical disk and evaluated after bringing the disk back to ground post-mission.

An additional on-board interface, realized e.g. by a standard link to a laptop, would provide MMA quick look data to the cosmonauts during mission.

The adaptation of MMA for MIR implies modification or reproduction of MMA system hardware and software. The real accommodation of MMA to MIR will be no problem due to the simple interfaces of the system. An adaptation to MIR is in any case possible.

SUMMARY

MMA is a reusable, centralized microgravity measurement facility to be operated autonomously and independent by any other payload operation. The system is currently designed for Spacelab application and has demonstrated its full functionality during approximately 200 h of uninterrupted operation while the D-2 mission in 1993.

The system was extended during its first usage by an impact hammer assembly to support, the first time in a Spacelab mission, determination of structural transfer functions on ground and in orbit.

The ground station of MMA has supported the whole test phase and the mission for both the control of the microgravity environment as well as the transfer function experiment.

Many experimenters requests during D-2 mission were supported, e.g. the breakage of a fluid column during an AFPM experiment could be explained on-line by a µg-disturbance detected by MMA.

Due to the modular system design of MMA and the current capability to accept seven three axial sensor packages the system can be accommodated for further Spacelab missions as well as in modified configuration for MIR without major modifications.

REFERENCES

1. Trappen, N.; Demond, F.J.: Post Flight Accelerometer Data Evaluation Proceedings of the Norderney Symposium: Scientific Results of the German Spacelab Mission D1, 27.-29- August 1986.

2. Eilers, D.; Gerhard, I.,; Hofer, B.; Rudolf, F., Brungs, W.: "Microgravity Measurement Assembly (MMA) for Spacelab Module Missions", IAF-88-343, 1988, pp. 1-8.

3. Gerhard, I.; Gilbert, C.: Microgravity Measurement Assembly (MMA) Description and Performance Summary Deutsche Aerospace / ERNO Raumfahrttechnik GmbH, Feb. 1993.

4. Research Program of the German Spacelab Mission D-2 DARA / WPF 1993 Second revised edition pp. 522-536.

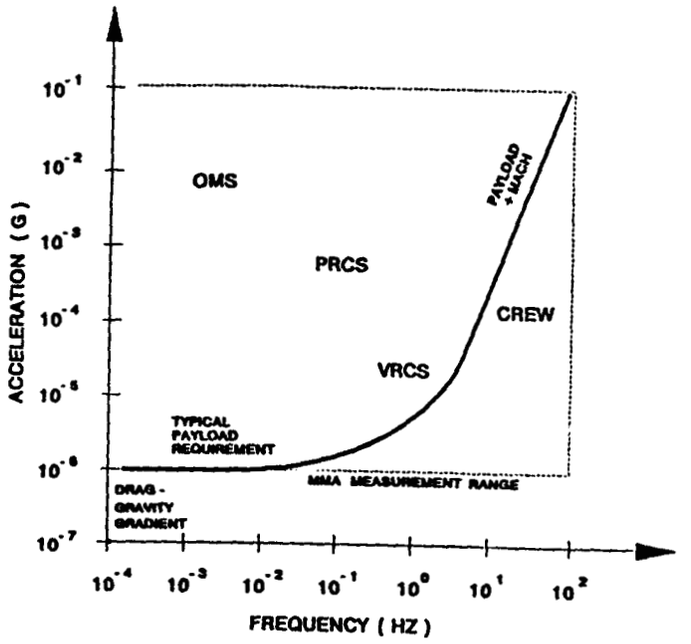

Figure 1 MMA Measurement Range.

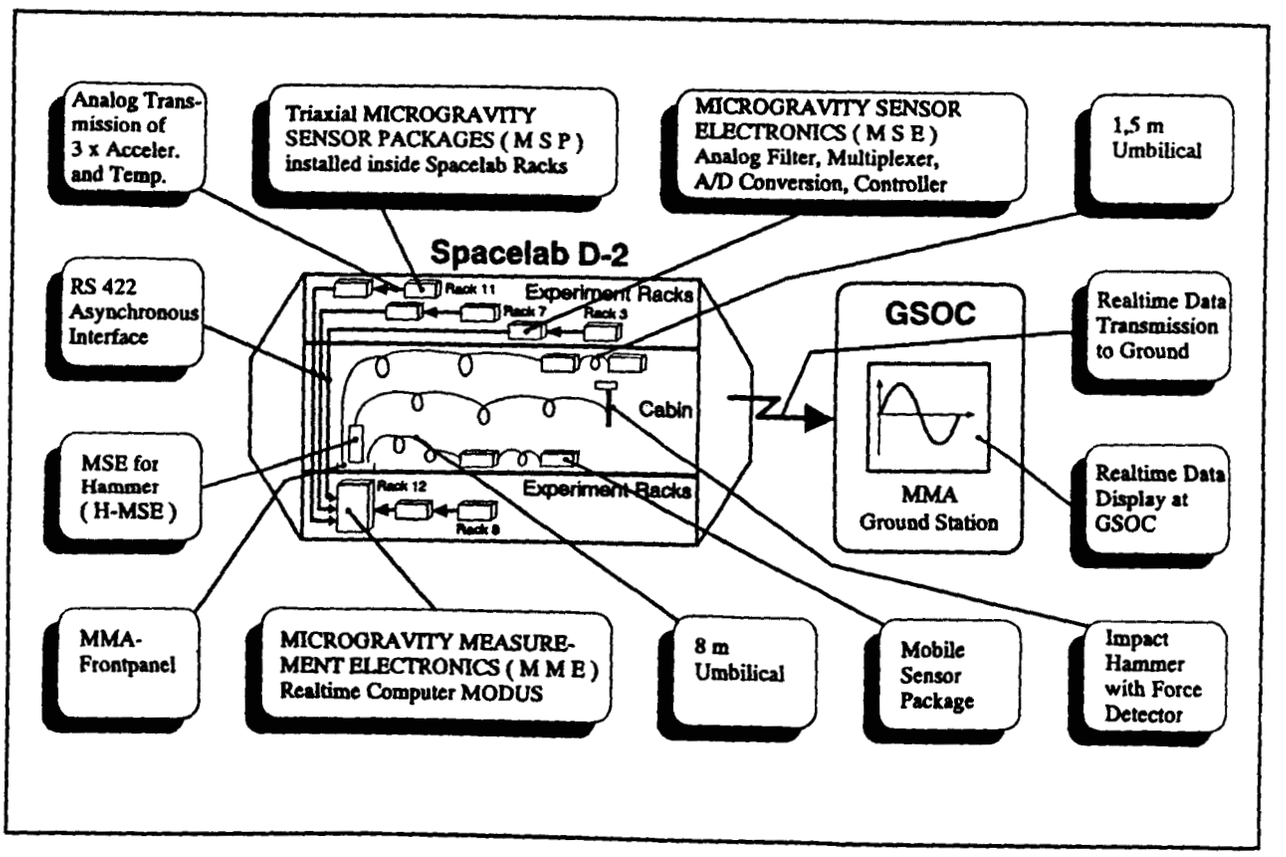

Figure 2 Microgravity Measurement Assembly Block Diagram.

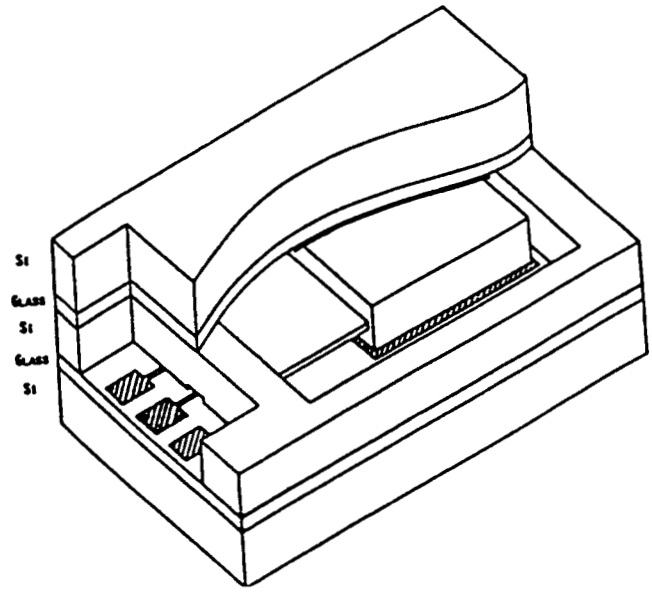

Figure 3 Schematic representation of the micromechanical accelerometer silicon chip.

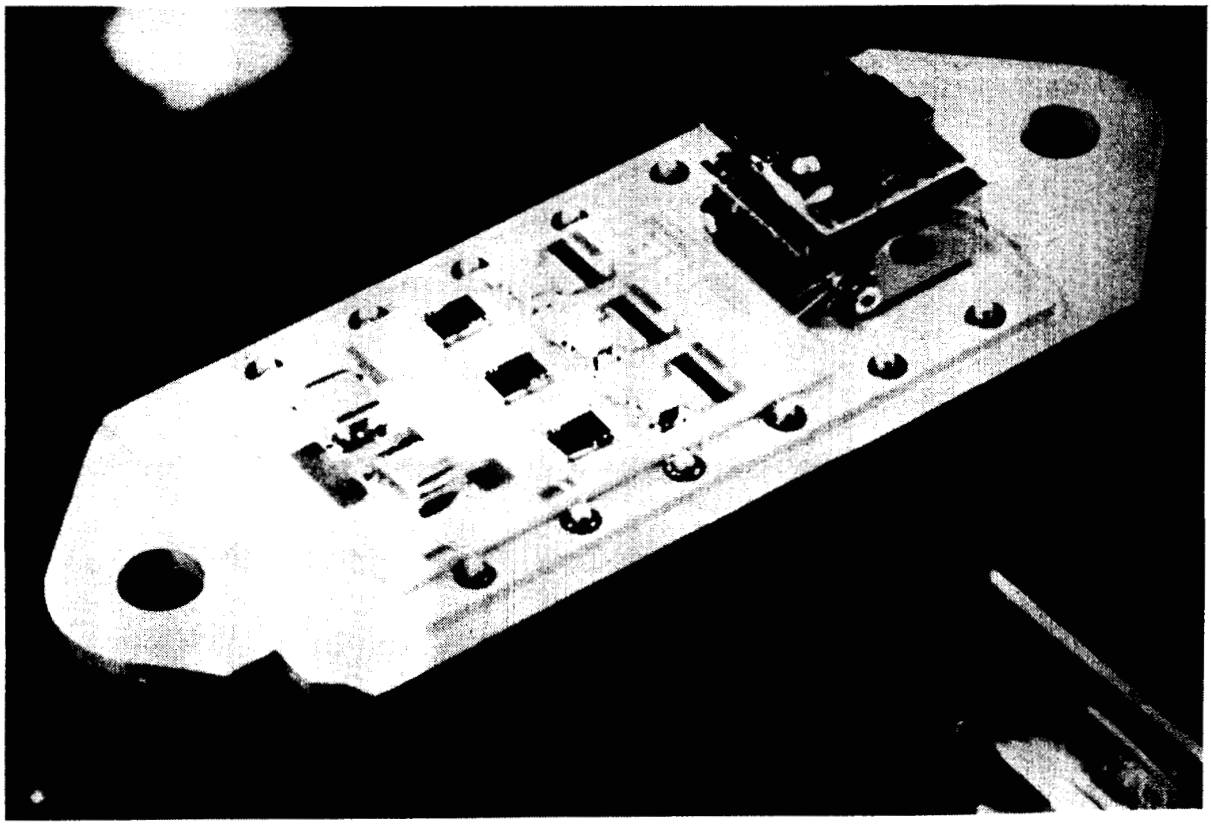

Figure 4 At the center of the Microgravity Sensor Package is a solid-state silicon accelerometer. Shown is the 3-axis hybrid sensor head, about 40 mm long, 15 mm wide, weight ca. 10 g.

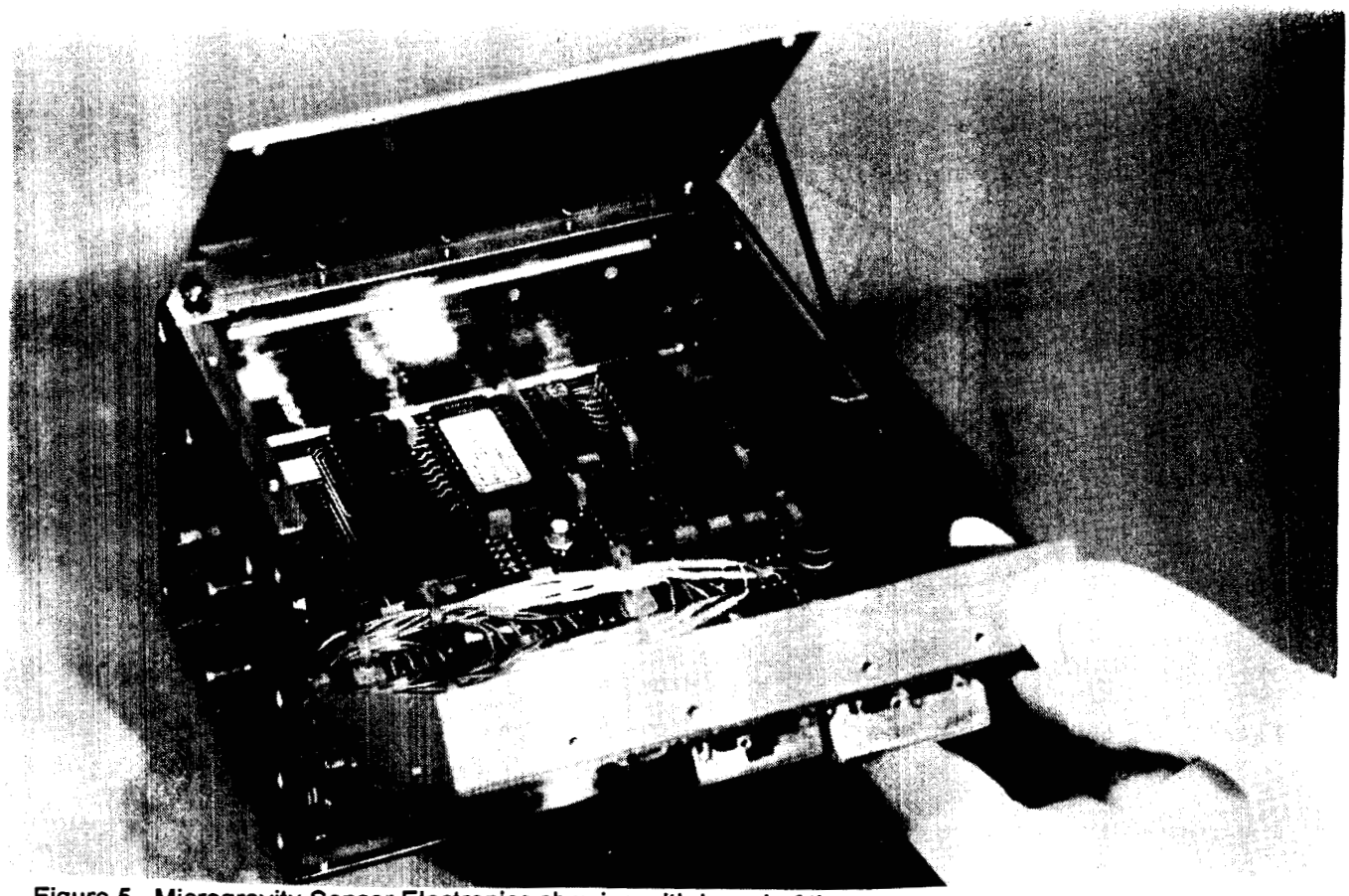

Figure 5 Microgravity Sensor Electronics showing withdrawal of the power supply module.

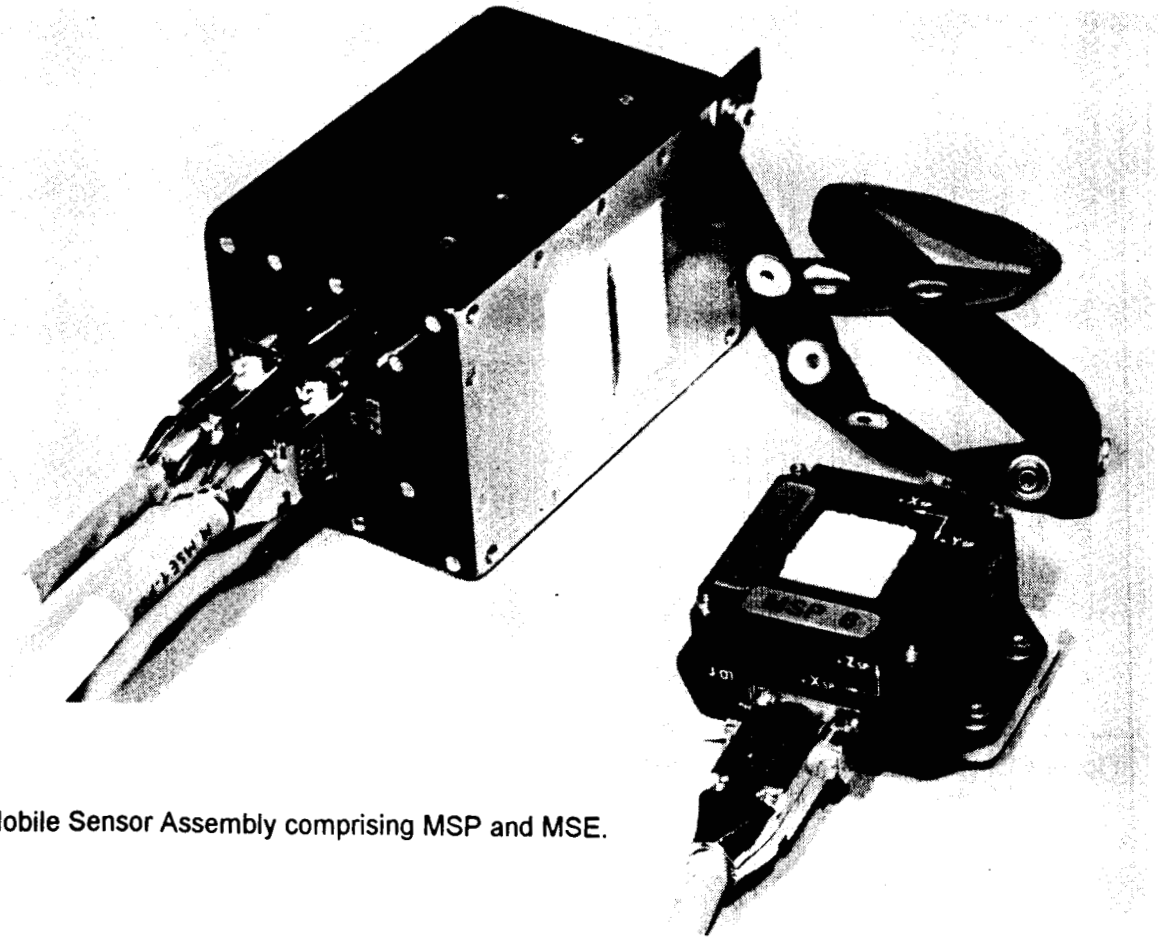

Figure 6 Mobile Sensor Assembly comprising MSP and MSE.

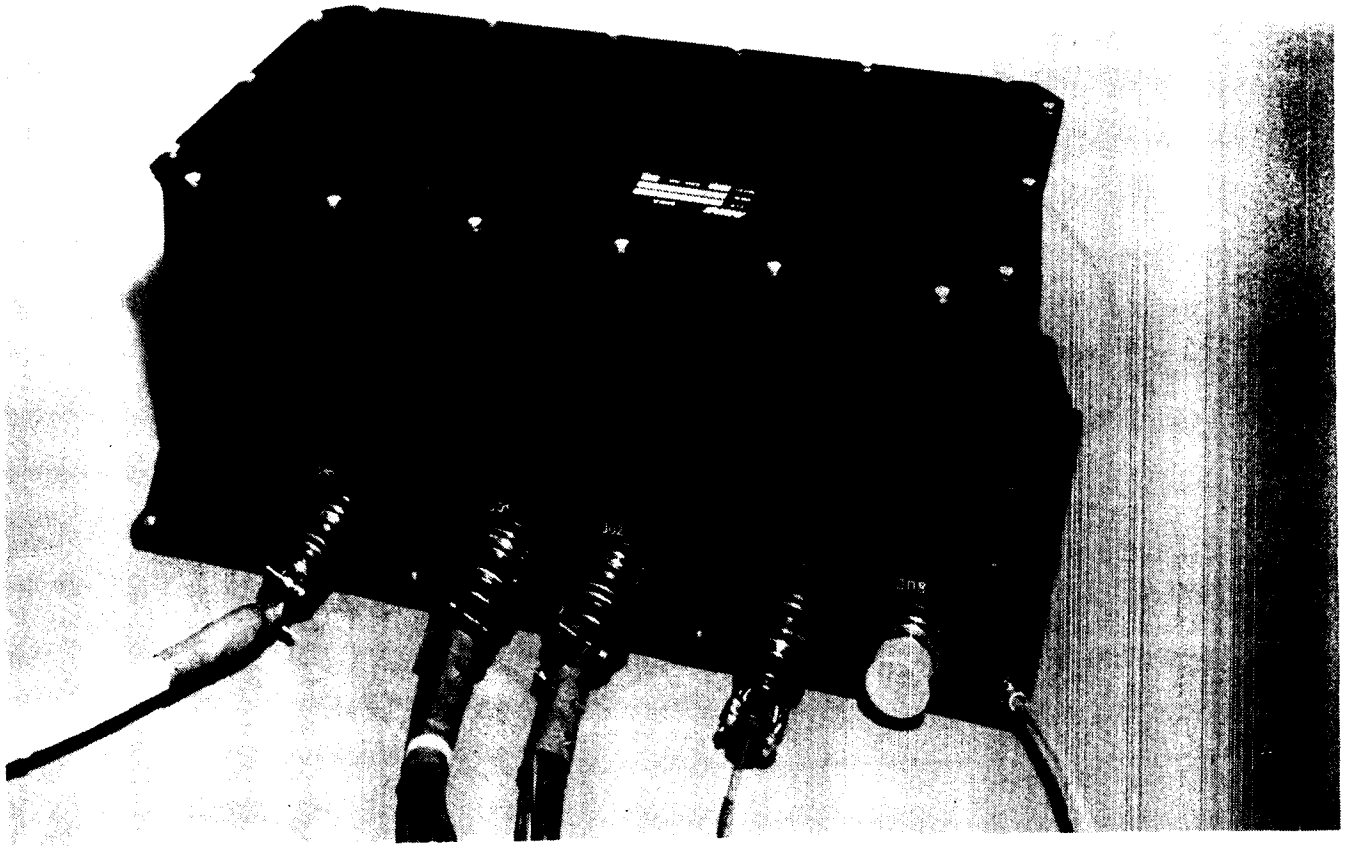

Figure 7 Flight Hardware of MMA On-board Computer.

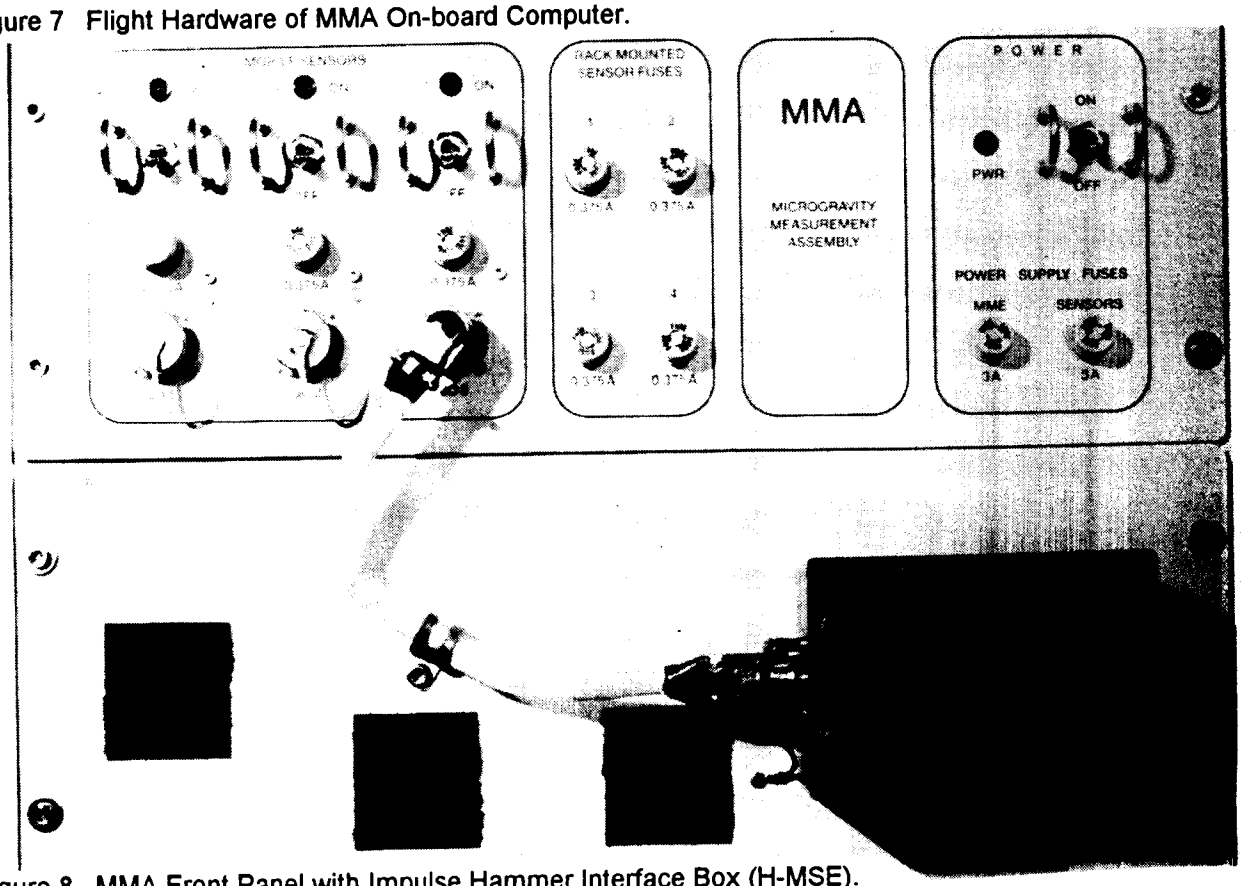

Figure 8 MMA Front Panel with Impulse Hammer Interface Box (H-MSE).

Figure 9 MMA Impact Hammer.

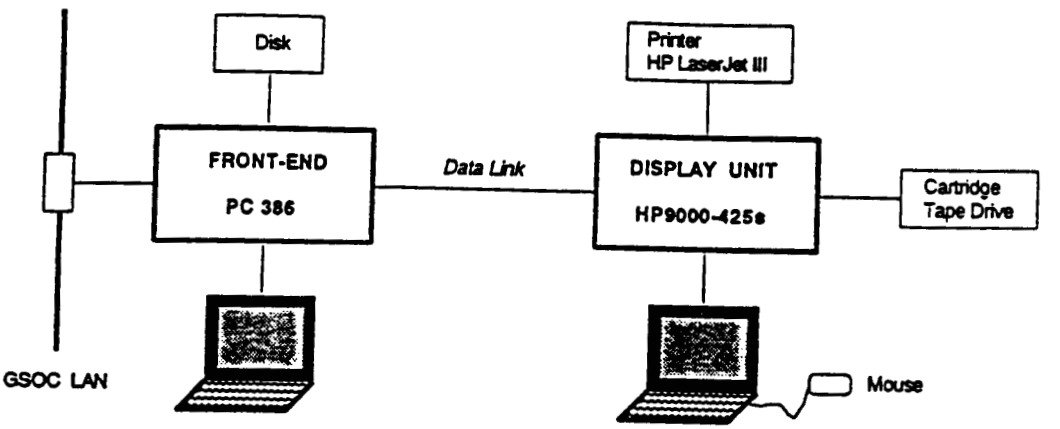

Figure 10 MMA Ground Station Block Diagram.

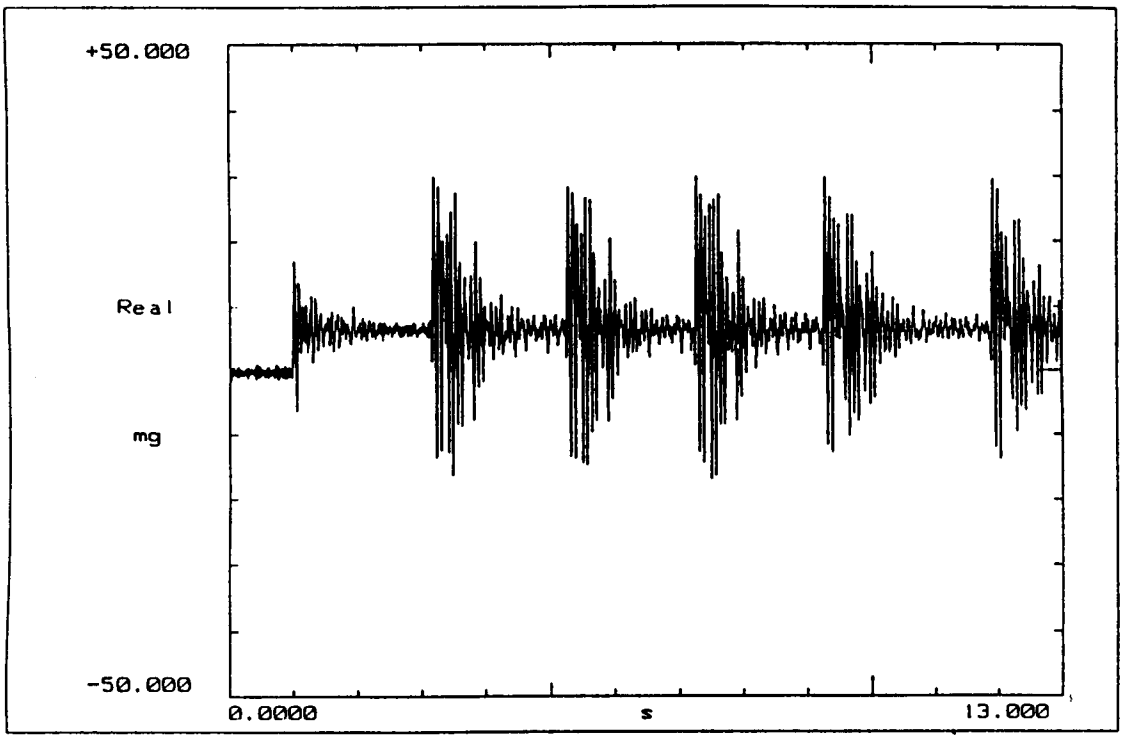

Figure 11 Typical Ground Station Printout (Trim Burn).

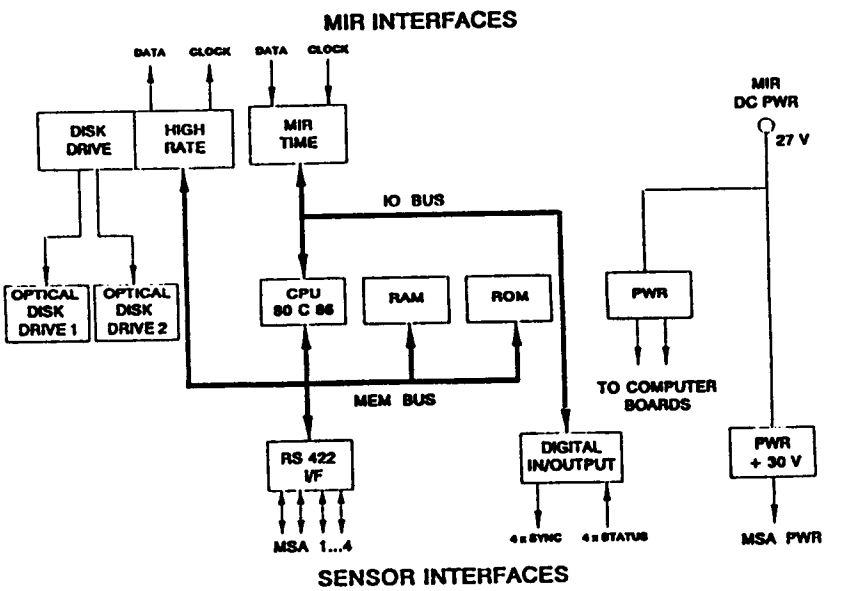

Figure 12 Proposal for a MIR MMA (Block Diagram).

Discussion

Question: *I have a question about the noise level for the instrument. Do you have a figure for that?*

Answer: Yes. I think about 5-6 micro-g

Question: *What is the maximum frequency of this module ?*

Answer: Our measurement range is from .1 to 100 Hz.

Question: *When do you plan to fly on the MIR ?*

Answer: As soon as possible. We have no date yet.

Question: *What is your sampling rate ?*

Answer: We have a sampling frequency of 300 Hz.

QSAM - AN APPROACH TO DETECT LOW FREQUENCY ACCELERATION IN SPACELAB

H. Hamacher, R. Jilg, and H.E. Richter

Deutsche Forschungsanstalt für Luft- und Raumfahrt (DLR)
Cologne, Germany

ABSTRACT

Most of the microgravity experiments show highest sensitivity to residual acceleration in the low frequency range, typically below 0.01 Hz, where atmospheric drag, gravity gradient and centrifugal forces are pre-dominant. QSAM is an instrument especially developed to detect this range where conventional methods are hampered by instrument bias and high amplitude noise problems entailing additional error contributions of detecting devices. Bias is generally varying in time due to unpredictable dependence on temperature, aging and other effects what precludes pre-mission calibration. In QSAM, signal modulation is applied by turning the sensor's sensitive axis. This allows the detection of accelerations in a frequency range between 0 and 0.02 Hz with a resolution better than 10^{-7} g_o.

INTRODUCTION

A free fall system simulates the state of weightlessness at its center of mass (CM) where gravity is locally canceled by inertia. This principle, approximated in a drifting spacecraft, is applied in space laboratories to carry out experiments under low gravity conditions. Complete weightlessness cannot be achieved in practice due to one or several of the following deviations from the free fall model:

(i) A drifting spacecraft is not in an ideal free fall condition as a consequence of residual external forces. Causes are atmospheric drag, solar radiation pressure, changes of the spacecraft's total mass (e.g. due to thruster firings, mass dumps, outgassing or sublimation of materials) etc.

(ii) There are residual forces acting on objects which do not coincide with the spacecraft CM:

a) Gravity is not completely canceled by inertia due to the gradient of the Earth's gravitational field (tidal effect).

b) Any rotation of the spacecraft creates centrifugal and tangential forces.

c) Changes in the mass allocation due to internal forces are a consequence of running machines, crew activities, etc.. Internal forces are compensated in time, so they do not affect the motion of the spacecraft CM.

Joint "L+1" Science Review for USML-1 and USMP-1 with the Microgravity Measurement Group, September 22-24, 1993, Huntsville, Alabama, USA.

Perturbing forces act on an interior object either directly as body forces (gravity, inertial forces) or indirectly as surface forces via the spacecraft structure (all external and internal forces). The acceleration of the object is thus determined by the time characteristics of the perturbing forces and the dynamic behavior of the spacecraft structure. The frequency range of the dynamic response function can be subdivided into two characteristic regimes: the regimes above and below the system's fundamental frequency f_f. The high frequency range is determined by the flexibility of the system. In the low or quasi-steady range the system behaves essentially as a rigid body. This is illustrated in Fig. 1 showing an example of a frequency analysis deduced from disturbance measurements during the Spacelab D1 mission [1]. The fundamental frequency of the Orbiter was $f_f \approx 1$ Hz. The symbols indicate harmonics of the system and excitation frequencies.

Only very few systematic measurements exist for the low frequency regime where the residual acceleration reaches the sub-μg range ($\mu g = 9.81 * 10^{-6}$ m/s^2) [2,3]. The reason for this lack is the difficulty to measure low signal amplitudes superimposed by noise levels, which are several orders of magnitude higher. Noise also includes sensor bias (offset) which has frequency components like the acceleration environment to be measured. Residual bias of state-of-the-art accelerometers is $>10^{-5}g$. The Orbiter's low frequency acceleration levels shown in Fig. 1 are therefore based on estimations of the main effects

> atmospheric drag

> gravity gradient forces

> spacecraft rotation.

There is a strong demand for a thorough analysis in the low frequency range, arising from investigations showing the majority of physical phenomena most sensitive to low frequency acceleration. The dashed line in Fig. 1 is typically the upper limit of acceleration tolerated by an experiment. It actually represents the specified maximum of residual acceleration allowed for the Global Space Station.

The measurement system QSAM (Quasi-Steady Acceleration Measurement) is an instrument especially developed to detect selectively the spacecraft's low frequency acceleration, free of any bias and noise, within an arbitrary vibration spectrum. Once the low frequency acceleration vector is known at one point the entire field can be calculated on the basis of rigid body kinematics. QSAM is selected to be part of the IML-2 payload (Second International Microgravity Laboratory). A second flight is planned for the Russian free flyer FOTON in fall 1995. In this paper the principle of QSAM is described together with its hardware design and data processing system.

I. A CONCEPT TO MEASURE QUASI-STEADY

There is a variety of available acceleration sensor heads. However, the performance characteristics are limited by error contributions typical for real detection devices what first precludes the measurement of the discussed quasi-steady accelerations. Figure 2 shows schematically a response curve of a linear servo accelerometer due to acceleration input within the full scale range, running from point A to B. The output signal a_r can be modeled by the expansion

$$a_r = b_0 + a + K_2 a^2 + K_3 a^3 + \ldots \qquad (1)$$

where a is the acceleration applied parallel to the sensor's sensitive axis, b_0 is the bias (offset), and K_2, K_3 are second and third order non-linearity coefficients. All values are generally affected by temperature, vibration, etc., and undergo hysteresis or non-repeatability.

Many of these variations can be neglected in most cases. For applications below 10^{-4}g, however, the bias b_0 and its stability becomes dominant. Bias thermal variations can be modeled or reduced by thermostats to a residual of about 10^{-5}g for state-of-the-art sensors, but there is still bias due to aging, vibrations and other causes, which cannot be calibrated or modeled. This becomes apparent for the high vibration levels during launch. The application in the 10^{-6}g range calls for other means of bias cancellation. In addition, the random vibration environment within a spacecraft -including electronics noise of the detection device itself- is classifying the measurement of quasi-steady acceleration as a problem to detect signals deeply buried in noise with the task to enhance signal-to-noise ratios by several orders of magnitude. The communication theory applies modulation techniques to mark such perturbed signals by frequency or phase transformation. A method to retrieve the modulated signal is the lock-in technique. The modulation applied to QSAM is based on turning the sensor axis by 180° as shown in figure 3. By taking the difference $a_r = a_{r,0} - a_{r,180}$ of a pair of readings in 0° and in 180° direction, eq. (1) yields

$$a = a_r / 2 - K_{2i+1}\, a^{2i+1};\ i = 1,2,\ldots \qquad (2)$$

Thus, a_r / 2 equals the true acceleration free of the instantaneous bias and non-linearity up to second order. This discussion in the time domain shows an improvement of the sensor performance parameters bias and non-linearity by applying signal modulation. However, the ability to increase noise rejection requires analysis in the frequency domain.

A. Lock-In Technique

Lock-in is a measurement technique, which combines the elimination of bias, drift and noise. The output of a lock-in analyzer is the component of the input signal, which has the same frequencies and phase than a given reference signal. Figure 4 shows the basic components of a lock-in analyzer. The incoming signal Ui(t) is pre-amplified by an ac-amplifier with gains as high as possible to unburden the dc-amplifier at the end of the circuit and so to minimize its drift. However, the ac-amplifier must not be overdriven by peaks in the incoming signal and all amplitudes have to be in its linear operating range. This requires a basic knowledge of the signal level to be measured and the superimposed noise. For noise reduction a low- or band-pass pre-filter increases the signal-to-noise ratio of the amplified signal. The filter roll-off has to be selected not to interfere with the frequency of the modulated signal. The following phase sensitive detector (PSD) functions as multiplier with the output Up(t) = Uf1(t).Ur(t) where Uf1 is composed of the modulated signal of interest and perturbing signals of all possible frequencies and phases within the bandwidth of the pre-filter. Assuming Ur to be a rectangular wave and expanding Ur and Uf1 in Fourier series, it can be shown that the output of the post-filter following the PSD has only components at frequencies [10]

$$fp = \sum_{n=1}^{\infty} fr(2n-1) \qquad (4)$$

This means that also odd harmonics of the reference frequency are passing the PSD (however, damped with 1/(2n-1)) and can perturb the modulated signal. It is a further task to suppress harmonic response by selecting the pre-filter with a roll-off near above the modulation frequency or by applying digital demodulation techniques, e.g..

Case A in figure 4 represents analyzer used for detection of signals with known modulation frequency, but which are covered by noise or drift (QSAM). Path B represents analyzers used as tracking-filter or phase-synchronizer. They are realized by a signal controlled oscillator, which uses the output amplitude of the post-filter to adjust the reference signal Ur(t) in phase and frequency so as to reduce the phase difference of the incoming signal Uf1(t) and the reference signal Ur(t).

B. The Adaptation of the Lock-In Technique for QSAM

The elements of an analog lock-in amplifier can be substituted by digital components. Digital technique is free of any drift, without build-up time flexible in changing parameters and has no limitations towards low frequencies. QSAM uses a hybrid concept as shown in figure 5.

A modulation of 0.07 Hz is applied to QA-3000 accelerometers, which are linear servo sensors with resolution better than 10^{-6}g, high bias stability, dynamic range and reliability. However, the initial

bias can be as high as 10^{-3}g what would overflow the following components. Since QSAM shall be an instrument with a minimum of calibration requirement, this offset is calculated and shifted during power-up with an input amplifier. The full scale factor of 10^3V/g is reached after the ac-amplifier with a programmable gain of up to 1000. The pre-filter with a 3 Hz roll-off still allows harmonics of the modulation frequency to pass. These are eliminated by the digital phase sensitive detector, which pulls out only components equal to the first Fourier component of the modulation frequency Ur(t). The adaptive post-filter increases the output stability and sets the overall bandwidth to $0 < f < 0.07$ Hz.

II. SYSTEM DESIGN

QSAM in the IML-2 version consists of two pairs of accelerometers each of which is mounted on a rotating device flipping the pairs by 180° as shown in fig. 6. The relative orientation of the two devices and the number of accelerometers used allow to detect the acceleration vector with a minimum redundancy of 100%. Resolution and absolute error are $< 5.10^7$ g.

QSAM is also equipped with static tri-axial (AC) accelerometer package to detect the frequency range up to 50 Hz. All data are analyzed on line, stored on board, and most are transmitted to ground. An on board display provides the crew with acceleration data and status of the instrument, etc. (fig. 7).

CONCLUSIONS

There is a strong need for in-flight measurement of the residual acceleration in the frequency range up to $\approx 10^2$ Hz, where most physical phenomena show highest sensitivity to residual acceleration. State-of-the-art accelerometers have residual bias levels at least one order of magnitude higher than the signal to be detected. The non predictable nature excludes bias modeling in the relevant range. QSAM cancels all bias by turning the sensor axis and applying a lock-in technique. A measurement at a single location within the spacecraft together with the knowledge of the orbiter attitude are sufficient to calculate the entire acceleration field due to the rigidity of the spacecraft in the low frequency range. QSAM is also suited to be applied for center of mass determination, detection of atmospheric drag and, indirectly, for the determination of atmospheric density and the drag coefficient.

Moreover, the application of QSAM is not restricted to space technology. There are many potential fields of applications in civil engineering and sciences.

REFERENCES

1. Hamacher, H., Jilg, R., Merbold, U., "Analysis of microgravity measurements performed during Spacelab 1", ESA SP-256, 1987, pp. 413-420.

2. "Spacelab payload accommodation handbook", NASA Spl/2104, main vol, issue 2, 1985.

3. Jacchia, L.G., "Variations in the Earth's upper atmosphere as revealed by satellite drag", Rev. Modern Phys., 35, 4, 1963, pp. 973-991.

4 Hedin, A.M., "MSIS-86 thermospheric model", J. Geophys. Res., 92, A5, 1987, pp. 4649-4662.

5. "Space and planetary environment criteria guidelines for use in space vehicle development, 1982 revision (volume 1)", NASA TM 82478, 1983.

6. Escobal, P.R., "Methods of astrodynamics", Wiley, New York 1968, pp. 23-28.

7. Walterscheid,R.L., "Solar cycle effects on the upper atmosphere: Implications for satellite drag", J. Spacecraft, 26, 6, 1989, pp. 439-444.

8. Blanchard, R.C., Hendrix, M.K., Fox, J., Thomas, D.J., Nicholson, J.Y., "Orbital acceleration research experiment", J. Spacecraft, 24, 6, 1987, pp. 504-511.

9. Probst, P.A., Collet, B., "Low-Frequency digital lock-In amplifier", Rev. Sci. Instrum., 56, 3, 1985, pp.466-470.

10. Winterhalder, M., "Theoretische Semesterarbeit: Signaltheoretische Gegenüberstellung analoger und digitaler Modulationsverfahren zur Messung Quasi-Statischer Orbitaler Beschleunigungen", Technische Universität München, 1990.

11. Toney, J.H., Demas, J.N., "Low-Frequency Computerized Lock-In Amplifier", Rev. SCI. Instrum. 53(7), 1982, p. 1082.

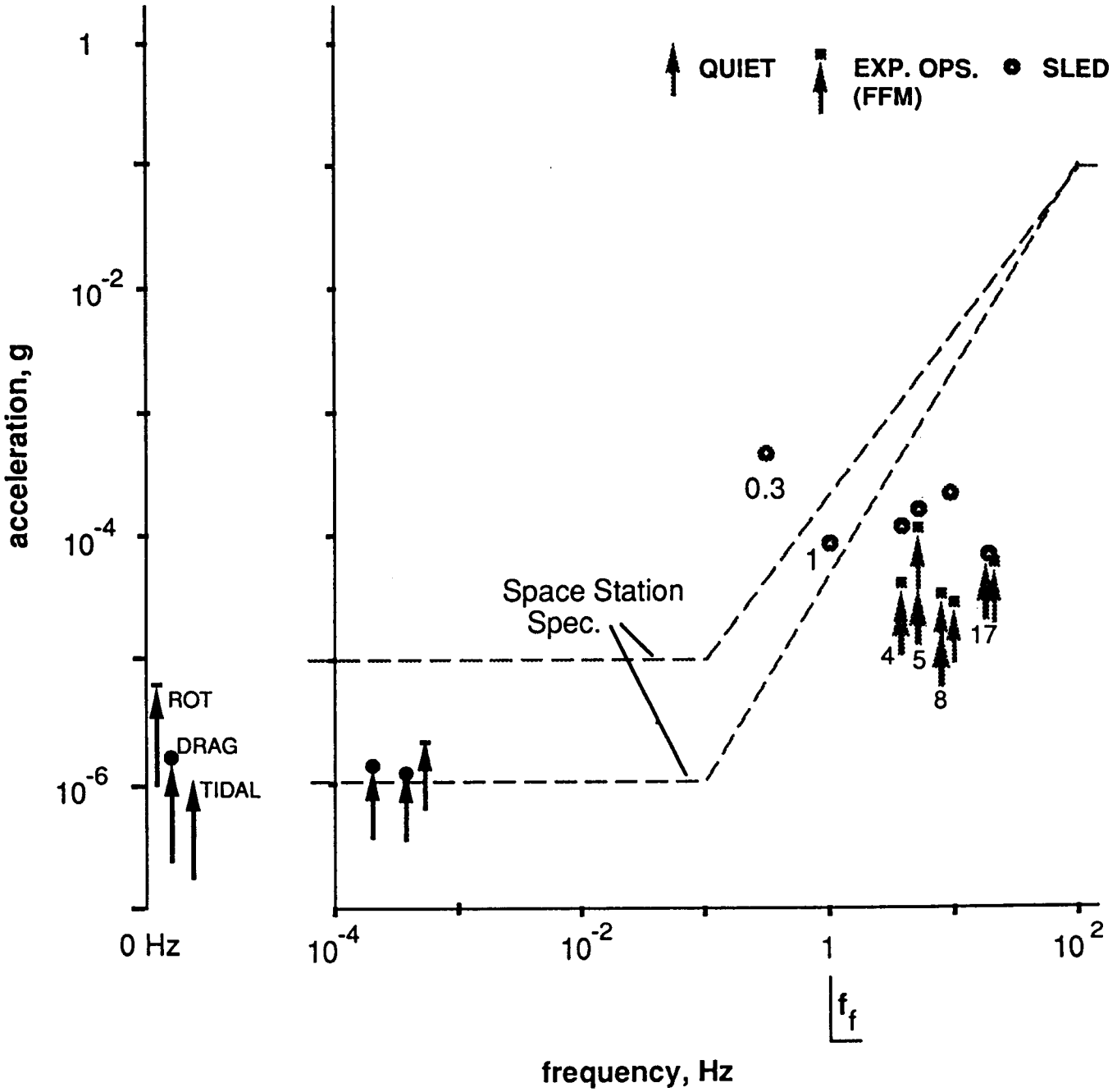

Figure 1 Frequency analysis of Spacelab D-1 data. The symbols refer to different mission events. Values above 0.1 Hz are based on measurements, data below 0.1 Hz result from analytical calculations for atmospheric drag, tidal and centrifugal acceleration [1]. The dashed line represents the upper acceleration limit tolerated for the Global Space Station Freedom.

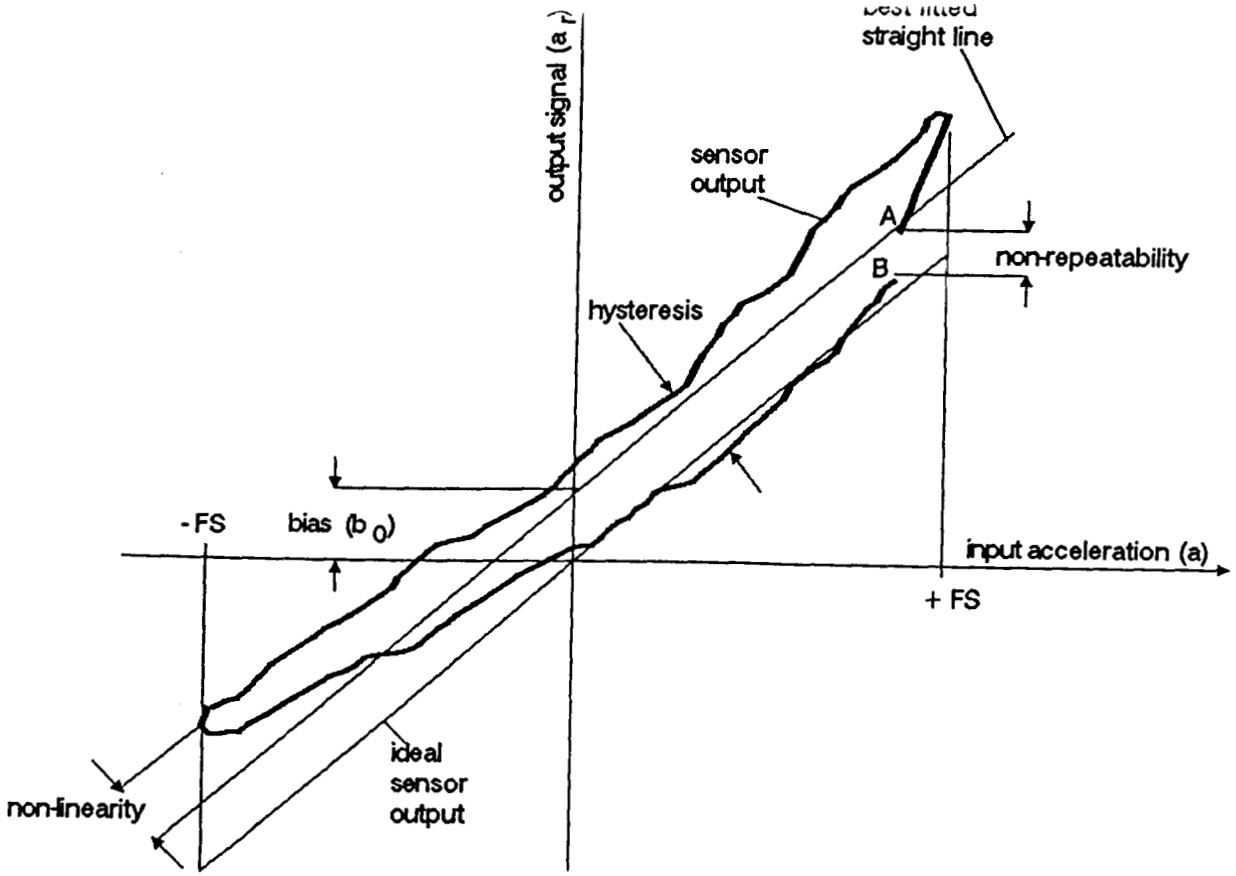

Figure 2 Output characteristic of a linear servo accelerometer and error contributions.

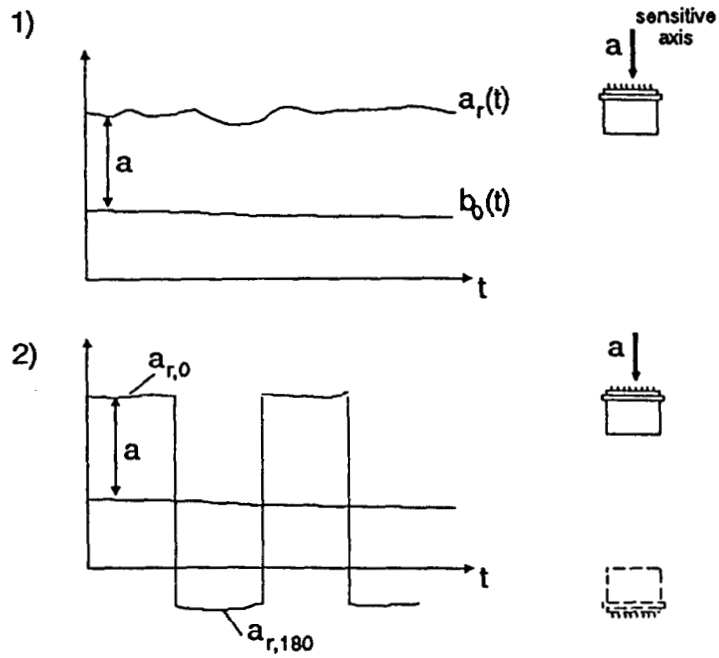

Figure 3 The concept of QSAM to cancel bias is based on flipping the sensor's sensitive axis by 180° continuously. This modulates the signal (1) to (2) and allows to determine the true acceleration from eq. (2).

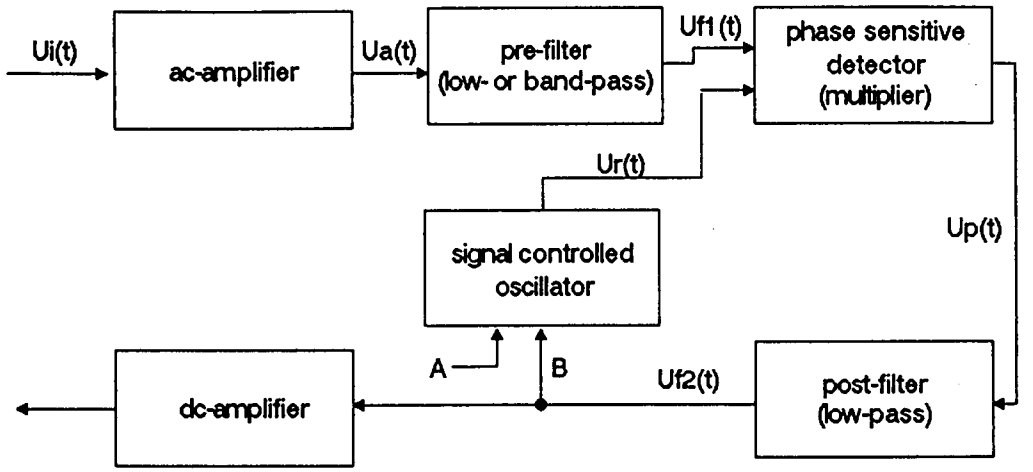

Figure 4 Basic components of a lock-in amplifier.

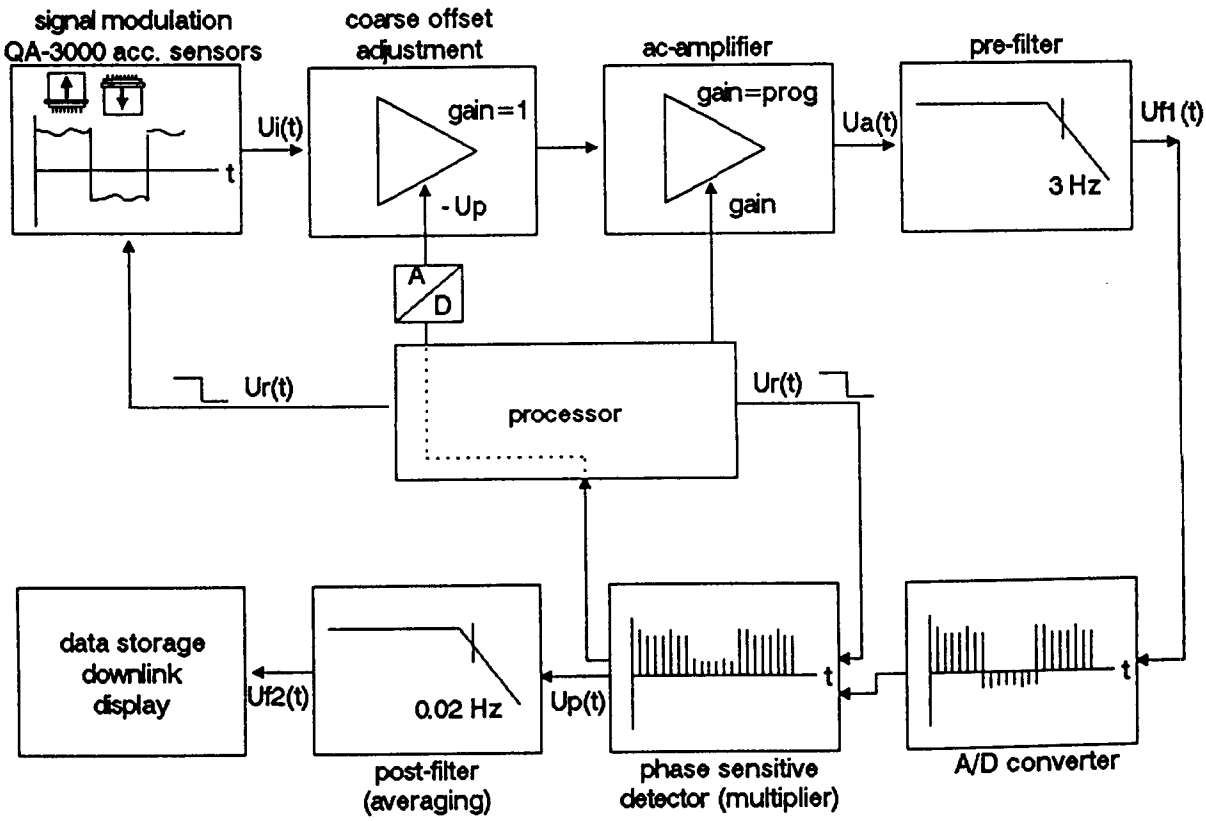

Figure 5 Setup of the lock-in technique for the experiment QSAM.

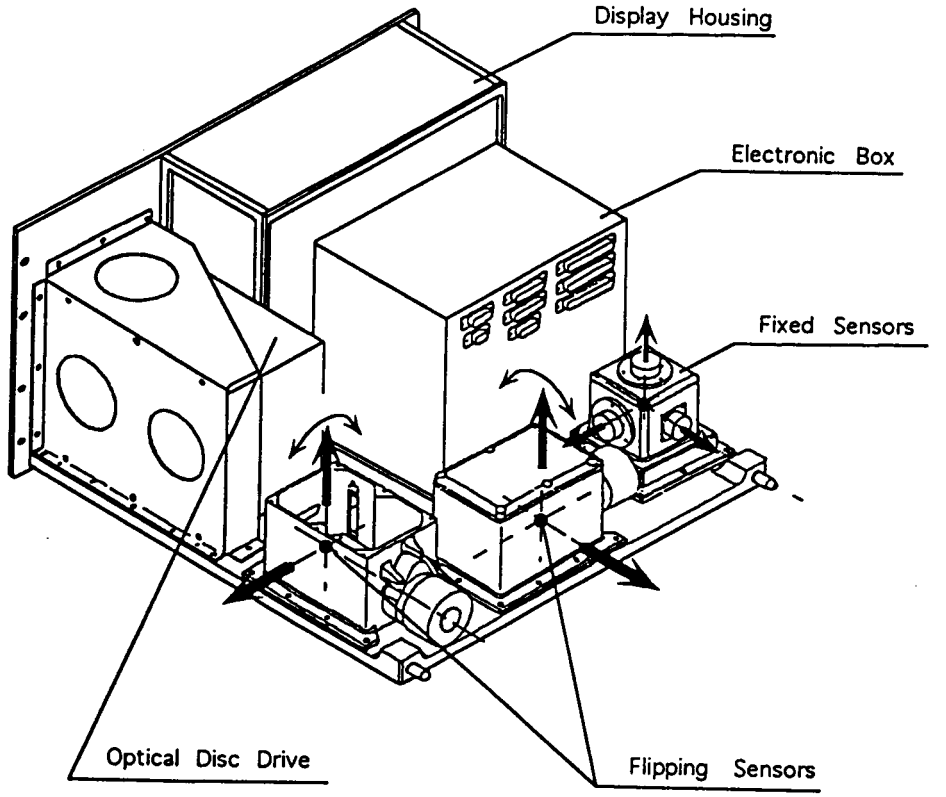

Figure 6 QSAM hardware for IML-2.

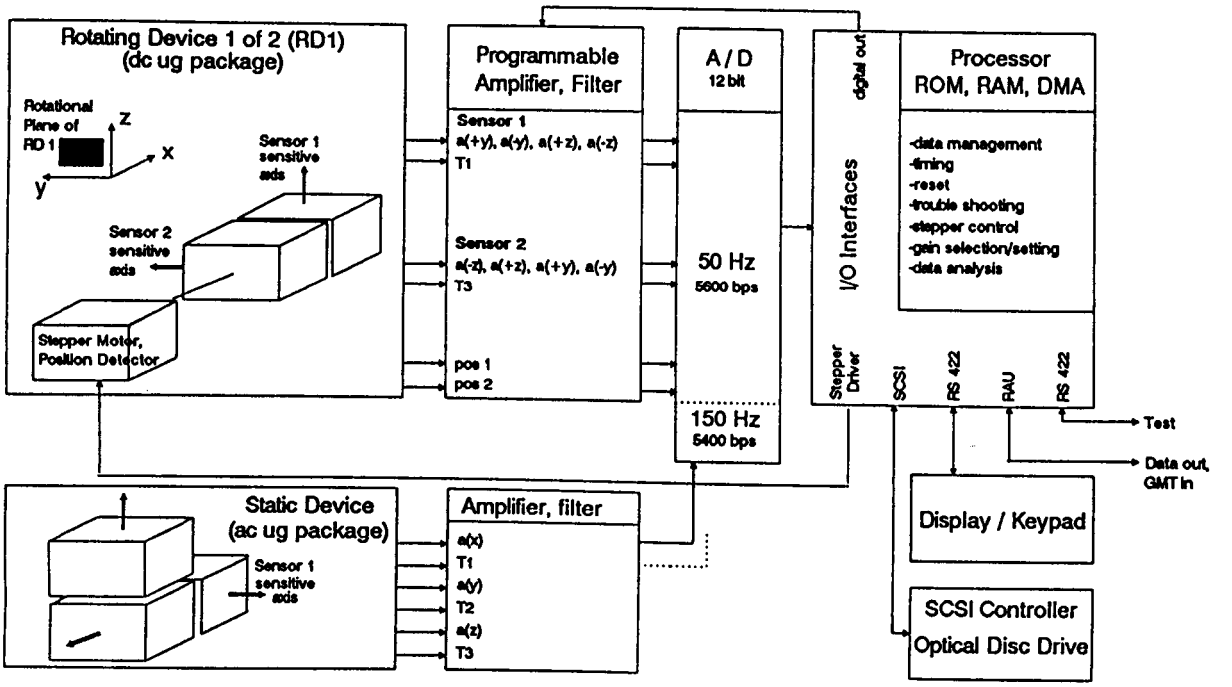

Figure 7 Block diagram of QSAM data management.

Discussion

Question: *How do you minimize the input put into the spacecraft by your device while making measurements ?*

Answer: Yes. We have selected very quiet stepper motors with the aim of not generating too much noise when measuring the acceleration. That was not easy. We found a system, finally, that is quite smooth but that turned out to be one of the serious problems.

Question: *What kind of rotational position accuracy do you achieve with the system ?*

Answer: The accuracy in the positioning of Z axis that is on the order of half a degree.

Question: *How long does the flipping procedure take ?*

Answer: It takes about 1 second to flip over. We are trying to keep that period short. On the other hand, it induces vibration and disturbance. That is a compromise between the requirements.

Question: *About the performance data, you talked about it. How about some results? Before flight what does your noise calibration look like ?*

Answer: Yes. We tested the system. The task as I said in the beginning, was to measure 10^{-7} g within very high level of noise. We did the following: We mounted our system on a plate and calibrated that system by very sensitive quartz actuators and we found resolutions better than 10^{-6} g on ground. After that calibration process, we mounted a shaker on to that plate, and the shaker excited the plate to about 5 g. Then we repeated our procedure by the actuators and we found the same signal, not affected by the high vibration level of the sinusoidal vibration with 5g amplitude. We did this with a variable frequency between 1 Hz and 50 Hz. That is a whole range of frequency we have qualified it for.

EURECA MICROGRAVITY ENVIRONMENT - PRELIMINARY FLIGHT DATA

D. Eilers* **and H. R. Stark+**
*ERNO Raumfahrttechhnik, Bremen, Germany
+ESA/ESTEC, Noordwijk, The Netherlands

ABSTRACT

EURECA, the European Retrievable Carrier, provides a new platform to perform microgravity research in a low gravity orbital environment over extended duration of at least six months. The first mission was launched in August 1992. After the free flying period, the EURECA spacecraft was successfully retrieved by the Space Shuttle and landed on June 24, 1993. EURECA has been designed for at least five launches and retrievals.

In order to comply with the stringent microgravity requirements, the EURECA system, subsystem and payload performances shall maintain a controlled microgravity environment and shall not exceed a limited acceleration response spectrum at the payload mechanical interfaces. Intensive design, development and optimization activities were implemented and verified by simulations, analyses and during an integrated system test on-ground. Finally, on-board acceleration measurement system completed the information about the quality of the micro-g environment.

This paper summarizes the preliminary review of the residual accelerations as measured during the first mission period of EURECA between 07.08.92 and the 1.10.92 in correlation with the previous analysis and ground test results, as well as some later data.

The on-board Microgravity Measurement Subsystem (MMS) detected the residual accelerations after command from ESOC, the European Space Operations Center, in Darmstadt, Germany. This review is namely based on a set of 906 acceleration measurements during the initial period, with a duration of 3.167 minutes and in some cases up to 657.6 minutes.

The MMS data were transmitted from ESOC to the Microgravity User Support Centre (MUSC) at DLR, Köln-Porz, for processing and presentation. The preliminary evaluation provided very interesting results. For instance, a dominant vibration frequency of 0.85 Hz is observed which can correspond to a FEM-mode shape. A modulation frequency of 0.04 Hz could also be caused by two adjacent mode shapes. Measurements over orbit periods show repetitive slight changes in the vibration behavior beginning with and during each eclipse phase, etc.

The paper will present these findings and the conclusion that the desire design goal for the microgravity quality on EURECA was met.

Joint "L+1" Science Review for USML-1 and USMP-1 with the Microgravity Measurement Group, September 22-24, 1993, Huntsville, Alabama, USA.

INTRODUCTION

EURECA, as a large and most complex European spacecraft, completed its first mission after eleven month on orbit and is back on Earth. The utilization of a very low gravity environment over an extended time period provided a dominant prospective of this space flight mission [1]. EURECA carried 1000 kg of payloads on board the 4400 kg spacecraft.

The quality of the microgravity environment, as a result of the EURECA system requirements and associated design and development activities, was monitored during the payload operational period with the Microgravity Measurement Subsystem (MMS). The MMS consists of a set of accelerators mounted at three outer locations with two sensitive axes in each package and a frequency bandwidth from DC to 5 Hz. The acceleration response data received from the MMS during the mission contained a lot of information about realistic spacecraft conditions in comparison with analytical predictions.

I. MICROGRAVITY ENVIRONMENT REQUIREMENTS FOR EURECA

EURECA is the first spacecraft designed for a specified micro-g environment. The EURECA mission, the spacecraft and payloads had to be designed such that the residual acceleration spectrum in Fig. 1 is not exceeded. That means, that during operation of microgravity sensitive payloads the microgravity environment at the spacecraft/payload interface should be equal or better than the tolerance level in Fig. 1. This acceleration spectrum should also be valid and applicable for pulse type and transient events. Sensitive payload operation was defined for a continuous and uninterrupted duration of 180 days with the exception of the orbital adjustment maneuvers as required to perform phase angle and ascending node corrections for retrieval by the Shuttle.

Similar specifications have been under consideration for the Spacelab D2-Mission and are considered in the Space Station Freedom (SSF) program and its COLUMBUS element.

For the purpose of direct comparison with the measured acceleration time histories, the EURECA limit acceleration spectrum is converted back into the time domain.

It is assumed that the EURECA requirement allows for a broad spectral response of a random vibration type acceleration in the frequency range from 0.1 Hz to 5 Hz. The upper frequency of 5 Hz corresponds to the MMS measurement bandwidth and the lower frequency of 0.1 Hz with first vibration modes of the flexible spacecraft. The amplitude spectrum of the EURECA requirement in Fig. 1 can be converted into an acceleration power spectral density spectrum, PSD in g^2 per Hz, considering a spectral resolution of $\Delta f = 1$ Hz, with 10^{-10} g^2/Hz form 0.1 Hz to 1 Hz and sloping up to 2.5×10^{-9} g^2/Hz at 5 Hz.

In order to determine the equivalent effective root-mean-squared acceleration value in g(rms) in the time domain, the PSD-spectrum is integrated of the frequency range from 0.1 Hz to 5 Hz (Fig. 2).

$$a(rms) = \sqrt{\int_{0.1Hz}^{5Hz} (g^2 / Hz)df}$$

The composite acceleration level in the time domain results with

$$a(rms) = 6.5 \times 10^{-5}\ g(rms)$$

II. EURECA MICRO-G ENVIRONMENT DESIGN AND DEVELOPMENT ACTIVITIES

Extensive design and development activities and optimization cycles were performed on all project levels and development periods [2], from equipment level up to system and for payloads, in order to maintain the micro-g specification. Design features, that had been considered and introduced, were for instance:

- The mission profile and initial orbital height was selected such that at the end of a 180 day mission period the minimum altitude still assures low drag acceleration without interim orbital re-boots, even under worst case atmospheric drag influenced by solar activity and geomagnetism.
- The spacecraft center body cross section is small, about 6 to 8 m^2, pending on the orbital position.
- The solar array cross section of about 50 m^2 was optimized with regard to the power needed and the drag accelerations limits.
- The payload is located on an upper deck very close to the spacecraft center of mass, at distances between 0.5 m and 2 m, in order to minimize the gravity gradient.
- The location of the spacecraft center of mass is stable during the mission, supported by symmetrical fuel consumption from the propulsion tanks.
- The complete spacecraft sun-orientation was chosen to avoid solar array drive mechanism and associated perturbations.
- The spacecraft attitude was stabilized through magneto-torques and fine 20 mN cold gas thruster with build-in controller strategies to suppress action of multiple actuators at a time.
- The use of reaction wheels for attitude stabilization was disregarded due to the vibrations induced at higher speeds and stiction/friction impacts at zero speed crossing.
- On-board data are stored by a bubble memory instead of an electromechanical data recorder which generates vibrations and shocks.

• Data transmission to ground is made via fixed antennae, such that a steerable antenna with electromechanical drives, fast acquisition and tracking motions is not necessary (the IDC tracking antenna is part of the payload and is operated only during selected periods).

• Some effort was spent to overcome thermal control tasks by fully passive means and heat pipe radiators, but an active fluid cooling loop could not be avoided.

• Pump package and fluid loop induced vibrations form the major disturbance sources of the spacecraft subsystems.

• The mechanism within the payload instruments form the other group of major vibration disturbance sources.

• The fluid loop pump package was mounted via vibration isolators.

Microgravity environment compatibility (MEC) tests were performed on component level with equipment, assemblies and, finally, with the integrated system. During integrated system testing, the EURECA spacecraft center body was supported quasi dynamically free/free via air bearings within its integration stand. Solar Array Wings and Antenna Booms were not deployed as on orbit. The subsystems and payloads were operated with a certain timeline. The induced vibrations were measured at several locations and directions with ground test accelerometers over a frequency range from below 3 Hz up to 1000 Hz. The ground measurements included also the on-board Micro-g Measurement Subsystem (MMS) Sensors locations.

The upper frequency limitation of the MMS with 5 Hz due to on orbit data storage restrictions and the lower frequency limitation of about 3 Hz for the ground test due to the non-representative low frequency dynamic behavior of the test suspension and the non-deployed appendages have not to be seen as supplementary to each other, such that the micro-g requirement verification is given in two steps both by ground testing and by on-orbit measurements over the entire frequency range of interest.

A typical vibration response spectrum from the integrated system test over the frequency range from 1 Hz to 1280 Hz is given in Fig. 3, with operation of the worst case subsystem equipment and payload instruments. This ground test vibration spectrum shows that the EURECA specification is basically met in that frequency range.

During this operational mode and the vibration environment described by Fig. 3, a container filled with fluid was attached to the EURECA structure. The container had the shape as shown in Fig. 4 and was filled with two separated fluids of different density and an air bubble on top within the enclosure. This device allowed for a simple visual check of the vibration sensitivity by means of that fluid dynamic system with free surfaces; even under gravity.

The observations made can be summarized such that no wave motions were visible at the fluids and the air bubble under the EURECA ground vibration environment. The only reaction, which could be seen, was that light reflections changed dynamically at mirror images at the fluid-to-fluid and fluid-to-air bubble separation planes. The result indicated the good quality of the residual perturbations of the EURECA upper frequency micro-g environment.

III. THE EURECA MICRO-G MEASUREMENT SUBSYSTEM (MMS)

The MMS measures residual quasi-static and low frequency acceleration levels during selectable time intervals of the operational phase in orbit. The instrumentation consists of 3 accelerometer package with each 2 sensors, which are mounted and oriented on the spacecraft body as shown in Fig. 5. This sensor configuration allows the reconstitution of the six-degrees-of-freedom motions of the rigid center body of EURECA and the interpolation among the three measurements locations for any other location and direction up to, at least, 5 Hz, where the center body can be considered as rigid.

The frequency bandwidth from 0 Hz to 5 Hz and the associated data rates of the MMS were adjusted to the available interim on-board data storage capabilities in between ground station contact and data dump.

The MMS provides the main functions:

- Measurement Range: 10^{-6} g to 10^{-2} g
  with amplitude resolution step of about 12.5% per decade and the maximum resolution of $1{,}25 \times 10^{-6}$ g.

Measurement Bandwidth: 0 Hz to 5 Hz

- Mode: Signal Sampling Frame;
  with temperature, calibration/bias-compensation value, peak value of proceeding period, n-numbers of acceleration samples
- Mode: Peak Selection Frame;
  with temperature, calibration/bias-compensation value, peak value of proceeding period.

On-orbit calibration/bias-compensation was performed after calculation of the mean acceleration value over certain periods by ESOC. The mean value should be determined over up to 3 orbits, where also the tidal natural accelerations from the gravity gradient and atmospheric drag should average to zero, such that the remaining offset can be declared as bias.

The EURECA sun pointing orientation supported this averaging process by rotation of the sensor axes in the quasi-static acceleration field. A minimum bias-compensation value of $\pm 8 \times 10^{-6}$ g could be commanded from ground. That means that this bias compensation is effective only for bias

levels above $5x10^{-6}$ g. During the initial EURECA mission period, the bias-value was determined and corrected such that the highest resolutions steps of the MMS with $1.25x10^{-6}$ g up to $3.875x10^{-5}$ g and $1.25x10^{-5}$ g up to $3.875x10^{-4}$ g are utilized. This resolution step change at $3.875x10^{-5}$ g can be observed in the acceleration time histories presented in Fig. 6.

The mean value calculated again from the calibrated/bias-compensated measurement data confirmed in general a minimum residual bias offset in the order of $2x10^{-6}$ g as given in Fig. 6.

IV. PRELIMINARY MMS FLIGHT DATA EVALUATION

A set of typical acceleration time histories were selected primarily from the available 906 measurement cycles over the payload operational time period from the 7.08.1992 to the 1.10.1992. The print outs of the processed data were made available by the Microgravity Users Support Center (MUSC) at DLR, Köln-Porz. Typical acceleration time histories of the six sensors over about two orbits are shown in Fig. 6. A set of Fast Fourier Transformed (FFT) acceleration spectra are given in Fig. 7. The presented spectral amplitudes need to be confirmed by a justification of the used FFT with well defined harmonic time functions, where the spectral amplitude is known.

A. General Observations

The signature and shape of the acceleration time histories look similar over all the observation periods. But the signal form is not stationary, nor fully repetitive. It varies with time.

During all measurements events the highest acceleration responses are in x-direction, followed by the y-direction and lowest in z-direction. The acceleration time functions show a more or less dynamic environment of vibrations mainly in x- and y-directions within the measurement bandwidth of up to 5 Hz. The acceleration mean values over the measurement periods are at about $2x10^{-6}$ g and, as such, within the resolution limit of the MMS.

Quasi-static and very low frequency residual accelerations are embedded in such mean values and can be lower than $2x10^{-6}$ g. All acceleration peak values in the time domain are below the composite rms-acceleration limit level of $6.5x10^{-5}$ g. The acceleration levels in z-direction, which are less than 10^{-5} g, satisfy already the very low frequency acceleration limits.

The maximum vibrational peak acceleration of $6.25x10^{-5}$ g or $5x10^{-5}$ g, observed over one orbit period, occur only rarely, as taken from Fig. 6 and listed in Table 1. The level increments of the MMS resolution with $1.25x10^{-5}$ g and $1.25x10^{-6}$ g are visible in Table 1 as well. The regular acceleration peaks are found to be in the order of $3.75x10^{-5}$ g, with maxima in x-direction.

Table 1: Number and Level of Peak Accelerations per Orbit (from Fig. 6)

ACCELEROMETER	PEAK LEVEL	NO. OF PEAKS PER ORBIT
MMS X-1B	6.25×10^{-5} g 5×10^{-5} g 3.75×10^{-5} g	3 appr. 30 n
MMS X-2B	5×10^{-5} g 3.75×10^{-5} g	appr. 12 n
MMS Y-3A	2.5×10^{-5} g 2×10^{-5} g	2 n
MMS Z-1A	8.75×10^{-6} g	n
MMS Z-2A	8.75×10^{-6} g	n
MMS Z-3B	1×10^{-5} g	n

The acceleration time histories in Fig. 6 do not provide an indication for any step function excitation with transient acceleration responses as they could have been occurred due to 20 mN cold gas thruster or magnetic torquer pulse activation of the attitude control subsystem.

B. Estimated Drag Accelerations based on Actual Solar Activity and Geomagnetic Activity

Quasi-static and very low frequency residual accelerations are determined by

- atmospheric drag - pending on actual conditions,
- gravity gradient, as defined in [1] with less than 5.4×10^{-7} g,
- attitude control disturbance torques and counteracting actuator torques, as defined in [1] with less than 2.6×10^{-6} g.

The most dominant atmospheric drag is a function of the actual air density, which changes with the solar activity and the geomagnetic activity. The solar activity $F_{10.7}$ and geomagnetic activity A_p for the actual EURECA flight period is given with

$F_{10.7}$ = 175/160

A_p = 21.5

They are smaller than the worst case numbers considered for earlier assessments with

$F_{10.7}$ = 310/230

K_p = 7.0

With the activity numbers, the date and time 1992/10/5 12:00 LST and the altitude of 508 km the air density can be calculated with the NASA/MSFC-J70 software program.

The air density results in the following table:

AIR DENSITY ρ	VALUE [kg/m^3]
max. ρ	2.4×10^{-12} kg/m^3
min. ρ	0.8×10^{-12} kg/m^3
mean ρ	1.4×10^{-12} kg/m^3

The maximum drag acceleration is calculated then with

$$a_D = c_D \cdot \frac{\rho}{2} \cdot v^2 \cdot \frac{A}{m} = 3.2 \times 10^{-7} \text{ g}$$

under the consideration of following factors:

VARIABLE	COEFFICIENT	VALUE
Drag Coefficient	c_D	2.2
Air Density	max. ρ	2.4×10^{-12} kg/m^3
Relative Velocity	$v = v_o + v_w$ and $v_o = \sqrt{\frac{GM}{r_0 + h}}$	
Gravitational Constant	GM	3.986×10^{14} m^{3}sec^{-2}
Earth Radius	r_0	508 km
Atmospheric Winds	v_w	1500 m/s
S/C Cross Section	A	59.2 m^2
S/C Mass	m	4200 kg

Thus, the actual drag accelerations with 3.2×10^{-7} g are very small and below the measurement resolution of the MMS.

Further analysis have been performed by ESOC to determine the influence of air drag on the EURECA microgravity environment. The software used to determine the air drag influence on the spacecraft implements a 8th order Adams-Bashford/Adams-Moulton integrator, using the MSIS air density model (Hedin 1983) to model the effects of air drag. The only modification performed with respect to the operational version was to output the acceleration due to air drag at each integration step (using 180 steps per revolution).

The information required by this drag model are the daily $F_{10.7}$ flux and geomagnetic index (A_p), and a mean value for the $F_{10.7}$ flux over the previous 30 days. On each of the two days in question, the orbit was propagated for 24 hours under both high and low levels of solar activity. The high values were taken from the operational solar flux file (which contains the actual solar activity history), for the period around August 1992 during which several solar flares were observed.

To obtain low values, the SOLMAG software for prediction of solar activity, available at ESOC, was used to predict the levels of activity in May 1993. The low values used for the analysis were then these predicted values minus the one sigma errors. The implicit assumption that the levels of solar activity seen in August would not be exceeded (due to the position in the solar cycle) was validated by events.

INFLUENCE BY AIR DRAG*			
DATE	RESIDUAL ACCELERATION [g] min. acceleration	max. acceleration	REMARKS
92/08/10 (beginning of the mission)	0.05×10^{-6} g	0.12×10^{-6} g	Low solar flux conditions
92/08/10 (beginning of the mission)	0.11×10^{-6} g	0.27×10^{-6} g	High solar flux conditions
93/05/04 (end of the mission)	0.08×10^{-6} g	0.17×10^{-6} g	Low solar flux conditions
93/05/04 (end of the mission)	0.16×10^{-6} g	0.39×10^{-6} g	High solar flux conditions

*propagation under extreme solar flux and geomagnetic index conditions (magnitude of acceleration due to air drag calculated at the rate of 180 observations per orbit

In fact, the solar activity during the second half of the mission was generally much lower than predicted, so that there would have been periods when the acceleration due to air drag was less than the minimum quoted in the table. The input values used in the study were as following.

SOLAR FLUX	DAILY $F_{10.7}$	MEAN $F_{10.7}$	A_p
high solar flux	150	140	88
low solar flux	110	120	1

C. The Effect of the Eclipse

The measurements over orbital periods show a reproducible slight change in the peak level vibration behavior beginning with and during each eclipse phase, see Fig. 6 dated 28.09.1992 and

the eclipse times of 13:57:58.72 plus 1900 sec for the beginning and plus 4000 sec for the end. Besides thermal changes, the only repetitive operational change of the spacecraft is that the attitude information is switched from Sun Sensor data to the Gyro reference, which could cause a different attitude control activity feed back.

D. Fluid Cooling Loop By-Pass Switching

A specific anomaly in the acceleration time histories was observed on the 19.09.1992, at 13:50:54.10 plus 28 sec (Fig. 8).

This time correlates with the ground command to switch the fluid cooling loop by-pass valve, which is part of the spacecraft thermal control subsystem. The by-pass valve opens or closes the branch of the fluid loop which is integrated into one thermal radiator panel (Fig. 9). The measured acceleration vectors indicate a reaction of the spacecraft with a rotational motion around the x-axis (Fig. 9). The accelerated mass flow of the fluid is partially compensated by symmetry around the x-axis; but a net torque remains from the loop sections in the off-set area.

E. On-Orbit Vibrations

As indicated by Fig. 6 and Fig. 8, the on-orbit acceleration measurements show a highly dynamic environment within the measurement bandwidth of up to 5 Hz. The typical acceleration spectra in Fig. 7 may be interpreted. A larger number of frequencies resulted after Fast Fourier Transformation (FFT), which can be associated to excited free vibrations or forced vibration of the spacecraft. The excitations sources of these vibrations should be subject of a more detailed investigation, but the vibration behavior allows already some correlation with the analytical description of the spacecraft structural dynamics. In an earlier stage of the project on-orbit Finite Element Model (FEM) was prepared. The FEM-Model resulted with a number of vibration modes, which are listed in Table 2.

The expanded time histories in Fig. 8 allow to extract particular frequencies. If the vibration cycles are counted individually in x-and y-direction over a certain time step, a vibration frequency of about $f = 0.85$ Hz appears. This 0.85 Hz frequency is also dominating in the x- and y-spectra of Fig. 7.

The vibrational deflections associated with the 0.85 Hz frequency can be drawn by acceleration vectors, as shown in Fig. 10. A vibration mode with a rotation around the z-axis results. The positive or negative sign of the y-vector need to be confirmed. If negative, the picture would be more conclusive for the z-axis rotation of the EURECA center body and the level arm ratio between sensor axes and inertia axes/center of mass.

Such a mode shape (elastic mode no. 5 with f_5 = 0.812 Hz) resulted also from the on-orbit dynamic mathematical model, which is shown in Fig. 11. The frequency response function in Fig. 12, which was calculated with the FE-Models, illustrates the sensitivity of the spacecraft structural dynamics modes to response with vibrations in X-direction at a frequency of about 0.85 Hz. One source, which excited the 0.85 Hz frequency, could be WATCH-Instrument, consisting of a rotating collimator with a speed of 1 Hz, continuously. A modulation of the 0.85 Hz vibration signal is observed in Fig. 8, as over almost all the acceleration time histories at other periods. The modulation period is T_m = 25 sec and the modulation frequency

$f_m = 1/T_m = 0.04$ Hz.

The modulation must result from two frequencies (f_1 and f_2), which are separated by f_m, like

$f_2 = f_1 + f_m = 0.85$ Hz + 0.04 Hz or

$f_1 = f_2 - f_m = 0.85$ Hz - 0.04 Hz.

The frequency spectra in Fig. 7 for the x- and y-direction do not show clearly two vibration frequencies f_1 and f_2, spaced by 0.04 Hz, around 0.85 Hz. The FE-model instead provides these close mode numbers of 0.812 Hz and 0.870 Hz.

The lowest first vibration frequency, which may be identified from the spectra in Fig. 7, could be at 0.11 Hz. The motion seems to be again mainly a rotation of the EURECA center body around the z-axis, see x- and y-amplitude at 0.11 Hz. According to Table 2, the first FE-model elastic structural mode was analyzed with 0.142 Hz.

Table 2: EURECA On-Orbit Structural Dynamics Mode Numbers

MODE NO.	FREQUENCY [HZ]	MODE NO.	FREQUENCY [HZ]
1	0.142 Hz	11	2.127 Hz
2	0.218 Hz	12	2.630 Hz
3	0.223 Hz	13	2.630 Hz
4	0.578 Hz	14	3.837 Hz
5	0.812 Hz	15	3.848 Hz
6	0.820 Hz	16	4.511 Hz
7	0.870 Hz	17	4.534 Hz
8	1.006 Hz	18	4.605 Hz
9	1.013 Hz	19	4.643 Hz
10	2.100 Hz	20	5.318 Hz

The calculated transfer function example in Fig. 12 does not show the 0.142 Hz frequency response under this particular excitation direction and location, but in other cases this is visible. By comparison of the response spectra in Fig. 7 with the transfer function example in Fig. 12 and the list of eigen frequencies in Table 2, another frequency of 0.22 Hz appears to be of interest, especially in conjunction with the observations made after the payload operational period.

F. Transient Vibrations After The Payload Operational Period At The End Of Mission

Typical transient acceleration time histories are monitored by MMS, as shown in Fig. 13 after the EURECA payload operation was finished and the EURECA stayed in dormant orbits, waiting for retrieval. The attitude control and maneuvers were performed not with hot gas thrusters. Thruster pulses excited transient accelerations with peak levels up to 10^{-3} g, which are a factor of 20 higher than the peak levels observed during payload operation.

The basic frequency, which can be counted from the example in Fig. 13, is 0.22 Hz in z-axis. This frequency in z can be identified in the spectra of Fig. 7 and from the vibration modes listed in Table 2. The mode shape of the analytical model at 0.223 Hz is given in Fig. 14 and corresponds again with the rotation of the center body around the y-axis, as it can be constructed by the z-axis acceleration amplitudes in Fig. 13 at t = 270 sec. A second frequency can be counted mainly in x- and y-axis with about 0.85 Hz. This frequency is well known from section 5.5, but not so regularly excited. It has to be noted that low accelerations are present before thruster activation. The transient behavior of the acceleration behavior allows to estimate the structural damping under orbital conditions by means of the logarithmic decrement. The degree of damping in the system may be defined by the logarithmic decrement Δ, which is the natural logarithm of the ratio of the amplitudes of successive cycles of the damped free vibration.

$$\Delta = \frac{1}{n} . \ln \frac{x_1}{x_{n+1}}$$

The fraction of critical damping z can be derived, as defined in [3], from the logarithmic decrement Δ with approximately

$$\zeta = \frac{\Delta}{2\pi}$$

The damping values z from the transients in Fig. 13 resulted with f = 0.22 Hz with z = 1.3 - 2%. This is a higher damping than expected and usually considered with 0.5 % in on-orbit structural dynamics modeling.

CONCLUSIONS

With the examples given in Fig. 6 and Fig. 7, it is shown that the on-orbit acceleration measurements confirmed the quality of the EURECA microgravity environment. Together with the ground test results in Fig. 3, it can be said that EURECA performed better than specified in Fig. 1. Many interesting findings could be evaluated from the on-orbit acceleration measurement which improves the understanding of on-orbit spacecraft system performances and analytical simulations. Some phenomena could be explained and correlation with structural dynamics models are found, but a more detailed investigation should provide a better disturbance source detection and a more direct recalculation an analytical simulation of the measured orbital conditions.

ACKNOWLEDGMENT

This paper was established, to a significant extent, as a result of a preliminary review of the EURECA residual accelerations of the microgravity environment performed by ERNO Raumfahrttechnik. The authors wish to thank Mr. H. P. Schmidt, MUSC (Microgravity User Support Center) at DLR, Köln-Porz, for the MMA flight data processing and presentation and Mr. Stuart Martin, ESOC, for his contribution on the analysis of the EURECA microgravity environment, in particular the investigations of the air drag effects.

REFERENCES

1. Stavrinidis, C., Stark, H., Eilers, D., Hornung, E.: "Microgravity Quality Provided By Different Flight Opportunities", Microgravity Science Technology III/4, February 1991

2. Herfs, W., Andresen, R.D., Eilers, D.: "The Measured and Predicted Micro-g EURECA Environment", IAF-88-341, 39th IAF-Congress, October 8-15, 1988, Bangalore, India

3. Harris, C.H.: "Shock and Vibration Handbook", 3rd Edition, 1988, McGraw-Hill Book Company, New York

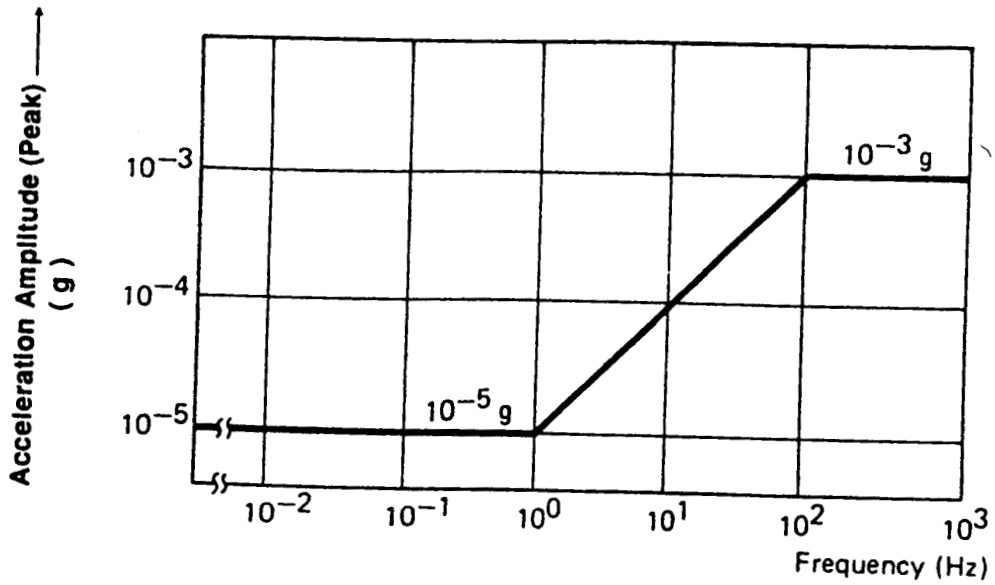

Figure 1 EURECA System Microgravity Environment Specification - The Allowable Natural and Induced Micro-G Environment at a Spacecraft/Payload Interfaces.

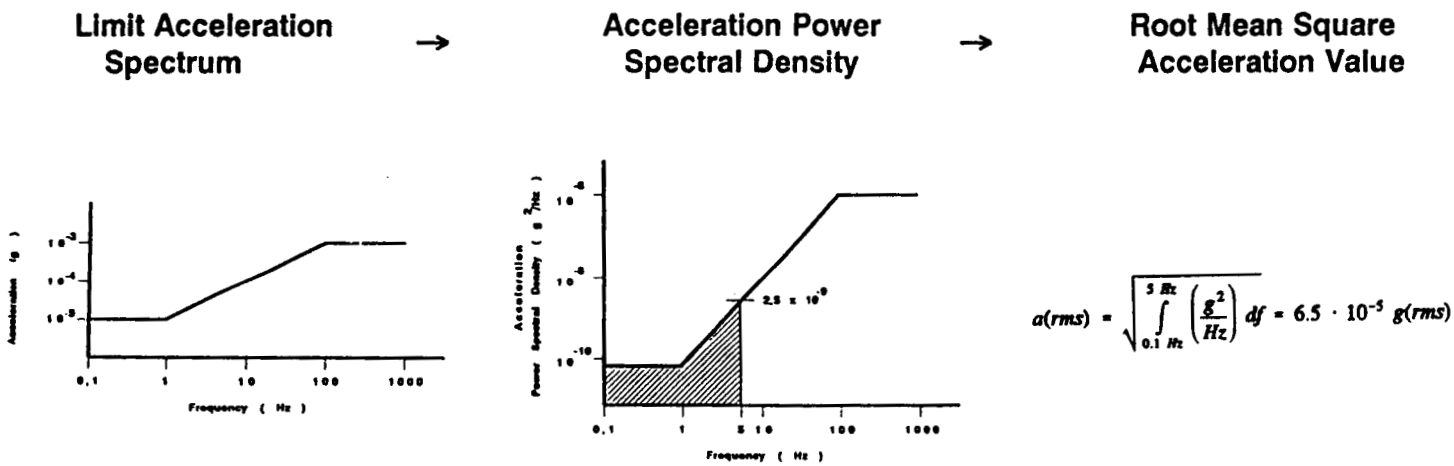

All Flight Measurements are Below the Specification Limit of $6{,}5 \cdot 10^{-5} g_{rms}$

Figure 2 Comparison of Flight Data with the EURECA Specification.

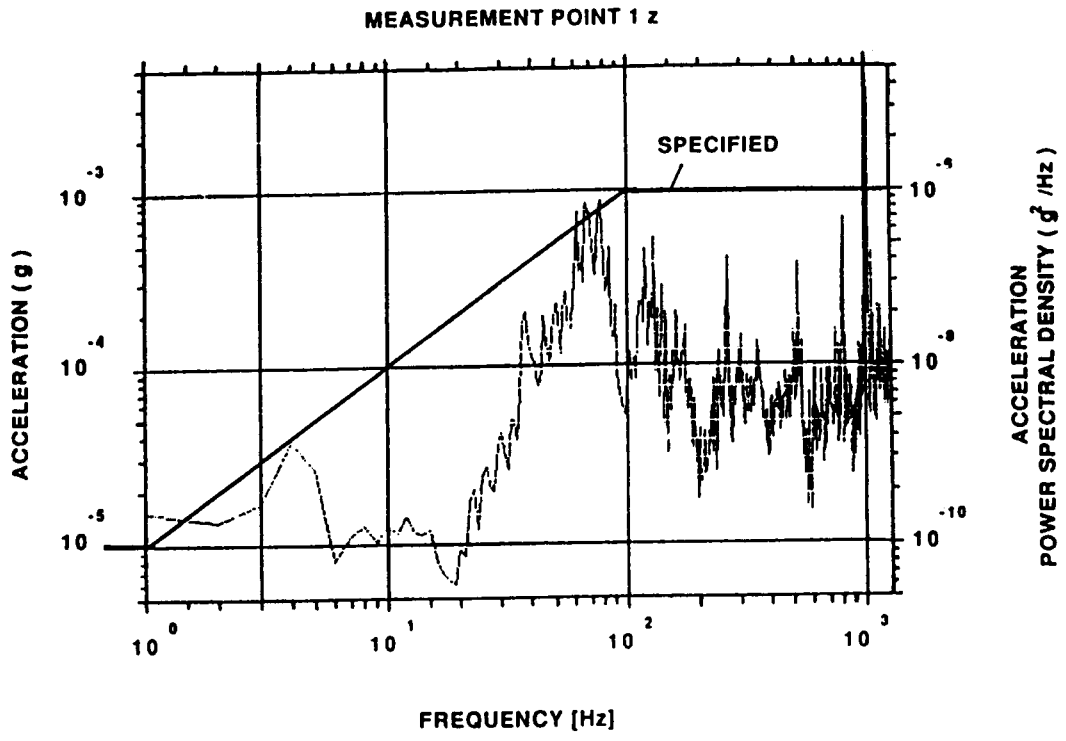

Figure 3 EURECA Integrated System Test (On Ground) - Typical Response Spectrum at a Micro-G Payload Interface (with all subsystems and the worst payload operated).

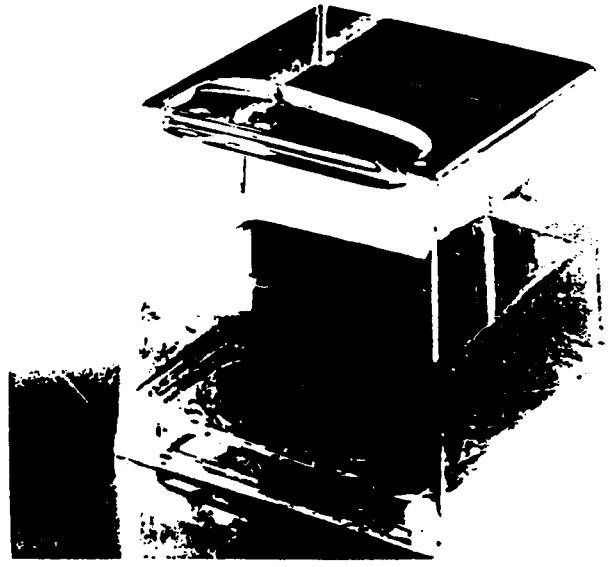

Figure 4 Fluid Dynamics Vibration Sensitivity Check-Out Equipment Mounted during EURECA Integrated System Test (On-Ground).

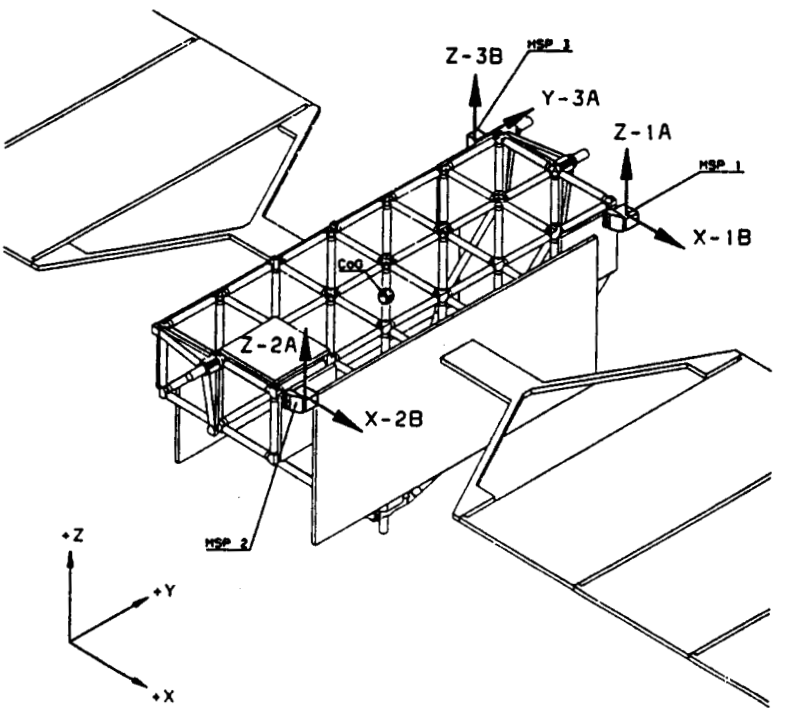

Figure 5 The EURECA Microgravity Measurement Subsystem (MMS) Sensor Configuration.

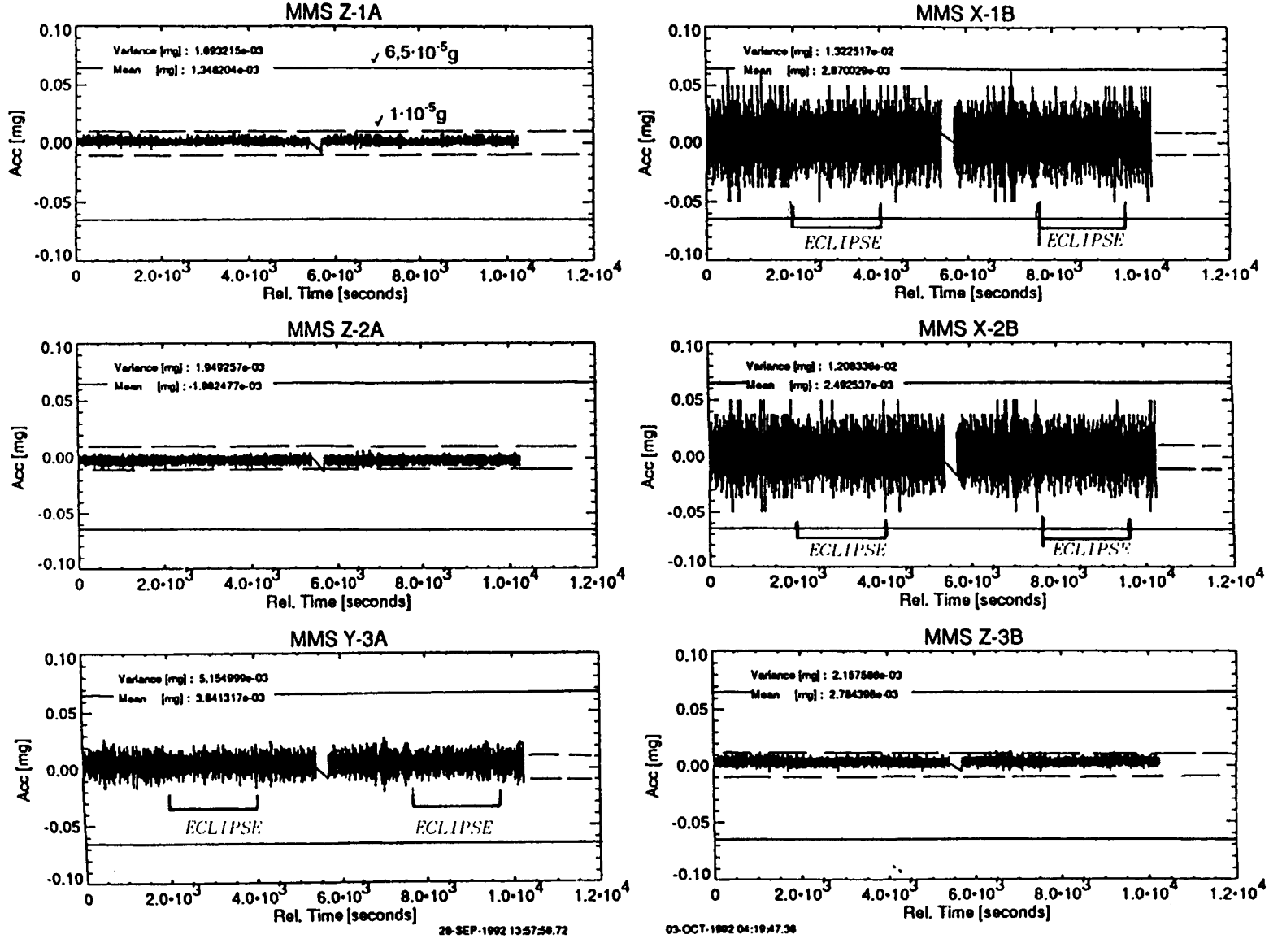

Figure 6 Typical On-Orbit Acceleration Measurement versus the EURECA Limit Acceleration Level.

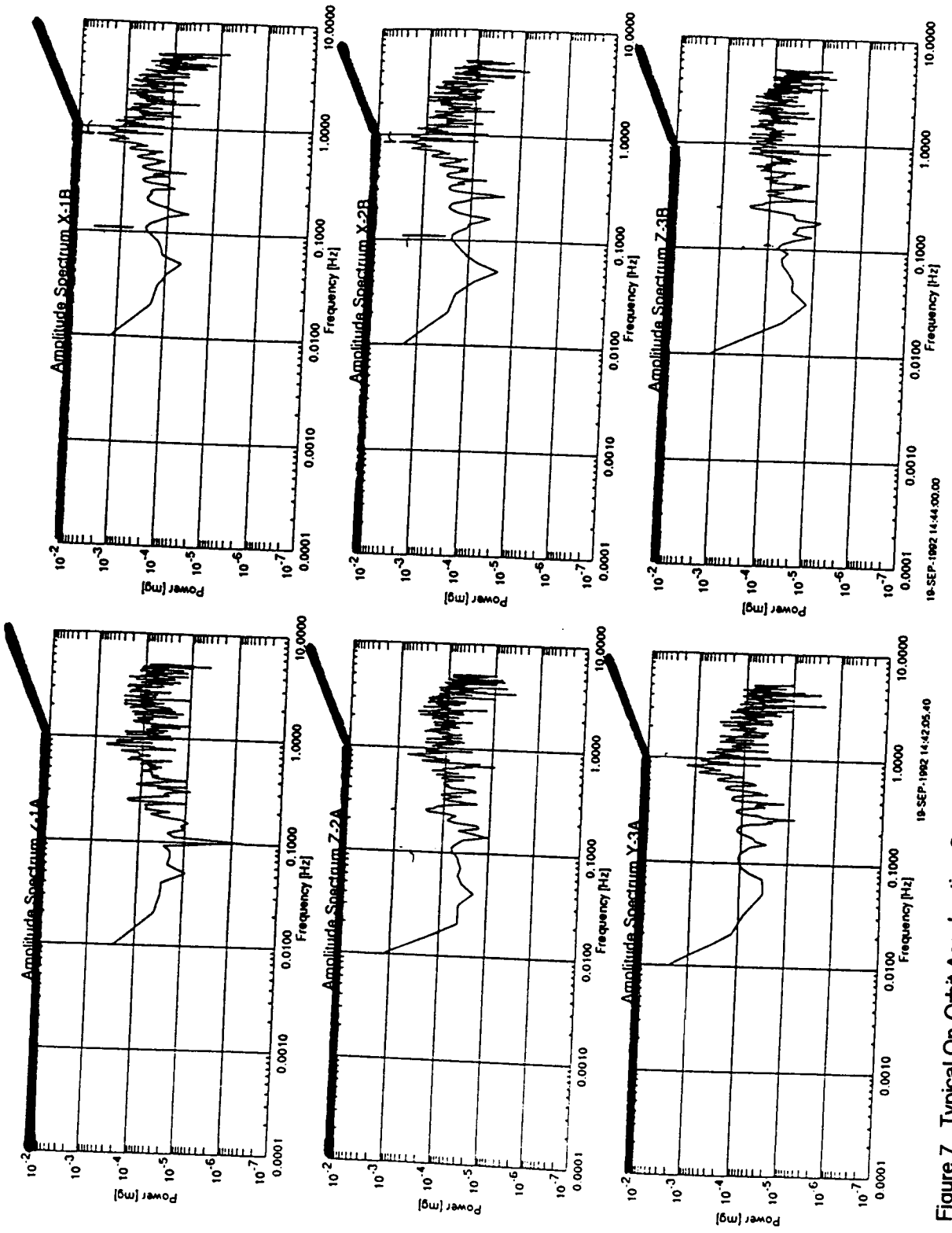

Figure 7 Typical On-Orbit Acceleration Spectra versus the EURECA Limit Acceleration Spectrum (see Fig. 1).

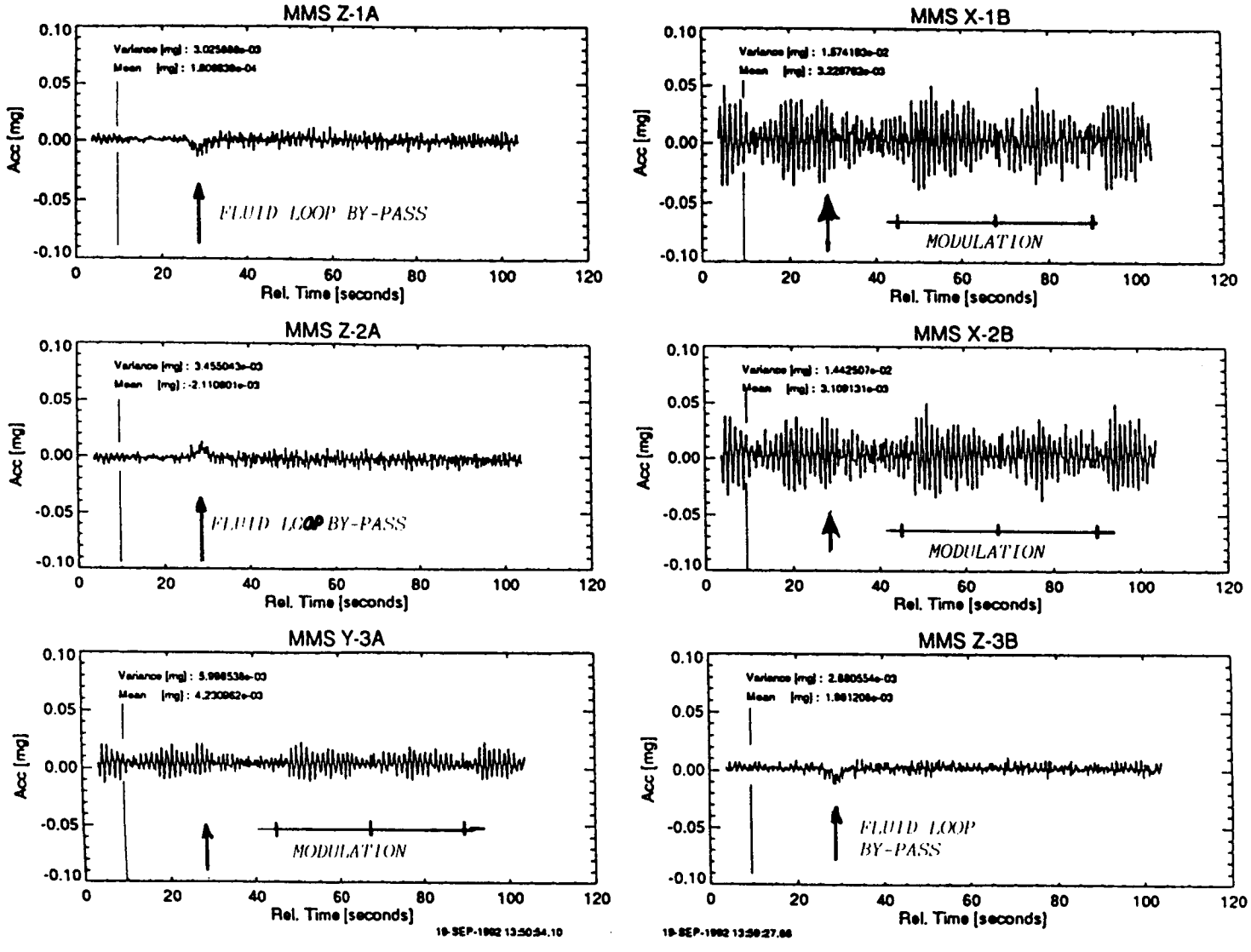

Figure 8 Fluid Cooling Loop By-Pass Switching Acceleration Response (19.09.92, 13:50:54.10 plus 28 sec).

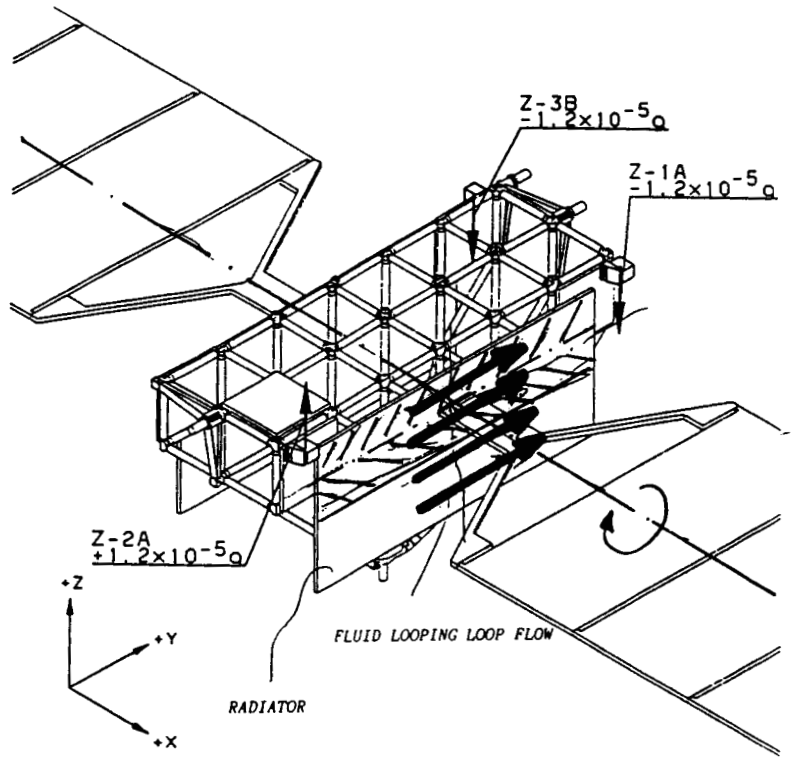

Figure 9 Rotational Motion due to Fluid Loop By-Pass Switching.

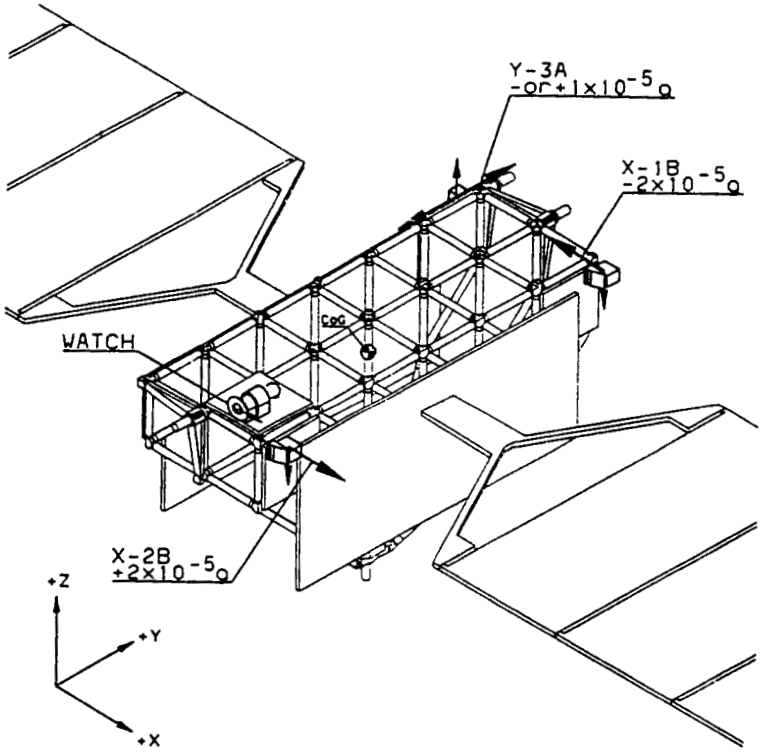

Figure 10 Vibration Deflection and Acceleration Vectors with f = 0.85 Hz (19.09.1992, 13:50:54.10 plus 9.5 sec from Fig. 8).

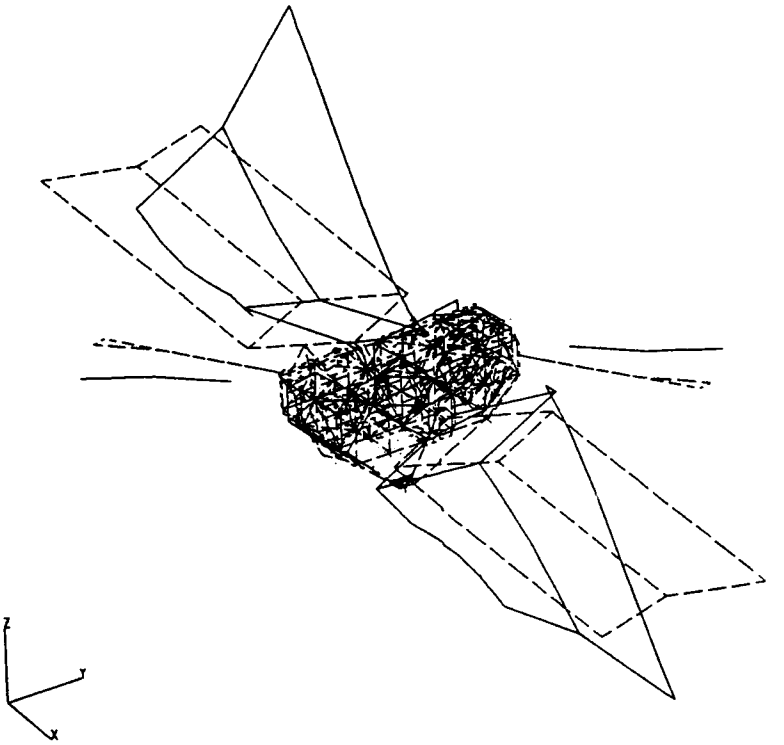

Figure 11 EURECA Vibration Mode Shape Analysis (mode 5, f_5 = 0.812 Hz, with similar deflections of the center body as in Fig. 10).

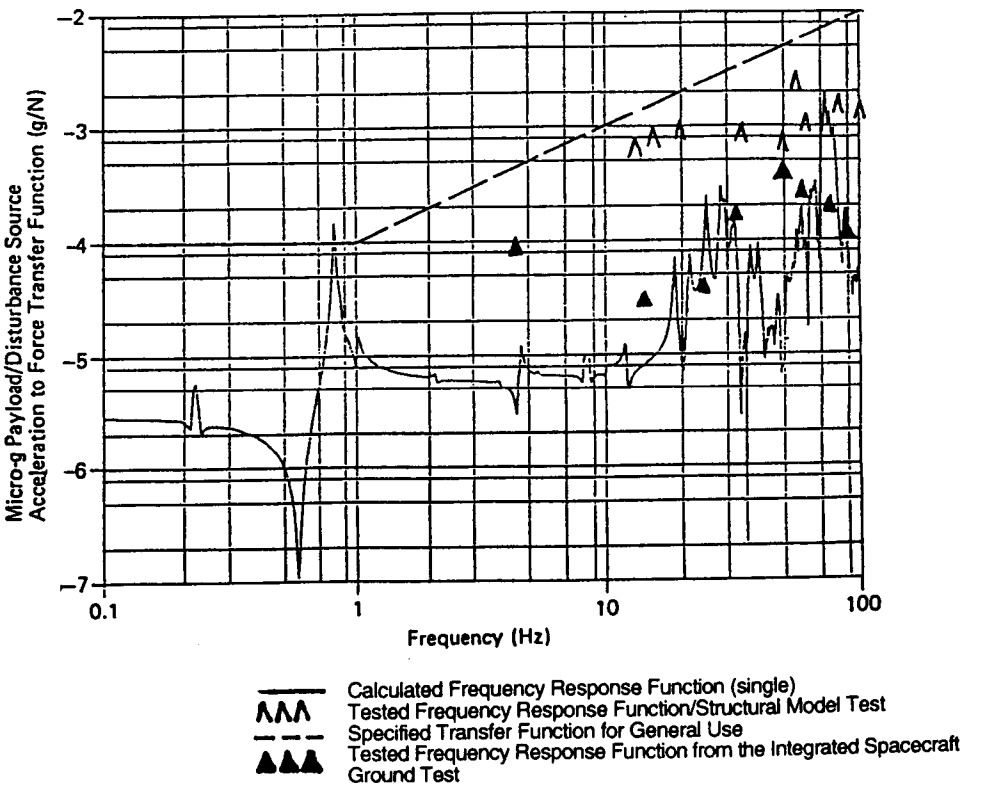

Figure 12 Typical EURECA On-Orbit Structural Dynamics Acceleration-to-Force Transfer Function (x-response due to y-excitation).

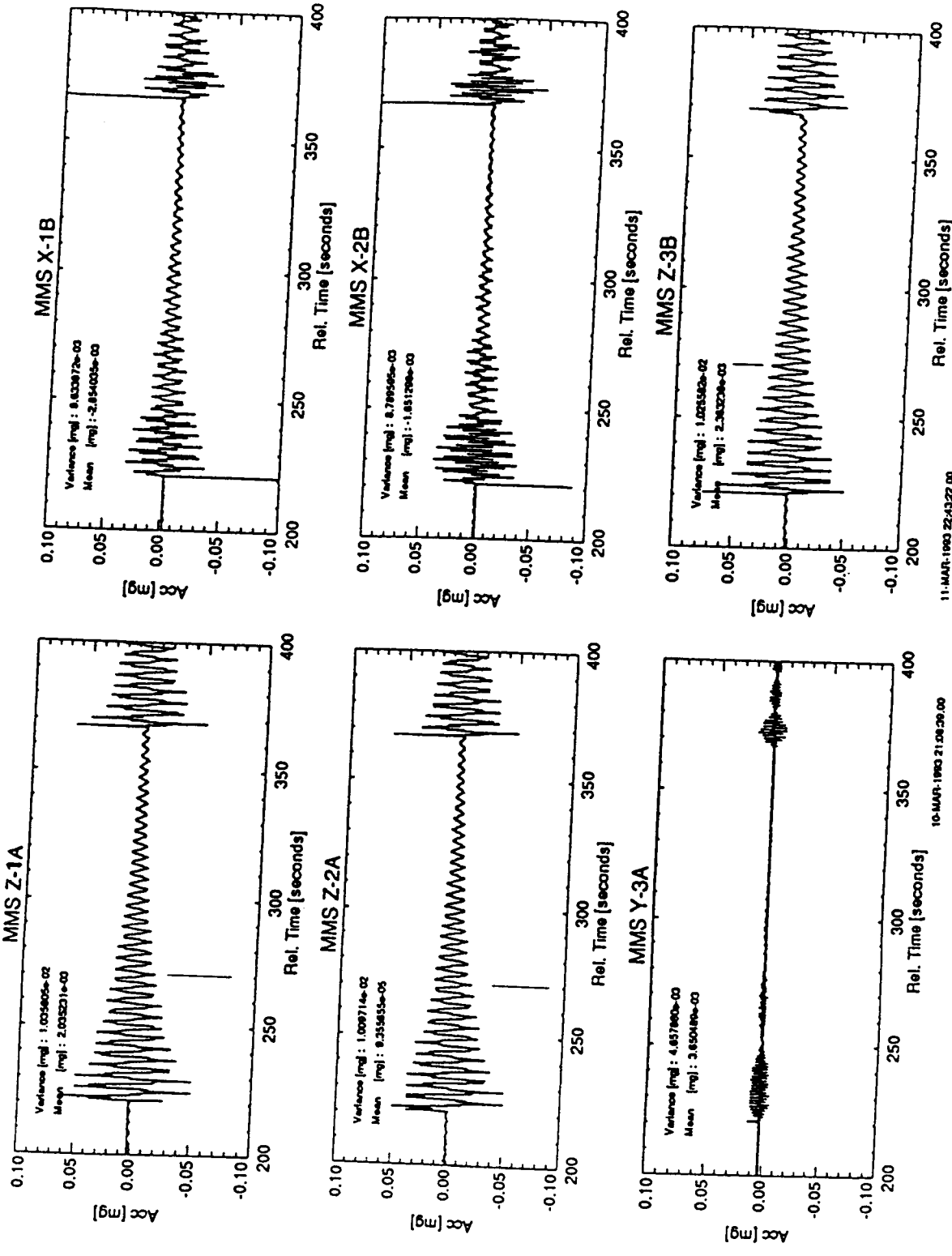

Figure 13 Typical Acceleration Time Histories after the Payload Operational Period at the End of Mission.

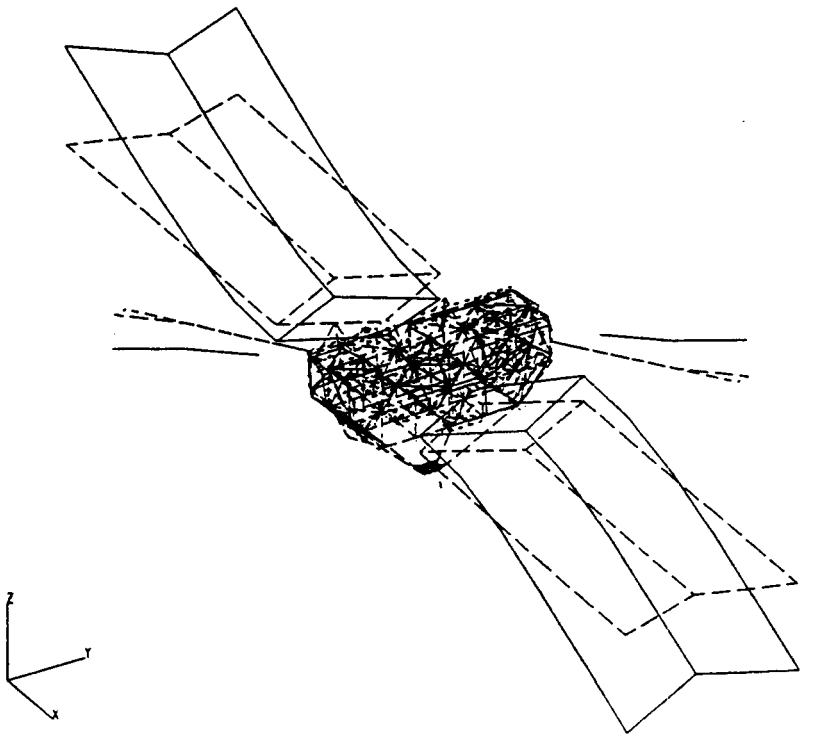

Figure 14 EURECA Vibration Mode Shape Analysis (mode 3, f_3 = 0.223 Hz, with similar deflections of the center body as in Fig. 13)

CORRELATION OF ACCELEROMETER DATA ON STS-50 (USML-1)

Melissa J. B. Rogers, Randall P. Wolf, and J. Iwan D. Alexander

Center for Microgravity and Materials Research
The University of Alabama in Huntsville, Huntsville, Alabama.

ABSTRACT

The quasi-steady acceleration and vibrational environment on STS-50 as measured and recorded by the Passive Accelerometer System (PAS), the Orbital Acceleration Research Experiment (OARE), and the Space Acceleration Measurement System (SAMS) is analyzed. The following disturbance sources are investigated: Flash Evaporator System and water dump activity, crew exercise, and Reaction Control System firings.

INTRODUCTION

First United States Microgravity Laboratory (USML-1) flew on Columbia on STS-50 from 25 June to 8 July 1992. Three accelerometer systems measured and recorded data during the mission which was dedicated to fluid physics, materials science, and combustion science experiments performed in the reduced gravity environment of low-Earth orbit. The Orbital Acceleration Research Experiment (OARE) is a triaxial electrostatic accelerometer package with complete on-orbit calibration capabilities [1-3]. It is designed to characterize the Orbiter's aerodynamic behavior in the rarefied-flow flight regime through measurement of low frequency (<5 Hz), low magnitude accelerations. The Space Acceleration Measurement System (SAMS) was developed to monitor and measure the low-gravity environment of MSAD-sponsored science payloads on the Orbiter [4,5]. SAMS consists of up to three remote triaxial sensor heads connected to a main unit by cables. The sensors use a pendulous proof-mass and force-rebalance coil system to measure acceleration. Both OARE and SAMS record the acceleration of the Orbiter with respect to a frame of reference fixed to the accelerometer sensor.

The Passive Accelerometer System (PAS) was designed to measure the quasi-steady residual acceleration caused by a combination of atmospheric drag and the gravity gradient. The system is used to determine the residual acceleration environment experienced by experiments with respect to a frame of reference fixed to the Orbiter. Acceleration is computed indirectly with Stokes' Law using the recorded motion of a small steel proof mass along an oriented tube filled with liquid.

Joint "L+1" Science Review for USML-1 and USMP-1 with the Microgravity Measurement Group, September 22-24, 1993, Huntsville, Alabama, USA.

I. EXPERIMENT LOCATIONS

The experiment carrier for USML-1 was the Spacelab. The Orbiter center of gravity was about (1091.9", -0.4", 374.0") halfway through the mission. The Passive Accelerometer System (PAS) measured the quasi-steady acceleration environment of the Flight Deck and Spacelab on USML-1. A description of the PAS and PAS results is given elsewhere in this document. Three SAMS heads recorded data in the Spacelab in Racks 3, 9, and 12, see Table 1 for locations. The OARE sensor was located at (1153.28", -1.33", 317.81"). Note that all locations are given in Orbiter structural coordinates, see Fig. 1. Quasi-steady accelerations and vibrations measured by these accelerometers are discussed in the following section.

II. DISTURBANCE SOURCES AND RESULTANT ACCELERATION LEVELS

The two main components of the low-gravity environment of the Orbiter are quasi-steady accelerations and vibrations caused by oscillatory and transient sources. These two components are discussed below in general and specific sources present during USML-1 are outlined.

A. Quasi-steady accelerations:

The three major, predictable components of the quasi-steady acceleration environment of orbiting laboratories are aerodynamic drag, gravity gradient, and rotational (tangential and radial) effects. These contributions are discussed at length in the literature [6-8]. Modeling of these effects at the CGF location on USML-1 indicate that predicted total contributions were between $7x10^{-8}$ g and $9x10^{-8}$ g in X-body, between $2x10^{-7}$ and $3x10^{-7}$ g in Y-body, and between $-8x10^{-7}$ and $-3x10^{-7}$ g in Z-body, see Fig. 2. Quasi-steady accelerations have a frequency component on the order of 10^{-4} Hz, consistent with the orbital period.

An additional acceleration in the same magnitude range was identified in OARE and PAS measurements taken during USML-1. A component of this acceleration was identified as the venting force of the Flash Evaporator System (FES) [9]. The FES is a component of the Orbiter Active Thermal Control Subsystem (ATCS) [10]. Along with the radiators and ammonia boilers, the FES acts to meet total system heat rejection requirements during flight. It is also used to dump excess potable water in flight. The FES is located in the Orbiter aft fuselage and is composed of a high-load and topping system contained in one envelope. Steam generated from the topping evaporator is ejected through two opposing sonic nozzles on each side of the aft Orbiter: (1506", ±128", 305") in structural coordinates, see Fig. 3. The high-load evaporator is not normally used on orbit because it has a propulsive vent; it was not used on orbit during USML-1 [Q. Carelock, personal communication].

During USML-1, two nozzle FES operations, in topping mode, occurred with about a 28 hour periodicity. The FES removed water at about 10.5 lb hr^{-1} for 14 hours, followed by a 14 hour off period, see Fig. 4. USML-1 FES operations caused total thrust along the X-body axis of -0.03 lbf and along the Z-body axis of 0.018 lbf [9]. The resultant linear accelerations caused by the FES activity are g_X=-1.2x10^{-7} g, g_Z=7.6x10^{-8} g, where g_X and g_Z are acceleration in the X-body and Z-body directions. Y-body accelerations due to FES operations cancel due to the opposing nozzle configuration.

Figs. 5 and 6 show the average orientation of the residual acceleration vector recorded by OARE when FES was off and on [11]. The data represented here were extrapolated to the CGF location [2] and the signs have been adjusted to transform the data into an Orbiter fixed reference frame. Note that the $-X_b$, $+Z_b$ nature of the FES venting force influences the acceleration vector.

Fig. 7 shows the average orientation of the residual acceleration vector recorded by PAS in the Flight Deck and extrapolated to the CGF location [11]. All PAS Flight Deck measurements were taken while the FES was on. Note that the vector orientation indicated by PAS is consistent with that shown by OARE when the FES was on.

B. Vibrational Environment:

The vibrational environment on-board a manned orbiting laboratory is influenced greatly by both spacecraft operations and crew activity. Large magnitude disturbances caused by Orbiter Reaction Control System firings and crew exercise, especially if not isolated, are propagated throughout the craft as vibrations at Orbiter, carrier, and subsystem structural modes. Oscillatory disturbances from spacecraft fans, motors, and pumps also cause excitation of structural modes. On a smaller scale, localized vibrations at experiment component structural modes can be excited by Orbiter operations and by experiment specific operations. In the remainder of this section we discuss the vibrational environment on USML-1 as caused by Orbiter Reaction Control System activity and crew exercise.

The Orbiter Reaction Control System (RCS) provides thrust for attitude (rotational) maneuvers and small velocity changes (translations) when the Orbiter is above 21,336 m [10]. RCS modules are located in the forward fuselage nose area and in the left and right OMS/RCS pods, attached to the aft fuselage. The forward RCS has 14 primary and 2 vernier RCS engines; the aft RCS has 12 primaries and 2 verniers in each pod. Primary RCS (PRCS) engines provide 870 lb of thrust each; vernier RCS (VRCS) engines provide 24 lb of thrust each. Both RCS engine types can be used in steady-state thrusting mode for one to 125 sec or in pulse mode with a minimum pulse time of 0.08 sec.

On average, 125 RCS thrusters fired per hour between MET day 3 and MET day 7 on STS-50. This is the count of total firings and does not take into account the fact that several thrusters often fire at the same time for attitude control. If simultaneous multiple firings are considered as a single event, the

average number of firings per hour decreases by about 65%. Fig. 8 is a histogram of the total RCS count from MET 92 hr to MET 184 hr. Note that the attitude deadband was changed from 0.5° to 0.1° at approximately 120 hr. RCS activity increases by about 98% after this change.

Instantaneous linear accelerations produced by a VRCS firing would be about $1x10^{-4}$ g. Instantaneous linear accelerations produced by a PRCS firing would be about $3.5x10^{-3}$ g. Various engine firing durations, simultaneous firings of opposing and/or complementary jets, the excitation of structural modes, and acceleration data sampling rates make it difficult to identify a single acceleration value from accelerometer data.

RCS activity for attitude control is generally necessary because the Orbiter tends to drift out of a desired attitude. Such drifting is due, for example, to orbit degradation related to aerodynamic drag and attitude instability. In addition, Orbiter induced accelerations will require attitude correction. An example of this which occurred during USML-1 involves supply water dumps.

Potable and waste water accumulated in flight is stored in 74 kg capacity tanks which can be dumped overboard via vents on the port side of the Orbiter: potable water ports at (620", -105.5", 342") and waste water ports at (620", -105.5", 336"), in structural coordinates, see Fig. 3. Three waste water dumps occurred during Spacelab operations on USML-1. Each water dump lasted one hour. The 0.09 lbf venting thrust along the Y-body axis caused linear accelerations of approximately $g_y=3.8x10^{-7}$ g. Because of the vent configuration, X-body and Z-body accelerations are negligible. RCS data for a water dump at MET 6/17 indicate that thruster activity increased from about 30 firings an hour prior to the dump, to about 30 firings a half hour during the dump, Fig. 9. This increase in activity was in response to Orbiter motion caused by the port side waste water dump which causes the Orbiter to yaw. Fig. 10 shows an acceleration vector magnitude for the period shown in Fig. 9. Note that transient acceleration magnitudes related to VRCS activity are in the $1\text{-}4x10^{-4}$ g range.

Fig. 11 shows OARE data for an earlier waste water dump. The acceleration magnitudes are different than the Fig. 10 SAMS data because of the different filtering applied to the data. Note, however, that the Y_b and Z_b (Fig. 11b & c) data clearly show the response of the Orbiter to the negative yaw VRCS jets fired to counteract the water dump torque [9].

Another vibration source which existed during USML-1 was crew use of exercise equipment. During this mission, ergometer exercise occurred in three configurations: with the cycle ergometer hard-mounted to the Flight Deck, with the cycle ergometer attached to the Ergometer Vibration Isolation System (EVIS) in the mid-deck, and with the cycle ergometer suspended by bungees in the aft Flight Deck area. A comparison of vibration levels among the three exercise configurations on USML-1 is presented in Ref. [4]. Vibration levels related to exercise are not particularly noticeable above the general background in SAMS Head B (CGF) data. Fig. 12 shows a period during which bungee isolated

exercise occurred. Exercise begins approximately 15 minutes into the plot. The pedaling frequency of about 1.2 Hz is easily seen in Fig. 12c. Excitation of Orbiter/Spacelab 3.5, 3.7, and 4.7 Hz structural modes can be seen, although no comment about the power in these modes can be made because this is above the SAMS filter cut-off frequency. These modes may, in part, be excited because of their coincidence with upper harmonics of the exercise frequency.

CONCLUSIONS

The three accelerometer systems flown on the First United States Microgravity Laboratory mission together provide a working characterization of the quasi-steady acceleration and vibration environment experienced by experiments during the mission. The OARE provided a measure of the quasi-steady acceleration environment over the extent of the mission. The PAS provided a more real-time spot check of the environment for up to 20 minute periods. The data sets resulting from these two systems give consistent values for the residual acceleration vector magnitude and appear to give a consistent estimate of the vector direction. Comparisons of the OARE and PAS data sets can only be made for the times when PAS was used. It is important to note that all PAS measurements were taken when the Flash Evaporator System was venting excess water.

Acceleration magnitudes obtained from OARE and SAMS cannot be compared because of the different filtering and processing applied to the data. The two data sets can be used, however, to confirm activity that both record. The OARE and the SAMS data sets both indicate that waste water venting forces at the port side vent site require increased RCS jet activity to counteract Orbiter torquing. RCS data from the mission also support this increase of RCS activity.

SAMS data collected during USML-1 also provide an indication of the vibration levels related to crew exercise. This subject has been covered quite thoroughly in the literature [4] and in this meeting. Neither OARE nor PAS is designed to measure exercise related vibration magnitudes or frequencies.

Table 1. Location and orientation of SAMS heads on USML-1

Sensor Head	Xs	Ys	Zs	Xs	Ys	Zs
A	992.5"	-63.2"	1.2"	Ysams	Xsams	-Zsams
B*	1088.8"	-44.0"	409.0"	-Xsams*	-Ysams*	Zsams*
C	1118.5"	49.2 "	396.4"	Ysams	Zsams	Xsams

*Accelerometer head was rotated -12° (clockwise) about Xs and +35° (counter clockwise) about Zs

REFERENCES

1. Blanchard, R. C., M. K. Hendrix, J. C. Fox, D. J. Thomas, J. Y. Nicholson, Orbital Acceleration Research Experiment. J. Spacecraft and Rockets 24 (1987) 504-511.

2. Blanchard, R. C., J. Y. Nicholson, J. R. Ritter, Preliminary OARE Absolute Acceleration Measurements on STS-50. NASA Technical Memorandum 107724, February 1993.

3. Blanchard, R. C., J. Y. Nicholson, J. R. Ritter, STS-40 Orbital Acceleration Research Experiment flight results during a typical sleep period, Microgravity Sci. Technol. V/2 (1992) 86-93.

4. Baugher, C. R., G. L. Martin, R. DeLombard, Low-Frequency Vibration Environment for Five Shuttle Missions, NASA Technical Memorandum 106059, March 1993.

5. Rogers, M. J. B., C. R. Baugher, R. C. Blanchard, R. DeLombard, W. W. Durgin, D. H. Matthiesen, W. Neupert, P. Roussel, A comparison of low-gravity measurements on-board Columbia during STS-40. Microgravity Sci. Technol., in print (1993).

6. Alexander, J. I. D. and C. Lundquist., Residual motions caused by micro-gravitational acceleration, J. Astronautical Sci. 35 (1987) 193-211.

7. Alexander, J. I. D. and C. Lundquist, Motions in fluids caused by microgravitational acceleration and their modification by relative rotation, AIAA Journal 26 (1988) 34-39.

8. Hamacher, H. Simulation of Weightlessness, in: Materials Sciences in Space, B. Feuerbacher, H Hamacher, R. J. Naumann (eds.), Springer-Verlag (1986) 31-52.

9. Rogers, M. J. B., B. P. Matisak, J. I. D. Alexander, Venting force contributions: Quasi-steady acceleration on STS-50, Microgravity Sci. Technol., submitted.

10. Shuttle Operational Data Book, Volume 1, JSC-08934, Rev. E, Johnson Space Center, Houston, TX, January 1988.

11. Alexander, J. I. D. and M. J. B. Rogers, A note on the extrapolation of PAS and OARE acceleration measurements to the CGF location on STS-50 (USML-1), Center for Microgravity and Materials Research, University of Alabama in Huntsville, September 1993.

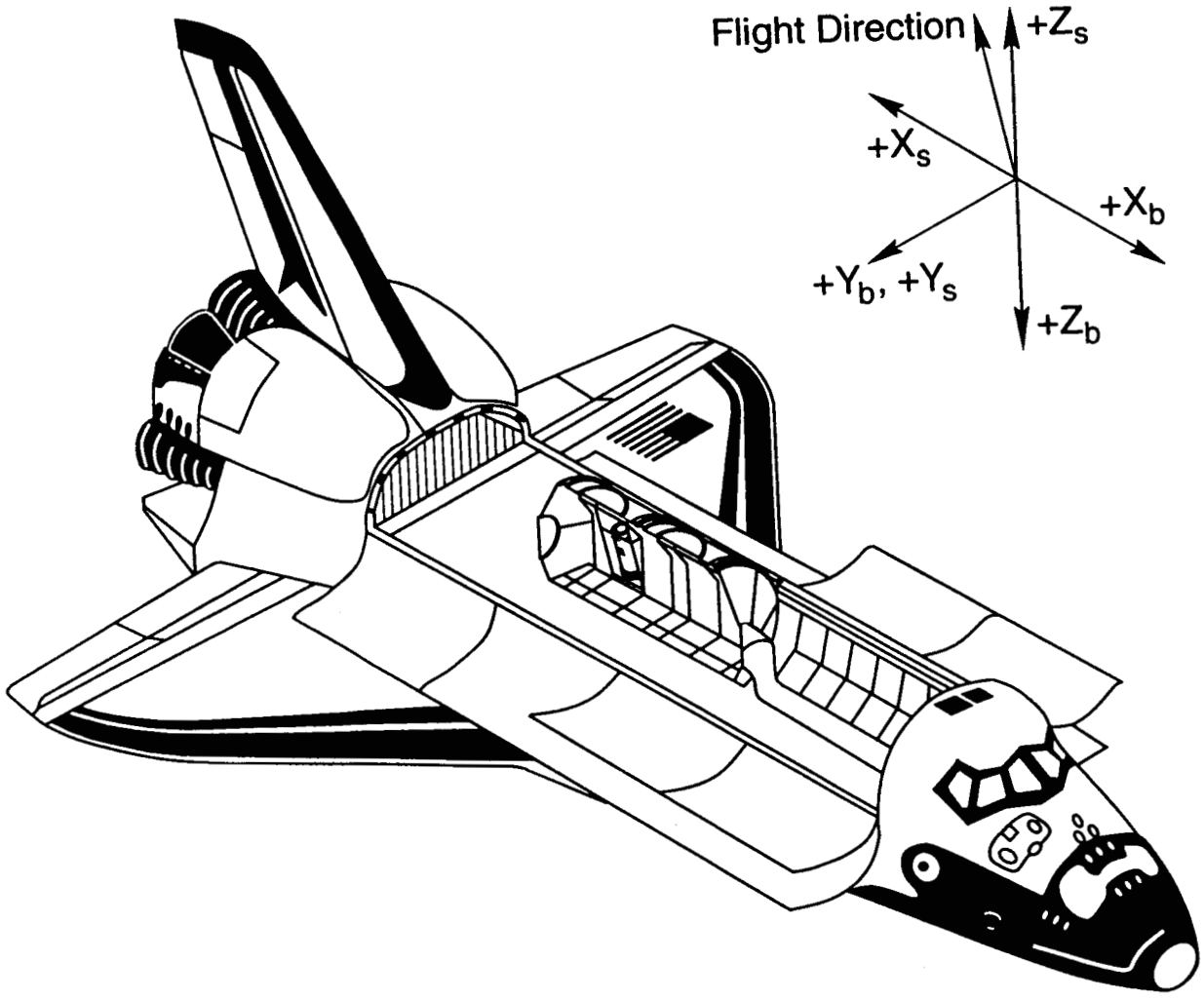

Figure 1 Cutaway view of Spacelab in Orbiter payload bay. Orbiter body coordinate system designated (X_b,Y_b,Z_b); Orbiter structural coordinate system designated (X_S,Y_S,Z_S).

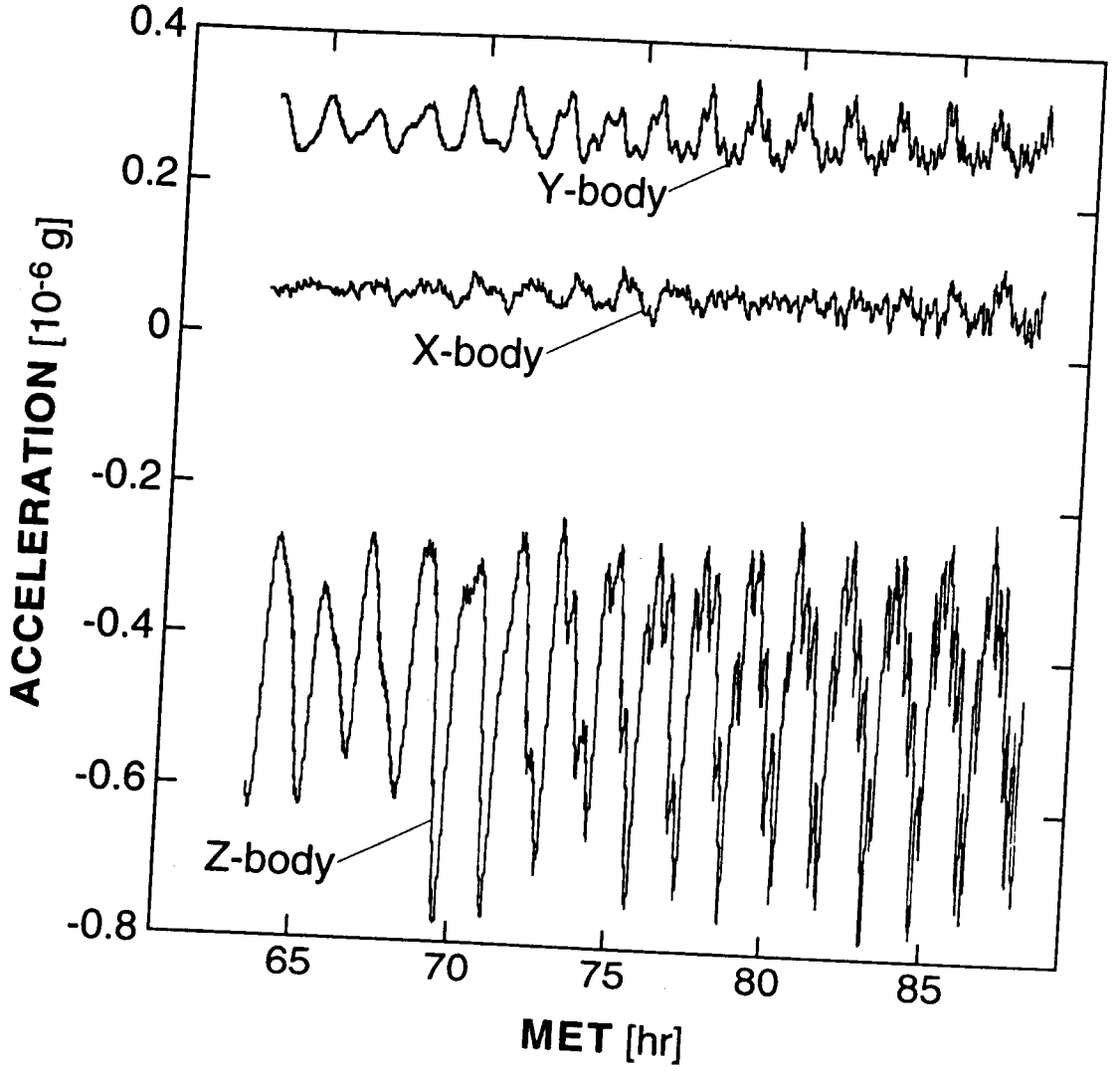

Figure 2 Modeled quasi-steady acceleration on USML-1 (aerodynamic drag, gravity gradient, tangential, and radial components). Accelerations at the Crystal Growth Furnace location modeled using actual Orbiter state vector data from MET 63 hr to 89 hr.

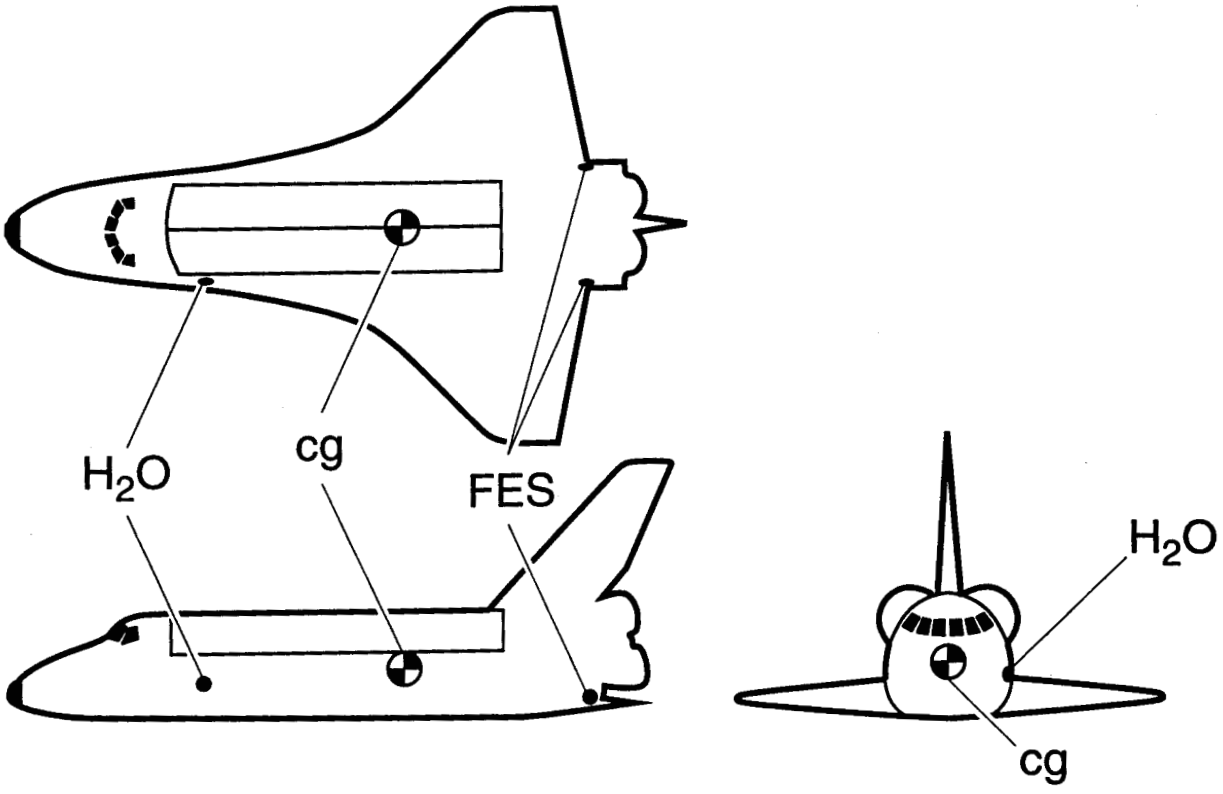

Figure 3 Approximate locations of Orbiter cg, waste and potable water vents (H_2O), and Flash Evaporator System vents (FES). See text for coordinates.

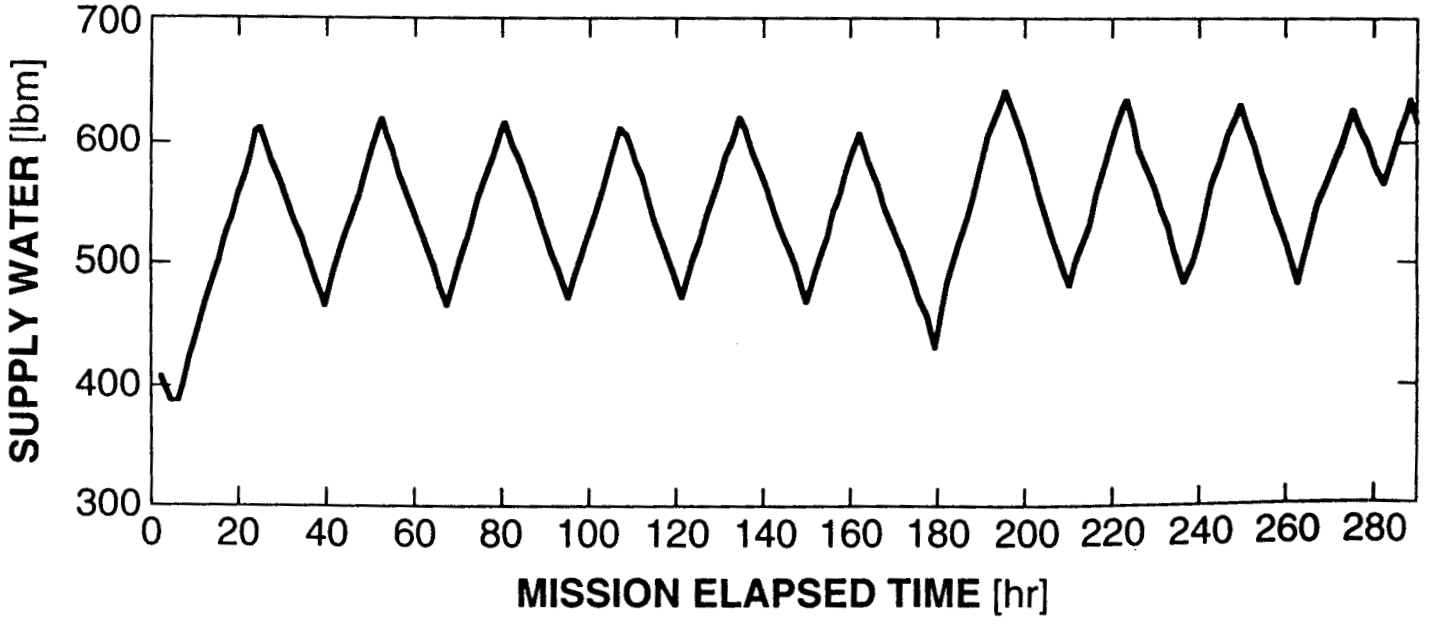

Figure 4 Supply water quantity history for STS-50. Downgoing segments of plot indicate water loss via FES activity. Note ~28 hr periodicity of venting.

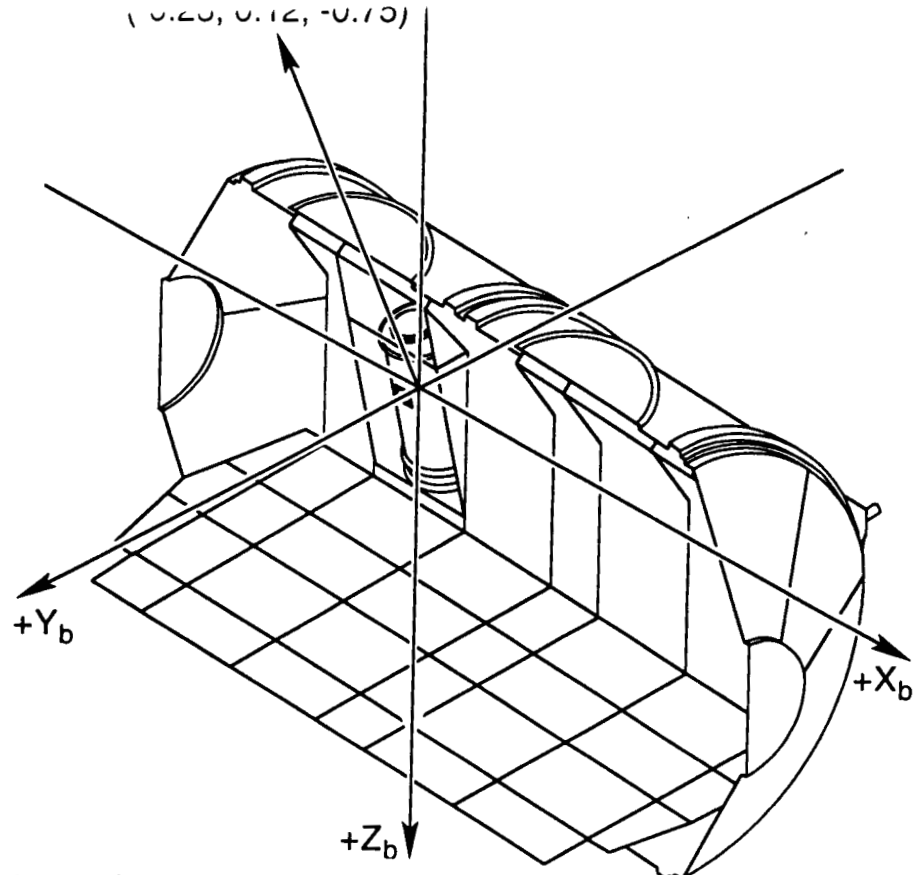

Figure 5 Average orientation of residual acceleration vector recorded by OARE when FES was off. Data recorded at OARE location and extrapolated to CGF location. From [11].

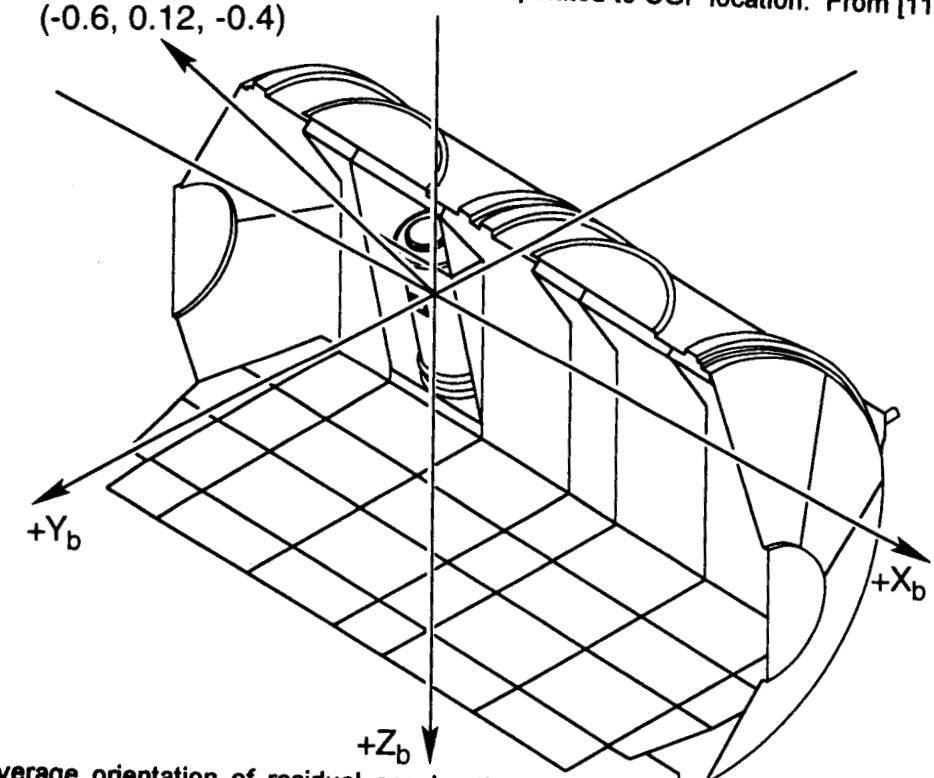

Figure 6 Average orientation of residual acceleration vector recorded by OARE when FES was on. Data recorded at OARE location and extrapolated to CGF location. From [11].

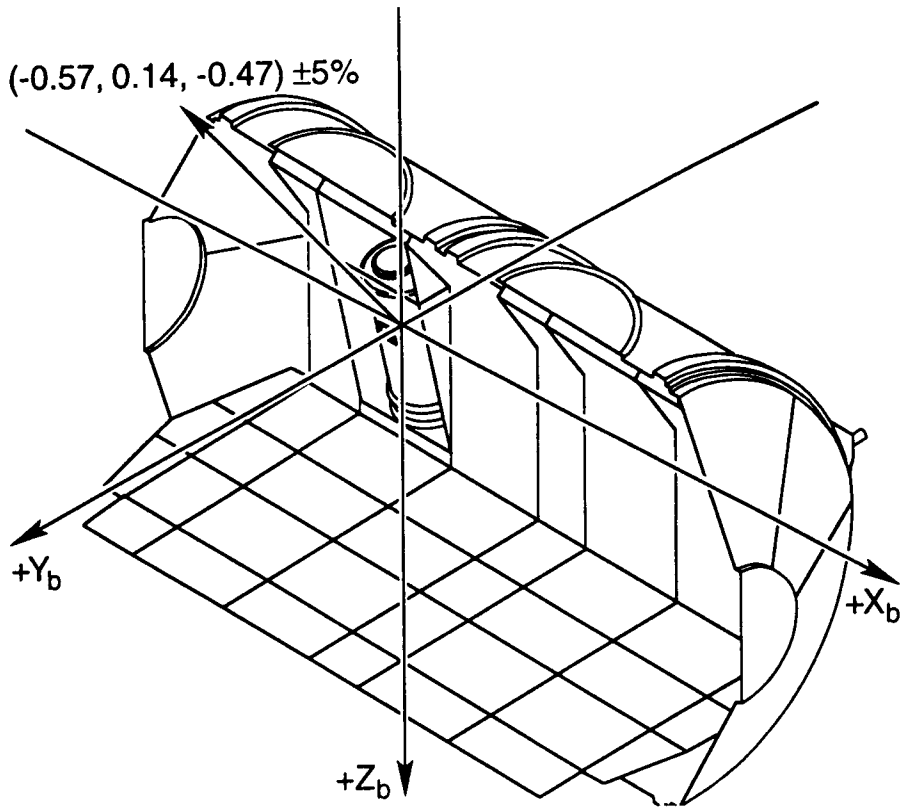

Figure 7 Average orientation of residual acceleration vector recorded by PAS when FES was on. Data recorded in Flight Deck and extrapolated to CGF location. From [11].

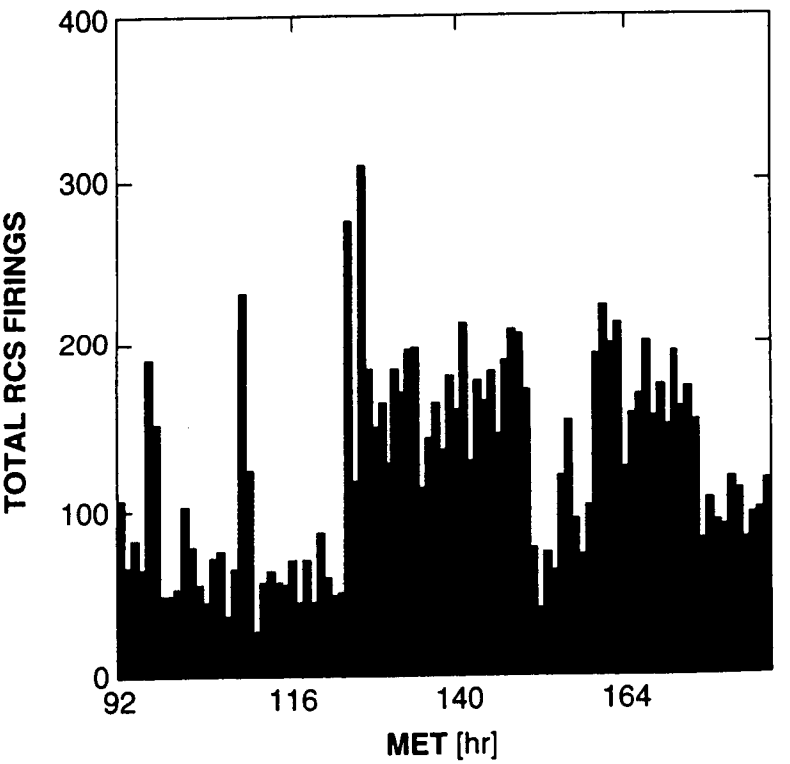

Figure 8 Total number of RCS jets fired in one hour periods. Note that simultaneous firings are considered as multiple events and that all firings are of VRCS jets.

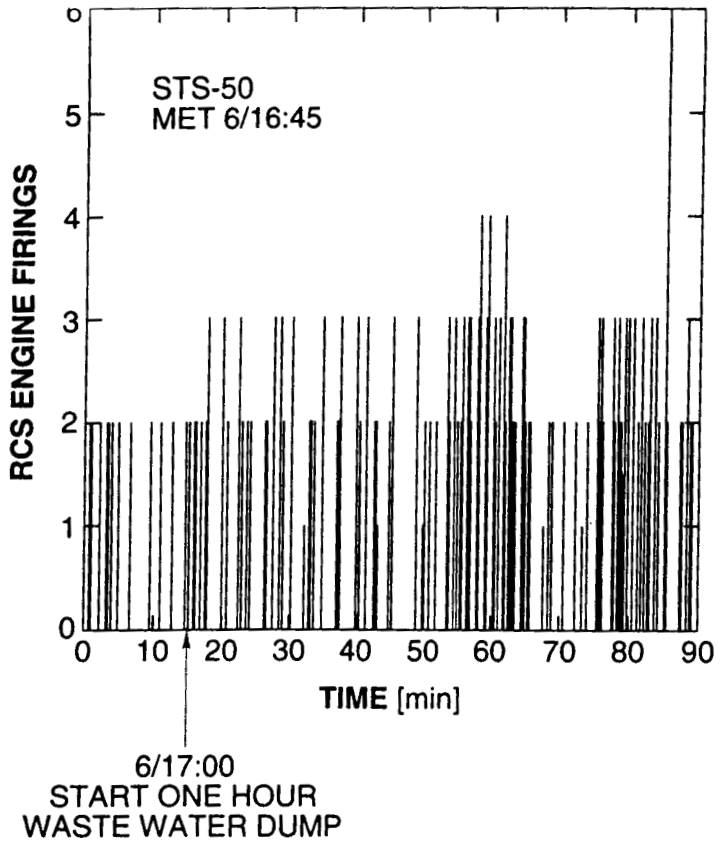

Figure 9 VRCS jet firing history before and during waste water dump. Plot shows jet firing occurrences versus time. For example, a bar of height 2 indicates that 2 VRCS engines fired. Width of bar indicates relative firing length and/or temporal spacing of firings.

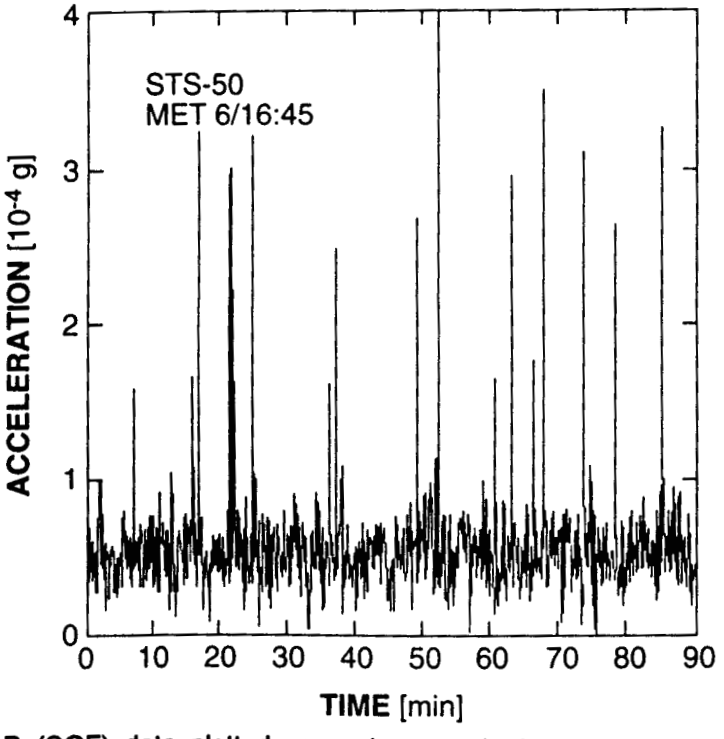

Figure 10 SAMS Head B (CGF) data plotted as vector magnitude for time shown in Fig. 9. Note acceleration transients related to thruster activity.

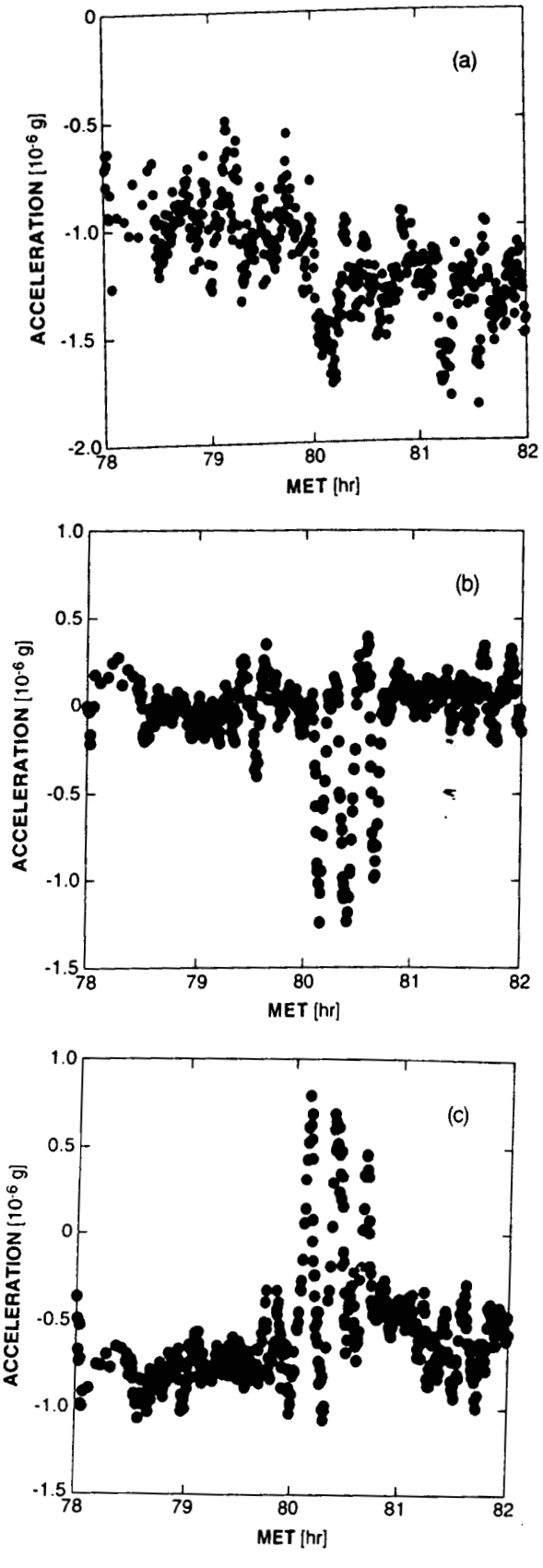

Figure 11 OARE data recorded during waste water dump activity (an earlier event than shown in Figs. 9 and 10). (a) X_b, (b) Y_b, (c) Z_b. Note response to thrusters, most evident in (b) and (c).

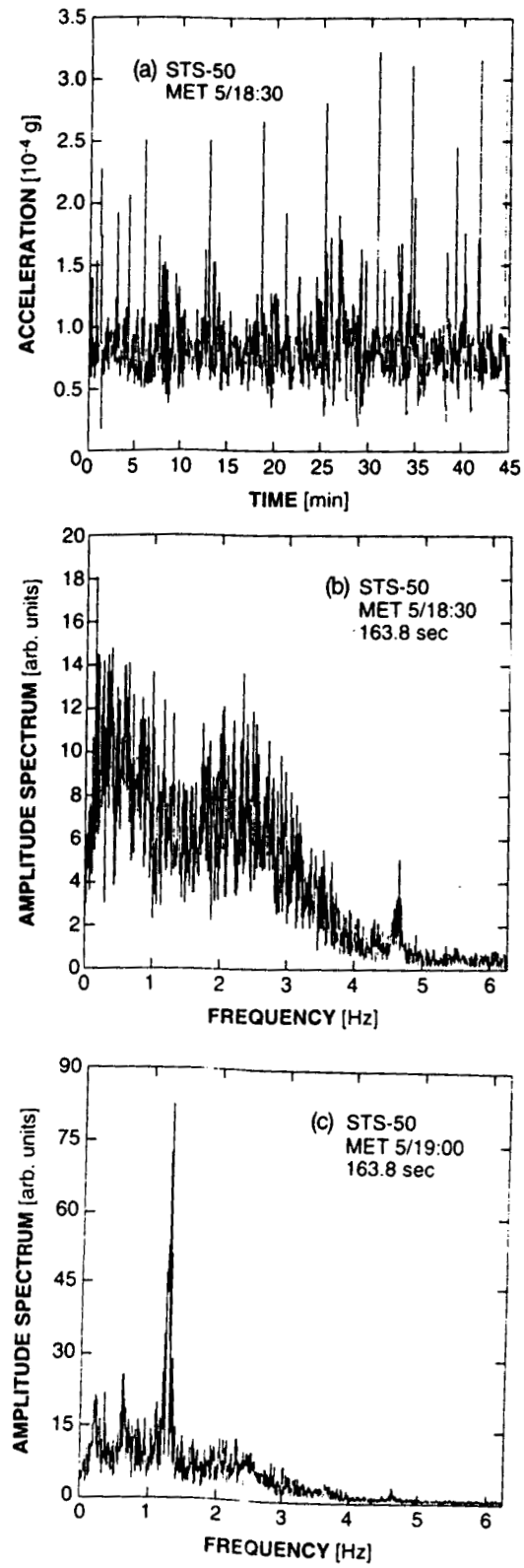

Figure 12 SAMS Head B (CGF) data during bungee isolated exercise. (a) Vector magnitude, exercise begins about 15 minutes into plot. (b) Combined amplitude spectrum, pre-exercise. (c) Combined amplitude spectrum, during exercise. Note excitation of 1.2 Hz pedaling frequency in (c).

Discussion

Question: *Why did they tighten the dead band ?*

Answer: I think Brian may have mentioned that earlier. What was happening was the CGF attitude was a gravity gradient attitude so that the tail of the orbiter was pointing towards Earth. But it was also not in it's natural position. That is, it wants to be in, which is at a slight angle. It was more upright than that, and so it was constantly wanting to drift down in that position and they had to keep firing the engines to get it to stay in this dead band that they wanted. The particular thrusters that had to be fired to do that were two of the aft thrusters, and as a consequence, the thrusters in the nose were not firing and they were having temperature problems. They have to fire so often to basically stay healthy and so the orbit people decided to tighten the dead band so that the thrusters in the nose area would fire and they would not lose the ability to fire those thrusters. It was not science driven, it was an Orbiter and safety type driven decision.

DESIGN CONSIDERATIONS FOR A MICROGRAVITY ISOLATION SYSTEM TO FLY ON SPACE SHUTTLE

D. L. Edberg

Senior Scientist
McDonnell Douglas Aerospace
Huntington Beach, California

ABSTRACT

The design of a microgravity isolation system must take into account predicted vibration levels, payload requirements, and logistic considerations. This paper describes the results of current research being carried out at MDA (McDonnell Douglas Aerospace) to produce a vibration attenuation system for possible use on Shuttle or Space Station. The system is a very low frequency, flexible interface between a scientific payload and the orbiting host platform. The platform's natural modes may be excited by on-board equipment and astronaut activities, and predictions indicate that these disturbances may be enough to upset the desired levels of microgravity.

The MDA isolator concept has been demonstrated in 3-axis testing in the laboratory and nearly meets the desired space station specifications. However, the design needs on-orbit testing to verify its performance in a true space environment. This paper discusses the practical aspects of the design and operation of a flight-test version. NASA has notified MDA that a Phase A award for an experiment will be made under the IN-STEP program.

INTRODUCTION

One of the main justifications for a space station is its potential use as a long-term microgravity science platform. Other space missions, such as the U.S. Microgravity Laboratory flown on the Space Shuttle have similar missions, but shorter duration. A number of scientific experiments to be carried out require extremely low levels of acceleration, on the order of one to ten *millionths* of one Earth gravity (1 to 10 x 10^{-6} x 9.8 m/sec^2 = 1 to 10 μg). These include both materials and biological science experiments such as very high quality semiconductors, metal alloys, and protein crystal growth. To get an idea of the required level of acceleration: if one were able to mount a scientific payload on the end of the second hand of a wristwatch, the experiment would experience an acceleration level of about 15 μg, higher than the space station specification!

Acceleration measurements made on Shuttle flights [1,2] as well as finite-element analyses of Space Station Freedom and other large orbiting platforms indicate that operation of on-board mechanical equipment and movement of personnel may cause acceleration levels well above their required μg levels. On-board machinery such as solar array and thermal radiator rotary joint actuators can excite a large number of natural vibration modes, as can crew activity.

The difficulty of maintaining microgravity on an orbiting platform may be simply assessed by the observation that the assembled SSF has an on-orbit mass on the order of 200 metric tonnes (440,000 lb_m). To accelerate it as a rigid body at 10^{-6} g (1 μg) requires a force of just 2 N (0.5 lb_f). It is not hard to imagine that nearly any source of forces such as crew pushing off a wall, typing on a keyboard, or even a sneeze could produce a force of this magnitude.

To make the problem even more difficult, the host vehicle is not a rigid body, but a flexible one with many vibratory modes below 100 Hz. Any excitation may supply energy to one or more of these modes, whose expected low damping provides very long settling times and makes the microgravity problem even more difficult. A 1 Hz mode with 0.5% critical damping takes more than 15 minutes to drop to one-hundredth of its initial amplitude. It is easy to see that unless on-board excitations are properly dealt with, many disturbances will prevent microgravity research from occurring.

One way to achieve the desired low acceleration levels is to curtail crew activities and operation of machinery, or at least schedule them for "nonsensitive" times. The curtailment of any of these activities is certain to reduce crew efficiency and productivity and strongly impact on-orbit performance. While a crew may be restricted for a few hours at a time, keeping them restrained for a 90 day period is not a realistic option for a manned platform.

With these issues in mind, MDA began to look for an alternative mechanical system that could provide microgravity levels of acceleration for selected payloads. The isolation properties of a soft suspension are very well known to the dynamics industry, but isolation to such very low levels has rarely been attempted.

Our design goal was to build a practical low-frequency suspension system that would accommodate a sensitive payload or experiment on an inner frame. The inner frame is very loosely connected to an outer frame which is mounted to the (noisy) platform. The details of the design process, the important variables, and the results of testing of our laboratory demonstrator will be given below.

I. SYSTEM DESIGN

An ideal isolation system consists of no mechanical connection at all. In this case, the isolated payload simply "flies freely" around with no connection to the outside world. The only physical requirement for such a system is "sway space" between the isolated experiment and the platform. The choice of the amount of sway space depends on the input accelerations that are expected.

The need to supply the experiment with power, data, and cooling facilities makes some connection to the outside world a necessity. Hence, our design baselined an inner payload elastically coupled to the outer frame/platform, where the elastic coupling comes about from two sources: the inherent stiffness of the umbilical cables performing the connection, and a set of actuators that may be used to improve isolation performance. The idea is to use the actuators to reduce the stiffness of the elastic coupling as much as possible.

The design of an isolation system is determined by the external inputs, desired performance, and system constraints. A simple passive spring-mass system has a natural frequency proportional to $\sqrt{(k/m)}$ where k is the spring stiffness and m is the system mass. Below this frequency, its transmissibility is unity, i.e. all disturbances are transferred directly to the payload without attenuation. Above the natural frequency, the transmissibility "rolls off" at a slope of 20 dB per decade, meaning that high frequency excitations are attenuated. In the vicinity of the natural frequency, disturbances are amplified as a function of the damping of the system.

(Because of the unity transmissibility at low frequencies, it is not possible for this — or any other isolation system — to isolate the quasistatic forces created by gravity gradients and atmospheric drag. These will act on all payloads whether isolated or not.)

Active control may be used to enhance system performance, especially in the vicinity of the system's natural frequency. One could feed back the acceleration of the inner platform to the actuators, in effect canceling out the stiffness of the suspension system.

External vibration inputs are the first part of the design analysis and can take one of two general forms, either steady state or transient. We assume that any steady state excitation is from some sort of rotating mechanical equipment and is sinusoidal in nature. In the case of a space station, sinusoidal excitation comes from the rotation of the solar arrays and thermal radiators, pumps, fans, exercising activities on a treadmill, and assorted other machinery (random noise could also be considered steady state but doesn't create as large a response, so has a smaller contribution). Many of these sources have sinusoidal contributions in the vicinity of fundamental vibration modes of the platform, which in the case of a space station is less than 1 Hz. This drives

the desired natural frequency of the suspension to even lower values, if natural attenuation is desired.

Transient acceleration is something that is applied for a short time period, and then released. Examples of transient phenomena are astronauts pushing off walls, sneezing, typing on keyboards, docking operations, thruster firings, and other such actions.

We assume that the excitation is an applied *displacement* rather than an applied force, since the platform upon which the experiment is mounted is orders of magnitude more massive than the experiment itself. This is justified in the case of Space Station Freedom, whose projected 200,000+ kg mass is more than four orders of magnitude higher than the mass of most scientific payloads. In simple terms, we are assuming that the actions of the scientific payload will not have any noticeable effect on the dynamics of the base platform.

Consider, then, the microgravity specification used for design purposes. The desired microgravity vibration levels determine the necessary "sway space" that separates the inner and outer frames. Considering a 1 μg acceleration at 0.01 Hz, it is easy to show that the needed amplitude is 10^{-6} x 9.8 m/sec^2 ÷ (2π x 0.01/sec)^2 = 2.5 x 10^{-3} m. In other words, if we have a half-centimeter around the payload to be isolated (because we need to have clearance for the double amplitude of motion), the space station could vibrate at a 1 μg level at 0.01 Hz without contact with the payload.

We now consider a transient event: four astronauts, each massing 80 kg, push off the wall of a module of Space Station and coast to the opposite end eight meters away. In this case, we use conservation of momentum to calculate that the Space Station would move the opposite direction 4 x 80 kg x 8 m ÷ 200,000 kg = 1.28 cm. This motion occurs during the few seconds of time that the astronauts take to travel to the other side of the module.

These factors must be used to size the space between the inner payload and outer frame, a term we define as "sway space." If we choose more sway space, less volume is available to the payload and vice versa. Our prototype finally settled on a 2 cm sway space, or ±1 cm of travel from neutral. This would *not* be able to accommodate the four-astronaut pushoff described above, but would be able to handle a two-astronaut pushoff.

However, the determination of sway space is only part of the design of the isolation system. Another part is the requirements that the payload be connected to the real world. The payload's needs dictate what connections are needed to the outside world, such as data transmission, power, and air or water cooling. These connections determine the necessary size of an umbilical cord connecting the outer and inner frames. Once the umbilical is sized, the minimum stiffness of the suspension system is determined, and the isolation performance is approximately pinned down.

Of course, it must be said that the umbilical connections must be designed for minimum stiffness. A stiff conduit connecting the inner and outer frames will "short-circuit" any soft suspension system, so the design of the umbilical must be done carefully to produce minimal stiffness. Work on some low stiffness umbilical designs at McDonnell Douglas and at Harvey Mudd College has recently been completed.

We mentioned earlier that the transmissibility of the suspension system is large in the vicinity of the natural frequency of the suspension. Early on in the design process it was determined that passive isolation could provide some, but not enough performance to guarantee low microgravity levels at the payload inner frame. It was decided to augment the passive isolation system with an actively-controlled set of actuators that could force the inner frame upon command.

The signals fed to the actuators originate from measurements made by accelerometers mounted on the inner frame. These are filtered appropriately by a compensation system and then amplified to high-voltage levels to drive the actuators. The actuators were fabricated from piezoelectric polymer material and capable of large stroke. These actuators would be used to "negate" forces being transmitted across the suspension system and in effect zero the effective stiffness connecting the inner and outer frames.

II. EXPERIMENTAL TEST-BED

The design of the testbed was dictated by the size of the external mounting frame. It was decided that a double Shuttle middeck locker equivalent (MLVE) space provided reasonable volume. Initially a double locker available from Wyle was considered for use for the flight experiment, as it appeared ideally suited to hold the isolation system. Once the outer dimensions are specified, the sway space dictates the size of the inner frame. Then, it was possible to concentrate on the details of the construction. Figure 1 shows a photograph of the laboratory testbed.

The outer frame is a base for the trapezoidal piezoelectric plastic film actuators, which are connected to the inner frame with stinger mechanisms to allow for unrestricted motion throughout the sway space. The circular items within the inner box represent a scientific experiment.

The construction of the laboratory testbed was done in order to facilitate testing to verify its isolation performance. This testing measured transfer functions between the outer and inner frames when a specified level of acceleration was applied to the outer frame. To conveniently carry out this measurement in the laboratory, the outer frame was suspended by cables attached to the ceiling, representing the interface to the host spacecraft. The cable suspension allowed electrodynamic shakers to easily be used to drive the outer frame. By applying the appropriate forcing to the outer

frame and measuring the response of the inner frame, it was possible to measure the system's actual performance.

Testing all six degrees of freedom (DOF) requires a zero stiffness suspension system with zero dissipation, an impossible requirement. As shown in Figure 2, we decided to test three axes at a time, rotate the assembly 90°, repeat the testing, again rotate the assembly 90°, and again repeat the testing. This procedure would test in all nine degrees of freedom, although only six of them are unique.

Of high importance was the requirement to simulate microgravity on the inner payload. The inner frame is placed on an air-bearing table, a *planar* zero friction system. The air bearing uses a higher pressure chamber underneath the experiment to provide a very low friction interface with the base. This arrangement provides three degrees of freedom for the simulated experiment: two transverse horizontal motions, and rotation about the vertical axis. This in turn means that three microgravity accelerometers and three electrodynamic shakers (to provide disturbances) need to be provided.

The inner frame is connected to the outer frame with a set of very soft laminated piezoelectric plastic spring/actuators, producing open-loop frequencies around 0.2 Hz. The springs are laminated from 12 layers of etched polyvinylidene fluoride with a slight curvature. Figure 3 depicts the shape and etched pattern of one of the actuator layers. A maximum of ±850 volts would drive these actuators several centimeters.

This construction choice allowed the actuators to be formed in a way that they could double as very soft elastic suspension members. Furthermore, with the application of voltage to the film, the piezoelectric effect created a mechanical strain that can be used to provide actuation forces. To operate properly, the actuators are sized to overcome the stiffness of the suspension and umbilicals in the system, so with a good design of the former, the forces in the actuation system may be kept reasonably small. Properties of the actuators are summarized in Table 1.

As mentioned earlier, the laminated piezoelectric springs also function as actuators, and the measured acceleration of the inner container is fed back to further improve the isolation performance. The acceleration was measured by three Sunstrand servo accelerometers, whose noise floor is well under the micro-g requirements. Very thin magnet wire was used to transmit their signals across the inner-outer frame interface.

III. SYSTEM PERFORMANCE

A number of tests were carried out on the testbed hardware[3,4]. These included system identification and transfer function measurement. The key performance measure is the transfer

function from input acceleration to acceleration of the platform. Figure 3 gives the transmissibility of the lab testbed. Noise levels shown are from both the noise floor of the laboratory at MIT and from the sensors themselves.

Enveloping this curve and inverting it gives the allowable levels versus frequency as shown in Figure 4. Note that the closed-loop feedback has removed almost all the second-order system resonance peak, and one may note the good performance at higher frequencies, where the second-order rolloff occurs and naturally attenuates inputs.

With this good performance in hand, various NASA officials were briefed on our progress in the lab, and we began campaigning for the natural next step – a flight experiment to verify performance at nominal zero-g levels.

IV. DEVELOPMENT OF FLIGHT EXPERIMENT

Both scientific and political considerations make a flight experiment worth pursuing. The ability to run a microgravity experiment without worrying about crew activities or on-board equipment vibration is a definite advantage, and NASA's interest and support for a flight experiment will show a commitment to microgravity both on-board its shuttle scientific flights as well as a space station.

We have considered the work necessary to demonstrate our microgravity isolation system in the space environment and expect to be able to plan on a shuttle flight approximately 24 months from start of work (Fig. 5). This schedule includes the time necessary for the design of the flight hardware, fabrication and testing, shuttle integration planning, safety reviews, training sessions, and other factors. We have coined the acronym SMITE to represent either Shuttle Middeck Isolation of Transient Events or SPACEHAB Microgravity Isolation of Transient Events, depending on the final location that the demonstration secures. MDA's Huntsville division is a equity-sharing partner in the SPACEHAB venture, and may have some interest in promoting microgravity isolation for its own sales efforts.

Prospective designs for the flight experiment place the actuators in the corners of the outer container so that the space available to the isolated volume is maximized. Depending on the configuration chosen, the payload efficiency (defined by the payload available to the scientific payload divided by the total volume consumed) ranges from 65 to 90%. Since the sway space is independent of the isolated volume, the larger the volume, the higher the payload efficiency.

The flight demonstration will be one of four options, depending on the final budget and space constraints on the shuttle middeck. The first and most inexpensive option places a small isolated volume along with the associated recording and control electronics within a single MLVE. The

second and third options consume two MLVEs, one with one MLVE volume completely isolated and electronics in a second MLVE, and the other with a double-MLVE space containing both isolated volume and electronics. The last option provides a full double-MLVE to be isolated, and a separate MLVE containing electronics. The fourth option will provide the most isolated volume to a prospective payload, and except for locker volume costs little more than the other options.

The cost of the demonstration depends on the development timeline as well as the option as given above. The cost of fabricating, testing, and integrating the demonstration is largely independent of its size, but the number of MLVEs consumed has a very large affect. We currently are predicting an approximate $2M cost for the hardware development. To this number must be added the cost of locker space and transportation to orbit. These costs may vary wildly depending on the availability of locker space and the possible sponsor.

We have considered options to reduce cost, the most significant one to make use of the government-owned Experiment Support Module (ESM) used on shuttle *Discovery* mission STS-48 to control the excitation and data acquisition of the Middeck Zero-gravity Dynamics Experiment (MODE). The modification would consist of the addition of drive electronics for the actuators for the six DOFs. The existing optical data recording system is capable of recording at least 160 hours of data from the accelerometers on board the isolated platform as well as three reference accelerometers mounted on the outer frame itself. All data are recorded onto a write-once, read-many (WORM) disc for subsequent data analysis.

One design feature necessary for operation is a "lock-out" mechanism that is used to secure the inner payload frame during high acceleration events, such as launch, orbital maneuvering, and reboost. For simplicity and to reduce possibility of failures, such a mechanism would have a manually-operated crank that would force the inner container onto some tapered pins that would lock the assembly onto the outer frame. To release, the crank would be retracted to allow the inner frame to move freely. Soft elastomeric stops will be provided in all possible degrees of freedom in the event of a large transient that the closed-loop control system cannot overcome.

Operation and monitoring of the flight by the crew is very simple. First, the inner volume is "unlocked" so as to be able to move as appropriate for microgravity considerations. Next, power to the control system, data acquisition system, and any scientific payload is turned on. Data acquisition is initiated, and the experiment may be left unattended until the mission is completed or data storage needs replenishment. Shutdown procedures are the opposite of the operations listed above.

CONCLUSIONS

We have designed and built an operational microgravity isolator system, and demonstrated its performance and usefulness to the scientific community. The hardware is now being evolved into a flight demonstration. The overall objective of the Shuttle Middeck/ SPACEHAB Microgravity Isolation of Transient Events (SMITE) flight experiment is to demonstrate that active isolation technology may provide a microgravity environment in space. A flight test could be completed within 24 months after project start at moderate cost.

POSTSCRIPT

On 13 October 1993, NASA's Office of Advanced Concepts and Technology announced the selection of MDA's SMITE microgravity isolator proposal for Phase A award. If fully funded, this program will lead to a flight demonstration on board a shuttle with at least one scientific payload to measure its performance. Negotiations are under way with several experimenters to obtain a candidate experiment for our isolator.

One goal of the SMITE flight experiment will be to measure the effects of vibrations on typical scientific payloads. By programming the feedback system to apply cyclic acceleration rather than null acceleration, the isolation system may be used to apply specific acceleration levels as well as to isolate. Thus, an experiment may be run at different base acceleration levels in order to assess the true effect of acceleration on the science return.

REFERENCES

1. Dunbar, B., Thomas, D, and Schoess, J, "The Microgravity Environment of the Space Shuttle Columbia Middeck During STS-32," NASA Technical Paper 3140, November 1991.

2. Dunbar, B., Giesecke, R., and Thomas, D, "The Microgravity Environment of the Space Shuttle Columbia Payload Bay During STS-32," NASA Technical Paper 3141, November 1991.

3. Mercadal, M., Blaurock, C., von Flotow, A., and Wereley, N., "Laboratory Prototype of a Six Axis Microgravity Isolation Mount," Report SERC#15-91-R, Massachusetts Institute of Technology, Sept. 1991.

4. Mercadal, M., Blaurock, C., von Flotow, A., and Wereley, N., Microgravity Isolation For Spacecraft Payload, Proceedings of the ADPA/AIAA/ASME/APIE Conference on Active Materials and Adaptive Structures, IOP Publishing, Nov. 1991.

Table 1. ACTUATOR PROPERTIES

Layer thickness	0.03 mm
Glue layer thickness	0.0002 mm
Number of layers	12
Total thickness	0.389 mm
Length	101.6 mm
Maximum voltage	840 V
Maximum force	0.089 N
Maximum displacement	20.3 mm
Total mechanical stiffness	0.0049 N/mm

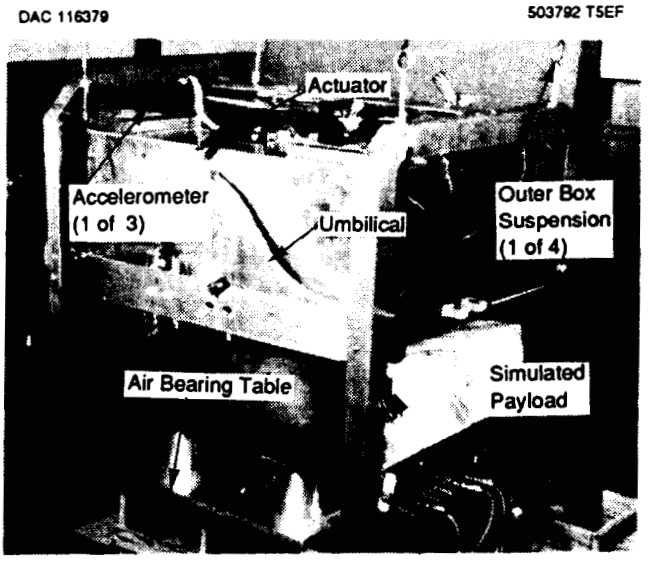

Figure 1 MDA Vibration Isolator Test-Bed.

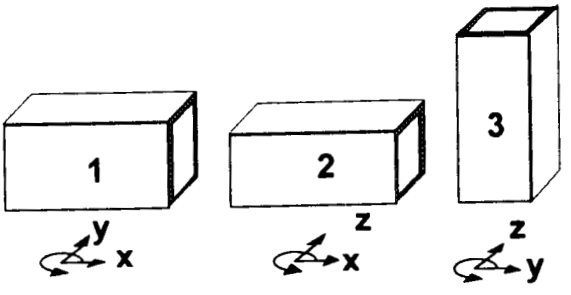

Figure 2 Sequential 3-DOF Testing Verifies 6-DOF Operations.

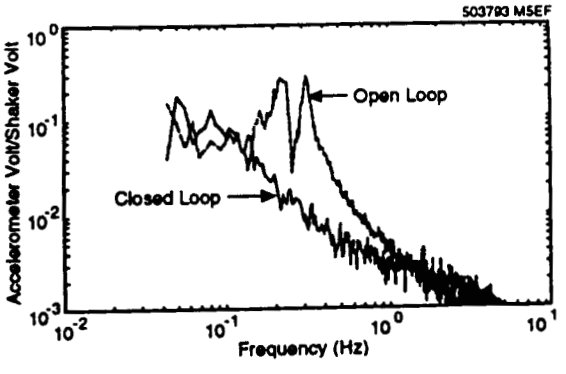

Figure 3 Our isolator increased the attenuation of at 0.3 Hz by a factor of 70.

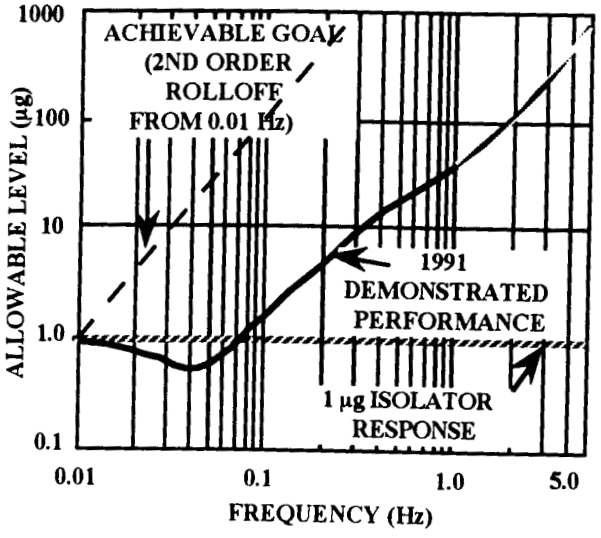

Figure 4 Measured and Predicted Transmissibility

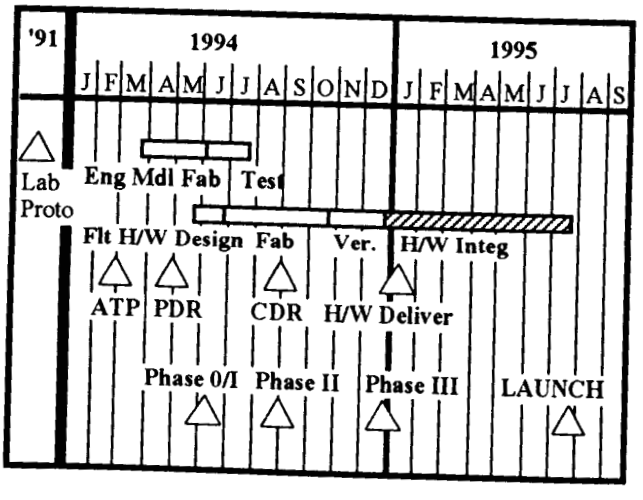

Figure 5 Our schedule predicts a flight demonstration within two years of ATP.

PRELIMINARY CALIBRATION REPORT OF AN APPARATUS TO MEASURE VIBRATION CHARACTERISTICS OF LOW FREQUENCY DISTURBANCE SOURCE DEVICES

James W. Russell*, Robert A. Marshall*, Tom D. Finley^ and George F. Lawrence^

*Lockheed Engineering & Sciences Company, Hampton, Virginia
^NASA Langley Research Center, Hampton, Virginia

ABSTRACT

This report presents a description of the test apparatus and the method of testing the low frequency disturbance source characteristics of small pumps, fans, camera motors, and recorders that are typical of those used in microgravity science facilities. The test apparatus will allow both force and acceleration spectra of these disturbance devices to be obtained from acceleration measurements over the frequency range from 2 to 300 Hz. Some preliminary calibration results are presented.

INTRODUCTION

The microgravity science facilities being developed employ devices which generate low frequency disturbances that could effect the science activities. Furthermore, the disturbance levels generated by these devices may exceed the payload vibroacoustic allocation as specified in Space Station Control Board Directive BB003262A to the Space Station Systems Requirements Document, SSP30000. Although it is thought that the vibroacoustic levels of these disturbance sources are low, the actual values need to be ascertained. Current analysis methods for determining the values of these devices are predicated on considerably larger, heavier equipment and may not be applicable to such devices as small camera motors, small water pumps, computer fan motors, data recorders, etc. Microgravity science experiments like fluid mixing and combustion flameballs are very sensitive to low frequency disturbances. Currently, there is very little data on the low frequency characteristics of small disturbance source devices such as those used in microgravity science facilities.

The NASA Langley Experiment Utilization Branch (EUB) has undertaken a task to measure the amount of disturbance of various source noise devices at low frequency. By measuring both the acceleration spectra and the forcing function for a particular device, the power spectra can be defined. Similarly, for each device, the impedance spectra can be calculated at any location for the particular

mounting system. The power spectra and impedance spectra can then be used to define both the force and acceleration at the specified location.

The purpose of this report is to show the test apparatus design and present the methodology for obtaining both forcing function and acceleration characteristics of the various disturbance source devices. The calibration methods for obtaining forcing functions from accelerometer measurements on three orthogonal axes are discussed. Preliminary calibration data are presented of force to acceleration ratios for the test apparatus on the Y and Z axes over the frequency range from 2 Hz to 300 Hz.

I. TEST APPARATUS DESIGN

To measure the acceleration spectra of a disturbance source device, a triaxial accelerometer package is hard mounted to the device. To measure the force spectra of the disturbance source device, it was initially planned to mount force transducers between the device and a hard surface. However, the preload source of several pounds on the transducer could significantly affect the dynamic measurements. Also each device would require a separate mounting system.

Therefore it was decided to employ a soft spring system with a large plate mass of high impedance which would vibrate as the dynamic force was applied. With a soft spring and a heavy plate, most of the force goes into the plate vibration, because the spring force is low relative to the plate vibration force. The force can then be determined from the acceleration spectra of the mass if the mass has a high impedance.

Figure 1 shows the test apparatus and the associated electronics equipment. The test apparatus consists of a 66 pound, 20 inch diameter aluminum plate supported by three zinc rods with turnbuckles, which in turn are suspended from a soft stainless steel spring which has a spring constant of 5 pounds per inch. The triaxial accelerometer package is mounted underneath the plate. The spring in turn is suspended from a 7 foot long 3/16 inch twisted steel cable which is mounted to an eyehook from the ceiling. The eyehook is welded to two steel bars which are mounted between the concrete crossbeams of the ceiling. Also shown is a 10 inch diameter, 7/8 inch thick steel plate, which is mounted to the test apparatus. The steel plate has a weight of 25.4 pounds. This allows the force to acceleration ratio calibration of the test apparatus to be performed at two different masses. The test apparatus is oriented such that the X and Y axes are parallel to the surface of the plate and the Z axis is perpendicular to the plate surface. The center of the three axes planes are at the center of gravity of the aluminum plate. Figure 2 shows the aluminum plate with a peristaltic pump mounted so that it is aligned with the X axis. The acceleration measurements will provide both acceleration and force characteristics of the pump on all three axes.

The test apparatus is designed to measure acceleration responses to force inputs over the frequency range from 2 to 300 Hz in the X, Y, and Z directions. For the suspended aluminum plate shown in Figure 1, the natural frequency in the X and Y directions is only dependent on the length of swing and is defined by:

$$f_X = (g/L)^{1/2}/(2\pi)$$

For our system where the suspended length is approximately 8.6 feet, the natural frequency on the X and Y axes is 0.307 Hz. In the vertical or Z direction, the natural frequency is dependent on the mass of the test apparatus, m, and the spring constant, K_S, in pounds per foot. Part of the force in the Z direction, F_Z, goes into the deflection of the spring, and part goes into the vibration of the mass. The equation for the spring assuming that there is negligible damping is as follows:

$$F_Z = -4\pi^2 m f^2 x_Z(f) + K_S x_Z(f)$$

The natural frequency on the Z axis, f_Z, is that frequency associated with the mass and the spring constant when the force, F_Z, is zero, and is defined by:

$$f_Z = (K_S/m)^{1/2}/(2\pi)$$

For the test apparatus shown in Figure 1, the weight, W, is 93.4 pounds with the steel plate and 68.0 pounds without the steel plate. The spring constant, K_S, is 5 pounds per inch or 60 pounds per foot. The natural frequency corresponding to these two calibration masses is 0.724 Hz and 0.848 Hz respectively.

II. CALIBRATION SETUP

Figure 3 shows a sinusoidal shaker and a force transducer hard mounted to the top of the aluminum plate and an accelerometer package hard mounted to the bottom of the aluminum plate. The shaker and force transducer are used to obtain the forcing function of force to acceleration ratio for both of the test apparatus masses on all three axes. Figure 3 shows the shaker mounted on the Z axis for calibration without the steel plate. The calibration is also performed on all three axes with the steel plate attached to provide a means of interpolation for determining the forces associated with the mass of the disturbance source device attached to the aluminum plate. Figure 3 also shows pieces of Styrofoam mounted in the eyehook plate supports. The purpose of the Styrofoam is to reduce or eliminate chatter in

the support rod mountings and make sure that the whole mounting system vibrates and not just the support plate.

For the X and Y axes, the shaker was aligned so that it was level and the force transducer was aligned between the shaker and the plate as shown in Figure 4. The steel mounting rod used to support the shaker was installed such that it was supported by a stand and butted against a 7 ton block, so that it would not move and cause forces other than the drive motor force to be input into the plate in the X or Y direction.

The electronics setup shown in Figure 1 consists of a General Radio Random-Noise Generator which creates random broadband white noise over the frequency range from 10 Hz to 50 KHz to drive the B&K Minishaker Type 410. The white noise output signal was passed through a Khron-Hite Model 3750R low bypass filter which provided for a 24 db per octave falloff in energy at frequencies above the selected bypass frequency. The signal was then passed through a Southwest Technical Products Power Amplifier 207A into the shaker. At low frequencies a Hewlett Packard 3325B Synthesizer/Function Analyzer was used in place of the random noise generator and low bypass filter. The synthesizer was used to generate signals from 2 to 10 Hz in 1 Hz increments. The shaker output was threaded to a PCB model 208A02 force transducer that in turn was threaded to the large support plate. The threaded connections insured that all the force transmitted to the plate from the shaker would be measured by the force transducer. The force transducer output was passed through a Kistler 5004 Dual Mode Amplifier, which amplifies the signal into an Ono Sokki CF-350 Portable Dual Channel Analyzer. Figure 5 shows a schematic of the force calibration system.

The triaxial orthogonal accelerometer package consists of three Sundstrand QA-700 accelerometers that have resolutions of 10^{-6} g's (1 micro-g). The accelerometers are powered by an Analog Devices Inc. Model 902 Dual Power Supply and the output signal goes directly into the Ono Sokki CF-350 Portable Dual Channel Analyzer. Figure 5 also shows the schematic of the accelerometer measurement system.

III. SYSTEM CALIBRATION

The force transducer and each of the three accelerometers were calibrated in the laboratory over the frequency range from 2 to 500 Hz. The force transducer was found to have a nominal value of 1000 millivolts per pound and the accelerometers were found to have a nominal value of 1 volt per g. Associated with each calibration is a frequency variation from the nominal value. The transducer calibration response was flat and varied from -2.9 to +0.5 percent over the frequency range from 2 to 300 Hz. Similarly the accelerometer calibration responses were also flat and varied from -0.0 to +5.0 percent over the same frequency range. The accelerometer calibrations are different for each

accelerometer. These frequency response calibrations have been incorporated into the test apparatus calibrations, but are not presented in this report .

The test apparatus is designed to measure acceleration responses to force inputs over the frequency range from 2 to 300 Hz. The ratio of force to acceleration is computed from the data and plotted as a function of frequency. Figures 6 and 7 show the normalized ratio of force to acceleration over the frequency range for the Y and Z axes respectively. At frequencies from 2 to 10 Hz there is data at each discrete integer frequency. From 10 Hz to 20 Hz there are four data sets. From 20 Hz to 50 Hz there are three sets of data. From 50 Hz to 200 Hz there are two data sets, and from 200 Hz to 300 Hz there is one set of data. The reason for this is that the Ono Sokki CF-350 analyzer performs a Fourier Transform on 400 discrete frequency values distributed evenly over the frequency range of interest. Therefore to maximize the number of discrete frequencies, the frequency data was taken over four ranges; 0 to 20 Hz, 0 to 50 Hz, 0 to 200 Hz, and 0 to 500 Hz. For each range the low bypass filter was adjusted to a value 50 percent higher than the maximum frequency. In processing the data from the white noise generator, the data below 10 Hz was removed, because the design operating range of the shaker begins at 20 Hz. As previously stated, measurements were made at discrete integer frequencies from 2 to 10 Hz using the HP 3325B Synthesizer to power the shaker.

The data presented in Figures 6 and 7 is preliminary and has not been analyzed to ascertain the forcing function statistics. It is planned to perform one more calibration on the Y axis
and two more calibrations on the X axis with the steel plate attached, before performing the statistical analysis. However, Figures 6 and 7 do present the normalized force to acceleration ratio, which is based on the calibration weight of 93.4 pounds. Figure 6 shows that at 160 Hz there is an anomaly in the Y axis measured calibration data. The explanation for this has not been determined. However, it is known that at 160 Hz, associated with the Y axis force there are significant accelerations on both the X and Z axes. It should be noted that in Figure 7 the normalized force to acceleration ratio is adjusted at low frequencies to account for that part of the force which goes into the spring deflection on the Z axis. Figure 7 shows that at 18.75 Hz there is an anomaly in the Z axis measured calibration data. This is due to the fact that the natural frequency of the steel spring is 18.75 Hz with a spring load of 93.4 pounds. Figures 6 and 7 show that the normalized force to acceleration level in the range from 10 to 200 Hz is approximately 0.96. This is 4 percent less than the theoretical value of 1.0.

IV. CALIBRATION PLANS

In order to obtain more precise forces from the acceleration measurements, it is necessary to understand the 4 percent discrepancy between the weight and the force to acceleration ratio. The most likely source for this discrepancy is the force transducer. It is planned to perform an independent

calibration of the force transducer, prior to continuing with the test apparatus calibrations. The transducer calibration will involve attaching the force transducer and two different masses of about 0.5 pounds and 1.0 pound to the shaker, with an accelerometer attached to the masses. All the force from the shaker should be transmitted through the force transducer to the mass and the accelerometer. By using two different masses, the force transducer tare weight and force spectra can be calibrated over the frequency range of interest. Once the force transducer is calibrated, the calibration of the test apparatus will continue with the two system masses of 68.0 and 90.4 pounds as previously stated. After the force to acceleration ratio calibrations are completed for both masses, the data can be applied to the acceleration measurements of the test apparatus with the various disturbance source devices installed to obtain both force and acceleration spectra. It is planned to test each source device three times, so that it is oriented on each of the three axes.

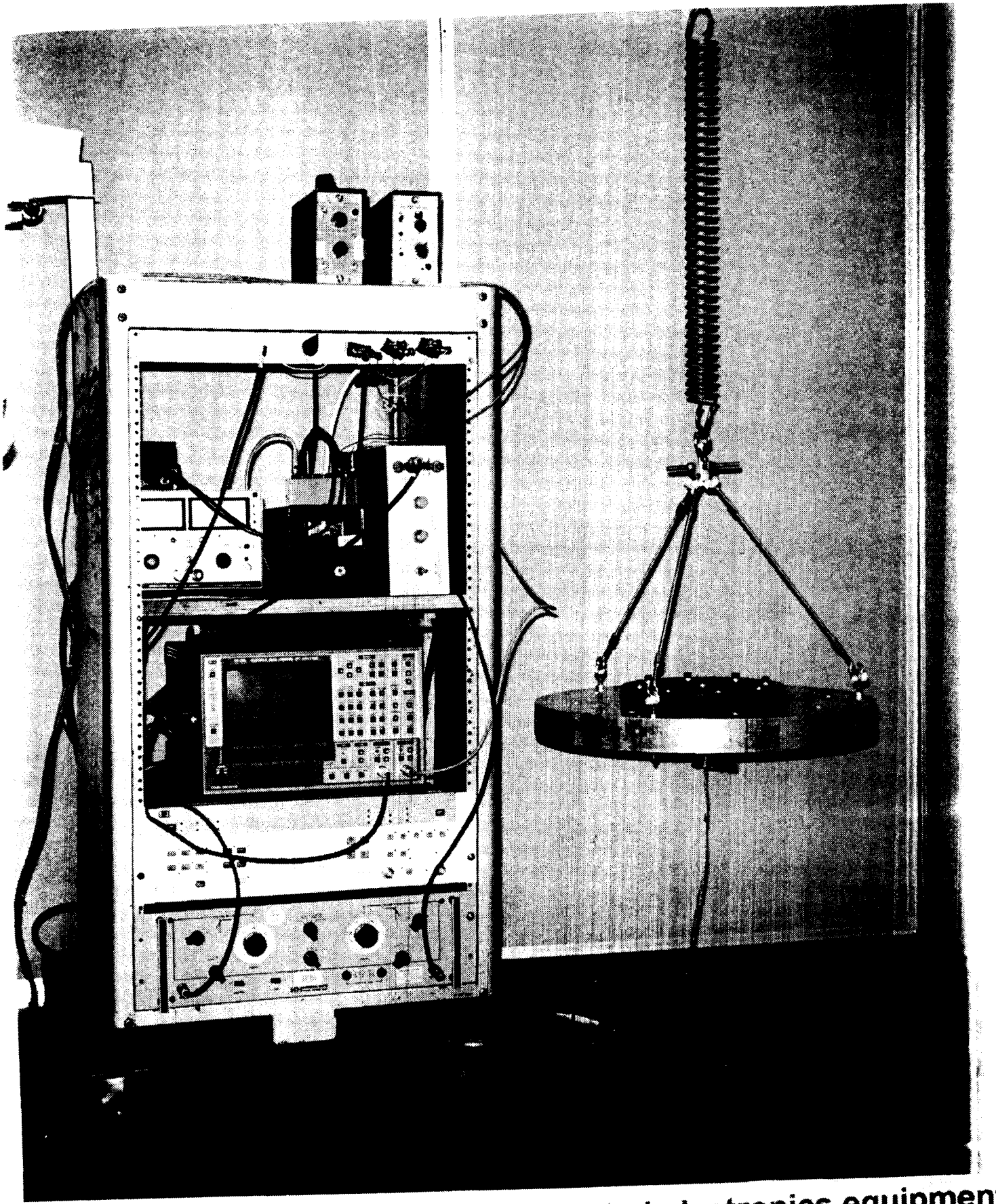

Figure 1. - Test apparatus and associated electronics equipment

Figure 2. - Installation of peristaltic pump aligned with X axis

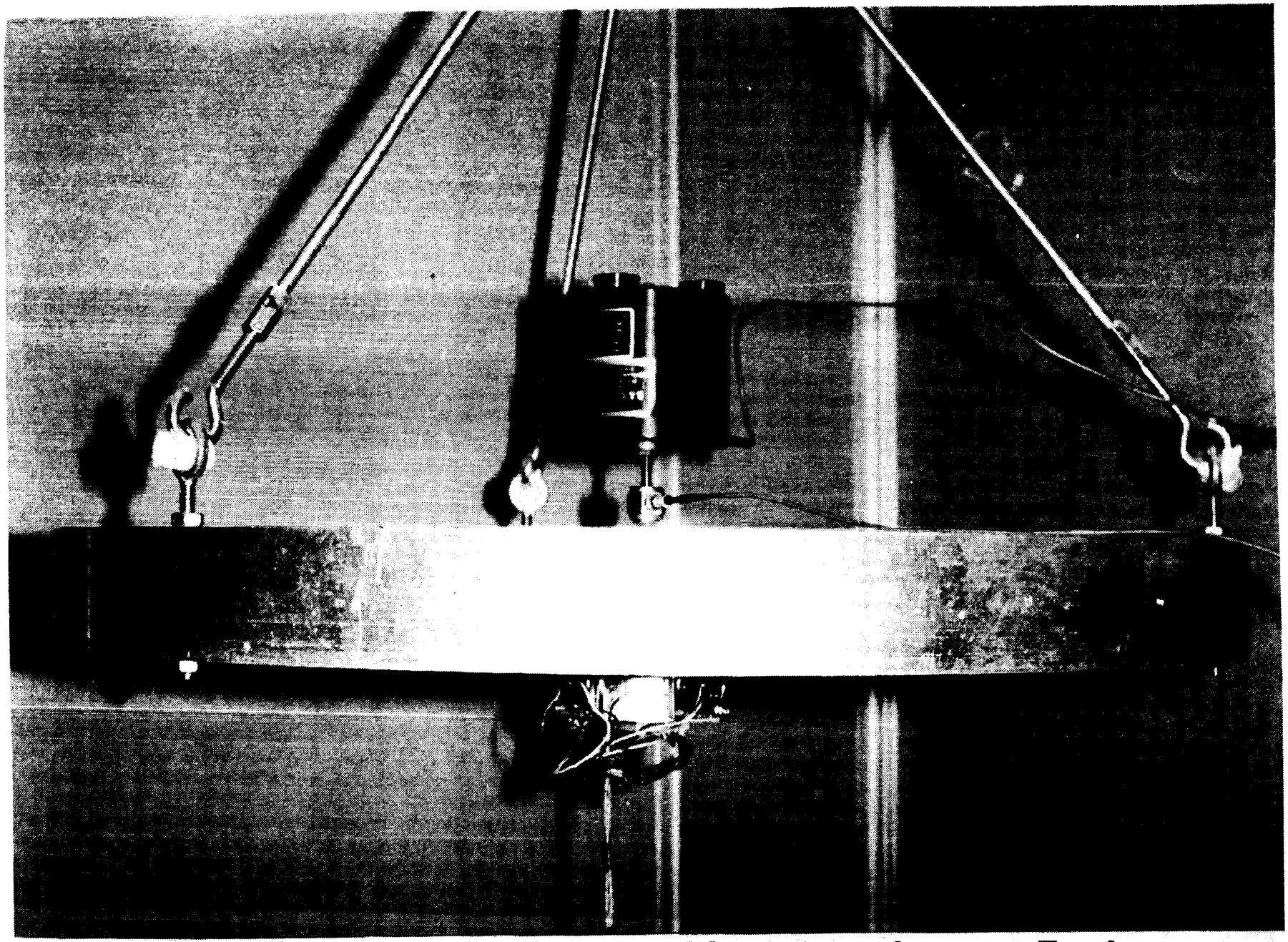

Figure 3. - Installation of shaker and force transducer on Z axis and triaxial accelerometer package

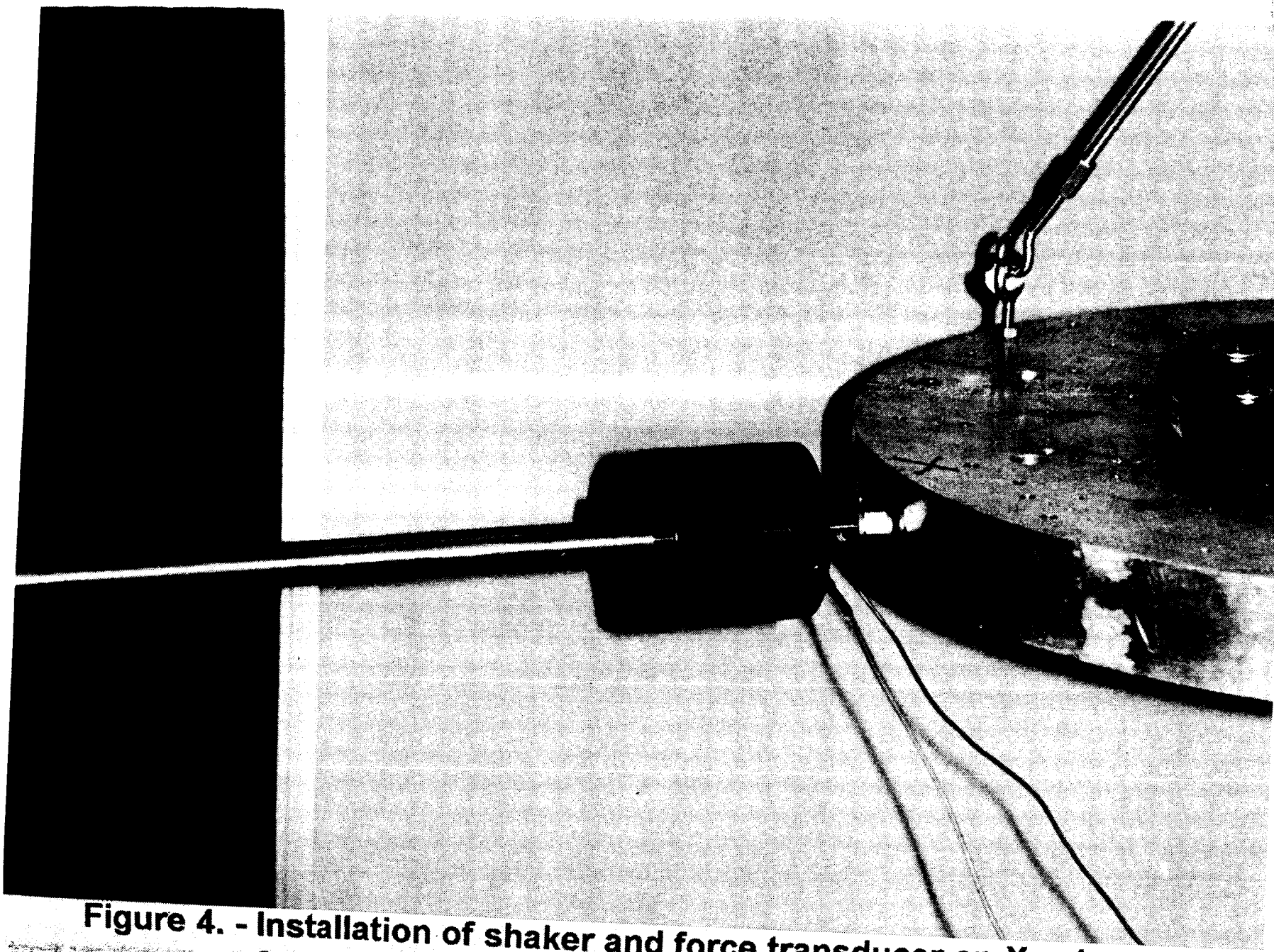

Figure 4. - Installation of shaker and force transducer on X axis for calibration with steel plate

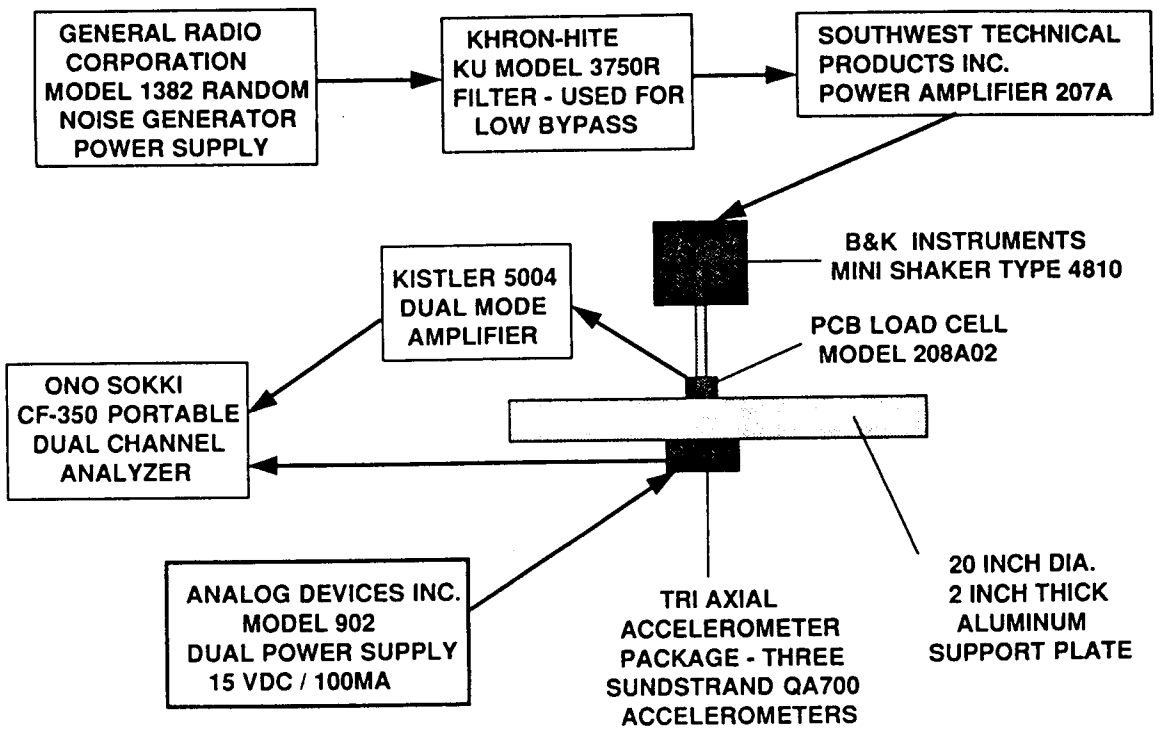

Figure 5 Schematic diagram of test rig calibration system.

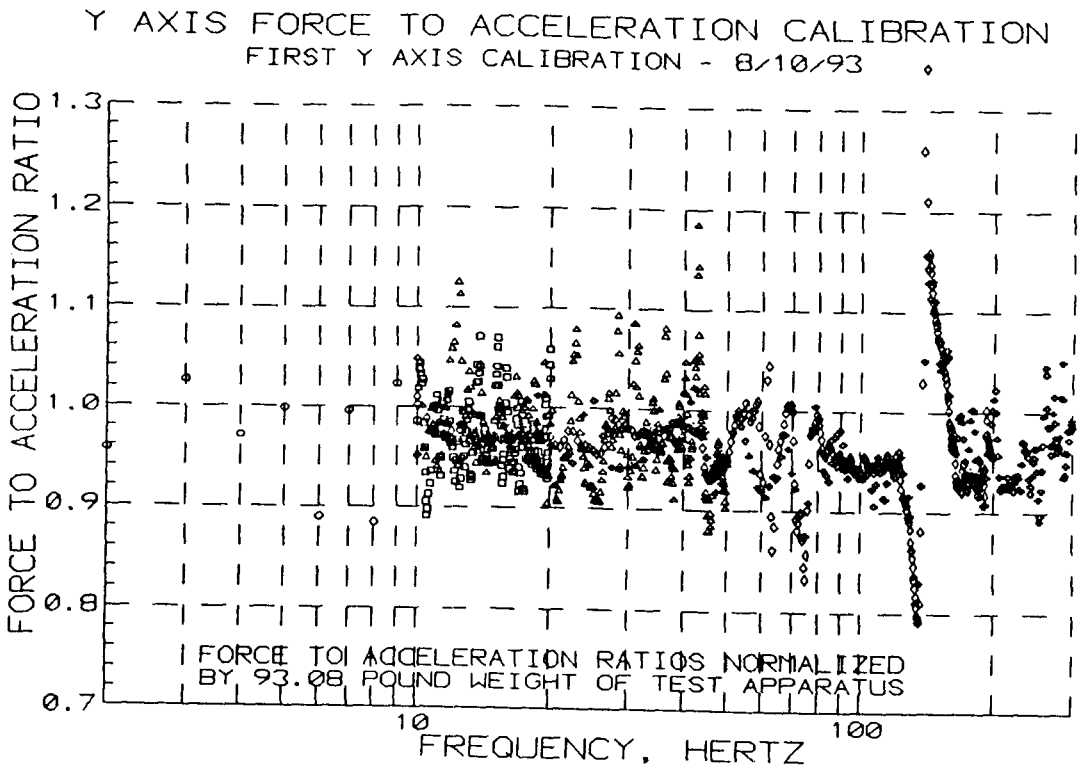

Figure 6 Preliminary results of measured force to acceleration levels with steel plate - first Y axis calibration.

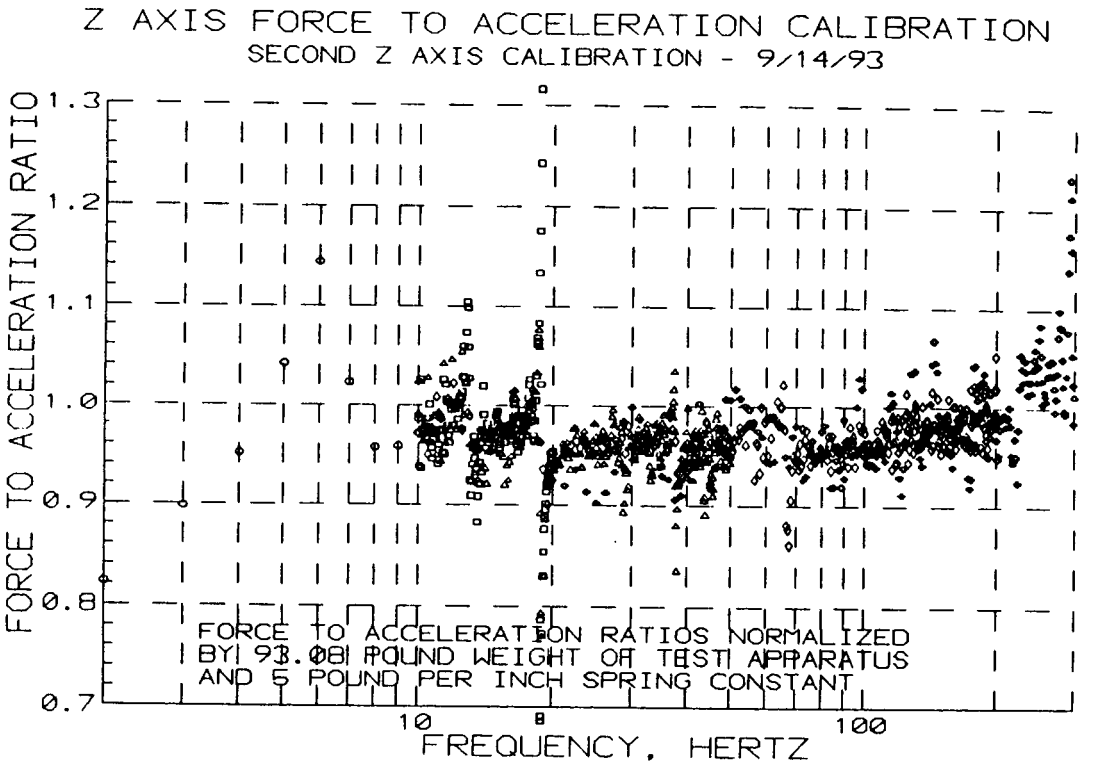

Figure 7 Preliminary results of measured force to acceleration levels with steel plate - second Z axis calibration.

KEYNOTE ADDRESS

(Banquet Speech at the Space and Rocket Center, Huntsville, Al, Sept. 23, 1993)

Dr. Bonnie Dunbar
NASA Johnson Space Flight Center, Houston, TX

First of all, I want to tell you what a distinct honor it is for me and a pleasure because most of us have had the opportunity to work together for over 2 years, some of us longer than that, to bring this mission to fruition and now to have the opportunity to share in some of the data, so this is a singularly pleasurable event for me and I do not know if I have all the words to express that. There are two themes that I would like to talk about this evening. One of them is vision and the other one is team work. You have to have vision to set the goals and decide on the direction in which you are traveling but it takes a team to really get there. Every individual in this room from the researchers to the controllers and the crew that I had the opportunity to fly with, and I see some of you out there, it takes a team to finally acquire that vision and there is a great deal of pleasure and rewards you find at the end of that journey in sharing that with the team. Jack Lee said some very important words tonight about how we fit into exploration. I got into spaceflight because I wanted to help explore the universe. As a young girl growing up on a farm in Washington State, I looked at the stars and I envisioned myself walking on the moon someday; that may not happen, but I certainly have enjoyed every minute of my participation in the journey there and participation in science because what you are doing is a part of that and without what you have done in the past, we simply could not have gone to the moon. I would like to bring this all together and show you some film from the flight and slides of the flight and kind of capsualize the experience for everyone, and for those of you who were not there with us onboard I hope to share that experience with you.

We are all inspired by the journey to the moon and the words that President Kennedy used to get us there and that is, "..not because it is easy but because it is hard." And for those of you involved in microgravity research, whether it be materials, fluids, combustion, or life sciences, you know that this is not the easiest route to research; your laboratory is 150 nautical miles up, you have to wait for the opportunity to persevere, and sometimes you will have to meet the skeptics, but what you have is a vision, just as a vision that brought us into this environment in the first place.

After we went to the moon, we used low-Earth orbit as a laboratory, and the first space station we launched was called Skylab, which some of you in this room helped put there. Skylab was a unique period of time for us. We had the opportunity to perform fluid physics experiments and directional

solidification experiments. We put crew members up for as long as 84 days and on those flights we acquired a wealth of physiological data. Some of the followon to that you saw in the EDOMP program presentations today. What we have acquired during Skylab is still considered the gold standard of physiological data for the world. The Russians still use our data. They have not replicated it but they use it as an operation base. It gave us a lot of experience and everyone who worked on it should be very proud of what Skylab was. I had the opportunity to participate in Skylab; I was a guidance and navigation officer at JSC. My job was to work with Marshall Space Flight Center as we glided it into the Indian ocean. I worked on that job for 9 months and obtained an emotional attachment to Skylab and as my data started disappearing from the screen I felt as if I was losing a friend. It certainly stayed intact longer than we thought it was going to. In fact, on its last orbit around the Earth I walked outside the mission control center at JSC and watched it flash over the dawning sky, went back in and followed the ground track, got a call in from a pilot on one of the Australian airlines who saw it streak by, and watched it disappear from our screen. I look forward to the day that we would have another space station in orbit and I think we are all working toward that day. Certainly we all hope to participate in it. But we have had another opportunity in spaceflight to share and research with a new platform and that was via the Space Shuttle and the Space Laboratory system and I want you to know that Spacelab, for those of you here at Marshall Space Flight Center who work on the program, has really been a work horse for us. I have flown with it twice now, first on the 7 day flight with the Germans and the opportunity on this flight (USML-1), and there was never a systems failure that interrupted the science. It just really performed flawlessly, and it was due in a large part to the support and personnel here at the Marshall Space Flight Center. It gave us an opportunity to extend our volume as a laboratory in a short-sleeved environment connected by a tunnel to the middeck and then to the flight deck. On USML-1, we planned a 13-day flight but actually we went to 14 because of the weather. When USML-2 flies in 1995 that will be the first 16-day flight. Right now if you stay with the given flight rate that we are hoping to have by the year 2000 we hope to extend to 25-30 days in the shuttle. We have to collect a number of physiological data points to work that extension.

On this mission we were divided into the red shift and the blue shift roughly half and half, four and three. The blue shift comprised of Ellen Baker (Mission Specialist II), EugeneTrinh (Payload Specialist II), and flight engineer Carl Meade. The red shift consisted of Ken Bowersox, the pilot, myself, Dick Richards, the commander, and Larry DeLucas, Payload Specialist I. Two other crew members that were always with us in spirit but not shown on the patch were Al Sacco and Joe Prahl. Once we activated the laboratory on the first day in orbit we put ourselves into appropriate attitude and looking out those back windows at the lab in the payload bay, we could see below us the coast of Florida a couple of weeks before Hurricane Andrew went through. We had some pretty spectacular views.

Here is a quick layout of the laboratory; this did not include, of course, the middeck experiments. We have the control center rack, the rack that had our four VCR's on it which recorded much of our video data; the Drop Physics Module complex where we saw some of the data generated today with the acoustical chamber; a rack called SMIDEX that allowed us to carry experiments that could be carried from middeck as well; the Solid Surface Combustion Experiments; and the Generic Bioprocessing Apparatus, as well as some of the EDOMP experiments. The other components are the Glovebox, which is just as valuable for supporting some of the experiments, the Crystal Growth Furnace in its complex; from Case Western and Lewis, the Surface Tension-Driven Convection Experiment; and next to that the rack used as a work bench with a table, supplies, and stowage. We had a number of center aisle stowage containers as well.

On the first day on orbit Larry and I started work loading the CGF. Then Larry started working back at the Glovebox. We were surprised to open up the CGF sample container and see an American flag there. We were very proud of the mission, but also proud since we were going to be up on the fourth of July. Larry worked many long hours at the Glovebox doing his protein crystal growth. He was very dedicated to that and I think the results show that. On the other shift, Carl also worked very hard at the Glovebox on many of the proteins as well. On the blue shift, Gene spent many hours at the drop physics module. You see lots of cables and wires and that is part of living in a zero-gravity environment. Without Velcro which were the white patches on the door and straps holding cables back, it is a little bit of a chaotic environment. We did hang up the flag for the fourth of July celebration. One of Carl's very favorite experiments was the Generic Bioprocessing Apparatus and here he is wearing the pressure as part of his physiological experiments. This is the candle burning experiment. I think this was exciting for all of us and both Carl and I had an opportunity to do that. This is probably one of the most popular slides I show when I go out and talk because it is a dramatic demonstration, for most people, on the difference between gravity and microgravity. Most people know what a birthday candle looks like. They think of how it ought to burn in low gravity and here is what it actually does. Larry and I spent many hours as subject and operator for the lower body negative pressure device. We both trained on operating the Echocardiograph the device that is used to image the heart, and we used Doppler to measure the blood flow velocities, it's all recorded on 8 mm tapes. It is an interesting type of work and I certainly enjoyed it and we got a lot of good data out of it. We looked at fluids we wanted to stabilize. We looked at fluid interfaces that we wanted to bifurcate. This particular experiment is the Drop Physics Module; I understand it had most of control mission hypnotized for the entire flight if you happened to watch any of those drops. When I talk to my friends at JSC that is the single thing they remember the most.

We saw some spectacular sights form orbit, we saw sunrises and sunsets, we looked at a lot of water, and many islands. We monitored some flooding in South America. I know this is a rather hazy

picture, but there is some significant river flooding and we were asked on real time to document that on orbit. We documented deserts and we looked at dust storms coming over the Atlantic off the coast of Africa. Any time you take over 4000 pictures on a flight it is a little difficult to find all the best ones to show. But certainly, this gives you a little flavor of the view we had from orbit.

This flight ended over a year ago from now. Here we look at the data and we are looking at the future of where we are going. We have been through some rather interesting months on the space station and I do not need to tell you that. What it means is we are going through a reorganization. We are going through a restructuring. But the intent is to continue on a space station track and to put a US space station up there and to provide a platform for you to continue research. Interjected in all of this is something that we have been working on for the last several months: an interim opportunity to work with the Russians on the MIR. We will be flying the first cosmonaut on the Space Shuttle on STS-60, Sergei Krikalev, and then we will be flying a second cosmonaut on STS-63, Vladimir Titov. We are going to be putting an astronaut on the MIR in early '95. We will be docking the Shuttle to the MIR-1 in mid-95. There is a plan for follow on flights. There are some opportunities to do some research in the biomedical and life sciences area, and then the microgravity area. Bob Rhome will enlighten the microgravity community and will be talking with some of you about what these potential opportunities are. The US and Russians are currently engaged in negotiations to end somewhere around November 1 to determine to what extent we will participate together in the International Space Station. Where we are going on that is not easy to say. We have a lot of unknowns at this point, but I think what is important is for everybody to remember the big picture; where the vision is. The research itself is important and we do not have exploration without research, regardless of what may be the prevailing concepts; life support systems require research. I have read articles about going to Mars and taking indigenous materials. Making materials is going to require research especially because Mars has one-third Earth gravity. We need to focus on the future and keep the path going. There are a lot of pictures in this museum and one of my favorites is of Robert Goddard because he was a rather unique individual. When I was getting ready for this mission, I know that a lot of people thought that maybe I was a little driven but I want you to know it was hard not to be. I would go to bed at night and dream about the mission. I know a lot of you did too. Only I would dream about day one or day five and how it ought to look. I saw a lot of problems in my dreams and I was never embarrassed about that because I figured Robert Goddard never was. You go out to the Goddard Space Flight Center and read the plaque out there and it says "Who is to say what is impossible, for it is the dreams of yesterday that are the hopes of today that are the realities of tomorrow." I had an opportunity to work this mission starting in 1988 and I want to thank everyone of you for helping my dreams come true.

INTERNATIONAL FLIGHT ACCELEROMETER DATA BASE

The International Flight Accelerometer Data Base is a collection of data on flight accelerometers and acceleration measurement systems captured in an Excel spreadsheet. The custom software can be used on IBM, IBM-compatible, and Macintosh personal computers. The data base currently contains data on the following accelerometers and acceleration measurement systems:

Accelerometer Name	Country
MASER Q-flex Accelerometers	Europe
General Active Micromotion Attenuator (GAMMA)	France
Micro Accelerometer	France
MICROMEDY	France
SPOT3 On-ground Microvibrations Test	France
D-1-MEDEA-ACC	Germany
Microgravity Measurement System (MMS) [EURECA]	Germany
Microgravity Measurement Assembly (MMA) for Spacelab D-2	Germany
Microgravity Measuring Assembly (MMA)	Germany
Quasi-Steady Acceleration Measurement (QSAM)	Germany
Triaxial Sensor Package of Japanese Sounding Rocket TT-500A	Japan
Microgravity Measurement Subsystem	The Netherlands
Solid State Micro-Accelerometer (SSMA)	The Netherlands
3-Dimensional Microgravity Accelerometer - COMET (3-DMA-C)	United States
3-Dimensional Microgravity Accelerometer - Complex Autonomous Payload (3-DMA-CAP)	United States
3-Dimensional Microgravity Accelerometer - SPACEHAB (3-DMA-SH)	United States
Accelerometer Package	United States
Aerodynamic Coefficient Identification Package (ACIP)	United States
Boeing Accelerometer Package	United States
Development Flight Instrumentation (DFI)	United States
GTE Triaxial Acceleration Measurement System (GTE-TAMS)	United States
High Resolution Accelerometer Package (HiRAP)	United States
Honeywell In-Space Accelerometer (HISA)	United States
Linear Triaxial Accelerometer (LTA)	United States

Accelerometer Name	Country
Low-Gravity Accelerometer System (LGAS)	United States
Micro "G" Acceleration Measurement System (M-GAMS)	United States
Miniature Electrostatic Accelerometer - Fluid Experiment System (MESA-FES)	United States
Office of Space and Terrestrial Applications Accelerometers (OSTA-1)	United States
Office of Space Sciences Accelerometers (OSS-1)	United States
Orbiter Acceleration Research Experiment (OARE)	United States
Orbiter Stability Experiment (OSE)	United States
Passive/Hand-Held Accelerometer	United States
Space Acceleration Measurement System - Unit A (SAMS-A)	United States
Space Acceleration Measurement System - Unit B (SAMS-B)	United States
Space Acceleration Measurement System - Unit C (SAMS-C)	United States
Space Acceleration Measurement System - Unit D (SAMS-D)	United States
Space Acceleration Measurement System - Unit E (SAMS-E)	United States
Space Acceleration Measurement System - Unit F/G (SAMS-F/G)	United States
Spacelab Module Low Level Accelerometer Package (SMLLAP) [VFI]	United States
Spacelab Pallet Low Level Accelerometer Package (SPLLAP) [VFI]	United States
Superfluid Helium Experiment Accelerometer (SHEA)	United States
Worcester Polytechnic Institute Accelerometer System (WPIAS)	United States

The information tracked for each accelerometer is listed and described in the field dictionary which is included as Appendix I.

I. GETTING STARTED

This data base was created using Microsoft Excel, Version 3.0. You can run the data base with either Excel, Version 3.0 for the Macintosh or Excel for Windows which runs on IBM and IBM-compatible computers. The spreadsheet is a file called ACCEL.DBS and the macro sheet is a filed called REPORTS.MCR. Both of these files should be placed in the same folder (or directory). To enter the data base, open the ACCEL.DBS file by either double clicking it or choosing open from the **File** menu. If the REPORTS.MCR file is in the same folder, the autoexec macro will open it automatically.

II. REPORT LAYOUTS

Report Layouts are views of the spreadsheet data. Different reports show different combinations of data base fields. You may change from one report layout to another by choosing **Change View** from the **Custom** menu. Change View brings up the Report Layout dialog box. The reports are listed on the dialog box:

Report 1 - which shows all of the fields in the data base
Report 2 - which shows the Instrument Name, Country, and Responsible Organization
Report 3 - which shows the Instrument Name, Country, and Contacts
Report 4 - which shows the Instrument Name, Contacts, and their Addresses
Report 5 - which shows the Instrument Name, Instrument Type, and Instrument Builder
Report 6 - which shows the Instrument Name, Country, and Flight History Information
Report 7 - which shows the Instrument Name and Abstract/Details

By changing the report layout, you can look at specific fields without having to scroll through other fields that are not of immediate interest. The report layouts essentially hide the data in the other data fields. When **Print** is selected from the **File** menu, only the columns in the current report layout are printed. You may search or sort on a field even if that field is not shown in the current layout report as described in the next section.

III. SEARCH

The **Search** command on the **Custom** menu allows you to find records in the data base that meet specified criteria. The search dialog box contains a scroll box for selecting the field to search and a text editing box for typing the criteria. If you type a text string as the criteria, the search looks for records where the selected search field begins with that text string. For example, if you choose "Instrument Name" as the search field and type "m" as the criteria, the search will find all accelerometers beginning with the letter "m"; case is ignored. In order to find an exact match, precede the text string with an equal sign "=". You may use the "?" wild card to designate one character in a text string and the "*" wild card to designate any number of characters. In order to search where a field contains a text string but does not necessarily begin with that text string, precede the string with "*". For example, if the search field is "Instrument Name", the criteria, "*micro", would find all accelerometers whose names contain the string "micro", including those beginning with the string "micro". When searching on numeric fields it is sometimes necessary to use comparisons in the criteria. To do this, begin the criteria with one of the following operators: *equal* "=", *greater than* ">", *less than* "<", *greater than or equal to* ">=", *less than or*

equal to "<=", or *not equal to* "<>". The last choice in the search field scroll box is "**Any Field**". This selection, when used with a contains criteria (i.e., "**text*"), finds all records that contain a specified text string anywhere in any of the fields.

The custom search only performs searches on one field. Selecting "Contact" as the search field searches in the "Principle Investigator" field as well as "Other Contact (1)" and "Other Contact (2)". Searching any of the flight history parameters (e.g., "Mission", "Mission Date", "Mission Comments") automatically searches all six missions. The custom search sets the criteria range, writes the criteria to the appropriate cells of the criteria range, extracts matching records to the extract range, and sets the extract range as the print area. To perform more complex searches with multiple criteria these steps must be performed manually. Refer to the Excel manual sections on "Criteria," "Data Find," and "Data Extract". The criteria range for this data base is the range A1:AQ2 (more rows are necessary for searches with OR-type criteria). The extract range is the range A89:AQ89.

After you perform a search, the matching records are shown in the extract range. To return to the data base range select **Show All Records** from the **Custom** menu.

IV. SORT

You can sort the records in the data base by choosing **Sort** from the **Custom** menu. You can sort on up to three fields. If you only wish to sort on one field, choose "**None**" as the second and third sort field. If you wish to sort on two fields, choose "**None**" as the third field. The sort will work whether you are viewing all records or have just done a search and are viewing the matching records only. If you perform a sort on the results of a search, only the extract range is sorted; when you select **Show All Records** from the **Custom** menu, the records are in the same order as the last time all records were viewed. If, however, all records are sorted, subsequent searches, which extract a subset of all records, will be in this sorted order.

V. ENTERING AND EDITING DATA

Data can be entered into any empty cells and the existing data can be edited. However, entering new records (i.e., accelerometers or acceleration measurement systems) into the data base is not possible without extensive modification of the macros that permit automation of the spreadsheet data base. The macros called from the **Custom** menu are found on the macro sheet, REPORTS.MCR. These macros address specific ranges of cells on the spread sheet. If additional rows or columns are added to the data base, the macros have to be edited to ensure correct display of all data.

VI. QUITTING OR EXITING THE DATA BASE

Upon quitting or exiting the data base you will be prompted to save changes to both the ACCEL.DBS and REPORTS.MCR files. You should save both of these files.

For Additional Information or Assistance Contact:

Charles R. Baugher
NASA/Marshall Space Flight Center
Space Science Laboratory
Microgravity Science & Applications Division
ES71, Marshall Space Flight Center, AL 35812
(205) 544-7417

(or)

Sarah Morgan
Essex Corporation
Microgravity Data Center
NASA/MSFC
(205) 544-5921

APPENDIX I: INTERNATIONAL FLIGHT ACCELEROMETER DATA BASE FIELD DICTIONARY

FIELD NAME	DATA TYPE	DEFINITION
Name of Instrument/Experiment	TEXT	Name of the accelerometer or accelerometer package.
Type of Instrument	TEXT	Description of accelerometer may include model number or method of measurement.
Country	TEXT	Accelerometer sponsor country.
Organization (1)	TEXT	Sponsoring organization.
Organization (2)	TEXT	If more than one sponsoring organization exists, the second organization is entered here.
Principle Investigator	TEXT	Principle investigator of the experiment.
Other Contact (1)	TEXT	Additional point of contact, may be a second Principle Investigator or Project Manager.
Other Contact (2)	TEXT	Additional point of contact.
PI Address	TEXT	Address of person listed in the Principle Investigator column.
Contact (1) Address	TEXT	Address of person listed in Other Contact (1) column.
Contact (2) Address	TEXT	Address of person listed in Other Contact (2) column.
Instrument Builder	TEXT	Name and address of the hardware builder.
Carrier	TEXT	Name of carrier(s).
Mission (1)	TEXT	Designation of first mission.
Mission Date (1)	DATE	Launch date of first mission.
Mission Comments (1)	TEXT	Comments on first mission.
Mission (2)	TEXT	Designation of second mission.

FIELD NAME	DATA TYPE	DEFINITION
Mission Date (2)	DATE	Launch date of second mission.
Mission Comments (2)	TEXT	Comments on second mission.
Mission (3)	TEXT	Designation of third mission.
Mission Date (3)	DATE	Launch date of third mission.
Mission Comments (3)	TEXT	Comments on third mission.
Mission (4)	TEXT	Designation of fourth mission.
Mission Date (4)	DATE	Launch date of fourth mission.
Mission Comments (4)	TEXT	Comments on fourth mission.
Mission (5)	TEXT	Designation of fifth mission.
Mission Date (5)	DATE	Launch date of fifth mission.
Mission Comments (5)	TEXT	Comments on fifth mission.
Mission (6)	TEXT	Designation of sixth mission and additional missions.
Mission Date (6)	DATE	Launch date of sixth mission and additional missions.
Mission Comments (6)	TEXT	Comments on most recent missions.
Location of Instrument/Experiment	TEXT	Flight location of the accelerometer.
Events Monitored	TEXT	Listing of what was measured.
Data Status	TEXT	Current status of the accelerometer data.
Data Amount	TEXT	Amount of bulk data that can be stored by the instrument.
Storage Media	TEXT	The media form on which the instrument stores bulk data.
Data Location	TEXT	The ground location where the data from this instrument now resides.
Data Availability	TEXT	Comment on availability of existing accelerometer data.

FIELD NAME	DATA TYPE	DEFINITION
Frequency	REAL	The frequency in Hz for which minimum and maximum acceleration levels are given in the next two columns.
Minimum Acceleration	REAL	The minimum acceleration measurable by the instrument at the given frequency.
Maximum Acceleration	REAL	The maximum acceleration measurable by the instrument at the given frequency.
Abstract/Details	TEXT	Details of the operation and performance of the instrument.
Bibliography	TEXT	Primary source of accelerometer information.

ATTENDANCE LIST

William Witherow
NASA MSFC
Huntsville, AL

Charles Walker
Arlington, VA

Ping Tcheng
NASA LaRC
Hampton, VA

Robert Snyder
NASA MSFC
Huntsville, AL

Richard Wisniewski
NASA AMES
Moffett Field, CA

Martin Volz
NASA MSFC
Huntsville, AL

Frank Szofran
NASA MSFC
Huntsville, Al

Damon Smith
Houston, TX

Jim Wise
JPL
Pasadena, CA

Marcus Vlasse
NASA MSFC
Huntsville, AL

Ching-Hua Su
USRA
Huntsville, AL

Leland Smith
McDonnell Douglas
Huntington Beach, CA

Marion Wise
Hampton, VA

Steve Vest
TBE
Madison, AL

Louise Strutzenberg
NASA MSFC
Huntsville, AL

Reginald Smith
Queens University
Kingston, Ontario

Ralph Will
NASA LaRC
Hampton, VA

Andrew Tygielski
TBE
Huntsville, AL

Don Strayer
JPL
Pasadena, CA

Byran Schrick
NASA MSFC
Huntsville, AL

Heribert Wiedemeier
RPI
Troy, NY

Bjarni Tryggvason
Canadian Astronaut
Program
Ottawa, Canada

Thomas Stoebe
University of
Washington
Seattle, Washington

Albert Sacco, Jr.
WPI
Worcester , MA

Michael Weinberg
University of Arizona
Tuscon, AZ

Eugene Trinh
JPL
Pasadena, CA

Dennis Stocker
NASA LeRC
Cleveland, OH

Alyson Rutledge
Mevatec Corp.
Huntsville, AL

Michael Wargo
NASA HQ
Washington DC

Larry Torre
Boeing
Huntsville, AL

Hendrik Stark
ESTEC
Noordwijk, The
Netherlands

J. W. Russell
Lockheed
Hampton, VA

Robert Waninger
DLR
Koln, Germany

Ted Tibbitts
Univ of Wisconsin
Madison, WI

Srini Srinivas
TBE
Huntsville, AL

Chris Rulison
Hattiesburg, MS

Taylor Wang
Vanderbilt Univ
Nashville, TN

Sarah Thornburg
Essex
Huntsville, AL

Charles Sprinkle
NASA MSFC
Huntsville, Al

Chuck Rudiger
Lockheed Missles &
Space Co
Sunnyvale, CA

Howard Ross
NASA LeRC
Cleveland, OH

John Pojman
Univ of Southern
Mississippi
Hattiesburgh, MS

Tony O'Neil
NASA MSFC
Huntsville, AL

James McGuire
NASA HQ
Washington D.C.

Melissa Rogers
CMMR - UAH
Huntsville, AL

Alexander Pline
NASA LeRC
Cleveland , OH

Vinit Nijhawan
Payload Systems Inc
Cambridge, MA

Charlien McGlothin
NASA MSFC
Huntsville, AL

Walt Roark
Mevatec Corp.
Huntsville, AL

Donald Pirich
Grumman
Bethpage, NY

Mark Nall
NASA HQ
Washington D.C.,

Rick McConnell
STC
Huntsville, AL

Robert Rhome
NASA HQ
Washington DC

Richard Peters
NASA MSFC
Huntsville, AL

Isao Nakatani
NASDA Tsukuba
Space Center
Tsukuba City, Japan

Philip McAlister

Washington DC

Nate Reynolds
Boeing Co.
Huntsville, AL

Ben Penn
NASA MSFC
Huntsville, AL

Mickie Nagy
Teledyne Brown
Engineering
Huntsville, AL

Todd Matthews

Athens, AL

Donald Reiss
NASA MSFC
Huntsville, AL

Jeff Patrick
NASA JSC
Houston, TX

Barry Musick
NASA MSFC
Huntsville, AL

David Mathiesen
GTE Laboratories
Waltham, MA

John Reimer
JPL
Pasadena , CA

Richard Ott
NASA HQ
Washington,
Washington DC

Robert Morrow
U Wisconsin
Madison, WI

Lon Mathias
Univ of Southern
Mississippi
Hattiesburg, MS

Dennis Readey
Colorado School of
Mines
Golden, CO

Simon Ostrach
Case Western Reserve
University
Cleveland, Ohio

Kim Eric Moore
Lockheed-ESC
Houston, TX

Gary Martin
NASA HQ
Washington, DC

N. Ramachandran
USRA/ NASA MSFC
Huntsville, AL

Sandra Olson
NASA LeRC
Cleveland, OH

Carl Meade
NASA JSC
Houston , TX

Philip Marston
Washington State Univ
Pullman, Washington

Joseph Prahl
Case Western Reserve
Univ
Cleveland , OH

Ed Okeefe
Boeing
Huntsville, AL

Patrick McNally
Canopus Systems
Ann Arbor, MI

Jennifer Majewski
CWRU
Cleveland, OH

Rhonda Mackey
Teledyne Brown
Engineering
Huntsville, AL

Roger Kroes
NASA MSFC
Huntsville, AL

Alan Johnston
NASA MSFC
Huntsville, Al

Lafett Hendrix
NASA MSFC
Huntsville, AL

Marvin Luttges
BioServe Technologies
Boulder, CO

Dave Knuteson
NASA LaRC
Hampton, VA

Catherine Johnson
NASA ARC
Moffett Field, CA

Fred Henderson
Teledyne Brown Eng
Huntsville, AL

Marvin Luttges
Bioserve
Boulder, CO

John Kline
Grumman Aerospace
& Electronics
Bethpage, NY

R. Jilg
DLR
Germany

Louis Hemmerdinger
Grumman Corp.
Bethpage, NY

Bill Lorson
TBE
Huntsville, AL

Jana Killebraw
TBE
Madison, AL

David Jex
NASA MSFC
Huntsville, Al

Steven Hegg
The Bionetics Corp.
Washington, DC

Robert Lochhead
Univ of Southern
Mississippi
Hattiesburg, MS

Akhtar Khan
Univ of Southern
Mississippi
Hattiesburg, MS

Tom Jacobson
NASA LeRC
Cleveland, OH

Frank Hartley
JPL
Pasadena, CA

Robert Little
NASA MSFC
Huntsville, AL

George Keiser
Stanford Univ.
Stanford, CA

Kaye Inman
NASA MSFC
Huntsville, Al

Hans Hamacher
DLR
Koeln, Germany

John Lipa
Stanford Univ
Stanford, CA

John Keating
DSP Development
Cambridge, MA

Ted Holtz
CTA Inc.
Hampton, VA

Tina Grubb
U of Southern
Mississippi
Hattiesburg, MS

Alex Lehoczky
NASA MSFC
Huntsville, AL

Akio Kanbayashi
NASDA
Tsukuba City, Japan

Anthony Hmelo
Vanderbilt Univ
Nashville, TN

Jean-Pierre Granier
CNES
31055 Toulouse
Cedex, France

Jack Lee
NASA MSFC
Huntsville, AL

Yasuhiro Kamotani
CWRU
Cleveland , OH

Robert Hill
TBE
Huntsville, Al

Sandra Graham
Bionetics Corp.
Washington DC,

Kevin Larman
Lockheed
Hampton , VA

James Kafalas

Wayland, MA

Roslin Hicks
NASA MSFC
Huntsville, AL

Martin Glicksman
RPI
Troy, NY

Ronald Giuntini
Huntsville, AL

Tom Finley
NASA Langley
Hampton, VA

Ken Demel
NASA JSC-SSPO
Houston, TX

William Daisak
Tracor Applied Sciences
Rockville, MD

Donald Gillies
NASA MSFC
Huntsville, AL

George Fichtl
NASA MSFC
Huntsville, Al

Lawrence DeLucas
UAB - CMC
Birmingham, AL

Peter Curreri
NASA MSFC
Huntsville, AL

Ingo Gerhard
ERNO
Raumfahrtechnik
Bremen, Germany

Carlos Fernandez-Pello
U California
Berkeley, CA

Richard Delombard
NASA LeRC
Cleveland, OH

Vince Cuda
CTA Inc.
Hampton, VA

Paul Galloway
Teledyne Brown Eng
Huntsville, AL

Jean-Jacques Favier
CNES
Grenoble, France

Anthony DeLoach
NASA MSFC
Huntsville, AL

Roger Crouch
NASA HQ
Washington, DC

Joseph Galate
Missouri City, TX

Barbara Facemire
NASA MSFC
Huntsville, AL

Steve DelBasso
Grumman/SSEIC
Reston, VA

Arvid Croonquist
JPL
Pasadena, CA

Archie Fripp
NASA LaRC
Hampton, VA

Barry Epstein
NASA Headquarters
Washington,
Washington DC

William Debnam
NASA LaRC
Hampton, VA

Pat Cooney
NASA MSFC
Huntsville, Al

Don Frazier
NASA MSFC
Huntsville, AL

Don Edberg
McDonnell Douglas
Huntington Beach, CA

James Dean
NASA JSC
Houston, TX

Mike Cooke
NASA JSC
Houston, TX

James Fox
Canopus Systems
Ann Arbor, MI

Bonnie Dunbar
NASA JSC
Houston, TX

James Dean
Barrios Tech
Houston, TX

Paul Concus
U California
Berkeley, CA

Jim Fountain
NASA MSFC
Huntsville, AL

Alice Dorries
NASA MSFC
Huntsville, Al

Stephan Davis
NASA MSFC
Huntsville, AL

Sharon Cobb
NASA MSFC
Huntsville, Al

Brian Finley
Sverdrup Tech
Cleveland, OH

Terry Dewandre
ESTEC/ESA
Noordwijk, The
Netherlands

Charles Darby
NASA MSFC
Huntsville, AL

Leonard Cipriano
CSAT
Fairfax, VA

Louis Chestney
NASA LeRC
Brunswick, OH

Michael Braun
Dornier
Germany

Robert Apfel
Yale Univ
New Haven , CT

Iwan Alexander
CMMR
Huntsville, AL

Roger Chassay
NASA MSFC
Huntsville , AL

Sheila Boettcher
Krug Life Sciences
Houston , TX

Basil Antar
UTSI
Tullahoma, TN

John Charles
NASA JSC
Houston, TX

Udo Bluemel
DLR
Koeln, Germany

V. Anilkumar
Vanderbilt Univ
Nashville , TN

Li Chang
NASA Ames Research Center
Moffett Field, CA

Robert Blanchard
NASA LaRC
Hampton , VA

Barry Andrews
UAB
Birmingham , AL

Holly Carr
Sverdurp Technology
Huntsville, AL

Jan Bijvoet
UAH
Huntsville, AL

Rosaile Andrews
UAB
Birmingham , AL

Cynthia Caldwell
Essex Corp.
Huntsville, Al

Thomas Berg

Huntsville, AL

Phil Anderson
TBE
Huntsville, AL

Robert Burdine
NASA MSFC
Huntsville, AL

Victoria Beckner
Bionetics Corp.
Wasington,
Washington DC

Tim Anderson
Univ. of Florida
Gainesville, Florida

Robert Buchholz
Lockheed Engineering & Sciences Co.
Houston, TX

Charles Baugher
NASA MSFC
Huntsville, AL

Robert Altenkirch
Mississippi State Univ.
Drawer, MS

Barbara Brown
JPL
Pasadena , CA

Ann Bathew
NASA MSFC
Huntsville , AL

Cheryl Allen
NASA LaRC
Hampton, VA

Joseph Brezovic
Clarkson University
Postdam, New York

Kumar Basu
U Southern Mississippi
Hattiesburg, MS

Helga Alexander
NASA MSFC
Huntsville, AL

REPORT DOCUMENTATION PAGE

Form Approved
OMB No. 0704-0188

1. AGENCY USE ONLY (Leave blank)	2. REPORT DATE	3. REPORT TYPE AND DATES COVERED
	May 1994	Conference Publication

4. TITLE AND SUBTITLE

Joint Launch + One Year Science Review of USML-1 and USMP-1 with the Microgravity Measurement Group

5. FUNDING NUMBERS

6. AUTHOR(S)

N. Ramachandran*, D.O. Frazier, S.L. Lehoczky and C.R. Baugher, Editors

7. PERFORMING ORGANIZATION NAME(S) AND ADDRESS(ES)

George C. Marshall Space Flight Center
Marshall Space Flight Center, Alabama 35812

8. PERFORMING ORGANIZATION REPORT NUMBER

M-750

9. SPONSORING/MONITORING AGENCY NAME(S) AND ADDRESS(ES)

National Aeronautics and Space Administration
Washington, DC 20546

10. SPONSORING/MONITORING AGENCY REPORT NUMBER

NASA CP - 3272
Volume II

11. SUPPLEMENTARY NOTES

*Universities Space Research Association, Huntsville, Alabama

Proceedings of papers presented at a 3-day meeting held in Huntsville, Alabama, September 22-24, 1993, and implemented by Universities Space Research Association under contract to NASA MSFC.

12a. DISTRIBUTION/AVAILABILITY STATEMENT

Unclassified --- Unlimited

Subject Category: 88

12b. DISTRIBUTION CODE

13. ABSTRACT *(Maximum 200 words)*

On September 22-24, 1993, investigators from the First United States Microgravity Laboratory (USML-1) and the First United States Microgravity Payload (USMP-1) Missions met with the Microgravity Measurement Group (MGMG) in Huntsville, Alabama, to discuss science results and the microgravity environments from the respective missions. USML-1 was launched June 1992, and USMP-1 was launched October 1992. This document summarizes from the various investigations, the comprehensive results and highlights, and also serves as a combined mission report for the two missions. USML-1 was the first totally U.S.-sponsored mission dedicated to microgravity research and included 31 investigations in fluid dynamics, crystal growth, combustion, biotechnology, and technology demonstrations supported by 11 facilities. The papers in these proceedings attest to the wealth of information gleaned from the highly successful mission. On the USMP-1 mission, both the MEPHISTO and the Lambda Point experiments exceeded by over 100% their planned science objectives. The mission also marked the first time that acceleration data were down-linked and analyzed in real-time. The meeting, which concentrated on flight results, brought low-gravity investigators, accelerometer designers, and acceleration data analysis experts together. This format facilitated a tremendous amount of information exchange between these varied groups. Several of the experimenters showed results, some for the very first time, of the effects of residual accelerations on their experiment. The proceedings which are published in two volumes also contain transcriptions of the discussion periods following talks and also submittals from a simultaneous poster session.

14. SUBJECT TERMS	15. NUMBER OF PAGES
Microgravity, Materials Processing, Bioprocessing, Fluid Physics, Human Physiology, Crystal Growth of Proteins and Semiconductors, G-Jitter, Acceleration Measurements, USML-1, USMP-1	432
	16. PRICE CODE: A19

17. SECURITY CLASSIFICATION OF REPORT	18. SECURITY CLASSIFICATION OF THIS PAGE	19. SECURITY CLASSIFICATION OF ABSTRACT	20. LIMITATION OF ABSTRACT
Unclassified	Unclassified	Unclassified	Unlimited